Synthesis and Electrochemical Operation of Crown/Ammonium Rotaxanes

Inaugural-Dissertation

to obtain the academic degree

Doctor rerum naturalium (Dr. rer. nat.)

submitted to the Department of Biology, Chemistry, Pharmacy

of Freie Universität Berlin

by

Marius Gaedke, M.Sc.

from Berlin

2021

The present research was carried out under the supervision of Prof. Dr. Christoph A. Schalley from November 2016 until October 2021. I certify that the work presented in this report is my own original work based on the research I performed by using the means and source materials as noted therein.

Marius Gaedke Berlin, 05.10.2021

First reviewer: Prof. Dr. Christoph A. Schalley

Second reviewer: Prof. Dr. Siegfried Eigler

Date of defense: 19.11.2021

“When a system of “meaningless” symbols has patterns in it that accurately track, or mirror, various phenomena in the world, then that tracking or mirroring imbues the symbols with some degree of meaning – indeed, such tracking or mirroring is no less and no more than what meaning is. Depending on how complex and subtle and reliable the tracking is, different degrees of meaningfulness arise.”

-Douglas R. Hofstadter, Gödel Escher, Bach: An Eternal Golden Braid

Acknowledgements

First of all, I would like to thank Prof. Dr. Christoph A. Schalley for giving me the chance to perform my doctoral thesis in his lab. I thank him for his mentorship involving honest opinions and constant support. He gave me a lot of freedom and resources for choosing my topics and finishing projects, while trying out original ideas along the way.

Furthermore, I want to express my thankfulness to Prof. Dr. Siegfried Eigler for taking the time to be the second reviewer.

I feel very thankful for our "TTF subgroup", Henrik Hupatz and Dr. Hendrik V. Schröder, who shaped my way of thinking about scientific problems and provided valuable help in the lab and for the writing in addition to proofreading this thesis. You two also introduced me to supramolecular electrochemistry and shared my joy and struggle with the potentiostat and the data.

I would also like to thank collaboration partners in and outside of Germany, namely Dr. Tuğrul Kaynak, Dr. Felix Witte, Dr. Jana Anhäuser, Dr. Arto Valkonen, Simon Suhr, Dr. Jan M. Wollschläger, Dr. Julia Beerhues, Prof. Dr. Beate Paulus, Prof. Dr. Kari Rissanen, Prof. Dr. Biprajit Sarkar, Prof. Dr. Sebastian Riedel and Prof. Dr. Arne Lützen,

I would like to thank my students Kurt F. Hoffmann, Jennifer Anders, Clara Douglas and Lukas Fischer for their help and their perspectives that helped me grow as a supervisor and person. I would like Pin-Wei Lee for proofreading this thesis. I am thankful to the group for the kind atmosphere and also the nice non-work related activities. I wish you all the best and hope that you are successful with your projects.

Same goes for Marta Da Pian, who is a very kind and open person and a great friend. Sebastian Müller, I want to thank you for the help with syntheses and the sympathetic ear every day.

As always I am very thankful for the services and spectra I get from the kind people of the service and analysis department, especially Dr. Andreas Springer, Fabian Klautzsch and Xuan Pham from mass spectrometry.

I would also like to thank the DAAD for the funding of my two research stays in Finland and additional financial support by the GdCh and the SFB 765 for conferences and material.

Last but not least I want to thank my family, which supports me in my studies and life in general, without which I would not be able to be where I am. Finally, my lovely wife Maria, you motivate and help me every day, even when you are struggling with your own projects. For that and for the joy and love you give me, I feel blessed every day.

Abstract

Functional molecules such as proteins and enzymes are the basis for a plethora of complex biochemical functions and thus a central aim for research in biology, chemistry and physics. Nature uses these molecular switches, motors and pumps to convert energy into work or information. Following their natural models, artificial molecular machines (AMMs) are comparably small functional molecules or assemblies with the goal to convert energy into harnessable work. In fact, many of the recent examples for switches, motors and pumps are mechanically interlocked molecules (MIMs) such as rotaxanes and catenanes. Taming these sophisticated molecules promises compelling applications in catalysts and stimuli-responsive materials.

Nethertheless, to achieve the complexity and functionality of natural nanomachines three main challenges need to be resolved: Introducing directionality to steer and utilize movement; gaining control over the kinetics of movement and controlling the assembly of complex molecules.

This work focuses on the synthesis and characterization of electrochemically switchable (pseudo)rotaxanes and the analysis with regard to their use as molecular switches and functional molecules. These challenges were adressed in three projects using crown/ammonium rotaxanes. The MIMs are equipped with either a reversibly oxidizable tetrathiafulvalene (TTF), a naphthalene diimide (NDI) or both.

In the first project, a new directional reversibly redox-switchable crown ether bound on a directional axle gave a new chiroptical switch, which is able reverse the electronic circular dichroism (ECD) spectrum upon oxidation. This observation could be rationalized to the change of electronic structure using quantumchemical calculations.

In the second project, kinetic control over co-conformational changes of the macrocycle upon deprotonation or oxidation was investigated. Thereby, considerable differences between pseudorotaxanes and rotaxanes were determined. While deprotonation led to instantaneous dethreading or shuttling, only in case of the pseudorotaxanes oxidation of the macrocycle led to expulsion of the binding site.

Finally, the third project was concerned with investigation of new redox-switchable crown ethers with different cavity sizes. Afterwards, a procedure to synthesize different self-

sorted hetero[3]rotaxanes was established. Notably, only the redox properties of NDI-moieties were found to be sequence-specific.

In conclusion, the results of this thesis broaden the versatility of chiral and non-chiral redox-switchable rotaxanes and describe a blueprint for the controlled synthesis of functional sequence-specific molecules. The three mentioned challenges directionality, controlled kinetics and assembly were addressed successfully.

Kurzzusammenfassung

Proteine und Enzyme sind natürliche molekulare Maschinen und die Basis einer Vielzahl von komplexen biochemischen Funktionen. Als molekulare Schalter, Motoren und Pumpen wandeln sie Energie in Arbeit oder Information um. Um ihre Eigenschaften zu imitieren und für neue Prozesse zugänglich zu machen, stehen sie im Fokus biologischer, chemischer und physikalischer Forschungsbereiche.

Entsprechend ihrer natürlichen Vorbilder haben künstliche molekulare Maschinen das Ziel, Energie in nutzbare Arbeit umzuwandeln. Besonders vielversprechende Kandidaten für die Erreichung dieses Ziels sind mechanisch verzahnte Moleküle wie Rotaxane und Catenane. Aktuelle Beispiele in der Literatur zeigen bereits ihre vielversprechende Verwendbarkeit als Schalter, Motoren und Pumpen. Diese anspruchsvollen Moleküle zu perfektionieren, wird zu ungeahnten Anwendungen unter anderem in der Katalyse und in stimuli-responsiven Materialien führen.

Um die Komplexität und Funktionalität der natürlichen Nanomaschinen zu erreichen, müssen noch mindestens drei Herausforderungen gemeistert werden: Die Einbindung von Direktionalität, um gerichtete Bewegung zu nutzen, die Erlangung der Kontrolle über die Kinetik der Bewegung und die kontrollierte Assemblierung der komplexen Moleküle.

Die vorliegende Promotionsarbeit befasst sich mit der Herstellung und Charakterisierung von elektrochemisch schaltbaren (Pseudo)rotaxanen und ihrer Verwendbarkeit als molekulare Schalter und Maschinen. Mittels Krone-Ammonium-Rotaxanen wurden die genannten Herausforderungen in drei Projekten angegangen und Lösungsansätze präsentiert. Dafür wurden mechanisch verzahnten Moleküle entweder mit einem reversibel oxidierbarem Tetrathiafulvalen (TTF), einem reversibel reduzierbarem Naphthalendiimid (NDI) oder mit beiden Bausteinen funktionalisiert.

Im ersten Projekt konnte ein neuer chiroptischer Schalter durch die Auffädelung eines neuen direktionalen und reversibel oxidierbaren Kronenethers auf einer direktionalen Achse realisiert werden. Er ist in der Lage das Vorzeichen des elektronischen Zirkulardichroismus (ECD) durch Oxidation umzukehren. Mittels quantenchemischer Berechnungen konnte diese Beobachtung im ECD-Spektrum Änderungen der elektronischen Struktur im Molekül zugeschrieben werden.

Im zweiten Projekt wurde der Einfluss der Kinetik auf co-konformationelle Änderungen des Makrozyklus durch Deprotonierung oder Oxidation untersucht. Es konnten dabei erhebliche Unterschiede zwischen Rotaxanen und Pseudorotaxanen festgestellt werden. Während Deprotonierung in allen untersuchten Beispielen zum sofortigen Abfädeln beziehungsweise Pendeln führte, wurde der Makrozyklus durch Oxidation nur im Fall des Pseudorotaxans von der Bindungsstelle abgestoßen.

Schließlich wurden im dritten Projekt neue redox-schaltbare Kronenether mit unterschiedlichen Ringgrößen untersucht. Anschließend wurde eine Vorschrift zur Herstellung verschiedener selbst-sortierter Hetero[3]rotaxane formuliert. Dabei ergab sich eine Änderung der Redoxeigenschaften der NDI-Bausteine in Abhängigkeit von der Sequenz der beiden Reife auf der Achse des Rotaxans.

Die Ergebnisse dieser Arbeit tragen zum allgemeinen Verständnis der Synthese und Verwendbarkeit von chiralen und nicht-chiralen Rotaxanen bei und liefern zusätzlich Ansätze zur kontrollierten Herstellung von redoxschaltbaren, sequenzspezifischen Molekülen. Dabei wurden die genannten Herausforderungen – Direktionalität, kontrollierte Kinetik und Assemblierung – erfolgreich angegangen.

Table of Contents

1 Introduction and Motivation

Mechatronic devices and integrated circuitry enable our modern world. They deliver mobility, healthcare, nutrition, communication, entertainment and overall productivity. The swift rise of electronics into our daily lives is linked to more affordable devices, which consume less power, while offering more computing power and features. Miniaturization of circuitry is one of the key aspects that drives the progress in electronics. The drastic development in feature sizes of processors in the last fifty years is displayed in Figure 1. In the last 30 years, the feature size of a processor shrank from approximately 600 nm to only 5 nm.

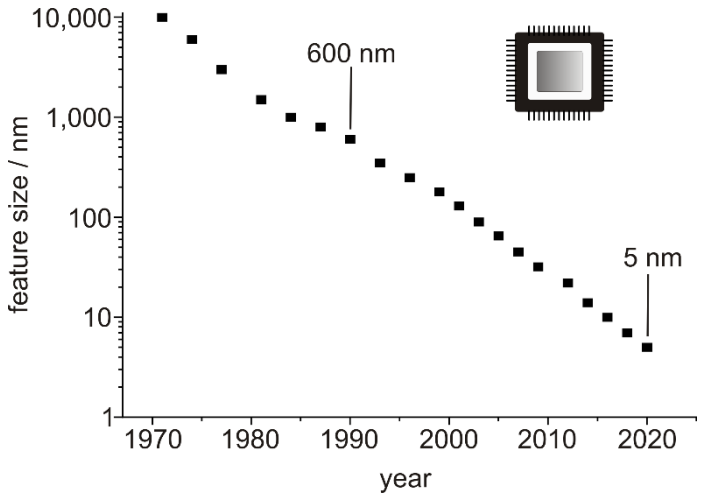

Figure 1: Shrinking feature sizes of processors.[1-2]

Although material science and manufacturing technology still progress expeditiously, the lower limits of sheer top-down miniaturization will inevitably be reached.[3] A possible solution could be the bottom-up approach. Instead of shrinking complex arrangements on silicon wafers, bottom-up approaches strife away from bulk material towards nanoscale molecular computing systems.[4] The goal is to envision nanometer sized molecular assemblies with the ability to perform tasks, such as Boolean operations or even allow directed and controlled motion on the molecular scale. Whereas artificial molecular machines (AMMs) or motors are molecules or molecular assemblies whose controlled movement can be used to perform work, molecular switches are merely limited to changing between defined states fueled by external stimuli, such as light, chemical/electric energy or mechanical force.[5]

Illustrative examples for molecular switches or machines with macroscale role models are shown in Figure 2, such as robotic arms that transport or manipulate cargo (Figure 2a). Modern car factories rely on their tireless welding and assembling of payload in the decimeter

to meter range. On the molecular scale a hydrazone switch picks up and releases a 3-mercaptopropanehydrazide cargo (shown in red in Figure 2b) thus transporting it from one side to the other. Furthermore, electric motors (Figure 2c) convert electrical energy into mechanical energy to propel toy vehicles as well as giant ships. The unidirectional motion of overcrowded alkenes (Figure 2d) paved the way for plenty examples where liquid crystals[6] and gels[7] changed their shape fueled by light.

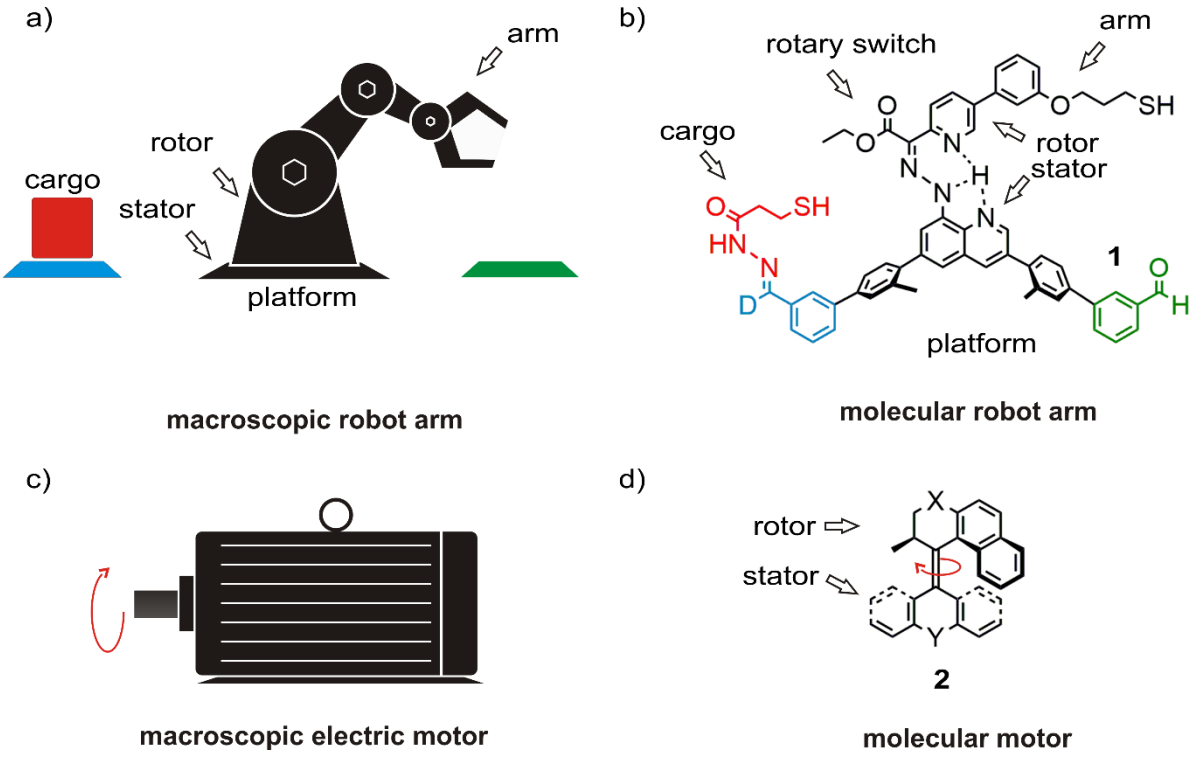

Figure 2: a) Scheme of a macroscopic robot arm capable of transporting a cargo. b) Molecular robot arm that can move a cargo molecule from one side to the other.[8] c) Scheme of a macroscopic electromotor. d) Feringa's 2nd generation molecular motor.[9]

Besides these two recent examples, plenty of research groups in the broad field of supramolecular chemistry are working to understand and mimic natural microscopic and technical macroscopic motors and machines. A blueprint to build in the nanometer scale is provided by the ingenious functions of the machinery of life.[10-11] How to attain this level of molecular function and control is an ongoing subject in the research community. Pioneering steps towards this direction were acknowledged, when the Nobel Prize in Chemistry 2016 was awarded jointly to Jean-Pierre Sauvage, Sir J. Fraser Stoddart and Bernard L. Feringa "for the design and synthesis of molecular machines".[12-14] There, a central research aim is the synthesis and characterization of mechanically interlocked molecules (MIMs). Despite the ongoing research on artificial molecular machines, we have merely scratched the surface of possible applications.

Owing to their physical circumstances, the properties of matter on a macroscopic scale such as friction, gravity, inertia, shear forces and adhesion are negligible in the sub-micrometer scale. Thermal motion dictates movement of particles in solution. For example, the molecular robot arm **1** in Figure 2b is a marvellous example for controlled molecular motion yet moving a cargo from left to right is meaningless, when there is no frame of reference and left and right are constantly changing due to thermal motion. Understanding and controlling all parameters is crucial for the operation of molecular switches and machines. Therefore, the following milestones can be phrased:[15-16]

- Directionality of motion to ensure that individual components do not work against each other, for example by using chiral or sequence-specific molecules or assemblies. Directionality can also be created by immobilization in ordered arrays for example on a surface instead of the solution phase in which the assemblies randomly diffuse. Additionally, the directional components need to be addressable by a stimulus with a high conversion efficiency.
- Control over the kinetic parameters of the motion is needed, because movement that is too fast or too slow is hardly useful. Cycle stability allows the continuous usage of a process without the need of constantly exchanging parts or removal of chemical waste.
- Synthetic accessibility by using a toolbox approach, where components are easily interchangeable. This way adjusting a part of the machine does not require to start over the whole synthesis.

These are only some of the milestones that need to be overcome in an interdisciplinary endeavor. Within the scope of our expertise, the main focus of this thesis is set on the synthesis and employment of a recently developed stimuli-responsive construction motif[17] as a seamless continuation of the works on mechanically interlocked molecules, unraveling emergent properties of stimuli-responsive rotaxanes. Thereby, three key projects of this thesis can be summarized (Figure 3):

I. Introduction of directionality into a tetrathiafulvalene-decorated crown ether macrocycle to establish a chiral environment upon rotaxane formation. A chiroptical switch resulted. (Figure 3 top left)
II. By incorporation of a steric ‘speed bump’ on the axle of a redox-switchable crown/ammonium (pseudo)rotaxane the diverging kinetic implication over the translational motion for the redox and acid-base switching was investigated. (Figure 3 top right)

III. By introducing a second binding site on the axle with a suitable spacer, a series of rotaxanes with differing macrocycle sequences could be synthesized and characterized. (Figure 3 bottom)

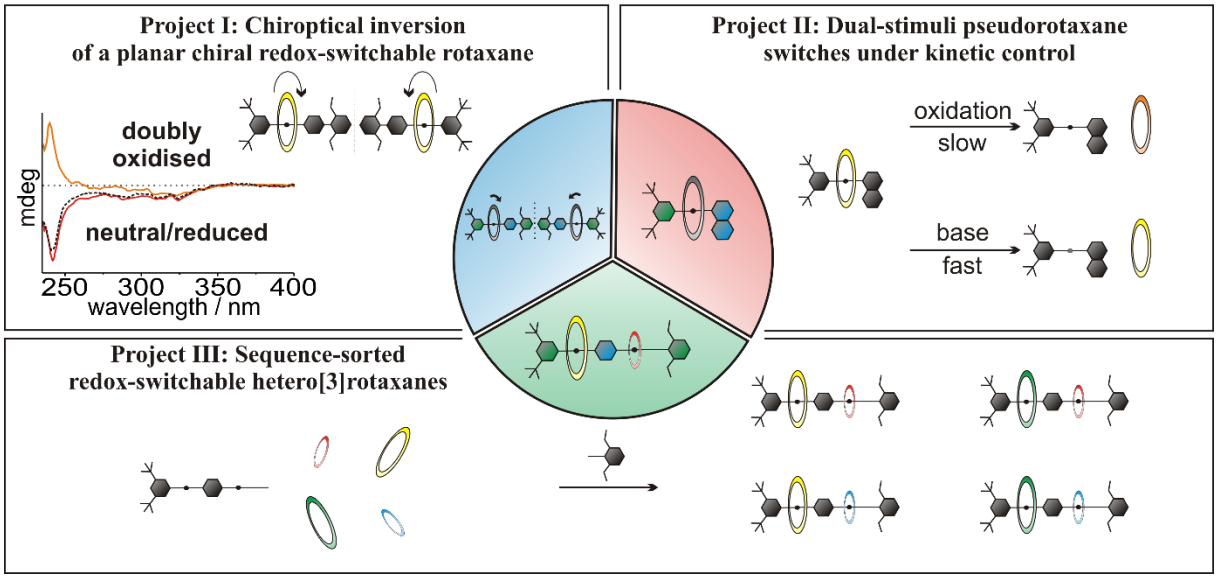

Figure 3: Overview of the three main projects of this thesis. Chiroptical inversion of a planar chiral redox-switchable rotaxane[18] (top left), Dual-stimuli pseudorotaxane switches under kinetic control[19] (top right) and Sequence-sorted redox-switchable hetero[3]rotaxanes[20] (bottom). Reproduced with permission from the Royal Society of Chemistry.

2 Theoretical Background

2.1 Concepts of Supramolecular Chemistry

2.1.1 Non-Covalent Interactions

Non-covalent interactions are of multidisciplinary relevance, as they are encountered in biology, chemistry and physics. Their dynamic and reversible nature unfolds when studying the examples that rely on them. Animals, such as geckos use dry adhesion[21] to climb the steepest surfaces or even upside down. Hierarchical surface structures, such as branching hairs (setae) on their feet maximize the interaction with their path. Due to the reversible nature of the interaction, the gecko can stick and unstick rapidly to run away.[22] When focusing on individual molecules or molecular arrays, protein folding[23] and DNA-(un)zipping[24-25] are very prominent examples, which are even at the core of life itself.[26-27] It is noteworthy to say, that there are also covalent examples for reversible or dynamic bonds.[28]

Apart from naturally occurring examples, supramolecular chemistry as the "chemistry beyond the molecule"[29] uses non-covalent interactions as a tool kit. For the common covalent bonds in organic chemistry namely C-C and C-H, single bond dissociation energies are in the range of 300–550 kJ/mol.[30] When comparing the energy ranges of non-covalent and covalent interactions, the non-covalent ones can be found at considerably lower energy. Various types of non-covalent interactions are depicted in Figure 4. Starting on the bottom end of the energy scale are van der Waals' forces and dispersion interactions between unpolar molecules such as alkanes. Slightly stronger interactions include (cat)ion-π (5–80 kJ/mol), which can be found in the interaction of enzymes with substrates,[31] and π-π interactions (1–50 kJ/mol), which facilitate the sandwich or slipped-parallel stack of benzene and hexafluorobenzene.[32] Stronger non-covalent bonds are ion-dipole interactions (50–200 kJ/mol), which are formed during the solvation of salts in highly polar media. Also, dipole-dipole interactions are electrostatic interactions between molecules with a permanent dipole, for example acetone. Hydrogen bonds are a directional interaction of a lone pair of an electronegative atom and a hydrogen atom bound to oxygen, sulfur, nitrogen or fluorine. For instance, dimers of organic acids are formed by hydrogen bonds. Halogen bonds are related to hydrogen bonds, as it is also the interaction of a Lewis acid and Lewis base. However, halogen bonds are much more directional and are always very close to 180°. Finally, the strongest non-covalent interactions are ion-ion and coordinative bonds (e.g. metal with ligand) with bond dissociation energies of around 100–

350 kJ/mol each.[30, 33] A hydrophobic – or more generally solvophobic – effect can be observed, when nonpolar substances aggregate in aqueous solution. It maximizes the interaction among the solvent molecules and minimizes the contact area of the nonpolar substances and drives for example the folding of globular proteins and the formation of membranes in cells.[34]

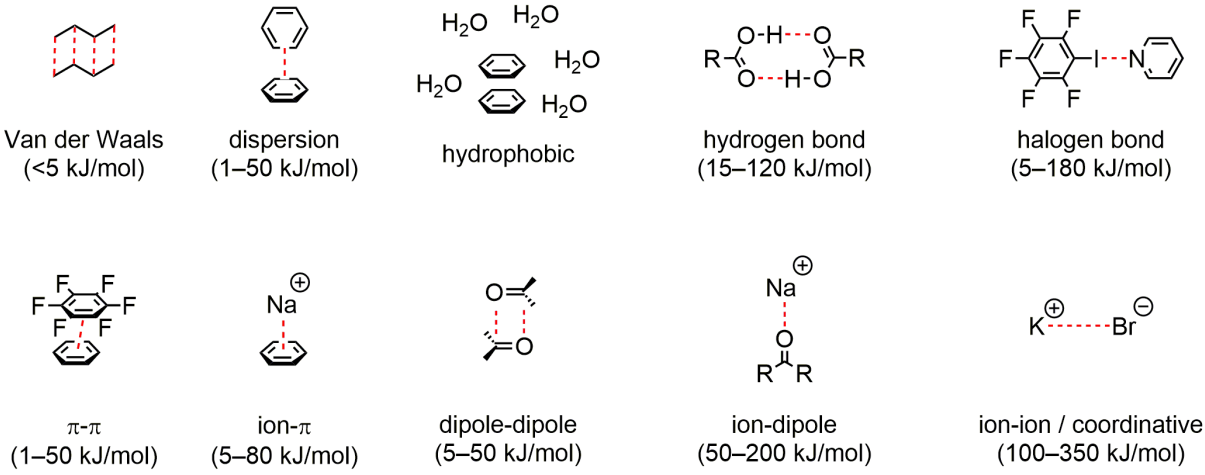

Figure 4: Non-covalent intermolecular interactions with examples roughly ordered by their bond dissociation energies.[30, 35]

Apart from the listed interactions, a central concept of supramolecular chemistry is the mechanical bond. This bond is made up by forming a steric or electrostatic barrier for the dissociation of two or more interlocked species.[36] As such, it is not a chemical bond in the classical sense, but rather a physical bond. The conditions under which the assembly can dissociate define the strength of the bond.[36] The mechanical bond is a main topic of this thesis and is discussed more thoroughly in chapter 2.2.

2.1.2 Host-Guest Chemistry

A major field of supramolecular chemistry is concerned with studying host-guest complexes, where a host – mainly in macrocyclic, bowl, or cage-like shape – binds a suitable guest by reversible and non-covalent interactions. In other words, the two (or more) components eventually find each other through Brownian motion of the molecules in solution and spontaneously form a self-assembled complex, without the input of external energy. A thermodynamic minimum is reached, with varying equilibrium constants depending on the combination of host and guest. The thermodynamic equilibrium between a host (H) and a guest (G) forming an associated complex (G@H) (Equation 1) for a classical 1:1 complex can be described by the association constant K_a (Equation 2). *Via* the Van't Hoff equation, also a

relation to Gibbs free energy (ΔG^0), with R the ideal gas constant and T the temperature can be formulated (Equation 3).

$$H + G \rightleftarrows G@H \qquad (1) \qquad K_a = \frac{[G@H]}{[H] \cdot [G]} \qquad (2) \qquad \Delta G^0 = -RT \cdot \ln(K_a) \qquad (3)$$

This concept of host guest chemistry is used since Donald J. Cram and his wife Jane M. Cram showed the selective binding of chiral amino acids to chiral crown ethers.[37] Their work is based on the papers by Pedersen starting in 1967, describing the synthesis of crown compounds that complex alkali metal, ammonium and alkylammonium salts.[38-39] Concerning the general design of hosts, the following key aspects need to be considered:[40]

- Preorganization lowers the entropic penalty upon binding;
- Size complementarity to the guest provides a good fit;
- Compatible electronic interaction sites between host and desired guest.

Host-guest complexes in thermodynamic equilibrium are mainly products of a self-assembling process, meaning a reversible and spontaneous association of building blocks that form organized aggregates.[33, 41] An important aspect is error correction through reversibility. While the formation of a simple 1:1 complex usually does not involve several sequential steps, larger and more complex assemblies containing multiple binding sites rely on the disassembly of mismatched building blocks in order to reach a thermodynamic equilibrium, which would otherwise end in a trap along the way. An aspect that will become more relevant in chapter 2.1.4.

In Figure 5 some examples for macrocyclic hosts and their corresponding guests are displayed. Along with the progress of supramolecular and macrocyclic chemistry more and more examples appear. The examples are starting with crown ethers in different sizes which bind cationic guests and hydrogen bond donors, such as metal ions and ammonium salts. Crown ether complexes are more thoroughly discussed in the next chapter (2.1.3). Secondly, prominent examples are cyclophanes, such as the π-electron deficient cyclobis(paraquat-*p*-phenylene), which is also called *Stoddart's Blue Box* after the 2016 Chemistry Nobel laureate Sir J. Fraser Stoddart. First synthesized in 1988,[42] it forms donor-acceptor complexes by binding electron rich aromatic guests, such as 1,4-dioxybenzene[43] moieties, as well as tetrathiafulvalene.[44] As radical cation it can also bind other radical cations through radical pairing, for example a viologen radical cation. Thirdly, cucurbiturils (CB*n*) comprised of 5 to 10 glycoluril units[45] can bind cations with the carbonyl portals (ion-dipole interaction) and encapsulate neutral

moieties through hydrophobic interactions. Water inside the hydrophobic cavity, also referred to high-energy water, is released into bulk solution upon binding of a guest.[46] Their name is derived from the botanical name of pumpkins (cucurbitaceae) due to their pumpkin-like shape.[47] Finally, the naturally occuring cyclodextrines (α,β,γ-CD) are cyclic oligosaccharides, which bind apolar organic guests through hydrophobic interaction in their bucket-shaped cavity.[48]

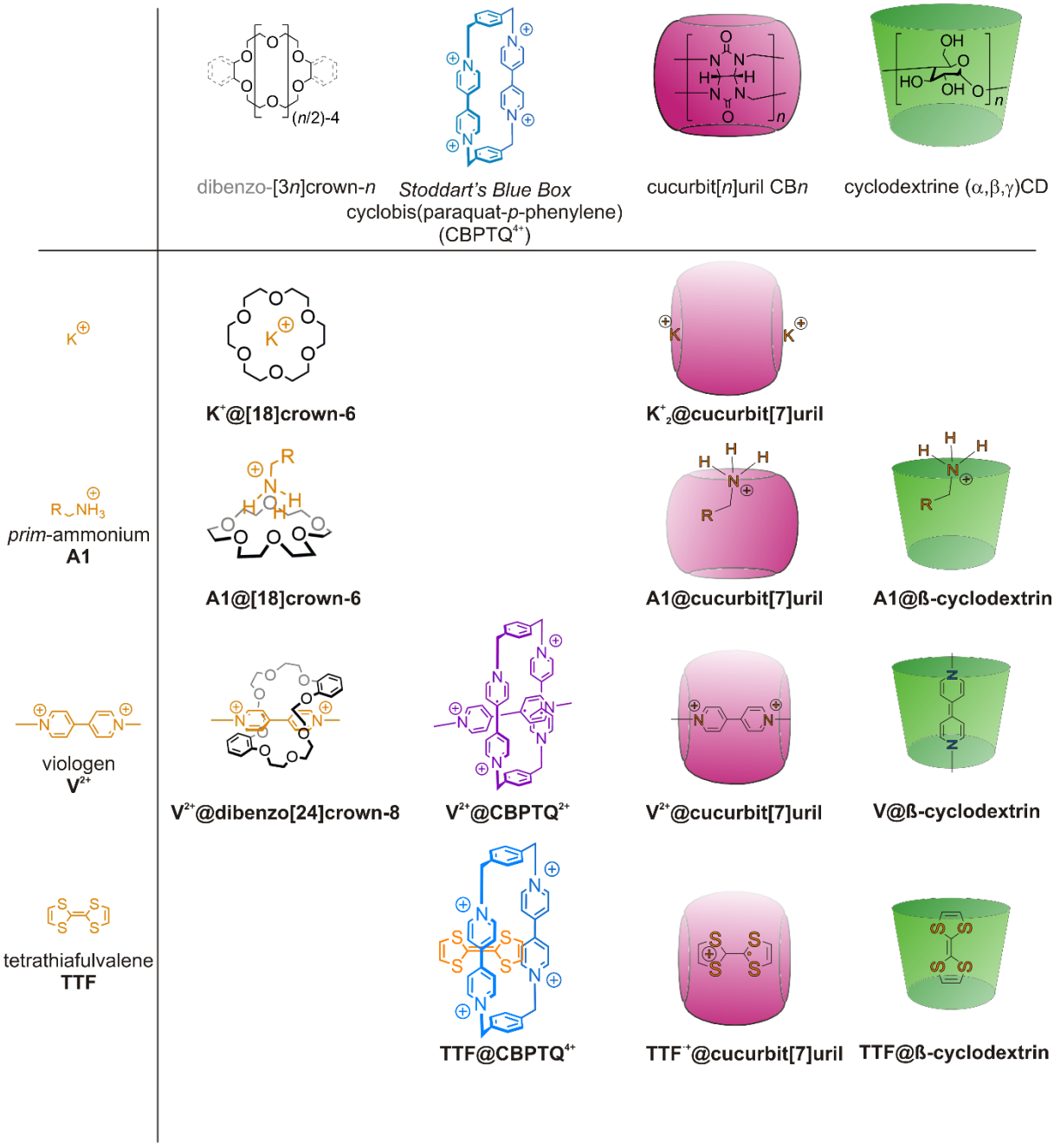

Figure 5: A selection of macrocyclic host molecules and favorable guests (counterions omitted for clarity).[49-54]

2.1.3 Crown/Ammonium Complexes

The discovery of crown ether compounds by C. J. Pedersen in the 1960s,[55] and the observation that they are able to bind and solubilize inorganic salts such as $KMnO_4$, NaCl, $AgNO_3$ in organic solvents[56] sparked the interest of researchers to investigate synthetic host molecules until today. Crown ethers are macrocyclic oligomers of ethylene oxide (nomenclature: [3*n*]crown-*n*, with *n* oxygens or other chalcogens in a 3*n* membered ring). Although crown ethers are used for decades, only a few structures are commercially available and the amount of functionalization protocols for aliphatic and aromatic crown ethers are rather limited.[57-58]

Apart from metal salts, a major focus is set on the complexation of ammonium guests starting from the ammonium cation (NH_4^+), which is similar in size to a potassium cation (1.38 Å),[59] to quaternary ammonium ions such as pyridinium ions. In Figure 6 examples for guests bound to differently sized crown ethers and their corresponding non-covalent interactions are shown. Depending on the size of the macrocycle/wheel cavity different binding modes are feasible. For small crown ethers such as [16]crown-6, the ammonium ion does not sit in the ring plane, but rather above forming a side-on complex involving three N^+-H···O interactions.[60] Threaded crown/ammonium complexes can be observed with ring sizes $n \geq 7$. Thereby, with increasing ring size bulkier ammonium residues can be overcome. For example, [21]crown-7 can thread over alkyl chains at room temperature, but not over phenyl rings. This can be accomplished by the slightly larger [24]crown-8. The reason why secondary and quaternary ammonium ions thread into the cavity of the crown are the additional C-H···O hydrogen bonds, which are beneficial to the free enthalpy of the complex formation in comparison to a mere side-on or face-to-face complex. The benzylic methylene protons on the ammonium add to the two to four stronger N^+-H···O bonds and ion-dipole interactions. Figure 7 includes a crystal structure of dibenzylammonium bound to **di**-**b**enzo[24]-**c**rown-**8** (**DBC8**).[61] There, the benzylic protons interact with the oxygens of the crown ether opposite to the N-H protons, which is not possible in non-threaded complexes. Many crown ether hosts are also decorated with benzyl or naphthyl groups to enable π-π interactions with the desired guest. For example, [38]crown-10 (Figure 6 bottom) binds the electron deficient and neutral naphthalene diimide (NDI) in a π-π stacking donor-acceptor complex between the two naphthalene moieties of the macrocycle/wheel.[62]

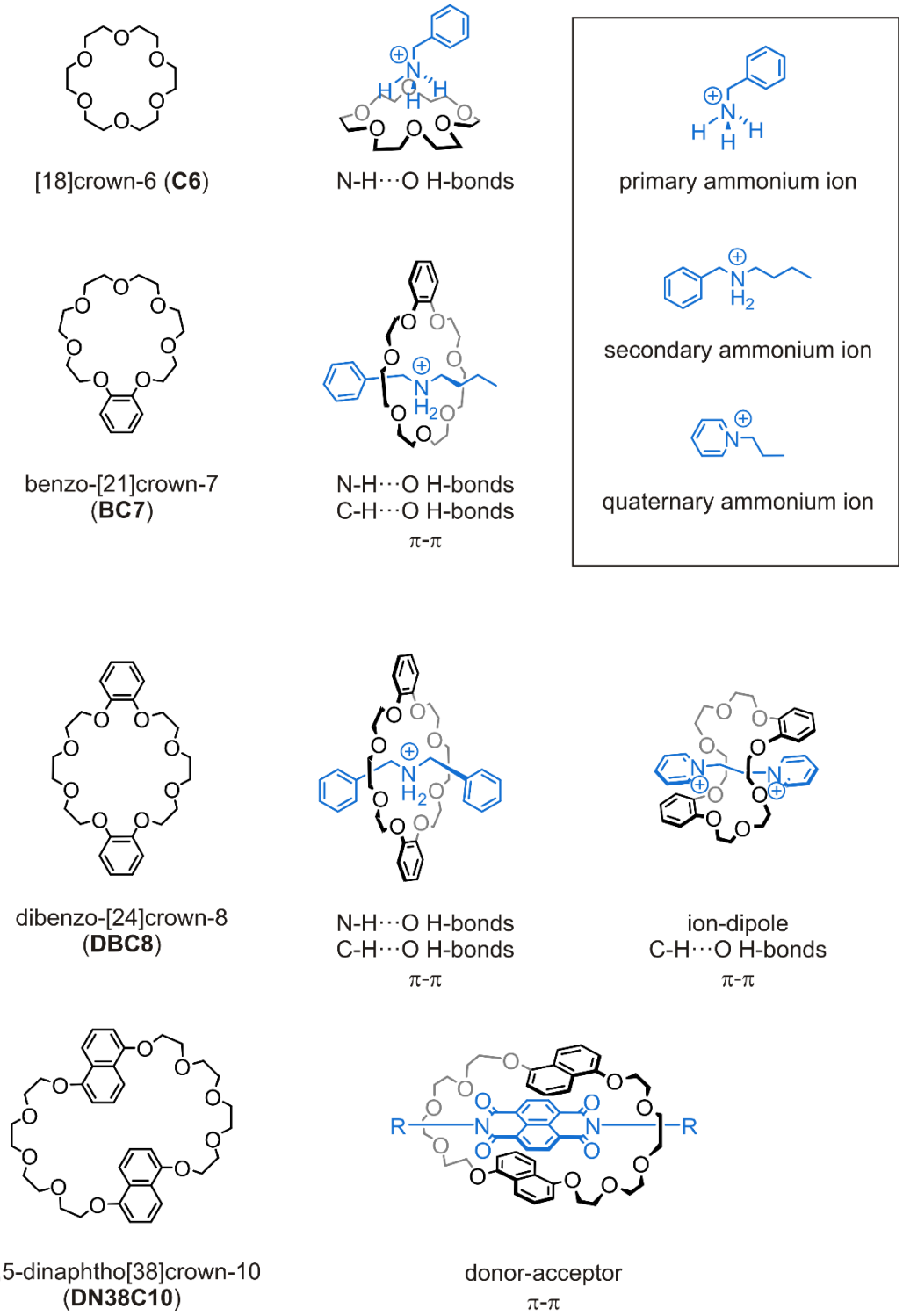

Figure 6: Most commonly used crown ethers for host-guest chemistry and corresponding guests with individual attractive interactions (counterions omitted for clarity).[63]

The association constants (K_a) of crown/ammonium complexes are typically in the range of 10^2 to 10^6 M^{-1}.[58, 63-65] Apart from the size and shape of the macrocycle, the counterion of the guest and the solvent are the key influencing factors. In increasingly polar solvents the association constants drop, as the solvent molecules more effectively compete with the host to stabilize the ammonium of the guest.[61] The trend Me_2SO < Me_2CO < MeCN < $MeNO_2$ < CH_2Cl_2/$CHCl_3$

with respect to K_a values compares well with the Gutmann donor numbers[66] of solvents. The highest association constants can be measured in halogenated solvents such as CH_2Cl_2 and $CHCl_3$, but with limited solubility, binary solvent systems with MeCN are often used. Solubility and association constants can be tuned by the right choice of anion for the ammonium guest. As shown by Gibson and co-workers,[64-65] the K_a of the macrocycle and ammonium guest complex is also influenced by the equilibrium of the ammonium axle with the corresponding anion. Figure 7 shows a selection of the most common counterions with increasing K_a values for the dibenzylammonium dibenzo-[24]crown-8 complex **DBA@DBC8**, where PF_6^- is the most commonly used, due to the low costs, noticeable solubility and considerably high association constants. With the rising interest of synthetic chemists in weakly coordinating anions (WCAs)[67] more examples of ammonium guests with WCAs are reported. They shine with high solubility and exceptional association constants for crown/ammonium complexes, when the constitution of the macrocycle is detrimental to high binding constants.[58, 68] In fact, all of the (pseudo)rotaxanes in this thesis are based on the exceptional K_a of dibenzylammonium tetrakis(3,5-bis(trifluoromethyl)phenyl)borate ($BArF_{24}^-$) with crown-8 macrocycles and the good solubility of the resulting complexes.

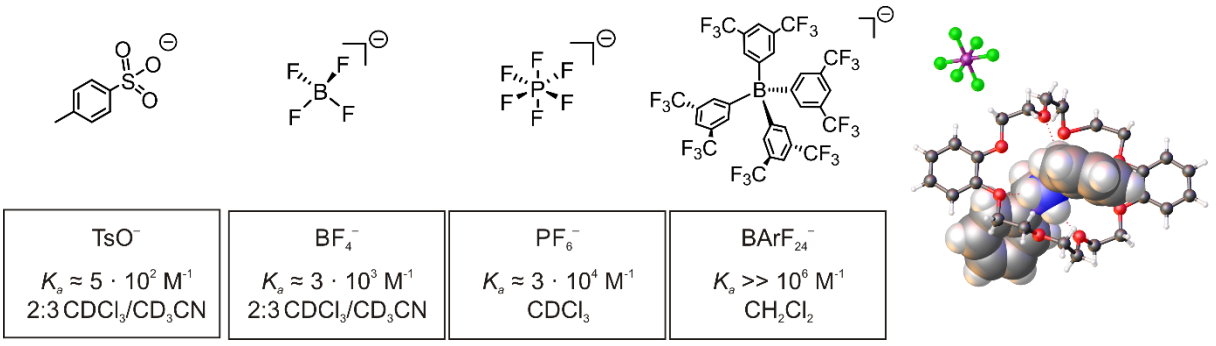

Figure 7: Typical anions used for crown/ammonium complexes in supramolecular chemistry and the superstructure of the 1:1 complex of dibenzylammonium hexafluorophosphate and dibenzo-[24]crown-8.[58, 61, 63]

2.1.4 Self-Assembly, Self-Organization and Self-Sorting

Although self-assembly and self-organization are often used synonymously, an important distinction has to be made, especially in the context of supramolecular chemistry. Both describe processes to form ordered structures from a disordered system. Self-assembly is a spontaneous process leading to a thermodynamic minimum (release of energy), which is in equilibrium with the individual components and other structures, for example the formation of a host-guest complex. It can be observed on nanometer to centimeter scales.[69] On the other hand, self-organization requires a concentration gradient or the constant input of energy (a dissipative

system) and leads to a local energetic minimum, or in other words, a non-equilibrium state. As such, all living things can be considered to be a self-organized system, since they also deteriorate when no more energy is provided to us.[70] An illustration of the energetic implication is provided in Figure 8.

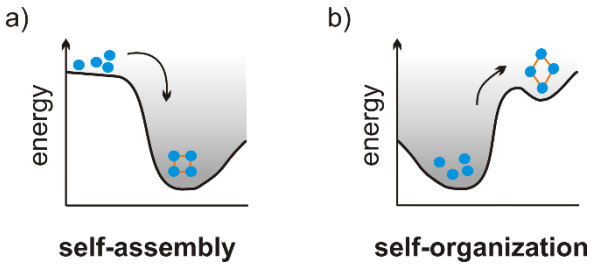

Figure 8: Simplified potential energy landscapes of two different organization principles, a) self-assembly and b) self-organization. While self-assembly occurs spontaneously under release of energy, self-organization requires energy to create patterns and structural order away from the thermodynamic minimum. It is noteworthy to mention that as long as energy is provided no minimum on the potential energy surface is required, because it is a flow equilibrium and no chemical equilibrium.

When we expand the concept of self-assembly to different participating agents, more possibilities arise. Are all compounds included in a self-assembled structure or are individual compounds left out? How many different structures are formed? The concept of self-sorting covers these considerations. The general term self-sorting refers to a high-fidelity recognition between molecules within complex mixtures. Only one or few structures are formed in contrast to a library, as suggested by Isaacs and co-workers.[71-72] The concept can be subdivided into assembly processes with high affinity towards other components (social self-sorting) or high affinity towards the same compound (narcissistic self-sorting) as shown in Figure 9.[73-74]

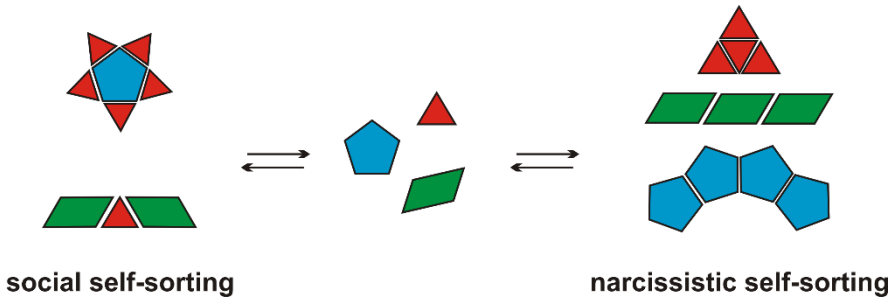

Figure 9: Representation of social (left) and narcissistic (right) self-sorting. The red, green and blue components will either aggregate with identical copies of themselves (narcissistic self-sorting) or form mixed assemblies, for example by complementary interactions (social self-sorting).

The basis for self-sorting is selective and complementary molecular recognition such as hydrogen bond complementarity, steric factors, coordination spheres, donor-acceptor interaction and the ability for error correction, which is the case for non-covalent

interactions.[29, 73] Also, social self-sorting is only observed in a stoichiometric window. When one component is much too abundant, the delicate balance of association constants is disturbed. Accordingly, the majority of self-sorted systems described in literature operate under thermodynamic control, although there are recent examples for kinetic selection of assemblies.[75-77]

For the uncommon case of a single assembly from a number of components programmed to arrange in specific positions, the term integrative self-sorting was coined.[74, 78] By proficiently merging or integrating two orthogonal recognition sites into one component, the desired assemblies become connected, hence integrated. In Figure 10b an example of integrative self-sorting in a crown/ammonium complex with two differently sized macrocycles is shown. The monovalent benzylalkylammonium guest **A3** in green (Figure 10a) can bind both the red **BC7** and the orange macrocycle **DBC8**. Due to a higher affinity, meaning a ratio of the binding constants in favor of the red macrocycle, the mixture will eventually end up in a self-sorted thermodynamic equilibrium (**A3@BC7** and **A2@DBC8**).

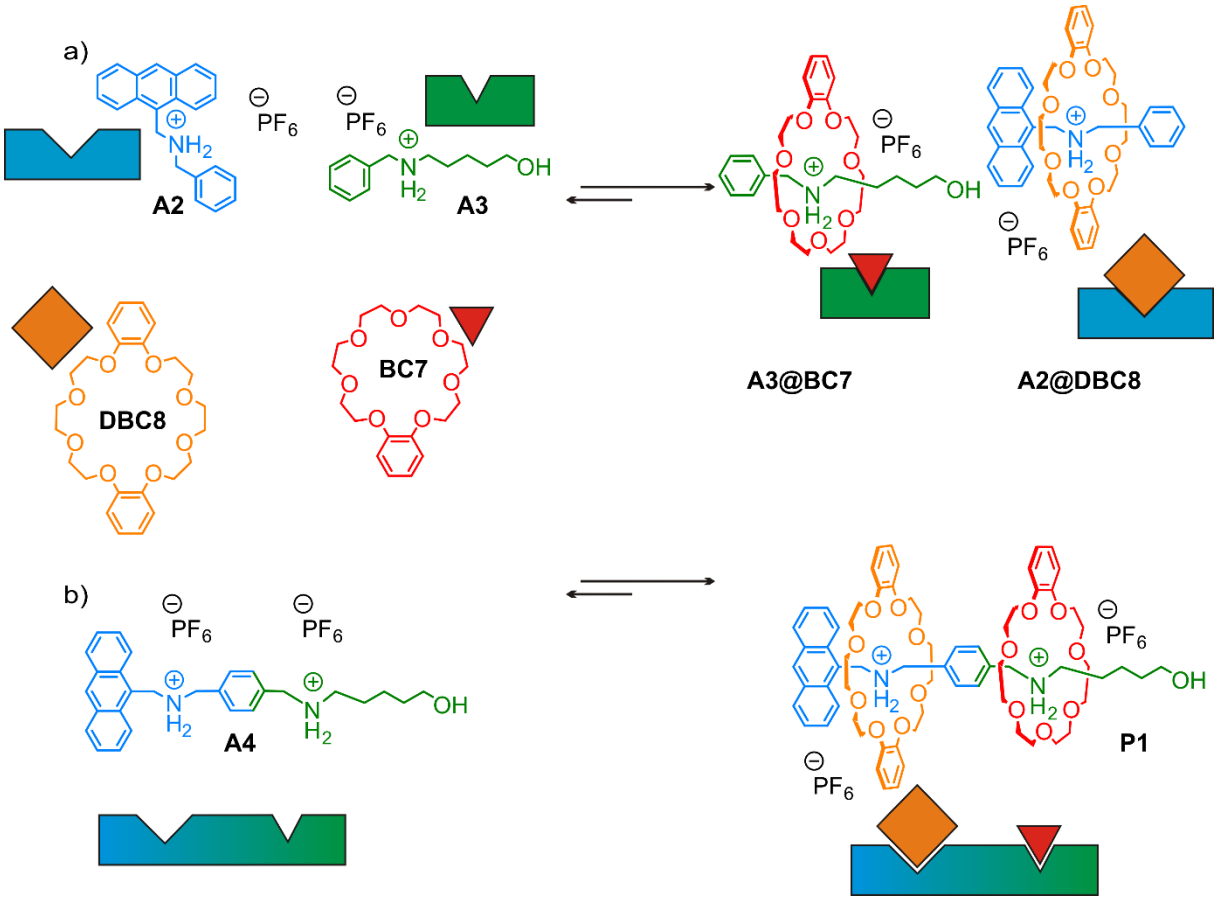

Figure 10: Integrative self-sorting in a crown/ammonium heteropseudo[3]rotaxane: a) the two individual guests bind their matching crown ether (blue/orange and green/red), b) The divalent guest (blue/green gradient) binds both crown ethers at their matching binding site.[78-79]

In the meanwhile, mismatched green guest **A3** with orange macrocycle **DBC8** that will occur with certainty (a local thermodynamic minimum), can disassemble due to the reversibility of the host-guest complex. Disassembling mismatched pairs and consequently being able to bind the better counterpart is called error correction. It can be regarded as a crucial feature that comes with the reversibility of the interaction, without whom higher order assemblies, such as the self-sorted complex with two macrocycles **P1** (Figure 10b), would not be possible. Without reversibility, the larger orange macrocycle **DBC8** is left out for complexation when the divalent guest is already bound to the smaller red macrocycle **BC7**, blocking the way to the second binding site. These design principles are powerful tools to reach dynamic structures that are not or incredibly hard to reach by classic covalent synthesis. Indeed, self-sorting enabled the synthesis of the new rotaxanes in the third project of this thesis.

2.2 Rotaxanes – A Class of Mechanically Interlocked Molecules (MIMs)

So far mostly covalent and non-covalent bonds were discussed in the previous chapters. But there is another type of bond, rather a physical bond, which can also be observed in the macroscopic world. Bruns and Stoddart describe the mechanical bond as "an entanglement in space between two or more molecular entities such that they cannot be separated without breaking or distorting chemical bonds between atoms".[63] Mechanical bonds are not an invention of supramolecular chemists, instead there are plenty of examples in nature as well as early examples in art from our everyday life (Figure 11). It has been shown that DNA enzymes called gyrase can form catenanes (mechanically interlocked rings) out of cyclic DNA fragments (Figure 11a).[80] Also, some peptides occur as lasso peptides, where a peptide chain is threaded through a lactam ring, giving rise to a proteolysis and heat resistant structure resembling artificial [1]rotaxanes (Figure 11b).[81]

The high stability and flexibility of chains is appreciated in all kinds of machines from bicycles to container ships that navigate the oceans. On a molecular level, chains are nothing more than polycatenanes (Figure 11c). Lastly, representations of knots are not only mathematically relevant, but they are also stylistic devices, which can represent eternity, love, friendship and loyalty. Figure 11d shows a celtic knot that is a common feature of Irish culture and tradition.

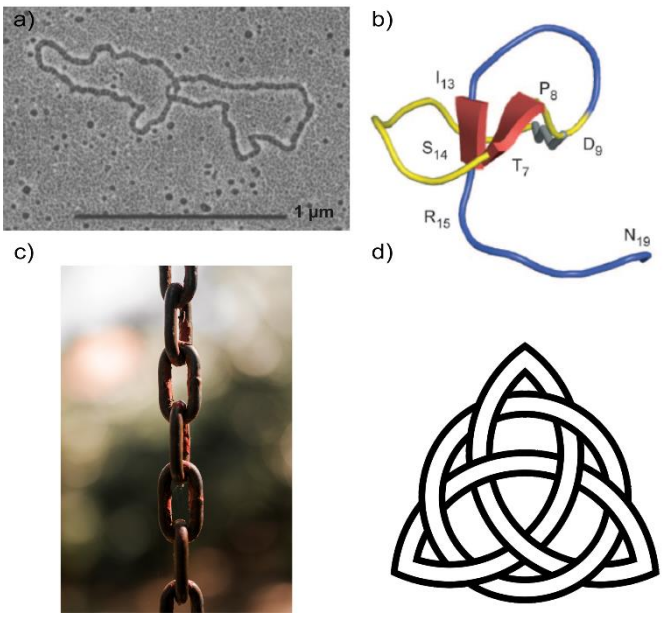

Figure 11: a) Electron micrograph of a gyrase-produced catenane. Reprinted from [80] Copyright 1980, with permission from Elsevier. b) Ribbon representation of the lasso peptide capistruin. Reprinted with permission from American Chemical Society[81]. Copyright 2008 American Chemical Society. c) Picture of a chain by Lola Russian. D) Celtic knot.

Mechanically interlocked molecules (MIMs) were discussed already a century ago.[82] By now they evolved from aesthetically appealing curiosities to molecular machinery with astonishing functions. The archetypes of MIMs are catenanes (mechanically interlocked rings), rotaxanes (a ring threaded onto a dumbbell-shaped axle from which it cannot escape) and knots (an entangled molecular chain). Figure 12 depicts the relationship of supramolecular complexes with MIMs. Pseudorotaxanes are at the intersection of supermolecules and interlocked species, because some of them are very stable under most conditions and hardly ever dissociate. The energetic barrier to dissociate is determined by the size, shape and electronic properties of the stopper groups, the wheel and the character of the medium. However, from a topological standpoint rotaxanes are not interlocked compounds, because the rules of topology allow the macrocycle to be stretched until it is not trapped anymore.[83]

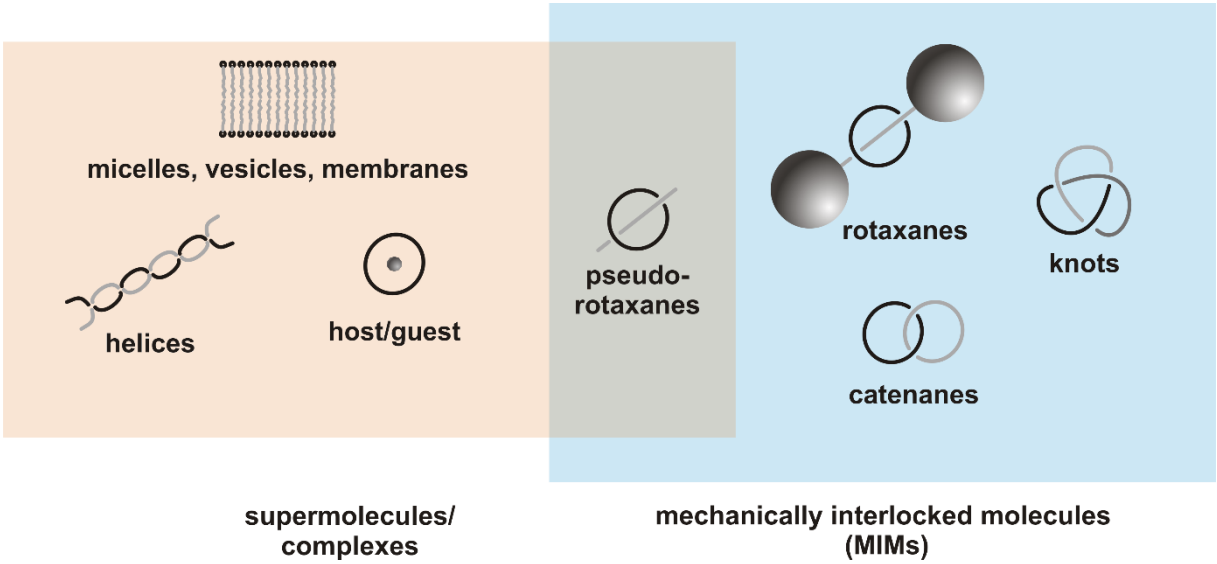

Figure 12: Schematic representation of the intersecting fields of supramolecular chemistry, host-guest complexes and mechanically interlocked molecules (MIMs).[63] Pseudorotaxanes are at the border of supermolecules and MIMs. Depending on the timescale and environment they can exhibit properties of both categories.[19]

As pseudorotaxanes are at the intersection of two individual and one mechanically bound molecule, they are very well suited to learn more about the mechanical bond and how it is formed. In the same way, ongoing research led to myriad examples with ingenious ideas on how to form rotaxanes.[84] The most common strategies are displayed in Figure 13, which can be distinguished into strategies that involve a preformed pseudorotaxane or not. If a pseudorotaxane is available, the mechanical bond can be formed by stoppering (attachment of bulky stopper groups), swelling (increasing the size of the stopper groups until the macrocycle cannot overcome them anymore) or shrinking (decreasing the circumference of the macrocycle after threading). Alternatively, slippage is the macrocycle slipping over the stopper groups under certain conditions and clipping is the formation of a macrocycle while preorganized around the dumbbell. Finally, dumbbell formation (often *via* active template)[85] is the formation of the mechanical bond by attaching the axle parts within the cavity of the macrocycle.

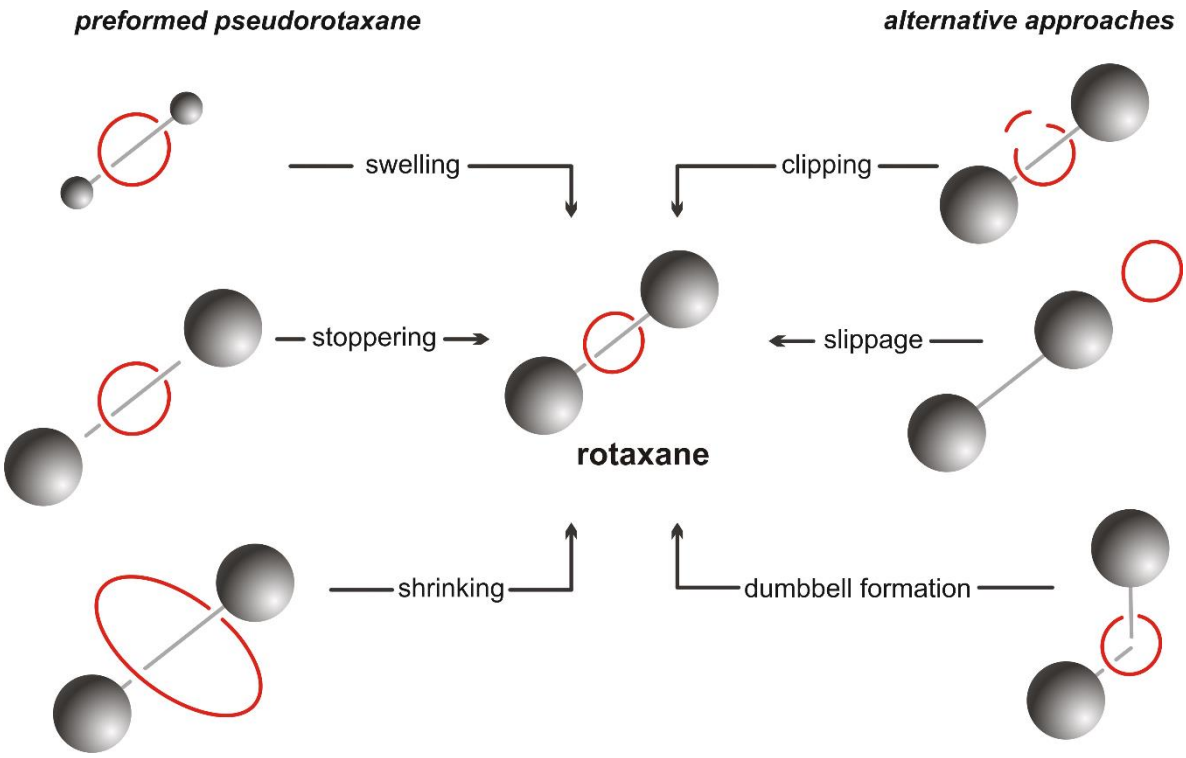

Figure 13: A selection of the most common strategies to generate rotaxanes.[63, 84] Either a preformed pseudorotaxane is interlocked or the macrocycle is clipped, slipped or the dumbbell is formed inside the macrocycle cavity.

For crown/ammonium rotaxanes stoppering is a very popular strategy because the macrocycle **DBC8** is commercially available and forms stable pseudorotaxanes with ammonium guests mostly within minutes. The stoppers are usually sterically demanding compounds, such as dimethyl- or di-*tert*-butylbenzene derivatives.[86] Attractive stoppering reagents are selective, high yielding and generate chemical bonds that tolerate desired follow-up reactions with the rotaxane. The stoppering – or rotaxanation – mostly proceeds by cycloadditions, esterification, amidation, formation of ureas/urethanes, disulfide formation or transition metal catalyzed coupling. Figure 14 features a selection of stoppering strategies. However, in this thesis the nitrile *N*-oxide click synthesis forming an isoxazole introduced by Takata and co-workers[87-88] was used for all rotaxanes (Figure 14a), to avoid side reactions of the macrocycles with metals in different oxidation states. This reaction was successfully employed for the addition of nitrile *N*-oxides to alkene, alkyne and nitrile end groups on pseudorotaxanes. It proceeds without catalyst at 40 °C and yields up to 98% are described in literature.[87]

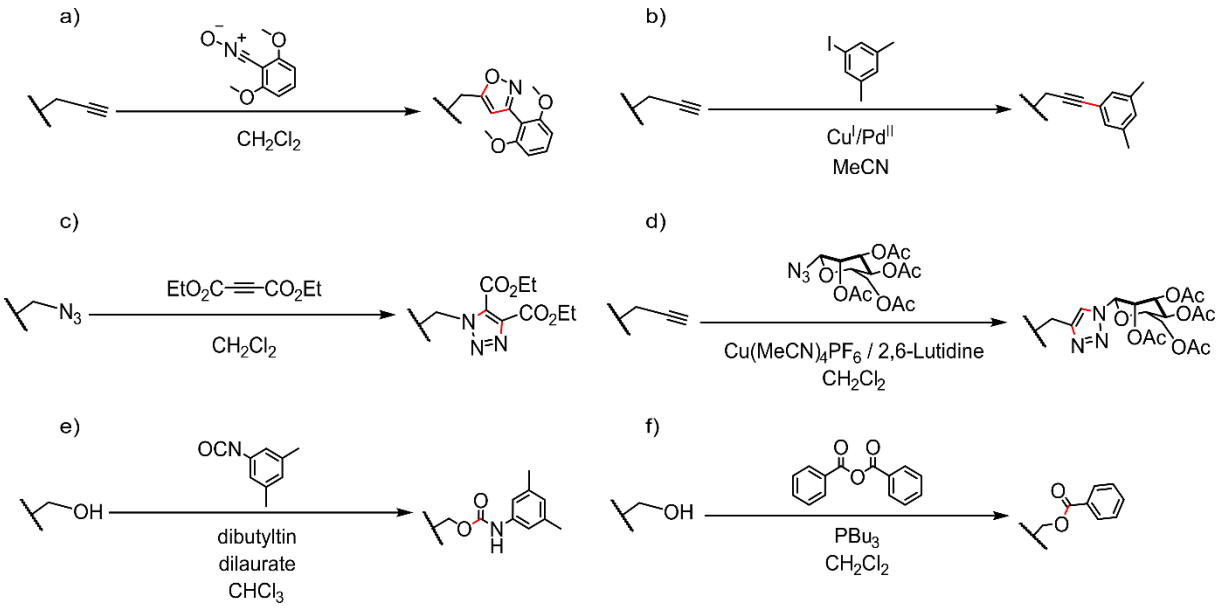

Figure 14: Selected examples of stoppering procedures for crown/ammonium rotaxanes: a) nitrile *N*-oxide click reaction,[87] b) Sonogashira coupling,[89] c) uncatalyzed Huisgen 1,3-dipolar cycloaddition,[90] d) CuAAC Huisgen cycloaddition,[91] e) urethane formation,[92] f) esterification.[93]

Once the macrocycle is trapped between the two bulky end groups, different types of motion can be defined. Due to the non-covalent interaction between axle and macrocycle, translational, pirouetting and rocking motions are possible (Figure 15a). For degenerate two-station [2]rotaxanes[43] the macrocycle engages in a shuttling motion between the two stations (Figure 15b). Degenerate two-station [2]rotaxanes have two equal binding sites on the axle encircled by one macrocycle. For the sake of lucidity the axle component is defined as stationary and the macrocycle as the moving component. Likewise, it also works the other way round, as it just depends on the frame of reference. This freedom of motion is the basis for stimuli-responsive rotaxanes that are in the spotlight in chapter 2.2.2.

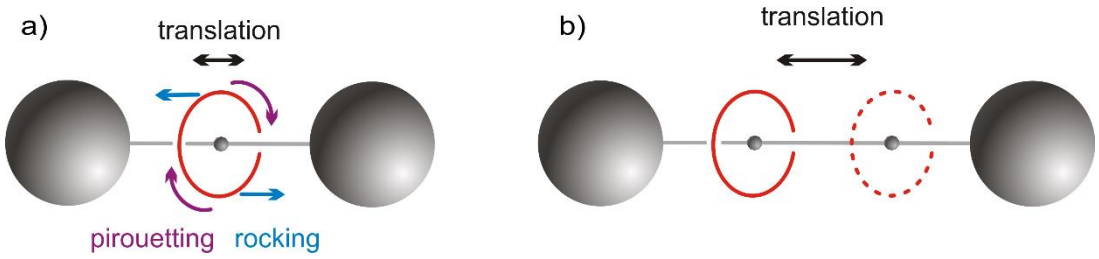

Figure 15: Illustration of different types of motion in rotaxanes. One-station [2]rotaxanes can exhibit pirouetting, rocking and translation (a). In degenerate two-station [2]rotaxanes the macrocycle also translates/shuttles between the two stations (b).

A subclass of rotaxanes that receive significant attention are heterorotaxanes.[94-95] In general, heterorotaxanes are made of at least three different components. Accordingly, hetero[3]rotaxanes are either made of two different macrocycles and an axle or two different axles trapped within the cavity of a macrocycle (Figure 16). The coexistence of different

macrocycles in heterorotaxanes allows for the investigation of properties that arise from sequence isomerism and controlled movement.[95]

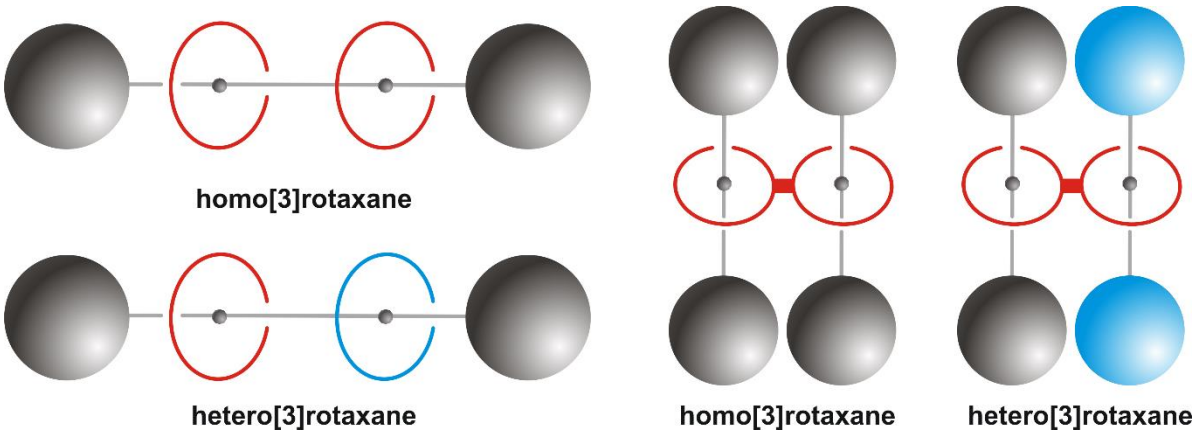

Figure 16: Archetypes of homo- and hetero[3]rotaxanes. Out of the three components, either the macrocycles or the dumbbells can be different

Studies on homorotaxanes are much more frequent than heterorotaxanes, most likely due to the synthetic challenge that comes with making them. Besides statistical approaches[96] to construct heterorotaxanes, the selective formation is achieved through orthogonal binding sites,[97-98] sequential macrocycle clipping/threading[99-100] or integrative self-sorting.[74, 78-79, 101-102] In Figure 17 some prominent examples from literature are shown. The first heterorotaxane example **R1** was reported 1995 by Stoddart and co-workers,[100] where a [2]rotaxane was formed first and then the larger macrocycle threads over the stopper units at high temperatures (Figure 17a). In an active-template kinetic self-sorting approach, Goldup and co-workers[103] describe the kinetic trapping of a larger behind a smaller 2,2'-bipyridin containing macrocycle, using a Cu-mediated alkyne-azide cycloaddition (AT-CuAAC) in the cavity of the macrocycles (Figure 17b). Additionally, Loeb and co-workers[99] synthesized hetero[3]rotaxane **R3** that exhibits a new type of shuttling motion, namely ring-through-ring shuttling (Figure 17c). Integrative self-sorting was used by Schalley and co-workers[79] to construct the cascade-stoppered hetero[3]rotaxane **R4**, where the smaller macrocycle prevents the larger from dethreading, whereas the phenyl stopper prevents the smaller macrocycle from dethreading (Figure 17d). Finally, Tian and co-workers[102] also used self-sorting to arrange three different crown ether macrocycles on two different threads and subsequently connecting them *via* a "click" reaction (Figure 17e).

However, it is noteworthy that in all examples with crown ethers or glycol chain containing macrocycles, only circumference is the main differentiating feature. So far, no additional functionalities, which are not necessary for the rotaxane formation, were introduced.

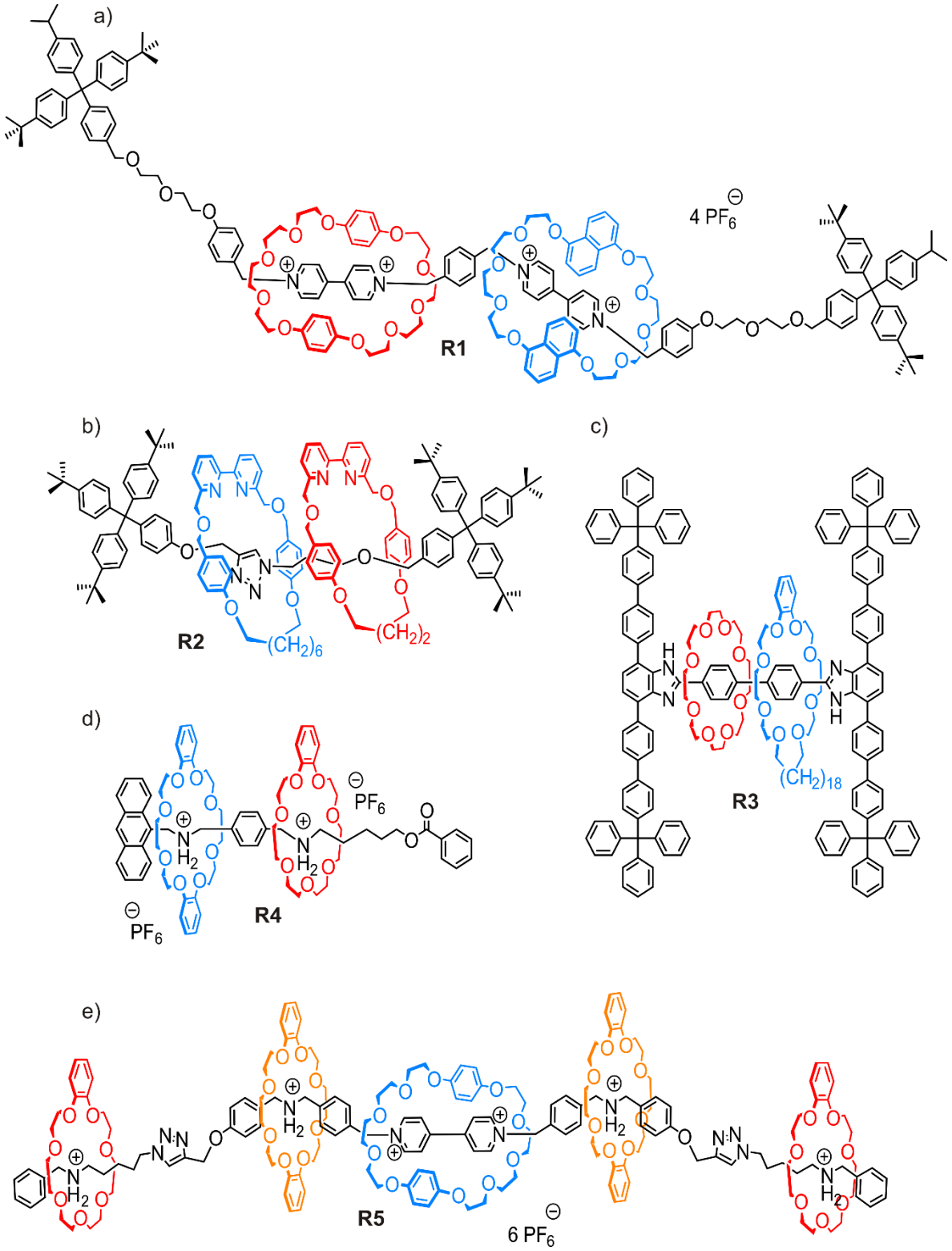

Figure 17: Examples of different heterorotaxanes a) The first controlled self-assembly of a [3]rotaxane incorporating three constitutionally different components,[100] b) kinetic self-sorting approach,[103] c) ring-through-ring molecular shuttling,[99] d) integrative self-sorting rotaxane,[79] e) one-pot hetero[6]rotaxane.[102]

2.2.1 Chirality in Rotaxanes

Directionality is an important topic in the development of nano-devices and molecular motors, because movement without directionality equals out on average. One way to achieve directionality in rotaxanes is to introduce a chiral element, which makes it more complex in the synthesis.[16] Biological systems are homochiral, therefore enantiopure molecules that need to be generated for biological applications. Chirality is a property of an object or a system which has no axis of improper rotation and the concept is not limited to molecules. For instance, the word *chirality* itself is derived from the Greek χειρ "*hand*". Although they all describe the same phenomenon, it is common to differentiate between point, axial, helical and planar chirality in chemistry. The corresponding terminology to assign absolute stereochemistry for the R/S enantiomers was originally developed by Cahn, Ingold and Prelog (CIP priority rules).[104] Generally, chiral centers can be introduced by carbon atoms with four different substituents or heteroatoms with three different substituents and a free electron pair, which is not prone to a pyramidal or umbrella inversion. An umbrella inversion is the stereochemical inversion at a heteroatom, e.g. nitrogen without the cleavage of a covalent bond.[105] Axial chirality can be found in molecules, where the rotation about a bond is hindered sterically or electronically to a degree where rotamers can be isolated. The stereoisomers are called atropisomers. Ortho-substituted biaryls, just like BINOL, often show this property. Furthermore, helical chirality is observed in molecules which form either a left- or right-handed helix. For example, the helix of a DNA double strand is usually right-handed in nature. Finally, planar chirality can be observed in systems with two dissymmetric non-coplanar rings, which cannot freely rotate about the bond connecting them. Some substituted metallocenes and substituted paracyclophanes are planar chiral.

The following examples are limited to rotaxanes, because they are the relevant category for this thesis, but there are also other chiral MIMs with compelling topologies, such as catenanes and knots (as seen in chapter 2.2).[106] Considerations on chemical topology and their theoretical treatment have already been published in 1961 by Frisch and Wasserman,[82] a few years before they were first synthesized in 1967.[107] Although rotaxanes are interlocked and can be isolated, they are topologically trivial. The rules of topology allow the deformation of the ring or the axle. The macrocycle can theoretically slide off the stoppered axle and rearrange its orientation without changing topology. In a chemical frame of reference, the mechanical bond of the macrocycle to the axle cannot be broken without scission of a covalent bond, the

enantiomers therefore cannot interconvert. Accordingly, only catenanes and knots are topologically chiral. As a result, one has to differentiate between topological and euklidian chirality.[108-109] The following statements refer to the euklidian chirality and are not valid in a topological frame of reference.

In Figure 18, comics of chiral [2]rotaxanes are displayed. Stereogenic elements can be part of the axle or macrocycle. However, here the chirality does not arise from the mechanical bond nor the co-conformation.

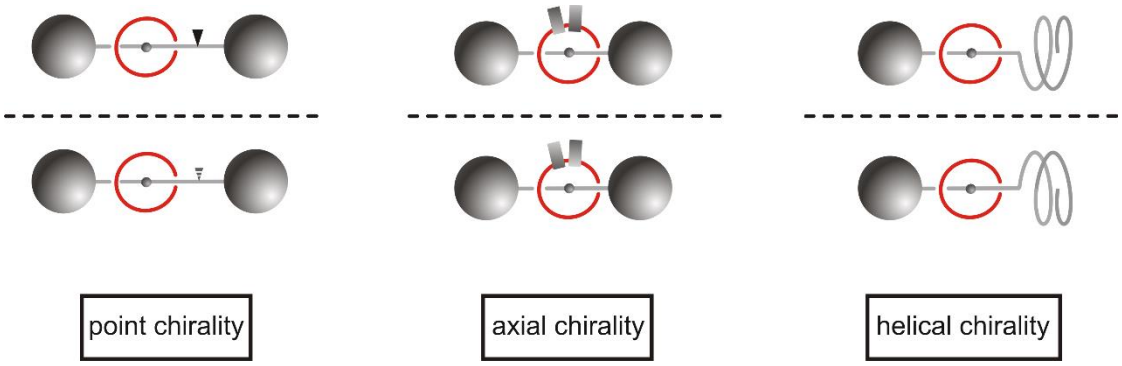

Figure 18: Universal examples of how stereogenic elements can be incorporated into a [2]rotaxane.

Additionally, the mechanical bond enables other possibilities beyond connecting stereogenic elements to a MIM. In Figure 19, chiral [2]rotaxanes are depicted where no single covalent stereogenic element is responsible for the chirality. In fact, it only arises from the arrangement which is fixed by a mechanical bond. Hence, these molecules are called “mechanically chiral”.[110] An achiral macrocycle with directionality in the atom sequence forms a mechanically planar chiral [2]rotaxane with two equal binding sites. The co-conformation determines the stereochemistry (Figure 19 mid). Finally, a prochiral axle can become chiral when a macrocycle is added on either side. The macrocycle alters the symmetry of the molecule, so that both sides are not equal anymore. This so called co-conformational covalent chirality can result in central/point, axial or planar chirality, depending on the moiety in the center of the axle (black wedge in Figure 19 on the right).

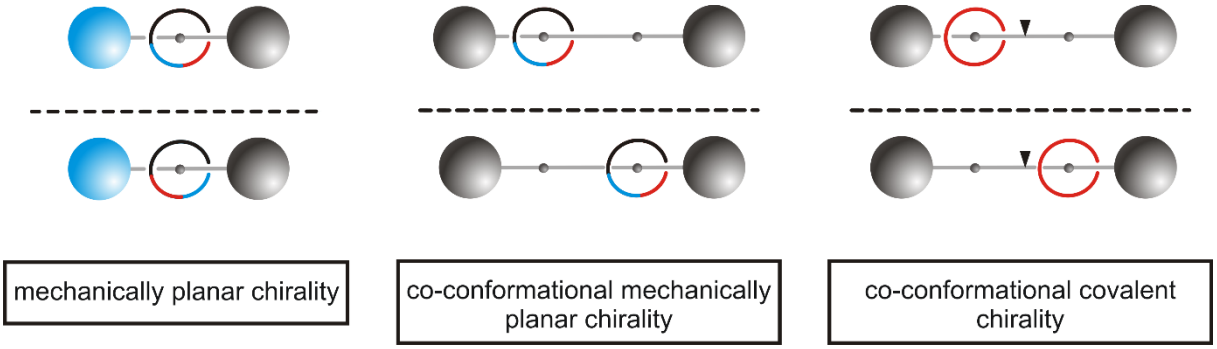

Figure 19: Chirality arising as a consequence of the mechanical bond in [2]rotaxanes.[110]

A first molecular example for planar chiral or cycloenantiomeric rotaxanes (Figure 19 left) was described by Vögtle and co-workers.[111] His group obtained two enantiomers of an amide-connected rotaxane with a directional tetralactam macrocycle on a directional axle, as shown in Figure 20.

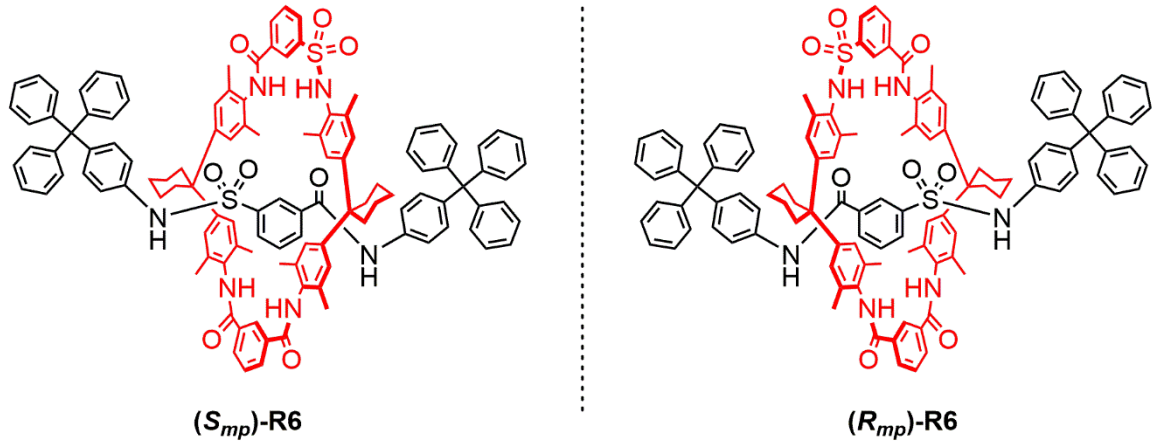

Figure 20: First example for cycloenantiomeric rotaxanes described by Vögtle and co-workers.[111]

A recent molecular example for a co-conformationally planar chiral [2]rotaxane (Figure 19 middle) was synthesized by Credi and co-workers (Figure 21). Upon deprotonation of the preferred dibenzlammonium site the prochiral [2]rotaxane **H-R7** on the top becomes a shuttle where the directional macrocycle rapidly changes between two triazolium binding sites. Additionally, a bias for one enantiomer could be induced by adding an enantiopure counteranion.[112] The rate of interconversion between the two enantiomers (which cannot be separated) is depending on the temperature. Therefore, the observers' timescale determines whether the deprotonated [2]rotaxane are to be reckoned as two distinct enantiomers or a transient achiral species. As a frame of reference, the two enantiomers interconvert with a rate of k_{rac} = 35 s^{-1}. A similar co-conformationally planar chiral [2]rotaxane with different interconversion barriers is described in a preprint article by Takata and Ishiwari.[113]

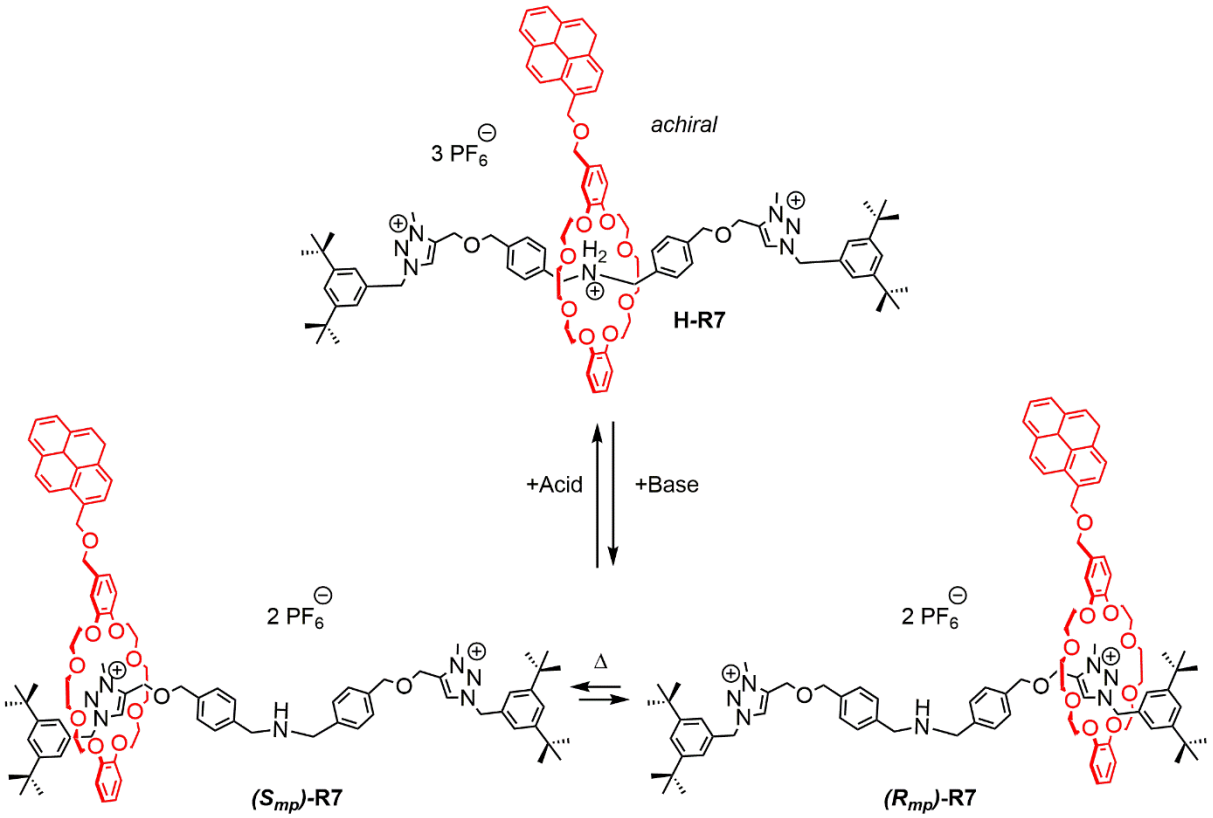

Figure 21: The prochiral [2]rotaxane **H-R7** reversibly shuttles between two planar chiral enantiomers upon deprotonation.[112]

Surprisingly, only one example for co-conformational covalent chirality (Figure 19 right) has been realized so far. Leigh and co-workers[114] synthesized the achiral bisfumaramide [2]rotaxane **R8** with two equal binding sites for a tetralactam macrocycle. Benzoylation of the central hydroxy group yielded two separable enantiomers (Figure 22).

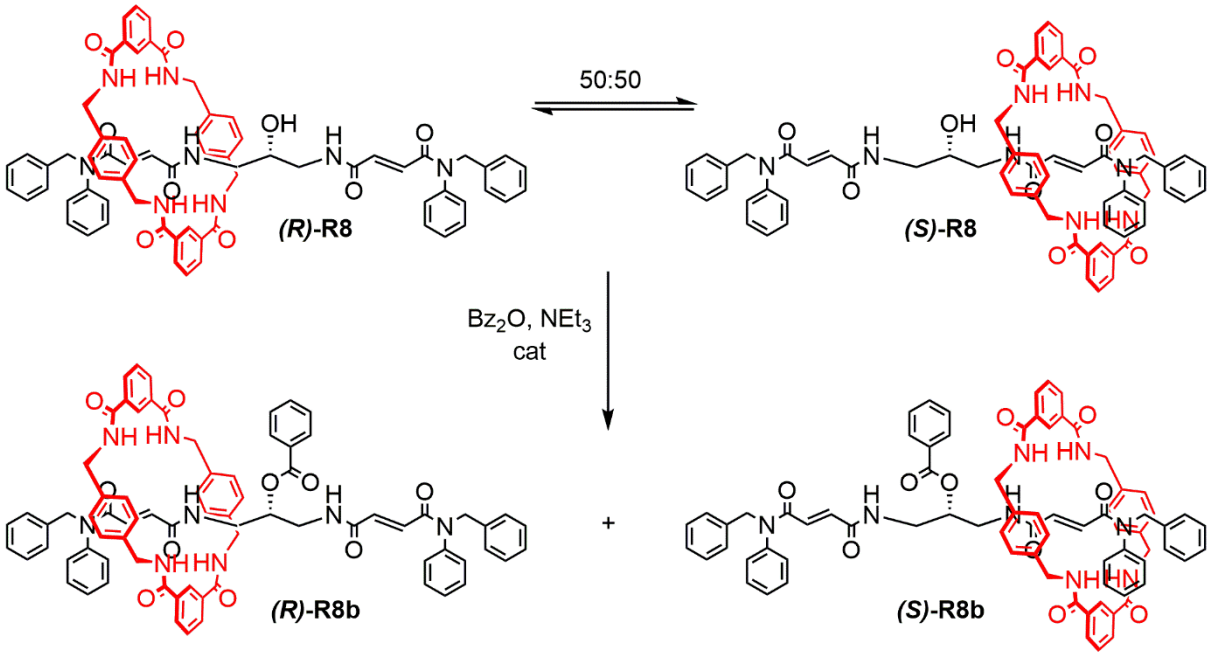

Figure 22: An achiral [2]rotaxane with two equal fumaramide binding sites yielded two separable enantiomers upon introduction of a bulky barrier (benzoyl group) at the central hydroxy group.[114]

With increasing number of components more isomers are possible. For a divalent symmetric axle with two identical directional macrocycles, three isomers are formed. Their stereochemical relationship is shown in Figure 23. Analogous to tartaric acid, the meso form in the middle is not chiral and a diastereomer of the two other isomers (enantiomers left and right). The first synthesis for planar chiral [3]rotaxanes was also described by Vögtle and co-workers.[109, 111]

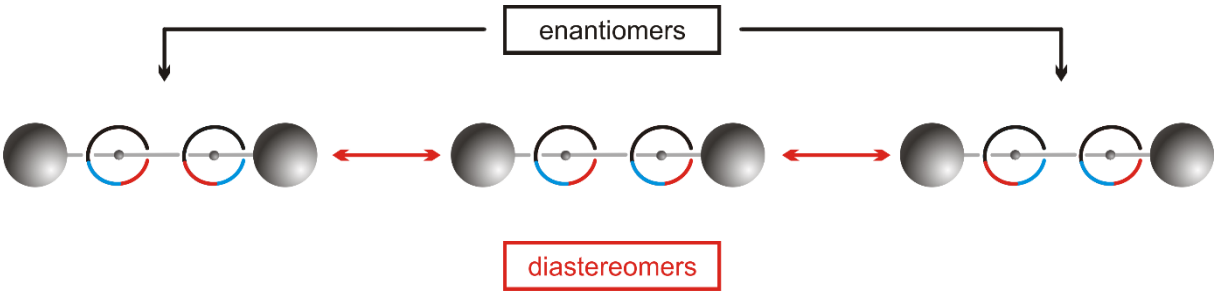

Figure 23: Possible isomers of [3]rotaxanes with directional macrocycle on a divalent symmetric axle.

Although an increasing amount of mechanically planar chiral rotaxanes appear in literature, the enantiopure synthesis is still a challenging task.[115] Most examples rely on the separation of stable enantiomers by chiral stationary-phase HPLC, but there are several strategies available to access enantioselectivity in the synthesis.[116]

A pioneering approach for catalytic enantioselective routes was demonstrated by Takata and co-workers in 2007. The approach relies on the stereoselective ester formation facilitated

by a chiral phosphine nucleophile. However, the reaction shown in Figure 24 only reached enantiomeric excess of 4.4%.[117]

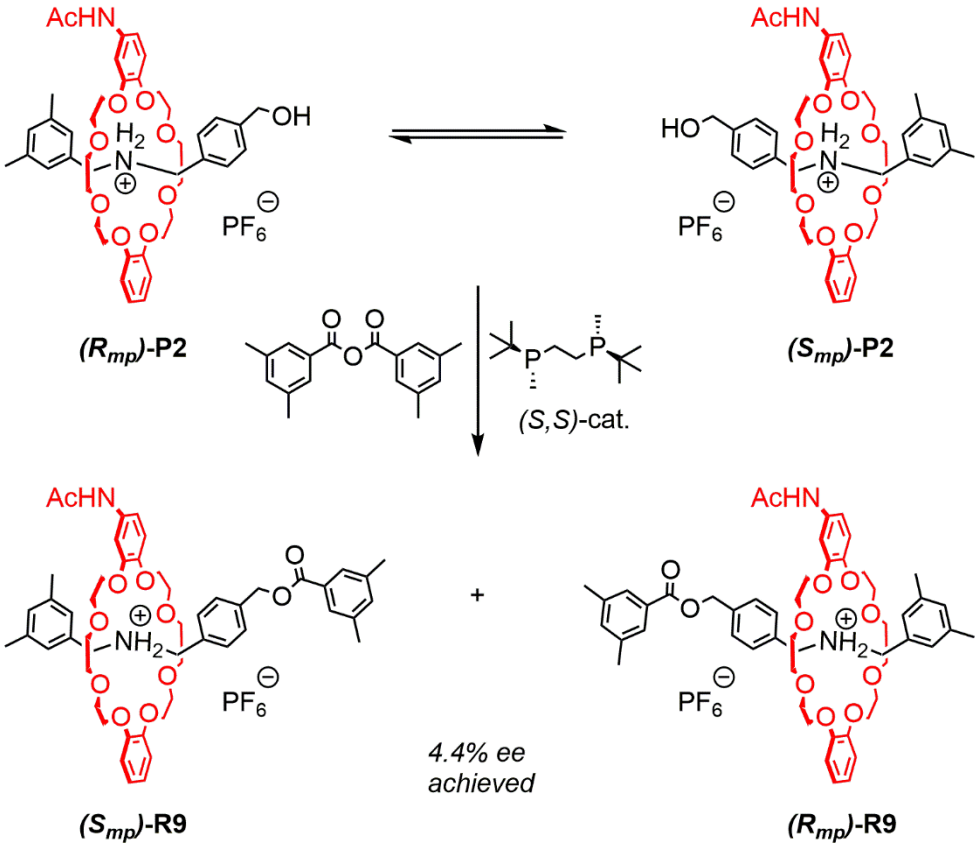

Figure 24: The stereoselective stoppering of an enantiomeric pseudo[2]rotaxane mixture by Takata and co-workers.[117]

Recently, a kinetic resolution approach by Kawabata and co-workers was reported. An enantiomeric solution of [2]rotaxanes by acylation of a hydroxyl group on the axle in the presence of a chiral catalyst could be achieved.[118] The unreacted enantiomer **R10** can be obtained from the reaction mixture in >99.9% *ee* in 29% yield, as the selectivity for the fast-reacting enantiomer with a chiral functionalized pyridine catalyst is 14.5 times faster than for the slower one (Figure 25). The challenge to discriminate one enantiomer of the substrate was overcome by adding a NHNs group (Ns = -SO_2-2-NO_2-C_6H_4) to the directional macrocycle. A beneficial hydrogen bond between the catalyst and the NHNs moiety in the transition state is key for the high selectivity factor.

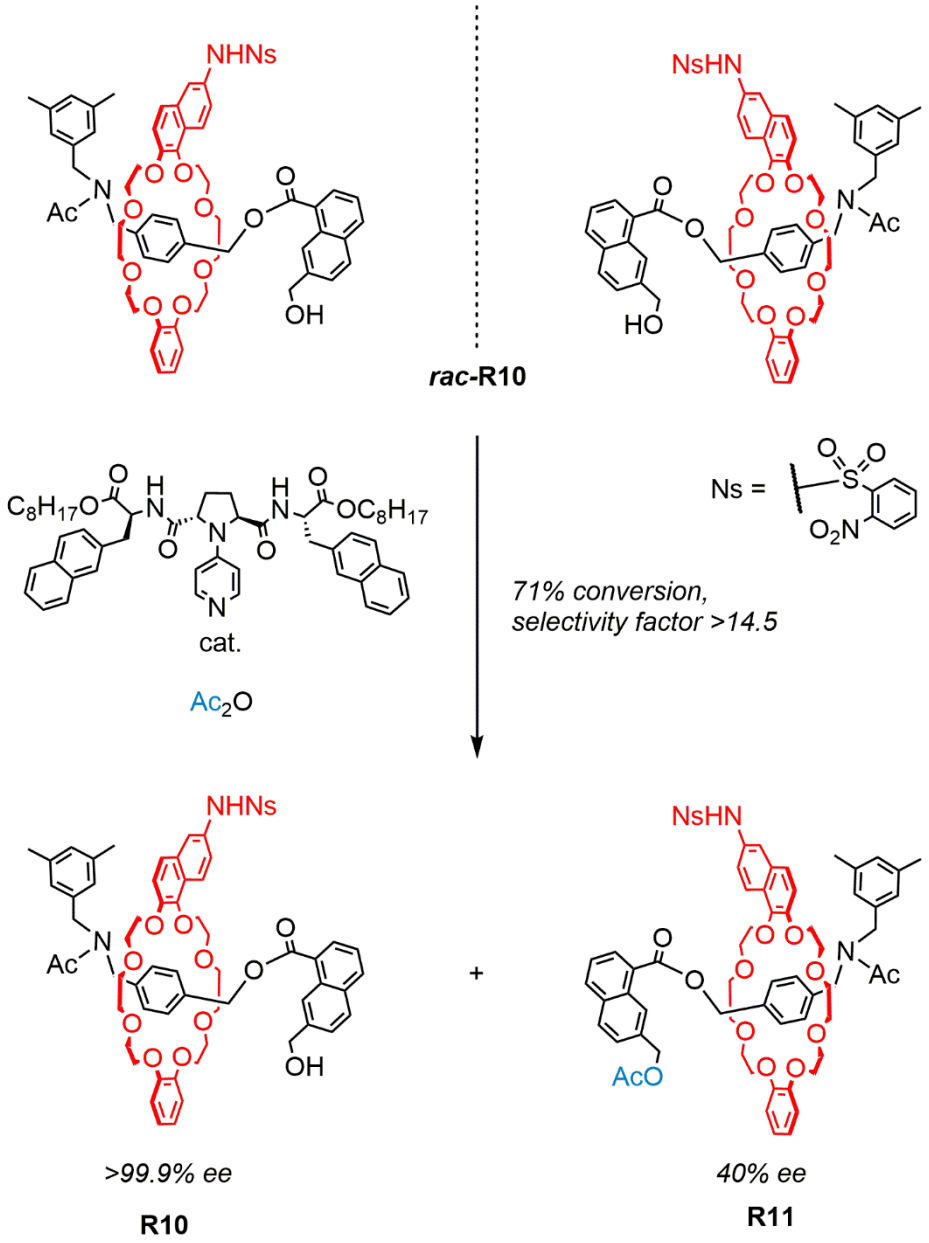

Figure 25: Kinetic resolution approach to enantiopure mechanically planar [2]rotaxanes.[118]

Another popular approach is the so-called chiral auxiliary approach. A stereogenic moiety is reversibly attached to the MIM and can be removed after diastereomeric separation on a regular chromatographic column. The first successful chiral auxiliary synthesis of a mechanically chiral MIM was reported by Goldup and co-workers (Figure 26).[119] The enantiopure sugar-based azide **4** formed a triazole with 1,3-di-*tert*-butyl-5-ethynylbenzene **3** within the bipyridine macrocycle **5** in an active template Cu-mediated alkyne-azide cycloaddition (AT-CuAAC).[85] The diastereomeric products **(D,*R/S*$_{mp}$)-R12** were separated and the sugar was exchanged for (3,5-di-*tert*-butylphenyl)methanamine **6** without cleaving the mechanical bond.

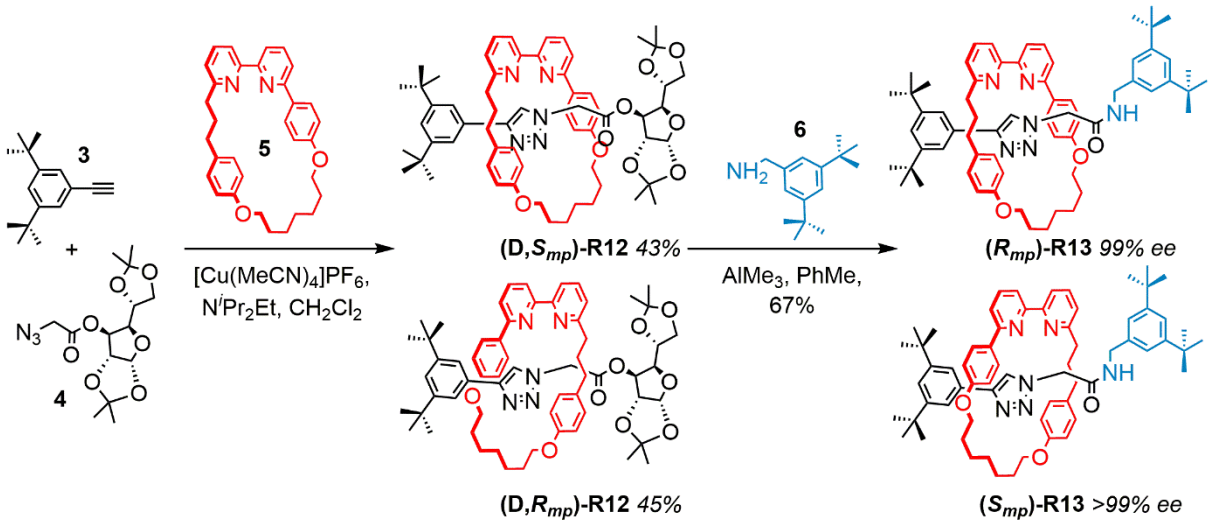

Figure 26: Goldup's synthesis of an enantiopure mechanically chiral [2]rotaxane *via* a chiral auxiliary.[119] After formation of the [2]rotaxanes **(D,*R*/*S*$_{mp}$)-R12** and separation on a regular chromatographic column. The chiral auxiliary sugar is exchanged with the final stopper **6** to obtain the final enantiopure products **R13**.

Similarly, Leigh and co-workers reported an enantioselective synthesis in up to 50% *ee* by a variation of their metal-free active template amide formation.[120-122] Stereoselectivity is delivered by a bulky (+)-cinchonidine moiety on the ester leaving group together with the directional naphthalene decorated crown ether **9**. According to molecular modeling, a selective formation of one of the four possible tetrahedral intermediates by macrocycle half-thread interactions give rise to the enantiomeric excess in the product **(–)-R14** (Figure 27).[123]

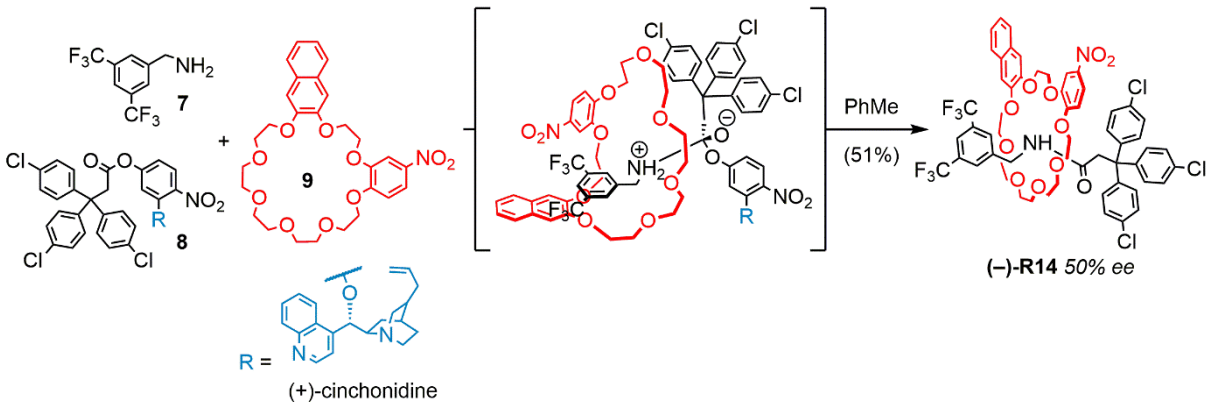

Figure 27: Leigh's direct enantioselective synthesis of the mechanically chiral [2]rotaxane **(–)-R14** by displacement of a chiral ester leaving group within the cavity of the directional crown ether **9**.[123]

In general, using non-covalent interactions to reach enantiomeric excess in the synthesis of MIMs, for example with enantiopure counterions remains underexplored. Only few examples for biasing a co-conformational racemic equilibrium after formation of the mechanical bond are reported for catenanes[124] and rotaxanes.[112] Nevertheless, consecutive examples used the planar chirality for studying the conformational changes and chiral induction.[125] For example, mechanically planar chiral rotaxanes were used to induce single-handed helicity of

polyacetylenes by Takata and co-workers (Figure 28).[126] Ethynyl groups (blue) on the enantiopure rotaxanes **R15** and **R16** are either located on the directional wheel or at a bulky end group of the axle. After polymerization with a Rh catalyst, the helicity of the polyacetylene chain had the opposite sense of the monomeric rotaxane. Hence, a chiral induction of the rotaxane to the chain occurred.

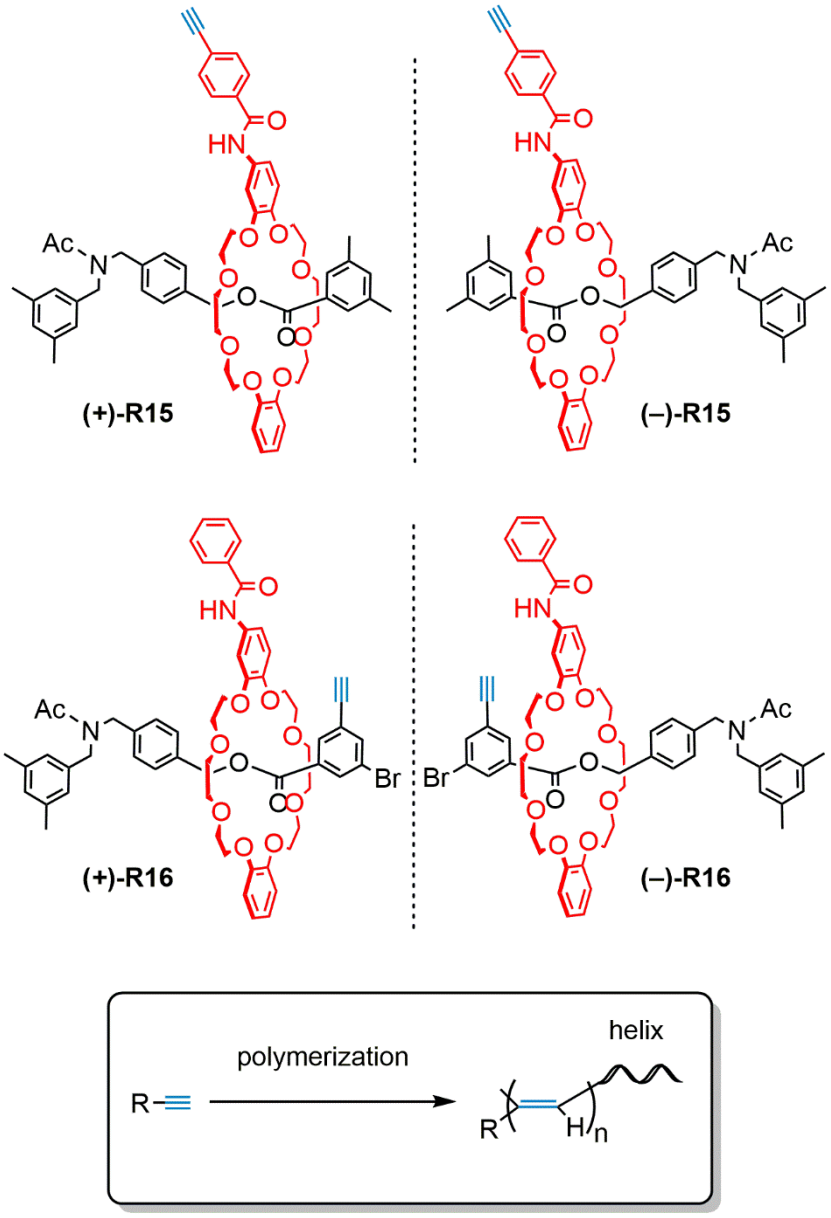

Figure 28: Enantiopure mechanically planar chiral [2]rotaxanes **R15** and **R16** induce a helical sense on a polymer chain grafted from them.[126]

Additionally, catalytic applications can benefit from the directionality of a planar chiral ligand. Goldup and co-workers used the mechanically planar chiral gold catalyst[**Au(*R*$_{mp}$)-R17(Cl)**] to stereoselectively catalyze a cyclopropanation reaction between **10** and **11** (Figure 29).[127] The stereoselectivities of the product **12** are comparable to other non-mechanically interlocked catalysts[128] without being structurally optimized for this purpose.

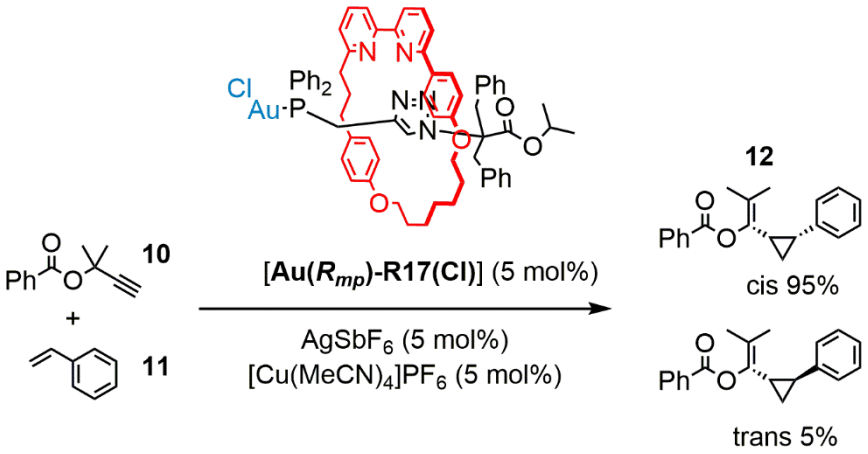

Figure 29: Stereoselective cyclopropanation catalyzed by the mechanically planar chiral gold catalyst [**Au(R$_{mp}$)-R17(Cl)**].[127]

All of the examples of chiral rotaxanes and MIMs have promising properties, but in order to perform more useful tasks it is beneficial to be able to switch them on and off and control their function.[129] Also, expressing and controlling chirality has possible applications in the storage and readout of information or as catalysts.[130]

2.2.2 Stimuli-Responsive Rotaxanes and Molecular Machines

Macroscopic switches surround us everywhere in our everyday life. Most of the time they appear in form of an electronic switch, like a button or light switch. As mentioned in the introduction, miniaturization of electronic devices is reaching a lower size limit. Therefore, the design of molecule-sized switches is a worthwhile topic for scientists and engineers.[131]

Molecular switches are stimuli-responsive molecules, that change their properties ideally reversibly after applying a stimulus. In the context of rotaxanes molecular switches are often designed to dislocate the macrocycle by diminishing the affinity towards a binding site. In Figure 30 the difference between a degenerate shuttle [2]rotaxane and a stimuli-responsive [2]rotaxane is shown.

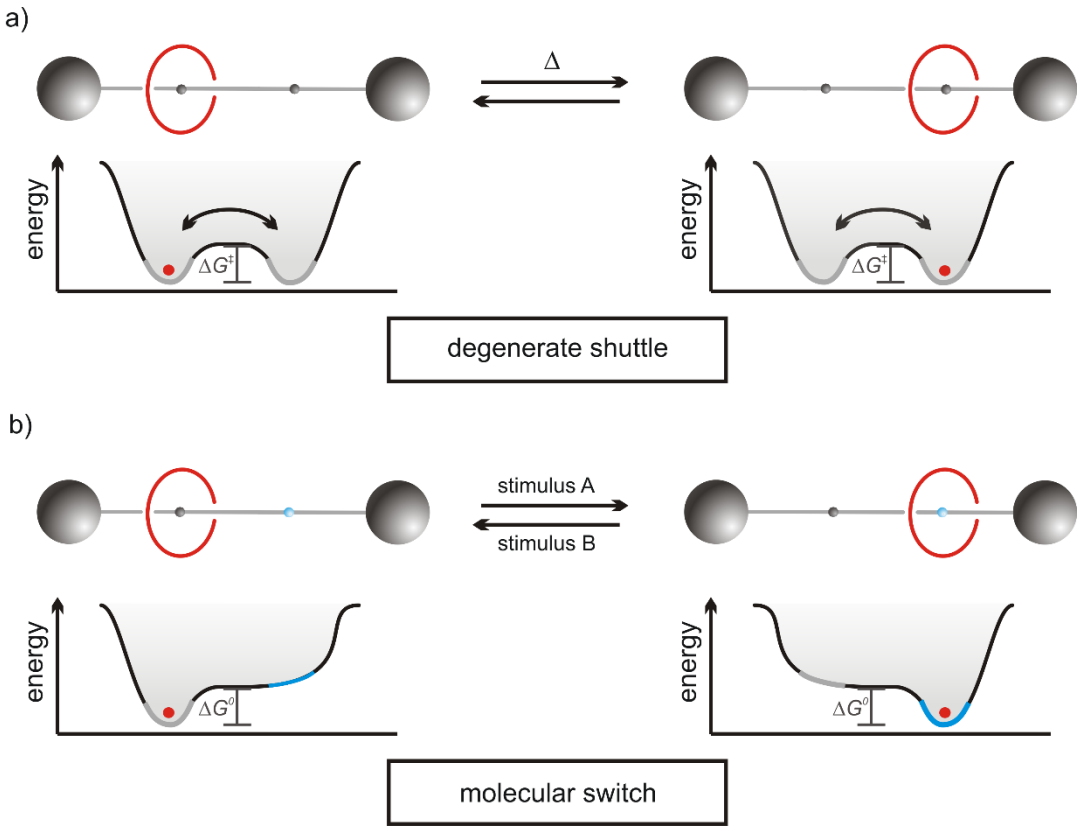

Figure 30: Schematic representation of a stimuli responsive rotaxane switch: A degenerate bistable [2]rotaxane (a) and a stimuli responsive [2]rotaxane shuttle (b) with potential energy landscapes for both states.[5]

The degenerate shuttle features two equal binding sites which are occupied with equal probability by the macrocycle (Figure 30a). The Eyring equation (Equation 4) describes the relationship between the rate of exchange between the two co-conformations or shuttling rate k and the activation barrier ($\Delta G^{\ddagger}$) of the conformational change, with T_c being the coalescence temperature usually obtained from NMR spectra,[132-133] R the gas constant, h the Planck's

constant and the Boltzmann constant k_B. The activation barrier depends on size and flexibility of the macrocycle cavity and bulkiness of the axle.[134-135] However, it does not depend on the length of the axle.[136]

$$\Delta G^{\ddagger} = -RT_c \cdot \ln\left(\frac{kh}{k_B T_c}\right) \qquad (4)$$

By introduction of a differing second binding station on the axle, the opportunity to create a supramolecular switch arises. In Figure 30b a drawing of a supramolecular switch, namely a bistable [2]rotaxane, is shown. The macrocycle resides on the energetically favored left site depicting the ground state co-conformation (GSCC). In this example, the grey binding station on the left is unfavored when the stimulus A is applied. As a consequence, the macrocycle will shuttle to the blue binding station on the right to reach the new energetic minimum. When the stimulus B is applied, the process is reversed, the rotaxane switch changes from the now unfavorable metastable state co-conformation (MSCC) with the macrocycle on the brown site back into the GSCC. The potential energy curves of the two states in Figure 30b show an energy difference (ΔG^0) of the two states. An important difference to macroscopic switches is that not 100% of the investigated species will adopt the preferred co-conformation. There is always a distribution between the two. The ratio depends on the binding energy difference between the two stations, an equilibrium constant of 100 equals an energy difference of only -11.2 kJ mol^{-1} at room temperature. Equation 5 shows the relation between the intramolecular equilibrium constant K_i and the energetic difference between the two states ΔG^0:

$$K_i = e^{\frac{-\Delta G^0}{RT}} \qquad (5)$$

With a suitably high equilibrium constant, cycle stability and a non-destructive readout, applications like Boolean algebra, molecular computation, logic gates and memory devices could be imagined.[137-139] In the course of the last decades, rotaxane switches operated by light, heat electrical or chemical energy were developed.[63, 140-141] Selected examples are summarized below. However, the characterization of different co-conformations and shuttling dynamics can be very complicated and often a combination of (temperature dependent) NMR spectroscopy, cyclic voltammetry (CV), UV/Vis, fluorescence spectroscopy, isothermal titration calorimetry (ITC) and mass spectroscopy among others is required to get a consistent picture.[132]

An early example of an acid/base-switchable [2]rotaxane was reported by Stoddart and co-workers in 1997.[142] The preferred dibenzylammonium binding site can be deprotonated by

base (*i*Pr$_2$NEt), which triggers the shuttling of **DBC8** towards the pH insensitive bipyridinium station of **R18**. The translocation of the macrocycle can be reversed by addition of acid, such as trifluoroacetic acid (TFA).

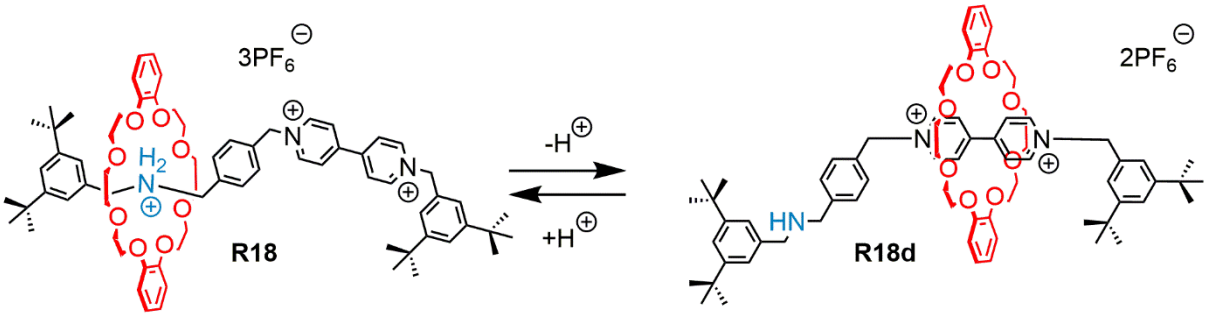

Figure 31: The pH-controlled shuttling of **DBC8** in a [2]rotaxane.[142]

The working principle was used in a [c2]daisy chain-based supramolecular polymer. Guiseppone and co-workers[143] combined a secondary ammonium and a triazolium binding site with two terpyridine stoppers which prevent disassembly of the [c2]daisy chain **R19**. By addition of either Zn(OTf)$_2$ or FeCl$_2$, two terpyridine stoppers connect daisy chain monomers by metal ion coordination (Zn^{2+} or Fe^{2+}) in bisterpyridine complexes. Small-angle neutron scattering (SANS) revealed a polymer length of 200 nm for the Fe-containing supramolecular polymer. The protonated ammonium station is the preferred binding site for the crown ether, whereas the triazolium is occupied after deprotonation (Figure 32). Thereby, acid-base switchable reversible contraction was achieved in a coupled muscle-like movement, as the macrocycle shuttles along the axle towards the preferred binding site in each monomer of the chain.

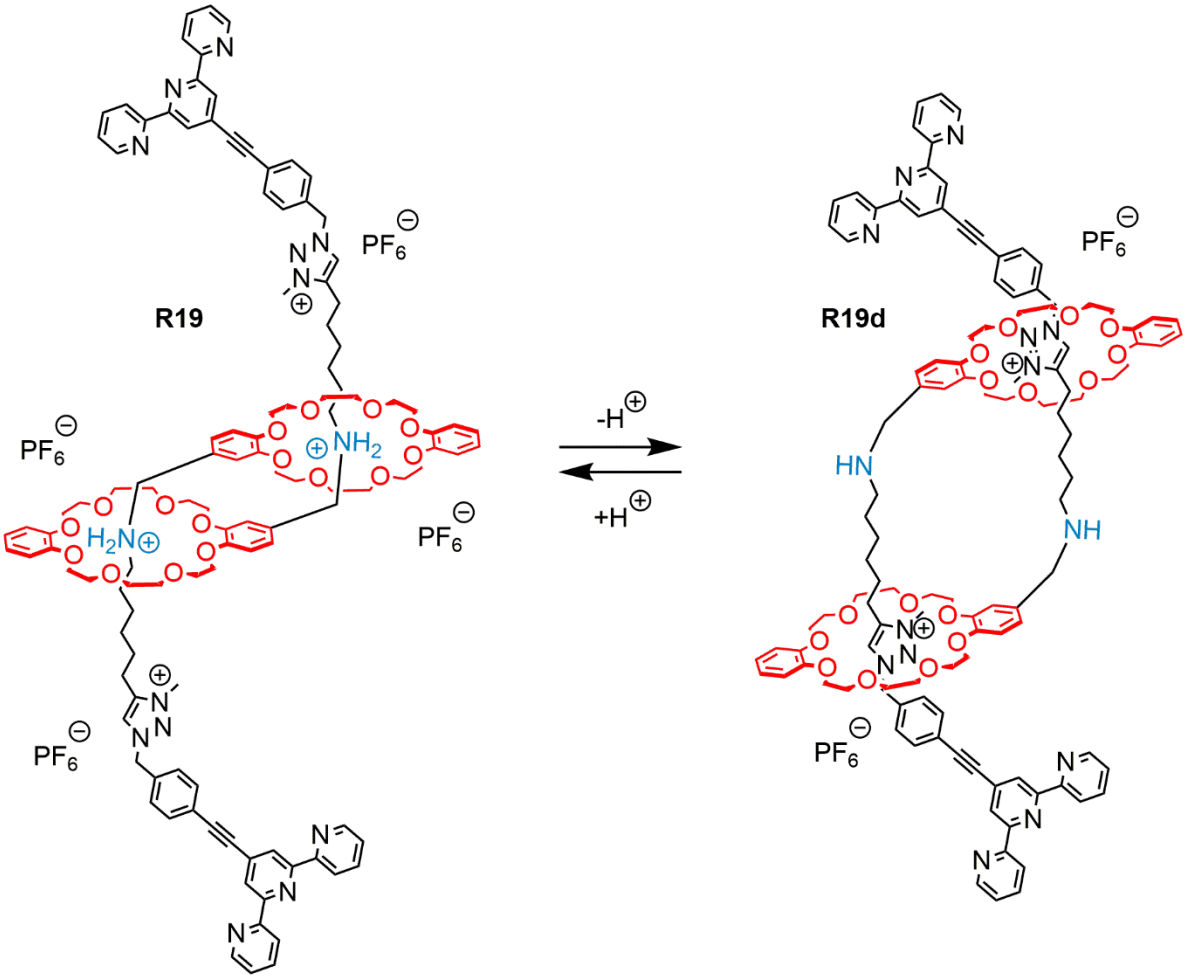

Figure 32: Muscle-like movement in the pH-responsive [c2]daisy chain **R19**.[143]

The examples mentioned so far allow an easy deprotonation of the ammonium station, as there is a second interaction site offered for the crown ether to bind. The acidity of ammonium salts is lowered significantly when it is encircled by a crown ether. This "rotaxane effect" may be explained with kinetic protection of the ammonium by the macrocycle cavity and charge stabilization through hydrogen bonding.[144] Takata and co-workers showed that even though deprotonation or neutralization of ammonium rotaxanes is much harder once no residual binding site is left for the macrocycle, N-acylation protocols can be used to yield stable and neutral crown/ammonium rotaxanes.[144-145] A permanent translocation of the macrocycle is achieved and non-charged molecules enable easier separation, for example on a chiral HPLC,[18, 126] as well as post rotaxanation modifications in general.[146] The higher mobility of the macrocycles in acetylated rotaxanes was used to change the properties of macromolecular [2]rotaxanes.[147]

A strategy for directional threading/dethreading controlled by light was described by Credi and co-workers (Figure 33).[148-149] Here, an azobenzene switch (Figure 33 box), which

changes with >95% yield from the (*E*) to the more bulky (*Z*) isomer upon irradiation with UV light, was attached at the end of an ammonium axle. The non-switchable cyclopentyl pseudo stopper on the other side is less bulky than the azobenzene (*Z*) isomer, but poses a larger threading barrier than the (*E*) isomer. When the axle **A5** and the macrocycle (**DBC8**) are mixed, the axle can thread from both sides, but due to a much higher rate constant the net threading occurs from the azobenzene ((*E*) isomer) side. Subsequent irradiation renders the azobenzene side too bulky and destabilizes the complex. Hence, dethreading proceeds on the cyclopentyl side. Subsequent irradiation with light with another wavelength or thermal relaxation recovers the initial (*E*) isomer, and the directional threading/dethreading cycle can repeat. An analogous axle with two azobenzene substituents in (*Z*,*Z*) configuration turns the assembly into a rotaxane, which is kinetically inert against dethreading.[148]

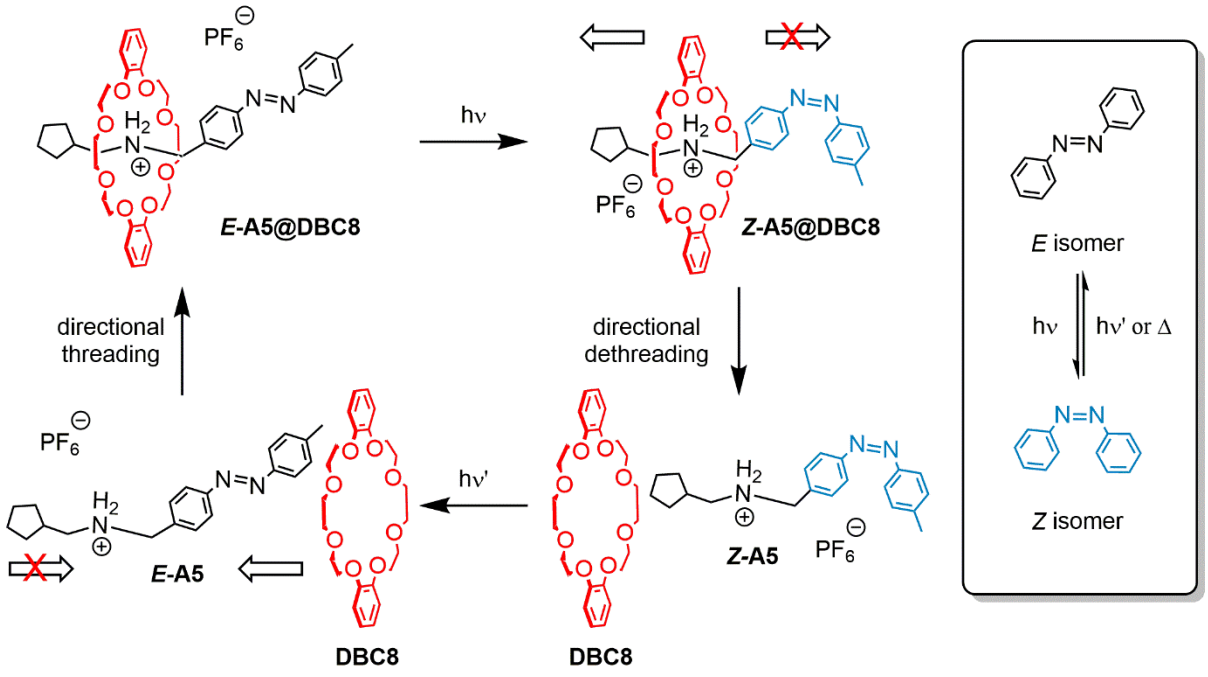

Figure 33: Directional threading and dethreading strategy with a photoswitchable stopper.[148-149]

Another important category, namely redox-driven switches are the most relevant for this thesis and are therefore thoroughly discussed in a separate chapter 2.3.

While rotaxane switches are well-explored, rotaxane based molecular motors that perform work are very rare and hard to realize. In contrast to their macroscopic counterparts, microscopic reversibility must be circumvented. Meaning that reversible forward and backward reactions must not be equal, which is not true for regular bistable rotaxanes. Either an information or energy ratchet mechanism is required to move systems energetically uphill.[5] The two mechanisms are schematically sketched in Figure 34.[5]

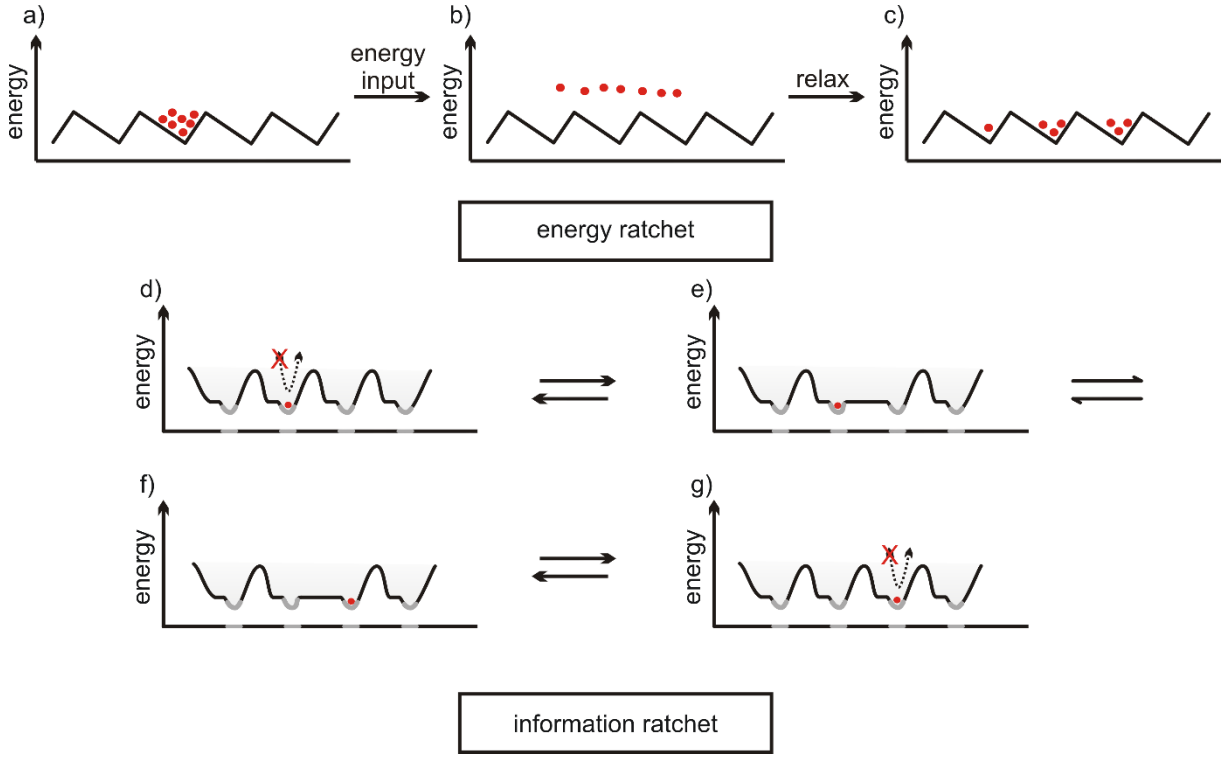

Figure 34: Schematic representation of ratcheting mechanisms. (a) An energy minimum is populated, the energy barriers exceed ambient thermal energy. (b) Energy is provided and thermal diffusion is allowed. (c) The particles relax back into energy minima, due to the asymmetric potential-energy surface a net movement to the right occured compared to the initial state. In (d) and (g) the black dotted arrows indicate the transfer of information about the position of the particle. (e) The barrier next to the particle is lowered. (f) Brownian motion facilitates the movement of the particle resulting in a net direction along with the lowered barriers.[5, 150]

Energy ratchets can be operated by thermal heat or chemical/electric energy. All of them have in common that the position of the particles on the potential-energy surface have no influence on the change or the height of barriers. The particle just diffuses along an asymmetric or tilted potential-energy surface, that changes constantly around them. In contrast, the information ratchet works differently. Depending on the position of the particle the potential-energy surface changes next to it. Barriers remote from the particle are not affected, which requires an information transfer from the particle to the potential-energy surface.

Ideally, machines are operated using only one fuel, which is operator-independent. Alternating addition of fuel and anti-fuel are operator-dependent to close a working cycle.[151] Only one fuel is used in a series of rotary and linear crown/ammonium based molecular motors by Leigh and co-workers.[152] The motor works by an energy ratchet mechanism, in which acid-base cycles proceed by addition of the chemical fuel trichloroacetic acid (Cl_3CCOOH), leaving only $CHCl_3$ and CO_2 as byproducts in base-promoted decarboxylation. The [2]catenane **C1** (Figure 35) consists of a [30]crown-10 host bound to a macrocycle decorated with a base-labile dibenzylammonium and a triazolium binding site. In between the binding sites two bulky blocking groups with orthogonal liabilities are placed, restricting co-conformational change for

the crown ether. Firstly, the base-labile disulfide bond is cleaved and exchanges with disulfides in the solution, also the ammonium site is deprotonated upon addition of excess base. On the contrary, the acid-labile hydrazone remains intact, leaving only clockwise direction for the crown ether to occupy the now preferred binding site (Figure 35 top to bottom). After addition of the fuel trichloroacetic acid, the hydrazone undergoes exchange *via* a transient aldehyde allowing the crown ether to traverse 180° clockwise back to the reprotonated ammonium site (Figure 35 bottom to top). Under these acidic conditions the disulfide is kinetically stable. Another 360° rotation is possible after 17 h, when trichloroacetic acid decomposed to CO_2 and $CHCl_3$ and the solution becomes sufficiently basic for the ammonium site to be deprotonated again. One fuel pulse enables 87% of the crown ethers to rotate 360° in [2]catenane **C1**.

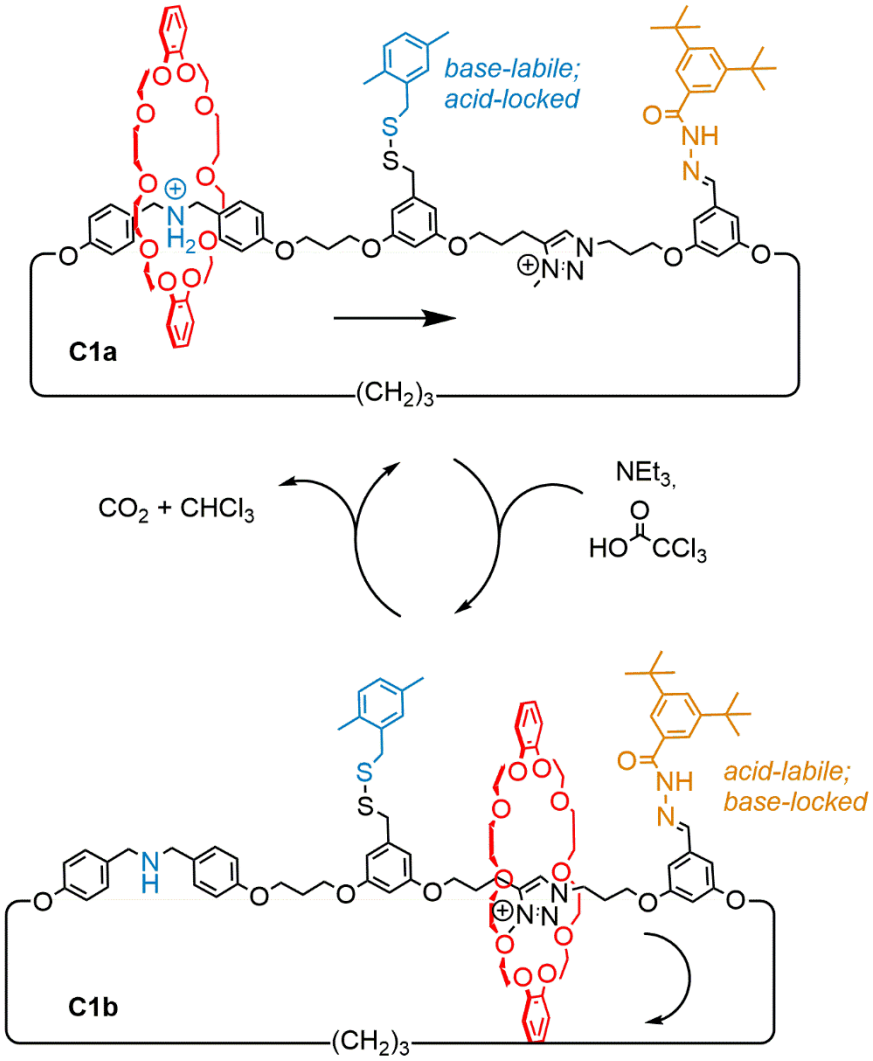

Figure 35: The switching cycle of chemically fueled rotary motor **C1**. Excess of base and the chemical fuel trichloroacetic acid enables a directional 360° rotation of a [30]crown-10 host (red) from the dibenzylammonium to the triazolium site and back.[152]

A very important kind of molecular machine are pumps, as they can transport molecular or ionic cargo along a specific direction while consuming energy. In contrast to channels, the cargo

is transported without concentration gradient or even against it.[153] Hence, molecular pumps in cells are crucial to sustain the life of organisms.[154] These out-of-equilibrium systems maintain their condition by constant decomposition of fuel, mostly adenosine triphosphate (ATP).[155]

Despite the high scientific significance, only few examples of artificial molecular pumps based on rotaxanes are available in literature.[156] In most examples, repetitive sequential addition of chemical fuel,[152, 157] variation of electric potential[158-159] or light[149, 160-162] is needed to keep the system out-of-equilibrium. Only a few months ago, Leigh and co-workers reported a catalysis-driven artificial molecular pump.[163] The information ratchet pumps crown ether macrocycles from solution onto a molecular axle. In contrast to earlier crown ether containing molecular machines, no permanently charged nitrogen species are involved. Instead, the formation of [2]rotaxanes from 24-crown-8 **C8**, an amine and several different electrophiles such as Fmoc-Cl in toluene was studied in a preceding work[122] and applied for the operation of this molecular pump.

The structure and operation cycle of a molecular pump is shown in Figure 36. A carbamate (blue moiety) is formed within the crown ether cavity during the first step of the cycle. After the [2]rotaxane is formed, the macrocycle (red) traverses over the trifluoromethyl ‘speed bump’ (orange) to the energetically favored triazole part of the axle **A6**. Once the macrocycle does not kinetically protect the carbamate anymore, base-catalyzed decomposition takes over. Afterwards, the free amine reacts again with Fmoc-electrophile **13**, preferably within the cavity of another crown ether, while the trifluoromethyl ‘speed bump’ acts as a bottleneck for dethreading of the first macrocycle. Thus, a [3]rotaxane is formed. Finally, it could be shown that up to three macrocycles can be pumped onto the axle completing the [4]rotaxane **R20**, as long as fuel in form of Fmoc-electrophiles **13** is provided. Even though decomposition of the carbamate is much slower when protected by a crown ether, it will occur eventually. When the bulky Fmoc group is not present at the axle terminus anymore and no new electrophile is available for the amine, all of the pumped macrocycles diffuse back into bulk solution restoring the thermodynamic equilibrium over time.

The delicate interplay of the trifluoromethyl ‘speed bump’ dethreading barrier and different reaction speeds, depending on the macrocycle position, enables this dissipative information ratchet mechanism.

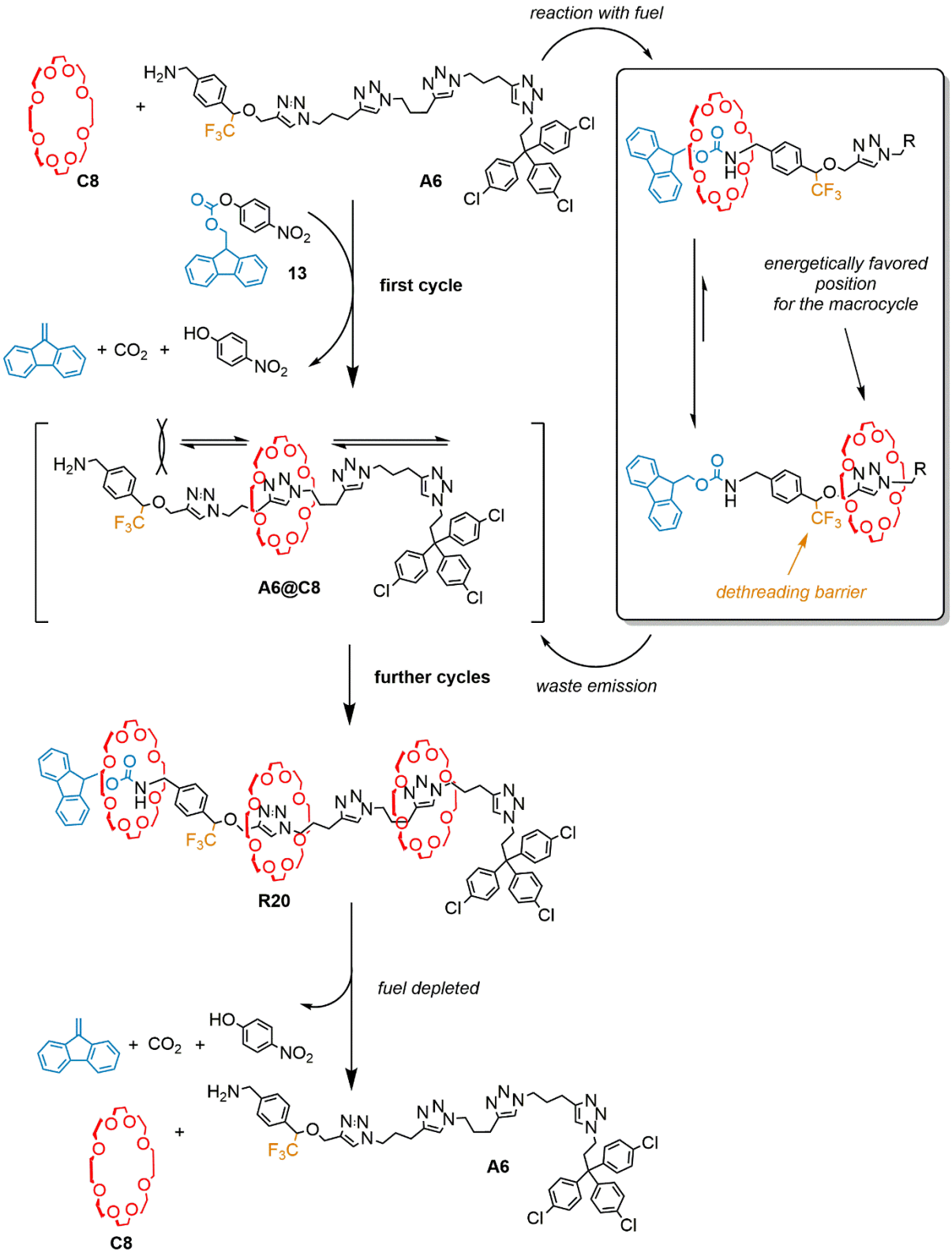

Figure 36: Structure and operation of a catalysis-driven molecular pump by Leigh and co-workers.[163] In the first cycle, a carbamate is formed from the amine **A6** and the Fmoc-electrophile **13** inside of the **C8** cavity. After shuttling of **C8** to the energetically favored triazole, the carbamate is cleaved in the basic solution. The cycle is repeated up to three times as long as the fuel **13** is present in solution.

2.3 Supramolecular Electrochemistry

Electrochemistry is a powerful tool used by organic, inorganic and physical chemists[164-167] to manipulate reactivities and gain insights into physicochemical processes and properties of the reactant species under investigation. A subtopic is supramolecular electrochemistry,[168-169] which is widely using non-invasive methods to determine and manipulate inter- and intramolecular interactions. Hence, manyfold host-guest complexes containing redox-active moieties are studied by electrochemical methods.[63]

For a general *n* electron transfer process:

$$Ox + ne^- \leftrightarrow Red \qquad (6)$$

Where *Ox* and *Red* represent the oxidized and reduced species of the redox couple the Nernst equation (Equation 7)[170] defines the thermodynamic potential (*E*):

$$E = E_0 + \frac{RT}{nF}\ln\frac{a_{Ox}}{a_{Red}} = E_0 + 2.3026\,\frac{RT}{nF}\log_{10}\frac{a_{Ox}}{a_{Red}} \qquad (7)$$

where E_0 is the potential under standard conditions, *R* is the gas constant, *F* is Faraday's constant, *T* is the temperature in Kelvin and *n* the number of transferred electrons. In dilute solutions the concentrations of the oxidized and reduced species are used instead of the activities *a*.

The basic kinetic description of electrochemical reactions in absence of mass transport limitations is named after John Alfred Valentine Butler[171] and Max Volmer[172] (Butler-Volmer equation).[168] It describes the relation between electrical exchange current at the electrode *i* and electrode potential *E* (Equation 8):

$$i = i_0 \cdot \left\{\exp\left[\frac{\alpha_a zF}{RT}\,(E - E_{eq})\right] - \exp\left[-\frac{\alpha_c zF}{RT}\,(E - E_{eq})\right]\right\} \qquad (8)$$

where E_{eq} is the potential under equilibrium conditions, *R* is the gas constant, *F* is Faraday's constant, *T* is the temperature in Kelvin and *z* the number of electrons involved in the electrode reaction. The cathodic and anodic charge transfer coefficients α_c and α_o are dimensionless. The relation between the left term (anodic component) and the right term (cathodic component) determines the sign of the current and therefore the direction and rate at which the

electrochemical reaction proceeds. As this is a discussion of unimolecular single step reactions, no additional electrode processes are considered.

In the context of supramolecular chemistry, we generally consider a host-guest equilibrium between a redox-active macrocycle (**M**), guest (**G**) and the corresponding 1:1 complex **M@G** with an association constant K_1 as shown in Figure 37. Upon one electron oxidation or reduction to $\mathbf{M}^{\pm 1}$ the affinity towards **G** is either increased or lowered, therefore a new equilibrium between $\mathbf{M}^{\pm 1}$, **G** and $\mathbf{M}^{\pm 1}$**@G** with the constant K_2 arises. The oxidation/reduction potentials of **M** and **M@G** ($E_{1/2}{}^{1}$ and $E_{1/2}{}^{1*}$) are in relation to each other, i.e. when K_1 is known and both potentials $E_{1/2}$ are measured, K_2 can be calculated or at least estimated (Equation 9). Sometimes electrochemical methods are the only way to determine these constants.

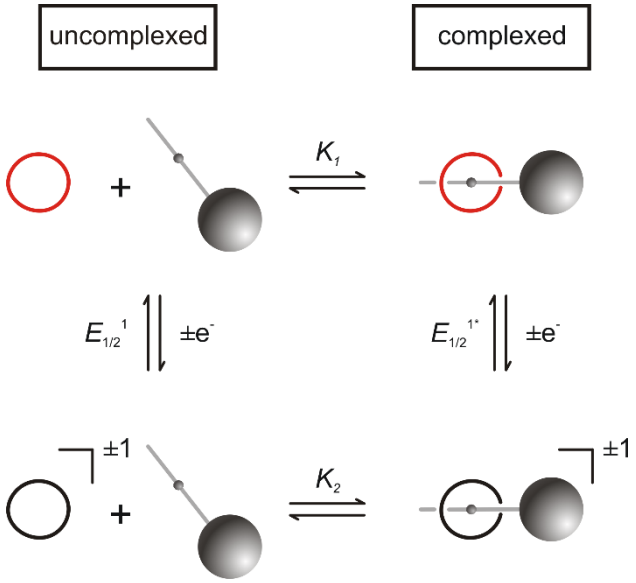

Figure 37: A square scheme to illustrate changing binding equilibria with a redox-switchable macrocycle.[168]

$$\Delta G = -zF\Delta E_{1/2} \qquad (9)$$

The concept also analogously applies for redox-active guests, or complexes where both components are redox-active. Coupled mechanisms with (ir)reversible chemical transformations and/or additional electron transfers will lead to arbitrarily complicated square schemes.

2.3.1 Analytical Methods of Supramolecular Electrochemistry

The most commonly used method to characterize redox-active molecules is voltammetry. Here, a voltage is varied between two electrodes and the corresponding amperage is recorded. In cyclic voltammetry (CV) the voltage is changed linearly back and forth in a circular fashion, whereas in differential pulse voltammetry (DPV) pulses of potential steps are induced and the differential current after the pulse is recorded (Figure 38).[168-169]

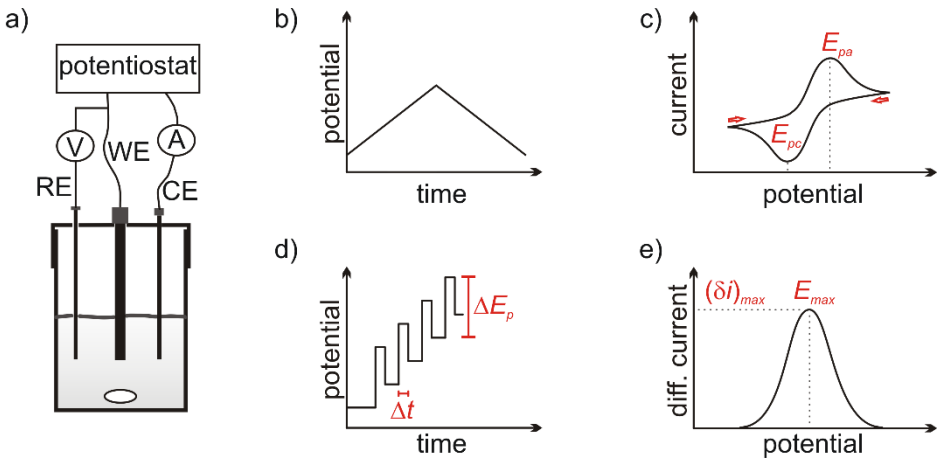

Figure 38: (a) Electrochemical setup for CV and DPV experiments in organic solvents. (b) Potential-time excitation setting for a CV experiment. (c) Resulting cyclic voltammogram for a reversible redox reaction with E_{pa} and E_{pc} as the peak potentials of the anodic and cathodic scans, respectively. (d) Potential-time excitation setting for a DPV experiment with ΔEp and Δt as the potential step and interval time between current measurements, respectively.[168]

The inexpensive voltammetry setup comprises of three electrodes in the analyte solution, connected to a potentiostat (Figure 38a). The voltage is varied between the working electrode (WE) and the counter electrode (CE). In order to measure the voltage-amperage curve, a reference electrode (RE) is introduced. The RE allows the correct determination of the voltage in a second circuit with the WE, because voltage and current cannot be measured simultaneously without interfering with each other. In a typical CV experiment the applied voltage is varied linearly over time within a preset potential window with a certain scan rate (Figure 38b). The corresponding voltammogram, often perceived as duck-shaped, reveals the peak potentials (E_{pa} and E_{pc}) of the oxidation and reduction of the analyte in solution (Figure 38c).

Although CV is already a powerful technique, DPV as a complementary method can add value to the analytic toolbox by having a lower detection limit (10^{-4} down to 10^{-8} M analyte) compared to CV. Also, detection of peak currents is easier as well as resolution of redox processes that have close E_0 values. Here, after each pulse the potential returns to a value slightly higher (anodic scan) or lower (cathodic scan) than before. Two current values are

measured one before and one at the potential peak of the pulse, giving rise to the difference between the currents δi corresponding to the applied potential (Figure 38d). The differential pulse voltammogram (Figure 38e) is the plot of δi against the potential E. Figure 39a shows how the peak potentials i_{pa} and i_{pc} can be determined, which is relevant to determine the reversibility of the electrochemical reaction. In non-reversible electron transfer reactions or coupled chemical reactions after oxidation/reduction peak shapes like in Figure 39b are observed. For example for a coupled electron transfer and (ir)reversible chemical reaction mechanism ($EC_{i/r}$). Many different kinds of these coupled electrochemical reaction mechanisms are feasible, such as EE, $EC_{i/r}E$, $EEC_{i/r}$ and so on.

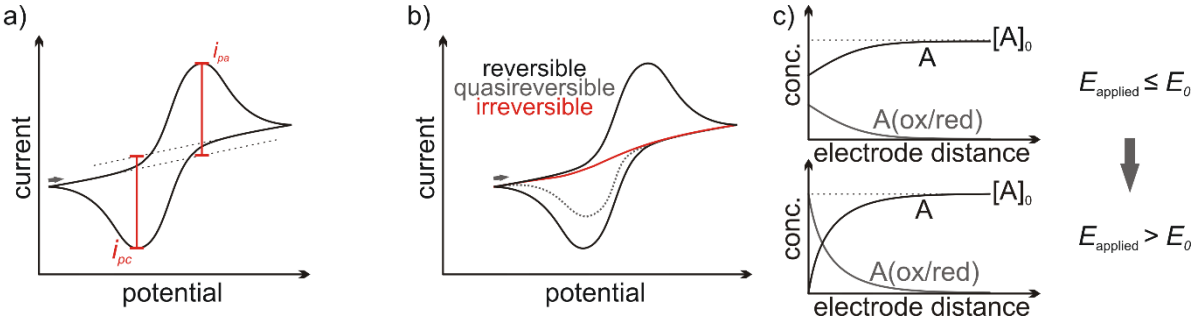

Figure 39: (a) Determination of peak potentials i_{pa} and i_{pc} from a CV experiment. (b) Voltammogram of a reversible (black), quasireversible (dottet grey) and irreversible (red) redox process. (c) Concentration of analyte (A) and oxidized or reduced analyte (A(ox/red)) as a function of the distance to the electrode, at the beginning ($E_{applied} \leq E_0$) and during oxidation/reduction ($E_{applied} > E_0$).

When a certain potential is reached during the CV experiment, the concentration of the analyte A changes depending on the distance to the electrode and the mobility of the analyte A until the analyte A is depleted and only oxidized or reduced species A(ox/red) is left (Figure 39c). The interfacial region at the surface of the electrode, which behaves as a capacitor working against the applied potential is classically termed electrical double layer.[173]

Changes in the shape of the voltammogram at different scan rates disclose the nature of the redox-process. For a reversible diffusion limited process peak potential i_p is defined by the Randles-Ševčík equation (Equation 9):

$$i_p = 0.446\, nFAC \left(\frac{nF\nu D}{RT}\right)^{1/2} \qquad (9)$$

where A is the working electrode surface, C is the concentration and D is the diffusion coefficient of the analyte, ν is the scan rate, R is the gas constant, F is Faraday's constant, T is the temperature in Kelvin and n the number of electrons involved in the electrode reaction. Hence, i_p and the square root of the scan rate ($\nu^{1/2}$) are linearly proportional. The veracity of this

relation for the analyte can be tested easily by collecting a data set at different scan rates. Additionally, diffusion coefficients of analytes can be determined using this equation.

Application-wise, many different geometries and materials of electrodes are commercially available. Working electrodes (WEs) are mostly made of glassy carbon or platinum/gold, because of their high conductivity and chemical inertness. When measuring in organic solvents, glassy carbon disk electrodes are used for most purposes.[174] Reference electrodes (REs) such as Ag/AgCl electrode, standard calomel electrode (SCE) or standard hydrogen electrode (SHE) are used in aqueous solutions. However, in organic solvents with low polarity a silver wire can only act as pseudo-reference since no ion exchange with the solution occurs. For determining the correct potential adding internal references such as the stable ferrocene/ferrocenium couple[175] are necessary. Internal references are redox couples with tabulated redox potentials that do not interfere with the analyte. Counter electrodes are usually made of platinum wire or mesh. Again, high conductivity and chemical robustness are the requirements.

To keep a high conductivity and inhibit migration of the analyte under the influence of the electric field, a 100-fold excess of an electrolyte is typically added to the analyte solution. Then, the charge migration is performed only by the dissociated inert electrolyte ions. A wide range of salts can be used as supporting electrolytes, as long as high solubility, electrochemical inertness in a wide potential window and highest purity are established. In supramolecular electrochemistry, tetrabutylammonium hexafluorophosphate is the most common conducting salt in use, due to the competitive price and availability in high purity.[168] In the recent years new weakly coordinating anions such as $BArF_{24}^-$ (tetrakis(3,5-bis(trifluoromethyl)-phenyl)borate) gained more interest, particularly for their exceptional stabilization of highly electrophilic cations.[67, 176]

The requirement of the solvent is a sufficiently wide potential window, in which the analyte is well solvated and the solvent does not get oxidized or reduced. Apart from water, dimethylformamide (DMF), acetonitrile (ACN) and very low polar solvents such as methylene chloride or 1,2-dichloroethane are used.[177]

2.3.2 Redox-Switchable Moieties

Along with the development of electrochemical methods, inorganic and organic redox-switchable molecules and complexes were synthesized and investigated. A selection of

supramolecular electrochemical workhorses and their respective redox states are displayed in Figure 40.

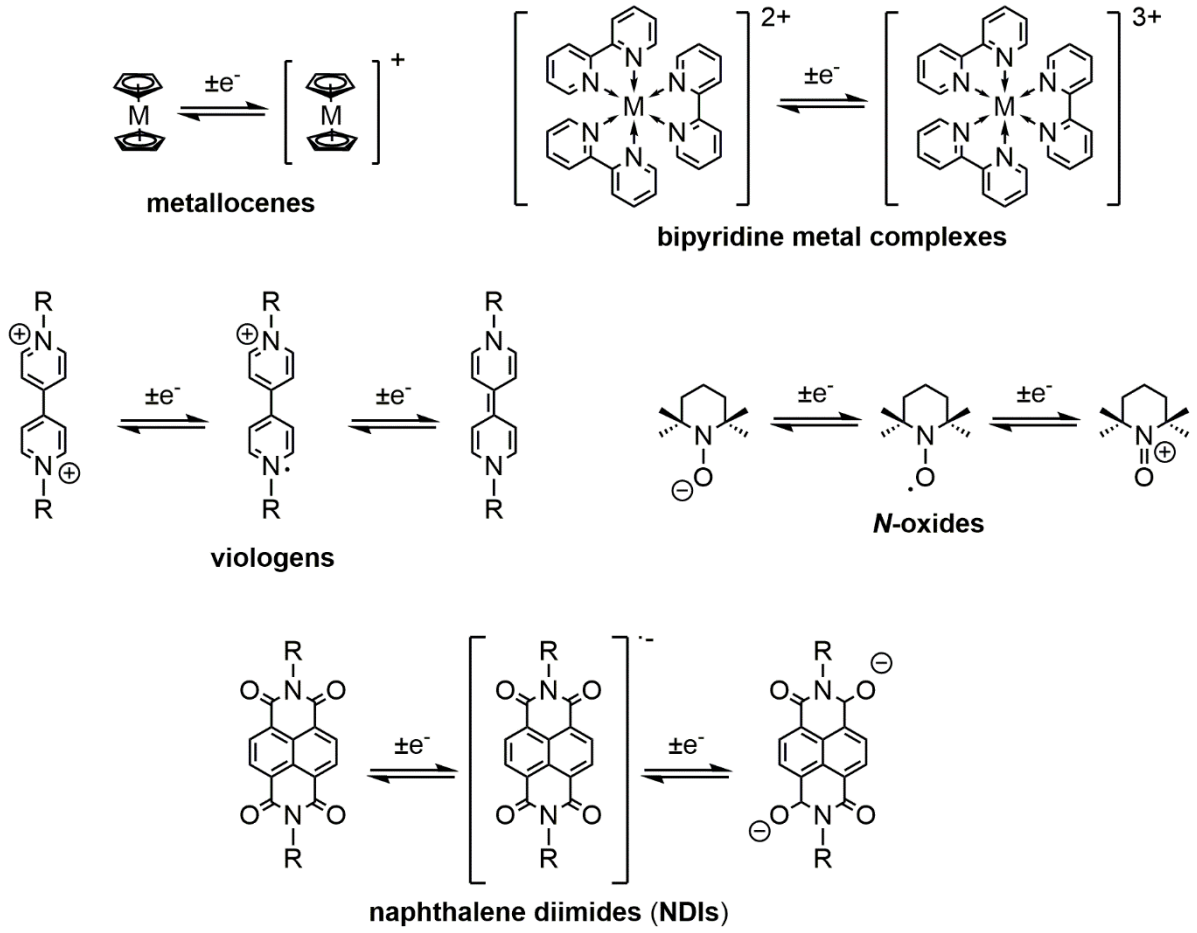

Figure 40: Common examples of reversibly redox-switchable moieties: metallocenes,[178] bipyridine metal complexes,[179] viologens,[180] *N*-oxides,[181] naphthalene diimides (NDIs)[182] and their respective stable redox states.

The common feature for the use in supramolecular electrochemistry are sufficiently stable electrogenerated species. To render the analysis feasible, the processes under investigation should be addressable within the laboratory time scale (minutes to hours) and the potential range of -3.0 - 2.0 V vs. SCE electrode.[183]

The intriguing spectroelectric properties of naphthalene diimides (**NDIs**) were exploited to construct self-assembled donor-acceptor complexes and sensors with an electrochemical probe.[184-185] Structurally **NDIs** are planar molecules with two electron withdrawing imide groups connected to a naphthalene core. The electron poor **NDIs** feature two reversible one-electron reductions (-1.10 V and -1.51 V vs. $FeCp_2/FeCp_2^+$),[186] high thermal and chemical stability, and broad synthetic chemistry. Therefore, NDIs are especially suited building blocks for the construction of complex supramolecular architectures.[187]

The most relevant building block for this thesis is tetrathiafulvalene (**TTF**), which is a well-studied heterocyclic structure motif for the development of electrically conducting materials, also called *organic metals*.[188] It can undergo two reversible one-electron oxidations at relatively low potentials (-74 mV and 311 mV vs. $FeCp_2/FeCp_2^+$).[189] The pro-aromatic 14π-electron molecules' reversible oxidations to $\mathbf{TTF}^{\cdot+}$ and $\mathbf{TTF}^{2+}$ are accompanied by conformational changes (Figure 41).[188, 190] Neutral **TTF** has a boat-shaped structure, whereas $\mathbf{TTF}^{\cdot+}$ is planar and appreciated for cofacial intermolecular stacking and radical pairing.[191-193] Finally, $\mathbf{TTF}^{2+}$ is twisted along the central bond. The stability of the radical cation $\mathbf{TTF}^{\cdot+}$ and the dication $\mathbf{TTF}^{2+}$ can be rationalized by the aromatic character of 1,3-dithiolium cations according to the Hückel rule. Each oxidation state shows distinct bands in UV/Vis spectra and can even be differentiated by the naked eye.[194] Additionally, oxidation decreases the π-electron-donor ability and increases the hydrophilicity. However, the central double bond is prone to electrophilic attacks that leads to a loss of the reversibility of oxidation, especially in acidic media.[189]

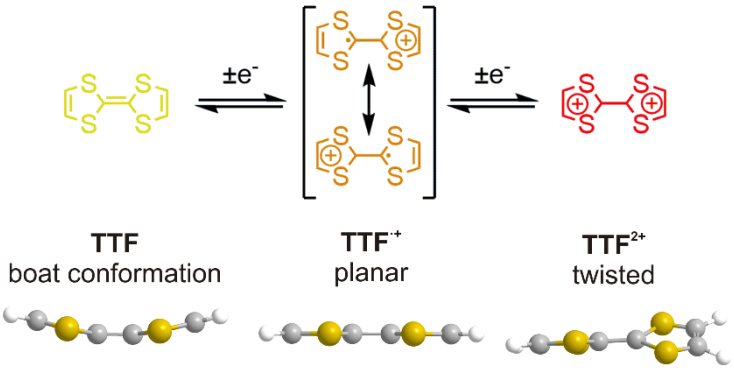

Figure 41: Oxidation states of **TTF**, which are accompanied by different conformational states. Taken from Tetrathiafulvalene: the advent of organic metals.[188]

TTF is known to form donor-acceptor complexes[195] with π-electron deficient molecules such as tetracyanoquinodimethane (**TCNQ**).[196] Intermolecular interactions in different oxidation states, mixed-valence- and radical cation dimer formation are also noticeable features that provoke the researchers' interest.[194, 197-198] For example, linking TTF-moieties using different spacers alter the spectroelectrochemical properties.[199] Furthermore, the versatile chemistry of **TTF** enabled material scientists to produce a plethora of TTF-derived structures.[200-201] Especially procedures for using the 1,3-dithiole-2-thione-4,5-dithiolate (**DMIT**) moiety,[202] cyanoethyl-protecting groups,[203] phosphite-mediated heterocoupling,[204-205] lithiated TTF[206] and further commercialization aided the dissemination of TTF-derivatives into synthetic organic contexts.

A strategy to incorporate **TTF** into supramolecular systems is the incorporation into macrocycles.[207] Especially sulfur-bridged crown ether derivatives combine the good solubility and ability to host cationic guests of crown ethers with the electrochemical switchability of TTF-moieties. A selection of mono- and divalent TTF-containing macrocycles with different cavity sizes is shown in Figure 42.

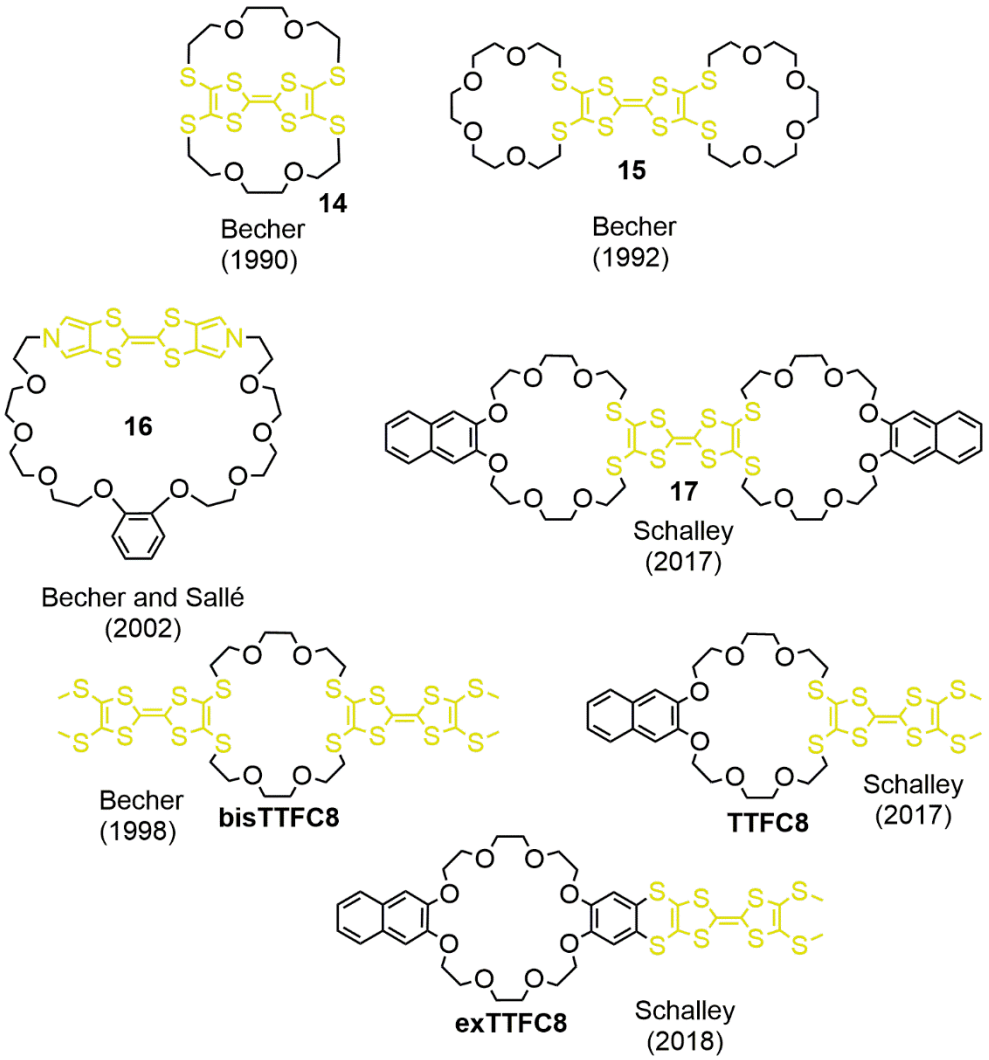

Figure 42: Selected examples of TTF-annelated crown ethers.[17, 208-213]

The examples with smaller crown ether ring sizes of ≤6 chalcogens **14** and **15** were used as sensors for alkali metal cations. Upon addition of the metal salts the first oxidation potential shifted anodically by up to 80 mV in acetonitrile, but required a large excess (250 equiv.) of the salt.[213] Salts with doubly charged metal cations such as Ba^{2+} or Pb^{2+} showed binding constants of ~500 M^{-1} to bis(pyrrolo)tetrathiafulvalene macrocycles. Again, charge repulsion of the cation to the oxidized TTF led to an anodic shift of 140 mV for the first oxidation.[207, 214-215]

To accommodate an ammonium guest inside of the crown ether cavity, a minimum of 7 chalcogens with a total of ≥21 atoms in the ring is necessary.[93] Because of the low

association constants of sulfur-containing crown ethers (thiacrowns) towards ammonium guests,[216] these compounds appeared unattractive for host-guest chemistry beyond metal ion sensing for over a decade. Along with the rise of weakly coordinating anions, thiacrowns became feasible hosts for stimuli responsive MIMs.[68] The macrocycles **17**,[210] **TTFC8**[17, 217] and **exTTFC8**[211] are examples from our group that were successfully incorporated into redox-switchable MIMs.

2.3.3 Redox-Switchable MIMs

Addressing a specific molecular building block and following intramolecular interactions and (co-)conformational changes after switching is a challenging task. Therefore, the controlled and waste-free electrochemical stimulus is gladly used by supramolecular chemists to investigate the kinetic and thermodynamic properties of mechanically interlocked molecular switches and motors.[141, 218] The following examples are merely a shortlist of mechanically interlocked electrochemical switches relevant for this thesis and will not provide a comprehensive view on the field. For a wider overview the consultation of relevant reviews is advised.[63, 218-220]

Although TTF-decorated macrocycles were used in host-guest complexes,[201, 207] examples in mechanically interlocked assemblies are still considerably sporadic. A series of crown/ammonium based redox-switchable rotaxanes with TTF-decorated crown ethers highlight the possibilities of this compound class.[17, 210-211, 217, 221]

The first example for rotaxanes with **TTFC8** as host for ammonium guests with $BArF_{24}^-$ anions was published in 2017.[17] There, the impact of the mechanical bond on the redox-switching of **TTFC8** was analyzed. Using $BArF_{24}^-$ as counterion raised the association constant to $(5.9 \pm 0.6)\ 10^5\ M^{-1}$, which is remarkably high for such crown/ammonium complexes.[61] Upon oxidation to $\mathbf{TTFC8^{2+}}$ the wheel expelled the ammonium guest **A6** from the cavity, whereas the charge repulsion of the singly oxidized $\mathbf{TTFC8^{\cdot+}}$ was not sufficient to achieve the same effect (Figure 43 top). In the mechanically interlocked complex **R21**, a rise of oxidation potentials compared to the free wheel is observed (**TTFC8** ($E^1_{1/2}$ = 610 mV, $E^2_{1/2}$ = 1060 mV vs. $FeCp_2^{*(+/0)}$) compared to **R21** ($E^1_{1/2}$ = 740 mV, $E^2_{1/2}$ = 1420 mV vs. $FeCp_2^{*(+/0)}$ in dichloromethane using tetrabutylammonium $BArF_{24}$ as electrolyte). The potential difference for the second oxidation ($\Delta E^2_{1/2}$ = 360 mV) is sufficiently high to overcome the binding energy determined by ITC (35 kJ mol^{-1} > 32.9 kJ mol^{-1}) Additionally, comparing fluorescence spectra

of axle **A6** and the rotaxane **R21** before and after oxidation suggest, that the macrocycle moves away from the stopper restoring the fluorescence band of the anthracene (Figure 43 bottom).

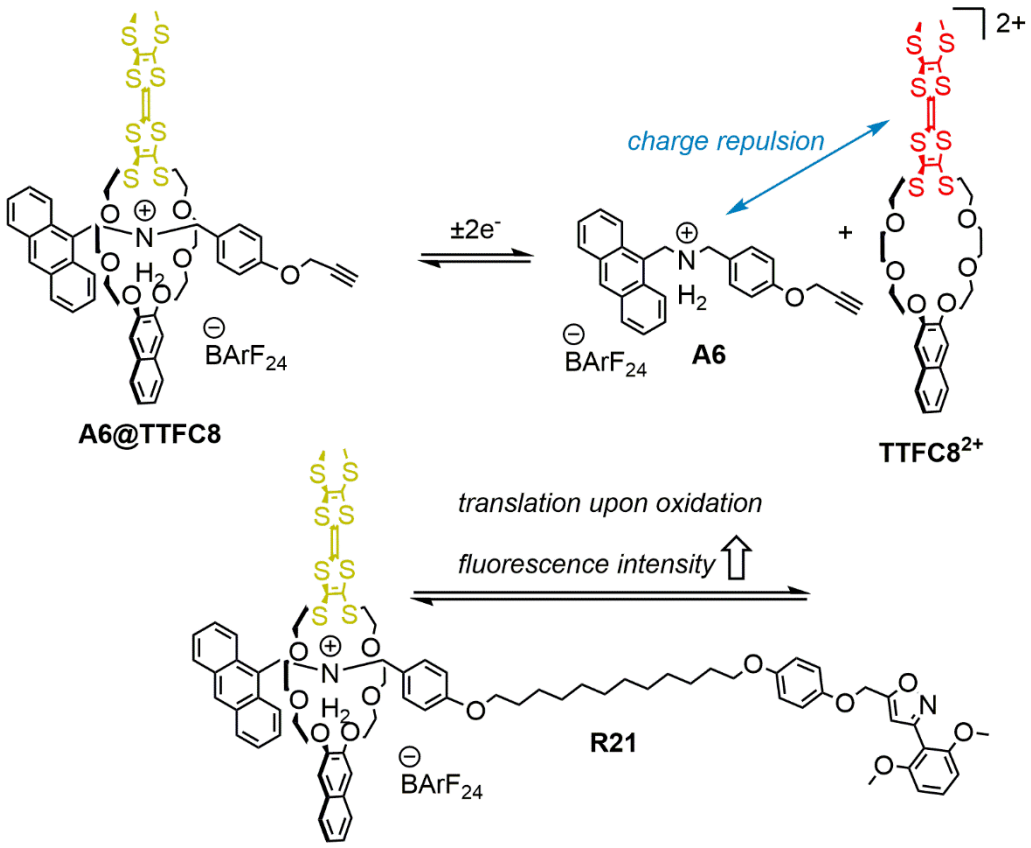

Figure 43: Impact of mechanical bonding on the redox-switching of a TTF-decorated crown ether macrocycle.[17] Oxidation induces expulsion of the ammonium guest **A6**, whereas in the [2]rotaxane **R21** a shuttling is induced upon oxidation.

In addition to macrocycle/axle interactions, a recent example reports remarkable results regarding intramolecular TTF/TTF-interactions of same macrocycles in a homo[4]rotaxane **R22** (Figure 44).[217] The three **TTFC8**, which are interlocked on a symmetrical axle, contracted upon one or three electron oxidation (**R22b)**. The contraction is caused by a mixed-valence interaction or radical cation pairing and is a common feature of covalently bound or physically constrained TTF moieties.[191, 222-223] Further oxidation to **TTFC8^{2+}** results in expansion of the macrocycles to reduce charge repulsion between TTF moieties and additionally the ammonium sites (Figure 44). In contrast, control compounds with spatially separated macrocycles did not exhibit those macrocycle interactions or conformational changes. In fact, contraction and expansion of wheels along an axle in a rotaxane was proposed in promising theoretical works about piston-type motor models to harness the (co-)conformational change to produce power.[224-226]

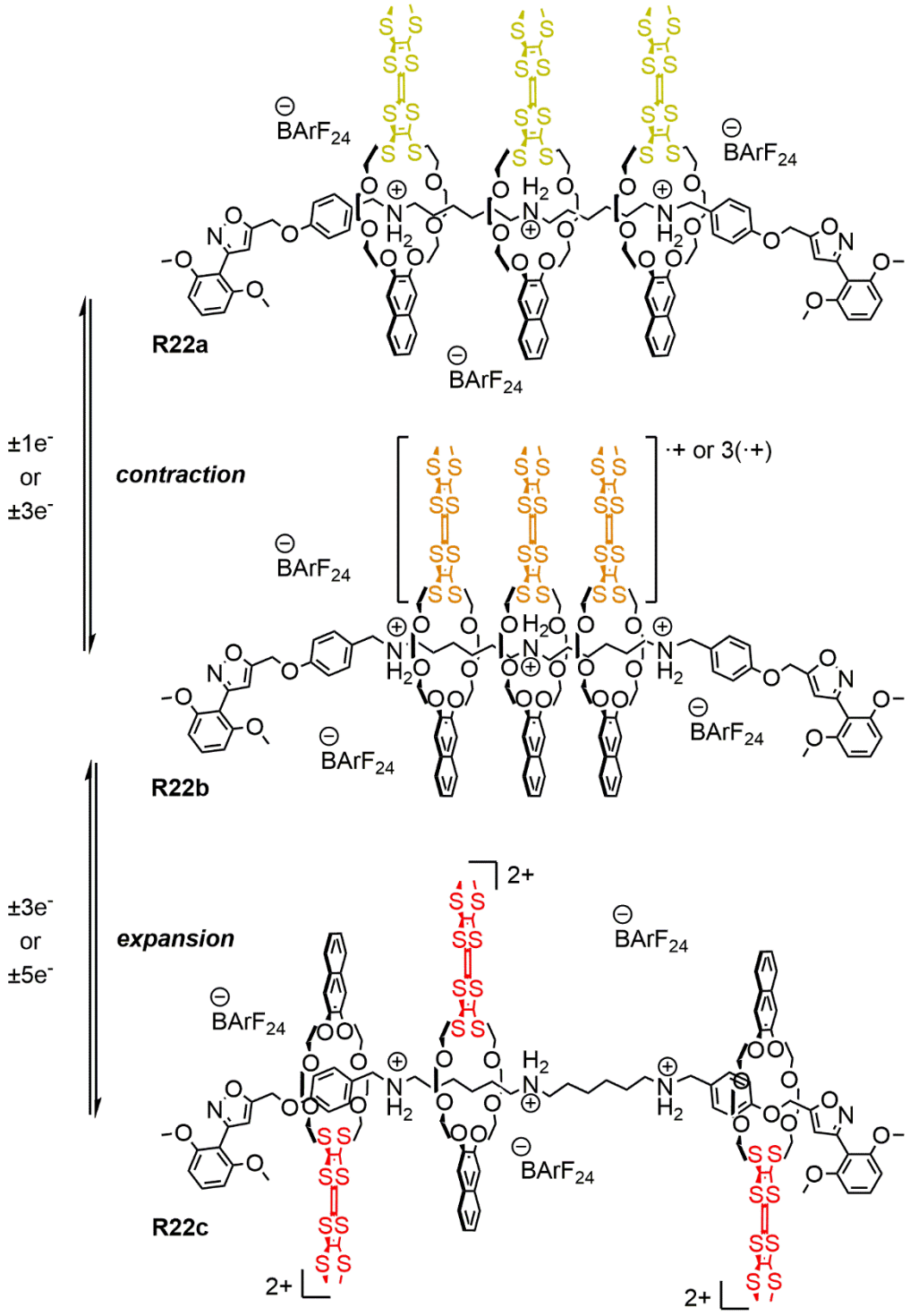

Figure 44: Contraction and expansion upon oxidation of homo[4]rotaxane **R22** with TTF-decorated crown ether macrocycles.[19, 217]

Crown/ammonium self-assembly can also be used to construct non-covalently linked donor-acceptor complexes with defined arrangements. The divalent TTF-decorated crown **17** interacts with an NDI building block on the guest (Figure 45).[210] The cofacial arrangement **R23** showed five reversible redox-states from 0 to +4 net charges, where the neutral forms of NDI and TTF

are stabilized in respect to their non-complexed counterparts. Also, the assembly features a solvatochromic[227] intramolecular charge transfer (ICT) band in the neutral state.

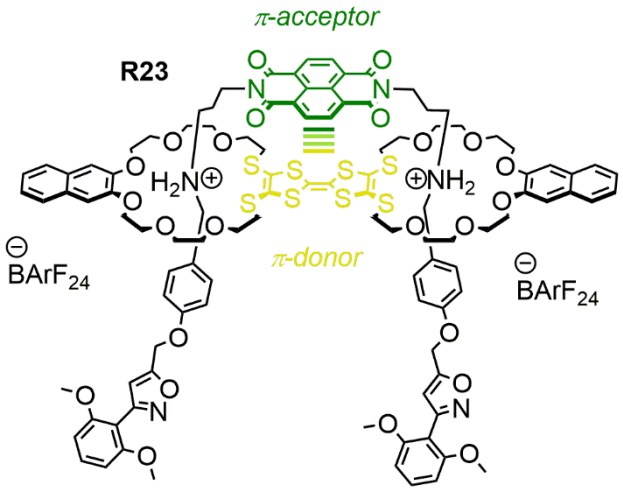

Figure 45: A donor-acceptor [2]rotaxane with cofacial arrangement of NDI and TTF.[19, 210]

Arguably the most sophisticated artificial electro-switchable molecular machines so far are pumps.[228] A series of progressing examples were published by Stoddart and co-workers[157-159, 229] where cyclobis(paraquat-*p*-phenylene) (**CBPQT^{4+}**) wheels are pumped away from concentration equilibrium either by chemical reduction and oxidation or an oscillating applied potential.

The minimalistic design[157] features a 3,5-dimethylpyridinium, a viologen, an isopropylphenyl group, a triazole and the diisopropylphenyl stopper (Figure 46). The pump is operated by reducing a solution of **CBPQT^{4+}** wheels and **A7^{3+}** axles in acetonitrile. The initial charge repulsion of the wheel and the viologen on the axle is flipped utilizing the attractive radical-radical pimerization.[230-231] In addition, the charge repulsion of the wheel and the 3,5-dimethylpyridinium is attenuated, allowing **CBPQT^{2+}** wheel to complex the reduced viologen on the axle. After reoxidation, the treaded **CBPQT^{4+}** wheel is pushed away from the viologen, due to the restored charge repulsion and the diminished attractive interaction. Now, the direction of the 3,5-dimethylpyridinium is less favorable than the steric 'speed bump' in form of an isopropylphenyl moiety. Relaxation of this metastable co-conformation occurs by traversing the **CBPQT^{4+}** wheel over the 'speed bump' towards the long oligomethylene chain that acts as a catchment region. Subsequent reduction leads to threading of another **CBPQT^{4+}** wheel. Dethreading of the first wheel is inhibited by the steric bulk of the isopropylphenyl and a faster threading of another **CBPQT^{2+}** wheel that complexes the reduced viologen. Up to two wheels could be pumped onto the axle, affording a [3]rotaxane in the example described (Figure 46).[157]

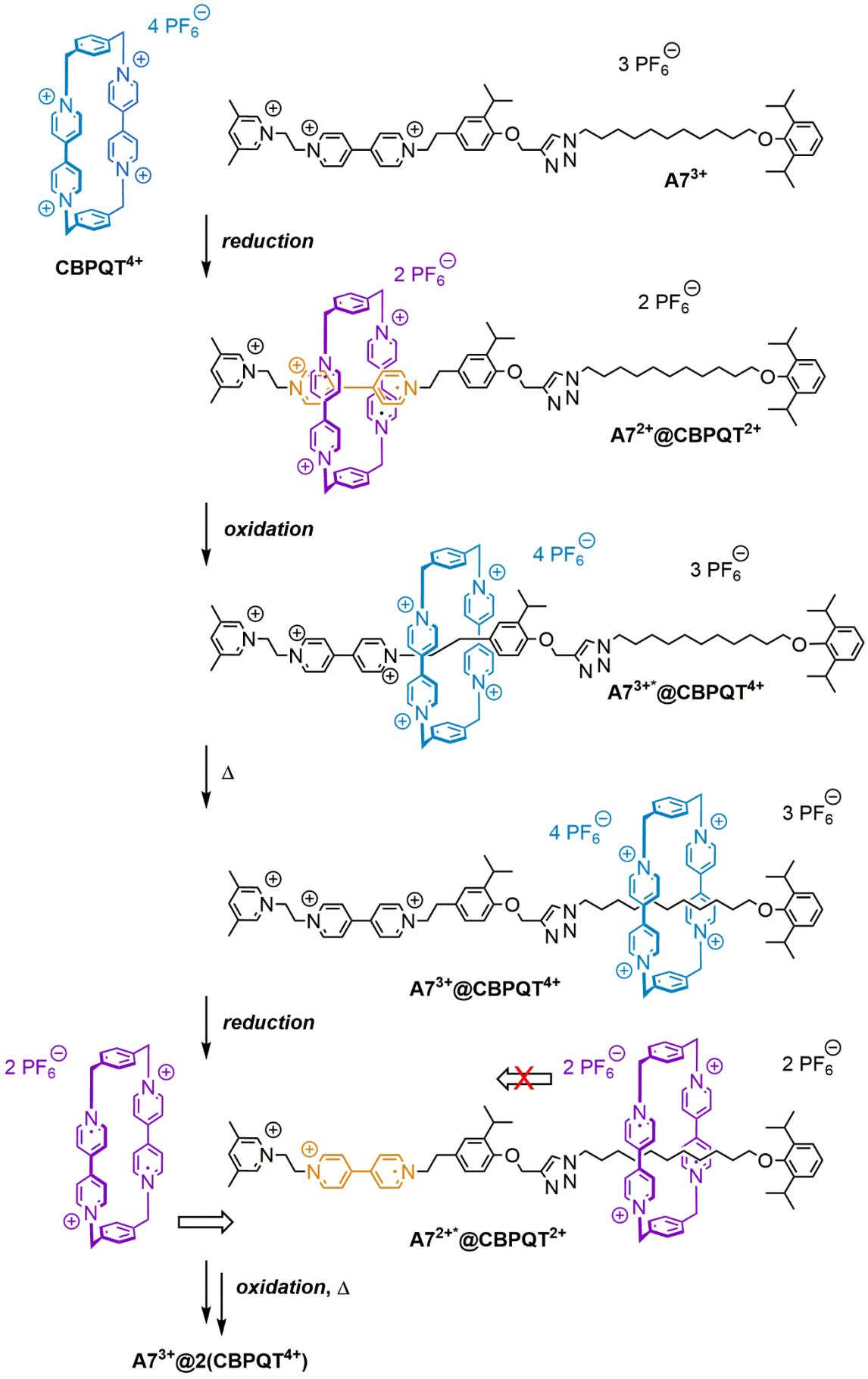

Figure 46: An artificial electrochemically operated molecular pump.[157]

In summary, redox-switchable MIMs using TTF-decorated crown ethers or the cyclobis(paraquat-*p*-phenylene) macrocycle are capable of large amplitude motion and utilized in for example molecular shuttles. Even pumping macrocycles out of the bulk solution onto an axle can be achieved. Also, spatial confinement of donor-acceptor moieties hold in place by a mechanical bond, gives rise to emergent switchable optical properties and can stabilize or destabilize certain oxidation states.

The development of redox-switchable MIMs has come a long way. However, the harnessing of motion and changing optical properties for the use in macroscopic devices remains a challenging task, that will lead to exciting new technologies.[15]

3 Summarized Results

3.1 Summarized Work

The publications summarized in this chapter are the result of collaborations with the groups of Arne Lützen (Friedrich-Wilhelms-Universität Bonn), Kari Rissanen (University of Jyväskylä), Beate Paulus (Freie Universität Berlin) and Biprajit Sarkar (Universität Stuttgart). The four publications can be divided into three main projects, that deepen the necessary knowledge for the construction of artificial molecular switches and machines. By focusing on different aspects in the design and using the same host-guest motif, the impact of each modification was investigated (Figure 47).

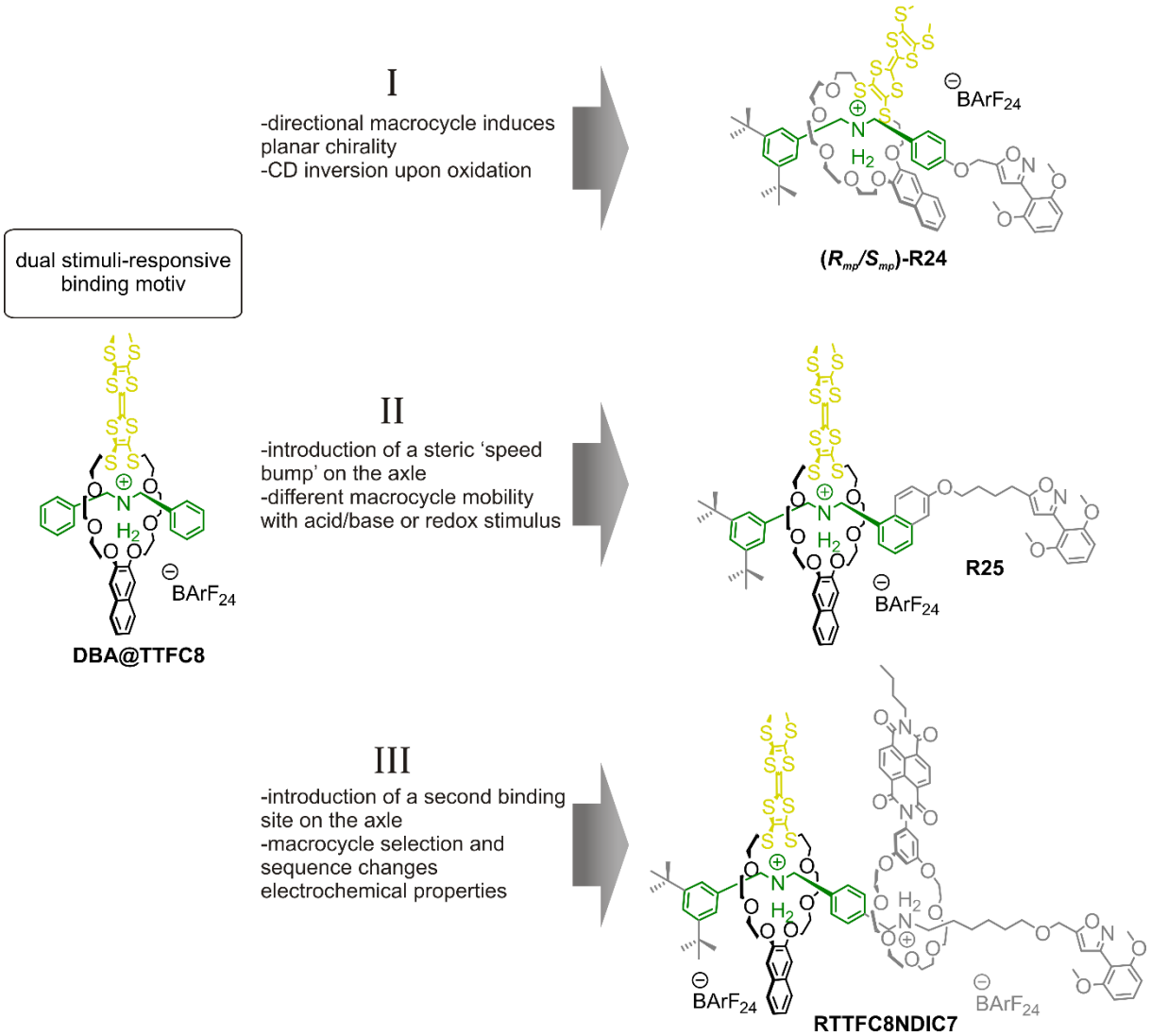

Figure 47: Overview on structural variations in the three projects of this thesis[18-20] based on the dual stimuli-responsive crown/ammonium binding motiv **DBA@TTFC8**.[17]

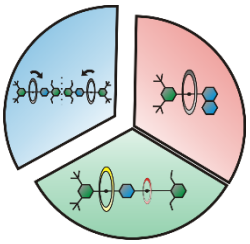

Project I:

Based on redox-switchable crown/ammonium rotaxanes,[17] in which crown ether wheels are decorated with TTF, a new directional wheel **dTTFC8** was envisioned to examine the influence of a chiral environment (Figure 48). As determined by ITC, altering the symmetry in the crown ether **dTTFC8** had only marginal influence on the association constant K_a = (3.6 ± 0.3) 10^5 M^{-1} to the desired axle in comparison to **TTFC8** (K_a = (4.4 ± 0.4) 10^5 M^{-1}). After rotaxanation using a catalyst-free end-capping protocol described by Takata and co-workers,[87] the rotaxane enantiomers were not separable as salts due to low interaction with the chiral stationary phase. Therefore, they were acetylated with Ac_2O.[145] Both the **(*rac*)-R24** and the acetylated **(*rac*)-R24Ac** showed the same electrochemical trends as observed for the non-chiral analogues.[17]

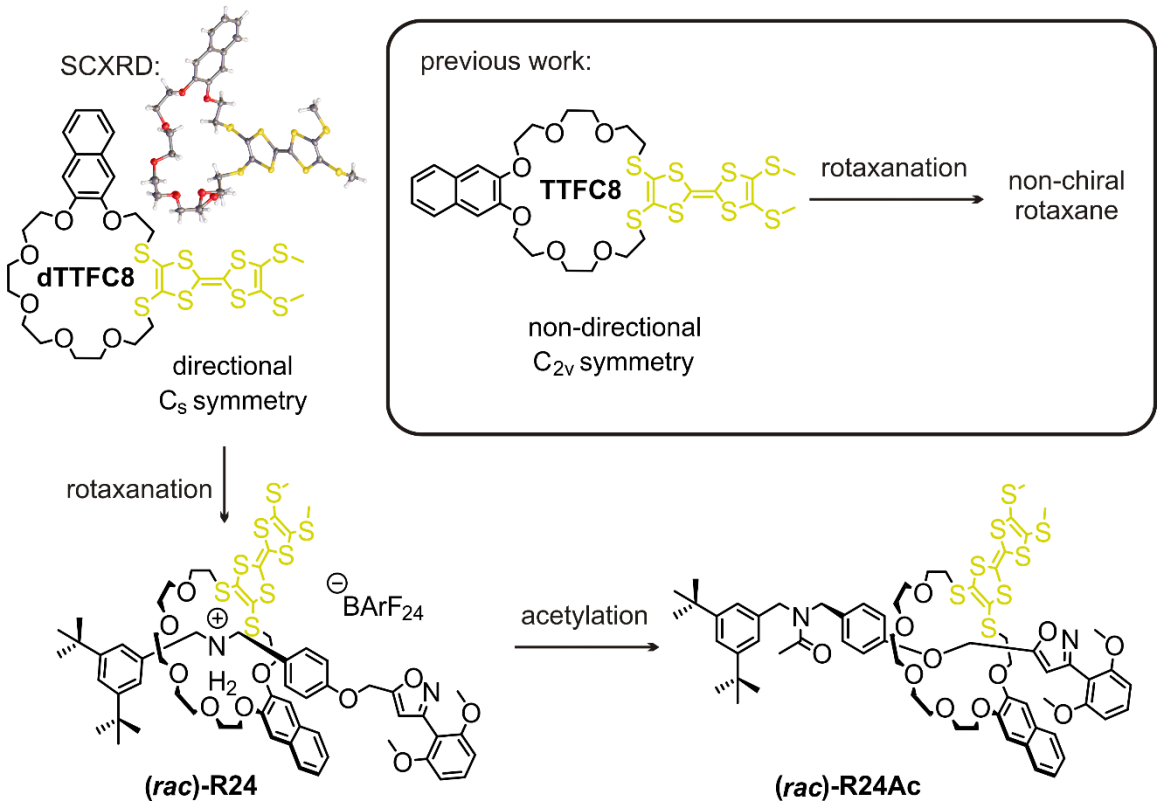

Figure 48: Synthesis of planar-chiral [2]rotaxane **(*rac*)-R24Ac**. Reproduced from Refs.[18, 232] with the permission from the Royal Society of Chemistry.

After separation of the enantiomers on a chiral HPLC, the ECD spectra of the individual enantiomers showed an inversion in the main feature at 242 nm upon oxidation (Figure 49). In addition, the chiroptical inversion is reversible upon reduction. In fact, before this study no TTF derivative was reported displaying a sign reversal in the ECD spectrum without a shift in the wavelength. The change in the ECD spectra could be rationalized by time-dependent density

functional theory (DFT) calculations. All of the optical transitions in the spectra region between 230 and 400 nm involve the TTF unit. While for the neutral TTF the electron transitions start from an orbital at the TTF core towards an orbital on the axle, the oxidized TTF receives electron transitions. Hence, the change in the electronic structure dictates the sign reversal in the ECD spectra, without changing the absolute configuration.

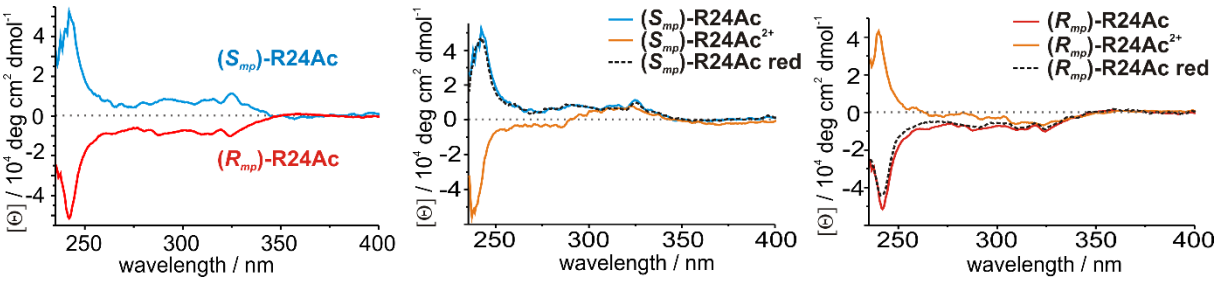

Figure 49: ECD spectra of the individual neutral enantiomers **(*S*$_{mp}$)/(*R*$_{mp}$)-R24Ac** as well as the oxidized (TTF^{2+}) and after reduction to the reduced state. Spectra were taken from 160 µM solutions in CH_2Cl_2 using bulk $Fe(ClO_4)_3$ as the oxidant and Zn powder as the reductant. Reproduced from Ref.[18, 233] with the permission from the Royal Society of Chemistry.

In summary, we constructed a new reversible chiroptical switch by introducing directionality into the macrocycle and the axle. This first chiroptical inversion of a TTF derivative was enabled by the mechanical bond using our redox-switchable crown/dibenzylammonium motif.

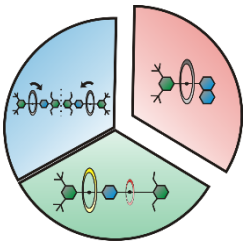

Project II:

After introducing directionality into the macrocycle, we focused the second project on dual-stimuli responsiveness of ammonium complexes with **TTFC8**. From an earlier study, it is known that **TTFC8** expels ammonium guests upon oxidation due to charge repulsion.[17] Additionally, deprotonation of the ammonium site disrupts the crown/ammonium interaction to control co-conformational isomerism of crown ether wheels in MIMs.[91, 142, 234-235] However, for kinetically hindered pseudorotaxanes and bistable rotaxanes the impact of the wheel exchange rate on dual-stimuli-induced switching has not been studied yet. Hence, the question arises, whether and how a kinetic ‘speed bump’ changes the timescales for macrocycle translation upon switching with different stimuli. For the pseudorotaxane, an additional entropic contribution supports the release of the macrocycle into bulk solution. The changes of the energy landscapes upon switching are schemed in Figure 50. A sufficiently slow dethreading rate is necessary to differentiate discrepancies between the two stimuli, otherwise both dethreading processes will

appear to be instant. On the other hand, if the barrier is too high, it would become impractical to measure.

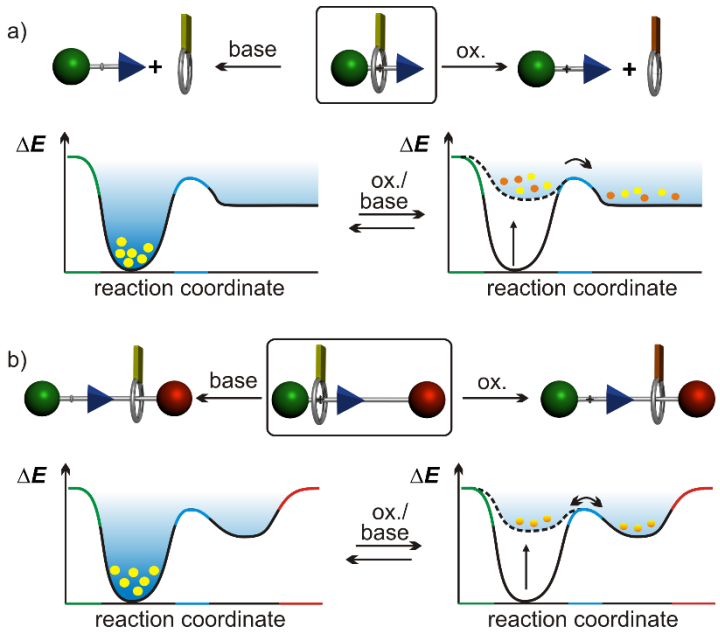

Figure 50: Stimuli-induced shuttling or dethreading with the corresponding changes in the energy landscape for pseudorotaxanes (a) and rotaxanes (b). Stoppers are highlighted in green/red, steric 'speed bump' on the axle in blue, TTF oxidation states in yellow (neutral) and orange (oxidized to TTF^{2+}). Reproduced from Ref.[19] with permission from the Chinese Chemical Society (CCS), Shanghai Institute of Organic Chemistry (SIOC), and the Royal Society of Chemistry.

The solid state structure obtained by single crystal X-ray diffraction (SCXRD) allowed us to appreciate the larger cavity of **TTFC8** compared to **DBC8**, although both share the same amount of atoms along their circumference (Figure 51).

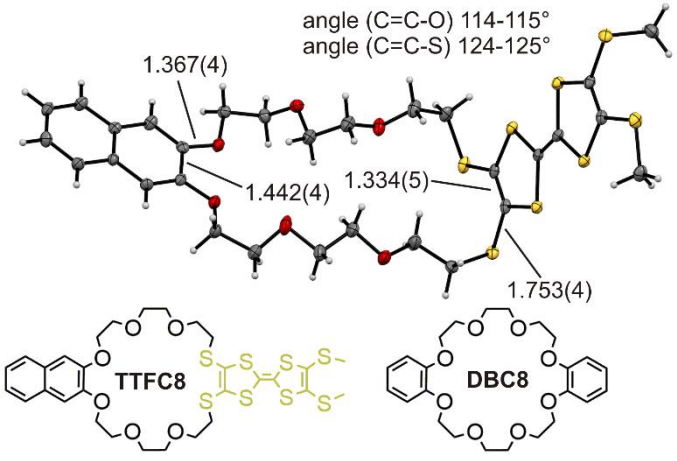

Figure 51: Solid-state structure of **TTFC8** with selected bond lengths (Å) and angles. Reproduced from Ref.[19] with permission from the Chinese Chemical Society (CCS), Shanghai Institute of Organic Chemistry (SIOC), and the Royal Society of Chemistry.

A series of 11 *sec*-ammonium $BArF_{24}^-$ salts with different bulky substituents were synthesized and ^1H NMR threading experiments with **DBC8** and **TTFC8** were conducted. Thereby, three

groups of axles with similar threading half-lives $t_{1/2}$ were distinguished: <<10 min, hours to days and >>14 days. It is noteworthy to say, that the small size difference between the crown ethers led to an up to 120 times faster threading of **TTFC8** compared to **DBC8**. We were also able to differentiate face-to-face from threaded complexes of **A8@TTFC8** by comparing survival yield voltages obtained from collision-induced dissociation (CID) experiments, as this information was not determinable by NMR experiments.

Based on this screening pseudorotaxane **A8@TTFC8**, rotaxane **R25** featuring a 1-naphthalene moiety on the axle and an analogous rotaxane **R25a** without 'speed bump' were synthesized (Figure 52). The threading $t_{1/2}$ of **A8** is 2 h, therefore it was the most suitable 'speed bump'.

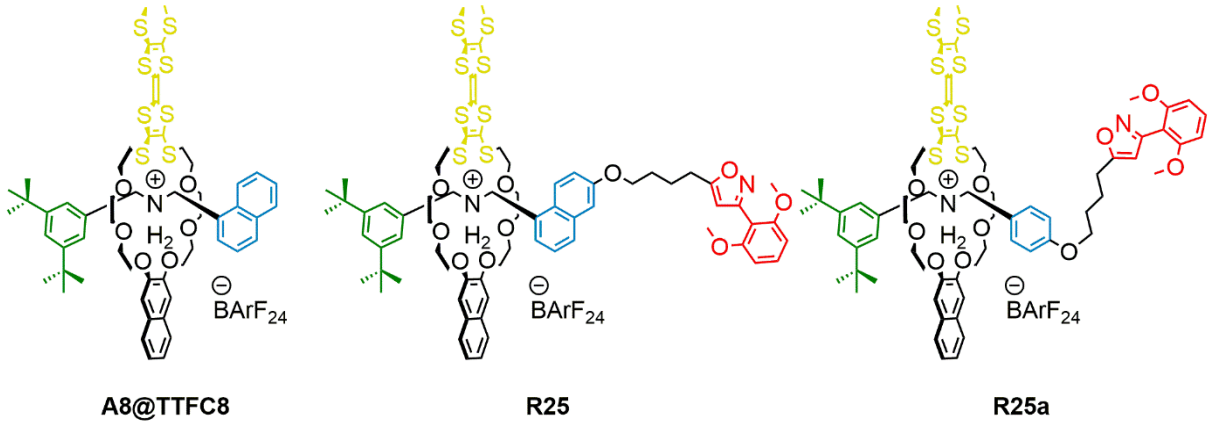

Figure 52: Pseudorotaxane **A8@TTFC8**, rotaxane **R25** and **R25a**. With stoppers in green/red, steric 'speed bump' on the axle in blue. Reproduced from Ref.[19] with permission from the Chinese Chemical Society (CCS), Shanghai Institute of Organic Chemistry (SIOC), and the Royal Society of Chemistry.

Dethreading experiments with **A8@TTFC8** using $NOSbF_6$ as oxidant and Schwesinger's P2 base on polystyrene as base revealed that dethreading upon deprotonation occurred before the first ^{1}H NMR spectrum could be recorded, whereas after oxidation to TTF^{2+} the wheel dethreads with a $t_{1/2}$ of 11 h. Other pseudorotaxanes showed similar trends: fast upon deprotonation, slow upon oxidation.

Deprotonation of the rotaxanes **R25** and **R25a** yielded comparable results for both rotaxanes indicating an immediate shuttling over the blue moiety on the axle, even low temperature NMR did not allow distinguishing co-conformational isomers for either rotaxane.

The ^{1}H NMR spectra of the oxidized rotaxanes indicated that **TTFC8**$^{2+}$ is still bound to the ammonium site. However, additional evidence could be obtained from bulk electrolysis of **A8@TTFC8**, **R25** and **R25a**. Since the oxidation potentials of the bound **TTFC8** are anodically shifted, a new set of redox couples arise for the uncomplexed wheel when no steric

bulk hampers dethreading. Bulk electrolysis for more than 2 h did not show a change in the DPV for all rotaxane species. However, **A8@TTFC8** features a new signal that can be attributed to accumulating dethreaded **TTFC8** (Figure 53d) which is in good agreement to the oxidation experiments monitored by ^{1}H NMR spectroscopy.

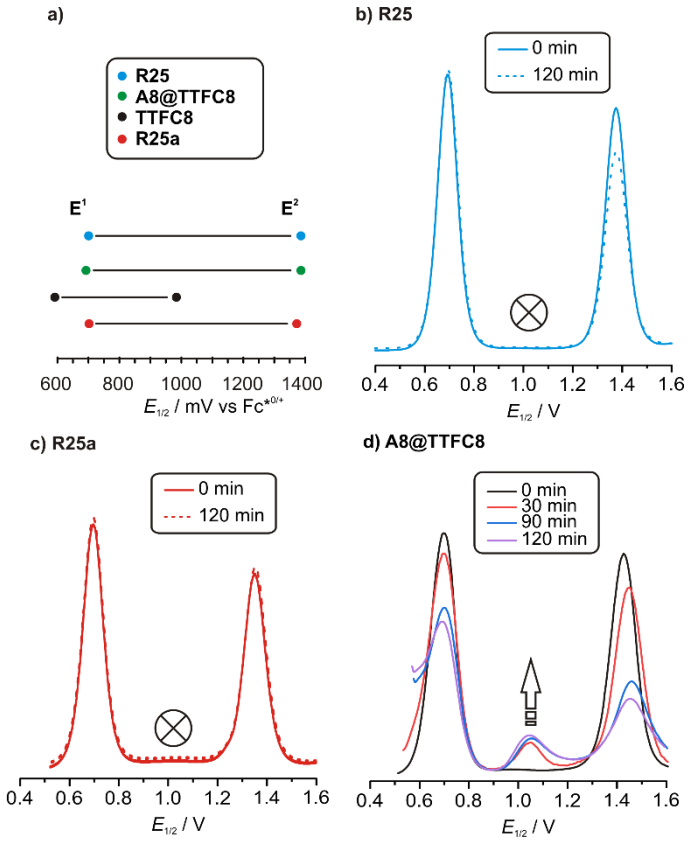

Figure 53: Electrochemical data: (a) Correlation diagram of DPV peak potentials of all relevant (pseudo)rotaxane species, DPVs before and after electrolysis of (b) **R25**, (c) **R25a**, (d) **A8@TTFC8** (CH_2Cl_2, with n-Bu_4NBArF_{24} as the electrolyte (0.1 M), 298 K, 1 mM analyte, 25 mVmodulation amplitude, 50 ms modulation time, 5 mV step potential, 0.5s interval time). Reproduced from Ref.[19] with permission from the Chinese Chemical Society (CCS), Shanghai Institute of Organic Chemistry (SIOC), and the Royal Society of Chemistry.

Overall, we investigated the impact of a steric 'speed bump' on the threading and dethreading of a TTF-decorated crown ether onto an ammonium axle. Our redox-switchable crown/dibenzylammonium motif rendered the assembly pH- and redox-switchable. The impact of the different stimuli was also distinguished between rotaxane and pseudorotaxane.

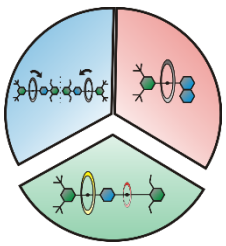

Project III:

As the interactions of same two or three **TTFC8** macrocycles threaded on one axle were found to give promising properties,[217] the interaction of **TTFC8** with another macrocycle is the focus of the third project. In general,

only few examples of crown /ammonium heterorotaxanes are described in literature due to their challenging synthesis, although they are excellent candidates to study sequence isomerism.[95] As shown by previous studies from our group,[74, 78-79, 236] to avoid statistic mixtures of homo- and heterorotaxanes the concept of integrative self-sorting is ideal for crown ethers of different circumference. However, we wanted to utilize new redox-switchable crown ethers to create more functional assemblies.

Before diving into the construction of hetero[3]rotaxanes we had to design and synthesize new redox-switchable crown ethers and systematically determine their thermodynamic binding and electrochemical properties.[58] Out of these a selection of new crown-8 ether and crown-7 ether analogs with their corresponding solid-state structures is depicted in Figure 54.

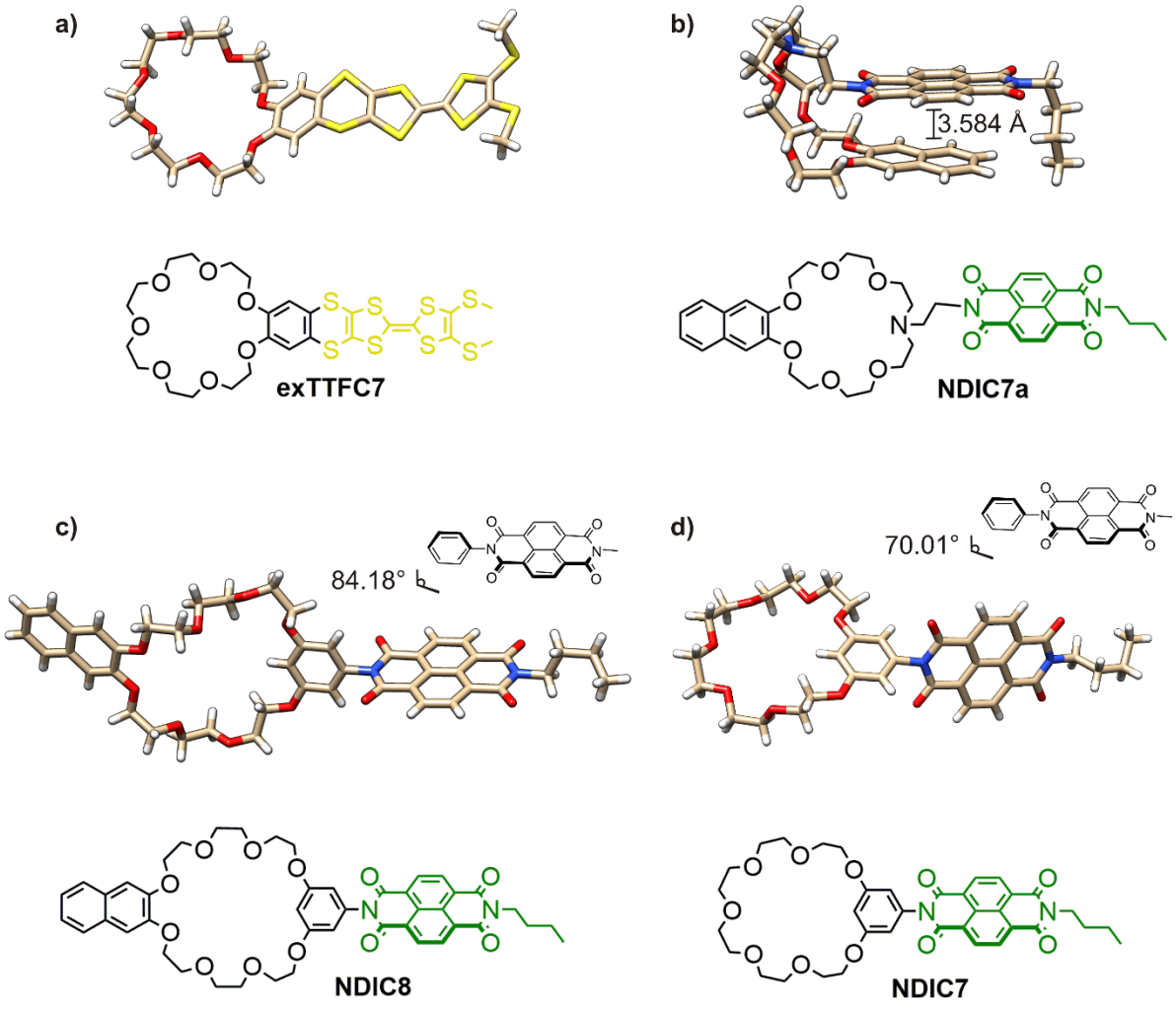

Figure 54: New redox-switchable crown ether macrocycles with their corresponding SCXRD structure: (a) **exTTFC7** (CH_3CN molecule omitted for clarity);[58] (b) **NDIC7a** (CH_3CN molecule omitted for clarity);[58] (c) **NDIC8**;[20, 58] (d) **NDIC7** (CH_3CN molecule omitted for clarity).[20]

Apart from TTF, we functionalized crown ethers with NDI to have an electron poor reversibly reducible counterpart to the electron rich TTF. Additionally, we already have synthetic and analytical experiences with a non-covalent donor-acceptor complex between TTF and NDI.[210]

In the crystal structure of **NDIC7** the torsional angle between the central phenyl and NDI moiety (70.01°) is flatter than for **NDIC8** (84.18°). Intermolecular π-π interactions of neighboring **NDIC7** are promoted by this flattened conformation in the solid state.[20] The azacrown-7 ether **NDIC7a**, which shows an intramolecular π-π interaction in the solid state, turned out to be unfit for threaded complexes with ammonium guests, as no 1:1 binding mode could be observed. A proton transfer from the *sec*-ammonium guests and nonthreaded complexation likely occurs. In contrast to the crown-8 ethers **TTFC8** and **NDIC8**, the crown-7 ethers **exTTFC7** and **NDIC7** could not overcome the phenyl groups to thread a dibenzylammonium guest. Generally, using $BArF_{24}^-$ as counterion for the ammonium guests instead of PF_6^- gave a 10- to 20-fold increase of the association constant.

After this preceding study,[58] we chose a library of five macrocycles, namely **DBC8**, **NDIC8**, **TTFC8**, **BC7** and **NDIC7** to synthesize redox-active hetero[3]rotaxanes.[20] The position on a divalent axle with dibenzylammonium and benzylalkyl ammonium binding sites is programmed by their cavity sizes. The divalent axle **dA** and the corresponding macrocycle positions are sketched in Figure 55.

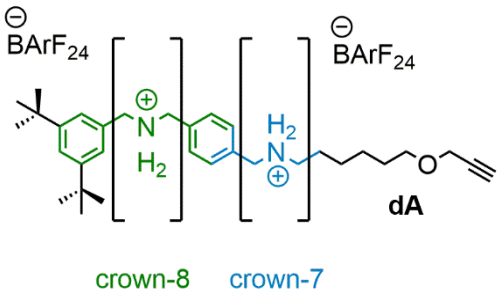

Figure 55: The divalent ammonium axle **dA** with the corresponding macrocycle positions for crown-8 and crown-7 wheels.[20]

The possible self-sorting pathways leading to heteropseudo[3]rotaxanes is exemplary shown for **PRTTFC8BC7** in Figure 56. The selective formation of the desired pseudo[3]rotaxane requires error-correction. When a 1:1:1 mixture of macrocycles and axle is dissolved, there are two possibilities for the first threading. Here **PRBC7** is a dead-end, because it cannot be surpassed by **TTFC8**. On the other hand, threading two **TTFC8** to form **PRTTFC8TTFC8** will also not lead to the desired complex. With error-correction, dead-ends will dissociate again, allowing to form the desired 1:1:1 complex eventually. The selectivity is programmed into the

structures. Whereas the crown-8 wheels will preferably bind to dibenzylammonium sites, benzylalkylammonium is the thermodynamically preferred binding site for crown-7 wheels. Additionally, the smaller crown-7 wheels cannot overcome the phenyl moiety on the axle, limiting them also kinetically to the smaller binding site.

The self-sorting equilibria for the combinations **DBC8**+**BC7**, **TTFC8**+**BC7**, **NDIC8**+**BC7, DBC8**+**NDIC7**, **TTFC8**+**NDIC7** and **NDIC8**+**NDIC7** on **dA** determined by correlated spectroscopy (COSY) NMR and electrospray ionization mass spectrometry (ESI-MS) showed a clear preference for heteropseudo[3]rotaxane formation from 58 % to 74 % in all combinations. However, the selectivity and the timescale are only governed by the crown ether-7 ether. **NDIC7** gave a highly selective (70-74 %) formation within hours, while **BC7** gave lower selectivity (56-58%) and the equilibration took days, rather than hours.

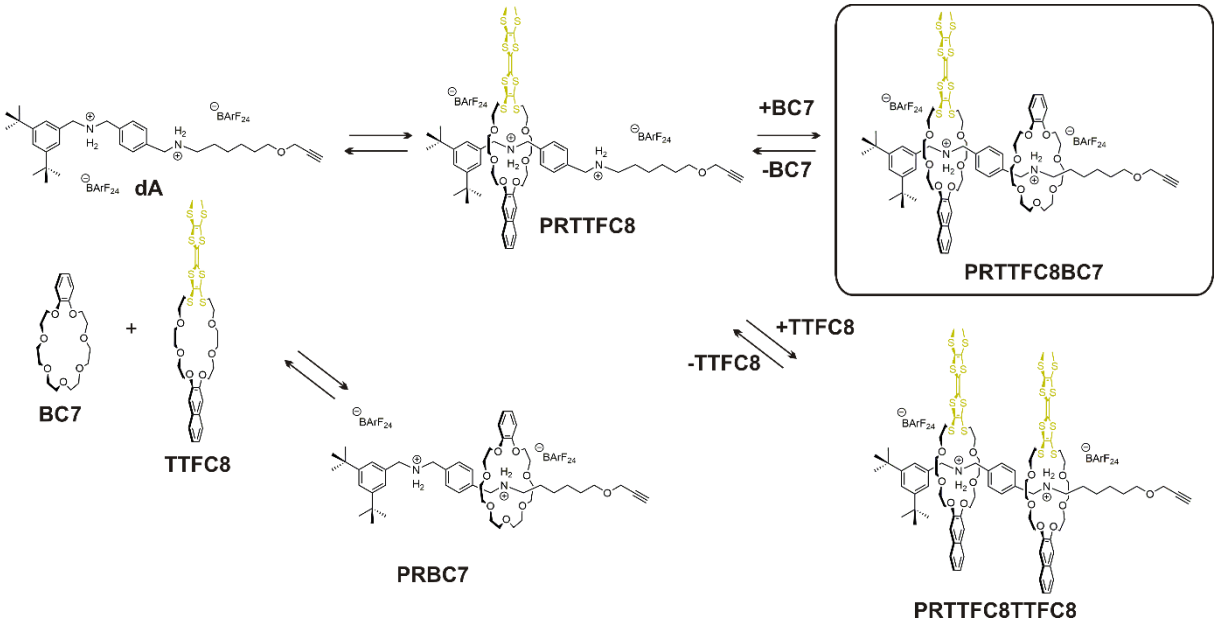

Figure 56: The self-sorting pathways of **PRTTFC8BC7**.[20]

Even though the formation was less selective, the **BC7**-containing pseudo[3]rotaxanes were more stable than the **NDIC7** counterparts, as determined by CID experiments with mass-selected heteropseudo[3]rotaxane ions. The higher stability presumably also leads to a worse error-correction, hence to a lower selectivity.

Remarkably, **PRTTFC8BC7** is stable enough to be isolated by column chromatography. So far, only few examples of chromatographically isolated crown/ammonium pseudorotaxanes are known.[19, 237] All other combinations dissociated on the silica column.

Comparison with the mechanically interlocked **RTTFC8BC7** (Figure 57) by CV and DPV gave similar oxidation potentials for the two TTF redox couples. Additionally, no

unbound **TTFC8** species could be determined after oxidation, although oxidation leads to dethreading of pseudorotaxanes, when no sterically demanding end group is in the way.[19] Therefore, it can be concluded that **BC7** acts as a kinetic barrier for dethreading, turning **PRTTFC8BC7** into an electrochemically "frustrated" pseudorotaxane.

After developing a generally applicable synthetic procedure using the prevalent catalyst-free stoppering protocol described by Takata and co-workers,[87] four new hetero[3]rotaxanes could be isolated from their pseudorotaxane mixtures (Figure 57). The desired macrocycle sequence and interlocked structure was confirmed by 2D NMR spectroscopy and tandem mass spectrometry.

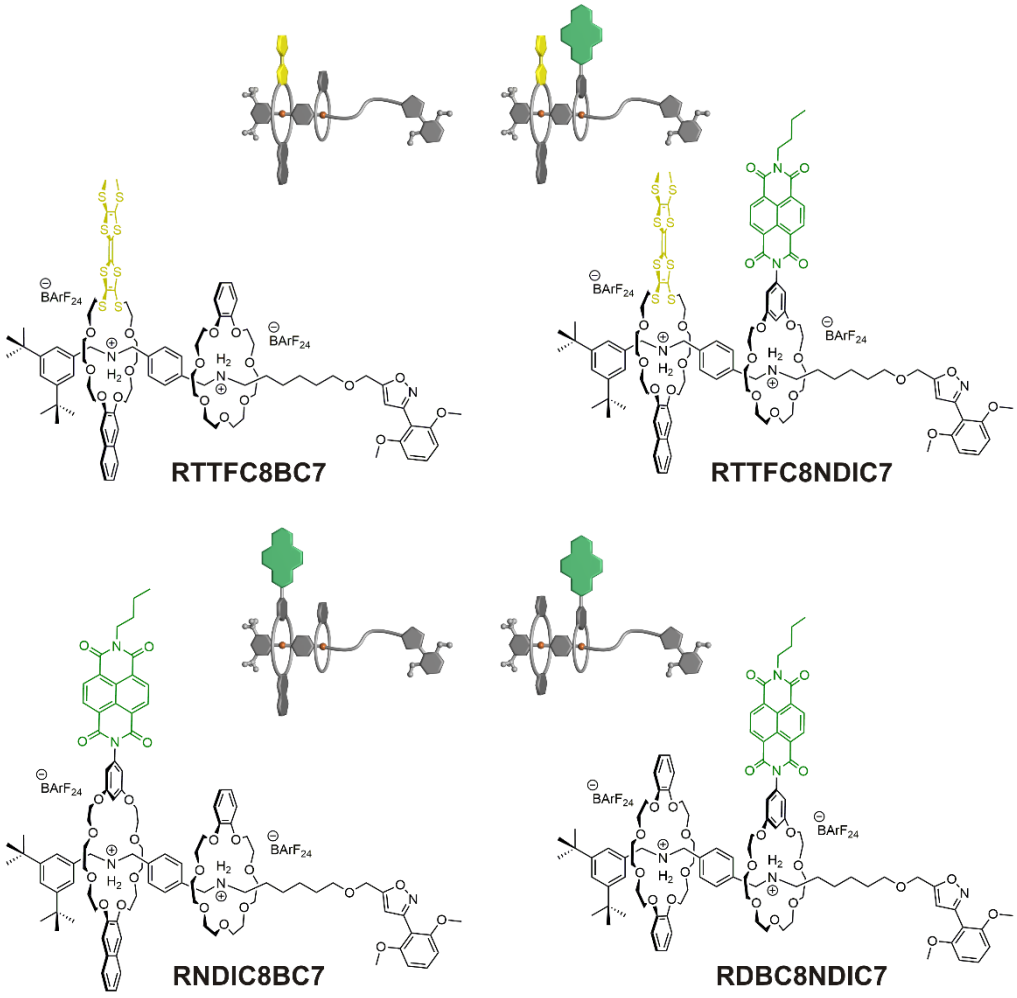

Figure 57: Hetero[3]rotaxanes synthesised from the pseudorotaxane mixtures.[20]

Since **NDIC8** and **NDIC7** have very similar spectroelectrical properties, the rotaxanes **RNDIC8BC7** and **RDBC8NDIC7** can be regarded as "sequence pseudoisomers". Assessing the electrochemical properties allows to determine the influence of the sequence on the axle. Figure 58 summarizes all half-wave potentials $E_{1/2}$. The peaks at positive potentials can be

attributed to the two oxidations at TTF, whereas the peaks at negative potentials are the two reductions of NDI.

The second macrocycle in the rotaxane does not have a strong impact on the oxidation of **TTFC8**. In contrast, **NDIC7** and **NDIC8** behave differently. Reduction potentials of **NDIC8** are more negatively shifted in the hetero[3]rotaxane compared to both hetero[3]rotaxanes with **NDIC7**. We conclude the sequence, rather than macrocycle combination, to be the reason for the different electrochemical properties.

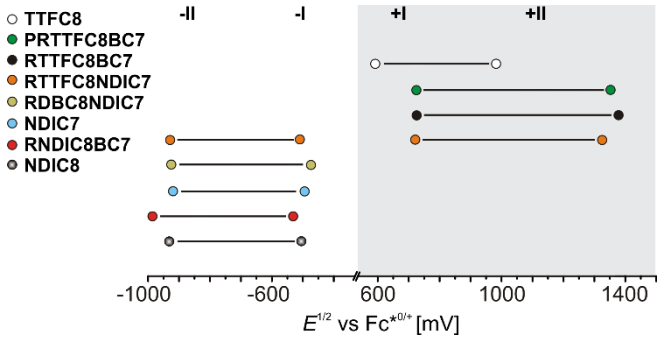

Figure 58: Correlation diagram of half-wave potentials for hetero[3]rotaxanes and free macrocycles determined by DPV in 1,2-dichloroethane with n-Bu_4NBArF_{24} as supporting electrolyte, referenced against the $FeCp_2^{*0/+}$ redox-couple.[20]

In summary, we investigated the impact of sequence on the electrochemical properties of self-sorted hetero[3]rotaxanes. After synthesizing and studying the thermodynamic and electrochemical properties of a suitable library of redox-switchable crown ethers in different sizes, we could design an axle for integrative self-sorting of hetero[3]rotaxanes. The smaller crown-7 ethers were found to dictate the self-sorting efficiency and timescale. One heteropseudo[3]rotaxane combination showed rotaxane-like behavior and could be isolated chromatographically. Our procedure allows the synthesis of donor-acceptor [3]rotaxanes in a one-pot reaction with individually addressable redox-switchable units. We could also show that the sequence on the axle has an impact on the redox properties of NDI.

4 List of Publications

4.1 Chiroptical Inversion of a Planar Chiral Redox-Switchable Rotaxane

M. Gaedke, F. Witte, J. Anhäuser, H. Hupatz, H. V. Schröder, A. Valkonen, K. Rissanen, A. Lützen, B. Paulus, C. A. Schalley, *Chem. Sci.* **2019**, 10, 10003-10009.

Submitted 26 Jul 2019, published 04 September 2019

Published by the Royal Society of Chemistry.[18]

The journal article is electronically available (https://doi.org/10.1039/C9SC03694F)

4.1.1 Authors' Contributions

The project was developed by me with help from Henrik Hupatz and Hendrik V. Schröder. Felix Witte, Jana Anhäuser, Henrik Hupatz, Hendrik V. Schröder, Christoph A. Schalley and I wrote the manuscript with main contributions from my side. I carried out the synthetic work including the preparation of single crystals, NMR, UV/Vis, CV, MS and CD measurements. All computational work was done by Felix Witte and Beate Paulus. The chiral HPLC separations were performed and analyzed by Jana Anhäuser and Arne Lützen. Henrik Hupatz measured and analyzed the ITC data. Arto Valkonen and Kari Rissanen measured and solved the SCXRD structure. Hendrik V. Schröder helped with synthetic work and data analysis. All authors contributed to the final version of the manuscript.

4.2 Thermodynamic and Electrochemical Study of Tailor-Made Crown Ethers for Redox-Switchable (Pseudo)rotaxanes

H. Hupatz, M. Gaedke, H. V. Schröder, J. Beerhues, A. Valkonen, F. Klautzsch, S. Müller, F. Witte, K. Rissanen, B. Sarkar, C. A. Schalley, *Beilstein J. Org. Chem.* **2020**, 16, 2576-2588.

Submitted 07 August 2020, published 20 October 2020

Published by the Beilstein-Institute.[58]

The journal article is electronically available: (https://doi.org/10.3762/bjoc.16.209)

4.2.1 Authors' Contributions

The project was developed by Henrik Hupatz with help coming from me and Hendrik V. Schröder. Henrik Hupatz, I, Hendrik V. Schröder and Christoph A. Schalley wrote the manuscript with main contributions from Henrik Hupatz. The synthetic work was carried out by Henrik Hupatz, me, Felix Witte, Sebastian Müller and Hendrik V. Schröder including NMR, UV/Vis, CV and MS measurements. I prepared the single crystals. Henrik Hupatz and Fabian Klautzsch measured ITC data and Henrik Hupatz analyzed the data. Julia Beerhues, Arto Valkonen, Biprajit Sarkar and Kari Rissanen measured and solved the SCXRD structures. All authors contributed to the final version of the manuscript.

4.3 Dual-Stimuli Pseudorotaxane Switches Under Kinetic Control

M. Gaedke, H. Hupatz, H. V. Schröder, S. Suhr, K. F. Hoffmann, A. Valkonen, B. Sarkar, S. Riedel, K. Rissanen, C. A. Schalley, *Org. Chem. Front.*, **2021**, 8, 3659-3667.

Submitted 31 March 2021, published 29 April 2021

Published by Royal Society of Chemistry.[19]

The journal article is electronically available: (https://doi.org/10.1039/D1QO00503K)

4.3.1 Authors' Contributions

I developed the general concept of this project with help of Hendrik V. Schröder. Henrik Hupatz, I, Hendrik V. Schröder and Christoph A. Schalley wrote the manuscript with main contributions from my side. The synthetic work was carried out by me, Kurt F. Hoffmann and Hendrik V. Schröder. I carried out the time-dependent NMR, as well as UV/Vis, CV and MS

measurements. Kurt F. Hoffmann, Sebastian Riedel and I conducted the low temperature, oxidation and deprotonation NMR experiments. Henrik Hupatz measured and analyzed the ITC data. Henrik Hupatz performed tandem mass spectrometry and analyzed and fitted the data. I prepared the single crystals. Simon Suhr and Biprajit Sarkar conducted the bulk electrolysis. Arto Valkonen, and Kari Rissanen measured and solved the SCXRD structure. All authors contributed to the final version of the manuscript.

4.4 Sequence-Sorted Redox-Switchable Hetero-[3]rotaxanes

M. Gaedke,* H. Hupatz,* Felix Witte, S. M. Rupf, C. Douglas, H. V. Schröder, L. Fischer, M. Malischewski, B. Paulus, C. A. Schalley, *submitted to Chem. Sci.*
Submitted 25th August 2021

A preprint of the journal article is electronically available:

(https://doi.org/10.33774/chemrxiv-2021-vj7k2-v2)[20]

4.4.1 Authors' Contributions

The project was developed by Henrik Hupatz and me. Henrik Hupatz, I and Christoph A. Schalley wrote the manuscript with main contributions from Henrik Hupatz and me. The synthetic work was carried out by me, Clara Douglas, Susanne Margot Rupf, Lukas Fischer and Henrik Hupatz with main contributions coming from my side. Henrik Hupatz conducted and evaluated all time dependent NMR and tandem MS experiments. I performed further NMR, UV/Vis and CV experiments and prepared the single crystals. Hendrik V. Schröder helped with data evaluation and conception. Henrik Hupatz measured and analyzed the ITC data. All computational work was done by Felix Witte and Beate Paulus. Susanne M. Rupf and Moritz Malischewski measured and solved the SCXRD structure. Both, Marius Gaedke and Henrik Hupatz contributed equally and have the right to list their name first in their CV. All authors contributed to the final version of the manuscript.

5 Conclusion and Outlook

In the course of this thesis, three topics relevant to the current research on functional molecules as well as artificial molecular switches and machines were covered: directionality,[110] kinetic control over stimuli-responsiveness,[84] and sequence-specificity.[95]

Directionality was achieved by introducing the directional isomer of crown ether **TTFC8** into rotaxanes. The isolated enantiomers of [2]rotaxane **R24Ac** interact differently with circularly polarized light, depending on the oxidation state − a result of the reversible directionality of optical transitions from or to the TTF moiety on the macrocycle. This feature of redox-active rotaxanes was not described so far.[18]

Being able to use different stimuli is of major interest to specifically address individual functions and thus allow the construction of more functional devices.[238] By choosing a kinetic barrier that matches the macrocyclic cavity of **TTFC8** and comparing the (pseudo)rotaxanes with and without kinetic barrier on the axle, we could investigate the influence of the mechanical bond on the co-conformational changes upon two different stimuli. As we have seen, different stimuli can have completely different timescales for the same 'speed bump' even when the same outcome, in this case dethreading, is achieved.[19]

Finally, a synthetic approach was devised to synthesize sequence-specific redox-switchable hetero[3]rotaxanes. The sequence-specific synthesis was established by modifying and expanding a known integrated self-sorting approach[74] towards more functional molecules and combinations.[58] We recognized the smaller macrocycle to have the main influence on the self-sorting efficiency in all cases. Although no electronic communication between the wheels could be observed, the sequence did have an impact on the electronic properties.[20] The modular approach is not limited to the examples that are described, by using integrative self-sorting and differently functionalized crown ether macrocycles new properties will emerge.

Tangible ideas for the further development of sequence-specific hetero[3]rotaxanes to involve increasing and tuning the interaction of macrocycles towards the stopper units, as all the computations that complemented our research point towards interactions of TTF or NDI with the dimethoxybenzyl stopper. Accordingly, the properties of the rotaxane will change depending on the sequence on the axle and the stopper. A starting point could be to exchange the binding site and stoppering unit on either side of the axle (Figure 59).

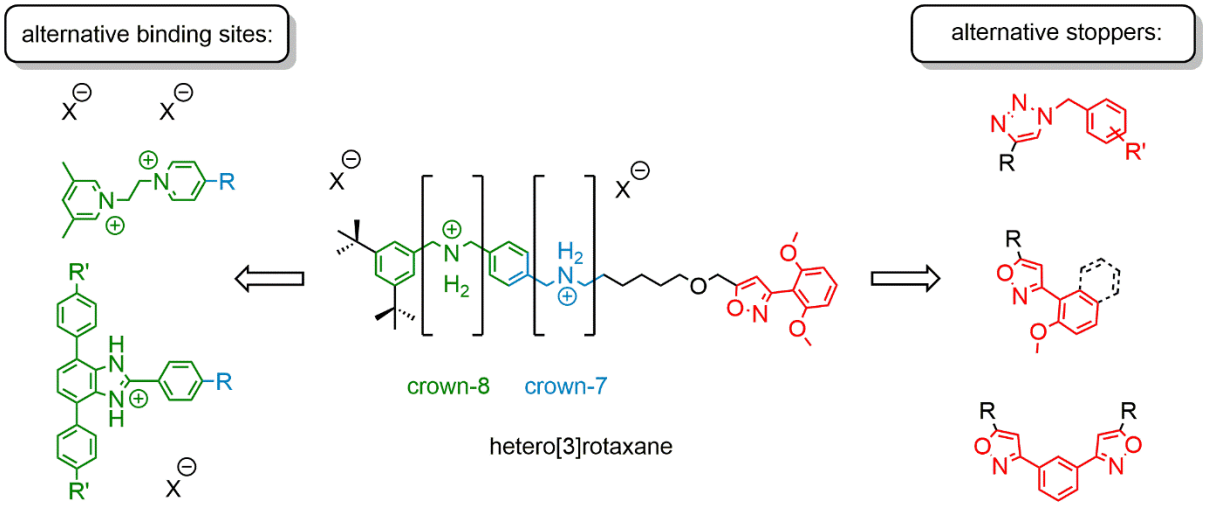

Figure 59: Structural alternatives for binding sites[99] and stopper moieties[239] for hetero[3]rotaxanes.

Another untapped parameter are counterions. The influence of counterions on co-conformational equilibria and redox potentials is often overlooked and underappreciated. In the publications of this thesis only PF_6^- and $BArF_{24}^-$ were employed. However, investigating the enthalpic and entropic contributions of counter anions to host-guest equilibria will complement the picture. There, electrochemical methods will be a powerful tool to gather quantitative data. The emerging field of WCAs[67] comes to mind. Additionally, chiral counterions (Figure 60) could be used to drive the racemic mixture of planar chiral pseudorotaxanes towards one diastereomer, rendering the tedious separation on a chiral stationary phase obsolete.

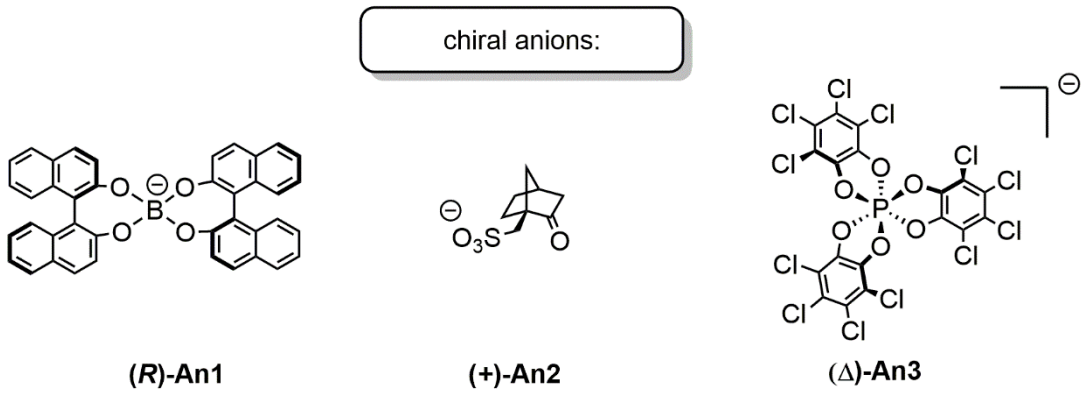

Figure 60: Exemplary counterion structures, that are used as chiral shift agents or in enantioselective catalysis. (**(*R*)-An1**[240] **(+)-An2**[241] **(Δ)-An3**[112]).

Overall, this thesis enlarged the scope of redox-switchable crown/ammonium (pseudo)rotaxanes for the construction of artificial molecular machines or switches. The projects are concerned with solution-phase studies, complemented with mass spectrometric measurements and quantum chemical calculations. However, the most influential studies in the field also point towards coupled motion in bulk,[242-243] on surfaces[244-245] or the controlled

release of cargo in biomedical applications.[246] Therefore, it is clear that we merely started to understand the interplay of inter- and intramolecular forces during switching processes. To actually build devices or materials that can amplify the switching motion or chiroptical properties, we as supramolecular chemists surely need the help from other disciplines and also think beyond the inspiring, yet often misleading technomimetic designs.

6 References

[1] M. M. Hussain, *Advanced Nanoelectronics*, Wiley-VCH, Weinheim, **2018**, pp. 1-23.
[2] T. S. M. C. Ltd., https://www.tsmc.com/english/dedicatedFoundry/technology/logic (accessed 20.05.2021), **2021**.
[3] T. Dietl, in *From Quantum Mechanics to Technology. Lecture Notes in Physics, Vol. 477* (Eds.: Z. Petru, J. Pryzystawa, K. Rapcewicz), Springer, New York, **1996**, pp. 75-85.
[4] Y. Luo, C. P. Collier, J. O. Jeppesen, K. A. Nielsen, E. DeIonno, G. Ho, J. Perkins, H.-R. Tseng, T. Yamamoto, J. F. Stoddart, J. R. Heath, *ChemPhysChem* **2002**, *3*, 519-525.
[5] S. Erbas-Cakmak, D. A. Leigh, C. T. McTernan, A. L. Nussbaumer, *Chem. Rev.* **2015**, *115*, 10081-10206.
[6] R. Eelkema, M. M. Pollard, J. Vicario, N. Katsonis, B. S. Ramon, C. W. Bastiaansen, D. J. Broer, B. L. Feringa, *Nature* **2006**, *440*, 163.
[7] Q. Li, G. Fuks, E. Moulin, M. Maaloum, M. Rawiso, I. Kulic, J. T. Foy, N. Giuseppone, *Nat. Nanotechnol.* **2015**, *10*, 161-165.
[8] S. Kassem, A. T. Lee, D. A. Leigh, A. Markevicius, J. Sola, *Nat. Chem.* **2016**, *8*, 138-143.
[9] E. M. Geertsema, S. J. van der Molen, M. Martens, B. L. Feringa, *Proc. Natl. Acad. Sci. USA* **2009**, *106*, 16919-16924.
[10] D. S. Goodsell, *Bionanotechnology: Lessons from Nature*, Wiley, Hoboken, **2004**, pp. 9-41.
[11] D. S. Goodsell, *The Machinery of Life 2nd Ed.*, Springer, New York, **2009**, pp. 8-26.
[12] J. F. Stoddart, *Angew. Chem. Int. Ed.* **2017**, *56*, 11094-11125.
[13] J. P. Sauvage, *Angew. Chem. Int. Ed.* **2017**, *56*, 11080-11093.
[14] B. L. Feringa, *Angew. Chem. Int. Ed.* **2017**, *56*, 11060-11078.
[15] I. Aprahamian, *ACS Cent. Sci.* **2020**, *6*, 347-358.
[16] C. A. Schalley, K. Beizai, F. Vögtle, *Acc. Chem. Res.* **2001**, *34*, 465-476.
[17] H. V. Schröder, S. Sobottka, M. Nössler, H. Hupatz, M. Gaedke, B. Sarkar, C. A. Schalley, *Chem. Sci.* **2017**, *8*, 6300-6306.
[18] M. Gaedke, F. Witte, J. Anhäuser, H. Hupatz, H. V. Schröder, A. Valkonen, K. Rissanen, A. Lützen, B. Paulus, C. A. Schalley, *Chem. Sci.* **2019**, *10*, 10003-10009.
[19] M. Gaedke, H. Hupatz, H. V. Schröder, S. Suhr, K. F. Hoffmann, A. Valkonen, B. Sarkar, S. Riedel, K. Rissanen, C. A. Schalley, *Org. Chem. Front.* **2021**, *8*, 3659-3667.
[20] M. Gaedke, H. Hupatz, F. Witte, S. M. Rupf, C. Douglas, H. V. Schröder, L. Fischer, M. Malischewski, B. Paulus, C. A. Schalley, *ChemRxiv* **2021**, *DOI: 10.33774/chemrxiv-2021-vj7k2-v2 This content is a preprint and has not been peer-reviewed.*
[21] K. Autumn, A. M. Peattie, *Integr. Comp. Biol.* **2002**, *42*, 1081-1090.
[22] C. Hu, P. Alex Greaney, *J. Appl. Phys.* **2014**, *116*, 074302.
[23] A. B. Harvey Lodish, S. Lawrence Zirpursky, Paul Matsudaira, David Baltimore, James Darnell, *Molecular Cell Biology, 4th Ed.*, W. H. Freeman, New York, **2000**.
[24] S. Amnuanpol, *J. Biol. Phys.* **2016**, *42*, 69-82.
[25] S. Cocco, R. Monasson, J. F. Marko, *Proc. Natl. Acad. Sci. USA* **2001**, *98*, 8608-8613.
[26] R. M. Pulselli, E. Simoncini, E. Tiezzi, *Biosystems* **2009**, *96*, 237-241.
[27] L. Strekowski, B. Wilson, *Mutat. Res.* **2007**, *623*, 3-13.
[28] S. J. Rowan, S. J. Cantrill, G. R. L. Cousins, J. K. M. Sanders, J. F. Stoddart, *Angew. Chem. Int. Ed.* **2002**, *41*, 898-952.
[29] J.-M. Lehn, *Angew. Chem. Int. Ed. Engl.* **1988**, *27*, 89-112.
[30] D. R. Lide, in *CRC Handbook of Chemistry and Physics*, Taylor and Francis, Boca Raton, **2007**.
[31] D. A. Dougherty, *Science* **1996**, *271*, 163-168.
[32] S. Tsuzuki, T. Uchimaru, M. Mikami, *J. Phys. Chem. A* **2006**, *110*, 2027-2033.
[33] J. W. Steed, D. R. Turner, K. Wallace, *Core Concepts in Supramolecular Chemistry and Nanochemistry*, Wiley, Hoboken, **2007**.
[34] M. Charton, B. I. Charton, *J. Theor. Biol.* **1982**, *99*, 629-644.
[35] J. W. Steed, J. L. Atwood, *Supramolecular Chemistry 2nd Ed.*, Wiley, Hoboken, **2009**.
[36] F. M. Raymo, J. F. Stoddart, *Chem. Rev.* **1999**, *99*, 1643-1664.
[37] D. J. Cram, J. M. Cram, *Science* **1974**, *183*, 803-809.

[38] C. J. Pedersen, *J. Am. Chem. Soc.* **2002**, *89*, 2495-2496.
[39] C. J. Pedersen, H. K. Frensdorff, *Angew. Chem. Int. Ed. Engl.* **1972**, *11*, 16-25.
[40] D. J. Cram, *Angew. Chem. Int. Ed. Engl.* **1988**, *27*, 1009-1020.
[41] T. K. Katsuhiko Ariga, *Supramolecular Chemistry - Fundamentals and Applications*, Springer, New York, **2006**.
[42] B. Odell, M. V. Reddington, A. M. Z. Slawin, N. Spencer, J. F. Stoddart, D. J. Williams, *Angew. Chem. Int. Ed. Engl.* **1988**, *27*, 1547-1550.
[43] P. L. Anelli, N. Spencer, J. F. Stoddart, *J. Am. Chem. Soc.* **1991**, *113*, 5131-5133.
[44] M. B. Nielsen, J. O. Jeppesen, J. Lau, C. Lomholt, D. Damgaard, J. P. Jacobsen, J. Becher, J. F. Stoddart, *J. Org. Chem.* **2001**, *66*, 3559-3563.
[45] S. J. Barrow, S. Kasera, M. J. Rowland, J. del Barrio, O. A. Scherman, *Chem. Rev.* **2015**, *115*, 12320-12406.
[46] F. Biedermann, V. D. Uzunova, O. A. Scherman, W. M. Nau, A. De Simone, *J. Am. Chem. Soc.* **2012**, *134*, 15318-15323.
[47] W. A. Freeman, W. L. Mock, N. Y. Shih, *J. Am. Chem. Soc.* **2002**, *103*, 7367-7368.
[48] G. Crini, *Chem. Rev.* **2014**, *114*, 10940-10975.
[49] T. Ogoshi, T. A. Yamagishi, Y. Nakamoto, *Chem. Rev.* **2016**, *116*, 7937-8002.
[50] K. Nakazono, S. Kuwata, T. Takata, *Tetrahedron Lett.* **2008**, *49*, 2397-2401.
[51] Y. L. Zhao, W. R. Dichtel, A. Trabolsi, S. Saha, I. Aprahamian, J. F. Stoddart, *J. Am. Chem. Soc.* **2008**, *130*, 11294-11296.
[52] H. J. Kim, W. S. Jeon, Y. H. Ko, K. Kim, *Proc. Natl. Acad. Sci. USA* **2002**, *99*, 5007-5011.
[53] M. Asakawa, W. Dehaen, G. L'Abbé, S. Menzer, J. Nouwen, F. M. Raymo, J. F. Stoddart, D. J. Williams, *J. Org. Chem.* **1996**, *61*, 9591-9595.
[54] T. Heinrich, C. H. Traulsen, M. Holzweber, S. Richter, V. Kunz, S. K. Kastner, S. O. Krabbenborg, J. Huskens, W. E. Unger, C. A. Schalley, *J. Am. Chem. Soc.* **2015**, *137*, 4382-4390.
[55] C. J. Pedersen, US Pat., US3361778, USA, **1968**.
[56] C. J. Pedersen, *J. Am. Chem. Soc.* **1967**, *89*, 7017-7036.
[57] F. Nicoli, M. Baroncini, S. Silvi, J. Groppi, A. Credi, *Org. Chem. Front.* **2021**, *8*, 5531-5549.
[58] H. Hupatz, M. Gaedke, H. V. Schröder, J. Beerhues, A. Valkonen, F. Klautzsch, S. Müller, F. Witte, K. Rissanen, B. Sarkar, C. A. Schalley, *Beilstein J. Org. Chem.* **2020**, *16*, 2576-2588.
[59] R. M. Izatt, G. A. Clark, J. D. Lamb, J. E. King, J. J. Christensen, *Thermochim. Acta* **1986**, *97*, 115-126.
[60] V. Rüdiger, H.-J. Schneider, V. P. Solov'ev, V. P. Kazachenko, O. A. Raevsky, *Eur. J. Org. Chem.* **1999**, *1999*, 1847-1856.
[61] P. R. Ashton, P. J. Campbell, P. T. Glink, D. Philp, N. Spencer, J. F. Stoddart, E. J. T. Chrystal, S. Menzer, D. J. Williams, P. A. Tasker, *Angew. Chem. Int. Ed. Engl.* **1995**, *34*, 1865-1869.
[62] D. G. Hamilton, J. E. Davies, L. Prodi, J. K. M. Sanders, *Chem. Eur. J.* **1998**, *4*, 608-620.
[63] C. J. Bruns, J. F. Stoddart, *The Nature of the Mechanical Bond: From Molecules to Machines*, Wiley, Hoboken, **2016**.
[64] H. W. Gibson, J. W. Jones, L. N. Zakharov, A. L. Rheingold, C. Slebodnick, *Chem. Eur. J.* **2011**, *17*, 3192-3206.
[65] J. W. Jones, H. W. Gibson, *J. Am. Chem. Soc.* **2003**, *125*, 7001-7004.
[66] V. Gutmann, E. Wychera, *Inorg. Nucl. Chem. Letters* **1966**, *2*, 257-260.
[67] I. M. Riddlestone, A. Kraft, J. Schaefer, I. Krossing, *Angew. Chem. Int. Ed.* **2018**, *57*, 13982-14024.
[68] H. Nagai, Y. Suzaki, K. Osakada, *Chem. Lett.* **2016**, *45*, 834-836.
[69] G. M. Whitesides, B. Grzybowski, *Science* **2002**, *295*, 2418-2421.
[70] J. D. Halley, D. A. Winkler, *Complexity* **2008**, *14*, 10-17.
[71] A. Wu, L. Isaacs, *J. Am. Chem. Soc.* **2003**, *125*, 4831-4835.
[72] P. Mukhopadhyay, A. Wu, L. Isaacs, *J. Org. Chem.* **2004**, *69*, 6157-6164.
[73] M. M. Safont-Sempere, G. Fernandez, F. Würthner, *Chem. Rev.* **2011**, *111*, 5784-5814.
[74] Z. He, W. Jiang, C. A. Schalley, *Chem. Soc. Rev.* **2015**, *44*, 779-789.
[75] F. J. Rizzuto, J. R. Nitschke, *J. Am. Chem. Soc.* **2020**, *142*, 7749-7753.
[76] K. Osowska, O. S. Miljanic, *J. Am. Chem. Soc.* **2011**, *133*, 724-727.
[77] R. C. Lirag, K. Osowska, O. S. Miljanic, *Org. Biomol. Chem.* **2012**, *10*, 4847-4850.

[78] W. Jiang, C. A. Schalley, *Proc. Natl. Acad. Sci. USA* **2009**, *106*, 10425-10429.
[79] W. Jiang, H. D. Winkler, C. A. Schalley, *J. Am. Chem. Soc.* **2008**, *130*, 13852-13853.
[80] K. N. Kreuzer, N. R. Cozzarelli, *Cell* **1980**, *20*, 245-254.
[81] T. A. Knappe, U. Linne, S. Zirah, S. Rebuffat, X. Xie, M. A. Marahiel, *J. Am. Chem. Soc.* **2008**, *130*, 11446-11454.
[82] H. L. Frisch, E. Wasserman, *J. Am. Chem. Soc.* **1961**, *83*, 3789-3795.
[83] R. S. Forgan, J. P. Sauvage, J. F. Stoddart, *Chem. Rev.* **2011**, *111*, 5434-5464.
[84] M. Xue, Y. Yang, X. Chi, X. Yan, F. Huang, *Chem. Rev.* **2015**, *115*, 7398-7501.
[85] V. Aucagne, J. Berna, J. D. Crowley, S. M. Goldup, K. D. Hanni, D. A. Leigh, P. J. Lusby, V. E. Ronaldson, A. M. Slawin, A. Viterisi, D. B. Walker, *J. Am. Chem. Soc.* **2007**, *129*, 11950-11963.
[86] D. Thibeault, J. F. Morin, *Molecules* **2010**, *15*, 3709-3730.
[87] T. Matsumura, F. Ishiwari, Y. Koyama, T. Takata, *Org. Lett.* **2010**, *12*, 3828-3831.
[88] T. Yuki, Y. Koyama, T. Matsumura, T. Takata, *Org. Lett.* **2013**, *15*, 4438-4441.
[89] J.-B. Giguère, D. Thibeault, F. Cronier, J.-S. Marois, M. Auger, J.-F. Morin, *Tetrahedron Lett.* **2009**, *50*, 5497-5500.
[90] J. Cao, M. C. Fyfe, J. F. Stoddart, G. R. Cousins, P. T. Glink, *J. Org. Chem.* **2000**, *65*, 1937-1946.
[91] F. Coutrot, E. Busseron, *Chem. Eur. J.* **2008**, *14*, 4784-4787.
[92] Y. Furusho, H. Sasabe, D. Natsui, K.-i. Murakawa, T. Takata, T. Harada, *Bull. Chem. Soc. Jpn.* **2004**, *77*, 179-185.
[93] C. Zhang, S. Li, J. Zhang, K. Zhu, N. Li, F. Huang, *Org. Lett.* **2007**, *9*, 5553-5556.
[94] E. A. Neal, S. M. Goldup, *Chem. Commun.* **2014**, *50*, 5128-5142.
[95] X. Q. Wang, W. J. Li, W. Wang, H. B. Yang, *Chem. Commun.* **2018**, *54*, 13303-13318.
[96] E. A. Wilson, N. A. Vermeulen, P. R. McGonigal, A. J. Avestro, A. A. Sarjeant, C. L. Stern, J. F. Stoddart, *Chem. Commun.* **2014**, *50*, 9665-9668.
[97] X. Hou, C. Ke, C. Cheng, N. Song, A. K. Blackburn, A. A. Sarjeant, Y. Y. Botros, Y. W. Yang, J. F. Stoddart, *Chem. Commun.* **2014**, *50*, 6196-6199.
[98] X. Hou, C. Ke, C. J. Bruns, P. R. McGonigal, R. B. Pettman, J. F. Stoddart, *Nat. Commun.* **2015**, *6*, 6884.
[99] K. Zhu, G. Baggi, S. J. Loeb, *Nat. Chem.* **2018**, *10*, 625-630.
[100] D. B. Amabilino, P. R. Ashton, M. Bělohradský, F. M. Raymo, J. F. Stoddart, *J. Chem. Soc., Chem. Commun.* **1995**, *7*, 747-750.
[101] C. Gao, Z. L. Luan, Q. Zhang, S. J. Rao, D. H. Qu, H. Tian, *Org. Lett.* **2017**, *19*, 3931-3934.
[102] S. J. Rao, Q. Zhang, J. Mei, X. H. Ye, C. Gao, Q. C. Wang, D. H. Qu, H. Tian, *Chem. Sci.* **2017**, *8*, 6777-6783.
[103] E. A. Neal, S. M. Goldup, *Angew. Chem. Int. Ed.* **2016**, *55*, 12488-12493.
[104] R. S. Cahn, C. Ingold, V. Prelog, *Angew. Chem. Int. Ed.Engl.* **1966**, *5*, 385-415.
[105] A. Rauk, L. C. Allen, K. Mislow, *Angew. Chem. Int. Ed. Engl.* **1970**, *9*, 400-414.
[106] J.-C. Chambron, C. Dietrich-Buchecker, J.-P. Sauvage, *Top. Curr. Chem.* **1993**, *165*, 131-162.
[107] I. T. Harrison, S. Harrison, *J. Am. Chem. Soc.* **1967**, *89*, 5723-5724.
[108] C. Wolf, *Dynamic Stereochemistry of Chiral Compounds*, Royal Society of Chemistry, Cambridge, **2007**.
[109] C. Reuter, R. Schmieder, F. Vögtle, *Pure Appl. Chem.* **2000**, *72*, 2233-2241.
[110] E. M. G. Jamieson, F. Modicom, S. M. Goldup, *Chem. Soc. Rev.* **2018**, *47*, 5266-5311.
[111] C. Yamamoto, Y. Okamoto, T. Schmidt, R. Jäger, F. Vögtle, *J. Am. Chem. Soc.* **1997**, *119*, 10547-10548.
[112] S. Corra, C. de Vet, J. Groppi, M. La Rosa, S. Silvi, M. Baroncini, A. Credi, *J. Am. Chem. Soc.* **2019**, *141*, 9129-9133.
[113] T. Takata, F. Ishiwari, *ChemRxiv* **2019**, *DOI: 10.26434/chemrxiv.10279208.v1 This content is a preprint and has not been peer reviewed. .*
[114] M. Alvarez-Perez, S. M. Goldup, D. A. Leigh, A. M. Slawin, *J. Am. Chem. Soc.* **2008**, *130*, 1836-1838.
[115] E. M. G. Jamieson, S. M. Goldup, *Nat. Chem.* **2019**, *11*, 765-767.
[116] J. R. J. Maynard, S. M. Goldup, *Chem* **2020**, *6*, 1914-1932.

[117] Y. Makita, N. Kihara, N. Nakakoji, T. Takata, S. Inagaki, C. Yamamoto, Y. Okamoto, *Chem. Lett.* **2007**, *36*, 162-163.
[118] A. Imayoshi, B. V. Lakshmi, Y. Ueda, T. Yoshimura, A. Matayoshi, T. Furuta, T. Kawabata, *Nat. Commun.* **2021**, *12*, 404.
[119] R. J. Bordoli, S. M. Goldup, *J. Am. Chem. Soc.* **2014**, *136*, 4817-4820.
[120] G. De Bo, G. Dolphijn, C. T. McTernan, D. A. Leigh, *J. Am. Chem. Soc.* **2017**, *139*, 8455-8457.
[121] S. D. P. Fielden, D. A. Leigh, C. T. McTernan, B. Perez-Saavedra, I. J. Vitorica-Yrezabal, *J. Am. Chem. Soc.* **2018**, *140*, 6049-6052.
[122] C. Tian, S. D. P. Fielden, G. F. S. Whitehead, I. J. Vitorica-Yrezabal, D. A. Leigh, *Nat. Commun.* **2020**, *11*, 744.
[123] C. Tian, S. D. P. Fielden, B. Perez-Saavedra, I. J. Vitorica-Yrezabal, D. A. Leigh, *J. Am. Chem. Soc.* **2020**, *142*, 9803-9808.
[124] S. A. Vignon, J. Wong, H. R. Tseng, J. F. Stoddart, *Org. Lett.* **2004**, *6*, 1095-1098.
[125] M. Asakawa, G. Brancato, M. Fanti, D. A. Leigh, T. Shimizu, A. M. Z. Slawin, J. K. Y. Wong, F. Zerbetto, S. Zhang, *J. Am. Chem. Soc.* **2002**, *124*, 2939-2950.
[126] F. Ishiwari, K. Nakazono, Y. Koyama, T. Takata, *Angew. Chem. Int. Ed.* **2017**, *56*, 14858-14862.
[127] A. W. Heard, S. M. Goldup, *Chem* **2020**, *6*, 994-1006.
[128] M. J. Johansson, D. J. Gorin, S. T. Staben, F. D. Toste, *J. Am. Chem. Soc.* **2005**, *127*, 18002-18003.
[129] L. Zhang, H. X. Wang, S. Li, M. Liu, *Chem. Soc. Rev.* **2020**, *49*, 9095-9120.
[130] A. H. G. David, J. F. Stoddart, *Isr. J. Chem.* **2021**, *61*, 1-15.
[131] B. L. Feringa, R. A. van Delden, N. Koumura, E. M. Geertsema, *Chem. Rev.* **2000**, *100*, 1789-1816.
[132] C. A. Schalley, *Analytical Methods in Supramolecular Chemistry, 2nd Edition*, Wiley-VCH, Weinheim, **2012**.
[133] H. S. Gutowsky, H. N. Cheng, *J. Chem. Phys.* **1975**, *63*, 2439-2441.
[134] D. D. Gunbas, A. M. Brouwer, *J. Org. Chem.* **2012**, *77*, 5724-5735.
[135] M. Hmadeh, A. C. Fahrenbach, S. Basu, A. Trabolsi, D. Benitez, H. Li, A. M. Albrecht-Gary, M. Elhabiri, J. F. Stoddart, *Chem. Eur. J.* **2011**, *17*, 6076-6087.
[136] P. G. Young, K. Hirose, Y. Tobe, *J. Am. Chem. Soc.* **2014**, *136*, 7899-7906.
[137] J. L. Zhang, J. Q. Zhong, J. D. Lin, W. P. Hu, K. Wu, G. Q. Xu, A. T. Wee, W. Chen, *Chem. Soc. Rev.* **2015**, *44*, 2998-3022.
[138] A. P. de Silva, I. M. Dixon, H. Q. N. Gunaratne, T. Gunnlaugsson, P. R. S. Maxwell, T. E. Rice, *J. Am. Chem. Soc.* **1999**, *121*, 1393-1394.
[139] T. Jasper-Toennies, M. Gruber, S. Karan, H. Jacob, F. Tuczek, R. Berndt, *Nano Lett.* **2017**, *17*, 6613-6619.
[140] A. Coskun, M. Banaszak, R. D. Astumian, J. F. Stoddart, B. A. Grzybowski, *Chem. Soc. Rev.* **2012**, *41*, 19-30.
[141] D. Dattler, G. Fuks, J. Heiser, E. Moulin, A. Perrot, X. Yao, N. Giuseppone, *Chem. Rev.* **2020**, *120*, 310-433.
[142] M. V. Martínez-Díaz, N. Spencer, J. F. Stoddart, *Angew. Chem. Int. Ed. Eng.* **1997**, *36*, 1904-1907.
[143] G. Du, E. Moulin, N. Jouault, E. Buhler, N. Giuseppone, *Angew. Chem. Int. Ed.* **2012**, *51*, 12504-12508.
[144] K. Nakazono, T. Takata, *Chem. Eur. J.* **2010**, *16*, 13783-13794.
[145] Y. Tachibana, H. Kawasaki, N. Kihara, T. Takata, *J. Org. Chem.* **2006**, *71*, 5093-5104.
[146] P. Waeles, M. Gauthier, F. Coutrot, *Angew. Chem. Int. Ed.* **2021**, *60*, 16778-16799.
[147] Z. Chen, D. Aoki, S. Uchida, H. Marubayashi, S. Nojima, T. Takata, *Angew. Chem. Int. Ed.* **2016**, *55*, 2778-2781.
[148] M. Baroncini, S. Silvi, M. Venturi, A. Credi, *Chem. Eur. J.* **2010**, *16*, 11580-11587.
[149] M. Baroncini, S. Silvi, M. Venturi, A. Credi, *Angew. Chem. Int. Ed.* **2012**, *51*, 4223-4226.
[150] P. Reimann, *Phys. Rep.* **2002**, *361*, 57-265.
[151] M. Baroncini, L. Casimiro, C. de Vet, J. Groppi, S. Silvi, A. Credi, *ChemistryOpen* **2018**, *7*, 169-179.

[152] S. Erbas-Cakmak, S. D. P. Fielden, U. Karaca, D. A. Leigh, C. T. McTernan, D. J. Tetlow, M. R. Wilson, *Science* **2017**, *358*, 340-343.
[153] B. Hille, Sinauer Associates, Inc., Sunderland, Massachusetts U.S.A., **2001**.
[154] Jeremy M. Berg, John L. Tymoczko, L. Stryer, *Biochemistry, 5th Edition*, W. H. Freeman, New York, **2002**.
[155] J. C. Skou, *Angew. Chem. Int. Ed. Engl.* **1998**, *37*, 2320-2328.
[156] Y. Feng, M. Ovalle, J. S. W. Seale, C. K. Lee, D. J. Kim, R. D. Astumian, J. F. Stoddart, *J. Am. Chem. Soc.* **2021**, *143*, 5569-5591.
[157] C. Cheng, P. R. McGonigal, S. T. Schneebeli, H. Li, N. A. Vermeulen, C. Ke, J. F. Stoddart, *Nat. Nanotechnol.* **2015**, *10*, 547-553.
[158] C. Pezzato, M. T. Nguyen, D. J. Kim, O. Anamimoghadam, L. Mosca, J. F. Stoddart, *Angew. Chem. Int. Ed.* **2018**, *57*, 9325-9329.
[159] C. Pezzato, M. T. Nguyen, C. Cheng, D. J. Kim, M. T. Otley, J. F. Stoddart, *Tetrahedron Lett.* **2017**, *73*, 4849-4857.
[160] V. Serreli, C. F. Lee, E. R. Kay, D. A. Leigh, *Nature* **2007**, *445*, 523-527.
[161] M. Canton, J. Groppi, L. Casimiro, S. Corra, M. Baroncini, S. Silvi, A. Credi, *J. Am. Chem. Soc.* **2021**, *143*, 10890-10894.
[162] I. M. Bennett, H. M. Farfano, F. Bogani, A. Primak, P. A. Liddell, L. Otero, L. Sereno, J. J. Silber, A. L. Moore, T. A. Moore, D. Gust, *Nature* **2002**, *420*, 398-401.
[163] S. Amano, S. D. P. Fielden, D. A. Leigh, *Nature* **2021**, *594*, 529-534.
[164] M. Yan, Y. Kawamata, P. S. Baran, *Chem. Rev.* **2017**, *117*, 13230-13319.
[165] Piero Zanello, F. F. d. Biani, C. Nervi, *Inorganic Electrochemistry: Theory, Practice and Application 2nd Ed.*, Royal Society of Chemistry, Cambridge, **2012**.
[166] K. J. Lee, N. Elgrishi, B. Kandemir, J. L. Dempsey, *Nat. Rev. Chem.* **2017**, *1*.
[167] D. Xiang, X. Wang, C. Jia, T. Lee, X. Guo, *Chem. Rev.* **2016**, *116*, 4318-4440.
[168] Angel Kaifer, M. Gomez-Kaifer, *Supramolecular Electrochemistry*, Wiley-VCH, Weinheim, **1999**.
[169] A. C. Paola Ceroni, Margherita Venturi, *Electrochemistry of Functional Supramolecular Systems*, Wiley, Hoboken, **2010**.
[170] J. S. Stock, *Electrochemistry, Past and Present*, American Chemical Society, Washington D.C., **1989**.
[171] W. V. Mayneord, *Biogr. Mem. Fellows R. Soc.* **1979**, *25*, 144-178.
[172] T. Erdey-Grúz, M. Volmer, *Z. Phys. Chem.* **1930**, *150A*, 203-213.
[173] A. J. Bard, H. D. Abruna, C. E. Chidsey, L. R. Faulkner, S. W. Feldberg, K. Itaya, M. Majda, O. Melroy, R. W. Murray, *J. Phys. Chem.* **1993**, *97*, 7147-7173.
[174] N. Elgrishi, K. J. Rountree, B. D. McCarthy, E. S. Rountree, T. T. Eisenhart, J. L. Dempsey, *J Chem. Educ.* **2018**, *95*, 197-206.
[175] J. R. Aranzaes, M.-C. Daniel, D. Astruc, *Can. J. Chem.* **2006**, *84*, 288-299.
[176] W. E. Geiger, F. Barriere, *Acc. Chem. Res.* **2010**, *43*, 1030-1039.
[177] K. Izutsu, *Electrochemistry in Nonaqueous Solutions 2nd Ed.*, Wiley-VCH Weinheim, **2009**.
[178] D. Stíbal, B. Therrien, in *Comprehensive Supramolecular Chemistry II* (Ed.: J. L. Atwood), Elsevier, Amsterdam, **2017**, pp. 305-329.
[179] H. Hofmeier, U. S. Schubert, *Chem. Soc. Rev.* **2004**, *33*, 373-399.
[180] J. Ding, C. Zheng, L. Wang, C. Lu, B. Zhang, Y. Chen, M. Li, G. Zhai, X. Zhuang, *J. Mater. Chem. A* **2019**, *7*, 23337-23360.
[181] J. E. Nutting, M. Rafiee, S. S. Stahl, *Chem. Rev.* **2018**, *118*, 4834-4885.
[182] J. Shukla, P. Mukhopadhyay, *Eur. J. Org. Chem.* **2019**, *2019*, 7770-7786.
[183] C. G. Zoski, *Handbook of Electrochemistry*, Elsevier, Amsterdam, **2007**.
[184] M. A. Kobaisi, S. V. Bhosale, K. Latham, A. M. Raynor, S. V. Bhosale, *Chem. Rev.* **2016**, *116*, 11685-11796.
[185] S. V. Bhosale, M. Al Kobaisi, R. W. Jadhav, P. P. Morajkar, L. A. Jones, S. George, *Chem. Soc. Rev.* **2021**.
[186] C. Thalacker, C. Roger, F. Würthner, *J. Org. Chem.* **2006**, *71*, 8098-8105.
[187] A. Diac, M. Matache, I. Grosu, N. D. Hădade, *Adv. Synth. Catal.* **2018**, *360*, 817-845.
[188] N. Martin, *Chem. Commun.* **2013**, *49*, 7025-7027.

[189] S. Adeel, M. E. Abdelhamid, A. Nafady, Q. Li, L. L. Martin, A. M. Bond, *RSC Adv.* **2015**, *5*, 18384-18390.
[190] D. Canevet, M. Salle, G. Zhang, D. Zhang, D. Zhu, *Chem. Commun.* **2009**, 2245-2269.
[191] S. V. Rosokha, J. K. Kochi, *J. Am. Chem. Soc.* **2007**, *129*, 828-838.
[192] J. B. Torrance, B. A. Scott, B. Welber, F. B. Kaufman, P. E. Seiden, *Phys. Rev. B* **1979**, *19*, 730-741.
[193] R. Bozio, I. Zanon, A. Girlando, C. Pecile, *J. Chem. Phys.* **1979**, *71*, 2282.
[194] H. V. Schröder, C. A. Schalley, *Beilstein J. Org. Chem.* **2018**, *14*, 2163-2185.
[195] M. R. Bryce, *Adv. Mater.* **1999**, *11*, 11-23.
[196] K. P. Goetz, D. Vermeulen, M. E. Payne, C. Kloc, L. E. McNeil, O. D. Jurchescu, *J. Mater. Chem. C* **2013**, *2*, 3065-3076.
[197] R. Klajn, J. F. Stoddart, B. A. Grzybowski, *Chem. Soc. Rev.* **2010**, *39*, 2203-2237.
[198] L. Chen, Y.-C. Zhang, W.-K. Wang, J. Tian, L. Zhang, H. Wang, D.-W. Zhang, Z.-T. Li, *Chin. Chem. Lett.* **2015**, *26*, 811-816.
[199] M. Hasegawa, K. Nakamura, S. Tokunaga, Y. Baba, R. Shiba, T. Shirahata, Y. Mazaki, Y. Misaki, *Chem. Eur. J.* **2016**, *22*, 10090-10101.
[200] J. L. Segura, N. Martín, *Angew. Chem. Int. Ed.* **2001**, *40*, 1372-1409.
[201] M. B. Nielsen, C. Lomholt, J. Becher, *Chem. Soc. Rev.* **2000**, *29*, 153-164.
[202] N. Svenstrup, J. Becher, *Synthesis* **1995**, *1995*, 215-235.
[203] K. B. Simonsen, N. Svenstrup, J. Lau, O. Simonsen, P. Mørk, G. J. Kristensen, J. Becher, *Synthesis* **1996**, *1996*, 407-418.
[204] P. Blanchard, M. Sallé, G. Duguay, M. Jubault, A. Gorgues, *Tetrahedron Lett.* **1992**, *33*, 2685-2688.
[205] A. Gese, M. Akter, G. Schnakenburg, A. García Alcaraz, A. Espinosa Ferao, R. Streubel, *New J. Chem.* **2020**, *44*, 17122-17128.
[206] J. Garin, *Adv. Heterocycl. Chem.* **1995**, *62*, 249-296.
[207] A. Jana, S. Bahring, M. Ishida, S. Goeb, D. Canevet, M. Salle, J. O. Jeppesen, J. L. Sessler, *Chem. Soc. Rev.* **2018**, *47*, 5614-5645.
[208] T. K. Hansen, T. Joergensen, F. Jensen, P. H. Thygesen, K. Christiansen, M. B. Hursthouse, M. E. Harman, M. A. Malik, B. Girmay, *J. Org. Chem.* **1993**, *58*, 1359-1366.
[209] K. Christiansen, J. Becher, T. K. Hansen, *Tetrahedron Lett.* **1992**, *33*, 3035-3038.
[210] H. V. Schröder, H. Hupatz, A. J. Achazi, S. Sobottka, B. Sarkar, B. Paulus, C. A. Schalley, *Chem. Eur. J.* **2017**, *23*, 2960-2967.
[211] H. V. Schröder, A. Mekic, H. Hupatz, S. Sobottka, F. Witte, L. H. Urner, M. Gaedke, K. Pagel, B. Sarkar, B. Paulus, C. A. Schalley, *Nanoscale* **2018**, *10*, 21425-21433.
[212] T. Akutagawa, Y. Abe, Y.-i. Nezu, T. Nakamura, M. Kataoka, A. Yamanaka, K. Inoue, T. Inabe, C. A. Christensen, J. Becher, *Inorg. Chem.* **1998**, *37*, 2330-2331.
[213] T. K. Hansen, T. Joergensen, P. C. Stein, J. Becher, *J. Org. Chem.* **1992**, *57*, 6403-6409.
[214] G. Trippe, E. Levillain, F. Le Derf, A. Gorgues, M. Salle, J. O. Jeppesen, K. Nielsen, J. Becher, *Org. Lett.* **2002**, *4*, 2461-2464.
[215] A. Jana, M. Ishida, J. S. Park, S. Bahring, J. O. Jeppesen, J. L. Sessler, *Chem. Rev.* **2016**.
[216] H. Nagai, Y. Suzaki, K. Osakada, *Eur. J. Inorg. Chem.* **2014**, *2014*, 4376-4384.
[217] H. V. Schröder, F. Stein, J. M. Wollschläger, S. Sobottka, M. Gaedke, B. Sarkar, C. A. Schalley, *Angew. Chem. Int. Ed.* **2019**, *58*, 3496-3500.
[218] M. Baroncini, S. Silvi, A. Credi, *Chem. Rev.* **2020**, *120*, 200-268.
[219] H. V. Schröder, C. A. Schalley, *Chem. Sci.* **2019**, *10*, 9626-9639.
[220] K. Cai, L. Zhang, R. D. Astumian, J. F. Stoddart, *Nature Rev. Chem.* **2021**, *5*, 447-465.
[221] H. V. Schröder, J. M. Wollschläger, C. A. Schalley, *Chem. Commun.* **2017**, *53*, 9218-9221.
[222] A. Saad, F. Barriere, E. Levillain, N. Vanthuyne, O. Jeannin, M. Fourmigue, *Chem. Eur. J.* **2010**, *16*, 8020-8028.
[223] J. M. Spruell, A. Coskun, D. C. Friedman, R. S. Forgan, A. A. Sarjeant, A. Trabolsi, A. C. Fahrenbach, G. Barin, W. F. Paxton, S. K. Dey, M. A. Olson, D. Benitez, E. Tkatchouk, M. T. Colvin, R. Carmielli, S. T. Caldwell, G. M. Rosair, S. G. Hewage, F. Duclairoir, J. L. Seymour, A. M. Slawin, W. A. Goddard III, M. R. Wasielewski, G. Cooke, J. F. Stoddart, *Nat. Chem.* **2010**, *2*, 870-879.
[224] E. M. Sevick, D. R. Williams, *ChemPhysChem* **2016**, *17*, 1927-1933.

[225] E. M. Sevick, D. R. Williams, *Langmuir* **2010**, *26*, 5864-5868.
[226] R. J. J. Boesten, E. M. Sevick, D. R. M. Williams, *Macromolecules* **2010**, *43*, 7244-7249.
[227] C. Reichardt, *Chem. Rev.* **1994**, *94*, 2319-2358.
[228] Y. Qiu, Y. Feng, Q.-H. Guo, R. D. Astumian, J. F. Stoddart, *Chem* **2020**, *6*, 1952-1977.
[229] C. Cheng, P. R. McGonigal, J. F. Stoddart, R. D. Astumian, *ACS Nano* **2015**, *9*, 8672-8688.
[230] Y. Wang, M. Frasconi, W. G. Liu, Z. Liu, A. A. Sarjeant, M. S. Nassar, Y. Y. Botros, W. A. Goddard, 3rd, J. F. Stoddart, *J. Am. Chem. Soc.* **2015**, *137*, 876-885.
[231] A. Trabolsi, N. Khashab, A. C. Fahrenbach, D. C. Friedman, M. T. Colvin, K. K. Coti, D. Benitez, E. Tkatchouk, J. C. Olsen, M. E. Belowich, R. Carmielli, H. A. Khatib, W. A. Goddard, 3rd, M. R. Wasielewski, J. F. Stoddart, *Nat. Chem.* **2010**, *2*, 42-49.
[232] A. C. Catalan, J. Tiburcio, *Chem. Commun.* **2016**, *52*, 9526-9529.
[233] Y. Koyama, M. Yonekawa, T. Takata, *Chem. Lett.* **2008**, *37*, 918-919.
[234] A. M. Elizarov, S. H. Chiu, J. F. Stoddart, *J. Org. Chem.* **2002**, *67*, 9175-9181.
[235] Y. Tokunaga, M. Kawabata, N. Matsubara, *Org. Biomol. Chem.* **2011**, *9*, 4948-4953.
[236] W. Jiang, A. Schäfer, P. C. Mohr, C. A. Schalley, *J. Am. Chem. Soc.* **2010**, *132*, 2309-2320.
[237] M. A. Soto, F. Lelj, M. J. MacLachlan, *Chem. Sci.* **2019**, *10*, 10422-10427.
[238] J. D. Harris, M. J. Moran, I. Aprahamian, *Proc. Natl. Acad. Sci. U. S. A.* **2018**, *115*, 9414-9422.
[239] H. Iguchi, S. Uchida, Y. Koyama, T. Takata, *ACS Macro Lett.* **2013**, *2*, 527-530.
[240] D. B. Llewellyn, D. Adamson, B. A. Arndtsen, *Org. Lett.* **2000**, *2*, 4165-4168.
[241] M. Brezgunova, K.-S. Shin, P. Auban-Senzier, O. Jeannin, M. Fourmigué, *Chem. Commun.* **2010**, *46*, 3926.
[242] W. Danowski, F. Castiglioni, A. S. Sardjan, S. Krause, L. Pfeifer, D. Roke, A. Comotti, W. R. Browne, B. L. Feringa, *J. Am. Chem. Soc.* **2020**, *142*, 9048-9056.
[243] F. Lancia, A. Ryabchun, N. Katsonis, *Nat. Rev. Chem.* **2019**, *3*, 536-551.
[244] B. K. Pathem, S. A. Claridge, Y. B. Zheng, P. S. Weiss, *Annu. Rev. Phys. Chem.* **2013**, *64*, 605-630.
[245] Y. Shirai, K. Minami, W. Nakanishi, Y. Yonamine, C. Joachim, K. Ariga, *Jpn. J. Appl. Phys.* **2016**, *55*, 1102A1102.
[246] J. Riebe, J. Niemeyer, *Eur. J. Org. Chem.* **2021**, DOI: 10.1002/ejoc.202100749.

7 Appendix

7.1 Additional Publications not Included in This Thesis

- ***Impact of mechanical bonding on the redox-switching of tetrathiafulvalene in crown ether-ammonium [2]rotaxanes***

H.V. Schröder, S. Sobottka, M. Nößler, H. Hupatz, M. Gaedke, B. Sarkar, C. A. Schalley, *Chem. Sci.* **2017**, 8, 6300-6306.

- ***An aryl-fused redox-active tetrathiafulvalene with enhanced mixed-valence and radical-cation dimer stabilities***

H.V. Schröder, Felix Witte, M. Gaedke, S. Sobottka, L. Suntrup, H. Hupatz, A. Valkonen, B. Paulus, K. Rissanen, B. Sarkar, C. A. Schalley, *Org. Biomol. Chem.* **2018**, 16, 2741-2747.

- ***Ion mobility and gas phase H/D exchange: revealing the importance of a single hydrogen bond for the chiral recognition of crown ether ammonium complexes***

J. M. Wollschläger, K. Simon, M. Gaedke, C. A. Schalley, *Chem. Commun.* **2018**, 54, 4967-4970.

- ***Switchable synchronisation of pirouetting motions in a redox active [3]rotaxane***

H.V. Schröder, A. Mekic, H. Hupatz, S. Sobottka, F. Witte, L.H. Urner, M. Gaedke, K. Pagel, B. Sarkar, B. Paulus, C. A. Schalley, *Nanoscale* **2018**, 10, 21425-21433.

- ***Accordion-like Motion in Electrochemically Switchable Crown Ether/Ammonium Oligorotaxanes***

H.V. Schröder, F. Stein, J.M. Wollschläger, S. Sobottka, M. Gaedke, B. Sarkar, C. A. Schalley, *Angew. Chem. Int. Ed.* **2019**, 58, 3496-3500; *Angew. Chem.* **2019**, 131, 3534-3538.

7.2 Curriculum Vitae

For reasons of data protection, the curriculum vitae is not published in the electronic version.

For reasons of data protection, the curriculum vitae is not published in the electronic version.

8 Appendix: Publications

The following publications are attached unmodified and therefore have no continuous page numbering:

Chiroptical Inversion of a Planar Chiral Redox-Switchable Rotaxane, M. Gaedke, F. Witte, J. Anhäuser, H. Hupatz, H. V. Schröder, A. Valkonen, K. Rissanen, A. Lützen, B. Paulus, C. A. Schalley, *Chem. Sci.* **2019**, 10, 10003-10009. (https://doi.org/10.1039/C9SC03694F)

Reproduced with permission from the Royal Society of Chemistry.

Thermodynamic and Electrochemical Study of Tailor-Made Crown Ethers for Redox-Switchable (Pseudo)rotaxanes, H. Hupatz, M. Gaedke, H. V. Schröder, J. Beerhues, A. Valkonen, F. Klautzsch, S. Müller, F. Witte, K. Rissanen, B. Sarkar, C. A. Schalley, *Beilstein J. Org. Chem.* **2020**, 16, 2576-2588. (https://doi.org/10.3762/bjoc.16.209)

Dual-Stimuli Pseudorotaxane Switches Under Kinetic Control, M. Gaedke, H. Hupatz, H. V. Schröder, S. Suhr, K. F. Hoffmann, A. Valkonen, B. Sarkar, S. Riedel, K. Rissanen, C. A. Schalley, *Org. Chem. Front.*, **2021**, 8, 3659-3667. (https://doi.org/10.1039/D1QO00503K)

Reproduced with permission from the Chinese Chemical Society (CCS), Shanghai Institute of Organic Chemistry (SIOC), and the Royal Society of Chemistry.

Sequence-Sorted Redox-Switchable Hetero[3]rotaxanes, M. Gaedke,* H. Hupatz,* Felix Witte, S. M. Rupf, C. Douglas, H. V. Schröder, L. Fischer, M. Malischewski, B. Paulus, C. A. Schalley, (https://doi.org/10.33774/chemrxiv-2021-vj7k2-v2)

Chemical Science

EDGE ARTICLE

View Article Online
View Journal | View Issue

Cite this: *Chem. Sci.*, 2019, **10**, 10003

All publication charges for this article have been paid for by the Royal Society of Chemistry

Received 26th July 2019
Accepted 4th September 2019

DOI: 10.1039/c9sc03694f

rsc.li/chemical-science

Chiroptical inversion of a planar chiral redox-switchable rotaxane†

Marius Gaedke,[a] Felix Witte,[a] Jana Anhäuser,[b] Henrik Hupatz,[a] Hendrik V. Schröder,[a] Arto Valkonen,[c] Kari Rissanen,[c] Arne Lützen,[b] Beate Paulus[a] and Christoph A. Schalley*[a]

A tetrathiafulvalene (TTF)-containing crown ether macrocycle with C_s symmetry was designed to implement planar chirality into a redox-active [2]rotaxane. The directionality of the macrocycle atom sequence together with the non-symmetric axle renders the corresponding [2]rotaxane mechanically planar chiral. Enantiomeric separation of the [2]rotaxane was achieved by chiral HPLC. The electrochemical properties – caused by the reversible oxidation of the TTF – are similar to a non-chiral control. Reversible inversion of the main band in the ECD spectra for the individual enantiomers was observed after oxidation. Experimental evidence, conformational analysis and DFT calculations of the neutral and doubly oxidised species indicate that mainly electronic effects of the oxidation are responsible for the chiroptical switching. This is the first electrochemically switchable rotaxane with a reversible inversion of the main ECD band.

Introduction

Evidenced by the homochirality in our biosphere,[1–3] chirality is a fundamental principle, which governs the molecular recognition and activity of virtually all biomolecules. Therefore, gaining control over the preferred isomer of a molecule or an assembly by carefully designing a molecular system is a worthwhile endeavour.

The term "chiroptical switch" has been used by Canary to refer to molecules, which are capable of "changes in their interaction with polarized light".[4] Potential applications are information processing, data storage and sensing. In this context, the ground breaking work of Feringa and co-workers[5–7] on overcrowded alkenes, which act as light triggered chiroptical switches was awarded with the Nobel Prize in chemistry 2016 "for the design and synthesis of molecular machines"[8] and underlines the general interest in this topic.

Mechanically interlocked molecules (MIMs)[9–12] consist of parts that can move relative to each other guided by intramolecular forces. Therefore, we envisioned them to be ideal candidates for chiroptical switches in which co-conformational or even configurational changes in the MIM occur.

An achiral wheel with directionality in its atom sequence forms a chiral [2]rotaxane, when threaded onto a directional

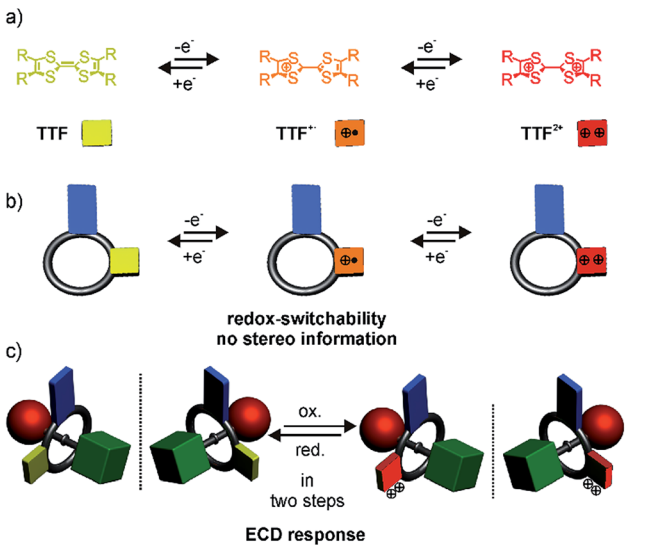

Scheme 1 (a) Reversible one-electron oxidations of the TTF moiety, (b) reversible oxidation of a directional crown ether wheel bearing a TTF unit, (c) chiroptical switching of the planar chiral [2]rotaxane enantiomers.

[a]Institut für Chemie und Biochemie, Freie Universität Berlin, Takustr. 3, 14195 Berlin, Germany. E-mail: c.schalley@schalley-lab.de

[b]Kekulé-Institut für Organische Chemie und Biochemie, Universität Bonn, Gerhard-Domagk-Str. 1, 53121 Bonn, Germany

[c]University of Jyvaskyla, Department of Chemistry, P.O. Box 35, 40014 Jyväskylä, Finland

† Electronic supplementary information (ESI) available: Synthetic procedures including full characterisation of new compounds, electrochemical data, crystallographic data and mass spectrometry data. CCDC 1910670. For ESI and crystallographic data in CIF or other electronic format see DOI: 10.1039/c9sc03694f

axle (Scheme 1). In 1997, Vögtle *et al.* reported on the first resolution of a racemate of such mechanically planar chiral rotaxanes.[13] Chiral rotaxanes may be chiral from inclusion of classical stereogenic elements or by virtue of being mechanically planar chiral. Since then, several examples followed,[14–25] in which the mechanically interlocked structure was used to induce directionality in polymers,[26–28] for sensing,[29–31] and to act as an enantioselective catalyst.[32] Today, sophisticated synthetic protocols allow an efficient enantioselective synthesis. For example, Goldup and co-workers[33,34] described elegant protocols to synthesise planar chiral enantiopure [2]rotaxanes using readily available chiral auxiliaries. However, switchable planar chiral rotaxanes remain rare. So far, the modulation of chirality relies on heat,[21] the choice of solvent, anion exchange,[35] or pH.[36]

Recently, we described redox-switchable rotaxanes, in which the wheels are decorated with tetrathiafulvalenes (TTF).[37–41] TTF can be reversibly oxidised to the $TTF^{\bullet+}$ and TTF^{2+} states (Scheme 1). Large-amplitude motion and co-conformational changes in (oligo)rotaxanes were triggered by redox chemistry.[38,42–50] Apart from rotaxanes, TTF derivatives with covalently bound chiral substituents exhibited a chiroptical response to a change of their redox-state.[51–57] Hence, our switchable rotaxanes display ideal optoelectronic properties since they are air stable in their neutral and oxidised form and show a clear-cut optical output,[37] which is even visible by the naked eye.

In this paper, we report the synthesis, characterisation and optical resolution of a new mechanically planar chiral tristable [2]rotaxane based on the 24-crown-8/secondary ammonium binding motif.[58] The rotaxane consists of the directional wheel **dTTFC8** (Scheme 2), which is derived from a C_{2v}-symmetric TTF-decorated crown ether **TTFC8** (Scheme 2) published by our group recently.[38] ECD measurements show reversible chiroptical switching, which can be explained mainly by electronic changes. The measurements are supported by quantum chemical calculations, which were also used to determine the absolute configuration. To the best of our knowledge, this is the first example of a chiroptical switch with a complete sign reversal of the main band in the ECD spectra based on electronic changes in a mechanically bound assembly.

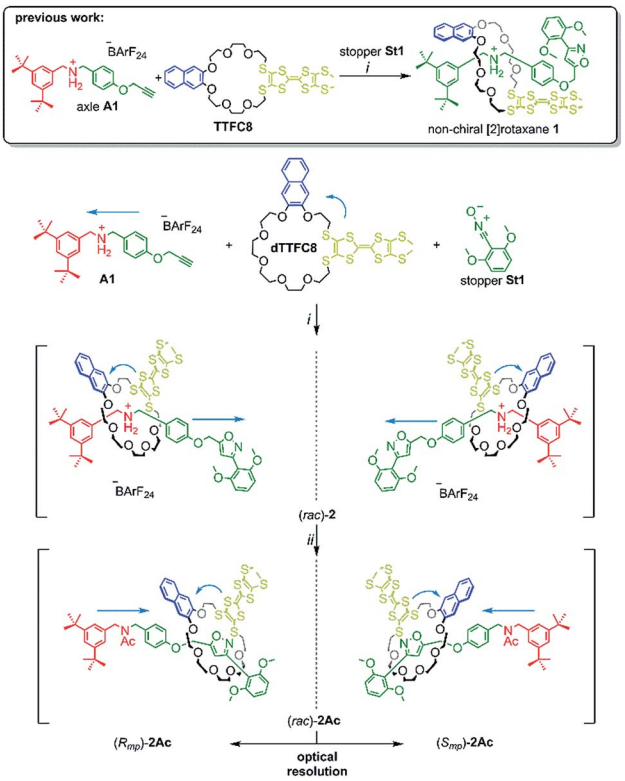

Scheme 2 Synthesis of rotaxanes (*rac*)-**2** and (*rac*)-**2Ac**. Conditions and reagents: (i) DCM, 35 °C, 12 h (73%); (ii) Ac_2O, NEt_3, ACN, 12 h, r.t. (95%).

Results and discussion

Synthesis and characterisation

The prerequisite for rotaxane formation is a sufficiently high binding constant between the crown ether and the ammonium axle. ITC experiments revealed an association constant of $K_a = (3.6 \pm 0.3)\ 10^5\ M^{-1}$ and a 1 : 1 stoichiometry for pseudorotaxane formation from **dTTFC8** and axle **A1** (Scheme 2). The binding constant is very similar to that of our previous non-directional TTF-decorated wheel **TTFC8** ($K_a = (4.4 \pm 0.4)\ 10^5\ M^{-1}$, for thermodynamic parameters see ESI,† Section 4),[38] which indicates the positional change of the TTF unit not to significantly affect the binding properties of the wheel.

As for the non-chiral [2]rotaxane **1**, rotaxane formation was achieved with nitrile-oxide stopper **St1** using a catalyst-free end-capping protocol established by Takata and co-workers[59] yielding a racemic mixture of rotaxane (*rac*)-**2** (73%). The non-ionic version (*rac*)-**2Ac** (95%) was obtained through *N*-acylation with Ac_2O[60] (Scheme 2). The ^1H NMR spectra of (*rac*)-**2** and (*rac*)-**2Ac** (Fig. 1) reveal a diastereotopic splitting of the macrocycle's methylene protons as well as of the axle methylene protons H_h.[37,38] The splitting of both macrocycle and axle protons is characteristic for the formation of a chiral, yet racemic [2]rotaxane. Isoxazole formation during stopper attachment leads to a strong downfield shift of 3.88 ppm for proton H_i.

In (*rac*)-**2**, the *S*-methyl protons on **dTTFC8** split into two singlets of the same intensity. Comparable rotaxanes also showed this behaviour on the same position.[27,28] HR-ESI mass and tandem MS experiments support the interlocked architecture (Fig. S1†).

For non-ionic (*rac*)-**2Ac**, the shift of H_i ($\Delta\delta = +0.28$ ppm) and H_h ($\Delta\delta = +0.76$ ppm) relative to (*rac*)-**2** suggests that the wheel translates towards the isoxazole moiety in the absence of attractive interactions with the ammonium ion. Two sets of signals are observed due to the *cis–trans* isomerism of the amide bond in (*rac*)-**2Ac**. Variable temperature NMR experiments (Fig. S3†) in DMSO-d_6 reveal the same barrier ($\Delta G^{\ddagger} = 74 \pm 2$ kJ mol^{-1}) for amide *cis–trans* isomerisation as observed for a similar acetylated rotaxane.[41]

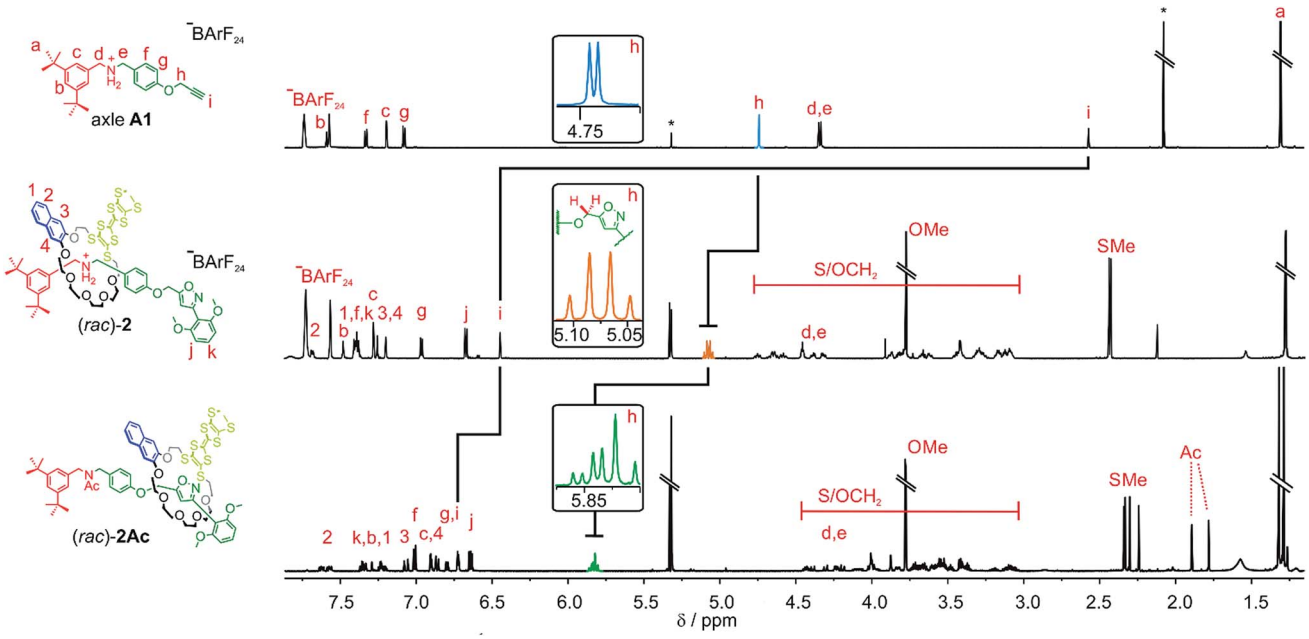

Fig. 1 Comparison of the shifts and splitting in the partial ^{1}H NMR spectra of the methylene groups on the axle **A1** (top), rotaxane (*rac*)-**2** (middle) and acetylated rotaxane (*rac*)-**2Ac** (bottom) (700 MHz, 298 K, CD_2Cl_2).

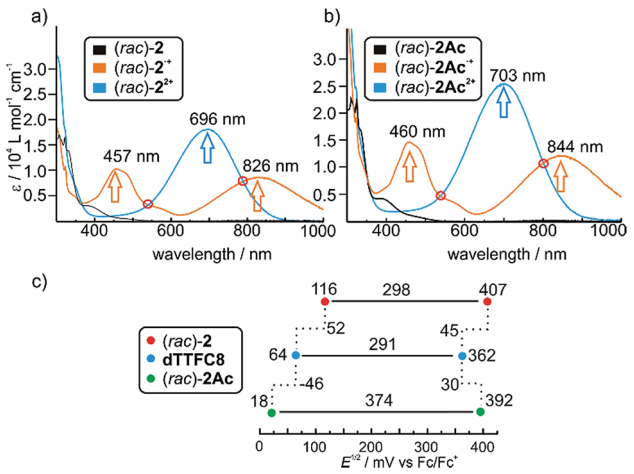

Fig. 2 UV/Vis spectra of (a) ionic (*rac*)-**2** and (b) non-ionic (*rac*)-**2Ac** in different oxidation states. Isosbestic points indicating a clean transition from $TTF^{\bullet+}$ to TTF^{2+} are highlighted with red circles. Spectra were obtained with 25 μM solutions in CH_2Cl_2 using bulk $Fe(ClO_4)_3$ as the oxidant; (c) correlation diagram of half-wave potentials obtained by cyclic voltammetry for the first and second redox process of (*rac*)-**2**, **dTTFC8** and (*rac*)-**2Ac** (each 1 mM) in CH_2Cl_2 referenced against $Fe(Cp)_2^{0/+}$ with NBu_4PF_6 (0.1 M) as the electrolyte.

Optoelectronic properties

Photometric titrations of (*rac*)-**2** and (*rac*)-**2Ac** with $Fe(ClO_4)_3$ (Fig. 2a and b) show similar bands for the three redox states (TTF, $TTF^{\bullet+}$ and TTF^{2+})[61–63] of both rotaxanes with distinct isosbestic points. These findings are consistent with structurally related rotaxanes featuring a non-directional TTF-decorated wheel.[38]

Cyclovoltammetric (CV) experiments were conducted with **dTTFC8**, (*rac*)-**2** and (*rac*)-**2Ac** in dichloromethane (Fig. 2c). The potentials for (*rac*)-**2** (116 mV and 407 mV) are considerably higher for both oxidation steps as compared to **dTTFC8** (64 mV and 362 mV). Both oxidations are thus energetically disfavoured because of the charge repulsion between the TTF cation radical as well as the TTF dication and the ammonium station. In case of (*rac*)-**2Ac** (18 mV and 392 mV) the first oxidation is more easily accomplished in comparison to the free macrocycle and the second oxidation is disfavoured. We attribute this behaviour to a stabilising interaction with the isoxazole moiety on the axle for the first oxidation.

For the second oxidation, the limited accessibility of the TTF^{2+} by counterions caused by the steric demand of the axle needs to be taken into account. Again these trends were already observed for the non-directional macrocycle and rotaxanes thereof.[38] The reversibility of the redox-waves of (*rac*)-**2** and (*rac*)-**2Ac** strongly indicated that the interlocked structures remain intact during the redox switching, however it is reasonable to assume conformational changes to occur due to charge repulsion and charge stabilisation. The data does not show any significant change in the electrochemical properties by introducing directionality into the TTF decorated wheel.

Enantiomer separation on chiral HPLC and CD spectroscopy

The two enantiomers of (*rac*)-**2Ac** could be separated using HPLC with a CHIRALPAK® IA stationary phase. The optical purity was determined (>99% ee; Fig. 3a) and mirror-image CD spectra were obtained for the neutral enantiomers with bands at 242 nm and 325 nm (Fig. 3b). We assigned the absolute configuration based on the computational results (see below).

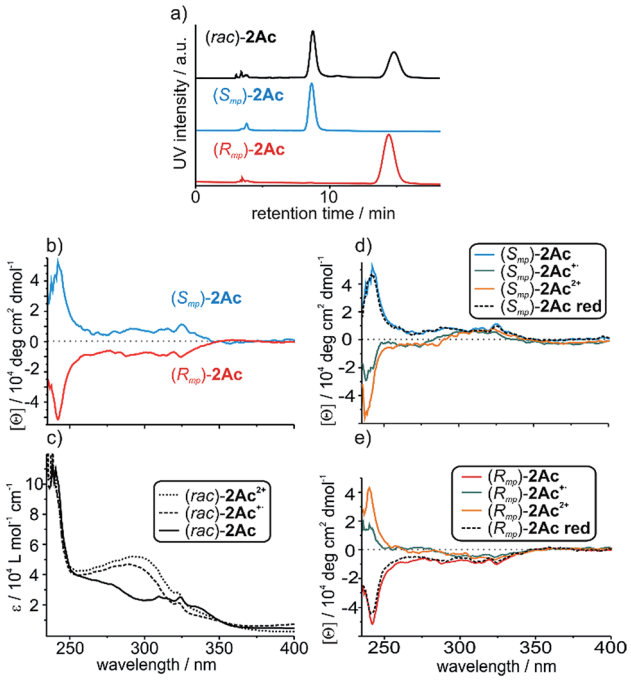

Fig. 3 (a) Traces of analytical chiral HPLC. The chromatographic resolution of (*rac*)-**2Ac** was realised by chiral phase HPLC on a CHIRALPAK® IA column using methyl *tert*-butylether/CH_2Cl_2 80 : 20 (v/v) as the eluent. (b) CD spectra of the individual neutral enantiomers and (c) partial UV/Vis spectra of the neutral, singly and doubly oxidized (*rac*)-**2Ac**. (d and e) CD spectra of the individual enantiomers in their three oxidation states and after reduction to the neutral state. Spectra were taken from 160 μM solutions in CH_2Cl_2 using bulk $Fe(ClO_4)_3$ as the oxidant and Zn dust as the reductant.

The oxidised species $\mathbf{2Ac}^{\bullet+}$ and $\mathbf{2Ac}^{2+}$ show bands at the same wavelengths. While no sign inversion occurs at 325 nm, the band at 242 nm exhibits a sign inversion during the first and a significant intensity increase during the second oxidation step. To exclude decomposition to be responsible for the switching, $\mathbf{2Ac}^{2+}$ was reduced back to the neutral state using Zn dust and then showed the initial CD spectrum again (Fig. 3d and e dashed lines). Surprisingly, no other CD signals are observed at a higher wavelength, although the change in UV/Vis absorption is most pronounced at 460 nm and 844 nm for the radical cation and at 703 nm for the dication (Fig. 2b). The reason for the sign change remains ambiguous. In fact, conformational changes were observed to induce transitions in CD spectra of non-interlocked TTF derivatives with centrochiral elements earlier.[53,64] Other examples show varying intensities[54] or shifts of the maxima[56] upon oxidation of the TTF attached.

Nevertheless, no TTF derivative is reported that shows a sign reversal in the maximum of an ECD spectrum without a shift in the wavelength. Apart from TTF derivatives, chiroptical switching *via* a redox process can be achieved with catechol,[65] viologen,[66] and tetraarylethylene[67] building blocks. Intense switching with a sign reversal was also observed for a viologen-type dicationic helquat.[68] Chiral inversion can also be achieved with metal ion complexation[69,70] acid–base-[71] and photoswitching.[6,68,72]

Computational results

To investigate whether the redox-induced sign inversion at 242 nm in the ECD spectra of (R_{mp})-**2Ac** is due to a change in its electronic properties or to a (co-)conformational change, density functional theory (DFT) calculations were performed at the TPSS-D3(BJ)[73–75] and ωB97X-D3 (ref. 76) levels. Conformational analyses reveal the structure depicted in Fig. 4 (left) to be the most stable one for (R_{mp})-**2Ac**. It is at least 18 kJ mol^{-1} more favourable than any other possible conformation found by theory (see Table S2†). For (R_{mp})-$\mathbf{2Ac}^{2+}$, there are two conformations relatively close in electronic energy: Conformer **A** (Fig. 4 middle) and **B** (Fig. 4 right) with a flipped naphthalene unit, *ca.* 9 kJ mol^{-1} more stable than **A**. This conformational change is explained by the oxidation of (R_{mp})-**2Ac** occuring fairly localised at the TTF unit.[77] The emerging charge of the oxidised TTF moiety is then stabilised by the naphthalene that moves into close proximity of the TTF^{2+}. Additionally, an atoms-in-molecules (AIM) analysis suggests that the electrostatic attraction between the naphthalene and TTF moieties outweighs all other non-covalent interactions for (R_{mp})-$\mathbf{2Ac}^{2+}$, while the maximisation of non-covalent interactions (C–H···π and π–π-stacking) is the most important factor in the neutral state (see ESI† for details).

The simulated CD spectra in Fig. 4 were obtained using simplified time-dependent DFT[78] at the ωB97X-D3 level. The spectrum of (R_{mp})-**2Ac** shows a deviation of around 40–50 nm, while that of (R_{mp})-$\mathbf{2Ac}^{2+}$ is off by less than 20 nm compared to experiment. The experimentally detected sign inversion at 242 nm is reproduced well by the calculations. The conformational change of (R_{mp})-**2Ac** upon oxidation, however, hardly influences the shape of the CD spectra as both conformations yield very similar CD spectra in the region between 230 and 400 nm. Therefore, we exclude the conformational change as the prime origin of the sign inversion.

To rationalise the optical behaviour of (R_{mp})-**2Ac** and (R_{mp})-$\mathbf{2Ac}^{2+}$, we examined its valence electronic structure, which is, as expected, dominated by orbitals localised at the TTF moiety (see Fig. S20†). Analysing the electronic transitions in the spectral region between 230 and 400 nm reveals that practically every excitation involves the TTF unit to some extent. While many transitions are of local nature, *i.e.*, between orbitals in close proximity, quite a few display a charge-transfer-like behaviour (insets Fig. 4 and S21†). For neutral (R_{mp})-**2Ac**, the vast majority of these transitions can be described by advancing an electron from an orbital centred at the TTF core, usually the HOMO, into an orbital located in another part of the rotaxane (*e.g.* the dimethoxy-phenyl moiety). For (R_{mp})-$\mathbf{2Ac}^{2+}$, the corresponding transitions progress from some orbital in the molecule into an orbital localised at the TTF moiety, usually the LUMO or LUMO+1. This induces differently oriented magnetic dipole transition moments leading to different signs in the CD spectrum. Hence, we conclude that the sign inversion in the CD spectra upon oxidation can be exclusively attributed to the change of the electronic structure.

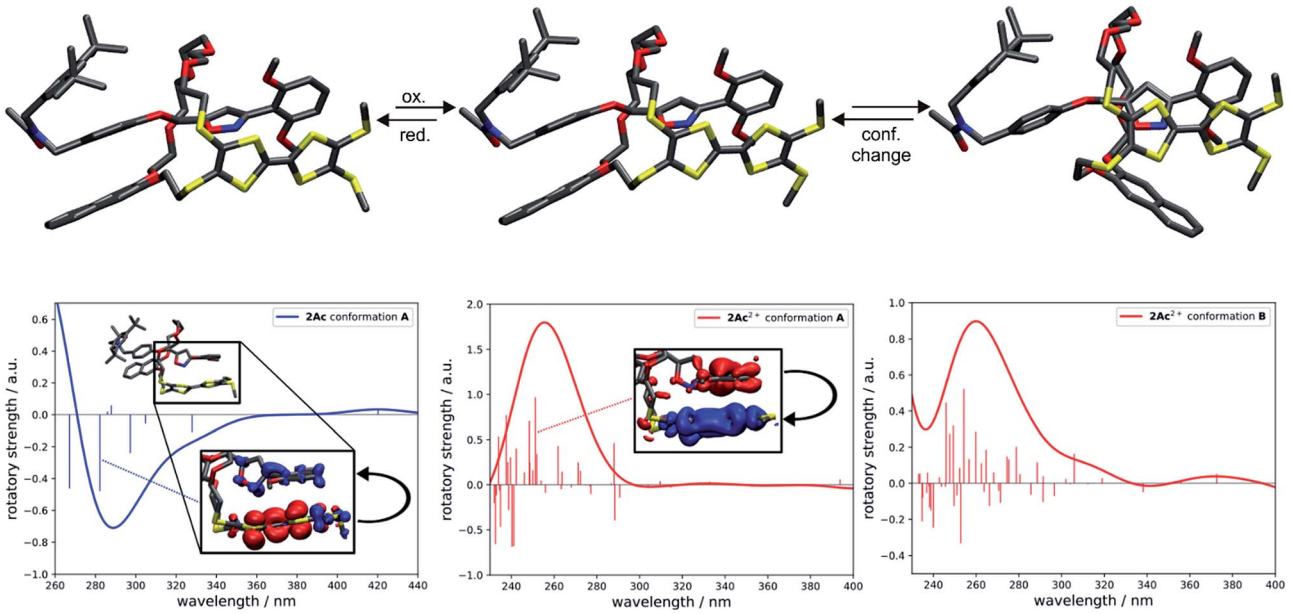

Fig. 4 Structural and spectral comparison of the most stable conformation of (R_{mp})-**2Ac** and the two most stable conformations, **A** and **B**, of (R_{mp})-**2Ac**$^{2+}$. Oxidation induces a flip of the naphthalene moiety in **A** towards the TTF unit yielding conformation **B**. The difference in electronic energy between **A** and **B** is around 9 kJ mol^{-1}. All structures were obtained at the TPSS-D3(BJ) level. Corresponding simulated CD spectra with excited state difference densities of selected transitions (insets) visualising the change in electronic structure upon photoexcitation of (R_{mp})-**2Ac** (left) and (R_{mp})-**2Ac**$^{2+}$ (middle). The difference in the CD spectra due to the conformational change of (R_{mp})-**2Ac**$^{2+}$ is negligible in the region of interest. The spectra were obtained at the ωB97X-D3 level using sTD-DFT. Gaussian line broadening with $\sigma = 20$ nm was applied. Insets: blue and red zones correspond to areas of electron enhancement and electron depletion, respectively. Isovalue = 0.001 a_0^{-3}.

Conclusions

In conclusion, electrochemically switchable crown ether/ammonium [2]rotaxanes bearing a directional wheel are reported. The wheel features a redox-switchable TTF unit. The directionality had no observable impact on the electrochemical and optical properties of the racemic mixtures determined by UV/Vis spectroscopy and CV measurements. Instead, the pure enantiomers of the acetylated non-ionic derivatives display a redox-induced reversible inversion of the sign in the ECD spectrum without a change of absolute configuration. The mechanism and the absolute configuration of this chiroptical switch has been examined by computational methods. While co-conformational changes have hardly any impact on the ECD spectra, the changes in electronic structure induced by oxidation play a pivotal role. These results underline the impact of the mechanical bond, which allows the construction of intriguing switchable chemical assemblies with unexpected properties. This is the first in class example of a redox-controlled chiroptical switch with a complete sign reversal based on a mechanically planar chiral rotaxane. In the future, these properties could be employed in materials science to construct novel optoelectronic building blocks.

Conflicts of interest

There are no conflicts to declare.

Acknowledgements

We thank the Deutsche Forschungsgemeinschaft (CRC 765) and Academy of Finland (KR proj. no. 309399, AV proj. no. 314343) for funding. We are grateful to the Alexander von Humboldt-Foundation for support of KR (AvH research award). JA thanks the Studienstiftung des deutschen Volkes for a doctoral scholarship. Furthermore, we thank Dr Lucia Volbach for help with the chiral separation and Dr Rakesh Puttreddy for help with the crystallisation.

Notes and references

1 R. Breslow and Z. L. Cheng, *Proc. Natl. Acad. Sci. U. S. A.*, 2009, **106**, 9144–9146.
2 F. Jafarpour, T. Biancalani and N. Goldenfeld, *Phys. Rev. E*, 2017, **95**, 032407.
3 D. G. Blackmond, *Cold Spring Harbor Perspect. Biol.*, 2010, **2**, a002147.
4 J. W. Canary, *Chem. Soc. Rev.*, 2009, **38**, 747–756.
5 N. Koumura, R. W. Zijlstra, R. A. van Delden, N. Harada and B. L. Feringa, *Nature*, 1999, **401**, 152–155.
6 B. L. Feringa, R. A. van Delden, N. Koumura and E. M. Geertsema, *Chem. Rev.*, 2000, **100**, 1789–1816.
7 B. L. Feringa, R. A. van Delden and M. K. J. ter Wiel, *Pure Appl. Chem.*, 2003, **75**, 563–575.
8 B. L. Feringa, *Angew. Chem., Int. Ed.*, 2017, **56**, 11060–11078.
9 J. F. Stoddart, *Angew. Chem., Int. Ed.*, 2017, **56**, 11094–11125.

10 E. A. Neal and S. M. Goldup, *Chem. Commun.*, 2014, **50**, 5128–5142.
11 J. F. Stoddart, *Chem. Soc. Rev.*, 2009, **38**, 1802–1820.
12 J. E. Lewis, M. Galli and S. M. Goldup, *Chem. Commun.*, 2016, **53**, 298–312.
13 C. Yamamoto, Y. Okamoto, T. Schmidt, R. Jäger and F. Vögtle, *J. Am. Chem. Soc.*, 1997, **119**, 10547–10548.
14 E. M. G. Jamieson, F. Modicom and S. M. Goldup, *Chem. Soc. Rev.*, 2018, **47**, 5266–5311.
15 N. H. Evans, *Chem.–Eur. J.*, 2018, **24**, 3101–3112.
16 P. E. Glen, J. A. T. O'Neill and A.-L. Lee, *Tetrahedron*, 2013, **69**, 57–68.
17 N. Kameta, K. Hiratani and Y. Nagawa, *Chem. Commun.*, 2004, 466–467.
18 J. Niemeyer and N. Pairault, *Synlett*, 2018, **29**, 689–698.
19 Y. Makita, N. Kihara, N. Nakakoji, T. Takata, S. Inagaki, C. Yamamoto and Y. Okamoto, *Chem. Lett.*, 2007, **36**, 162–163.
20 Y. Tachibana, N. Kihara, Y. Ohga and T. Takata, *Chem. Lett.*, 2000, **29**, 806–807.
21 Y. Mochizuki, K. Ikeyatsu, Y. Mutoh, S. Hosoya and S. Saito, *Org. Lett.*, 2017, **19**, 4347–4350.
22 M. Asakawa, G. Brancato, M. Fanti, D. A. Leigh, T. Shimizu, A. M. Z. Slawin, J. K. Y. Wong, F. Zerbetto and S. Zhang, *J. Am. Chem. Soc.*, 2002, **124**, 2939–2950.
23 T. Ogoshi, D. Yamafuji, T. Aoki, K. Kitajima, T. A. Yamagishi, Y. Hayashi and S. Kawauchi, *Chem.–Eur. J.*, 2012, **18**, 7493–7500.
24 G. Bottari, D. A. Leigh and E. M. Pérez, *J. Am. Chem. Soc.*, 2003, **125**, 13360–13361.
25 P. R. Ashton, J. A. Bravo, F. M. Raymo, J. F. Stoddart, A. J. P. White and D. J. Williams, *Eur. J. Org. Chem.*, 1999, 899–908.
26 Y.-G. Lee, Y. Koyama, M. Yonekawa and T. Takata, *Macromolecules*, 2010, **43**, 4070–4080.
27 S. Suzuki, F. Ishiwari, K. Nakazono and T. Takata, *Chem. Commun.*, 2012, **48**, 6478–6480.
28 F. Ishiwari, K. Nakazono, Y. Koyama and T. Takata, *Angew. Chem., Int. Ed.*, 2017, **56**, 14858–14862.
29 N. Kameta, Y. Nagawa, M. Karikomi and K. Hiratani, *Chem. Commun.*, 2006, 3714–3716.
30 J. Y. C. Lim, I. Marques, V. Felix and P. D. Beer, *Angew. Chem., Int. Ed.*, 2018, **57**, 584–588.
31 K. Hirose, M. Ukimi, S. Ueda, C. Onoda, R. Kano, K. Tsuda, Y. Hinohara and Y. Tobe, *Symmetry*, 2018, **10**, 20.
32 Y. Tachibana, N. Kihara and T. Takata, *J. Am. Chem. Soc.*, 2004, **126**, 3438–3439.
33 R. J. Bordoli and S. M. Goldup, *J. Am. Chem. Soc.*, 2014, **136**, 4817–4820.
34 M. A. Jinks, A. de Juan, M. Denis, C. J. Fletcher, M. Galli, E. M. G. Jamieson, F. Modicom, Z. Zhang and S. M. Goldup, *Angew. Chem., Int. Ed.*, 2018, **57**, 14806–14810.
35 S. Corra, C. de Vet, J. Groppi, M. La Rosa, S. Silvi, M. Baroncini and A. Credi, *J. Am. Chem. Soc.*, 2019, **141**, 9129–9133.
36 C. E. Gell, T. A. McArdle-Ismaguilov and N. H. Evans, *Chem. Commun.*, 2019, **55**, 1576–1579.
37 H. V. Schröder, H. Hupatz, A. J. Achazi, S. Sobottka, B. Sarkar, B. Paulus and C. A. Schalley, *Chem.–Eur. J.*, 2017, **23**, 2960–2967.
38 H. V. Schröder, S. Sobottka, M. Nößler, H. Hupatz, M. Gaedke, B. Sarkar and C. A. Schalley, *Chem. Sci.*, 2017, **8**, 6300–6306.
39 H. V. Schröder, J. M. Wollschläger and C. A. Schalley, *Chem. Commun.*, 2017, **53**, 9218–9221.
40 H. V. Schröder, A. Mekic, H. Hupatz, S. Sobottka, F. Witte, L. H. Urner, M. Gaedke, K. Pagel, B. Sarkar, B. Paulus and C. A. Schalley, *Nanoscale*, 2018, **10**, 21425–21433.
41 H. V. Schröder, F. Stein, J. M. Wollschläger, S. Sobottka, M. Gaedke, B. Sarkar and C. A. Schalley, *Angew. Chem., Int. Ed.*, 2019, **58**, 3496–3500.
42 H. V. Schröder and C. A. Schalley, *Beilstein J. Org. Chem.*, 2018, **14**, 2163–2185.
43 A. Coskun, M. Banaszak, R. D. Astumian, J. F. Stoddart and B. A. Grzybowski, *Chem. Soc. Rev.*, 2012, **41**, 19–30.
44 S. Erbas-Cakmak, D. A. Leigh, C. T. McTernan and A. L. Nussbaumer, *Chem. Rev.*, 2015, **115**, 10081–10206.
45 A. Jana, M. Ishida, J. S. Park, S. Bahring, J. O. Jeppesen and J. L. Sessler, *Chem. Rev.*, 2017, **117**, 2641–2710.
46 M. Fumanal, M. Capdevila-Cortada, J. S. Miller and J. J. Novoa, *J. Am. Chem. Soc.*, 2013, **135**, 13814–13826.
47 M. Yoshizawa, K. Kumazawa and M. Fujita, *J. Am. Chem. Soc.*, 2005, **127**, 13456–13457.
48 M. R. Bryce, *J. Mater. Chem.*, 2000, **10**, 589–598.
49 D. Canevet, M. Salle, G. Zhang, D. Zhang and D. Zhu, *Chem. Commun.*, 2009, 2245–2269.
50 J. L. Segura and N. Martín, *Angew. Chem., Int. Ed.*, 2001, **40**, 1372–1409.
51 A. Saad, F. Barriere, E. Levillain, N. Vanthuyne, O. Jeannin and M. Fourmigue, *Chem.–Eur. J.*, 2010, **16**, 8020–8028.
52 M. Hasegawa, J. Endo, S. Iwata, T. Shimasaki and Y. Mazaki, *Beilstein J. Org. Chem.*, 2015, **11**, 972–979.
53 F. Pop, S. Laroussi, T. Cauchy, C. J. Gomez-Garcia, J. D. Wallis and N. Avarvari, *Chirality*, 2013, **25**, 466–474.
54 E. Gomar-Nadal, J. Veciana, C. Rovira and D. B. Amabilino, *Adv. Mater.*, 2005, **17**, 2095–2098.
55 Y. Zhou, D. Zhang, L. Zhu, Z. Shuai and D. Zhu, *J. Org. Chem.*, 2006, **71**, 2123–2130.
56 T. Biet, A. Fihey, T. Cauchy, N. Vanthuyne, C. Roussel, J. Crassous and N. Avarvari, *Chem.–Eur. J.*, 2013, **19**, 13160–13167.
57 F. Riobe and N. Avarvari, *Chem. Commun.*, 2009, 3753–3755.
58 P. R. Ashton, P. J. Campbell, P. T. Glink, D. Philp, N. Spencer, J. F. Stoddart, E. J. T. Chrystal, S. Menzer, D. J. Williams and P. A. Tasker, *Angew. Chem., Int. Ed.*, 1995, **34**, 1865–1869.
59 T. Matsumura, F. Ishiwari, Y. Koyama and T. Takata, *Org. Lett.*, 2010, **12**, 3828–3831.
60 Y. Tachibana, H. Kawasaki, N. Kihara and T. Takata, *J. Org. Chem.*, 2006, **71**, 5093–5104.
61 S. V. Rosokha and J. K. Kochi, *J. Am. Chem. Soc.*, 2007, **129**, 828–838.
62 M. B. Kirketerp, L. A. Leal, D. Varsano, A. Rubio, T. J. Jorgensen, K. Kilsa, M. B. Nielsen and S. B. Nielsen, *Chem. Commun.*, 2011, **47**, 6900–6902.

63 V. Khodorkovsky, L. Shapiro, P. Krief, A. Shames, G. Mabon, A. Gorgues and M. Giffard, *Chem. Commun.*, 2001, 2736–2737.
64 T. Cauchy, F. Pop, J. Cuny and N. Avarvari, *Chimia*, 2018, **72**, 389–393.
65 M. Fukui, T. Mori, Y. Inoue and R. Rathore, *Org. Lett.*, 2007, **9**, 3977–3980.
66 J. Deng, N. Song, Q. Zhou and Z. Su, *Org. Lett.*, 2007, **9**, 5393–5396.
67 T. Mori and Y. Inoue, *J. Phys. Chem. A*, 2005, **109**, 2728–2740.
68 L. Pospisil, L. Bednarova, P. Stepanek, P. Slavicek, J. Vavra, M. Hromadova, H. Dlouha, J. Tarabek and F. Teply, *J. Am. Chem. Soc.*, 2014, **136**, 10826–10829.
69 E. Lee, H. Ju, I. H. Park, J. H. Jung, M. Ikeda, S. Kuwahara, Y. Habata and S. S. Lee, *J. Am. Chem. Soc.*, 2018, **140**, 9669–9677.
70 A. Homberg, E. Brun, F. Zinna, S. Pascal, M. Gorecki, L. Monnier, C. Besnard, G. Pescitelli, L. Di Bari and J. Lacour, *Chem. Sci.*, 2018, **9**, 7043–7052.
71 T.-Y. Tai, Y.-H. Liu, C.-C. Lai, S.-M. Peng and S.-H. Chiu, *Org. Lett.*, 2019, **21**, 5708–5712.
72 C. Petermayer and H. Dube, *J. Am. Chem. Soc.*, 2018, **140**, 13558–13561.
73 J. Tao, J. P. Perdew, V. N. Staroverov and G. E. Scuseria, *Phys. Rev. Lett.*, 2003, **91**, 146401.
74 S. Grimme, S. Ehrlich and L. Goerigk, *J. Comput. Chem.*, 2011, **32**, 1456–1465.
75 F. Weigend and R. Ahlrichs, *Phys. Chem. Chem. Phys.*, 2005, **7**, 3297–3305.
76 J. D. Chai and M. Head-Gordon, *J. Chem. Phys.*, 2008, **128**, 084106.
77 R. F. W. Bader, *Chem. Rev.*, 1991, **91**, 893–928.
78 H. J. C. Berendsen, J. P. M. Postma, W. F. van Gunsteren, A. DiNola and J. R. Haak, *J. Chem. Phys.*, 1984, **81**, 3684–3690.

Supporting Information

Chiroptical inversion of a planar chiral redox-switchable rotaxane

Marius Gaedke,[a] Felix Witte,[a] Jana Anhäuser,[b] Henrik Hupatz,[a] Hendrik V. Schröder,[a] Arto Valkonen,[c], Kari Rissanen,[c] Arne Lützen,[b] Beate Paulus[a] and Christoph A. Schalley*[a]

[a] Institut für Chemie und Biochemie, Organische Chemie, Freie Universität Berlin, Takustraße 3, 14195 Berlin, Germany.
[b] Kekulé-Institut für Organische Chemie und Biochemie, Universität Bonn, Gerhard-Domagk-Str. 1, 53121 Bonn, Germany.
[c] University of Jyvaskyla, Department of Chemistry, P.O. Box 35, 40014 Jyväskylä, Finland.
*Corresponding author e-mail: c.schalley@fu-berlin.de

Table of contents

1. Experimental details

1.1. General methods

All reagents and solvents were obtained from commercial sources and used without further purification. Dry solvents were purchased from Acros Organics or obtained from the M. BRAUN Solvent purification system SPS 800. 2-Hydroxyethyl 4-methylbenzenesulfonate **S4**,[1] 2-[(tetrahydropyran-2-yl)oxy]ethyl *p*-toluenesulfonate) **S5**,[2] 2,3-bis(2-cyanoethylthio)-6,7-bis(methylthio)tetrathiafulvalene **S12**,[3] axle **A1**,[4] and 2,6-dimethoxybenzonitrile oxide stopper **St1**[5] were synthesised according to literature procedures. Thin-layer chromatography was performed on silica gel-coated plates with fluorescent indicator F254 (Merck). For column chromatography, silica gel (0.04-0.063 mm, Merck) was used.

^{1}H and ^{13}C NMR experiments were performed on JEOL ECX 400, JEOL ECP 500, Bruker AVANCE 500 or Bruker AVANCE 700 instruments. Residual solvent signals were used as the internal standards. All shifts are reported in ppm and NMR multiplicities are abbreviated as s (singlet), d (doublet), t (triplet), m (multiplet) and br (broad). Coupling constants *J* are reported in Hertz. Compounds containing the tetrakis[3,5-bis(trifluoromethyl)phenyl]borate ($BArF_{24}^-$) anion show ^{13}C NMR spectra with ^{19}F, ^{10}B and ^{11}B couplings. These signals were denoted as one signal.

Melting points were determined on a SMP 30 (Stuart) instrument and are uncorrected.

High-resolution ESI mass spectra were measured on an Agilent 6210 ESI-TOF device. Tandem MS and infrared multiphoton dissociation (IRMPD) experiments were performed on a Varian Inc. Ionspec Q FT-7 equipped with a 7 T superconducting magnet and a Micromass Z-spray ESI source. HPLC grade solvents were used for sample preparation and the samples introduced into the ion source with a flow rate of 2-4 µL/min.

UV/Vis spectra were recorded with a Varian Cary 50 Bio spectrometer equipped with a xenon lamp. Solvents with HPLC grade and Suprasil glass cuvettes with a path-length of 1 cm were used.

ECD spectra were recorded on a JASCO-8-10 spectropolarimeter at 20°C. Solvents with HPLC grade and Suprasil glass cuvettes with a path-length of 2 mm were used. During the measurements, a constant flow of 3.2 L/min N_2 was provided. Each dataset is an average of three subsequent measurements.

CV measurements were carried out with an Autolab PGSTAT302N potentiostat in a 2 mL measuring cell in dichloromethane with 0.1 M n-Bu_4NPF_6 as the conducting salt. The working electrode was made of glassy carbon, the reference Ag electrode was etched with conc. aq. HCl. A Pt wire worked as a counter electrode. The cyclic voltammogram traces were recorded with 10, 25, 50, 100, 250, 500, 1000 and 2500 mV/s scan rates, to ensure that the observed

processes are reversible and diffusion-limited. For better comparability, only the 100 mV/s traces were plotted and compared in the discussion. In order to obtain the correct half-wave potentials, FeCp*/FeCp*$^{+}$ was used as the reference. These values were afterwards referenced to Fc/Fc^{+} as described in the literature.[6] The raw data was treated with Nova 1.5 by Metrohm and the plots were made with Origin *8* by OriginLab.

The chromatographic resolution was performed on a Shimadzu Prominence LC-20 HPLC system, equipped with two LC20-AT pumps, a DGU-20A3 solvent degasser, a diode array detector SPD-M20A (190-640 nm) and a fraction collector FRC-10A. For the analytical HPLC resolution, a Daicel CHIRALPAK® IA column (0.46 cm Ø, 25 cm) was used as the chiral stationary phase and *tert*-butyl methyl ether/CH_2Cl_2 (HPLC grade, 80:20 v/v) as the eluent with a flow rate of 1 mL/min. For the semi-preparative HPLC resolution, a CHIRALPAK® IA column (1 cm Ø, 25 cm) was used as the chiral stationary phase and *tert*-butyl methyl ether/dichloromethane (HPLC grade, 80:20 v/v) as the eluent with a flow rate of 4 mL/min.

1.2. Synthesis of dTTFC8

The directional wheel **dTTFC8** was synthesised starting from naphthalene-2,3-diol through consecutive substitution[7] with tetrahydropyranyl-protected mono- and pentaethylene glycol. After deprotection[8] to the diol and tosylation,[9] the corresponding diiodide was formed through a Finkelstein reaction.[4] In the last step, a CsOH•H_2O-mediated macrocyclisation[10] with the dicyanoethyl-protected TTF derivative[11] was carried out.

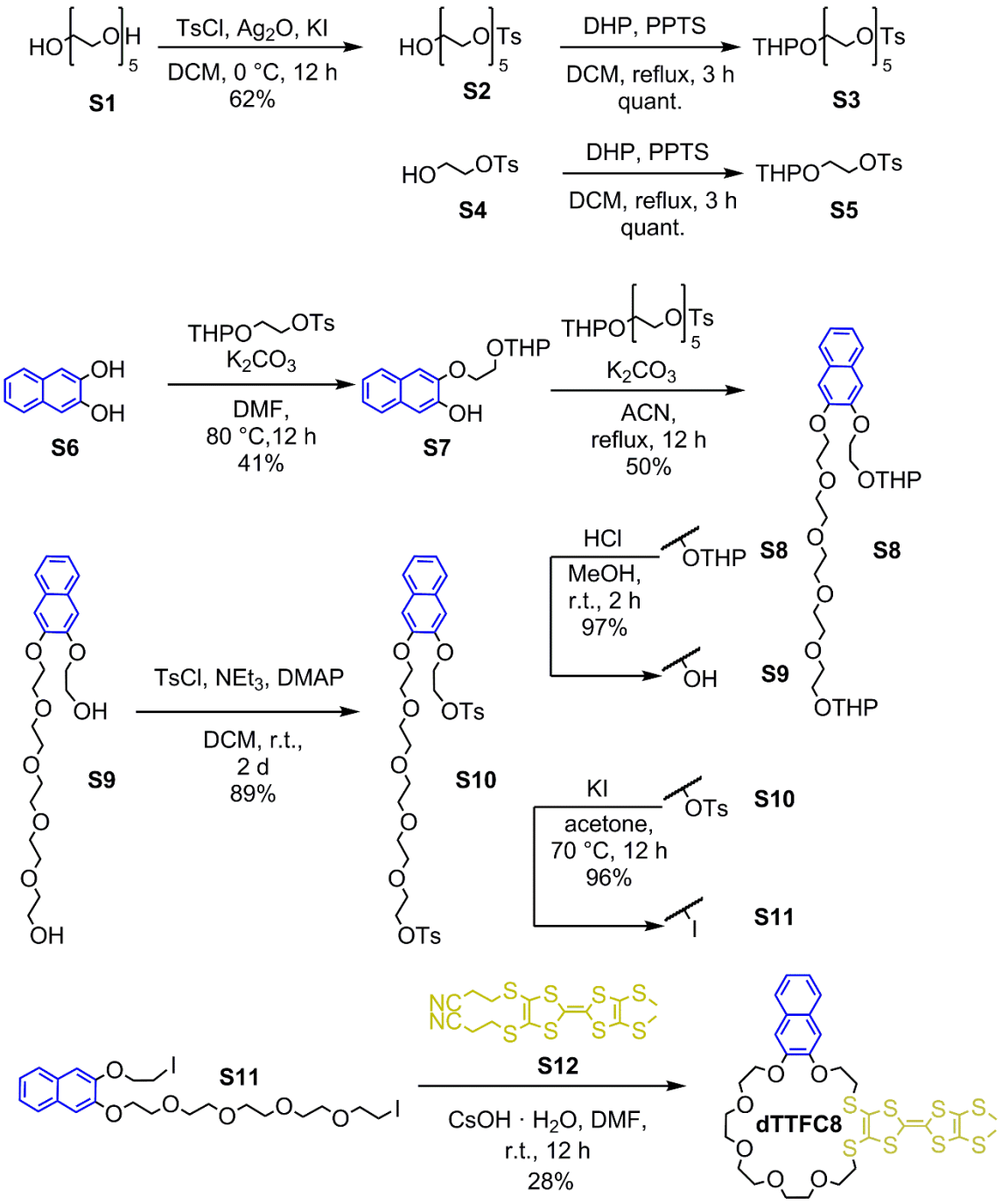

Scheme S1 Synthesis of wheel **dTTFC8** with a directional atom sequence.

14-Hydroxy-3,6,9,12-tetraoxatetradecyl 4-methylbenzenesulfonate[12]

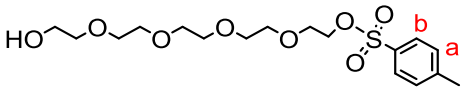

S2

4-Toluenesulfonyl chloride (444 mg, 2.3 mmol, 1.1 equiv.) was slowly added to a suspension of pentaethylene glycol **S1** (0.45 mL 1.9 mmol, 1.0 equiv.), KI (71.0 mg 0.42 mmol, 0.2 equiv.) and fresh Ag_2O (770 mg 3.3 mmol, 1.5 eq) in CH_2Cl_2 (21 mL) at 0 °C. The mixture was stirred overnight in a thawing ice bath. Afterwards, the mixture was filtered through a short celite pad and rinsed with EtOAc. After removal of the solvent, the crude product was purified by column chromatography (SiO_2, EtOAc/hexane = 2:1 → EtOAc, R_f ~ 0.3 in EtOAc) to isolate the desired product **S2** as a colourless oil in a 62% yield (466 mg, 1.2 mmol). **^{1}H NMR** (500 MHz, $CDCl_3$): δ = 2.42 (s, 3H, -C$\underline{H}_3$), 2.69 (s, 1H, -O$\underline{H}$), 3.47 – 3.70 (m, 18H, -OC$\underline{H}_2$), 4.08 – 4.17 (m, 2H, TsO-C$\underline{H}_2$-), 7.31 (d, J = 8.1 Hz, 2H, a), 7.76 (d, J = 8.1 Hz, 2H, b) ppm. **^{13}C NMR** (126 MHz, $CDCl_3$): δ = 21.7, 61.7, 68.7, 69.3, 70.3, 70.5, 70.6, 70.6, 70.6, 72.5, 128.0, 129.9, 133.0, 144.9 ppm. **ESI-HRMS**(ACN): *m/z* calcd. for $[C_{17}H_{28}O_8S]$: 415.1398 $[M+Na]^+$, found: 415.1394; calcd. for $[M+K]^+$:431.1137, found: 431.1130.

14-((Tetrahydro-2*H*-pyran-2-yl)oxy)-3,6,9,12-tetraoxatetradecyl 4-methylbenzenesulfonate[12]

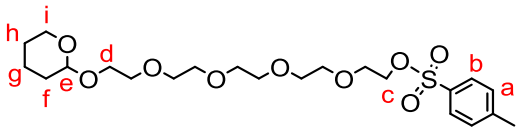

S3

A solution of monotosylate **S2** (1.00 g, 2.6 mmol, 1.0 equiv.), pyridinium tosylate (132 mg, 0.5 mmol, 0.2 equiv.) and 3,4-dihydro-*2H*-pyran (360 µL, 3.8 mmol, 97%, 1.5 equiv.) in CH_2Cl_2 (40 mL) was refluxed for 3 h. Afterwards, the mixture was poured into ice water, then extracted with CH_2Cl_2, washed with brine and dried with $MgSO_4$. After removal of the solvent, the crude product was purified by column chromatography (SiO_2, EtOAc, R_f ~ 0.6 in EtOAc) to isolate the desired product **S3** as a colourless oil in quantitative yield (1.26 g, 2.6 mmol). **^{1}H NMR** (500 MHz, $CDCl_3$): δ = 1.38 – 1.84 (m, 6H, f, g, h), 2.38 (s, 3H, -C$\underline{H}_3$), 3.38 – 3.49 (m, 2H, d), 3.49 – 3.65 (m, 16H, O-CH_2), 3.73 – 3.86 (m, 2H, i), 4.04 – 4.13 (m, 2H, c), 4.56 (dd, J = 4.3, 2.9 Hz, 1H, e), 7.29 (d, J = 8.1 Hz, 2H, a), 7.73 (d, J = 8.1 Hz, 2H, b) ppm. **^{13}C NMR:** (126 MHz, $CDCl_3$) δ = 19.4, 19.7, 21.6, 25.4, 30.5, 30.6, 43.6, 62.1, 62.8, 66.6, 68.6, 69.2, 70.4, 70.5, 70.6, 94.5, 94.5, 98.8, 98.9, 127.9, 129.8, 132.9 ppm. **ESI-HRMS**(ACN): *m/z* calcd. for $[C_{22}H_{36}O_9S]$: 499.1972 $[M+Na]^+$, found: 499.1955; calcd. for $[M+K]^+$: 515.1712, found: 515.1694.

3-(2-((Tetrahydro-2*H*-pyran-2-yl)oxy)ethoxy)-2-naphthol[7]

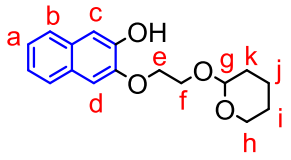

S7

A solution of protected monotosylate **S5** (96.0 mg, 0.32 mmol, 1.0 equiv.), naphthol **S6** (51.0 mg, 0.32 mmol, 1.0 equiv.) and K_2CO_3 (190 mg, 1.4 mmol, 4.3 eq) in dry DMF (20 mL) was stirred at 80 °C in an argon atmosphere for 12 h. Afterwards, residual K_2CO_3 was filtered off and the solvent was removed under reduced pressure. The crude product was then purified by column chromatography (SiO_2, CH_2Cl_2/MeOH = 100:1, R_f ~ 0.8 in CH_2Cl_2/MeOH = 50:1) to isolate the desired product **S7** as a colourless oil in a 41% yield (37.5 mg, 0.13 mmol). **^{1}H NMR** (500 MHz, $CDCl_3$): δ = 1.50 – 1.91 (m, 6H, j, k, l), 3.53 – 3.60 (m, 1H, h'), 3.89 – 3.97 (m, 2H, h'', f'), 4.07 – 4.16 (m, 1H,f''), 4.31 – 4.35 (m, 2H, e), 4.73 (dd, J = 4.6, 2.9 Hz, 1H, g), 7.20 (s, 1H, c), 7.27 (s, 1H, d), 7.28 – 7.34 (m, 2H, a, a'), 7.63 – 7.67 (m, 2H, b, b') ppm. **^{13}C NMR** (126 MHz, $CDCl_3$): δ = 19.7, 25.4, 30.7, 30.8, 62.8, 66.4, 69.5, 99.7, 109.0, 110.0, 123.5, 123.9, 124.6, 126.5, 126.7, 128.9, 130.4, 146.7, 147.0 ppm. **ESI-HRMS**(MeOH): *m/z* calcd. for $[C_{17}H_{20}O_4]$: 311.1254 $[M+Na]^+$, found: 311.1279; calcd for $[M+K]^+$ 327.0993, found: 327.1018.

2-(2-((3-((14-((Tetrahydro-2*H*-pyran-2-yl)oxy)-3,6,9,12-tetraoxatetradecyl)oxy)naphthalen-2-yl)oxy)ethoxy)tetrahydro-2*H*-pyran[7]

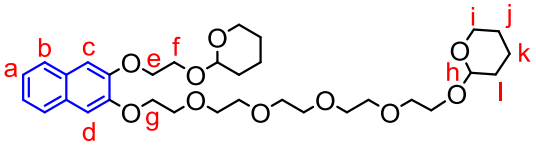

S8

A suspension of protected monotosylate **S3** (3.10 g, 6.44 mmol, 1 equiv.), monosubstituted naphthol **S7** (1.86 g, 6.44 mmol, 1 equiv.) and K_2CO_3 (3.80 g, 27.7 mmol, 4.3 equiv.) in dry ACN (100 mL) was refluxed under an argon atmosphere overnight. Afterwards K_2CO_3 was filtered off and the solvent was removed under reduced pressure. The crude product was then purified by column chromatography (SiO_2, EtOAc, R_f ~ 0.5 in EtOAc) to isolate the desired product **S8** as a colourless oil in a 50% yield (1.90 g, 3.21 mmol). **^{1}H NMR** (500 MHz, $CDCl_3$): δ = 1.44 – 1.90 (m, 12H, j, k, l), 3.45 – 3.61 (m, 4H, i), 3.61 – 3.91 (m, 15H, O-C$\underline{H}_2$), 3.91 – 3.96 (m, 2H, f), 3.96 – 4.02 (m, H, O-C$\underline{H}_2$), 4.11 – 4.16 (m, 1H, O-C$\underline{H}_2$), 4.17 – 4.23 (m, 1H, O-C$\underline{H}_2$), 4.25 – 4.33 (m, 4H, e, g), 4.59 – 4.63 (m, 1H, h), 4.73 – 4.78 (m, 1H, h'), 7.16 (s, 1H, d), 7.18 (s, 1H, c), 7.29 – 7.35 (m, 2H, a, a'), 7.63 – 7.67 (m, 2H, b, b') ppm. **^{13}C NMR** (126 MHz,

$CDCl_3$): δ = 19.4, 19.6, 19.9, 25.5, 25.6, 30.6, 30.7, 30.8, 62.2, 62.3, 65.7, 66.7, 68.3, 68. 6, 69.7, 70.6, 70.7, 70.7, 70.8, 71.1, 99.0, 108.7, 108.8, 124.3, 124.3, 124.5, 124.5, 126.4, 126.4, 126.5, 126.5, 129.4, 129.5, 129.6, 149.2, 149.3 ppm. **ESI-HRMS**(MeOH): *m/z* calcd. for $[C_{32}H_{48}O_{10}]$: 615.3140 $[M+Na]^+$, found: 615.3136; calcd for $[M+K]^+$: 631.2879, found: 631.2876.

14-((3-(2-Hydroxyethoxy)naphthalen-2-yl)oxy)-3,6,9,12-tetraoxatetradecan-1-ol[8]

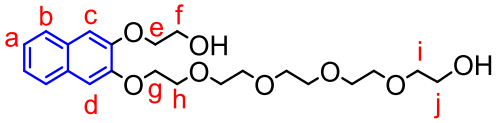

S9

A solution of diprotected glycol ether **S8** (1.90 g, 3.21 mmol) in MeOH (50 mL) was acidified with conc. HCl, until the solution reached pH = 1. After 2 h stirring at r.t. the solvent was removed under reduced pressure and the oily residue was stirred at 40 °C in oil pump vacuum for 5 h to obtain the desired product **S9** as a colourless oil in a 96% yield (1.31 g, 3.08 mmol). **^{1}H NMR** (500 MHz, $CDCl_3$): δ = 3.53 – 3.58 (m, 2H, j), 3.61 – 3.73 (m, 12H, O-C$\underline{H}_2$), 3.73 – 3.77 (m, 2H, i), 3.91 – 3.95 (m, 2H, h), 3.97 – 4.02 (m, 2H, f), 4.14 – 4.19 (m, 2H, e), 4.25 – 4.29 (m, 2H, g), 7.09 (s, 2H, d), 7.15 (s, 2H, c), 7.28 – 7.34 (m, 2H ,a, a'), 7.61 – 7.68 (m, 2H, b, b') ppm. **^{13}C NMR** (126 MHz, $CDCl_3$): δ = 60.9, 61.7, 68.2, 69.5, 70.3, 70.4, 70.6, 70.6, 70.7, 71.1, 72.7, 108.0, 108.1, 124.3, 124.5, 124.5, 126.4, 126.4, 129.2, 129.5, 148.7, 148.9 ppm. **ESI-HRMS**(ACN): *m/z* calcd. for $[C_{22}H_{32}O_8]$: 447.1989 $[M+Na]^+$, found: 447.1968; calcd for $[M+K]^+$: 463.1729, found: 463.1706.

2-((3-((14-(Tosyloxy)-3,6,9,12-tetraoxatetradecyl)oxy)naphthalen-2-yl)oxy)ethyl 4-methylbenzenesulfonate[9]

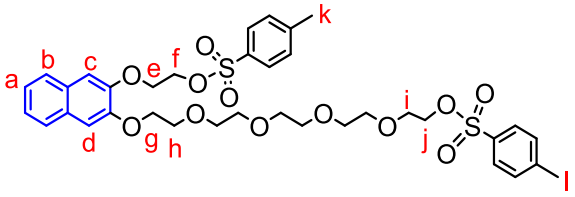

S10

A solution of 50 mg (0.12 mmol, 1.0 equiv.) diol **S9**, 100 µL (0.71 mmol, 6.0 eq) NEt_3, 0.1 mg (0.6 µmol, 0.5 mol%) DMAP and 135 mg (0.71 mmol, 6 eq) 4-toluenesulfonyl chloride in dry methylene chloride (25 mL) was left stirring at r.t. for 2 days. The reaction mixture was washed with saturated NH_4Cl aq. solution and dried with $MgSO_4$. The crude product was then purified by column chromatography (SiO_2, CH_2Cl_2 → EtOAc, R_f ~ 0.8 in EtOAc) to obtain the desired product **S10** as a colourless oil in 89% yield (77 mg, 0.11 mmol). **^{1}H NMR** (500 MHz, $CDCl_3$):

δ = 2.38 (s, 3H, l), 2.41 (s, 3H, k), 3.52 – 3.69 (m, 12H, O-CH_2), 3.75 – 3.78 (m, 2H, i), 3.91 – 3.95 (m, 2H, h), 4.11 – 4.15 (m, 2H, j), 4.22 – 4.26 (m, 2H, g), 4.27 – 4.32 (m, 2H, e), 4.41 – 4.47 (m, 2H, f), 7.04 (s, 1H, d), 7.14 (s, 1H, c), 7.27 – 7.36 (m, 6H, a, a', H-Ar-CCH_3), 7.58 – 7.67 (m, 2H, b, b'), 7.76 – 7.83 (m, 4H, H-Ar-CSO_3R) ppm. **^{13}C NMR** (126 MHz, $CDCl_3$): δ = 21.7, 21.7, 66.7, 68.2, 68.6, 68.7, 69.4, 69.6, 70.6, 70.6, 70.7, 70.8, 70.8, 71.0, 100.1, 108.9, 110.0, 110.0, 124.4, 124.7, 126.4, 126.5, 128.0, 128.1, 129.2, 129.9, 129.9, 129.9, 130.0, 133.0, 133.1, 144.9, 144.9, 145.0, 148.2, 149.1 ppm. **ESI-HRMS**(ACN): *m/z* calcd. for [$C_{36}H_{44}O_{12}S_2$]: 755.2166 [M+Na]$^+$, found: 755.2168; calcd for [M+K]$^+$: 771.1906, found: 771.1905.

1-Iodo-14-((3-(2-iodoethoxy)naphthalen-2-yl)oxy)-3,6,9,12-tetraoxatetradecane[4]

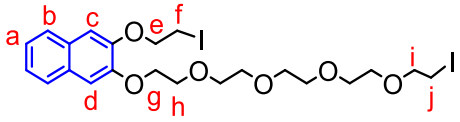

S11

A solution of 61.4 mg (83.8 µmol, 1.0 eq) ditosylate **S10** and 55.6 mg (335 mmol, 4.0 eq) KI in acetone (5 mL) was stirred at 70 °C overnight. When the reaction mixture turned yellow and a white precipitate formed, the solvent was removed under reduced pressure. The residue was dissolved in EtOAc and washed with brine. After drying with $MgSO_4$, the solvent was removed to isolate the desired product **S11** as a yellowish oil in a 96% yield (52 mg, 80.9 µmol). **^{1}H NMR** (500 MHz, $CDCl_3$): δ = 3.21 – 3.25 (m, 2H, j), 3.49 – 3.53 (m, 2H, f), 3.61 – 3.71 (m, 10H, O-CH_2), 3.71 – 3.74 (m, 2H, i), 3.78 – 3.82 (m, 2H, O-CH_2), 3.94 – 3.97 (m, 2H, h), 4.26 – 4.30 (m, 2H, g), 4.35 – 4.40 (m, 2H, e), 7.15 (s, 1H, d), 7.18 (s, 1H, c), 7.31 – 7.34 (m, 2H, a, a'), 7.64 – 7.67 (m, 2H, b, b') ppm. **^{13}C NMR** (126 MHz, $CDCl_3$): δ = 68.8, 69.7, 69.9, 70.3, 70.3, 70.7, 70.7, 70.8, 70.8, 71.1, 72.1, 72.1, 109.0, 109.9, 124.5, 124.7, 126.5, 126.5, 129.3, 129.8, 148.1, 149.1 ppm. **ESI-HRMS**(ACN): *m/z* calcd. for [$C_{22}H_{30}I_2O_6$]: 667.0024 [M+Na]$^+$, found: 666.9996; calcd. for [M+K]$^+$: 682.9763, found: 682.9730.

2-(4,5-Bis(methylthio)-1,3-dithiol-2-ylidene)-5,6,8,9,11,12,14,15,17,18,27,28-dodeca-hydro-[1,3]dithiolo[4,5-t]naphtho[2,3-b][1,4,7,10,13,16]hexaoxa[19,22]dithiacyclo-tetracosane[10]

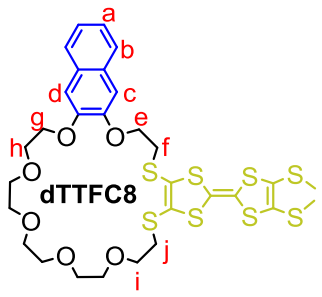

A solution of 74 mg (0.44 mmol, 2.0 equiv.) CsOH · H_2O in dry MeOH (2 mL) was added over 30 min to 104 mg (0.22 mmol, 1.0 equiv.) TTF precursor **S12** in dry DMF (5 mL). After the mixture turned dark red, it was added over 1 h to 143 mg (0.22 mmol, 1.0 equiv.) to diiodide **S11** in dry DMF (25 mL) and stirred at r.t. under argon overnight. Afterwards, the solvent was removed under reduced pressure and the residue was dissolved in CH_2Cl_2. The solution was washed with water and brine. After drying with $MgSO_4$, the crude product was purified by column chromatography (SiO_2, CH_2Cl_2, R_f ~ 0.5 in CH_2Cl_2/MeOH = 100:1) to isolate the desired product **dTTFC8** as an orange powder in a 28% yield (45.7 mg, 61 µmol). **M.p.** 79.3°C; **^{1}H NMR** (700 MHz, CD_2Cl_2): δ = 2.43 (s_{br}, 6H, S-CH_3), 3.02 (s_{br}, 4H, j), 3.30 (t, J = 6.5 Hz, 2H, f), 3.49 – 3.52 (m, 2H, O-C$\underline{H}_2$), 3.53 – 3.56 (m, 2H, O-C$\underline{H}_2$), 3.56 – 3.59 (m, 2H, O-C$\underline{H}_2$), 3.59 – 3.65 (m, 4H, i, O-C$\underline{H}_2$), 3.65 – 3.68 (m, 2H, O-C$\underline{H}_2$), 3.76 – 3.79 (m, 2H, O-C$\underline{H}_2$), 3.89 – 3.97 (m, 2H, h), 4.25 (m, 2H, O-C$\underline{H}_2$), 4.38 (s_{br}, 2H, e), 7.17 (s, 1H, c), 7.20 (s, 1H, d), 7.30 – 7.35 (m, 2H, a), 7.66 – 7.70 (m, 2H, b).ppm. **^{13}C NMR** (176 MHz, CD_2Cl_2): δ = 23.3, 29.9, 30.3, 32.5, 68.4, 69.5, 70.0, 71.0, 71.1, 71.2, 71.3, 71.7, 109.1, 109.8, 124.8, 124.9, 126.8, 126.9, 129.8, 130.2, 149.1, 149.7 ppm. **ESI-HRMS**(ACN): *m/z* calcd. for [$C_{30}H_{36}O_6S_8$]: 771.0170 [M+Na]$^+$, found: 771.0182; calcd. for [M+K]$^+$: 786.9909, found: 786.9916.

1.3. Synthesis of [2]rotaxane (*rac*)-2 and (*rac*)-2Ac

[2]Rotaxane (*rac*)-2

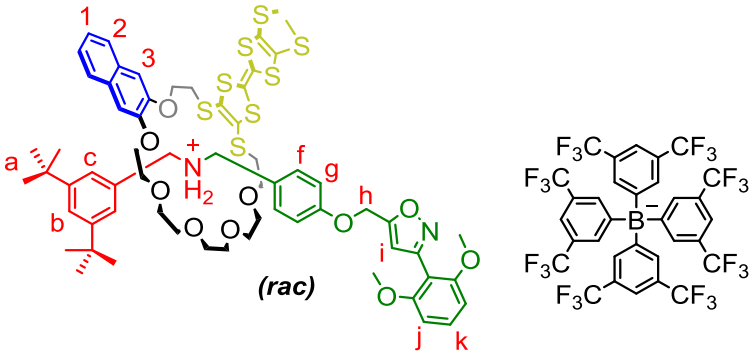

(*rac*)-**2**

Axle **A1** (74 mg, 60 µmol, 1.0 equiv.) and macrocycle **dTTFC8** (50 mg, 67 µmol, 1.1 equiv.) were dissolved in dry CH_2Cl_2 (200 µL) and stirred at r.t. for 10 min. Afterwards 2,6-dimethoxybenzonitrile oxide **St1** (14 mg, 78 µmol, 1.3 equiv.) was added and the mixture was stirred in a sealed tube under argon at 35 °C overnight. Then, the mixture was applied directly onto a preparative thin layer chromatography plate (SiO_2 2000 µm, CH_2Cl_2, R_f ~ 0.6 in CH_2Cl_2) to obtain the desired racemic product (*rac*)-**2** (129 mg, 60 µmol, 73 %) as a yellowish oil. **^{1}H NMR** (700 MHz, CD_2Cl_2): δ = 1.25 (s, 18H, a), 2.42 (s, 3H, -SMe), 2.43 (s, 3H, -SMe), 3.05 – 3.18 (m, 6H, O-C$\underline{H}_2$), 3.23 – 3.33 (m, 4H, O-C$\underline{H}_2$), 3.37 – 3.46 (m, 4H, O-C$\underline{H}_2$), 3.58 – 3.68 (m, 2H, O-C$\underline{H}_2$), 3.75 – 3.91 (m, 10H, O-C$\underline{H}_2$, -OMe), 4.28 – 4.40 (m, 2H, O-C$\underline{H}_2$), 4.43 – 4.46 (m, 2H, O-C$\underline{H}_2$), 4.53 – 4.77 (m, 4H, C$\underline{H}_2$-NH_2), 5.04 (d, *J* = 12.8 Hz, 1H, h), 5.08 (d, *J* = 13.0 Hz, 1H, h), 6.44 (s, 1H, i), 6.66 (d, *J* = 8.5 Hz, 2H, j), 6.95 (d, *J* = 8.7 Hz, 2H, g), 7.19 (s, 1H, 3), 7.24 (s, 1H, 3), 7.27 (d, *J* = 1.6 Hz, 2H, c), 7.35 – 7.41 (m, 5H, f, k, 1), 7.47 (t, *J* = 1.8 Hz, 1H, b), 7.55 (s_{br}, 4H, $BArF_{24}$), 7.66 – 7.69 (m, 2H, 2), 7.69 (s_{br}, 8H, $BArF_{24}$) 7.77 – 7.86 (m, 2H, NH_2) ppm. **^{13}C NMR** (176 MHz, CD_2Cl_2): δ = 19.6, 31.7, 35.4, 36.3, 37.3, 53.3, 56.5, 61.6, 68.7, 69.4, 70.5, 70.6, 71.0, 71.2, 71.2, 71.3, 71.5, 104.7, 107.3, 107.4, 109.1, 109.3, 109.6, 113.8, 115.6, 118.0, 118.1, 124.4, 124.7, 124.8, 125.0, 125.7, 126.0, 126.9 127.5, 127.8, 128.2, 128.2, 128.8, 129.4, 129.8, 129.9, 130.9, 132.0, 132.0, 135.4, 148.3, 148.4, 152.4, 157.8, 159.5, 162.3, 166.2 ppm. **ESI-HRMS**(MeOH): *m/z* calcd. for $[C_{64}H_{79}N_2O_{10}S_8]^+$: 1291.3495 $[M]^+$, found: 1291.3479.

[2]Rotaxane (*rac*)-2Ac

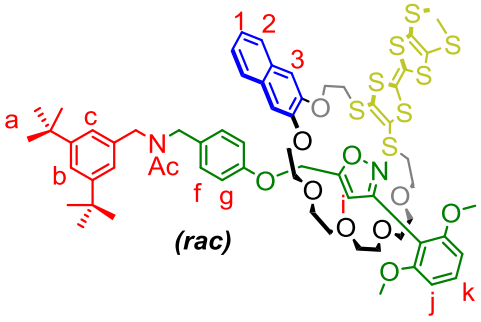

(*rac*)-**2Ac**

Rotaxane (*rac*)-**2** (14 mg, 6.5 µmol, 1.0 equiv.), NEt_3 (27 µL, 190 µmol, 30.0 equiv.) and Ac_2O (18 µL, 190 µmol, 30.0 equiv.) were dissolved in ACN (5 mL) and stirred at r.t. overnight. Then, the crude mixture was purified by preparative TLC (SiO_2 2000 µm, CH_2Cl_2/MeOH 50:1, R_f ~ 0.3 in CH_2Cl_2/MeOH = 50:1) to isolate the desired racemic product (*rac*)-**2Ac** as a yellowish oil in 95% yield (8.2 mg, 3.5 µmol). **^{1}H NMR** (700 MHz, CD_2Cl_2): δ = 1.29 (s, 9H, a), 1.32 (s, 9H, a), 1.78 (s, 1.5H, Ac), 1.90 (s, 1.5H, Ac), 2.24 (s, 1.5H, SMe), 2.30 (s, 1.5H, SMe), 2.33 (s, 1.5H, SMe), 2.34 (s, 1.5H, SMe), 3.02 – 3.15 (m, 3.6H, O-CH_2), 3.16 – 3.22 (m, 1.4H, O-CH_2), 3.34 – 3.44 (m, 4.5H, O-CH_2), 3.45 – 3.62 (m, 8H, O-CH_2), 3.64 – 3.74 (m, 5H, O-CH_2), 3.78 (d, *J* = 3.9 Hz, 6H, OMe), 3.81 – 3.83 (m, 0.7H, O-CH_2), 3.83 – 3.85 (m, 0.7H, O-CH_2), 3.95 – 4.04 (m, 4H, CH_2-N, O-CH_2), 4.05 – 4.13 (m, 2H, O-CH_2), 4.18 – 4.21 (m, 1H, CH_2-N), 4.22 – 4.26 (m, 1H, O-CH_2), 4.29 – 4.32 (m, 1H, CH_2-N), 4.37 – 4.40 (m, 1H, CH_2-N), 4.41 – 4.46 (m, 1H, CH_2-N), 5.80 – 5.87 (m, 2H, h), 6.64 (dd, *J* = 8.4, 5.6 Hz, 2H, j), 6.71 – 6.73 (m, 2H, g, i), 6.78 – 6.81 (m, 1H, g), 6.85 (s, 0.5H, 3), 6.87 (d, *J* = 1.8 Hz, 1H, c), 6.90 (s, 0.5H, 3), 6.91 (d, *J* = 1.8 Hz, 1H, c), 7.00 – 7.02 (m, 2H, f), 7.05 (*s*, 0.5H, 3), 7.07 (*s*, 0.5H, 3), 7.19 – 7.25 (m, 2H, 1), 7.29 (t, *J* = 1.9 Hz, 0.5H, b), 7.33 (t, *J* = 1.8 Hz, 0.5H, b), 7.35 (td, *J* = 8.4, 4.6 Hz, 1H, k), 7.55 – 7.59 (m, 1H, 2), 7.60 – 7.64 (m, 1H, 2) ppm. **^{13}C NMR** (176 MHz, CD_2Cl_2): δ = 19.2, 19.3, 19.3, 19.4, 21.8, 21.8, 30.3, 31.8, 32.5, 34.6, 35.2, 35.3, 35.5, 35.6, 46.59, 47.9, 48.8, 50.9, 51.3, 56.5, 56.5, 61.4, 61.4, 67.5, 67.5, 69.1, 69.2, 70.1, 70.2, 70.2, 70.5, 70.5, 71.2, 71.3, 71.3, 71.5, 71.5, 71.7, 71.7, 71.9, 104.5, 104.6, 107.1, 107.4, 107.5, 108.0, 108.1, 108.4, 108.4, 110.0, 110.1, 110.8, 115.2, 115.4, 121.0, 121.6, 121.8, 122.4, 123.9, 124.3, 124.6, 124.6, 124.6, 126.6, 126.7, 126.7, 126.7, 127.6, 127.7, 128.8, 129.0, 129.5, 129.6, 129.6, 129.9, 131.5, 131.5, 134.2, 134.5, 136.7, 137.3, 148.8, 148.9, 149.0, 149.1, 151.9, 157.4, 158.2, 158.3, 159.3, 168.9, 169.1, 171.1, 171.2 ppm. **ESI-HRMS**(MeOH): *m/z* calcd. for [$C_{66}H_{80}N_2O_{11}S_8$]: 1333.3606 [M+H]$^+$, found: 1333.3505; calcd. for [M+Na]$^+$: 1355.3425, found: 1355.3442; calcd. for [M+K]$^+$: 1371.3165, found: 1371.3185.

2. FTICR mass spectroscopy

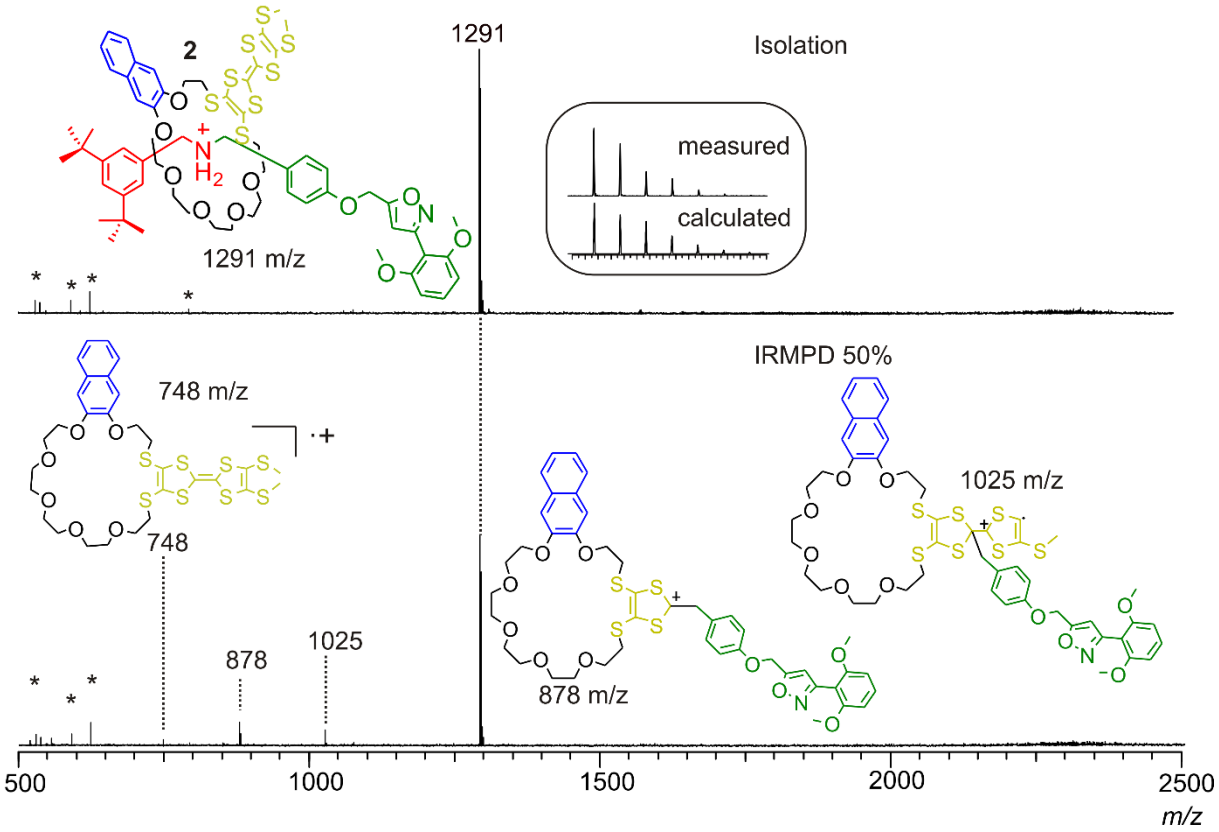

Fig. S1 ESI-FTICR infrared multiphoton dissociation (IRMPD) experiment with mass-selected rotaxane ions at *m/z* 1291 obtained from a MeOH solution (10 µM) of [2]rotaxane (*rac*)-**2**: (top) after mass-selection; (bottom) after fragmentation. The fragment peaks could be assigned to the free macrocycle as a radical cation (748 *m/z*) and two adducts, which arise from an attack of the TTF moiety on the benzylic position next to the nitrogen of the axle. These fragments are in line with the fragments obtained from rotaxanes of the non-directional **TTFC8** macrocycle.[4] As no free axle is observed as the fragmentation product, it can be concluded that the ionised and mass selected species are in fact mechanically interlocked. Electromagnetic stray radiation is marked with asterisks.

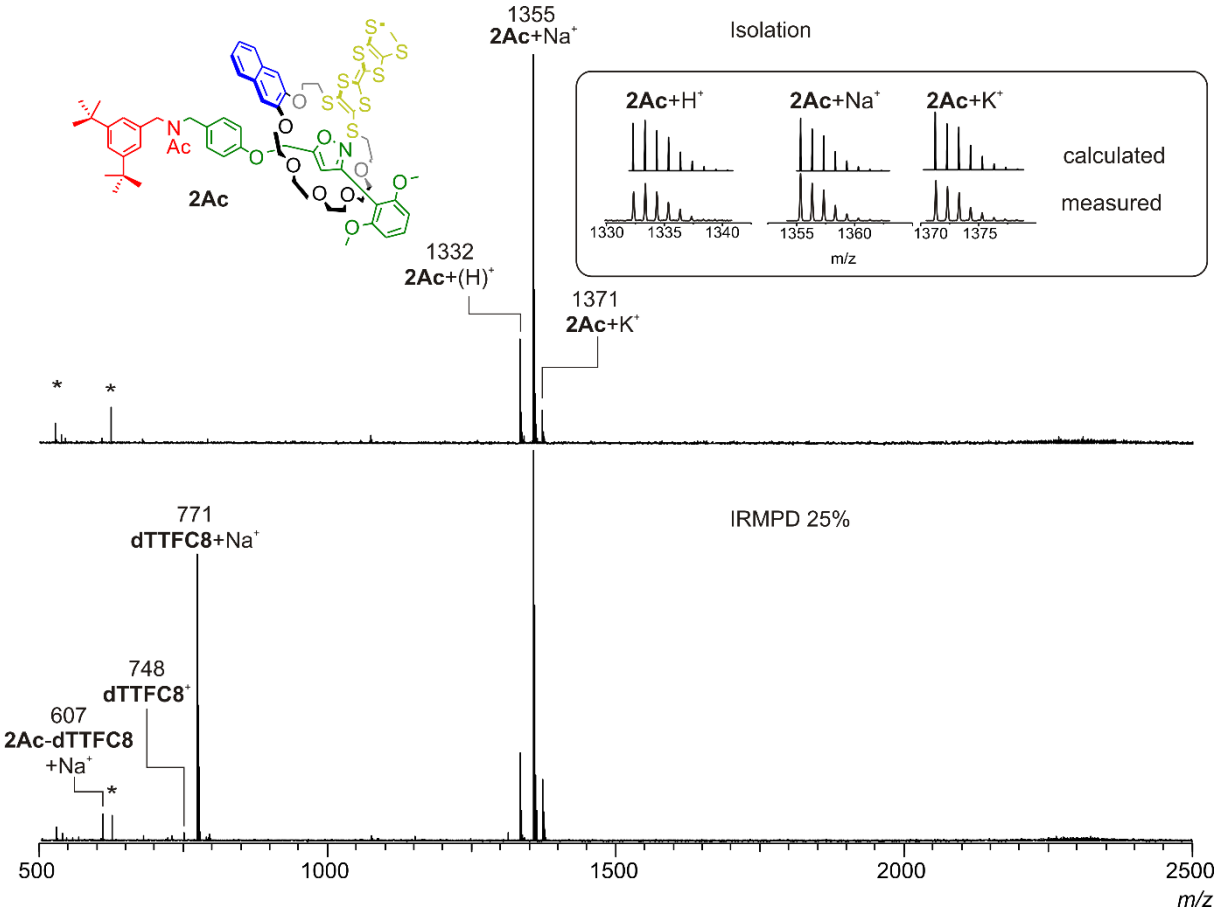

Fig. S2 ESI-FTICR infrared multiphoton dissociation (IRMPD) experiment with mass range-selected rotaxane ions obtained from a MeOH solution (10 µM) of [2]rotaxane (*rac*)-**2Ac**. The acetylated [2]rotaxane **2Ac** ions do not show the same fragmentation pattern as **2,** as no fragments from an intramolecular attack could be observed. Fragmentation proceeds by either losing the macrocycle (607 m/z) or fragmenting the axle leaving the charge on the macrocycle (748 and 771 m/z)

3. Variable Temperature NMR Spectroscopy

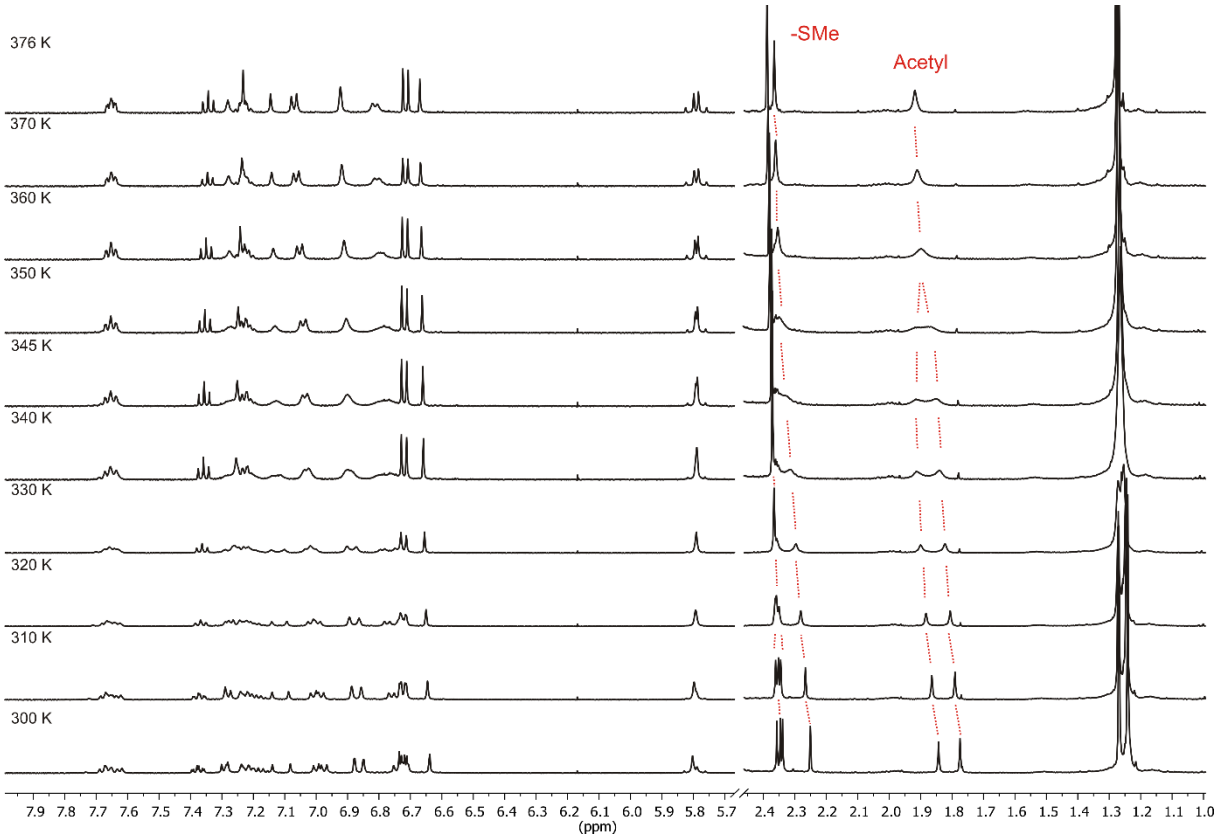

Fig. S3 Partial spectra of [2]rotaxane (*rac*)-**2Ac** in a VT ^{1}H NMR (500 MHz, DMSO-d6) experiment (gradual heating from 300 to 375 K), showing the coalescence of the acetyl groups and merging of the four singlets corresponding to SMe on the TTF into two singlets upon heating.

The free energy of activation ($\Delta G^{\ddagger}$) was calculated using the modified Eyring equation (eq. 1), where R is the ideal gas constant, T_c the coalescence temperature and $\Delta\nu$ the peak to peak separation between the signals for the two interconverting isomers in Hz.

$$\Delta G^{\ddagger} = R\,T_c\,(22.96 + \ln(T_c/\Delta\nu))\ \text{kJ mol}^{-1} \qquad \text{(eq. 1)}$$

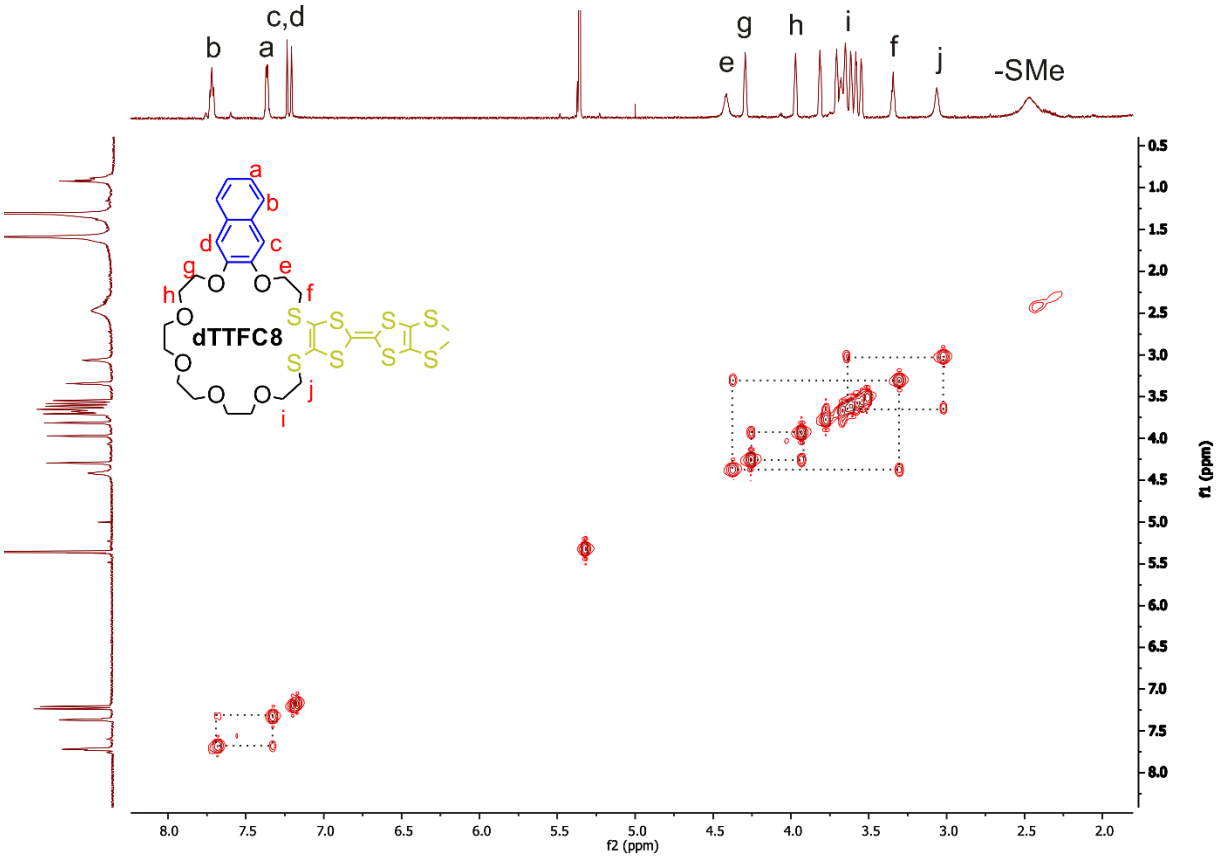

Fig. S4 COSY spectrum of **dTTFC8** in a (700 MHz, CD_2Cl_2).

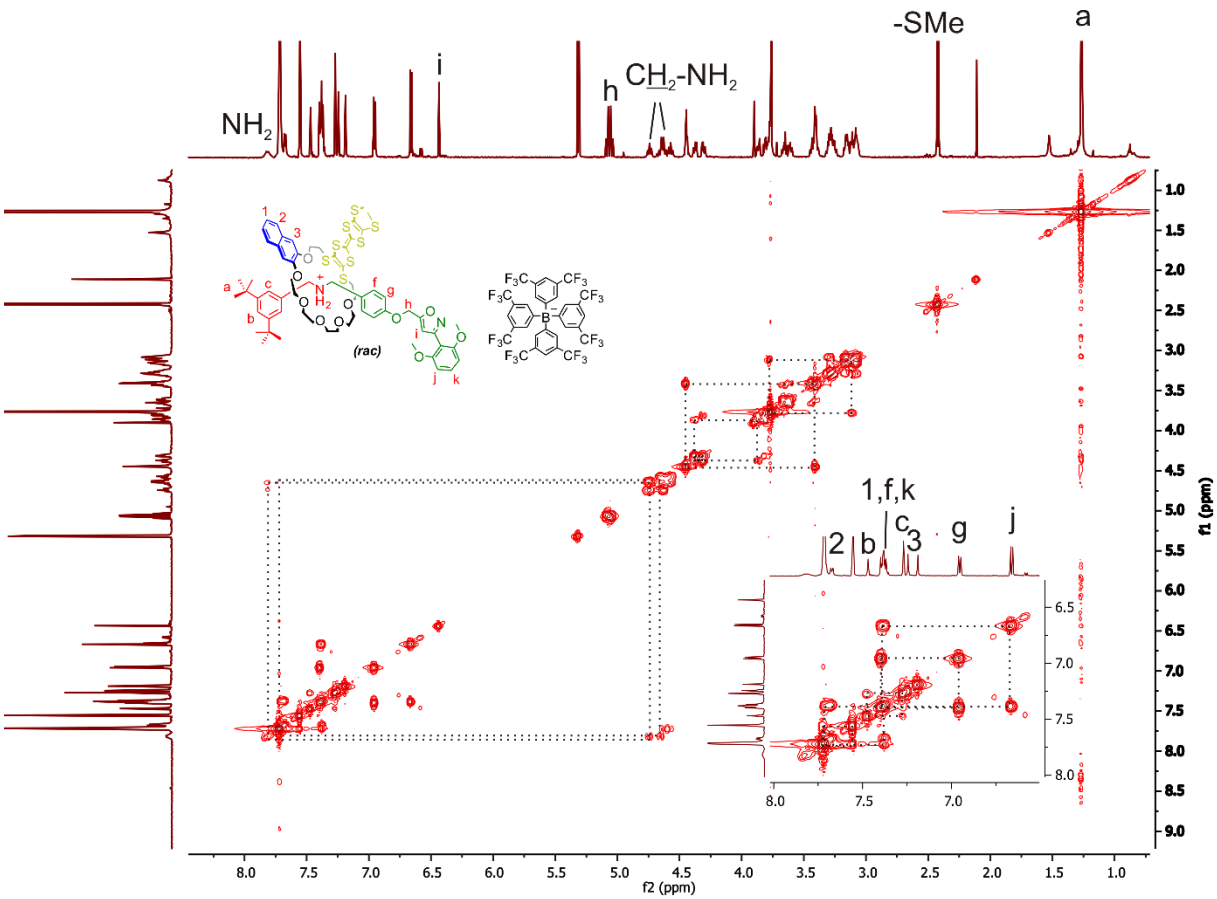

Fig. S5 COSY spectrum of (*rac*)-**2** in a (700 MHz, CD_2Cl_2).

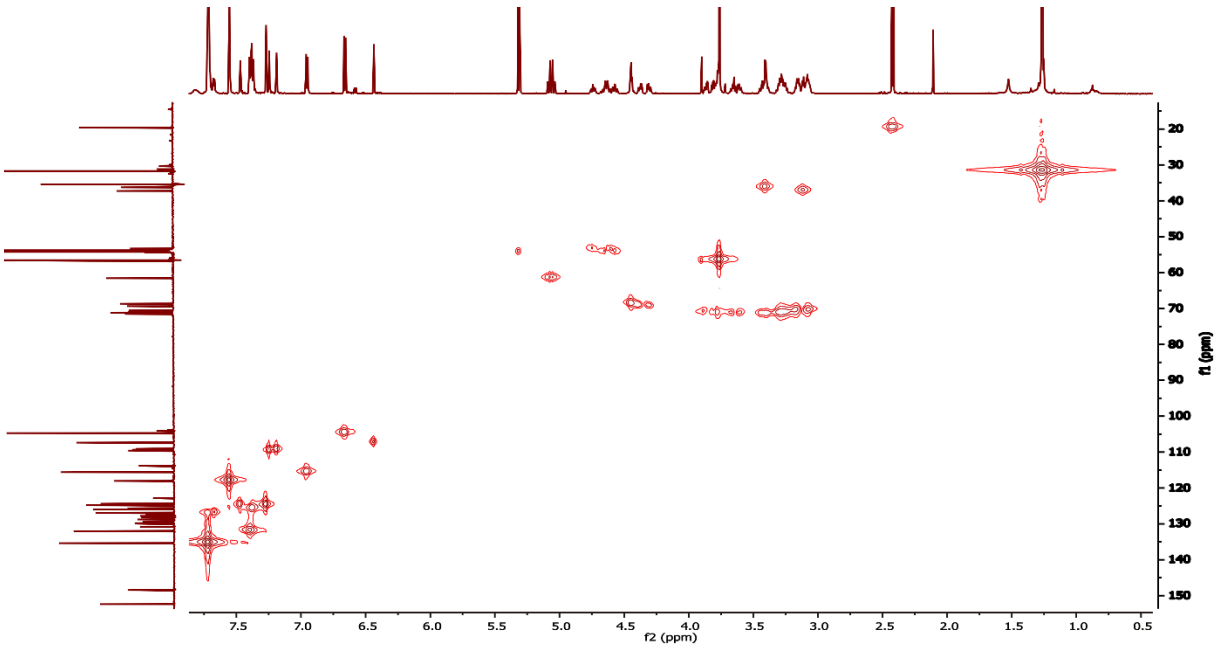

Fig. S6 HMQC spectrum of (*rac*)-**2** in a (700 MHz, CD_2Cl_2).

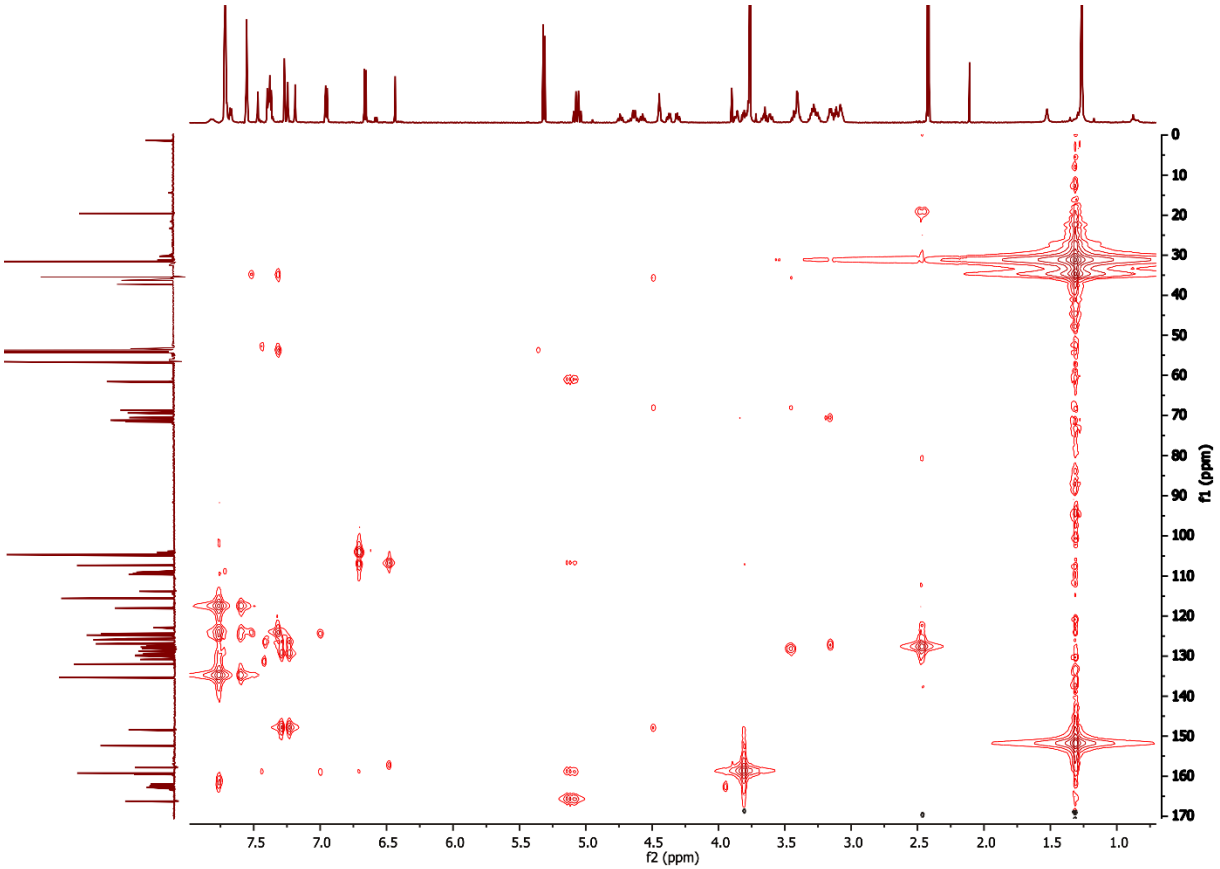

Fig. S7 HMBC spectrum of (*rac*)-**2** in a (700 MHz, CD_2Cl_2).

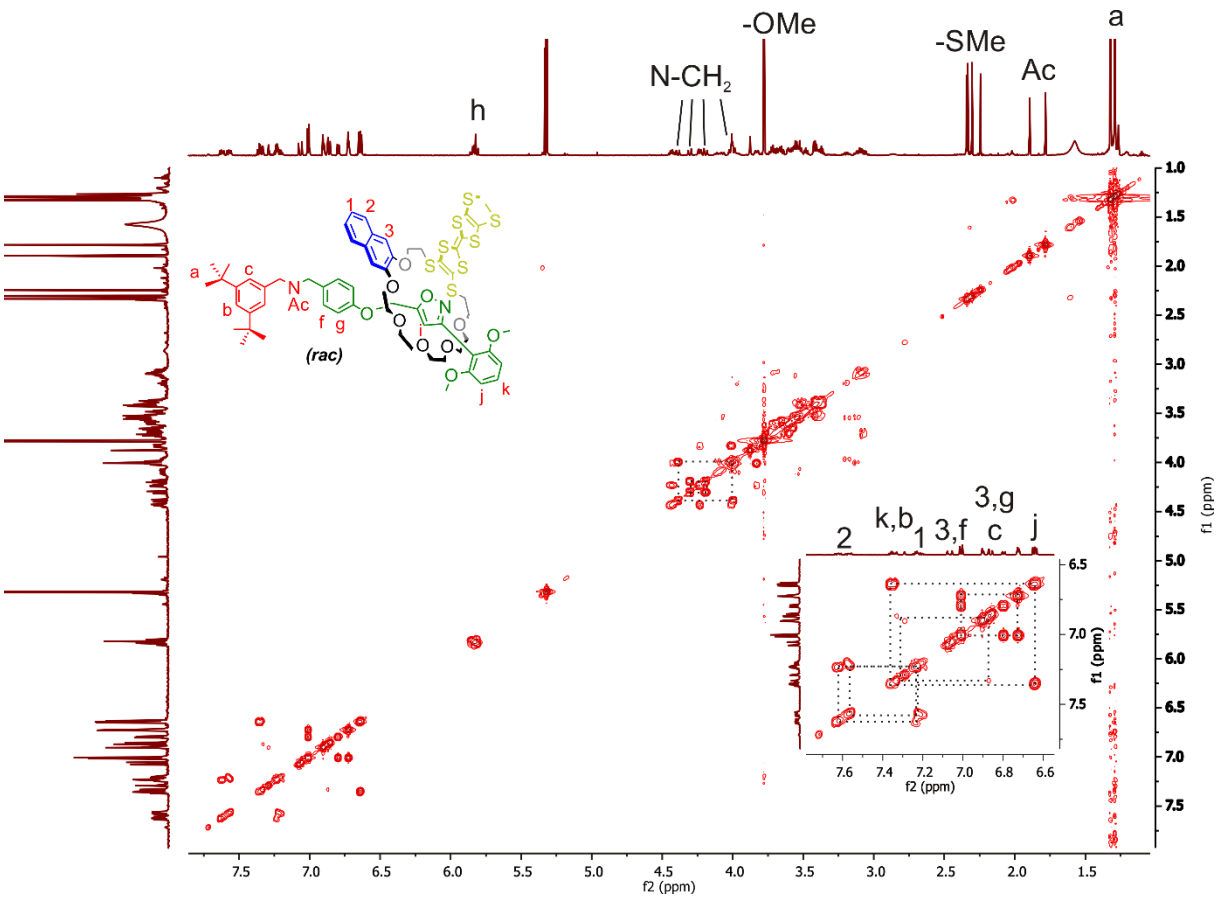

Fig. S8 COSY spectrum of (*rac*)-**2Ac** in a (700 MHz, CD_2Cl_2).

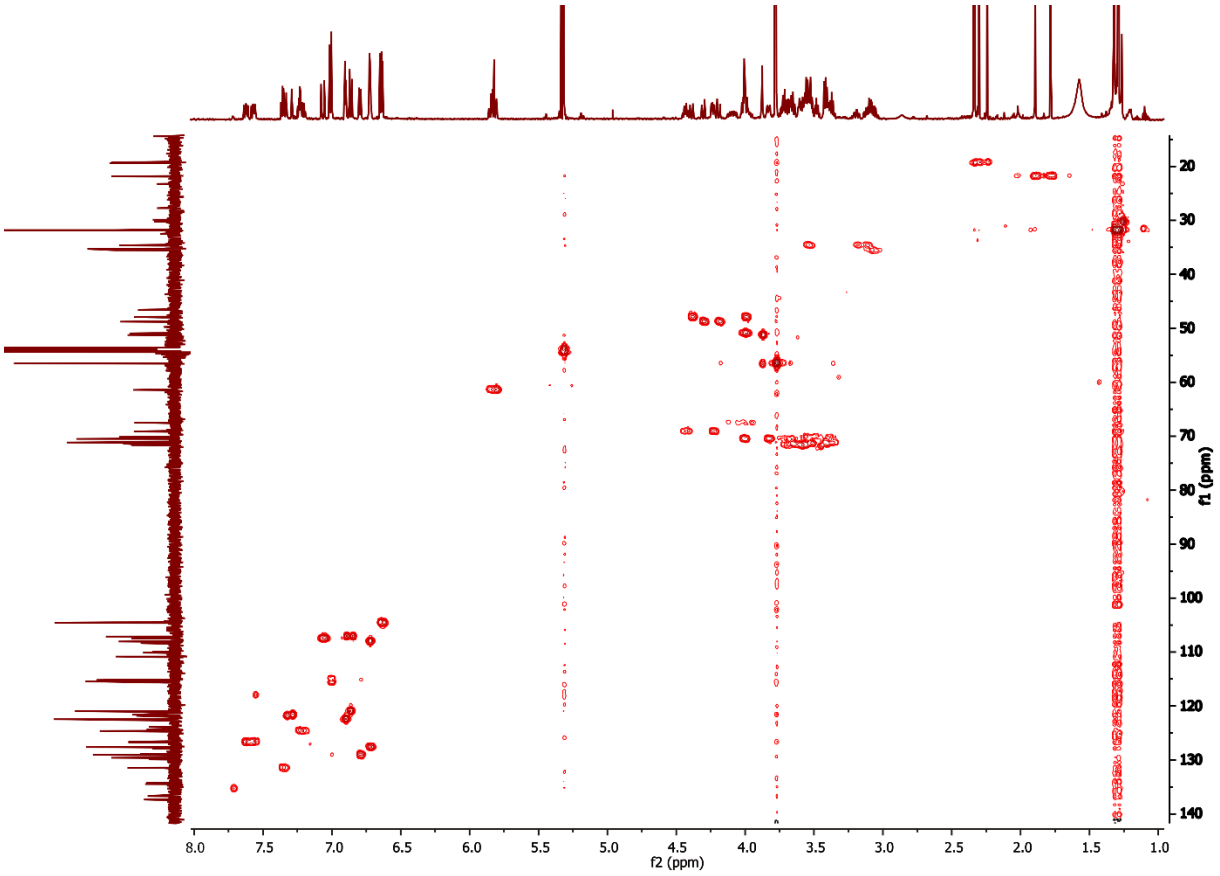

Fig. S9 HMQC spectrum of (*rac*)-**2Ac** in a (700 MHz, CD_2Cl_2).

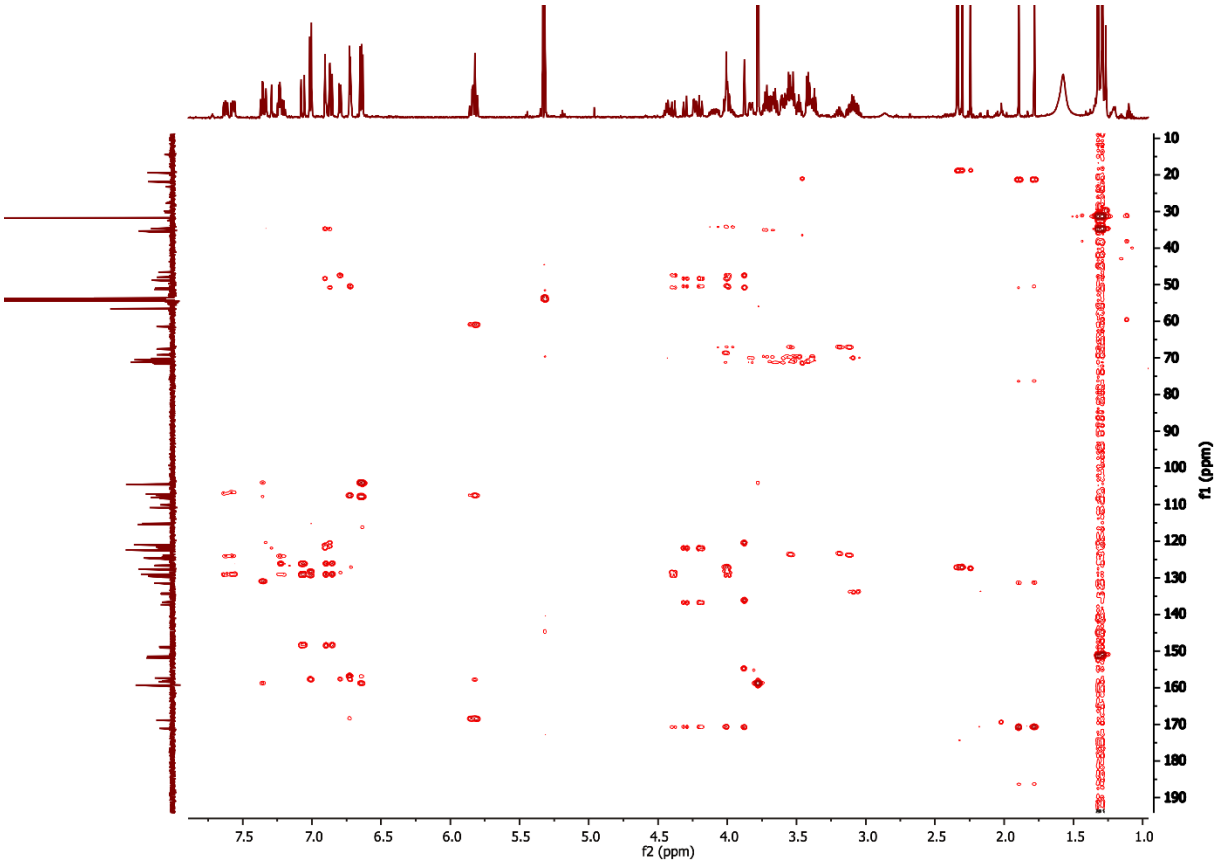

Fig. S10 HMBC spectrum of (*rac*)-**2Ac** in a (700 MHz, CD_2Cl_2).

4. Isothermal titration calorimetry

ITC experiments were carried out in dry 1,2-dichloroethane at 298 K on a TAM III microcalorimeter (Waters GmbH, TA Instruments, Eschborn, Germany). In a typical experiment, an 800 µL solution of crown ether was placed in the sample cell at a concentration of 1.1 mM, and 250 µL of a solution of the ammonium salt (8.0 mM) were put into the syringe. The titrations consisted of 32 consecutive injections of 8 µL each with a 15 min interval between injections. Heats of dilution were determined by titration of ammonium salt solutions into the sample cell containing blank solvent and were subtracted from each data set. The heat flow generated in the sample cell is measured as a differential signal between sample and reference cell. Hence, an exothermic event results in a positive and an endothermic in a negative heat flow. The data were analysed using the instrument's internal software package and fitted with a 1:1 binding model. Each titration was conducted three times and the measured values for *K* and Δ*H* were averaged.

Tab. S1: Thermodynamic data obtained from the ITC experiments.

	K_a /10^5 M^{-1}	ΔG / kJ mol^{-1}	ΔH / kJ mol^{-1}	$T\Delta S$ / kJ mol^{-1}
axle **A1⊂TTFC8**	4.4 ± 0,4	-32.2 ± 0.3	-46.2 ± 0.7	-14.0 ± 1.0
axle **A1⊂dTTFC8**	3.6 ± 0.3	-31.7 ± 0.2	-41.1 ± 1.1	-11.0 ± 1.3

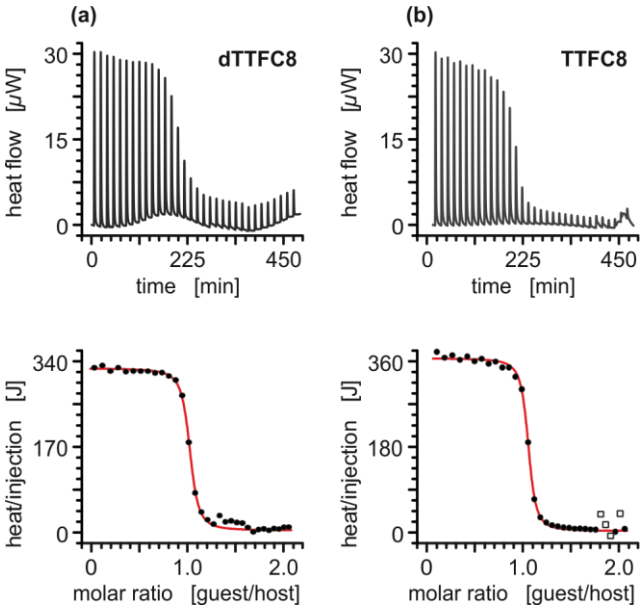

Figure S11. Titration plots (heat flow versus time and heat/volume versus guest/host ratio) obtained from ITC experiments at 298 K in 1,2-dichloroethane**: (a)** vial: **dTTFC8**, syringe: axle **A1**; **(b)** vial: **TTFC8**, syringe: axle **A1**; Points marked with non-filled squares were not considered in the fitting process.

5. Electrochemical measurements

Redox-potentials reported in this study were obtained by cyclic voltammetry. All measurements were at least conducted twice. Measurements were conducted in CH_2Cl_2 with 0.1 M electrolyte and 1 mM analyte concentration.

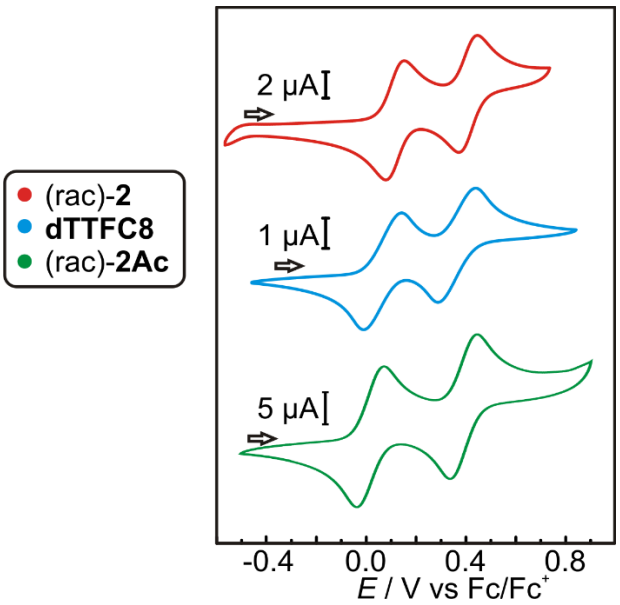

Fig. S12 Stacked cyclic voltammograms (CH_2Cl_2, n-Bu_4NPF_6, 298 K) of (*rac*)-**2**, **dTTFC8** and (*rac*)-**2Ac**

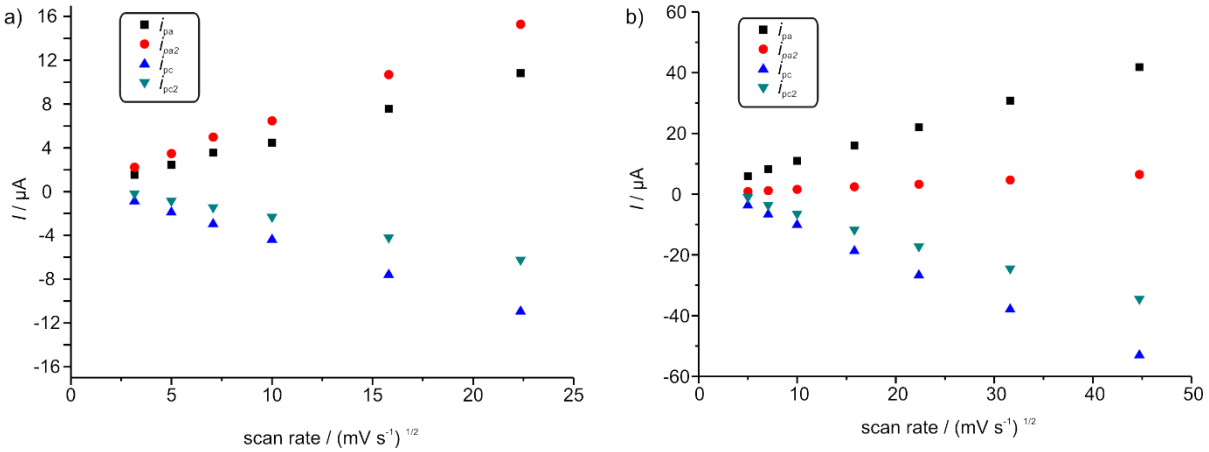

Fig. S13 Peak currents plotted against the square root of scan speed based on cyclic voltammograms of a) (*rac*)-**2** and b) (*rac*)-**2Ac** (CH_2Cl_2, with n-Bu_4NPF_6 as the electrolyte, 298 K). The peak currents can be approximated by linear functions, showing the reversibility of the redox process.

6. CD spectra

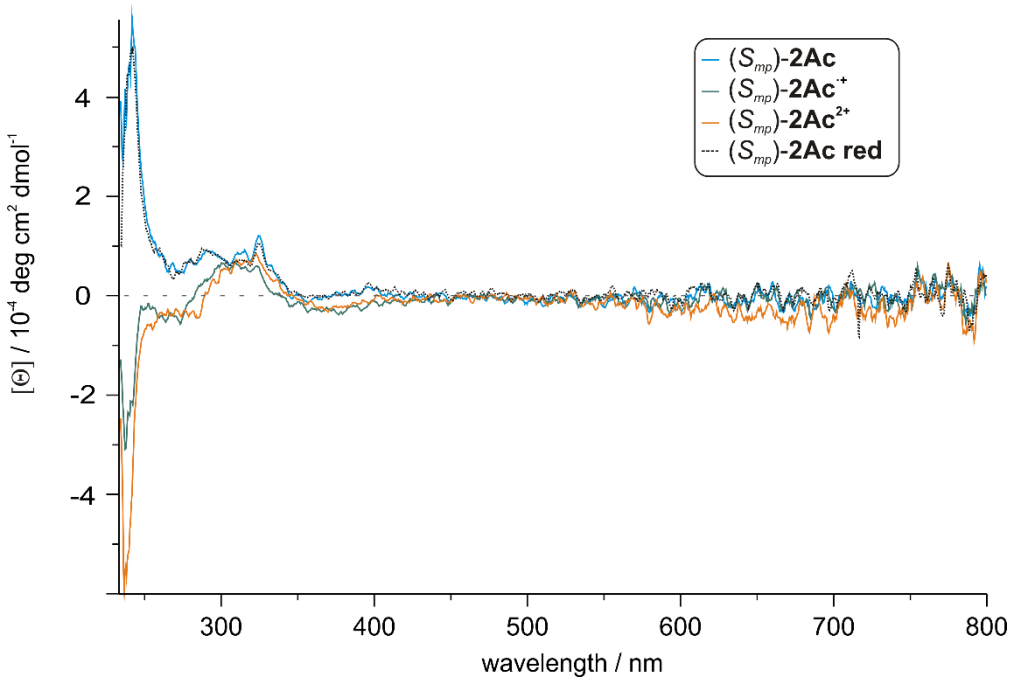

Fig. S14 CD spectra of (S_{mp})-**2Ac** (160 µM in CH_2Cl_2, 298 K, bulk $Fe(ClO_4)_3$ as the oxidant) in the TTF^0, $TTF^{\bullet+}$ and TTF^{2+} state and after reduction to the neutral form with Zn dust.

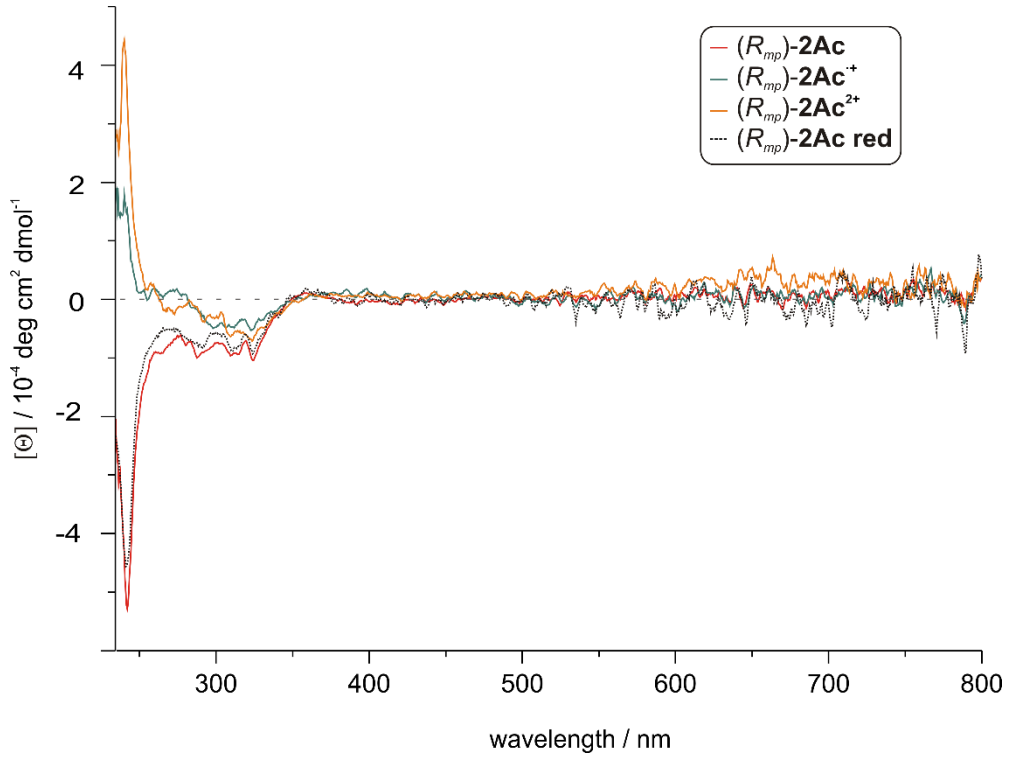

Fig. S15 CD spectra of (R_{mp})-**2Ac** (160 µM in CH_2Cl_2, 298 K, bulk $Fe(ClO_4)_3$ as oxidant) in the TTF^0, $TTF^{\bullet+}$ and TTF^{2+} state and after reduction to the neutral form with Zn dust.

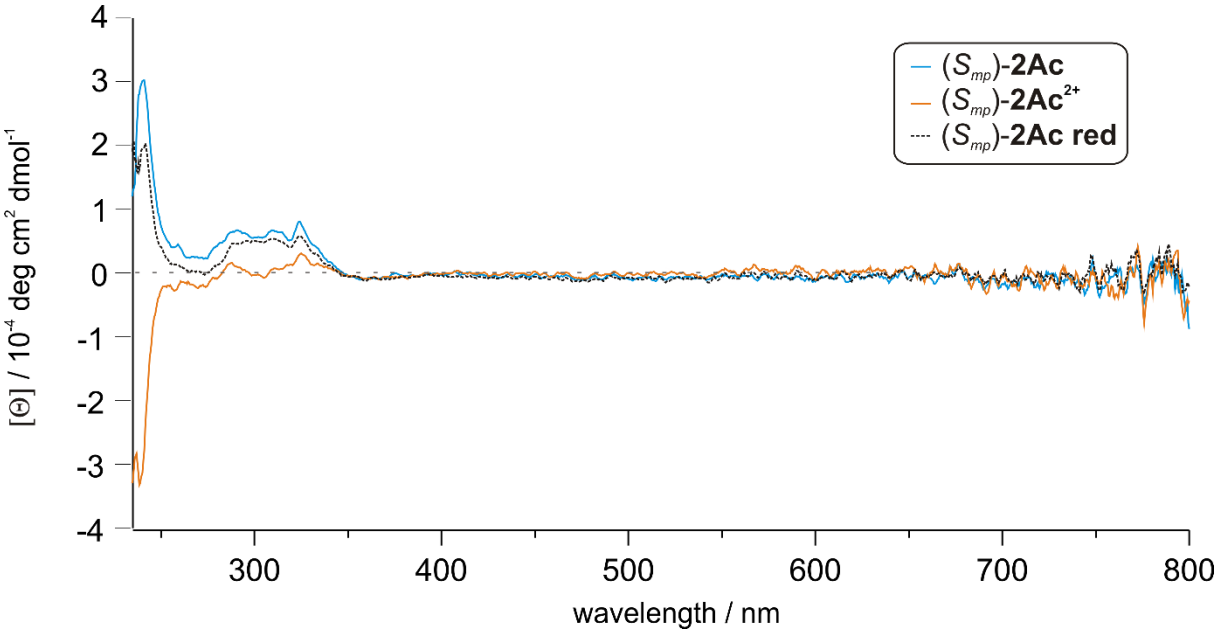

Fig. S16 CD spectra of (S_{mp})-**2Ac** (220 µM in ACN, 298 K, bulk $Fe(ClO_4)_3$ as the oxidant) in the TTF^0 and TTF^{2+} state and after reduction to the neutral form with Zn dust.

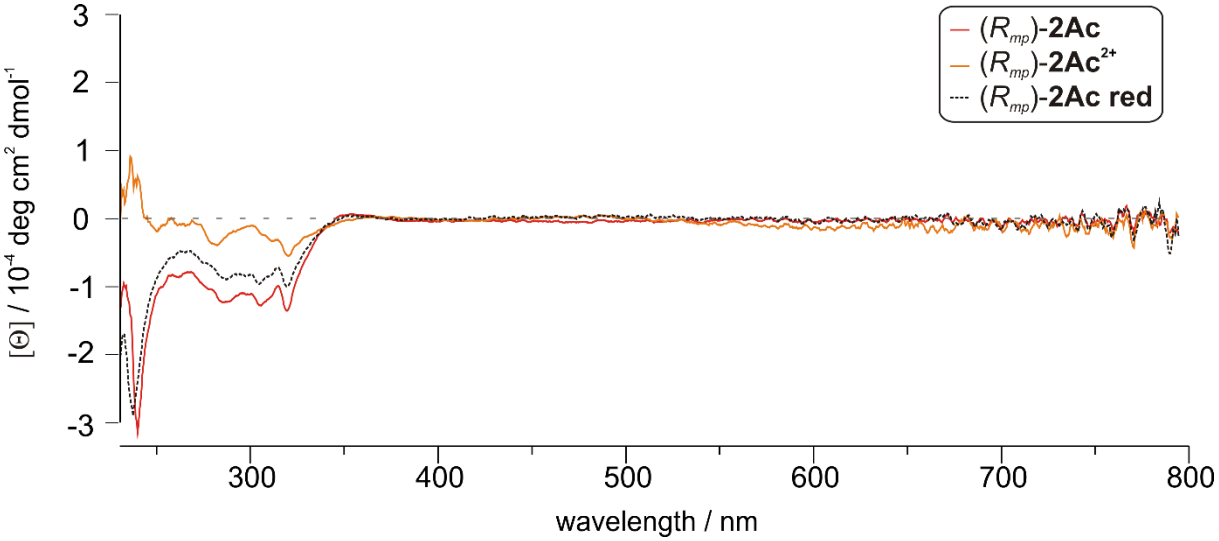

Fig. S17 CD spectra of (R_{mp})-**2Ac** (220 µM in ACN, 298 K, bulk $Fe(ClO_4)_3$ as oxidant) in the TTF^0 and TTF^{2+} state and after reduction to the neutral form with Zn dust.

7. Computational details

Conformational search. To study the influence of different conformations on the optical activity of *(*R_{mp}*)*-**2Ac**, we performed simulated annealing with the xTB (extended tight-binding) programme by Stefan Grimme.[13] This approach is based on DFTB (density functional tight binding)[14] and has been optimised for non-covalent interactions. GBSA (generalised Born accessible surface area)[15] was included as an implicit solvent model in the calculation. Using the Berendsen thermostat,[16] a maximum and minimum temperature of 1000 K and 300 K were chosen for annealing, respectively. The run time for each annealing step was 50 ps, the time step was 2 fs, and structures were dumped every 50 fs. Furthermore, the SHAKE algorithm[17] was applied to restrain hydrogen atoms from dissociating.

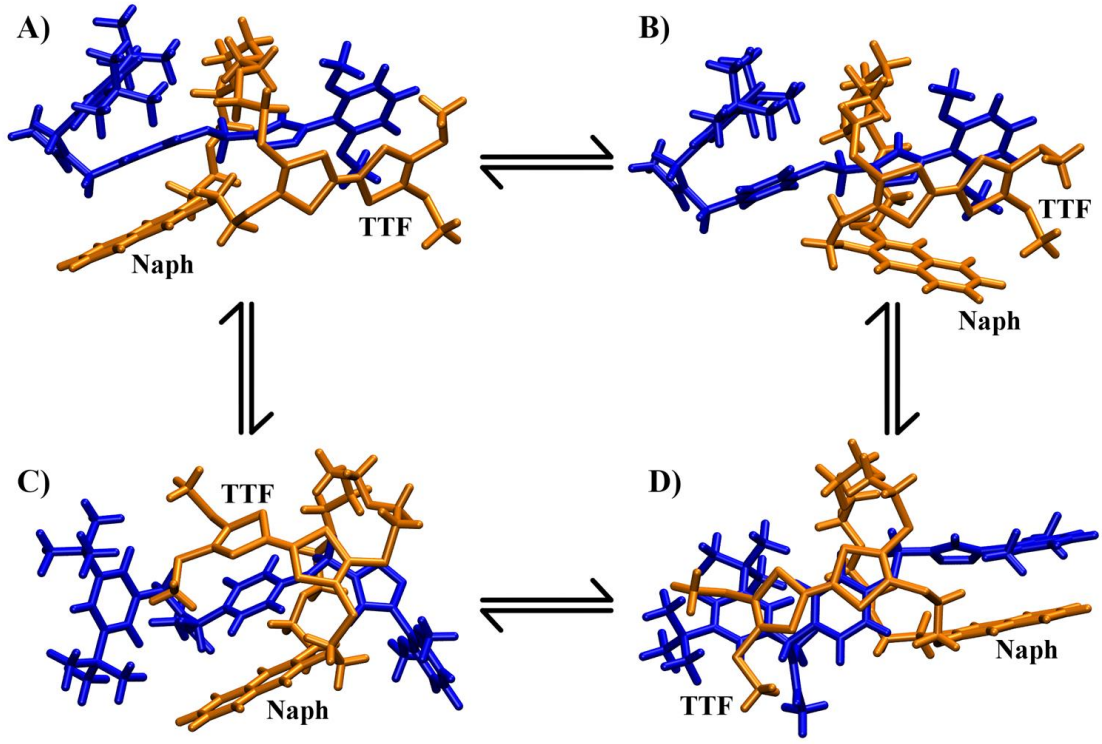

Fig. S18: The four most favourable conformations of (*R_{mp}*)-**2Ac**: **A**, **B**, **C**, and **D**. The conformations differ in the way the TTF core, the naphthalene unit, and the axle are positioned with respect to each other. Every conformation can be interconverted into another by flipping the TTF or the naphthalene unit or both.

Fig. S18 displays the four most stable conformations re-optimised at the RI*J*-TPSS-D3(BJ)/def2-SVP[18-22] level of density functional theory (DFT) with the programme package Turbomole (version 7.1)[23]. COSMO (ε = 8.9 for CH_2Cl_2)[24] was employed as the solvent model. Subsequent single-point calculations to assess the relative stabilities of the four conformations (see Table S2) were performed at the RI*J*COSX-ωB97X-D3/def2-TZVP[25, 26] level with CPCM[27]

as solvent model using ORCA (version 4.0.1)[28]. Finally, Grimme's sTD-DFT (simplified time-dependent DFT)[29] approach was used at the same level to connect electronic properties and optical activity, i.e. the ECD spectra (Fig. 4 in main text) of (R_{mp})-**2Ac**. The entire procedure was conducted for both (R_{mp})-**2Ac** and (R_{mp})-**2Ac^{2+}**.

Tab. S2: Relative electronic energies of all conformations in charge states 0 and 2+ calculated at the ωB97X-D3 level of DFT (values in kJ/mol)

charge state	conformer A	conformer B	conformer C	conformer D
0	0.0	30.4	43.9	17.9
2+	8.5	0.0	54.6	58.6

Calculations at other levels of theory (PBE0[30], CAM-B3LYP[31], and M06-2X[32]) confirm the relative stabilities of the four conformers. Moreover, the shapes of the simulated ECD spectra are considered reliable as they agree with each other regarding the signs of the CD bands. Nevertheless, a systematic red-shift in wavelengths of sometimes up to 50 nm compared to experiment is observed, which is however expected for different density functionals (see Fig. S19 for an illustrative example).

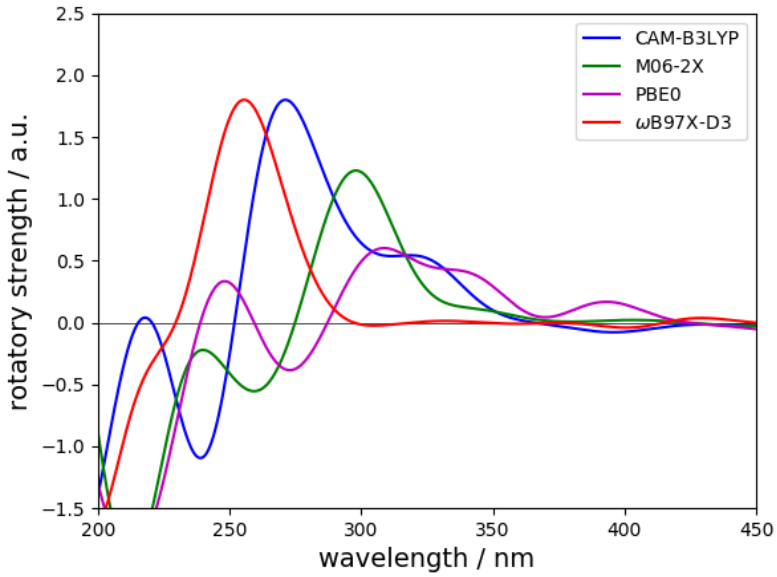

Fig. S19: ECD spectra of (R_{mp})-**2Ac**$^{2+}$ in conformation **A** computed at the sTD-DFT level with various functionals. Gaussian line broadening with σ = 20 nm was applied. Vertical transition lines are omitted for clarity. It can be observed that the general shapes of the spectra agree while the absolute positions of the signals vary in wavelengths to some extent.

Furthermore, it should be noted that (R_{mp})-**2Ac**$^{2+}$ in all four conformations displays non-negligible rotarory strengths for the TTF-centered transition at around 650-700 nm (not shown in Fig. S19) which is caused by an overestimation of the magnetic dipole transition moment

owing to a seemingly poor description of the TTF-TTF transition within the sTD-DFT framework.

Electronic structure and transitions.

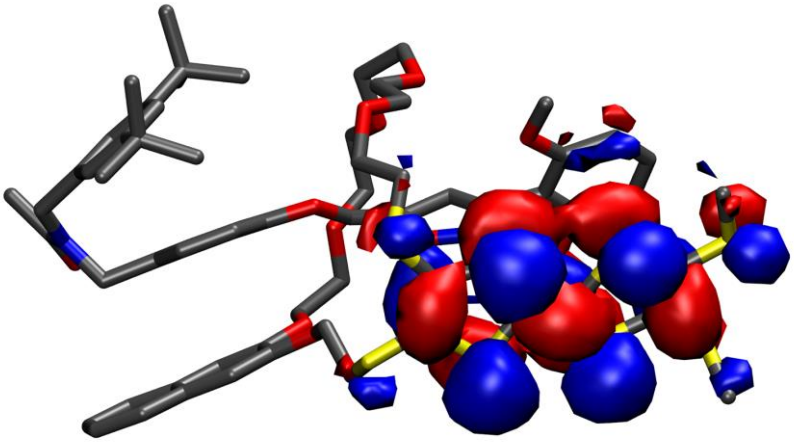

Fig. S20: HOMO of **2Ac** in conformation **A** (the same nodal shape can be observed for the LUMO of **2Ac**$^{2+}$), isovalue = 0.01 a_0^{-3}.

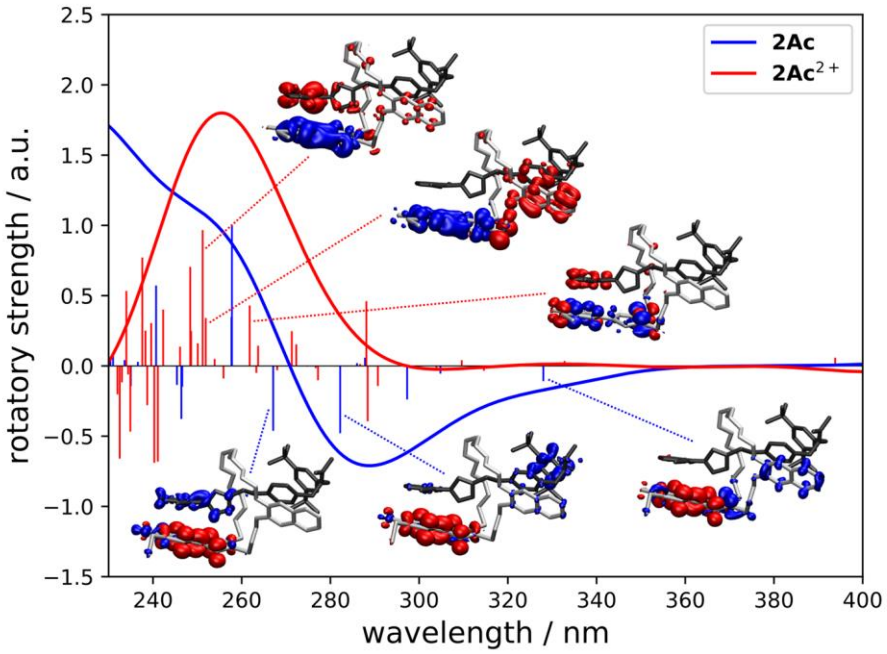

Fig. S21: Simulated ECD spectra of (R_{mp})-**2Ac** and (R_{mp})-**2Ac^{2+}** both in conformation **A** obtained at the ωB97X-D3/def2-TZVP level of sTD-DFT. Gaussian line broadening with σ = 20 nm was applied. Insets: Excited state difference densities of selected transitions to visualise the electron flow during these excitations. Blue and red zones correspond to areas of electron-enhancement and electron-depletion, respectively. Isovalue: 0.001 a_0^{-3}.

Intramolecular interactions. An atoms-in-molecules (AIM)[33] bonding analysis was performed for *(R_{mp})*-**2Ac** in all *four* conformations and charge state 0 and 2+. Fig. S22 shows *(R_{mp})*-**2Ac** in conformation **A** with its bond critical points as a representative example. An AIM analysis is useful for studying non-covalent interactions. C-H···π and π-π-stacking interactions can thus be easily identified within *(R_{mp})*-**2Ac**. Together with the results from our DFT calculations at the RI*J*COSX-ωB97X-D3/def2-TZVP level, we can deduce what is likely responsible for the conformational behaviour of *(R_{mp})*-**2Ac** and *(R_{mp})*-**2Ac**$^{2+}$. Important aspects are the energetic gain through π-π-stacking between the various (aromatic) units and the delocalisation of electron density near the TTF unit.

First, we will discuss the neutral molecule *(R_{mp})*-**2Ac**. Conformation **A** exhibits a large amount of intramolecular interactions especially through π-π-stacking of aromatic units. Furthermore, the TTF unit's proximity to the isoxazole core and the dimethoxy-phenyl moiety yield non-covalent interactions. In conformation **B**, many of the π-π-stacking interactions are lost as the naphthalene moiety attaches itself to the TTF unit, which makes this conformation around 30 kJ/mol less stable. The energetic gain in conformation **D** is based on the interaction

between the naphthalene, the isoxazole core, and the dimethoxy-phenyl unit and the stacking of the TTF unit and the phenyl spacer. However, the di-*tert*butyl-phenyl unit is not able to stack with any of the other aromatic units anymore, which results in a net loss of almost 18 kJ/mol with respect to conformation **A**. Finally, conformation **C** is the least stable structure (ca. 44 kJ/mol with respect to **A**) since effective π-π-stacking is neither achieved by the isoxazole unit nor by the dimethoxy-phenyl ring nor by the di-*tert*butyl-phenyl moiety. The energetic gain through non-covalent interactions is solely based on the arguably inefficient stacking between TTF core, phenyl spacer and naphthalene unit.

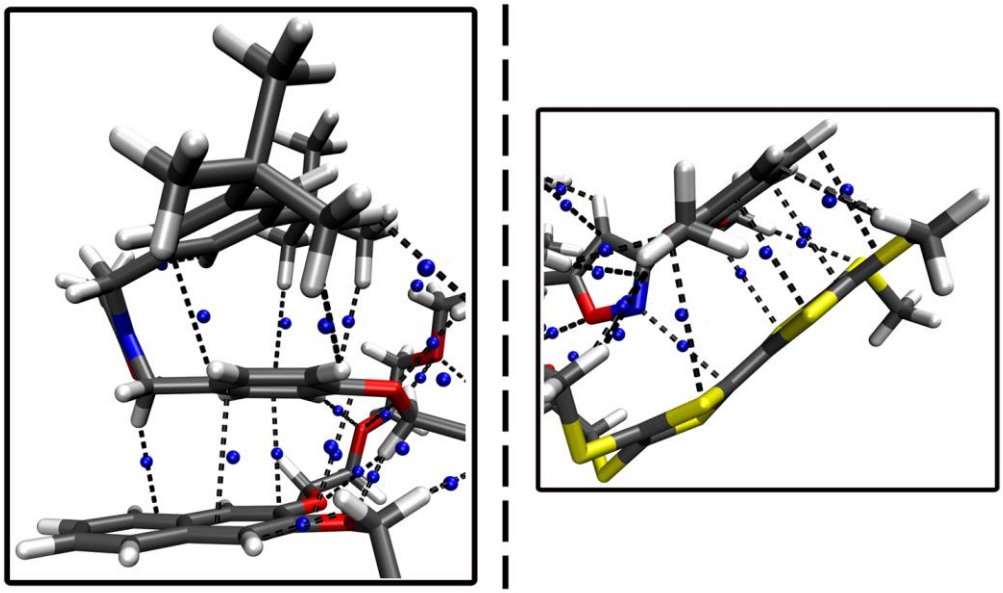

Fig. S22: Bond critical points (blue spheres) obtained at the ωB97X-D3/def2-TZVP level utilising the Multiwfn programme[34] near the naphthalene moiety (left) and the TTF unit (right) illustrating the non-covalent interactions within **2Ac** in conformation **A**.

For *(R_{mp})*-**2Ac**$^{2+}$ the picture is quite different. Now conformation **B** is the most stable structure since the charge, which is mostly localised on the TTF unit, can be delocalised over the TTF core, the naphthalene unit, the isoxazole ring, and the dimethoxy-phenyl moiety. Additionally, there is still the π-π-stacking interaction between the di-*tert*butyl-phenyl unit and the phenyl spacer contributing to its energetic stability. The charge delocalisation over four different units in the molecule is missing in conformation **A**, which makes it somewhat less stable than **B** (~ 9 kJ/mol). Similar arguments account for conformation **D**, which is – maybe somewhat surprisingly - by far the least stable structure now (over 58 kJ/mol), as the charge is not efficiently delocalised which seems to massively overcompensate any π-π-stacking interactions. In conformation **C**, the charge can be somewhat better delocalised than in **D**,

however, due to its lack of more efficient π-π-stacking interactions it is also somewhat less stable than **B** (ca. 55 kJ/mol).

8. Crystallographic data

General details. Single crystal X-ray data in the present study were collected at 170 K on a Bruker-Nonius KappaCCD diffractometer with APEX-II detector and graphite monochromatized Mo-Kα (λ = 0.71073 Å) radiation. The *COLLECT*[35] software was used for data collection (θ and ω scans) and *DENZO-SMN*[36] for the processing. Lorentzian polarization correction was applied on all data and absorption effects were corrected with multi-scan method (*SADABS*[37]). The structures were solved by intrinsic phasing methods (*SHELXT*[38]) and refined by full-matrix least squares on F^2 using *SHELXL*-2018/3.[39] The *SQUEEZE* module of *PLATON*[40, 41] was utilized in the structure refinement to remove the residual electron densities, which could not be reliably assigned and refined. Anisotropic displacement parameters were assigned to non-H atoms. Positional disorder in the structures was treated by gently restraining geometric and anisotropic displacement parameters. All hydrogen atoms were refined using riding models with U_{eq}(H) of 1.5U_{eq}(C) for terminal methyl groups and of 1.2U_{eq}(C) for other groups. The main details of crystal data collection and refinement parameters are presented below. CCDC 1910670 contains the supplementary crystallographic data for this paper. These data can be obtained free of charge via http://www.ccdc.cam.ac.uk/conts/retrieving.html (or from the CCDC, 12 Union Road, Cambridge CB2 1EZ, UK; Fax: +44 1223 336033; E-mail: deposit@ccdc.cam.ac.uk).

Structure of dTTFC8: Compound **dTTFC8** was crystallised as orange needles with vapour diffusion of Et_2O into CH_2Cl_2 solution of the compound. Crystal data and refinement parameters of **dTTFC8**: $C_{30}H_{36}O_6S_8$, M = 749.07, monoclinic, space group $P2_1/n$ (no. 14), a = 25.1361(6), b = 5.09490(10), c = 30.6018(9) Å, β = 109.649(2)°, V = 3690.8(2) Å^3, Z = 4, ρ_{calc} = 1.348 Mgm^{-3}, μ = 0.522 mm^{-1}, F_{000} = 1568, θ range = 1.82-26.37°, 14025 reflections collected of which 7554 unique (R_{int} = 0.1129), No. of reflections with $I>2\sigma(I)$ = 3856, which were used in all calculations, 409 parameters and 32 restraints, Goodness-of-fit (F^2) = 1.018. The final R indices [$I>2\sigma(I)$]: R1 = 0.0734 and wR2 = 0.1436. R indices (all data): R1 = 0.1606 and wR2 = 0.1770. Largest residual electron densities: 0.598 and -0.408 e.Å^{-3}.

Structure description for dTTFC8: Crystal structure solution of **dTTFC8** shows nicely that the substituted TTF is attached to the naphthalene crown ether macrocycle. There is a slight disorder in one oxygen atom of crown ether, which is divided over two spatial positions. The substituted TTF moiety exhibits typical bond distances for neutral TTF derivatives,[42-44] like

characteristically short C=C distance of 1.345(7) Å between the 1,3-dithiole rings and a distance range of 1.749(6) to 1.764(5) Å for C-S bonds. An Interesting geometric feature is the planarity of substituted TTF moiety with both 1,3-dithiole rings and all S atoms, as well lying in the same plane. The notably acute angle between the naphthalene and TTF planes (74.8°) can be attributed to the connecting ethylene bridge which avoids ecliptic and gauche conformations by maintaining an OCCS dihedral angle of 159.4°. In the crystal packing, the molecules are arranged in columnar stacks. Naphthalenes stack with naphthalenes with a plane-to-plane distance of 3.29 Å shifted sideways by 3.88 Å and TTFs on top of each other. Instead, TTFs stack with plane-to-plane distances of 3.47 Å, and a sideways slip of 3.73 Å, respectively.

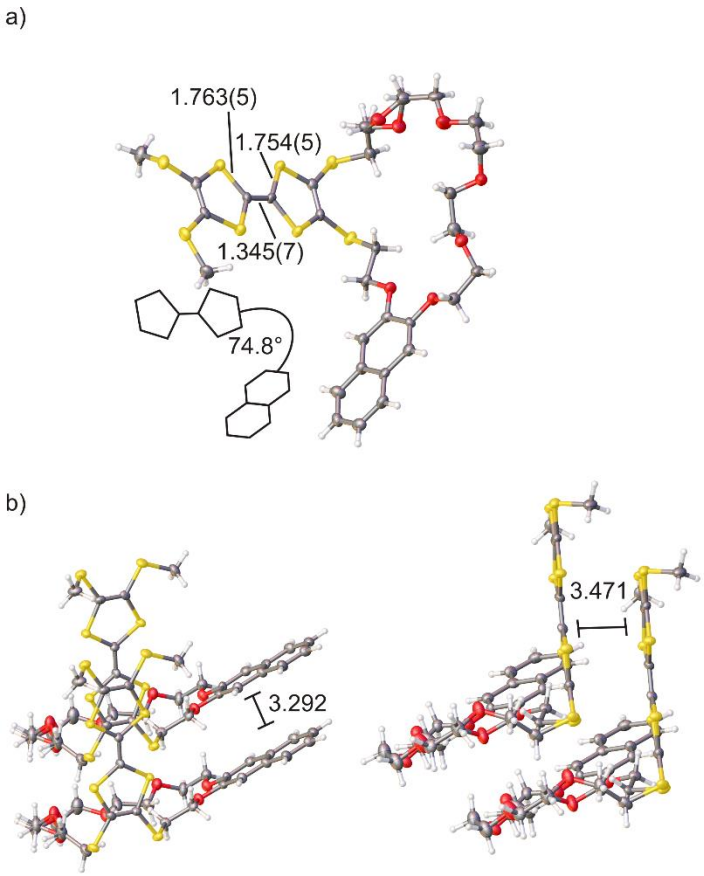

Figure S23: Solid-state structure of **dTTFC8**. (a) Top view with selected bond lengths (Å) and the angle between the naphthalene and the TTF plane. (b) Side view of two stacked **dTTFC8** molecules in the crystal with distances (Å) between molecule planes. Colour codes: S = yellow; O = red; C = grey; H = black (spheres).

9. ^{1}H, ^{13}C NMR

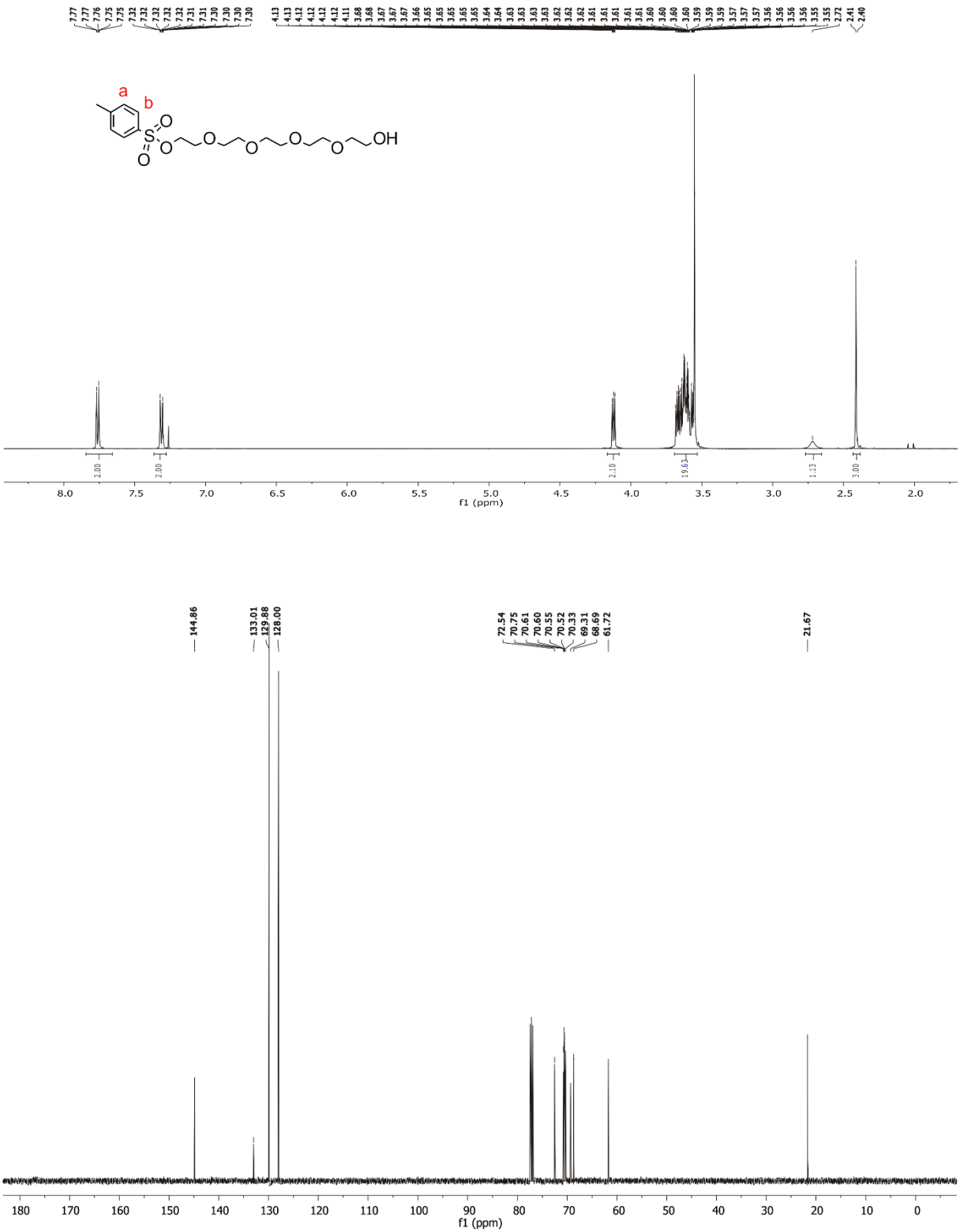

Fig. S24 ^{1}H (top) and ^{13}C (bottom) NMR spectrum (500/126 MHz, $CDCl_3$, 298 K) of **S2**.

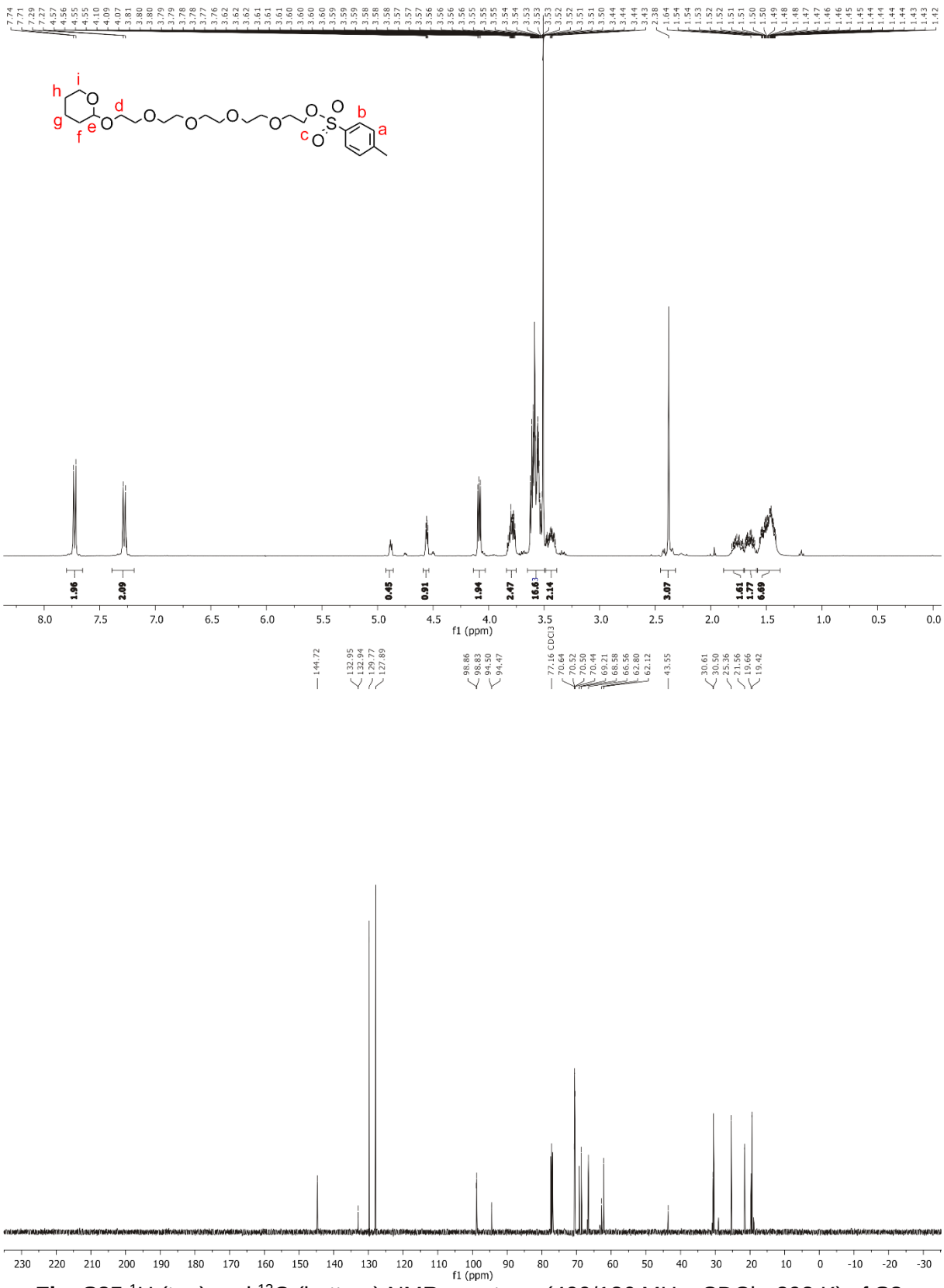

Fig. S25 ^{1}H (top) and ^{13}C (bottom) NMR spectrum (400/126 MHz, $CDCl_3$, 298 K) of **S3**.

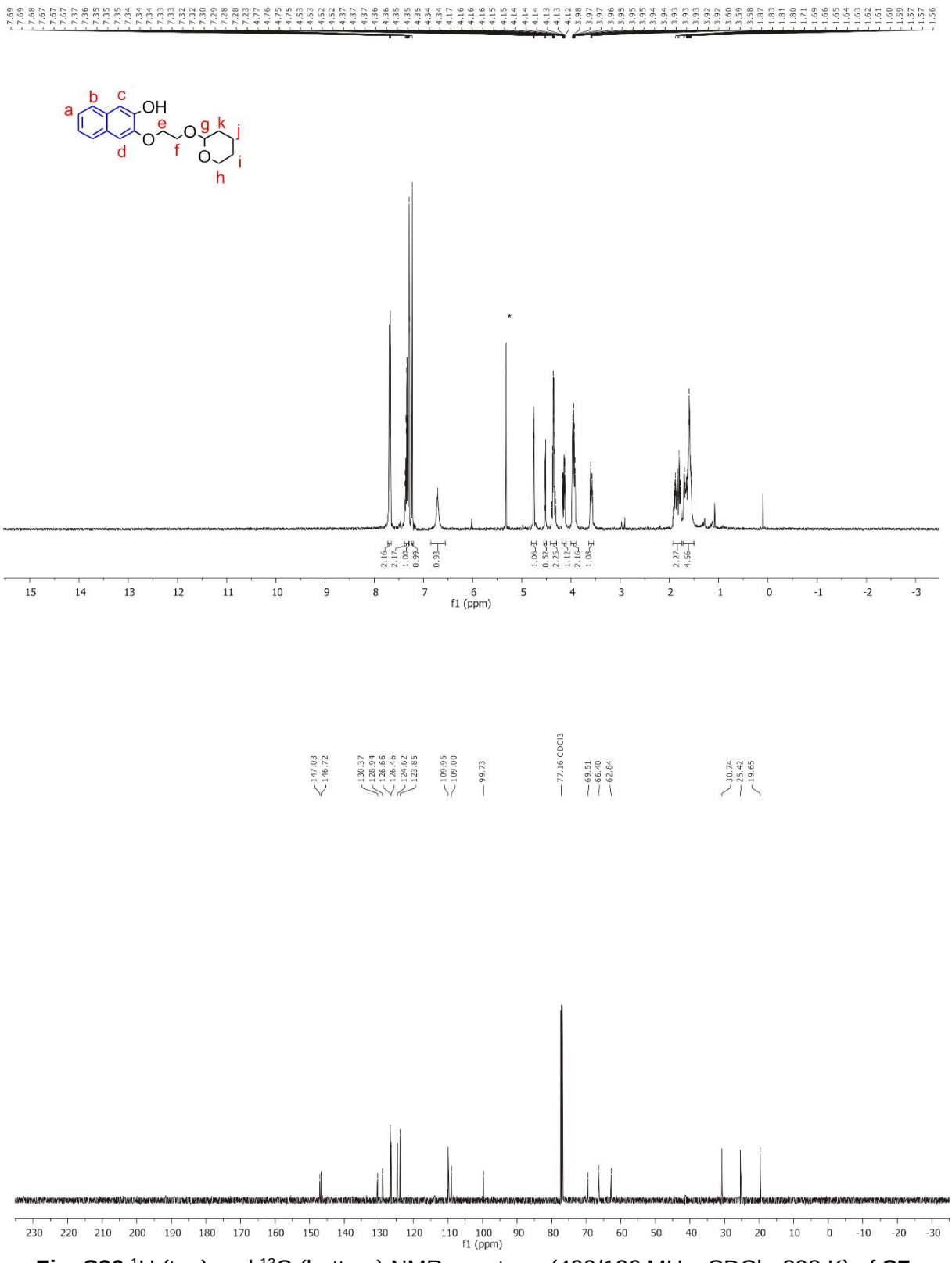

Fig. S26 ^{1}H (top) and ^{13}C (bottom) NMR spectrum (400/126 MHz, $CDCl_3$, 298 K) of **S7**.

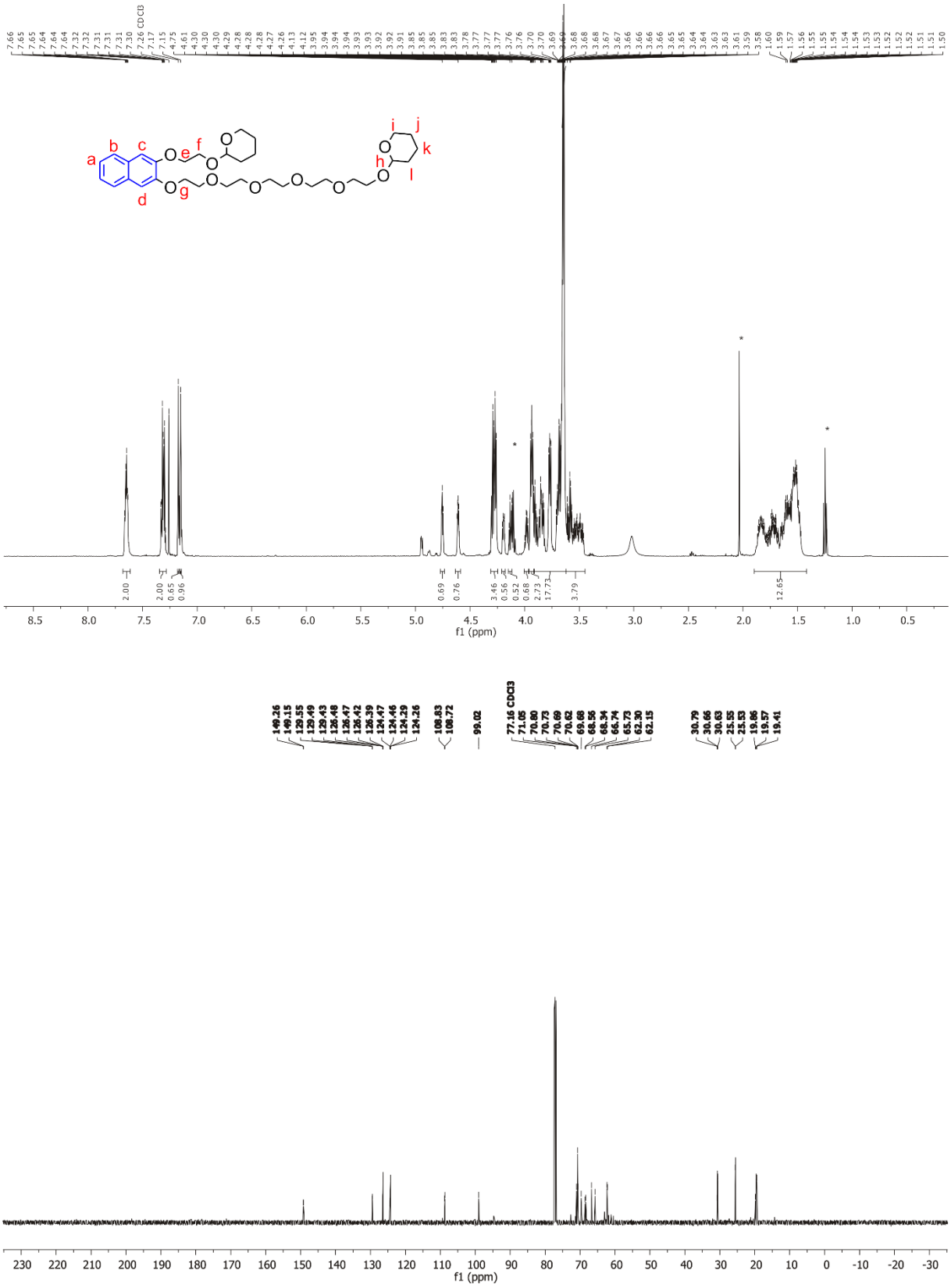

Fig. S27 ^{1}H (top) and ^{13}C (bottom) NMR spectrum (500/126 MHz, $CDCl_3$, 298 K) of **S8**.

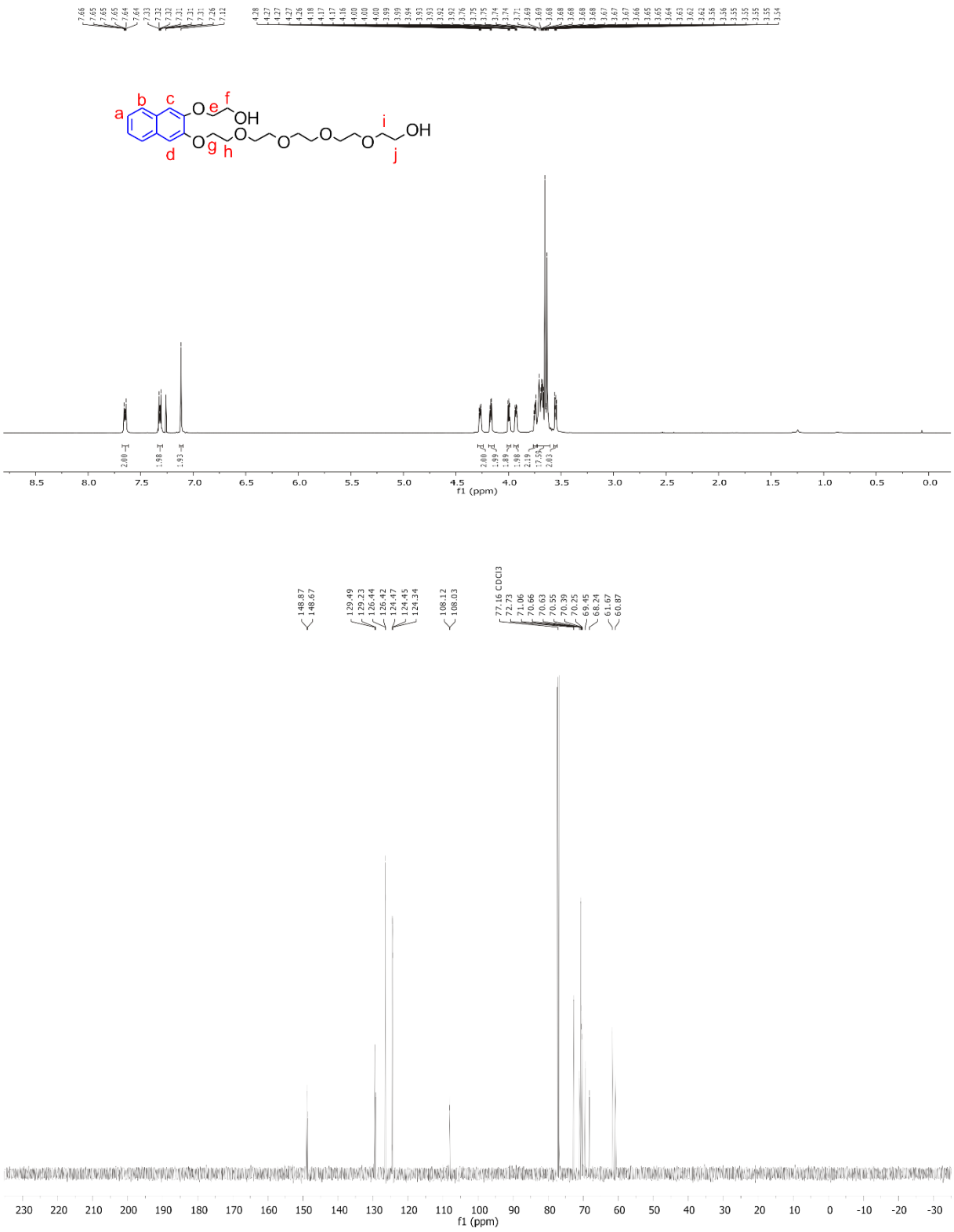

Fig. S28 ^{1}H (top) and ^{13}C (bottom) NMR spectrum (500/126 MHz, $CDCl_3$, 298 K) of **S9**.

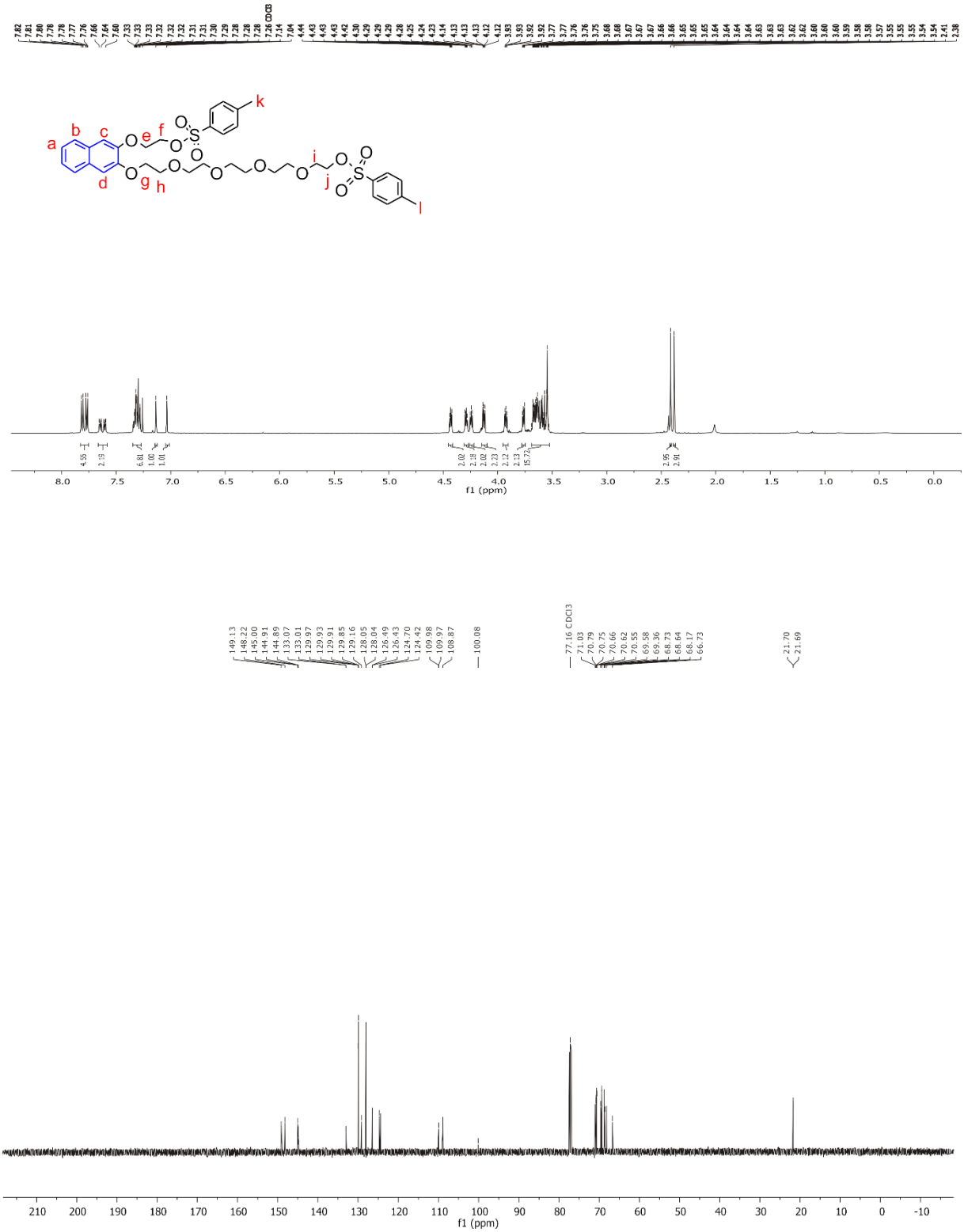

Fig. S29 ^{1}H (top) and ^{13}C (bottom) NMR spectrum (500/126 MHz, $CDCl_3$, 298 K) of **S10**.

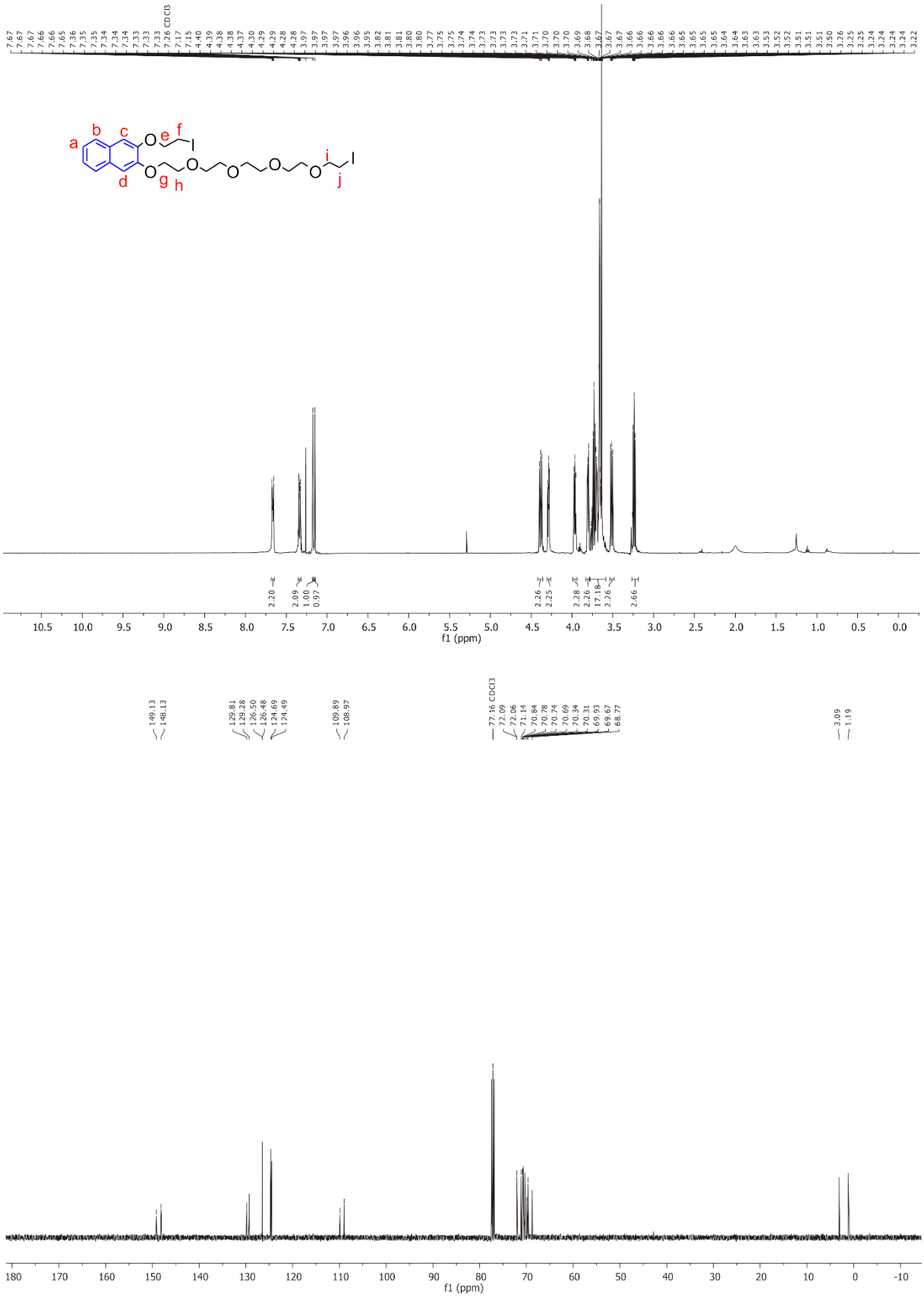

Fig. S30 ^{1}H (top) and ^{13}C (bottom) NMR spectrum (500/126 MHz, $CDCl_3$, 298 K) of **S11**.

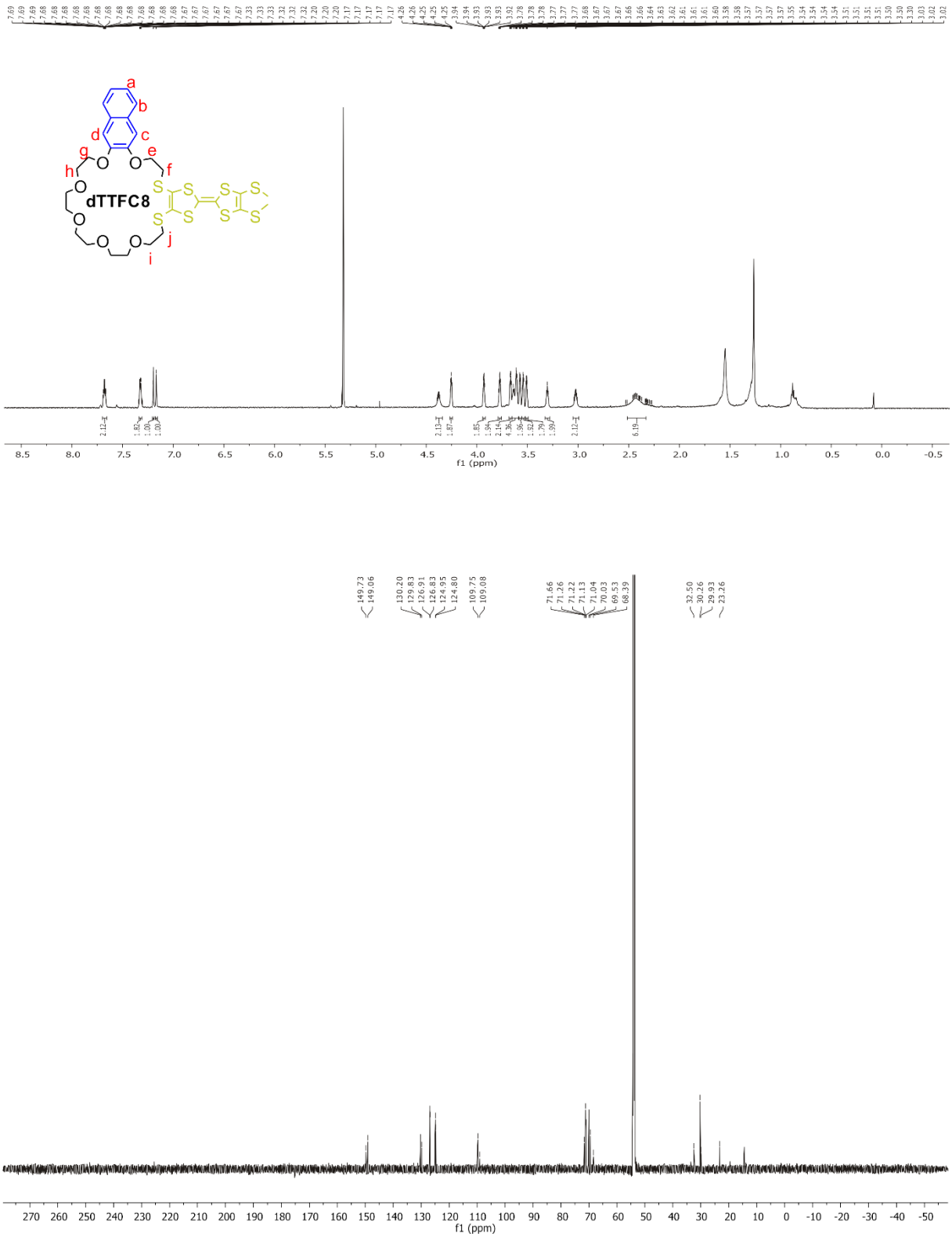

Fig. S31 ^{1}H (top) and ^{13}C (bottom) NMR spectrum (700/176 MHz, $CDCl_3$, 298 K) of **dTTFC8**.

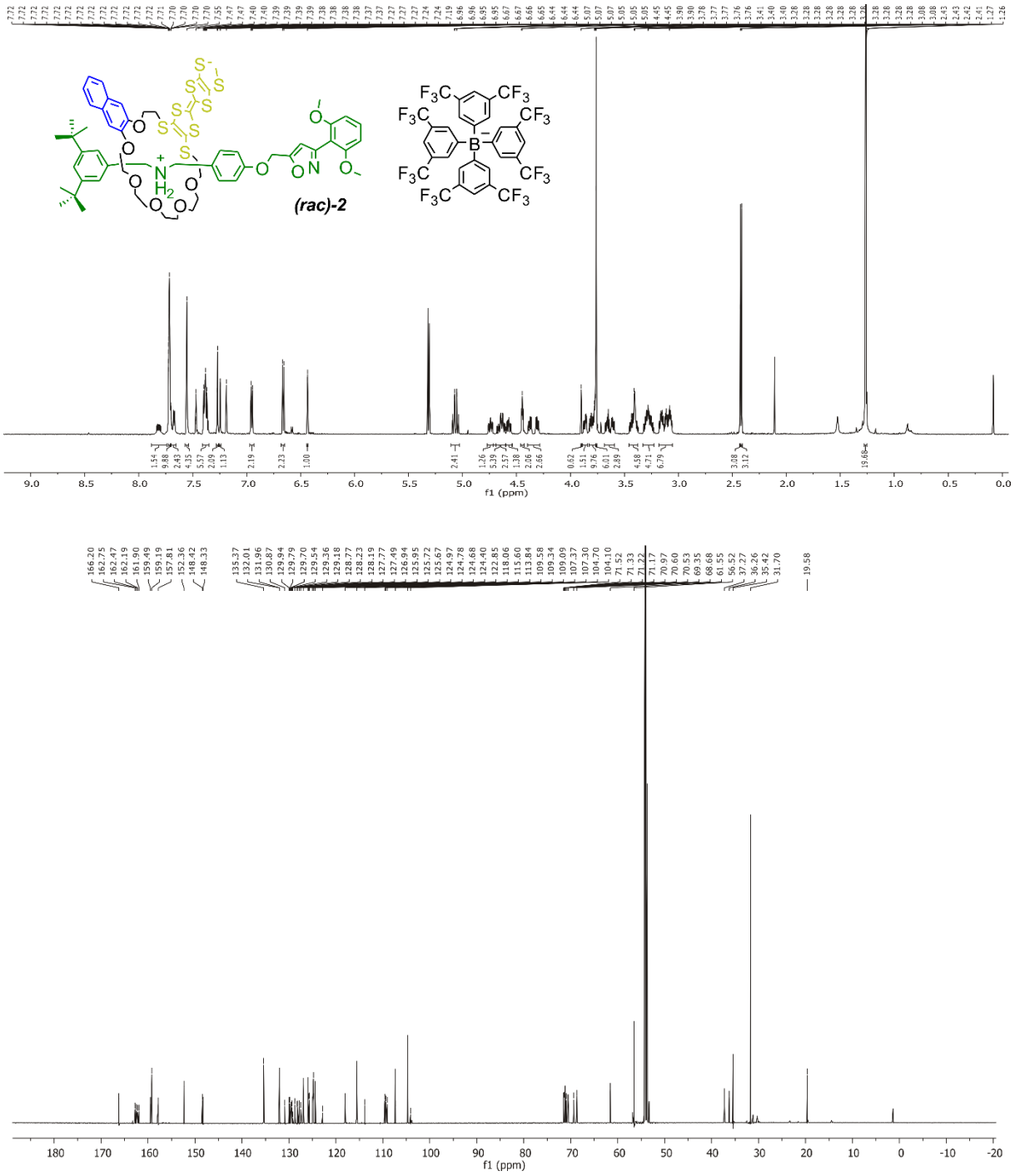

Fig. S32 ^{1}H (top) and ^{13}C (bottom) NMR spectrum (700/176 MHz, CD_2Cl_2, 298 K) of the racemic mixture of **2**.

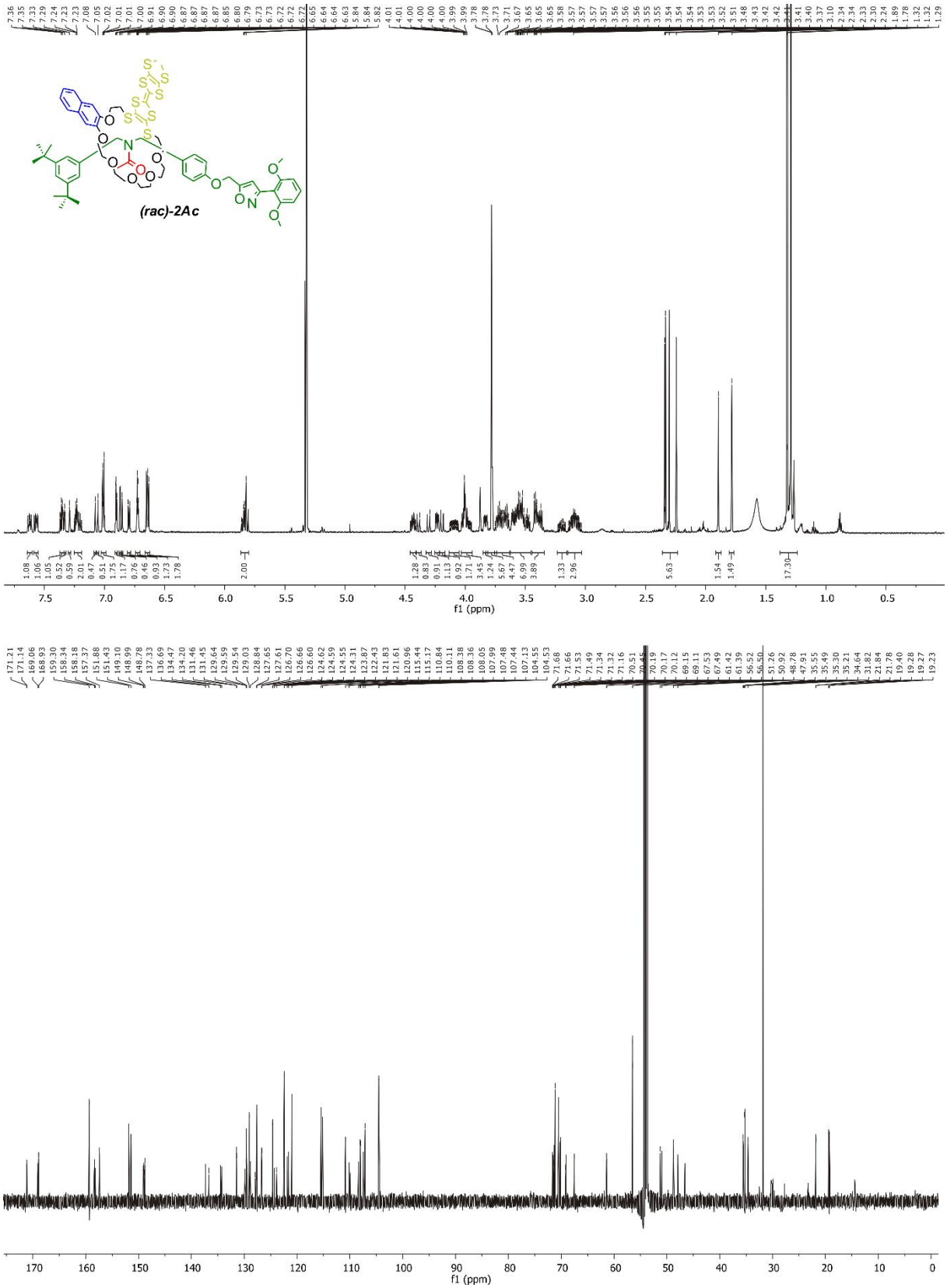

Fig. S33 ^{1}H (top) and ^{13}C (bottom) NMR spectrum (700/176 MHz, CD_2Cl_2, 298 K) of the racemic mixture of **2Ac**.

9. HR-MS

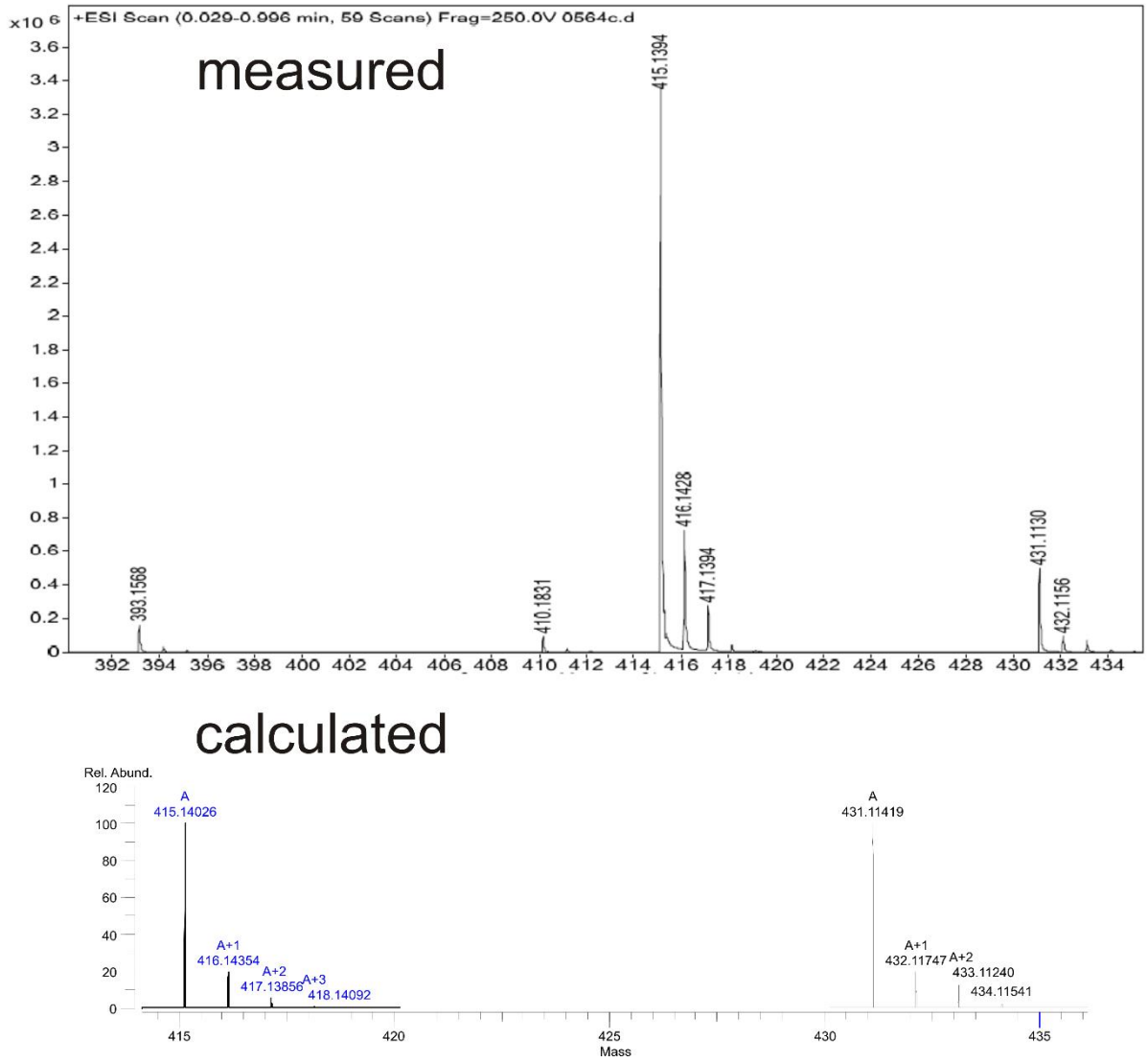

Fig. S34 HRMS ESI$^+$ (top) and calculated (bottom) of **S2**.

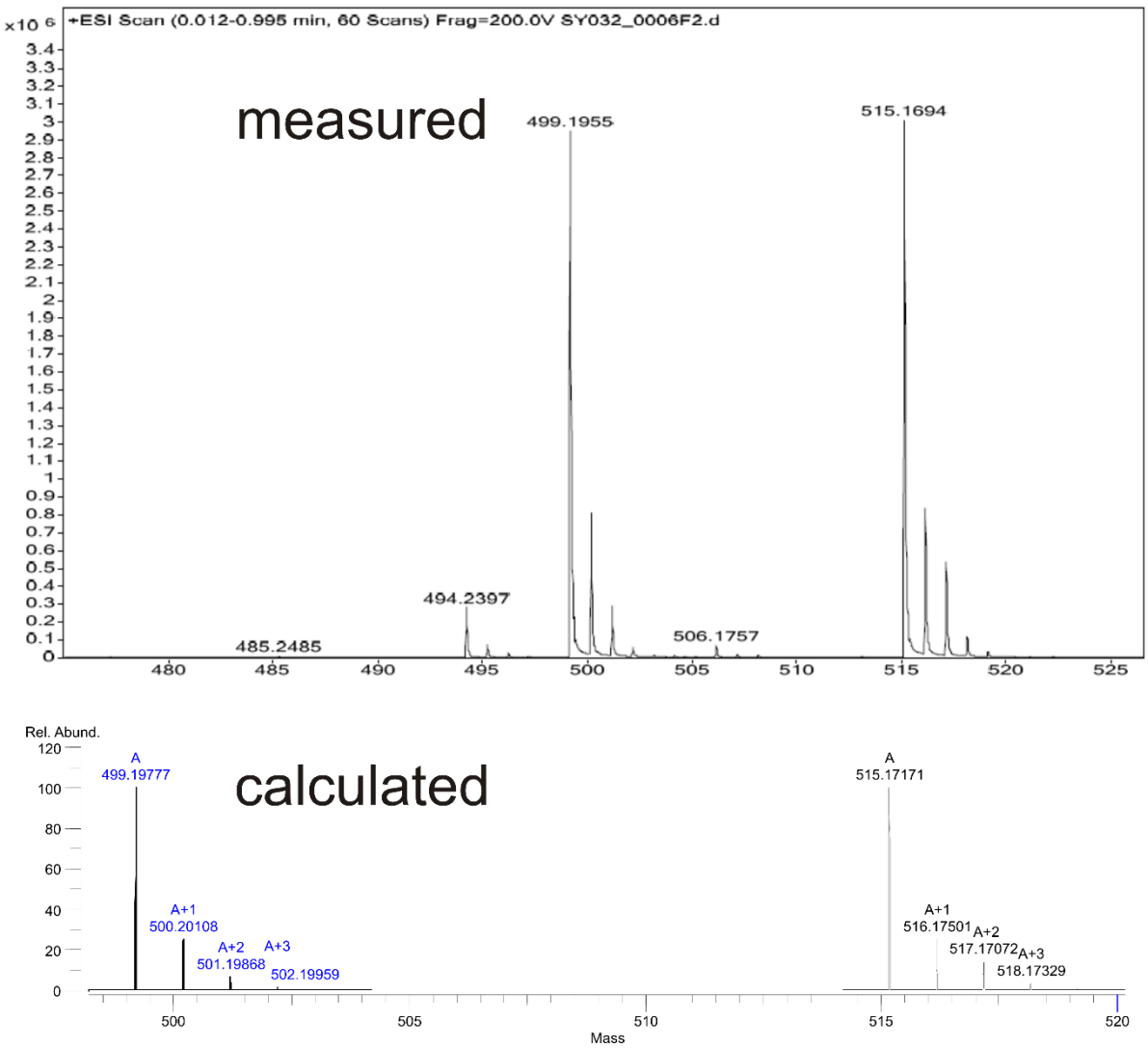

Fig. S35 HRMS ESI$^+$ (top) and calculated (bottom) of **S3**.

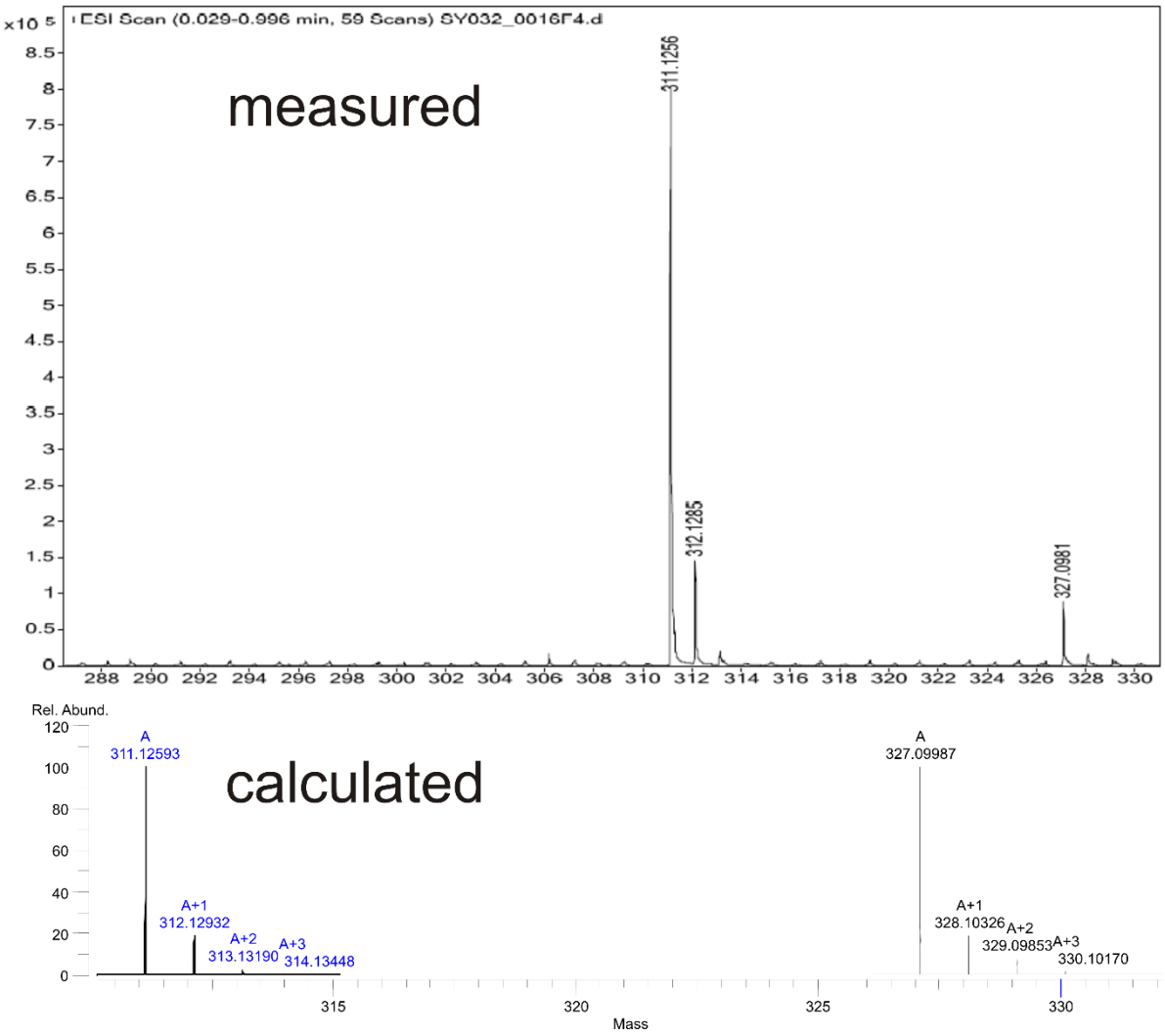

Fig. S36 HRMS ESI$^+$ (top) and calculated (bottom) of **S7**.

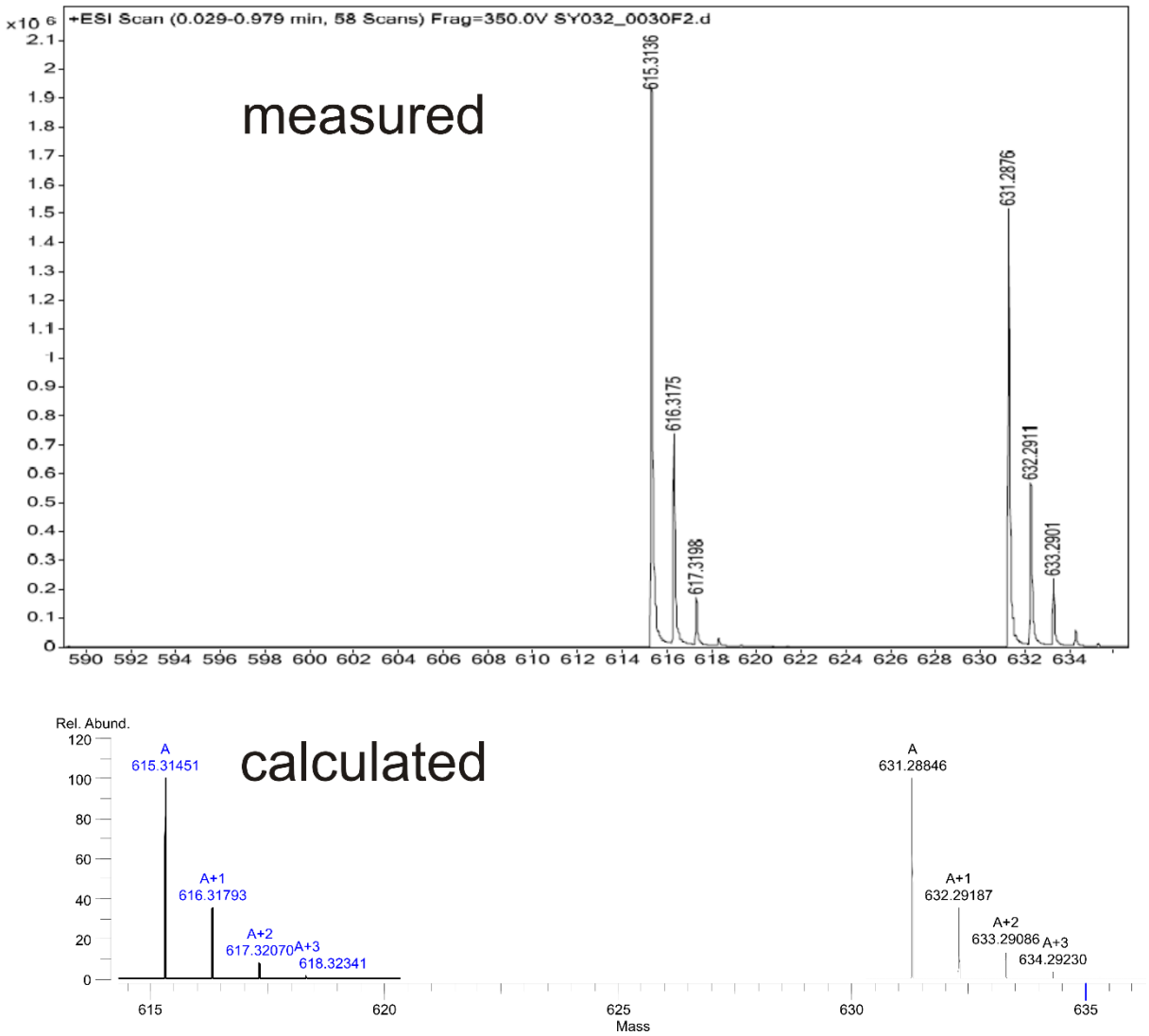

Fig. S37 HRMS ESI$^+$ (top) and calculated (bottom) of **S8**.

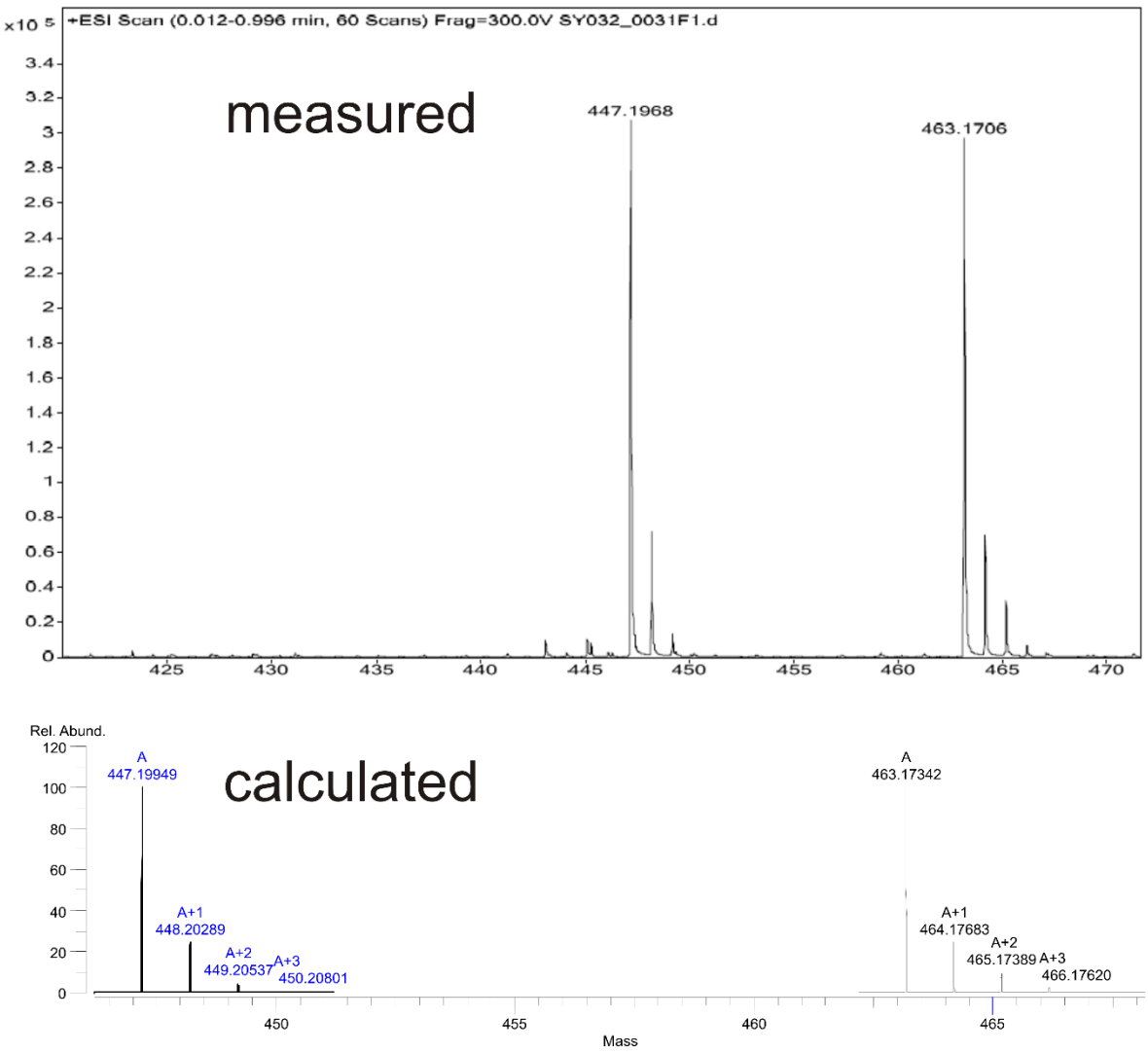

Fig. S38 HRMS ESI$^+$ (top) and calculated (bottom) of **S9**.

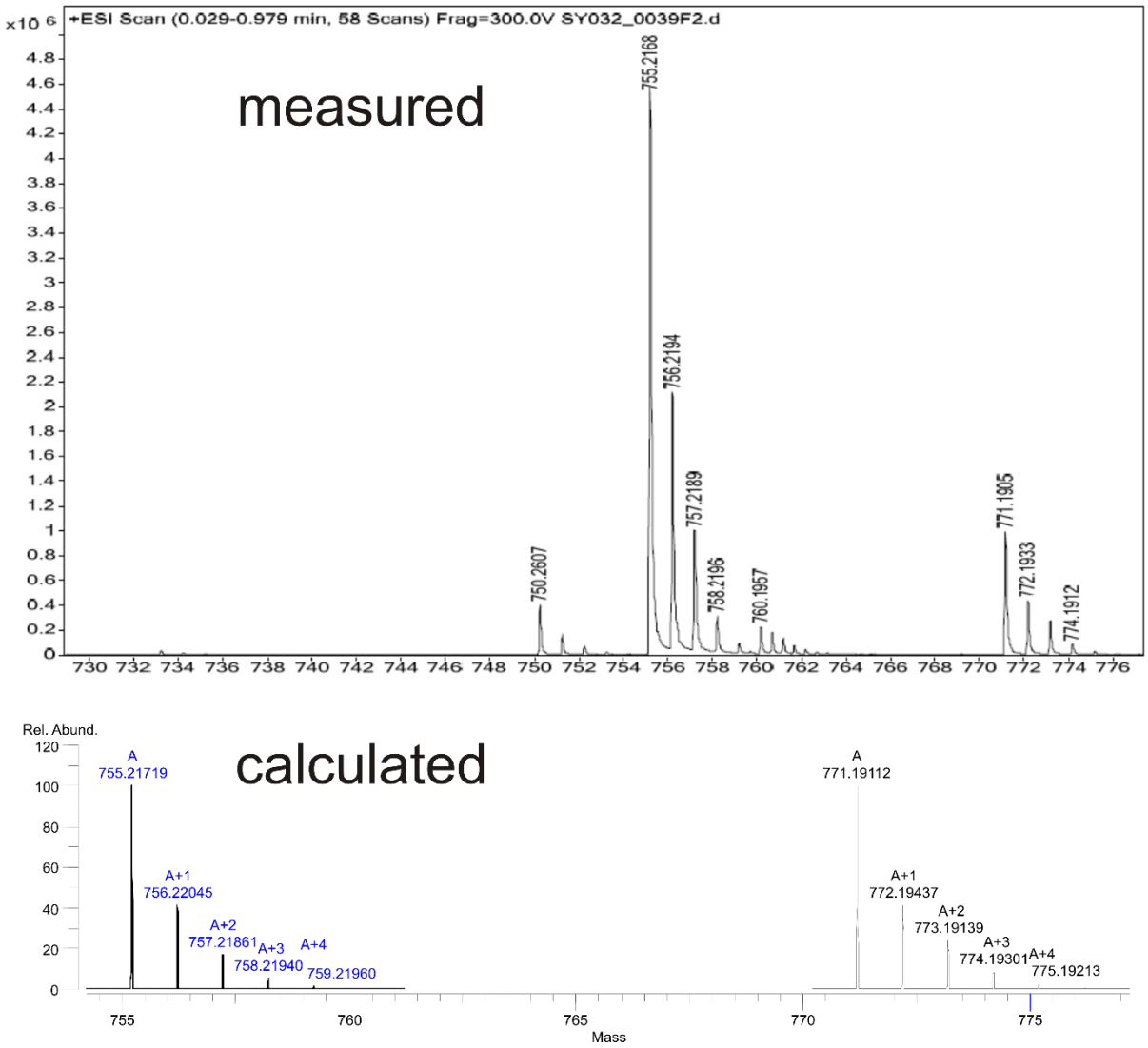

Fig. S39 HRMS ESI$^+$ (top) and calculated (bottom) of **S10**.

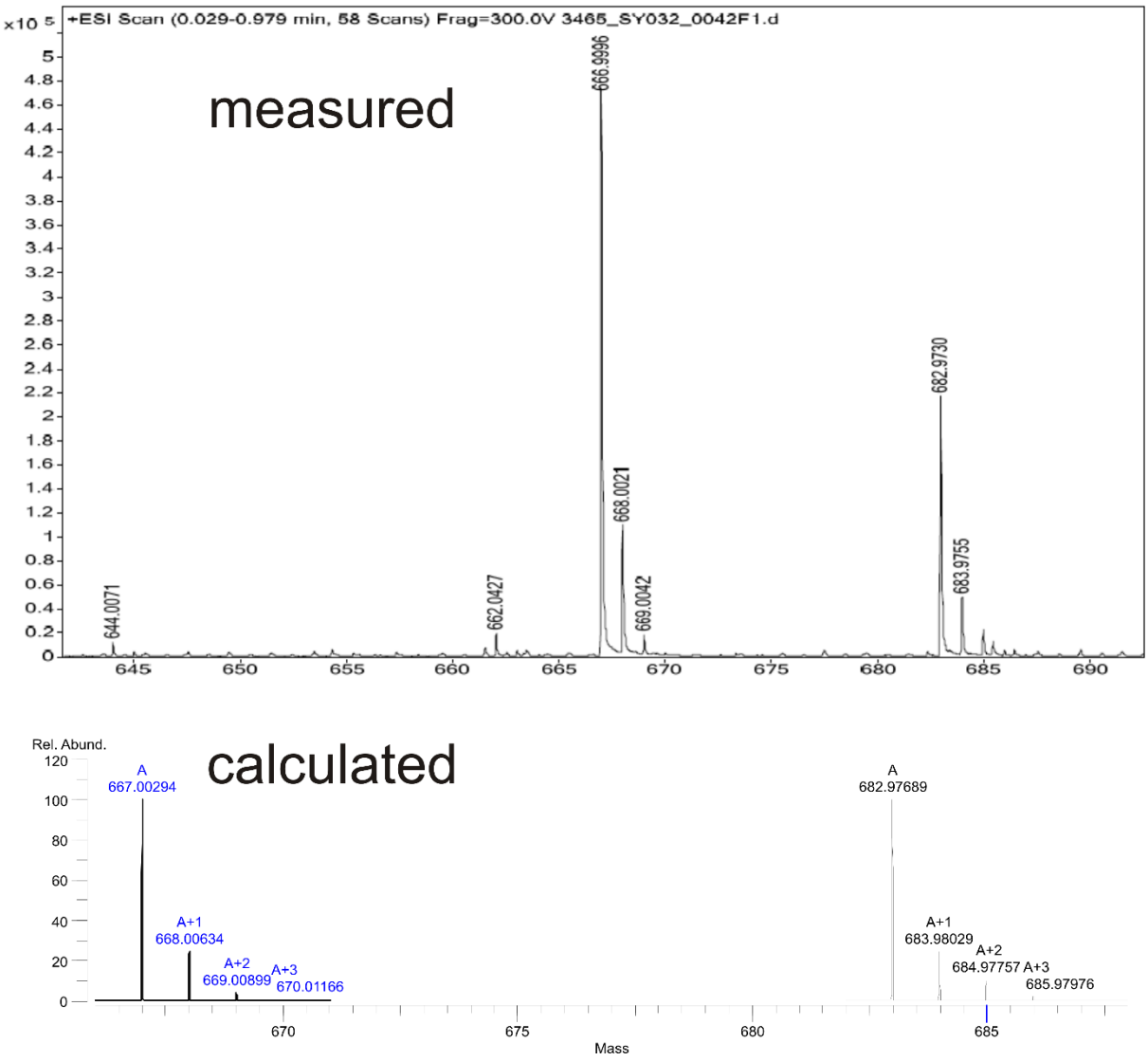

Fig. S40 HRMS ESI$^+$ (top) and calculated (bottom) of **S11**.

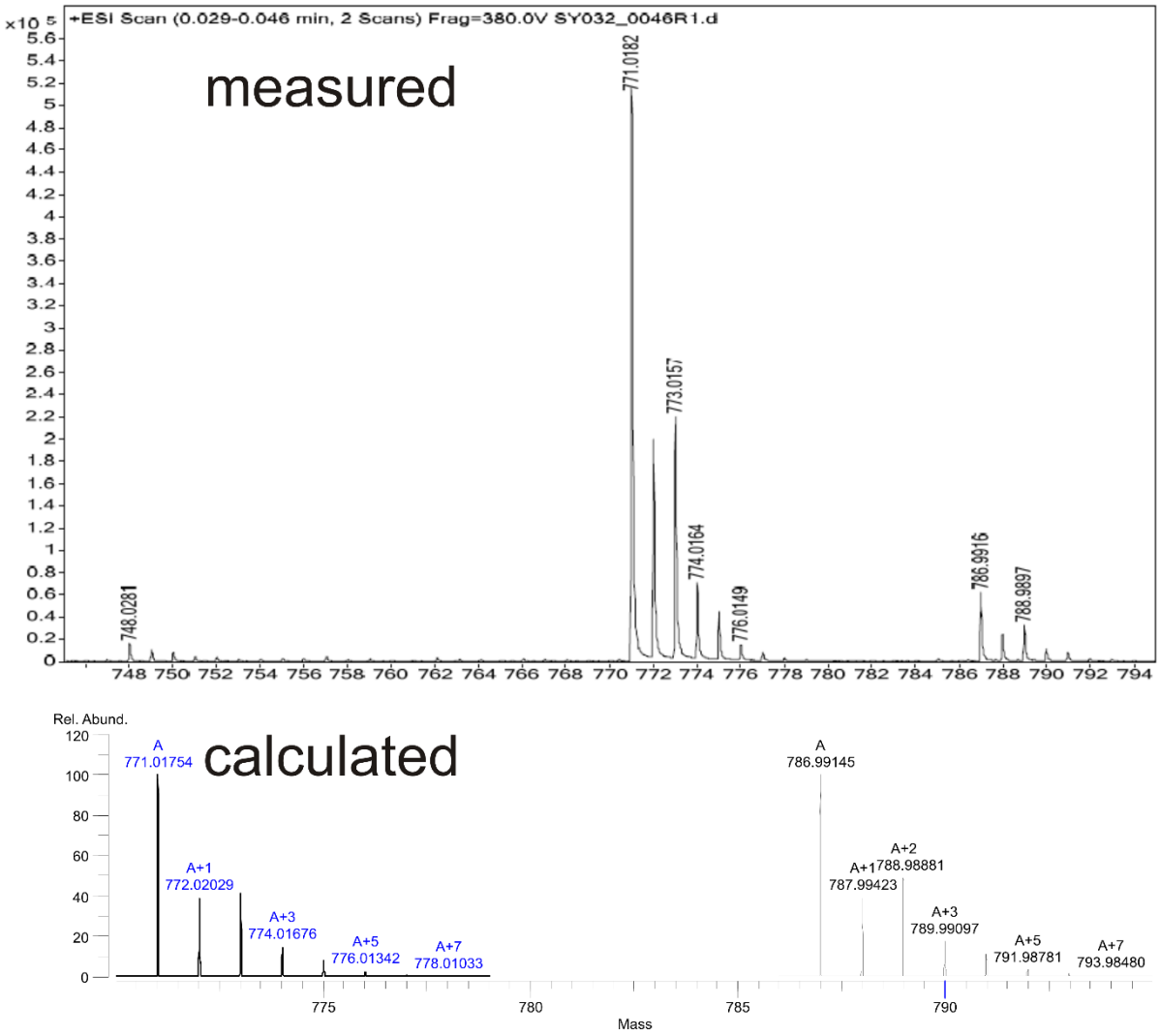

Fig. S41 HRMS ESI$^+$ (top) and calculated (bottom) of **dTTFC8**.

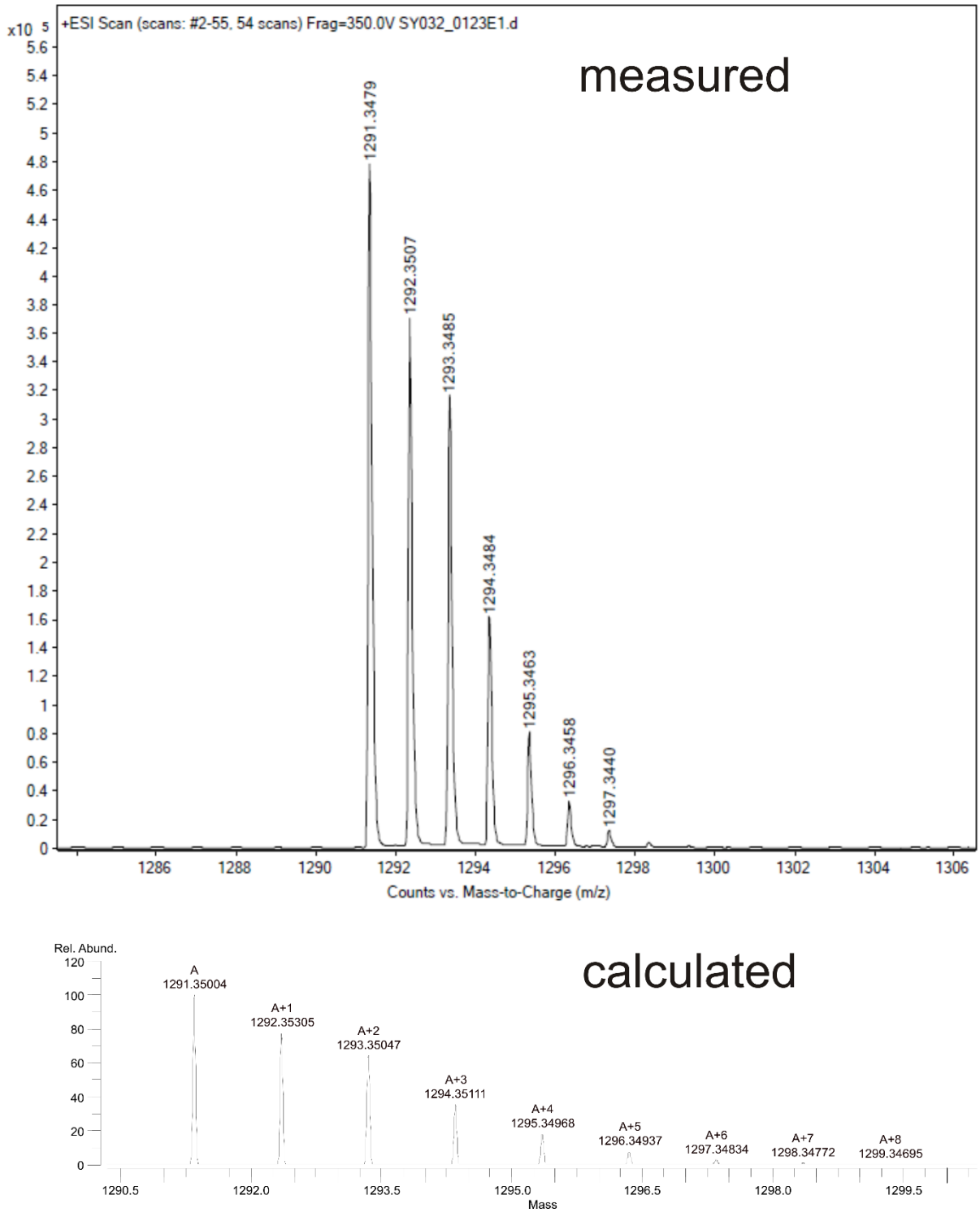

Fig. S42 HRMS ESI$^+$ (top) and calculated (bottom) of (*rac*)-**2**.

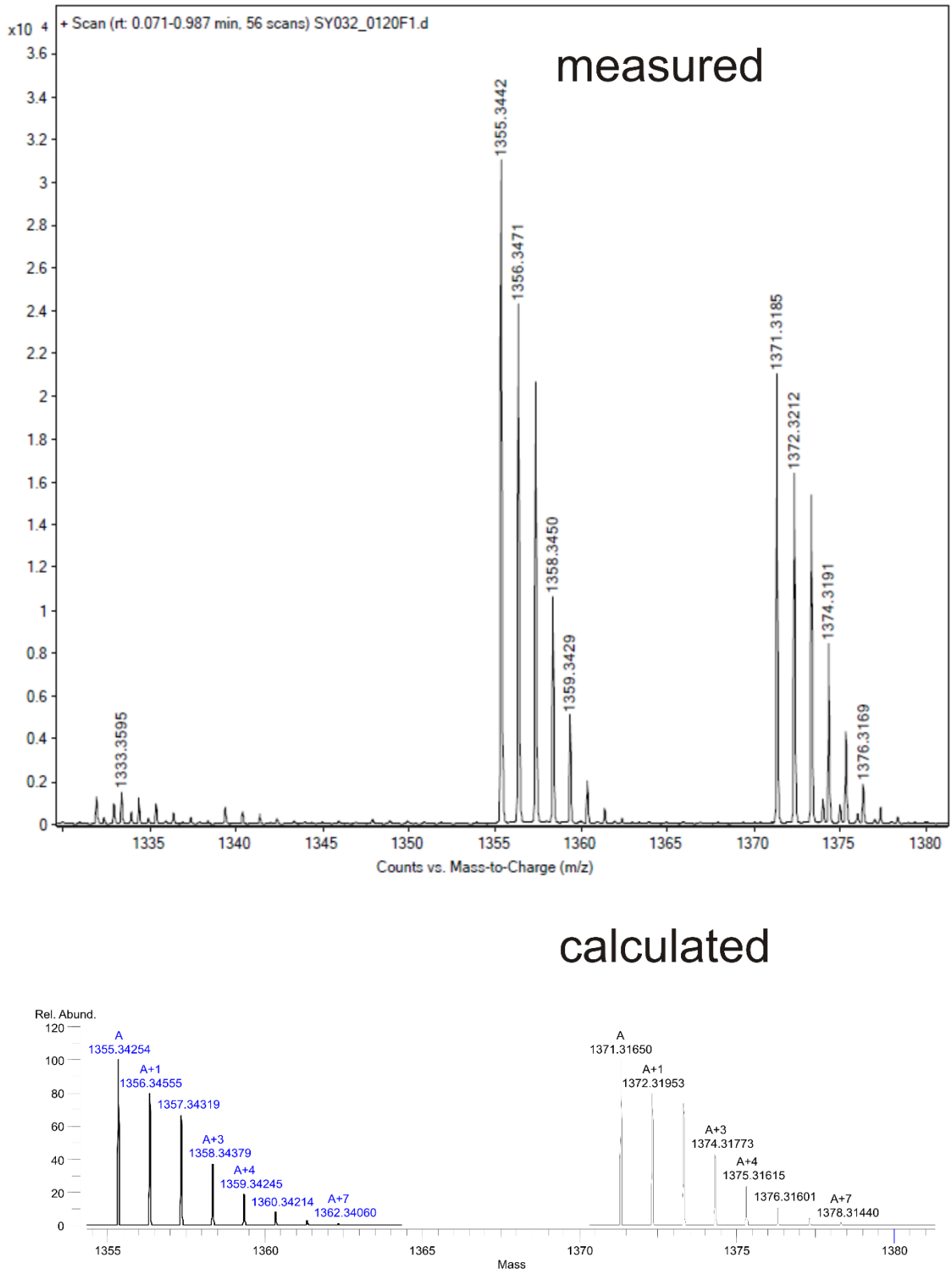

Fig. S43 HRMS ESI$^+$ (top) and calculated (bottom) of (*rac*)-**2Ac**.

11. References

1. M. Popr, S. Hybelbauerova and J. Jindrich, *Beilstein J. Org. Chem.*, 2014, **10**, 1390-1396.
2. W. Mamdouh, I. H. Uji, A. E. Dulcey, V. Percec, S. De Feyter and F. C. De Schryver, *Langmuir*, 2004, **20**, 7678-7685.
3. N. Svenstrup, K. M. Rasmussen, T. K. Hansen and J. Becher, *Synthesis*, 1994, **1994**, 809-812.
4. H. V. Schröder, S. Sobottka, M. Nößler, H. Hupatz, M. Gaedke, B. Sarkar and C. A. Schalley, *Chem. Sci.*, 2017, **8**, 6300-6306.
5. T. Matsumura, F. Ishiwari, Y. Koyama and T. Takata, *Org. Lett.*, 2010, **12**, 3828-3831.
6. J. R. Aranzaes, M.-C. Daniel and D. Astruc, *Can. J. Chem.*, 2006, **84**, 288-299.
7. X. Z. Zhu and C. F. Chen, *J. Am. Chem. Soc.*, 2005, **127**, 13158-13159.
8. K. Zimmermann, *Synth. Commun.*, 1995, **25**, 2959-2962.
9. S. Passemard, D. Staedler, L. Ucnova, G. S. Schneiter, P. Kong, L. Bonacina, L. Juillerat-Jeanneret and S. Gerber-Lemaire, *Bioorg. Med. Chem. Lett.*, 2013, **23**, 5006-5010.
10. J. Sly, P. Kasak, E. Gomar-Nadal, C. Rovira, L. Gorriz, P. Thordarson, D. B. Amabilino, A. E. Rowan and R. J. Nolte, *Chem. Commun.*, 2005, **10**, 1255-1257.
11. K. B. Simonsen, N. Svenstrup, J. Lau, O. Simonsen, P. Mørk, G. J. Kristensen and J. Becher, *Synthesis*, 1996, **1996**, 407-418.
12. F. A. Loiseau, K. K. Hii and A. M. Hill, *J. Org. Chem.*, 2004, **69**, 639-647.
13. S. Grimme, C. Bannwarth and P. Shushkov, *J. Chem. Theory. Comput.*, 2017, **13**, 1989-2009.
14. D. Porezag, T. Frauenheim, T. Köhler, G. Seifert and R. Kaschner, *Phys. Rev. B*, 1995, **51**, 12947-12957.
15. *Grimme et. al.*
16. H. J. C. Berendsen, J. P. M. Postma, W. F. van Gunsteren, A. DiNola and J. R. Haak, *J. Chem. Phys.*, 1984, **81**, 3684-3690.
17. J.-P. Ryckaert, G. Ciccotti and H. J. C. Berendsen, *J. Comput. Phys.*, 1977, **23**, 327-341.
18. K. Eichkorn, O. Treutler, H. Öhm, M. Häser and R. Ahlrichs, *Chem. Phys. Lett.*, 1995, **240**, 283-290.
19. J. Tao, J. P. Perdew, V. N. Staroverov and G. E. Scuseria, *Phys. Rev. Lett.*, 2003, **91**, 146401.
20. S. Grimme, J. Antony, S. Ehrlich and H. Krieg, *J. Chem. Phys.*, 2010, **132**, 154104.
21. S. Grimme, S. Ehrlich and L. Goerigk, *J. Comput. Chem.*, 2011, **32**, 1456-1465.
22. F. Weigend and R. Ahlrichs, *Phys. Chem. Chem. Phys.*, 2005, **7**, 3297-3305.
23. R. Ahlrichs, M. Bär, M. Häser, H. Horn and C. Kölmel, *Chem. Phys. Lett.*, 1989, **162**, 165-169.
24. A. Klamt and G. Schüürmann, *Perkin Trans. 2*, 1993, **5**, 799-805.
25. F. Neese, F. Wennmohs, A. Hansen and U. Becker, *Chem. Phys.*, 2009, **356**, 98-109.
26. J. D. Chai and M. Head-Gordon, *J. Chem. Phys.*, 2008, **128**, 084106.
27. V. Barone and M. Cossi, *J. Phys. Chem. A*, 1998, **102**, 1995-2001.
28. F. Neese, *Wiley Interdiscip. Rev.-Comput. Mol. Sci.*, 2012, **2**, 73-78.
29. C. Bannwarth and S. Grimme, *Comput. Theor. Chem.*, 2014, **1040-1041**, 45-53.
30. J. P. Perdew, M. Ernzerhof and K. Burke, *J. Chem. Phys.*, 1996, **105**, 9982-9985.
31. T. Yanai, D. P. Tew and N. C. Handy, *Chem. Phys. Lett.*, 2004, **393**, 51-57.
32. Y. Zhao and D. G. Truhlar, *Theor. Chem. Acc.*, 2007, **120**, 215-241.
33. R. F. W. Bader, *Chem. Rev.*, 1991, **91**, 893-928.
34. T. Lu and F. Chen, *J. Comput. Chem.*, 2012, **33**, 580-592.
35. COLLECT, Bruker AXS, Inc., Madison, Wisconsin, USA, 2008.
36. Z. O. a. W. Minor, *Methods Enzymol., vol. 276, Macromolecular Crystallography, Part A,* , Academic Press, New York, 1997.
37. G. M. Sheldrick, *SADABS*. University of Göttingen, Germany, **1996**.
38. G. M. Sheldrick, *Acta Crystallogr., Sect. A: Found. Adv.*, 2015, **71**, 3-8.
39. G. M. Sheldrick, *Acta Crystallogr., Sect. C: Struct. Chem.*, 2015, **71**, 3-8.
40. A. L. Spek, *Acta Crystallogr., Sect. C: Struct. Chem.*, 2015, **71**, 9-18.

41. A. L. Spek, *Acta Crystallogr., Sect. D: Biol. Crystallogr.*, 2009, **65**, 148-155.
42. J. Sun, X. Lu, J. Shao, X. Li, S. Zhang, B. Wang, J. Zhao, Y. Shao, R. Fang, Z. Wang, W. Yu and X. Shao, *Chem. Eur. J.*, 2013, **19**, 12517-12525.
43. H. Kobayashi, R. Kato, T. Mori, A. Kobayashi, Y. Sasaki, G. Saito, T. Enoki and H. Inokuchi, *Mol. Cryst. Liq. Cryst.*, 2011, **107**, 33-43.
44. P. R. Ashton, J. Becher, M. C. T. Fyfe, M. B. Nielsen, J. F. Stoddart, A. J. P. White and D. J. Williams, *Tetrahedron*, 2001, **57**, 947-956.

BEILSTEIN JOURNAL OF ORGANIC CHEMISTRY

Thermodynamic and electrochemical study of tailor-made crown ethers for redox-switchable (pseudo)rotaxanes

Henrik Hupatz[1], Marius Gaedke[1], Hendrik V. Schröder[1,2], Julia Beerhues[3,4], Arto Valkonen[5], Fabian Klautzsch[1], Sebastian Müller[1], Felix Witte[1], Kari Rissanen[5], Biprajit Sarkar[3,4] and Christoph A. Schalley[*1]

Full Research Paper

Open Access

Address:
[1]Institut für Chemie und Biochemie, Freie Universität Berlin, Arnimallee 20, 14195 Berlin, Germany, [2]present address: Department of Chemical and Biological Engineering, Princeton University, Princeton, NJ08544, USA, [3]Institut für Chemie und Biochemie, Freie Universität Berlin, Fabeckstr. 34/36, 14195 Berlin, Germany, [4]present address: Lehrstuhl für Anorganische Koordinationschemie, Institut für Anorganische Chemie, Universität Stuttgart, Pfaffenwaldring 55, 70569 Stuttgart, Germany and [5]Department of Chemistry, University of Jyvaskyla P. O. Box 35, 40014 Jyväskylä, Finland

Email:
Christoph A. Schalley[*] - c.schalley@schalley-lab.de

* Corresponding author

Keywords:
crown ether; isothermal titration calorimetry; redox chemistry; rotaxanes; supramolecular chemistry

Beilstein J. Org. Chem. **2020,** *16,* 2576–2588.
https://doi.org/10.3762/bjoc.16.209

Received: 07 August 2020
Accepted: 02 October 2020
Published: 20 October 2020

This article is part of the thematic issue "Molecular recognition" and is dedicated to the memory of Carsten Schmuck.

Guest Editor: T. Schrader

Abstract

Crown ethers are common building blocks in supramolecular chemistry and are frequently applied as cation sensors or as subunits in synthetic molecular machines. Developing switchable and specifically designed crown ethers enables the implementation of function into molecular assemblies. Seven tailor-made redox-active crown ethers incorporating tetrathiafulvalene (TTF) or naphthalene diimide (NDI) as redox-switchable building blocks are described with regard to their potential to form redox-switchable rotaxanes. A combination of isothermal titration calorimetry and voltammetric techniques reveals correlations between the binding energies and redox-switching properties of the corresponding pseudorotaxanes with secondary ammonium ions. For two different weakly coordinating anions, a surprising relation between the enthalpic and entropic binding contributions of the pseudorotaxanes was discovered. These findings were applied to the synthesis of an NDI-[2]rotaxane, which retains similar spectroelectrochemical properties compared to the corresponding free macrocycle. The detailed understanding of the thermodynamic and electrochemical properties of the tailor-made crown ethers lays the foundation for the construction of new types of molecular redox switches with emergent properties.

Introduction

Pedersen discovered crown ethers in 1967 while searching for multidentate ligands for the vanadyl group [1-3]. He was later awarded the Nobel Prize in Chemistry for his studies on the crown ether selective binding properties towards alkali metal ions [2]. Crown ethers and their binding properties nowadays find frequent application, e.g., as cation sensors [4-7], as phase-transfer catalysts [8-10], or as drug delivery systems [11-13].

Already at the early stages of crown ether research, considerable effort has been made towards switchable macrocyclic receptors, in which crown ethers are functionalized with a stimuli-responsive unit [14,15]. These studies were mainly motivated by a biomimetic approach and included examples such as crown ethers incorporating photo-responsive azobenzene [15,16] or redox-active ferrocene [14,17]. Yet, switchable crown ethers are also widely applied as cation sensors, where the sensor activity can be controlled by external stimuli, e.g., light, the redox potential or chemical reagents [14,17]. Redox-switchable crown ethers have been shown to sense cations by the generation of an electrochemical output. For example, crown ethers containing tetrathiafulvalene (TTF) derivatives, which enable two reversible oxidation processes from the neutral to the dicationic state, were applied to sense various cations, e.g., alkali metal ions, Pb^{2+}, and Ba^{2+} [18-21].

Furthermore, with the first synthesis of crown ether-based rotaxanes in 1995, crown ethers played a crucial role in the development of mechanically interlocked molecules (MIMs) [22,23]. This rotaxane synthesis was facilitated by the formation of a threaded complex (pseudorotaxane) between a secondary ammonium ion and dibenzo-24-crown-8 (**DBC8**, Figure 1), which bind through noncovalent interactions. In detail, these interactions are strong hydrogen bonds between ether oxygen atoms and ammonium protons. In addition, weaker C–H···O hydrogen bonds with the CH_2 groups adjacent to the ammonium nitrogen as well as π–π-interactions between the catechol ring of the crown ether and aromatic moieties of the secondary ammonium ion contribute to the complex formation [22-25].

Over the last 25 years, a detailed understanding of the thermodynamic and kinetic properties of crown ether/ammonium complexes has developed enabling the construction of more complex molecular structures [24,26,27]. With the introduction of stimuli-responsive units, crown ether/ammonium-based MIMs have evolved into molecular switches and motors [24,28]. Intriguing examples among them are a light-powered molecular pump [29], a chemical-fuel-driven molecular rotary motor [30], and an acid/base-switchable asymmetric organocatalyst [31].

In addition to MIMs switchable by light or chemical reagents, redox-switchable molecular assemblies are of particular interest, since redox switching at electrodes is considered to operate without chemical waste and electrochemical analytical tools, e.g., cyclic voltammetry (CV), exhibit great potential to investigate the kinetic and thermodynamic parameters of the switching processes [32,33]. Although various redox-active crown ethers have been described [14,21,34], they are not commonly implemented into crown ether/ammonium (pseudo)rotaxanes. One reason is that functionalized crown ethers can cause major obstacles in the synthesis of (pseudo)rotaxanes, as their functionalization can strongly interfere with the binding properties of the crown ether [24,25]. Recently, we have investigated examples for redox-switchable MIMs based on two 24-crown-8 ethers functionalized with TTF **TTFC8** [35,36] and **exTTFC8** [37] (Figure 1). Several **TTFC8**-derived molecular assemblies have been studied and provided access to new switching modes [35,36,38] and emergent optoelectronic properties [35,36,39,40], demonstrating the great potential of tailor-made redox-active crown ethers for the development of new molecular switches.

Yet, a careful design of tailor-made redox-active crown ethers is of great importance for tuning the crown ether binding and redox properties to achieve the desired molecular structure and switching mode, which motivated us to conduct the present study on the thermodynamic and electrochemical properties of seven redox-active crown ethers of different ring sizes in comparison to the unfunctionalized analogs **DBC8** and **BC7** (Figure 1). Crown ethers incorporating TTF, an extended TTF, and naphthalene diimide (NDI) as redox-active units were investigated with respect to the impact of the functionalization on the thermodynamic binding properties towards secondary ammonium axles using isothermal titration calorimetry (ITC). The electrochemical switching properties of the redox-active crown ethers were examined using differential pulse voltammetry (DPV) and compared to those of their corresponding pseudo[2]rotaxanes. Additionally, we report the synthesis of a novel NDI-[2]rotaxane and study the impact of the mechanical bond on the optoelectronic properties of the NDI unit by CV and spectroelectrochemical measurements.

Results and Discussion

Design considerations

The nine crown ether wheels and two ammonium axles used in this study are depicted in Figure 1. Previously, we investigated the thermodynamic and electrochemical properties of pseudorotaxanes made from **TTFC8** and **exTTFC8** in two separate studies [35,37]. Herein, we compare these two crown ethers, their smaller analogs and add a two TTF-units containing crown

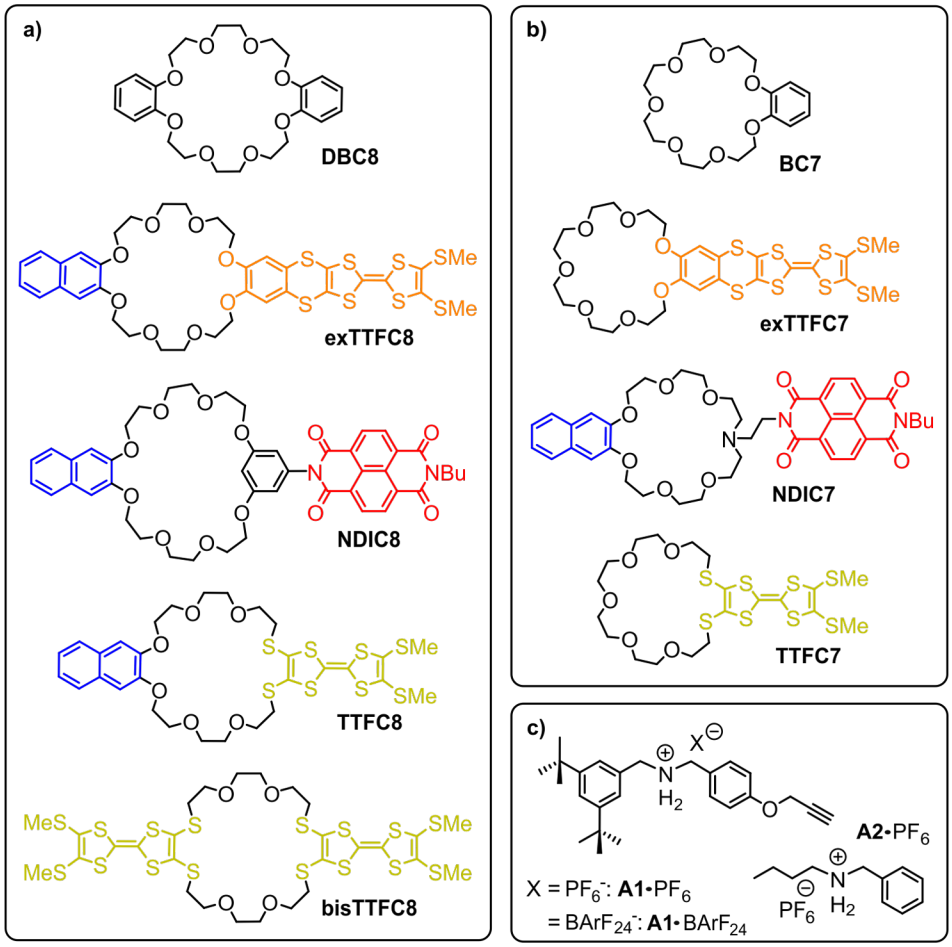

Figure 1: Structures of the compounds used in this study: a) crown-8 analogs; b) crown-7 analogs; c) secondary ammonium axles. $BArF_{24}^-$ represents tetrakis(3,5-bis(trifluoromethyl)phenyl)borate.

ether **bisTTFC8**, which was previously synthesized by Becher and co-workers [41]. These TTF-containing crown ethers become positively charged upon electrochemical oxidation, resulting in Coulomb repulsion with the ammonium axle [35,36,38].

A second goal was to add crown ethers, that can be reversibly reduced from the neutral to the dianionic state, as these crown ethers become negatively charged upon electrochemical switching and thus are expected to cause a Coulomb attraction between the ammonium axle and the crown ether. The NDI moiety, which is readily applied in various redox-active MIMs, was selected because of its high stability and synthetic accessibility [42].

An NDI-containing crown ether was reported by Sanders and co-workers, where the NDI unit is directly connected into the oligoglycol ring framework of the crown ether by the two nitrogen atoms [43]. However, the increased ring size and altered binding properties, which are dominated by the large π-systems of the NDI units, rendered this design unsuitable for our study. Therefore, we chose a similar design for the targeted NDI-functionalized crown ether as for the TTF crown ethers, where the NDI unit is in a position more remote from the crown ether binding site. Yet, keeping the formal C_2-symmetry of the macrocycle is important to avoid mixtures of isomers upon the threading of directional axles, such as **A1**·PF_6 (Figure 1c) [40]. Consequently, we chose to use a resorcinol-connected crown ether motif introduced by Stoddart and co-workers [44] for the NDI-crown-8 **NDIC8** (Figure 1).

To compare the larger crown ethers with smaller analogs, benzo-21-crown-7 (**BC7**) and the derivatives were also included, as at least the parent compound forms stronger complexes with secondary ammonium ions than the larger analog. But since phenyl groups already act as a stopper for **BC7**, one

side of the ammonium axle must be an alkyl chain, as in **A2**·PF_6 to enable pseudo[2]rotaxane formation (Figure 1c) [45,46].

The smaller TTF-containing crown ethers **TTFC7** and **exTTFC7** were designed in analogy to their crown-8 analogs (Figure 1). To access the NDI-functionalized crown-7 analog **NDIC7**, we chose an aza-crown-7 core, similar to the divalent crown ether described by Das and co-workers [47]. Comparing both NDI-containing crown ethers, **NDIC8** exhibits a rather rigid connection to the crown ether core, and in **NDIC7**, a more flexible ethylenediamine linker is used.

Crown ether synthesis and crystal structures

With respect to the synthesis of previously reported **TTFC8** and **exTTFC8** [35,37], we synthesized the novel 21-crown-7 analogs following a similar synthetic route, yielding **TTFC7** in one step and with good yield of 69% from the diiodide **1**, and **exTTFC7** with a good yield (31% over 4 steps) from **BC7** (Scheme 1, for the detailed synthetic procedure and characterization data, see Supporting Information File 1, section 1). Both NDI macrocycles **NDIC8** and **NDIC7** were synthesized in moderate yields of 24% and 26%, respectively, over three steps from the same two building blocks, the ditosylate **5** and the monobutyl-protected NDI precursor **7** (Scheme 1).

The connectivity and conformation of **exTTFC7** was observed in the crystal structure obtained from crystals generated through slow evaporation of a CH_2Cl_2/CH_3CN solution. The structure of the exTTF unit does not exhibit any significant changes upon incorporation into the crown ether [48]. No intermolecular stacking between the exTTF units was observed in the crystal structure of **exTTFC7** (Figure 2a and section 2 in Supporting Information File 1). Slow diffusion of CH_3CN into a concentrated solution of **NDIC7** in CH_2Cl_2 yielded single crystals suitable for X-ray diffraction (Figure 2b). The macrocycle displays a folded conformation in the solid state due to the flexible linker, featuring an intramolecular NDI/naphthalene stacking with a typical π-stacking distance of 3.58 Å and a tilt angle of 5.8°. The free electron pair of the tertiary amine points towards the inside of the crown ether. In contrast, single crystals of **NDIC8** (Figure 2c), obtained by slow evaporation of a concentrated dimethylformamide (DMF) solution, exhibit a non-folded conformation. The torsional angle between the central phenyl ring and the NDI is 84.2° in order to avoid strain between the protons of the resorcinol and the carbonyl groups of the NDI. Consequently, an intramolecular π–π-interaction with the naphthalene on the other side of the macrocycle is impeded. **NDIC8** therefore does not fold but stacks with the naphthalene and NDI moieties of the neighbors alternatingly in the solid state and with a typical plane/plane distance of 3.57 Å [49].

Thermodynamic analysis of crown ether/ammonium complexes

For the investigation of the thermodynamic binding properties, isothermal titration calorimetry is an advantageous method as it yields the binding stoichiometry, the binding constant K_a and the binding enthalpy ΔH^0 in one measurement. From these data, the Gibbs free binding energy ΔG^0 and the binding entropy ΔS^0 can be calculated. Pseudo[2]rotaxanes formed from crown ethers and ammonium axles are generally more strongly bound in solvents with low dielectric constants and in combination with weakly coordinating anions (WCAs) [24,50,51]. Therefore, we chose 1,2-dichloroethane (DCE) as the solvent and hexafluorophosphate (PF_6^-) as the counter ion, which resulted in binding constants in the optimal range for ITC titrations [52,53]. The even more weakly coordinating tetrakis(3,5-bis(trifluoromethyl)phenyl)borate ($BArF_{24}^-$) anion exemplarily served for comparison to study the influence of the anion on the binding constant.

Two different ammonium axles were employed: On the one hand, **A1**·PF_6 can only form a threaded complex with crown-8 ether derivatives due to the two bulky benzyl substituents on the ammonium ion. On the other hand, **A2**·PF_6 possesses one narrow alkyl substituent allowing both crown-8 and crown-7 ethers to form threaded complexes.

All possible pseudo[2]rotaxanes show strongly enthalpy-driven binding – with the notable exception of **NDIC7** (Table 1). The unfunctionalized crown ethers **BC7** and **DBC8** are the strongest binders among the corresponding derivatives with ΔG^0 of −34.6 kJ/mol and −34.8 kJ/mol, respectively (Table 1, entries 1 and 9).

Focusing on the combinations of crown-8 ethers and **A1**·PF_6, **exTTFC8** also forms a strong complex, with ΔG^0 being only ≈1 kJ/mol (Table 1, entry 10) lower than that of the **A1**·PF_6@**DBC8** complex. In contrast, the binding of **TTFC8** is more than 9 kJ/mol weaker (Table 1, entry 12), caused by the weaker hydrogen-bond-acceptor ability of the sulfur atoms incorporated in the **TTFC8** crown ether ring [34,54]. **NDIC8** also exhibits a comparably low binding energy, likely due to the increased ring size and the consequently weakened hydrogen-bonding pattern (Table 1, entry 11) [44].

However, **NDIC8** and **TTFC8** differ significantly in the entropic and enthalpic contributions to the binding energy (Table 1, entries 11 and 12). The comparably rigid structure of **NDIC8** is unable to adjust the conformation in the complex to achieve an optimal hydrogen-bonding pattern with the ammonium axle, and simultaneously, maximized π–π-interactions with the axle because of the 84° torsional angle between the resorcinol and

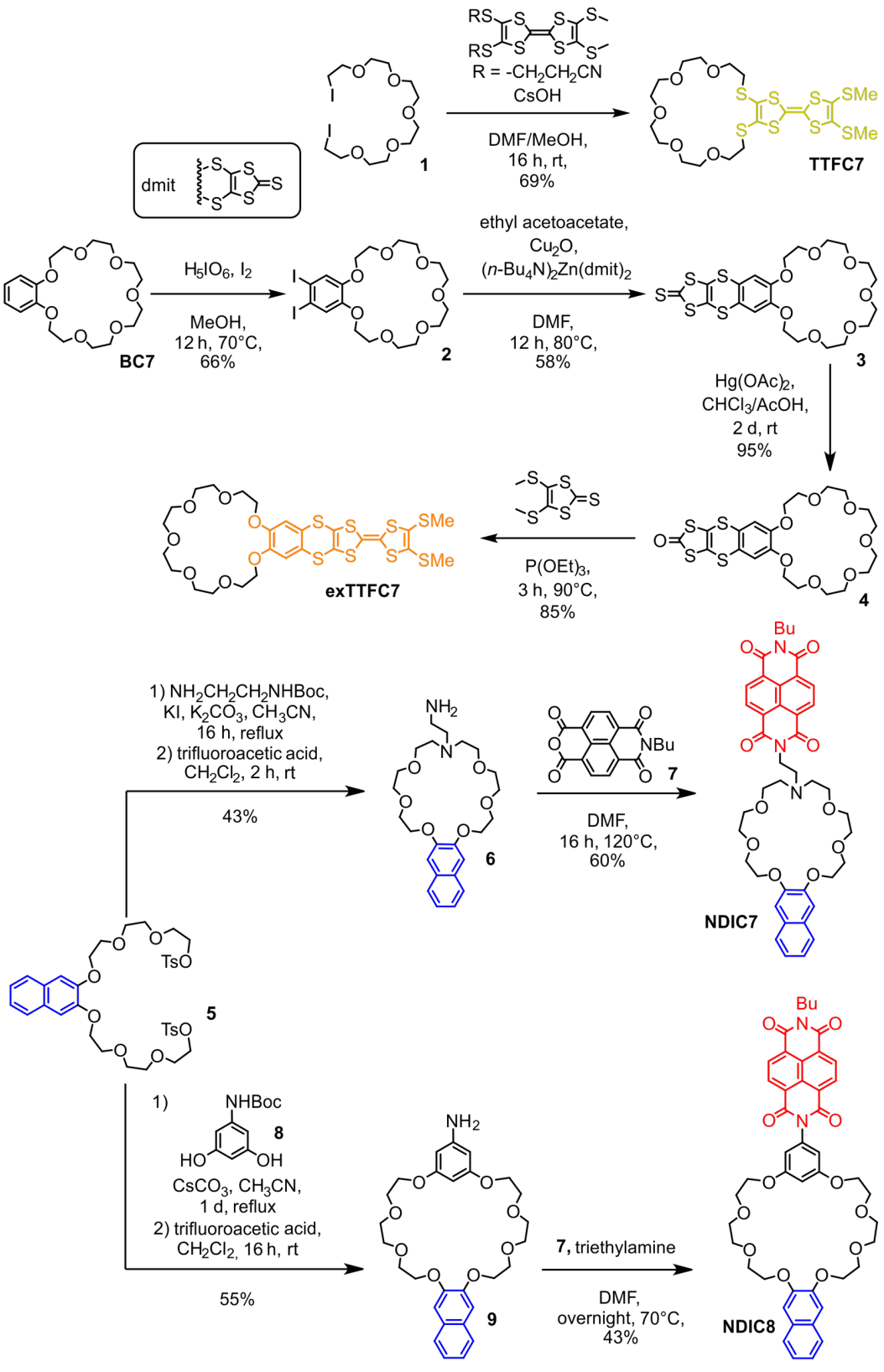

Scheme 1: Schematic representation of synthetic routes towards **TTFC7**, **exTTFC7**, **NDIC7**, and **NDIC8**.

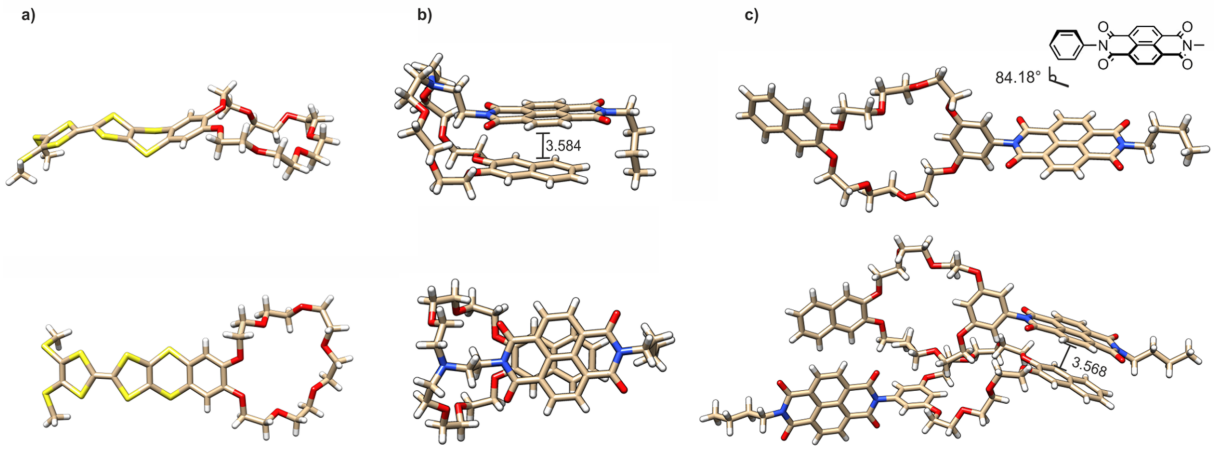

Figure 2: Solid-state structures of a) **exTTFC7** (CH_3CN molecule omitted for clarity), b) **NDIC7** (CH_3CN molecule omitted for clarity) and c) **NDIC8**.

Table 1: Thermodynamic binding data of different crown ether/secondary ammonium axle complexes obtained by ITC titrations in DCE at 298 K (for full data set and titration curves, see Supporting Information File 1, section 3).

entry	macrocycle	axle	K_a [10^3 M^{-1}]	ΔG^0 [kJ/mol]	ΔH^0 [kJ/mol]	$T\Delta S^0$ [kJ/mol]
1	**BC7**	**A2**·PF_6	1200 ± 100	−34.6 ± 0.2	−63.0 ± 0.5	−28.3 ± 0.7
2	**exTTFC7**		260 ± 30	−30.9 ± 0.3	−63.6 ± 1.0	−32.7 ± 1.3
3	**NDIC7**[a]		n. d.	n. d.	n. d.	n. d.
4	**TTFC7**		8.0 ± 1.0	−22.3 ± 0.2	−55.8 ± 1.5	−33.4 ± 1.7
5	**DBC8**	**A2**·PF_6	480 ± 70	−32.4 ± 0.3	−60.4 ± 1.5	−28.0 ± 1.8
6	**exTTFC8**		160 ± 20	−29.7 ± 0.3	−57.2 ± 2.0	−27.5 ± 2.3
7	**NDIC8**		13 ± 1	−23.4 ± 0.2	−48.1 ± 1.0	−24.7 ± 1.2
8	**TTFC8**		7.0 ± 1.0	−22.1 ± 0.2	−50.3 ± 1.0	−28.3 ± 1.2
9	**DBC8**	**A1**·PF_6	1300 ± 100	−34.8 ± 0.3	−60.9 ± 2.0	−26.1 ± 2.3
10	**exTTFC8**		780 ± 70	−33.6 ± 0.2	−58.6 ± 0.9	−25.0 ± 1.1
11	**NDIC8**		49 ± 6	−26.7 ± 0.3	−46.6 ± 2.0	−19.9 ± 2.3
12	**TTFC8**		33 ± 3	−25.7 ± 0.2	−51.5 ± 0.9	−25.9 ± 1.1
13	**NDIC8**	**A1**·$BArF_{24}$	1000 ± 100	−34.2 ± 0.2	−42.9 ± 1.2	−8.7 ± 1.4
14	**TTFC8**[b]		440 ± 100	−32.2 ± 0.3	−46.2 ± 0.7	−14.0 ± 1.0
15	**bisTTFC8**		2.0 ± 0.5	−18.7 ± 0.6	−21.0 ± 2.0	−2.2 ± 2.6

[a]ITC titrations cannot be fitted to a 1:1 pseudo[2]rotaxane binding model (for details, see text below and Supporting Information File 1, Figure S5).
[b]Taken from a previous report [40].

the NDI unit. Consequently, the complexation of **NDIC8** is less enthalpically favored than that of **TTFC8**. However, the more rigid structure of **NDIC8** also leads to a lower degree of conformational fixation in the pseudorotaxane of **NDIC8**, and thus to a more favorable binding entropy compared to the pseudorotaxane of **TTFC8**. For **TTFC8**, the increased binding enthalpy can be explained by additional π–π-interactions between the naphthalene and TTF unit of the crown ether and the ammonium axle, resulting in a rather rigid crown ether conformation in the complex as compared to the free macrocycle. This loss of conformational flexibility rationalizes the increased entropic penalty. A similar trend is observed for the binding enthalpy and entropy of **NDIC8** and **TTFC8** with the axles **A2**·PF_6 (Table 1, entries 7 and 8) and **A1**·$BArF_{24}$ (Table 1, entries 13 and 14), showing that this effect is caused by the macrocycle and not the ammonium axle.

The Gibbs free binding energy ΔG^0 of all four crown-8 ethers to axle **A2**·PF_6 is collectively 2–4 kJ/mol lower (Table 1, entries 5–8) in comparison to that of **A1**·PF_6. On the one hand, additional π–π-interactions of the phenyl ring in **A1**·PF_6 to the crown ether aromatic rings favor the complex formation. On the other hand, the flexibility of the alkyl substituent in **A2**·PF_6 is diminished upon complexation, inducing a larger entropic penalty visible in the overall more negative binding entropies in pseudo[2]rotaxanes of **A2**·PF_6 as compared to those formed from **A1**·PF_6.

Furthermore, the three crown-7 macrocycles **BC7**, **exTTFC7**, and **TTFC7** bind **A2**·PF_6 with a binding energy (entries 1, 2, and 4 in Table 1) slightly higher than the crown-8 analogs (entries 5, 6, and 8 in Table 1). Moreover, ΔG^0 follows the same trend as observed for crown-8 analogs with **A1**·PF_6 (entries 9, 10, and 12 in Table 1) and discussed above: the binding energy decreases from **BC7** over **exTTFC7** to **TTFC7**.

The azacrown-7 **NDIC7** is an exception: The ITC titration with the ammonium axle **A2**·PF_6 does not exhibit the anticipated sigmoidal shape of a 1:1 bonded complex (see Figure S5a in Supporting Information File 1). The curve shape suggests a more complex chemical equilibrium that involves more than one chemical process generating heat, taking place in the titration experiment. One process is likely a proton transfer from the secondary ammonium group of the axle to the tertiary amine in the crown ether wheel. An ITC titration with **A1**·PF_6 gave a similar curve shape (see Figure S5b in Supporting Information File 1), though crown-7 ethers are too small to thread over the phenyl ring of **A1**·PF_6 under the conditions of the experiment. The folded structure observed in the crystal structure hints towards a possible "side-on" complex, where the ammonium axle is not threading through the ring of the macrocycle, yet still forms hydrogen bonds to the crown ether [24,25] (see spectroelectrochemical measurements below). These results suggest that both ammonium axles form a similar type of equilibrium with **NDIC7**, where the protonation of the tertiary amine and the complexation in a nonthreaded complex might contribute.

When using $BArF_{24}^-$ as the counterion for **A1**, the binding energies increase by 6–8 kJ/mol, which results in a 10–20-fold increase of the binding constants as observed for the weaker binding macrocycles **TTFC8** and **NDIC8** (Table 1, entries 13 and 14). **A1**·$BArF_{24}$ even allows the formation of a pseudo[2]rotaxane with the **bisTTFC8** macrocycle (Table 1, entry 15), to which **A1**·PF_6 binds too weakly to determine the binding data by ITC. The observed decrease of the binding energy with more sulfur atoms in the crown ether ring from **DBC8** over **TTFC8** to **bisTTFC8** is consistent with a systematic study on thiacrown ethers [54].

Surprisingly, the increased Gibbs free binding energy ΔG^0 for **A1**·$BArF_{24}$ compared to **A1**·PF_6, is not caused by the binding enthalpy ΔH^0 (entries 11–14 in Table 1), as one might have expected, assuming the ion pairing to compete with the pseudorotaxane formation. In contrast, the enthalpic contribution is 4–6 kJ/mol less negative with **A1**·PF_6 than in **A1**·$BArF_{24}$ complexes, but the formation of the **A1**·$BArF_{24}$ pseudo[2]rotaxanes is less entropically disfavored, reflected by 11–12 kJ/mol less negative $T\Delta S^0$ (Table 1, entries 13 and 14). To the best of our knowledge, the study of weakly coordinating anions in the formation of pseudorotaxane complexes has been limited to their impact on the binding constant, but enthalpic and entropic contributions have not yet been studied [50,51,55]. As PF_6^- is more strongly coordinating than $BArF_{24}^-$, a larger fraction of **A1**·PF_6 ion pairs is present in nonpolar solvents such as DCE. Upon complexation, the ion pair of **A1**·PF_6 must dissociate, releasing PF_6^- anions into the bulk solution where they are solvated by a number of solvent molecules. The charge-induced order of the solvent dipoles in the solvent shell is entropically unfavorable and more pronounced for PF_6^-. Consequently, the main reason for the observed effects is likely a change in the solvation entropy. However, to further elucidate the role of WCAs in crown/ammonium complexes, more detailed studies are certainly indicated.

Electrochemistry

The electrochemical properties of the TTF and NDI-bearing macrocycles and pseudorotaxanes are summarized in Table 2. To get some insight into the solvent dependence of the electrochemical data, the measurements were performed in 1:1 DCE/CH_3CN (increased solubility of the axle salts, weaker pseudo[2]rotaxane binding) and in pure DCE (stronger pseudo[2]rotaxane binding). Generally, the oxidation potentials are shifted to higher values, and the reduction potentials are shifted to lower values in pure DCE due to decreased charge stabilization.

As expected, all TTF macrocycles display two reversible oxidation processes ($E_{1/2}^{ox1}$, $TTF \rightarrow TTF^{\bullet+}$ and $E_{1/2}^{ox2}$, $TTF^{\bullet+} \rightarrow TTF^{2+}$). $E_{1/2}^{ox1}$ and $E_{1/2}^{ox2}$ of the free **exTTFC8** and **exTTFC7** crown ethers are anodically shifted compared to those of **TTFC8** and **TTFC7**, in which the TTF units are directly incorporated into the crown ethers. This behavior is known also for the two redox-active TTF building blocks **exTTF** and tetramethylene-TTF, which are not part of a macrocycle [48].

The addition of the axles **A1**·PF_6 or **A2**·PF_6 to **TTFC8** and **TTFC7**, respectively, in a DCE/CH_3CN 1:1 solution has no significant effect on $E_{1/2}^{ox1}$ and $E_{1/2}^{ox2}$ (see Supporting Information File 1). However, an increase in the oxidation potential

Table 2: Electrochemical data obtained by differential pulse voltammetry (for voltammograms and experimental details see Supporting Information File 1, section 4).

entry	compound	solvent[a]	$E_{1/2}^{red2}$ [V][b]	$E_{1/2}^{red1}$ [V][b]	$E_{1/2}^{ox1}$ [V][b]	$E_{1/2}^{ox2}$ [V][b]
			reversible reductions		reversible oxidations	
1	**exTTFC7**	DCE/CH_3CN 1:1	/	/	0.66	0.95
2	**exTTFC8**[c]		/	/	0.66	0.93
3	**TTFC7**		/	/	0.59	0.83
4	**TTFC8**		/	/	0.59	0.83
5	**bisTTFC8**[c]		/	/	0.57	0.93
6	**NDIC7**		–0.96	–0.54	/	/
7	**NDIC7** + **A2**·PF_6[d]		–0.70	–0.46	/	/
8	**NDIC8**[c]		–0.95	–0.49	/	/
9	**NDIC8**[c] + **A1**·PF_6[d]		–0.72	–0.49	/	/
10	**NDIC8**[c] + $(CH_3)_2NH_2PF_6$[d]		–0.78	–0.45		
11	**NDIC8Rot**		–0.95	–0.50		
12	**exTTFC7**	DCE	/	/	0.65	1.01
13	**exTTFC7** + **A2**·PF_6[d]		/	/	0.67	1.01
14	**TTFC7**		/	/	0.59	0.87
15	**TTFC7** + **A2**·PF_6[d]		/	/	0.63	0.87
16	**bisTTFC8**		/	/	0.56	0.95
17	**NDIC8**[c]		–0.97	–0.53	/	/
18	**NDIC8Rot**		–0.96	–0.51	/	/

[a]With *n*-Bu_4NPF_6 (0.1 M) as the electrolyte. [b]Half-wave potentials are given against the decamethylferrocene/decamethylferrocenium couple as the reference; error = ±0.01 V. [c]The compound showed only moderate solubility in the corresponding solvent. [d]Five equivalents of the ammonium guest were added.

($\Delta E_{1/2}^{ox1}$ = +0.04 V) was observed for the **A2**·PF_6@**TTFC7** complex in pure DCE, which can be attributed to the increased strength of the hydrogen bonds in the neutral complex and Coulomb repulsion in the oxidized complex [35]. This effect is less pronounced for the complex **A2**·PF_6@**exTTFC7** because the TTF unit is more distant to the ammonium unit [37].

The macrocycle **bisTTFC8**, bearing two TTF units, shows a broadening of the signal for the first oxidation (Figure S9 in Supporting Information File 1), presumably due to intramolecular TTF–TTF interactions [35,36,56]. In comparison to the wheel **TTFC8**, the second oxidation of **bisTTFC8** is anodically shifted by $\Delta E_{1/2}^{ox2}$ = +0.10 V, indicating intramolecular Coulomb repulsion between the two TTF^{2+} units. The addition of **A1**·PF_6 does not have any impact on the redox properties of **bisTTFC8**, as hardly any pseudo[2]rotaxane forms with this axle.

The NDI-decorated wheels **NDIC8** and **NDIC7** undergo two reversible reduction processes ($E_{1/2}^{red1}$, $NDI \rightarrow NDI^{\bullet -}$ and $E_{1/2}^{red2}$, $NDI^{\bullet -} \rightarrow NDI^{2-}$). Here, the addition of the corresponding ammonium axles **A1**·PF_6 and **A2**–PF_6 drastically shifts the reduction potentials in DCE/CH_3CN 1:1 (**NDIC7**: +0.08 V and +0.26 V; **NDIC8**: 0 V and +0.23 V, for $\Delta E_{1/2}^{red1}$ and $\Delta E_{1/2}^{red2}$, respectively). We assume that the negatively charged reduced forms $NDI^{\bullet -}$ and NDI^{2-} form strong electrostatic interactions to ammonium ions and act as strong, competitive hydrogen-bond acceptors [57]. The high anodic shifts indicate strong attractive interactions between the wheels and axles, which compete with the coordination of the crown ether moiety. Thus, the secondary ammonium axles form presumably a non-threaded complex with the reduced NDI crown ethers, where the charged ions are in closer proximity than in the pseudo[2]rotaxane. This assumption was further confirmed by the addition of the hydrogen bond donor $(CH_3)_2NH_2PF_6$ to a solution of the wheel **NDIC8**, which again leads to strong anodic shifts in the voltammogram ($\Delta E_{1/2}^{red1}$ = +0.04 V, $\Delta E_{1/2}^{red2}$ = +0.17 V, Table 2, entry 10) and will be further elucidated below.

Synthesis and spectroelectrochemical characterization of [2]rotaxane with NDI crown ether

For **TTFC8**, we have recently shown, that rotaxane formation influences the optoelectronic properties of the TTF unit [35],

yet for **exTTFC8** the [2]rotaxane shows very similar properties as compared to the free macrocycle [37]. As **NDIC8** and the **A1**·PF_6@**NDIC8** pseudo[2]rotaxane also reveal distinctly different electrochemical potentials, we investigated the impact of mechanical bonding on the optoelectronic properties of the NDI unit. The binding properties suggest that the combination of the **A1**·$BArF_{24}$ axle and **NDIC8** is optimal for the synthesis of an NDI-containing [2]rotaxane. We applied Takata's catalyst-free stoppering approach [58] using the nitrile oxide **St** for the preparation of the [2]rotaxane **NDIRot**, which was obtained in 43% yield (Figure 3a).

The formation of the isoxazole can be recognized by the strong downfield shift of the proton H^j in the ^{1}H NMR spectrum (Figure 3b, for 2D spectra and signal assignment, see Supporting Information File 1, section 5.1). Furthermore, a diastereotopic splitting of the crown ether methylene protons and downfield shifts of the axle methylene protons H^d and H^f clearly point at the rotaxane formation. Additionally, a strong upfield shift observed for the resonance of the phenylic proton H^h ($\Delta\delta$ = 0.5 ppm) is in line with rotaxane formation, even though it has not previously been observed for similar TTF-containing rotaxanes [35,40]. This finding indicates a different conformation of the macrocycles in the NDI and TTF [2]rotaxanes.

Even though the signals of the NDI protons H^6 and $H^{6'}$ do not shift significantly which would be expected for strong π–π-interactions, they split from one pseudo singlet into two doublets upon rotaxane formation, indicating a lower symmetry of the NDI unit. The resorcinol proton H^4 exhibits a significant upfield shift ($\Delta\delta$ = −0.2 ppm), which can be rationalized by the position in the crown ether cavity close to the positively charged ammonium ion.

The collision-induced dissociation of mass-selected rotaxane ions occurs only at comparably high collision energy. Only axle fragments are observed while the intact axle is not seen among

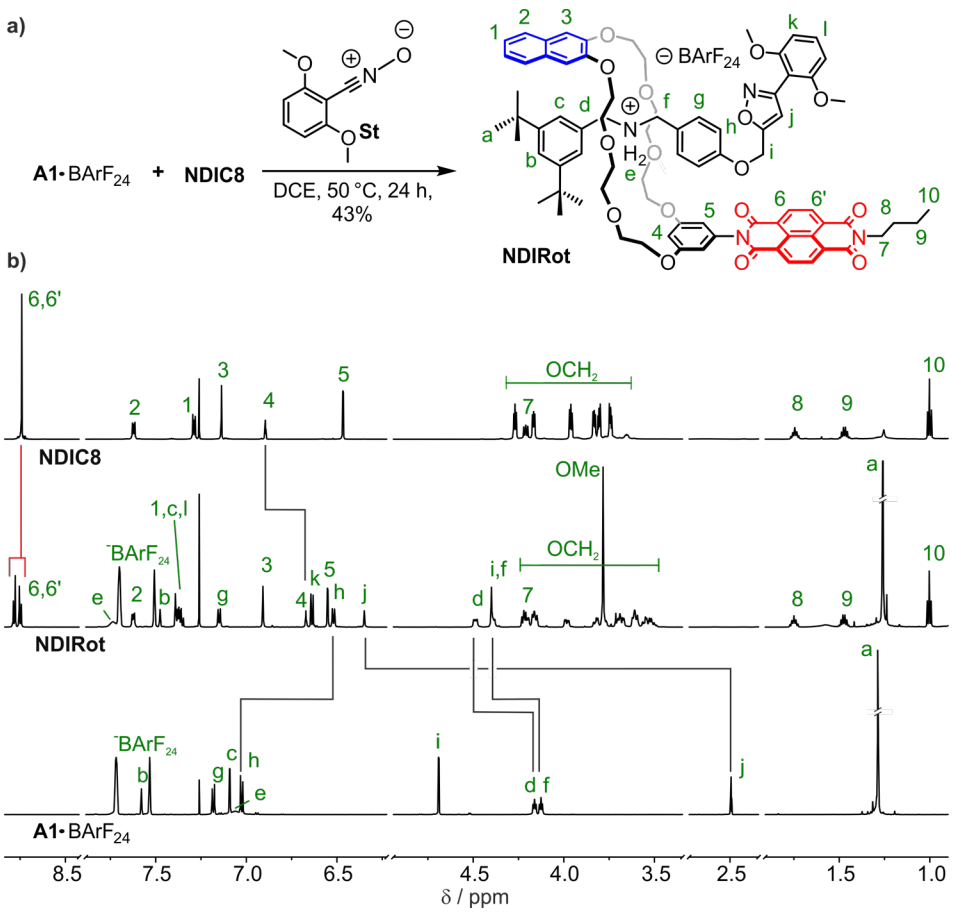

Figure 3: a) Synthesis of the [2]rotaxane **NDIRot**. b) Stacked ^{1}H NMR spectra (700 MHz, $CDCl_3$, 298 K) of **NDIC8** (top), **NDIRot** (middle), and **A1**·$BArF_{24}$ (bottom). The signal assignment was done by 2D NMR spectroscopy.

the fragments (Figures S15 and S16 in Supporting Information File 1). This clearly supports the mechanically interlocked structure for **NDIRot** in analogy to similar structures investigated by tandem mass spectrometry earlier [35,40].

Cyclic voltammograms of **NDIRot** show two reversible reductions $E_{1/2}^{red1}$ and $E_{1/2}^{red2}$ independent of the used solvent (pure DCE or DCE/CH_3CN 1:1, Figure S11 and Table S2 in Supporting Information File 1). Additionally, the two reduction potentials are very similar to those of free **NDIC8** and not the pseudo[2]rotaxane **A1**·PF_6@**NDIC8** (see Table 2, entries 8–11). This agrees well with the assumption that the reduction of the NDI leads to a complete rearrangement of the pseudo[2]rotaxane into a non-threaded complex as discussed above. As dethreading is impossible in **NDIRot**, the electrochemical data are significantly different from those of the non-threaded complexes formed from the pseudorotaxane and the $(CH_3)_2NH_2PF_6$ complex of **NDIC8**.

The optoelectronic properties of the rotaxane **NDIRot** were investigated by UV–vis–NIR spectroelectrochemistry in a CH_2Cl_2/CH_3CN 1:1 mixture and compared to **NDIC8** and **NDIC7** (Figure 4 and Table S3 in Supporting Information File 1). In the neutral state, the rotaxane displays the typical absorption pattern of an *N*,*N'*-disubstituted NDI monomer between 300 and 380 nm (Figure 4a–c, black) [59]. A weak charge-transfer band at ≈450 nm is observed for the free macrocycle **NDIC7** (Figure 4a, black), which is most likely caused by an intramolecularly folded naphthalene–NDI complex in solution, similar to the crystal structure. In contrast, no charge-transfer band is present, neither for **NDIRot** nor for **NDIC8**, ruling out the formation of similar charge-transfer complexes in **NDIC8** or in the corresponding rotaxane.

After one-electron reduction (NDI → $NDI^{\bullet-}$), a complex absorption band pattern emerges in the visible region of all three spectra. These bands are indicative of the radical anion $NDI^{\bullet-}$ (Figure 4a–c, red curves) [59]. The radical character of **NDIC8** was additionally confirmed by spectroelectrochemical EPR measurements, which showed an isotropic signal with a g-value of 2.004 (Figure S17 in Supporting Information File 1).

Upon further reduction, a new absorption pattern emerges for **NDIC7**, in accordance to a second electrochemical reduction ($NDI^{\bullet-}$ → NDI^{2-}) (Figure 4a, blue curve). However, only small shifts and intensity changes are observed for **NDIC8** and the rotaxane **NDIRot** when going to a more negative potential (−1.2 V), which can be explained by diffusion and comproportionation of the dianion, as it was observed earlier for other NDI^{2-} species [59]. Applying more positive potentials gradually converts the spectra back to the initial forms, which confirms the reversibility of the reduction processes. Overall, the comparison of all absorption spectra clearly demonstrates that the rotaxane formation does not significantly influence the optoelectronic properties of the NDI unit. This can be explained by the position of the NDI moiety being rather remote from the binding site of the crown ether.

Conclusion

In conclusion, the comparison of the thermodynamic properties of a series of functionalized crown ethers showed a small effect of redox-active units remotely attached to the crown ether on the binding of secondary ammonium ions. However, if the redox-active unit is incorporated directly into the crown ether core, as in **TTFC8** and **TTFC7**, the binding properties are altered significantly. The redox properties do not depend much on the crown ether core, irrespective of whether the redox-

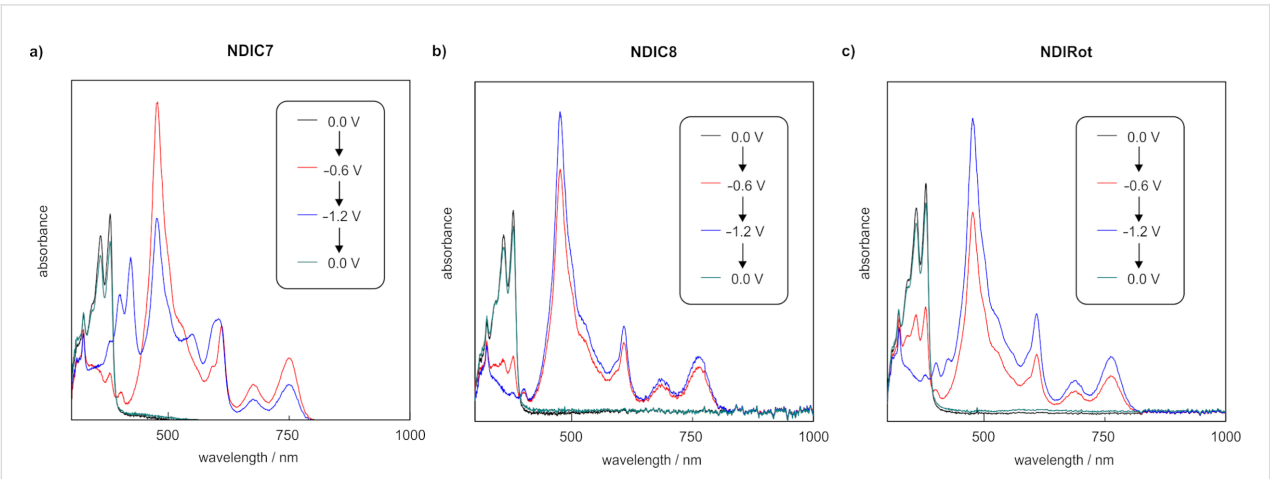

Figure 4: UV–vis–NIR spectra obtained by spectroelectrochemical measurements (0.1 M *n*-Bu_4PF_6, CH_2Cl_2/CH_3CN 1:1, 298 K) of a) **NDIC7** (0.5 mM), b) **NDIC8** (0.5 mM), and c) **NDIRot** (1 mM). Potentials are referenced against a silver wire pseudo-reference electrode.

active unit is attached in a remote position or incorporated in the crown ether.

Our findings provide some guidelines for how the binding and redox-switching properties can be fine-tuned for the construction of a desired crown ether-based switchable MIM: while **bisTTFC8** shows interesting redox properties but very low binding constants and **exTTFC8** displays a high binding constant, yet no strong interaction of the ammonium-binding site and the redox unit, **TTFC8** offers the best compromise of sufficiently high binding constants combined with sufficient Coulomb repulsion between the oxidized TTF and the ammonium ion to construct a molecular switch [35]. This trend can directly be translated to the smaller **exTTFC7** and **TTFC7**, which exhibit very similar thermodynamic and redox properties as compared to the corresponding crown-8 derivatives.

The important role that weakly coordinating counterions play in the binding of crown ether/ammonium pseudorotaxanes needs to be emphasized: a significant binding enhancement is achieved when $BArF_{24}$ anions are used compared to hexafluorophosphate. Surprisingly, this increased binding energy is not caused by a higher binding enthalpy, but can be attributed to a favorable change in the solvation entropy.

Two novel NDI-containing crown ethers have been successfully synthesized and characterized. Both compounds exhibit two reversible reduction processes. The lariat ether **NDIC7** is not suitable for rotaxane synthesis as it forms a complex equilibrium involving the deprotonation of the secondary ammonium axle and does not form 1:1 pseudorotaxanes. Additionally, the pseudorotaxane is hampered by intramolecular folding which was observed in the solid-state structure and is likely also present in solution, as indicated by a charge-transfer band. Nevertheless, it might be applicable for redox-controlled metal-sensing [60-62].

On the contrary, **NDIC8** forms pseudo[2]rotaxanes and facilitates the synthesis of a [2]rotaxane. Due to the remote position of the NDI unit and the rigid linker, rotaxane formation does not have a significant impact on the optoelectronic properties of the NDI moiety. The electrostatic interaction observed for NDI^{2-} and ammonium ions observed in the pseudo[2]rotaxane **A1**·PF_6@**NDIC8**, which even results in dethreading of the pseudorotaxane, may give rise to new switching modes in more complex molecular structures.

Overall, these findings demonstrate the benefit of detailed and systematic studies on the noncovalent interactions cohering the components of switchable MIMs for the construction of new architectures with emergent properties.

Supporting Information

Supporting Information File 1

Experimental section, including synthetic procedures, copies of NMR spectra, ITC, electrochemical, mass spectrometric and spectroelectrochemical data.
[https://www.beilstein-journals.org/bjoc/content/supplementary/1860-5397-16-209-S1.pdf]

Supporting Information File 2

Crystallographic data (cif) for **exTTFC7**, **NDIC7**, and **NDIC8**.
[https://www.beilstein-journals.org/bjoc/content/supplementary/1860-5397-16-209-S2.zip]

Acknowledgements

We thank Sebastian Sobottka for help with spectroelectrochemical measurements and Maite Nößler for help with synthesis.

Funding

This research was funded by the Deutsche Forschungsgemeinschaft and the Academy of Finland (decision no. 314343).

ORCID® iDs

Henrik Hupatz - https://orcid.org/0000-0002-2789-6279
Hendrik V. Schröder - https://orcid.org/0000-0002-6126-0055
Arto Valkonen - https://orcid.org/0000-0003-2806-3807
Felix Witte - https://orcid.org/0000-0002-6396-0178
Christoph A. Schalley - https://orcid.org/0000-0002-8634-3578

References

1. Pedersen, C. J. *J. Am. Chem. Soc.* **1967,** *89,* 2495–2496. doi:10.1021/ja00986a052
2. Pedersen, C. J. *Angew. Chem., Int. Ed. Engl.* **1988,** *27,* 1021–1027. doi:10.1002/anie.198810211
3. Pedersen, C. J. *J. Am. Chem. Soc.* **1967,** *89,* 7017–7036. doi:10.1021/ja01002a035
4. Cox, R. P.; Sandanayake, S.; Scarborough, D. L. A.; Izgorodina, E. I.; Langford, S. J.; Bell, T. D. M. *New J. Chem.* **2019,** *43,* 2011–2018. doi:10.1039/c8nj05666h
5. Li, J.; Yim, D.; Jang, W.-D.; Yoon, J. *Chem. Soc. Rev.* **2017,** *46,* 2437–2458. doi:10.1039/c6cs00619a
6. Pedersen, C. J.; Frensdorff, H. K. *Angew. Chem., Int. Ed. Engl.* **1972,** *11,* 16–25. doi:10.1002/anie.197200161
7. Gokel, G. W.; Leevy, W. M.; Weber, M. E. *Chem. Rev.* **2004,** *104,* 2723–2750. doi:10.1021/cr020080k
8. Landini, D.; Montanari, F.; Pirisi, F. M. *J. Chem. Soc., Chem. Commun.* **1974,** 879–880. doi:10.1039/c39740000879
9. Gokel, G. W.; Durst, H. D. *Synthesis* **1976,** 168–184. doi:10.1055/s-1976-23980

10. Stuart, A. M.; Vidal, J. A. *J. Org. Chem.* **2007,** *72,* 3735–3740. doi:10.1021/jo062606x
11. Morrison, P. W. J.; Porfiryeva, N. N.; Chahal, S.; Salakhov, I. A.; Lacourt, C.; Semina, I. I.; Moustafine, R. I.; Khutoryanskiy, V. V. *Mol. Pharmaceutics* **2017,** *14,* 3528–3538. doi:10.1021/acs.molpharmaceut.7b00556
12. You, X.-R.; Ju, X.-J.; He, F.; Wang, Y.; Liu, Z.; Wang, W.; Xie, R.; Chu, L.-Y. *ACS Appl. Mater. Interfaces* **2017,** *9,* 19258–19268. doi:10.1021/acsami.7b05701
13. Chehardoli, G.; Bahmani, A. *Supramol. Chem.* **2019,** *31,* 221–238. doi:10.1080/10610278.2019.1568432
14. Beer, P. D. *Chem. Soc. Rev.* **1989,** *18,* 409–450. doi:10.1039/cs9891800409
15. Shinkai, S.; Nakaji, T.; Nishida, Y.; Ogawa, T.; Manabe, O. *J. Am. Chem. Soc.* **1980,** *102,* 5860–5865. doi:10.1021/ja00538a026
16. Shinkai, S.; Nakaji, T.; Ogawa, T.; Shigematsu, K.; Manabe, O. *J. Am. Chem. Soc.* **1981,** *103,* 111–115. doi:10.1021/ja00391a021
17. Saji, T. *Chem. Lett.* **1986,** *15,* 275–276. doi:10.1246/cl.1986.275
18. Hansen, T. K.; Joergensen, T.; Stein, P. C.; Becher, J. *J. Org. Chem.* **1992,** *57,* 6403–6409. doi:10.1021/jo00050a010
19. Le Derf, F.; Mazari, M.; Mercier, N.; Levillain, E.; Trippé, G.; Riou, A.; Richomme, P.; Becher, J.; Garín, J.; Orduna, J.; Gallego-Planas, N.; Gorgues, A.; Sallé, M. *Chem. – Eur. J.* **2001,** *7,* 447–455. doi:10.1002/1521-3765(20010119)7:2<447::aid-chem447>3.0.co;2-a
20. Trippé, G.; Levillain, E.; Le Derf, F.; Gorgues, A.; Sallé, M.; Jeppesen, J. O.; Nielsen, K.; Becher, J. *Org. Lett.* **2002,** *4,* 2461–2464. doi:10.1021/ol0260829
21. Jana, A.; Bähring, S.; Ishida, M.; Goeb, S.; Canevet, D.; Sallé, M.; Jeppesen, J. O.; Sessler, J. L. *Chem. Soc. Rev.* **2018,** *47,* 5614–5645. doi:10.1039/c8cs00035b
22. Ashton, P. R.; Campbell, P. J.; Glink, P. T.; Philp, D.; Spencer, N.; Stoddart, J. F.; Chrystal, E. J. T.; Menzer, S.; Williams, D. J.; Tasker, P. A. *Angew. Chem., Int. Ed. Engl.* **1995,** *34,* 1865–1869. doi:10.1002/anie.199518651
23. Kolchinski, A. G.; Busch, D. H.; Alcock, N. W. *J. Chem. Soc., Chem. Commun.* **1995,** 1289–1291. doi:10.1039/c39950001289
24. Bruns, C. J.; Stoddart, J. F. *The Nature of the Mechanical Bond: From Molecules to Machines;* John Wiley & Sons, Inc.: Hoboken, NJ, USA, 2017. doi:10.1002/9781119044123
25. Ashton, P. R.; Chrystal, E. J. T.; Glink, P. T.; Menzer, S.; Schiavo, C.; Spencer, N.; Stoddart, J. F.; Tasker, P. A.; White, A. J. P.; Williams, D. J. *Chem. – Eur. J.* **1996,** *2,* 709–728. doi:10.1002/chem.19960020616
26. Zhang, M.; Yan, X.; Huang, F.; Niu, Z.; Gibson, H. W. *Acc. Chem. Res.* **2014,** *47,* 1995–2005. doi:10.1021/ar500046r
27. Clifford, T.; Abushamleh, A.; Busch, D. H. *Proc. Natl. Acad. Sci. U. S. A.* **2002,** *99,* 4830–4836. doi:10.1073/pnas.062639799
28. Balzani, V.; Gómez-López, M.; Stoddart, J. F. *Acc. Chem. Res.* **1998,** *31,* 405–414. doi:10.1021/ar970340y
29. Ragazzon, G.; Baroncini, M.; Silvi, S.; Venturi, M.; Credi, A. *Nat. Nanotechnol.* **2015,** *10,* 70–75. doi:10.1038/nnano.2014.260
30. Erbas-Cakmak, S.; Fielden, S. D. P.; Karaca, U.; Leigh, D. A.; McTernan, C. T.; Tetlow, D. J.; Wilson, M. R. *Science* **2017,** *358,* 340–343. doi:10.1126/science.aao1377
31. Blanco, V.; Leigh, D. A.; Marcos, V.; Morales-Serna, J. A.; Nussbaumer, A. L. *J. Am. Chem. Soc.* **2014,** *136,* 4905–4908. doi:10.1021/ja501561c
32. Schröder, H. V.; Schalley, C. A. *Chem. Sci.* **2019,** *10,* 9626–9639. doi:10.1039/c9sc04118d
33. Baroncini, M.; Silvi, S.; Credi, A. *Chem. Rev.* **2020,** *120,* 200–268. doi:10.1021/acs.chemrev.9b00291
34. Ashton, P. R.; Becher, J.; Fyfe, M. C. T.; Nielsen, M. B.; Stoddart, J. F.; White, A. J. P.; Williams, D. J. *Tetrahedron* **2001,** *57,* 947–956. doi:10.1016/s0040-4020(00)01062-0
35. Schröder, H. V.; Sobottka, S.; Nößler, M.; Hupatz, H.; Gaedke, M.; Sarkar, B.; Schalley, C. A. *Chem. Sci.* **2017,** *8,* 6300–6306. doi:10.1039/c7sc02694c
36. Schröder, H. V.; Stein, F.; Wollschläger, J. M.; Sobottka, S.; Gaedke, M.; Sarkar, B.; Schalley, C. A. *Angew. Chem., Int. Ed.* **2019,** *58,* 3496–3500. doi:10.1002/anie.201813265
37. Schröder, H. V.; Mekic, A.; Hupatz, H.; Sobottka, S.; Witte, F.; Urner, L. H.; Gaedke, M.; Pagel, K.; Sarkar, B.; Paulus, B.; Schalley, C. A. *Nanoscale* **2018,** *10,* 21425–21433. doi:10.1039/c8nr05534c
38. Schröder, H. V.; Wollschläger, J. M.; Schalley, C. A. *Chem. Commun.* **2017,** *53,* 9218–9221. doi:10.1039/c7cc05259f
39. Schröder, H. V.; Hupatz, H.; Achazi, A. J.; Sobottka, S.; Sarkar, B.; Paulus, B.; Schalley, C. A. *Chem. – Eur. J.* **2017,** *23,* 2960–2967. doi:10.1002/chem.201605710
40. Gaedke, M.; Witte, F.; Anhäuser, J.; Hupatz, H.; Schröder, H. V.; Valkonen, A.; Rissanen, K.; Lützen, A.; Paulus, B.; Schalley, C. A. *Chem. Sci.* **2019,** *10,* 10003–10009. doi:10.1039/c9sc03694f
41. Akutagawa, T.; Abe, Y.; Nezu, Y.-i.; Nakamura, T.; Kataoka, M.; Yamanaka, A.; Inoue, K.; Inabe, T.; Christensen, C. A.; Becher, J. *Inorg. Chem.* **1998,** *37,* 2330–2331. doi:10.1021/ic971623p
42. Diac, A.; Matache, M.; Grosu, I.; Hădade, N. D. *Adv. Synth. Catal.* **2018,** *360,* 817–845. doi:10.1002/adsc.201701362
43. Hansen, J. G.; Feeder, N.; Hamilton, D. G.; Gunter, M. J.; Becher, J.; Sanders, J. K. M. *Org. Lett.* **2000,** *2,* 449–452. doi:10.1021/ol991289w
44. Cantrill, S. J.; Fulton, D. A.; Heiss, A. M.; Pease, A. R.; Stoddart, J. F.; White, A. J. P.; Williams, D. J. *Chem. – Eur. J.* **2000,** *6,* 2274–2287. doi:10.1002/1521-3765(20000616)6:12<2274::aid-chem2274>3.0.co;2-2
45. Zhang, C.; Li, S.; Zhang, J.; Zhu, K.; Li, N.; Huang, F. *Org. Lett.* **2007,** *9,* 5553–5556. doi:10.1021/ol702510c
46. Jiang, W.; Schalley, C. A. *Beilstein J. Org. Chem.* **2010,** *6,* No. 14. doi:10.3762/bjoc.6.14
47. Mandal, A. K.; Suresh, M.; Das, A. *Org. Biomol. Chem.* **2011,** *9,* 4811–4817. doi:10.1039/c0ob01106a
48. Schröder, H. V.; Witte, F.; Gaedke, M.; Sobottka, S.; Suntrup, L.; Hupatz, H.; Valkonen, A.; Paulus, B.; Rissanen, K.; Sarkar, B.; Schalley, C. A. *Org. Biomol. Chem.* **2018,** *16,* 2741–2747. doi:10.1039/c8ob00415c
49. Blackburn, A. K.; Sue, A. C.-H.; Shveyd, A. K.; Cao, D.; Tayi, A.; Narayanan, A.; Rolczynski, B. S.; Szarko, J. M.; Bozdemir, O. A.; Wakabayashi, R.; Lehrman, J. A.; Kahr, B.; Chen, L. X.; Nassar, M. S.; Stupp, S. I.; Stoddart, J. F. *J. Am. Chem. Soc.* **2014,** *136,* 17224–17235. doi:10.1021/ja509442t
50. Gibson, H. W.; Jones, J. W.; Zakharov, L. N.; Rheingold, A. L.; Slebodnick, C. *Chem. – Eur. J.* **2011,** *17,* 3192–3206. doi:10.1002/chem.201002522
51. Jones, J. W.; Gibson, H. W. *J. Am. Chem. Soc.* **2003,** *125,* 7001–7004. doi:10.1021/ja034442x
52. Wiseman, T.; Williston, S.; Brandts, J. F.; Lin, L.-N. *Anal. Biochem.* **1989,** *179,* 131–137. doi:10.1016/0003-2697(89)90213-3
53. Turnbull, W. B.; Daranas, A. H. *J. Am. Chem. Soc.* **2003,** *125,* 14859–14866. doi:10.1021/ja036166s

54. Nagai, H.; Suzaki, Y.; Osakada, K. *Eur. J. Inorg. Chem.* **2014,** 4376–4384. doi:10.1002/ejic.201402465
55. Suzaki, Y.; Nagai, H.; Osakada, K. *Chem. Lett.* **2014,** *43,* 714–716. doi:10.1246/cl.131213
56. Rosokha, S. V.; Kochi, J. K. *J. Am. Chem. Soc.* **2007,** *129,* 828–838. doi:10.1021/ja064166x
57. Altieri, A.; Gatti, F. G.; Kay, E. R.; Leigh, D. A.; Martel, D.; Paolucci, F.; Slawin, A. M. Z.; Wong, J. K. Y. *J. Am. Chem. Soc.* **2003,** *125,* 8644–8654. doi:10.1021/ja0352552
58. Matsumura, T.; Ishiwari, F.; Koyama, Y.; Takata, T. *Org. Lett.* **2010,** *12,* 3828–3831. doi:10.1021/ol101543x
59. Andric, G.; Boas, J. F.; Bond, A. M.; Fallon, G. D.; Ghiggino, K. P.; Hogan, C. F.; Hutchison, J. A.; Lee, M. A.-P.; Langford, S. J.; Pilbrow, J. R.; Troup, G. J.; Woodward, C. P. *Aust. J. Chem.* **2004,** *57,* 1011–1019. doi:10.1071/ch04130
60. Hangarge, R. V.; La, D. D.; Boguslavsky, M.; Jones, L. A.; Kim, Y. S.; Bhosale, S. V. *ChemistrySelect* **2017,** *2,* 11487–11491. doi:10.1002/slct.201702085
61. Lin, H.; Cinar, M. E.; Schmittel, M. *Dalton Trans.* **2010,** *39,* 5130–5138. doi:10.1039/c000449a
62. Pond, S. J. K.; Tsutsumi, O.; Rumi, M.; Kwon, O.; Zojer, E.; Brédas, J.-L.; Marder, S. R.; Perry, J. W. *J. Am. Chem. Soc.* **2004,** *126,* 9291–9306. doi:10.1021/ja049013t

License and Terms

BEILSTEIN JOURNAL OF ORGANIC CHEMISTRY

Supporting Information

for

Thermodynamic and electrochemical study of tailor-made crown ethers for redox-switchable (pseudo)rotaxanes

Henrik Hupatz, Marius Gaedke, Hendrik V. Schröder, Julia Beerhues, Arto Valkonen, Fabian Klautzsch, Sebastian Müller, Felix Witte, Kari Rissanen, Biprajit Sarkar and Christoph A. Schalley

Beilstein J. Org. Chem. **2020,** *16,* 2576–2588. doi:10.3762/bjoc.16.209

Experimental section, including synthetic procedures, copies of NMR spectra, ITC, electrochemical, mass spectrometric and spectroelectrochemical data

Table of contents

1. Experimental details

1.1. General Methods

All reagents and solvents were obtained from commercial sources and used without further purification. Dry solvents were purchased from Acros Organics or obtained from the M. BRAUN Solvent purification system SPS 800. 2,3-bis(2-cyanoethylthio)-6,7-bis(methylthio)tetrathiafulvalene [1], diiodide **1** [2], **BC7** [3], ditosylate **5** [4], monoanhydride **7** [5], (4-(prop-2-yn-1-yloxy)phenyl)methanaminium chloride [6], **A2**·PF_6 [7], **A1**·$BArF_{24}$ [8], and 2,6-dimethoxybenzonitrile oxide stopper **St1** [9], were synthesized according to literature procedures. Thin-layer chromatography was performed on silica gel-coated plates with fluorescent indicator F254 (Merck). For column chromatography, silica gel (0.04–0.063 mm, Merck) was used.

^{1}H and ^{13}C NMR experiments were performed on JEOL ECX 400, JEOL ECP 500, Bruker AVANCE 500 or Bruker AVANCE 700 instruments. Residual solvent signals were used as the internal standards. All shifts are reported in ppm and NMR multiplicities are abbreviated as s (singlet), d (doublet), t (triplet), m (multiplet), and br (broad). Coupling constants *J* are reported in hertz. Compounds containing the tetrakis[3,5-bis(trifluoromethyl)phenyl]borate ($BArF_{24}^{-}$) anion show ^{13}C NMR spectra with ^{19}F, ^{10}B, and ^{11}B couplings. These signals were denoted as one signal.

Electrospray ionization high-resolution mass spectra (HRMS) were measured on an Agilent 6210 ESI-TOF device.

1.2. Synthetic procedures

TTFC7

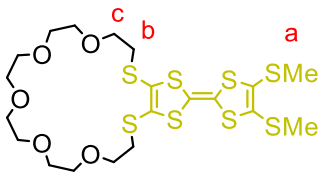

2,3-Bis(2-cyanoethylthio)-6,7-bis(methylthio)tetrathiafulvalene (50.0 mg, 0.11 mmol, 1 equiv) was dissolved in dry DMF (4 mL) and CsOH·H_2O (35.8 mg, 0.22 mmol, 2 equiv) dissolved in dry MeOH (1.5 mL) was added dropwise over 30 min under an Ar atmosphere. After stirring for 1 h, the resulting dark red solution was dropped to a solution of diiodide **1** (53.7 mg, 0.11 mmol, 1 equiv) in DMF (20 mL) in an ice bath over 1 h. The mixture was stirred in the thawing ice bath overnight. Afterwards, the solvent was removed under reduced pressure and the resulting residue was dissolved in CH_2Cl_2 (50 mL). The organic layer was washed with water (50 mL) and brine (50 mL). After drying over $MgSO_4$, the solution was concentrated under reduced pressure and the residue was purified by column chromatography (SiO_2, CH_2Cl_2

→ CH_2Cl_2/MeOH 100:1, R_f ≈ 0.6 in CH_2Cl_2/MeOH 50:1). The desired product (45 mg, 0.07 mmol, 69%) was obtained as dark red oil.

^{1}H NMR (700 MHz, CD_2Cl_2): δ = 2.42 (s, 6H, a), 3.03 (t, ^3J = 6.2 Hz, 4H, b), 3.62 – 3.61 (m, 16H, OCH_2), 3.69 (t, ^3J = 6.2 Hz, 4H, c) ppm. **^{13}C NMR** (176 MHz, CD_2Cl_2): δ = 19.6, 36.4, 70.2, 71.2, 71.2, 71.3, 71.3, 111.2, 128.1, 128.7 ppm. **ESI-HRMS** (CH_3CN): m/z calcd. for $[C_{20}H_{30}O_5S_8]$: $[M]^+$ 605.9853, found: 605.9843; calcd. for $[M+Na]^+$ 628.9751, found: 628.9734; calcd. for $[M+K]^+$ 644.9490, found: 644.9492.

21,22-Diiodo-2,3,5,6,8,9,11,12,14,15,17,18-dodecahydrobenzo[*b*][1,4,7,10,13,16,19]-heptaoxacyclohenicosine (**2**)

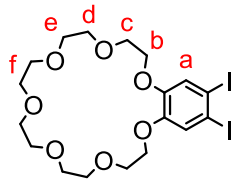

Periodic acid (231 mg, 1.01 mmol, 1.8 equiv) and iodine (114 mg, 0.45 mmol, 0.8 equiv) were dissolved in dry MeOH (5 mL) and stirred for 5 min under argon at rt. Afterwards, **BC7** (200 mg, 0.56 mmol, 1.0 equiv) dissolved in dry MeOH (7 mL) was added to the mixture and stirred for 12 h at 70 °C. The reaction mixture was quenched with a saturated aqueous $Na_2S_2O_3$ solution. The solvent was removed under reduced pressure and the residue dissolved in CH_2Cl_2 (50 mL). The organic phase was washed three times with water and brine. The organic phase was dried over $MgSO_4$ and the solvent was removed to isolate the desired product **2** (240 mg, 0.4 mmol, 66%) as light-yellow oil.

^{1}H NMR (500 MHz, $CDCl_3$): δ = 3.64 – 3.68 (m, 8H, f), 3.70 – 3.73 (m, 4H, e), 3.75 – 3.78 (m, 4H, d), 3.87 – 3.90 (m, 4H, c), 4.09 – 4.12 (m, 4H, b), 7.28 (s, 2H, a) ppm. **^{13}C NMR** (176 MHz, $CDCl_3$) *δ* = 69.6, 69.6, 70.7, 71.1, 71.1, 71.3, 96.7, 124.4, 149.6. ppm. **ESI-HRMS** (CH_3CN): m/z calcd. for $[C_{18}H_{26}I_2O_7]$: 626.0106 $[M+NH_4]^+$ found: 626.0094; calcd. for $[M+Na]^+$ 630.9660, found: 646.9644; calcd. for $[M+K]^+$ 646.9399, found: 646.9397.

7,8,10,11,13,14,16,17,19,20,22,23-Dodecahydro[1,3]dithiolo[4'',5'':5',6'][1,4]dithiino-[2',3':4,5]benzo[1,2-*b*][1,4,7,10,13,16,19]heptaoxacyclohenicosine-2-thione (**3**)

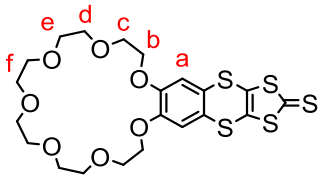

The diiodide **2** (235 mg, 0.38 mmol, 1.0 equiv), $(NEt_4)_2[Zn(dmit)_2]$ (dmit = 1,3 dithiole-2-thione-4,5-dithiolate (183 mg, 0.19 mmol, 0.5 equiv), Cu_2O (7 mg, 0.05 mmol, 0.1 equiv), and ethyl

acetoacetate (50 µL, 0.4 mmol, 1.0 equiv) were suspended in dry DMF (10 mL) and stirred for 12 h at 80 °C. Afterwards, the solvent was removed under reduced pressure and the residue was dissolved in CH_2Cl_2 (50 mL). The organic phase was washed three times with water and brine. The organic phase was dried over $MgSO_4$ and the solvent was removed. The crude product was purified via column chromatography (SiO_2, CH_2Cl_2 → CH_2Cl_2/EtOH 20:1, $R_f \approx 0.3$ in CH_2Cl_2/EtOH 20:1) to isolate the desired thione **3** as yellowish powder in 58% yield (121 mg, 0.22 mmol).

^{1}H NMR (500 MHz, $CDCl_3$): δ = 3.64 – 3.68 (m, 8H, f), 3.71 – 3.73 (m, 4H, e), 3.76 – 3.79 (m, 4H, d), 3.90 – 3.93 (m, 4H, c), 4.13 – 4.17 (m, 4H, b), 6.97 (s, 2H, a) ppm. **^{13}C NMR** (176 MHz, $CDCl_3$) *δ* = 69.7, 69.9, 70.7, 71.2, 71.2, 71.4, 114.6, 125.8, 131.9, 149.7, 212.7 ppm. **ESI-HRMS** (MeOH): m/z calcd. for $[C_{21}H_{26}O_7S_5]$: $[M+NH_4]^+$ 568.0620 found: 568.0631; calcd. for $[M+Na]^+$ 573.0174, found: 573.0185; calcd. for $[M+K]^+$ 588.9914, found: 588.9926.

7,8,10,11,13,14,16,17,19,20,22,23-Dodecahydro[1,3]dithiolo[4'',5'':5',6'][1,4]dithiino[2',3':4,5]-benzo[1,2-*b*][1,4,7,10,13,16,19]heptaoxacyclohenicosine-2-one (**4**)

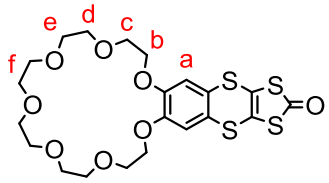

The thione **3** (58 mg, 0.11 mmol, 1 equiv) and mercury(II) acetate (101 mg, 0.33 mmol, 3 equiv) were dispersed in a mixture of $CHCl_3$ (5 mL) and acetic acid (2 mL). After stirring for 2 days at rt the reaction mixture was filtered through a celite pad, diluted with $CHCl_3$, and quenched with saturated aq. $NaHCO_3$ (20 mL). The organic phase was washed with brine, dried over $MgSO_4$, and the solvent was removed. The desired product **10** could be isolated as yellow powder in 95% yield (53 mg, 0.10 mmol).

^{1}H NMR (600 MHz, $CDCl_3$): δ = 3.63 – 3.67 (m, 8H, f), 3.69 – 3.72 (m, 4H, e), 3.75 – 3.78 (m, 4H, d), 3.89 – 3.92 (m, 4H, c), 4.13 – 4.17 (m, 4H, b), 6.97 (s, 2H, a) ppm. **^{13}C NMR** (126 MHz, $CDCl_3$) *δ* = 69.6, 69.8, 70.7, 71.1, 71.2, 71.3, 114.3, 122.0, 126.1, 149.7, 191.4 ppm. **ESI-HRMS** (MeOH): m/z calcd. for $[C_{21}H_{26}O_8S_4]$: $[M+K]^+$ 573.0142, found: 573.0126.

exTTFC7

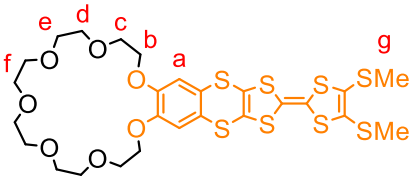

The one **4** (53 mg, 0.10 mmol, 1.0 equiv) and 4,5-bis(methylthio)-1,3-dithiole-2-thione (25 mg, 0.11 mmol, 1.1 equiv) were dissolved in $P(OEt)_3$ (20 mL). After stirring for 2 h at 80°C the solvent was removed in oil pump vacuum and the residue was dissolved in CH_2Cl_2 (50 mL). The crude product was purified by preparative thin layer chromatography plate (2000 µm, SiO_2, CH_2Cl_2/EtOH 30:1, $R_f \approx 0.4$ in CH_2Cl_2/EtOH 20:1) to isolate the desired product **exTTFC7** as yellow powder in 85% yield (61 mg, 0.09 mmol).

^{1}H NMR (700 MHz, CD_2Cl_2): δ = 2.42 (s, 6H, g), 3.59 – 3.61 (m, 8H, f), 3.63 – 3.65 (m, 4H, e), 3.68 – 3.71 (m, 4H, d), 3.83 – 3.86 (m, 4H, c), 4.10 – 4.12 (m, 4H, b), 6.94 (s, 2H, a) ppm. **^{13}C NMR** (176 MHz, $CDCl_3$) δ = 19.6, 70.0, 70.0, 71.1, 71.3, 71.4, 71.6, 113.3, 114.8, 116.7, 123.9, 127.0, 128.1, 149.7 ppm. **ESI-HRMS** (MeOH): m/z calcd. for $[C_{26}H_{32}O_7S_8]$: $[M+K]^+$ 750.9545, found: 750.9572.

2-(5,6,8,9,11,12,14,15,17,18-Decahydro-2H-naphtho[2,3-*h*][1,4,7,10,13,16,19]-hexaoxaazacyclohenicosin-10(3*H*)-yl)ethanamine (**6**)

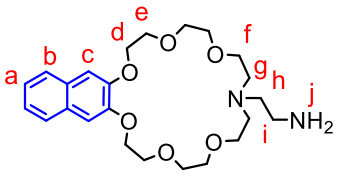

Ditosylate **5** (800 mg, 1.09 mmol, 1.0 equiv), EDABoc (174 mg, 1.09 mmol, 1.0 equiv), potassium iodide (262 mg, 1.58 mmol, 1.5 equiv), and K_2CO_3 (1506 mg, 10.9 mmol, 10 equiv) were dissolved in acetonitrile (25 mL) and heated to reflux overnight. After cooling to rt and filtration, the solvent was removed under reduced pressure and the residue was purified by column chromatography (SiO_2, CH_2Cl_2→ CH_2Cl_2/MeOH 10:1, $R_f \approx 0.1$ in CH_2Cl_2) to obtain pure protected amine (410 mg, 0.75 mmol, 69%) as pale yellow oil.

The protected amine was dissolved in CH_2Cl_2/trifluoroacetic acid (3:2, 2.5 mL) and stirred for 2 h at rt. The solution was concentrated under reduced pressure and the residue was solved in saturated $NaHCO_3$ solution (40 mL). The aqueous phase was extracted with CH_2Cl_2 (3 × 40 mL) and the combined organic phases were dried over $MgSO_4$. After removing the solvent, the crude product was purified by column chromatography (SiO_2, CH_2Cl_2 → CH_2Cl_2/MeOH 20:1, $R_f \approx 0.3$ in CH_2Cl_2/MeOH 20:1) to yield the desired product (204 mg, 0.46 mmol, 62%) as colorless oil. The product was obtained in an overall yield of 43%.

^{1}H NMR (500 MHz, $CDCl_3$): δ = 2.16 (s, 2H, j), 2.75 – 2.77 (m, 4H, g), 2.78 (br, 4H, h,i), 3.54 – 3.56 (m, 4H, f), 3.71 – 3.72 (m, 4H, OCH_2), 3.78 – 3.79 (m, 4H, OCH_2), 4.00 – 4.02 (m, 4H, e), 4.30 – 4.32 (m, 4H, d), 7.27 (s, 2H, c), 7.35 (AA'XX' spin system, $J_{AA'XX'}$ = 3.3, 6.2 Hz, 2H, a), 7.67 (AA'XX' spin system, $J_{AA'XX'}$ = 3.3, 6.2 Hz, 2H, b) ppm. **^{13}C NMR** (176 MHz, $CDCl_3$) δ

= 38.9, 51.8, 56.2, 68.6, 69.6, 69.9, 70.5, 70.6, 108.6, 124.9, 126.6, 129.5, 148.0 ppm. **ESI-HRMS** (CH_3CN): m/z calcd. for $[C_{24}H_{36}O_6N_2]$: $[M+H]^+$ 449.2646, found: 449.2661.

NDIC7

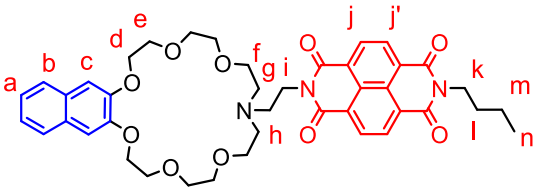

To a solution of amine **6** (170 mg, 0.38 mmol, 1.1 equiv) in DMF (2 mL) was added dropwise a solution of monoanhydride **7** (107 mg, 0.35 mmol, 1.0 equiv) in DMF (1 mL). The solution was stirred at 120 °C under Ar in a sealed tube overnight. After cooling to rt, the solvent was removed and the residue was purified by column chromatography (SiO_2, CH_2Cl_2/MeOH 20:1 → 10:1, $R_f \approx 0.4$ in CH_2Cl_2/MeOH 10:1) to yield the desired product **NDIC7** (158 mg, 0.21 mmol, 60%) as orange solid.

^{1}H NMR (500 MHz, $CDCl_3$): δ = 1.00 (t, ^3J = 7.4 Hz, 3H, n), 1.43 – 1.51 (m, 2H, m), 1.70 – 1.76 (m, 4H, l), 2.80 – 2.83 (m, 2H, h), 2.87 – 2.89 (m, 4H, g), 3.66 (br, 4H, f) 3.71 – 3.73 (m, 4H, OCH_2), 3.78 – 3.80 (m, 4H, OCH_2), 3.96 – 3.97 (m, 4H, e), 4.14 – 4.17 (m, 6H, d,k), 4.28 – 4.31 (m, 2H, i), 6.76 (s, 2H, c), 7.00 – 7.02 (m, 2H a), 7.24 – 7.26 (m, 2H, b), 8.56 – 8.60 (m, 4H, j, j') ppm. **^{13}C NMR** (176 MHz, $CDCl_3$) δ = 14.0, 20.5, 30.3, 39.4, 40.8, 52.3, 55.7, 68.8, 69.8, 70.2, 71.0, 71.2, 107.7, 123.8, 126.1, 126.5, 126.5, 126.5, 126.6, 128.9, 130.5, 130.7, 148.9, 162.8, 162.9 ppm. **ESI-HRMS** (CH_3CN): m/z calcd. for $[C_{42}H_{47}N_3O_{10}]$: $[M+H]^+$ 754.3334 found: 754.3361; calcd. for $[M+Na]^+$ 776.3154, found: 776.3180; calcd. for $[M+K]^+$ 792.2893, found: 792.2922.

tert-Butyl (3,5-dihydroxyphenyl)carbamate (**8**)

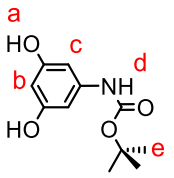

Aqueous NH_3 (28%, 100 mL) was purged with argon for 20 min. Benzene-1,3,5-triol (20.0 g, 0.16 mol, 2 equiv) was added and the mixture was stirred at rt for 2 h. The solvent was removed at reduced pressure, to the residue, toluene was added and removed at reduced pressure. The crude product was suspended in THF (150 mL) and Boc anhydride (17.5 g, 0.08 mol, 1 equiv) was added. The mixture was stirred under Ar overnight at rt and the solvent was

removed at reduced pressure. The crude product was purified by column chromatography (SiO_2, CH_2Cl_2/MeOH 15:1) and yielded a white solid (8.8 g, 0.04 mol, 25%).

^{1}H NMR (700 MHz, DMSO-d_6): δ = 1.43 (s, 9H, e), 5.80 (s, 1H, b), 6.40 (s, 2H, c), 9.01 (br, 1H, d), 9.02 (br, 2H, a) ppm. **^{13}C NMR** (176 MHz, DMSO-d_6) δ = 28.2, 78.7, 96.8, 96.6 140.9, 152.6, 158.3 ppm. **ESI-HRMS** (MeOH): m/z calcd. for $[C_{11}H_{15}NO_4]$: $[M+Na]^+$ 248.0893, found: 248.0884.

2,5,8,11,13,16,19,22-Octaoxa-1(2,3)-naphthalena-12(1,3)-benzenacyclodocosaphan-12^5-amine (**9**)

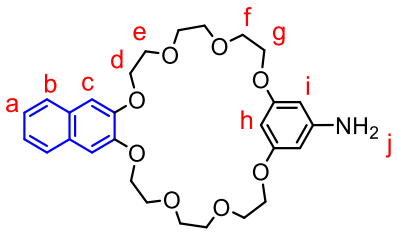

Cs_2CO_3 (5.0 g, 15.5 mmol, 5 equiv) was dissolved in acetonitrile (500 mL) and heated to reflux. A solution of ditosylate **5** (2.3 g, 3.1 mmol, 1 equiv) in acetonitrile (250 mL) and a solution of diol **8** (0.7 g, 3.1 mmol, 1 equiv) in acetonitrile (250 mL) were added dropwise and simultaneously. The mixture was stirred under reflux for 3 d. After cooling to rt and filtration, the solvent was removed under reduced pressure. The residue was dissolved in CH_2Cl_2 (300 mL) and washed three times with water and brine. After evaporation of the solvent, the crude product was purified by column chromatography (SiO_2, pentane/EtOAc/Et_3N 300:200:1 → 50:450:1, R_f ≈ 0.7 in 50:450:1) to obtain pure protected amine (1.1 g, 1.7 mmol, 55%) as yellow solid.

The protected amine and trifluoroacetic acid (2.6 mL, 34 mmol, 20 equiv) were dissolved in CH_2Cl_2 (100 mL) at 0 °C. The solution was warmed to rt and stirred for 16 h. The solvent was removed under reduced pressure and the residue was dissolved in saturated $NaHCO_3$ solution (200 mL). The aqueous phase was extracted with CH_2Cl_2 (3 × 200 mL). The combined organic phases were washed with water and dried over $MgSO_4$. After removing of the solvent, the crude product was purified by column chromatography (SiO_2, EtOAc/Et_3N 10:1, R_f ≈ 0.3) to yield the desired product (0.86 g, 1.7 mmol, quantitative) as pale yellow solid. The product was obtained in an overall yield of 55%.

^{1}H NMR (700 MHz, $CDCl_3$): δ = 3.61 (s, 2H, j), 3.72 – 3.73 (m, 4H, OCH_2), 3.77 – 3.78 (m, 4H, OCH_2), 3.79 – 3.80 (m, 4H, f), 3.93 – 3.95 (m, 4H, e), 4.07 – 4.09 (m, 4H, g), 4.24 – 4.26 (m, 4H, d), 5.85 (d, 2H, ^4J = 2.2 Hz, i), 6.12 (t, 1H, ^4J = 2.2 Hz, h), 7.15 (s, 2H, c), 7.31 (AA'XX' spin system, $J_{AA'XX'}$ = 3.3, 6.1 Hz, 2H, a), 7.65 (AA'XX' spin system, $J_{AA'XX'}$ = 3.3, 6.1 Hz, 2H, b) ppm. **^{13}C NMR** (176 MHz, $CDCl_3$) δ = 68.0, 68.9, 69.8, 70.0, 71.1, 71.3, 93.3, 95.5, 109.0, 123.3, 126.4, 129.5, 148.4, 149.2, 160.9 ppm. **ESI-HRMS** (CH_3CN): m/z calcd. for

[$C_{24}H_{36}O_8N_1$]: [M+Na]$^+$ 536.2255, found: 536.2276; calcd. for [M+K]$^+$ 552.1994, found: 552.2011.

NDIC8

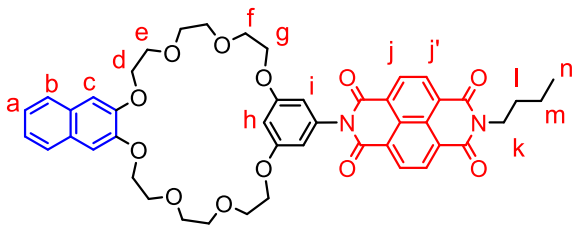

Monoanhydrate **7** (510 mg, 1.6 mmol, 1.1 equiv) was dissolved in dry DMF (55 mL) and stirred at 70 °C for 10 minutes in an Ar atmosphere. Et_3N (0.6 mL, 4.3 mmol, 3.0 equiv) and amine **9** (737 mg, 1.4 mmol, 1.0 equiv) were added and the solution was stirred at 70 °C for 24 h. The mixture was diluted in H_2O (200 mL) and extracted with EtOAc (2 × 200 mL). The solution was washed with brine and dried over MgSO4. The solvents were removed under reduced pressure and the crude product was purified by column chromatography (SiO_2, CH_2Cl_2/EtOAc 1:3, $R_f \approx$ 0.6 in EtOAc/Et_3N 40:1) to yield an orange solid (502 mg, 0.60 mmol, 43%)
^{1}H NMR (700 MHz, $CDCl_3$): δ = 1.00 (t, ^3J = 7.4 Hz, 3H, n), 1.47 (h, 2H, ^3J = 7.4 Hz, m), 1.72 – 1.77 (m, 2H, l), 3.74 – 3.75 (m, 4H, OCH_2), 3.80 – 3.81 (m, 4H, OCH_2), 3.83 – 3.84 (m, 4H, f) 3.95 – 3.97 (m, 4H, e), 4.16 – 4.17 (m, 4H, g), 4.20 – 4.21 (m, 2H, k), 4.26 – 4.28 (m, 4H, d), 6.47 (d, 2H, ^4J = 2.2 Hz, i), 6.89 (t, 1H, ^4J = 2.2 Hz, h), 7.14 (s, 2H, c), 7.29 (AA'XX' spin system, $J_{AA'XX'}$ = 3.3, 6.1 Hz, 2H, a), 7.62 (AA'XX' spin system, $J_{AA'XX'}$ = 3.3, 6.1 Hz, 2H, b), 8.74 (m, 4H, j, j') ppm. **^{13}C NMR** (176 MHz, $CDCl_3$) δ = 13.9, 20.5, 30.3, 40.9, 68.5, 68.8, 69.9, 70.1, 71.2, 71.3, 103.5, 108.6, 109.0, 124.3, 126.4, 126.8, 126.9, 127.0, 127.1, 129.5, 131.1, 131.4, 136.0, 149.3, 160.8, 162.8, 162.9 ppm. **ESI-HRMS** (CH_3CN): m/z calcd. for [$C_{46}H_{46}O_{12}N_2$]: [M+NH_4]$^+$ 836.3389 found: 836.3397; calcd. for [M+Na]$^+$ 841.2943, found: 841.2962; calcd. for [M+K]$^+$ 857.2682, found: 857.2701.

A1·PF_6

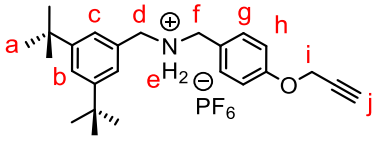

(4-(Prop-2-yn-1yloxy)phenyl)methanaminium chloride (473 mg, 2.4 mmol, 1 equiv) was dispersed in dry EtOH (40 mL) and Et_3N (242 mg, 2.4 mmol, 1 equiv) was added. Afterwards, 3,5-di-*tert*-butylbenzaldehyde (522 mg, 2.4 mmol, 1 equiv) was added and the mixture was stirred at reflux under Ar atmosphere for 3 h. The solution was cooled to 0 °C and $NaBH_4$ (454 mg, 12 mmol, 5 equiv) was added. After stirring at rt overnight, the suspension was

quenched with sat. $NaHCO_3$ solution. The mixture was filtered and the solid residue was washed with CH_2Cl_2 (150 mL). The combined filtrate was phase separated and the organic phase was washed with water (3 × 100 mL). It was dried with $MgSO_4$ and the solvent was removed at reduced pressure. The crude product was purified by column chromatography (SiO_2, CH_2Cl_2/MeOH 80:1 → 50:1) to yield a colorless oil.

The amine (745 mg, 2.0 mmol, 83 %) was dissolved in acetonitrile (10 mL), NH_4PF_6 (379 mg, 2.3 mmol) was added and argon was bubbled through the solution for 4 h. The solvent was removed at reduced pressure and the residue was suspended in water (100 mL). The suspension was extracted with Et_2O (3 × 100 mL) and the combined organic phases were washed with water (100 mL). After drying with $MgSO_4$, the solvent was removed at reduced pressure to yield the desired product **A1**•PF_6 (1010 mg, 2.0 mmol, quantitative) as white solid. **^{1}H NMR** (700 MHz, $CDCl_3$): δ = 1.32 (s, 18H, a), 2.50 (t, ^4J = 2.4 Hz, 1H, j), 4.09 (s, 2H, f), 4.13 (s, 2H, d), 4.63 (d, ^4J = 2.4 Hz, 2H, i), 6.10 (br, 2H, e), 6.97 – 6.98 (m, 2H, h), 7.18 (d, ^4J = 1.8 Hz, 2H, c), 7.27 – 7.28 (m, 2H, g), 7.47 (t, ^4J = 1.8 Hz, 1H, b) ppm. **^{13}C NMR** (176 MHz, $CDCl_3$) δ = 31.4, 35.1, 50.7, 52.0, 55.9, 76.1, 78.1, 115.9, 122.4, 124.0, 124.2, 128.7, 131.5, 152.7, 158.9. **ESI-HRMS** (CH_3CN): m/z calcd. for $[C_{25}H_{34}F_6NOP]$: $[M\text{-}PF_6]^+$ 364.2635, found: 364.2639.

NDIC8Rot

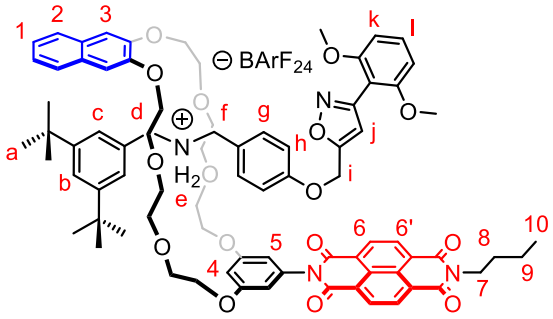

NDIC8 (28 mg, 34 µmol, 1.1 equiv) and **A1**•$BArF_{24}$ (38 mg, 31 µmol, 1.0 equiv) were dissolved in dry 1,2-dichloroethane (1.5 mL) and ultra-sonicated for 10 min. **St** (11 mg, 62 µmol, 2.0 equiv) was added and the solution was stirred at 50 °C for 3 days. The solvent was removed under reduced pressure and the crude product was purified by column chromatography (SiO_2, CH_2Cl_2/MeOH 100:1, R_f ≈ 0.4) and preparative thin layer chromatography plate (SiO_2, 500 µm, CH_2Cl_2/MeOH 100:1) to yield an orange solid (30 mg, 14 µmol, 45%).

^{1}H NMR (700 MHz, $CDCl_3$): δ = 1.00 (t, ^3J = 7.4 Hz, 3H, 10), 1.26 (s, 18H, a), 1.45 – 1.53 (m, 2H, 9), 1.73 – 1.77 (m, 2H, 8), 3.50 - 3.57 (m, 4H, OCH_2), 3.59 – 3.62 (m, 4H, OCH_2), 3.67 – 3.71 (m, 4H, OCH_2), 3.76 – 3.78 (m, 8H, OMe, OCH_2), 3.81 – 3.83 (m, 2H, OCH_2), 3.97 – 4.00 (m, 2H, OCH_2), 4.15 – 4.17 (m, 4H, OCH_2), 4.19 – 4.23 (m, 4H, 7, OCH_2), 4.38 – 4.40 (m, 4H,

i, f), 4.48 – 4.50 (m, 2H, d), 6.35 (s, 1H, j), 6.51 – 6.52 (m, 2H, h), 6.55 (d, ^{4}J = 2.2 Hz, 2H, 5), 6.64 (d, ^{3}J = 8.4 Hz, 2H, k), 6.67 (t, ^{4}J = 2.2 Hz, 1H, 4), 6.91 (s, 2H, 3), 7.14 – 7.15 (m, 2H, g), 7.35 – 7.39 (m, 5H, 1, c, l), 7.48 (t, ^{4}J = 1.8 Hz, 1H, b), 7.50 – 7.51 (m, 4H, $BArF_{24}$), 7.62 (AA'XX' spin system, $J_{AA'XX'}$ = 3.3, 6.1 Hz, 2H, 2), 8.56 – 8.60 (m, 4H, j), 7.69 – 7.70 (m, 8H, $BArF_{24}$), 7.73 (br, 2H, e), 8.75 (d, ^{3}J = 7.6 Hz, 2H, 6/6'), 8.78 (d, ^{3}J = 7.6 Hz, 2H, 6/6') ppm. **^{13}C NMR** (176 MHz, $CDCl_3$) δ = 13.9, 20.5, 30.3, 31.4, 35.1, 41.0, 52.4, 53.0, 56.2, 60.6, 68.0, 68.2, 69.4, 70.5, 70.9, 71.6, 104.3, 104.6, 106.6, 106.9, 108.0, 108.7, 114.8, 117.6, 123.2, 123.3, 124.1, 124.7, 125.7, 126.5, 127.0, 127.1, 127.3, 129.0, 130.5, 131.1, 131.1, 131.5, 131.5, 134.9, 137.1, 146.4, 152.3, 157.3, 158.7, 159.0, 160.5, 161.9, 162.8, 163.0, 165.7 ppm. **ESI-HRMS** (CH_3CN): m/z calcd. for $[C_{112}H_{101}BF_{24}N_4O_{16}]$: $[M\text{-}BArF_{24}]^+$ 1361.6274 found: 1361;6277.

.

2. Crystallographic data

General details. Single crystal X-ray data for **exTTFC7** were collected at 120 K on an Agilent Super-Nova dual wavelength diffractometer with a micro-focus X-ray source and multilayer optics monochromatized CuKα (λ = 1.54184 Å) radiation. Program *CrysAlisPro* [10] was used for collection and reduction of data. The diffraction intensities were corrected for absorption using analytical face index absorption correction method [11] for the data. The structures were solved with direct methods (*SHELXT*) [12] and refined by full-matrix least squares on F^2 using *SHELXL*-2018/3 [13]. Anisotropic displacement parameters were assigned to non-hydrogen atoms. All hydrogen atoms were constrained to their idealised positions and refined using riding models with U_{eq}(H) of 1.5U_{eq}(C) for terminal methyl groups, and of 1.2U_{eq}(C) for other groups. The summary details of crystal data, data collection, and the refinement results are documented below.

Single crystal X-ray data for **NDIC8** and **NDIC7** were collected on a Bruker D8 Venture system at 100(2) K using graphite-monochromated MoKα (λα = 0.71073 Å) and CuKα (λ = 1.54184 Å) radiation. The strategy for the data collection was evaluated using APEX3 software and the data were collected by the omega + phi scan techniques. The data were scaled and reduced using SAINT+ and SADABS software. The structure was solved by intrinsic phasing using SHELXT-2014/7. It was refined by full matrix least-squares using SHELXL-2014/7 and was refined on F^2. Non-hydrogen atoms were refined anisotropically [13-19].

Deposition numbers CCDC 1977518 (**exTTFC7**), 1902746 (**NDIC7**), and 1906086 (**NDIC8**) contains the supplementary crystallographic data for this paper. These data are provided free of charge by the joint Cambridge Crystallographic Data Centre and Fachinformationszentrum Karlsruhe Access Structures service www.ccdc.cam.ac.uk/structures.

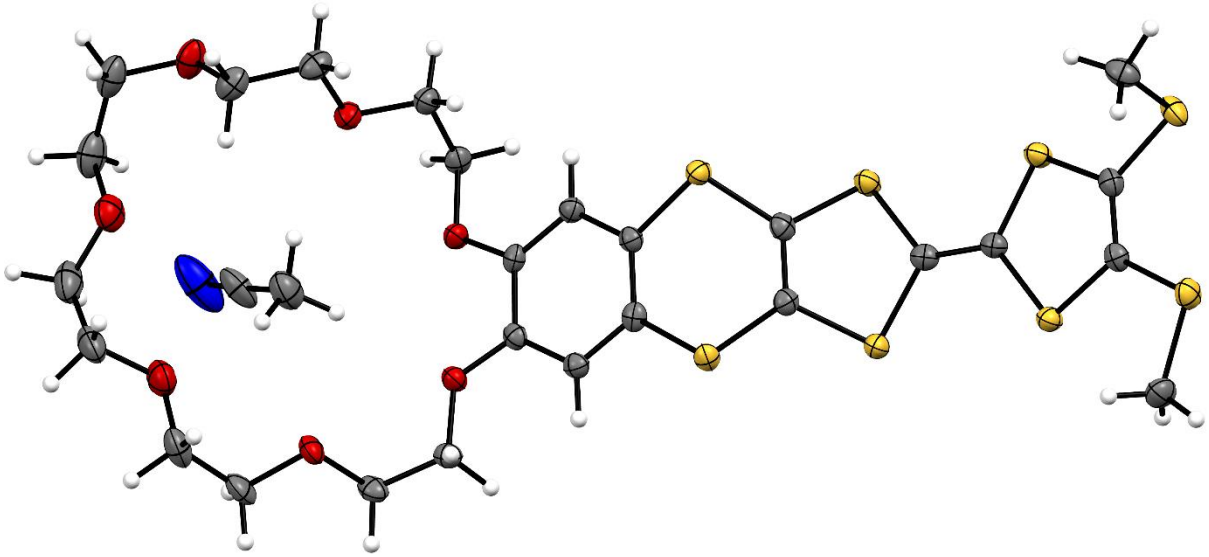

Figure S1: Thermal ellipsoid diagram of **exTTFC7** with 50% ellipsoid probability level. Colour codes: C (dark grey), H (white), N (blue), O (red) and S (yellow).

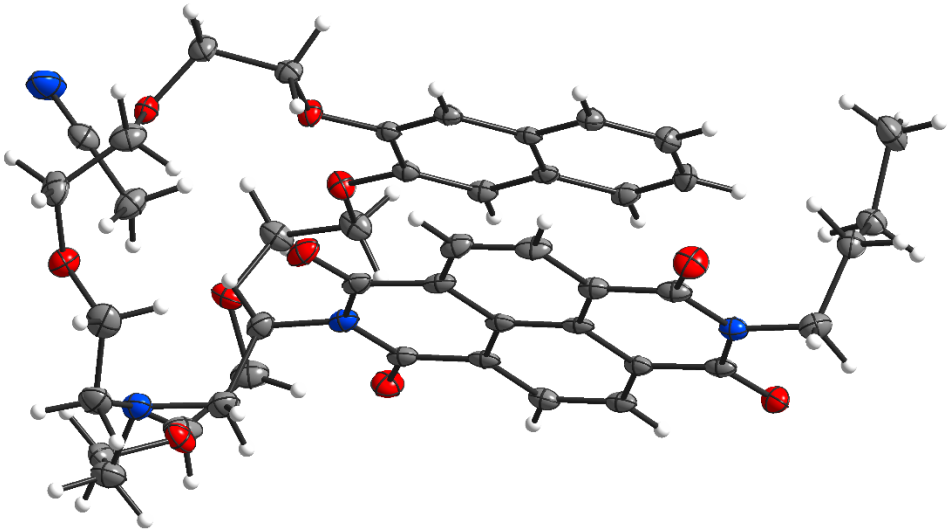

Figure S2: Thermal ellipsoid diagram of **NDIC7** with 50% ellipsoid probability level. Colour codes: C (dark grey), H (white), N (blue) and O (red).

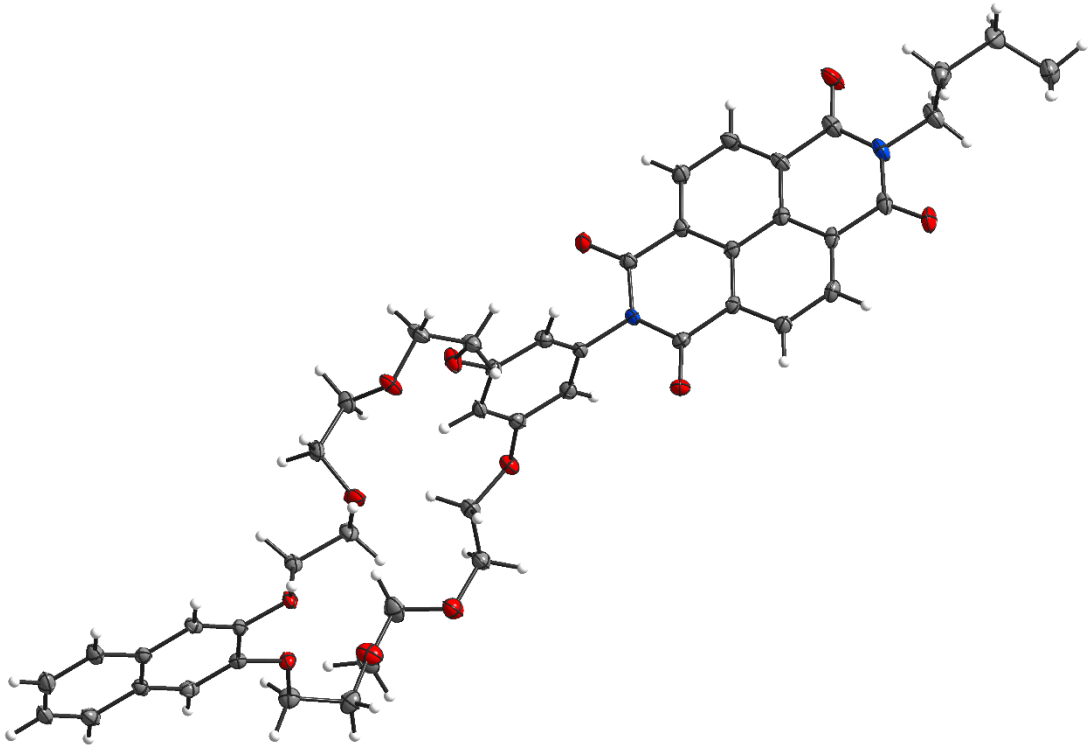

Figure S3: Thermal ellipsoid diagram of **NDIC8** with 50% ellipsoid probability level. Colour codes: C (dark grey), H (white), N (blue) and O (red).

Table S1: Crystallographic data.

compound	exTTFC7	NDIC7	NDIC8
chemical formula	$C_{28}H_{35}NO_7S_8$	$C_{44}H_{50}N_4O_{10}$	$C_{46}H_{46}N_2O_{12}$
*M*r / g mol^{-1}	754.05	794.88	818.85
crystal system	monoclinic	monoclinic	monoclinic
space group	*P2$_1$/c*	*P2$_1$/c*	*P2$_1$*
a / Å	31.5592(13)	13.6717(13)	19.695(4)
b / Å	12.8309(5)	9.8821(10)	9.1282(16)
c / Å	8.3107(3)	28.639(3)	21.618(4)
α / °	90	90	90
β / °	94.379(3)	90.657(4)	96.451(11)
γ / °	90	90	90
V / Å	3355.5(2)	3869.1(7)	3861.8(13)
Z	4	4	4
density / g cm^{-3}	1.493	1.365	1.408
F(000)	1576	1688	1728
radiation type	CuK_α	MoK_α	CuK_α
μ / mm^{-1}	5.317	0.097	0.845
crystal size / mm	0.12 x 0.09 x 0.05	0.42 x 0.22 x 0.10	0.31 x 0.09 x 0.07
meas refl.	13226	134093	125951
indep. refl.	6545	7104	16640
obsvd. [I > 2σ(I)] refl.	5274	5843	14307
max. and min. transmission	0.842, 0.629	0.745, 0.708	0.727, 0.654
R_{int}	0.0344	0.0678	0.0897
R [$F^2 > 2\sigma(F^2)$], wR(F^2), S	0.0487, 0.0860, 1.034	0.0522, 0.1254, 1.103	0.0449, 0.1064, 1.033
$\Delta\rho$max, $\Delta\rho$min (e Å^{-3})	0.487, -0.326	0.597, -0.285	0.663, -0.319

3. Isothermal titration calorimetry

ITC titrations were carried out in dry 1,2-dichloroethane (DCE) at 298 K on a TAM III microcalorimeter (Waters GmbH, TA Instruments, Eschborn, Germany). In a typical experiment, an 800 µL solution of the crown ether was placed in the sample cell at a concentration of 1.1 mM, and 250 µL of a solution of the ammonium salt (8.0 mM) were put into the syringe. The titrations consisted of 32 consecutive injections of 8 µL each with a 20 min interval between the injections. The heat of dilution was determined by titration of ammonium salt solutions into the sample cell containing blank solvent and were subtracted from each data set. The heat flow generated in the sample cell was measured as a differential signal between sample and reference cell. Hence, an exothermic event results in a positive and an endothermic in a negative heat flow. The data were analysed using the instrument's internal software package and fitted with a 1:1 binding model. Each titration was conducted at least three times and the measured values for K and ΔH were averaged.

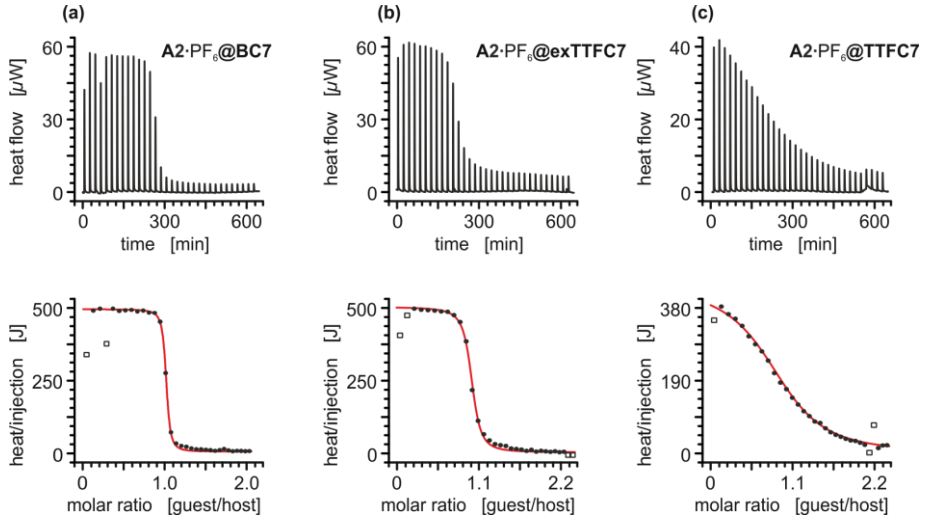

Figure S4: Titration plots (heat flow versus time and heat/volume versus guest/host ratio) obtained from ITC experiments at 298 K in 1,2-dichloroethane: (a) vial: **BC7**, syringe: axle **A2**•PF_6; (b) vial: **exTTFC7**, syringe: axle **A2**·PF_6; (c) vial: **TTFC7**, syringe: axle **A2**•PF_6. Points marked with non-filled squares were not considered in the fitting process.

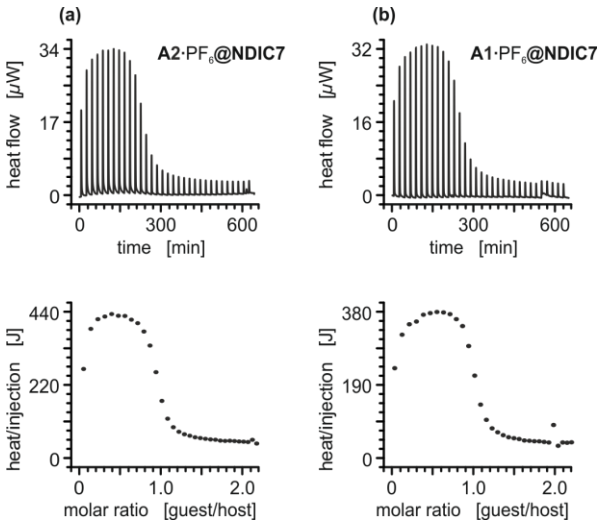

Figure S5: Titration plots (heat flow versus time and heat/volume versus guest/host ratio) obtained from ITC experiments at 298 K in 1,2-dichloroethane: (a) vial: **NDIC7**, syringe: axle **A2**•PF_6; (b) vial: **NDIC7**, syringe: axle **A1**•PF_6.The data points of the **A2**•PF_6@**NDIC7** do not agree with a 1:1 binding model. The increasing heat generated in the first 5 data points suggests a second process taking place in the mixture, which could be explained with the protonation of the tertiary amine of **NDIC7** by **A2**•PF_6. **A1**•PF_6 is sterically too big to thread **NDIC7** for a pseudo[2]rotaxane. Yet, the titration of **NDIC7** with the larger axle **A1**•PF_6 exhibits very similar results as with the smaller axle **A2**•PF_6. These results suggest that both ammonium axles undergo a similar type of reaction with **NDIC7**, which could be the protonation of the tertiary amine or the complexation in a non-threaded complex.

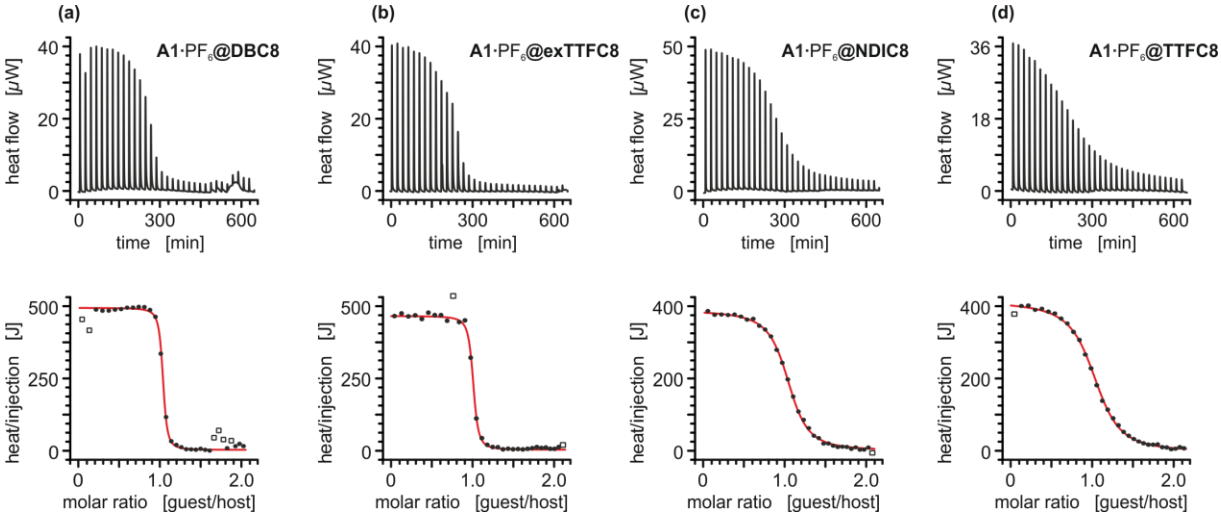

Figure S6: Titration plots (heat flow versus time and heat/volume versus guest/host ratio) obtained from ITC experiments at 298 K in 1,2-dichloroethane: (a) vial: **DBC8**, syringe: axle **A2**•PF_6; (b) vial: **exTTFC8**, syringe: axle **A2**•PF_6; (c) vial: **NDIC8**, syringe: axle **A2**•PF_6; (d) vial: **TTFC8**, syringe: axle **A2**•PF_6. Points marked with non-filled squares were not considered in the fitting process.

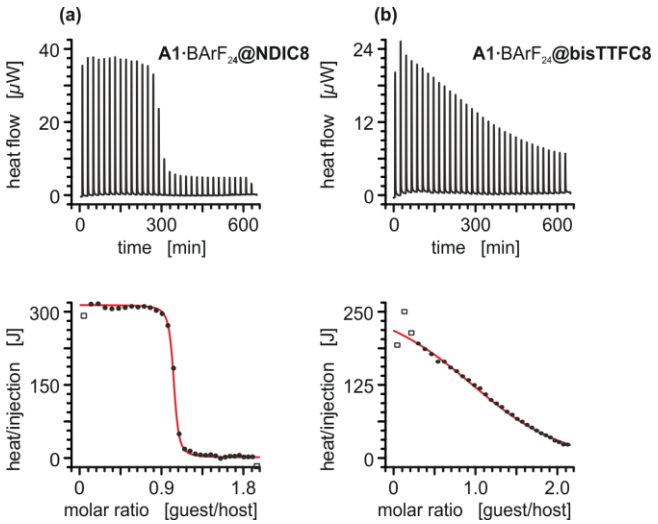

Figure S7: Titration plots (heat flow versus time and heat/volume versus guest/host ratio) obtained from ITC experiments at 298 K in 1,2-dichloroethane: (a) vial: **DBC8**, syringe: axle **A1**•PF_6; (b) vial: **exTTFC8**, syringe: axle **A1**•PF_6; (c) vial: **NDIC8**, syringe: axle **A1**•PF_6; (d) vial: **TTFC8**, syringe: axle **A1**•PF_6. Points marked with non-filled squares were not considered in the fitting process.

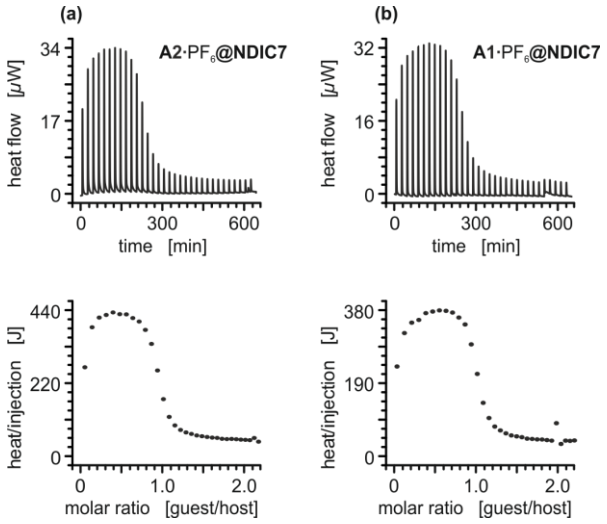

Figure S8: Titration plots (heat flow versus time and heat/volume versus guest/host ratio) obtained from ITC experiments at 298 K in 1,2-dichloroethane: (a) vial: **NDIC8**, syringe: axle **A1**•$BArF_{24}$; (b) vial: **bisTTFC8**, syringe: axle **A1**•$BArF_{24}$. Points marked with non-filled squares were not considered in the fitting process.

4. Electrochemical measurements

Cyclic voltammetry (CV) and differential pulse voltammetry (DPV) were performed on an Autolab PGSTAT302N potentiostat using a three-electrode configuration: a freshly polished glassy carbon working electrode, a platinum wire counterelectrode and a silver wire pseudoreference electrode. The decamethylferrocene/decamethylferrocenium ($FeCp^*_2^{(0/+)}$) couple was used as internal reference. Dry and argon purged solvents were used. Half-wave potentials were determined by DPV measurements and confirmed with CV (scan rate 100 mV s^{-1}), which also ensured reversibility of the reduction or oxidation processes. During experiments using axle **A1**•PF_6, an irreversible oxidation at ≈1.4 V vs. $FeCp^*_2^{(0/+)}$ was observed after addition of the axle. We address this signal to the oxidation of the axle phenol ether unit. The cyclic voltammogram traces of **NDIRot** were recorded with 10, 25, 50, 100, 250, 500, 1000, and 2500 mV/s scan rates, to ensure that the observed processes are reversible and diffusion limited. In order to obtain the correct half-wave potentials, $FeCp^{*0}$/$FeCp^{*+}$ was used as the reference. These values were later referenced to $FeCp/FeCp^+$ as described in the literature [20]. The raw data was treated with Nova 1.5 by Metrohm and the plots were made with Origin *8* by OriginLab.

Table S2: Electrochemical data obtained by differential pulse voltammetry.

entry	compound	solvent[a]	$E_{1/2}^{r2}$ / V[b]	$E_{1/2}^{r1}$ / V[b]	$E_{1/2}^{o1}$ / V[b]	$E_{1/2}^{o2}$ / V[b]
			reversible reductions		reversible oxidations	
1	**exTTFC7**	DCE/	/	/	0.67	0.95
2	**exTTFC7** + **A2**·PF_6[d]	CH_3CN	/	/	0.67	0.95
3	**exTTFC8**[c]	(1:1)	/	/	0.66	0.93
4	**exTTFC8** + **A1**·PF_6[d]		/	/	0.67	0.91
5	**TTFC7**		/	/	0.59	0.83
6	**TTFC7** + **A2**·PF_6[d]		/	/	0.60	0.84
7	**TTFC8**		/	/	0.59	0.83
8	**TTFC8** + **A1**·PF_6[d]		/	/	0.59	0.82
9	**bisTTFC8**[c]		/	/	0.57	0.93
10	**bisTTFC8** + **A1**·PF_6[d]		/	/	0.57	0.92
11	**NDIC7**		-0.96	-0.54	/	/
12	**NDIC7** + **A2**·PF_6[d]		-0.70	-0.46	/	/
13	**NDIC8**[c]		-0.95	-0.49	/	/
14	**NDIC8**[c] + **A1**·PF_6[d]		-0.72	-0.49	/	/
15	**NDIC8**[c] + $(CH_3)_2NH_2PF_6$[d]		-0.78	-0.45		
16	**NDIC8Rot**		-0.95	-0.50		
17	**exTTFC7**	DCE	/	/	0.65	1.01
18	**exTTFC7** + **A2**·PF_6[d]		/	/	0.67	1.01
19	**TTFC7**		/	/	0.59	0.87
20	**TTFC7** + **A2**·PF_6[d]		/	/	0.63	0.87
21	**bisTTFC8**		/	/	0.56	0.95
22	**NDIC8**[c]		-0.97	-0.53	/	/
23	**NDIC8Rot**		-0.96	-0.51	/	/

[a]With *n*-Bu_4NPF_6 (0.1 M) as the electrolyte. [b]Half-wave potentials are given against the decamethylferrocene/decamethylferrocenium couple as the reference; error = ± 0.01 V. [c]The compound showed only moderate solubility in the corresponding solvent. [d]Five equiv of the ammonium guest were added.

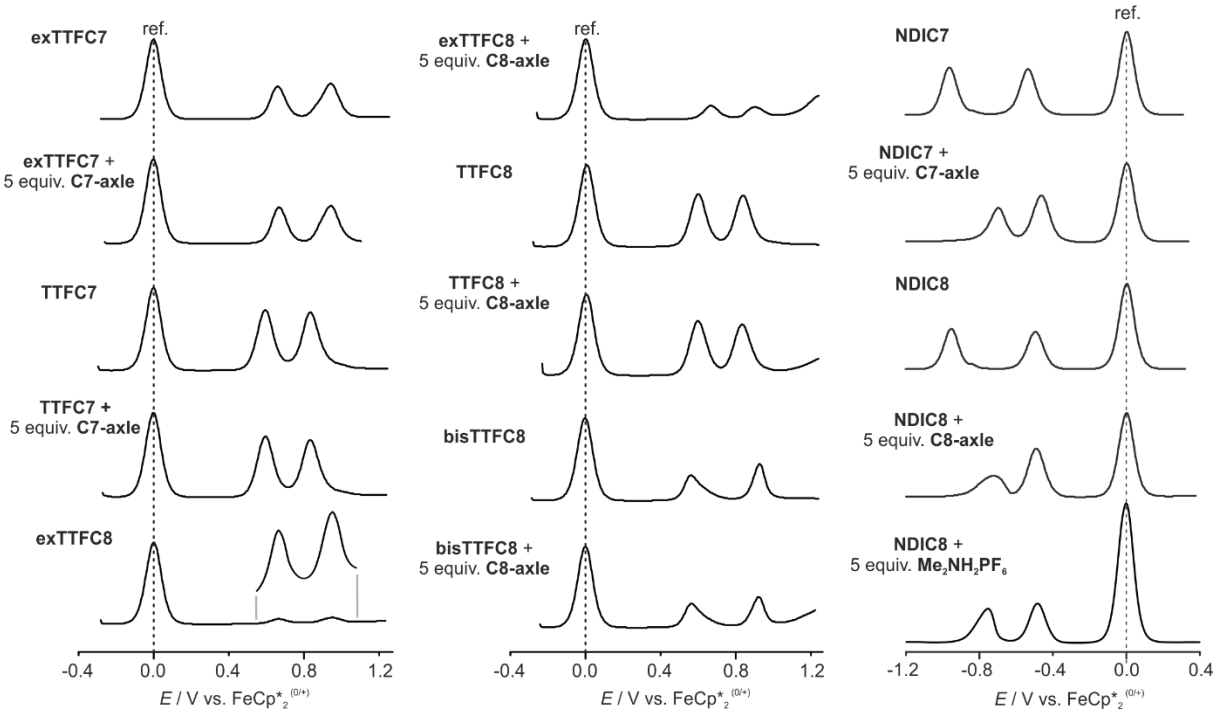

Figure S9: Differential pulse voltammograms (1 mM analyte, DCE/CH_3CN 1:1, 0.1 M *n*-Bu_4PF_6, 10 mV s^{-1} scan rate, 25 mV modulation amplitude, 50 ms modulation time, 5 mV step potential, 0.5 s interval time).

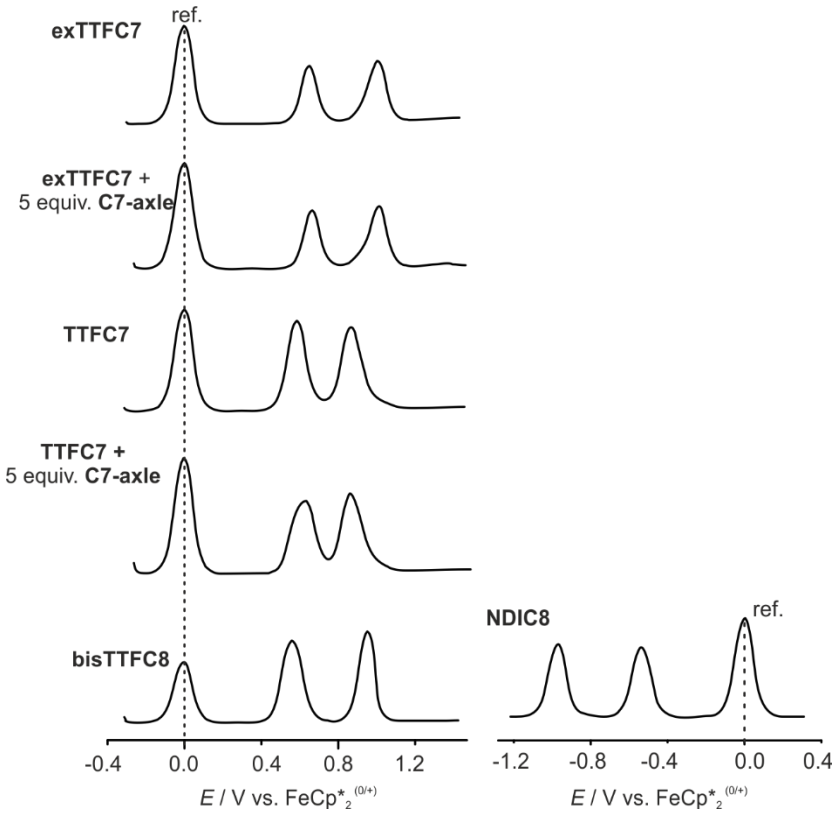

Figure S10: Differential pulse voltammograms (1 mM analyte, DCE, 0.1 M *n*-Bu_4PF_6, 10 mV s^{-1} scan rate, 25 mV modulation amplitude, 50 ms modulation time, 5 mV step potential, 0.5 s interval time).

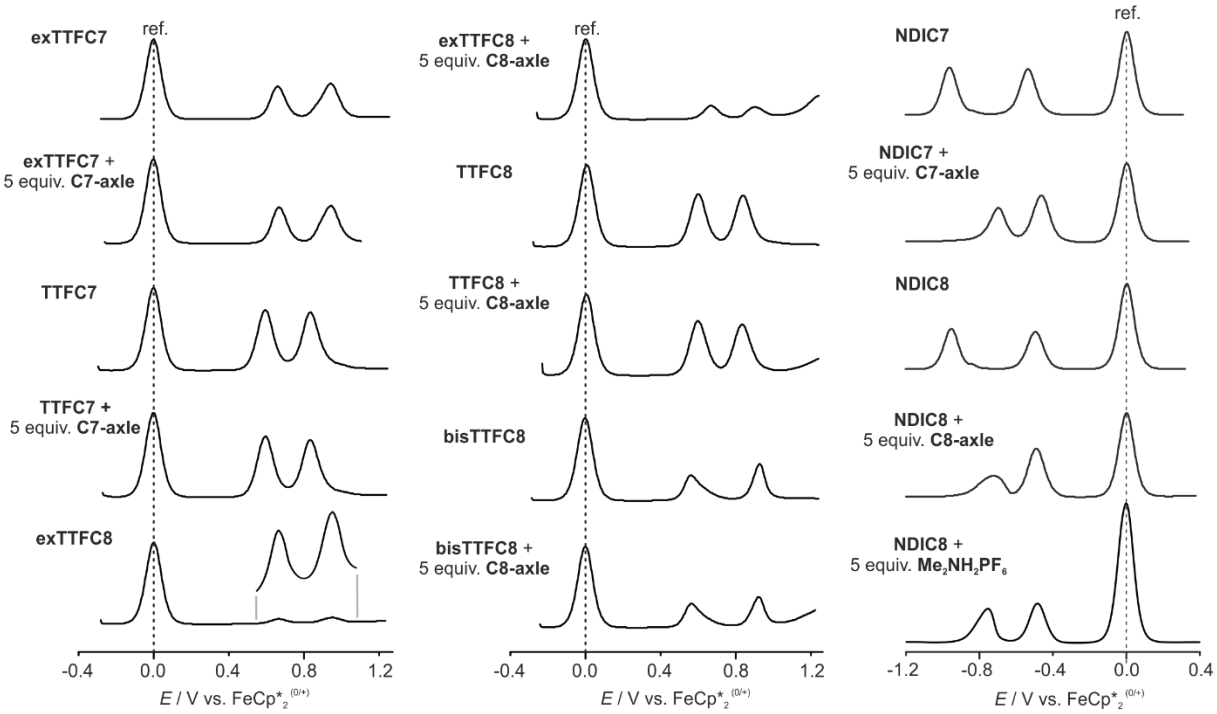

Figure S11: Differential pulse voltammogram (10 mV s^{-1} scan rate, 25 mV modulation amplitude, 50 ms modulation time, 5 mV step potential, 0.5 s interval time) and cyclic voltammogram (100 mV s^{-1}) of [2]rotaxane **NDIRot** (1.0 mM) in mixture of DCE/CH_3CN 1:1 and pure DCE (0.1 M *n*-Bu_4PF_6). The small signal at approximately −0.8 V was observed before adding the rotaxane and is addressed to an impurity. The decamethylferrocene/decamethylferrocenium couple was used as reference.

5. Rotaxane characterization

5.1. 2D NMR spectroscopy

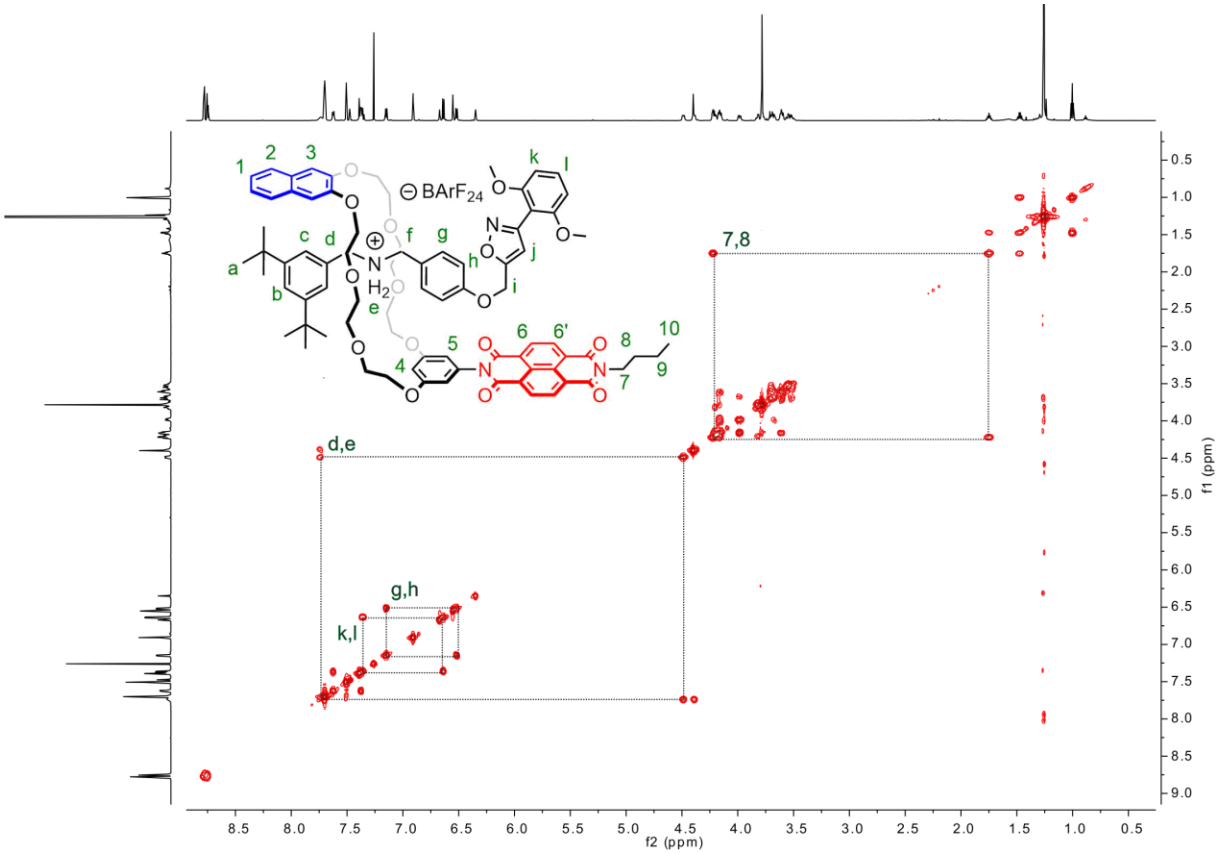

Figure S12: ^{1}H, ^{1}H COSY NMR spectrum (700 MHz, $CDCl_3$, 298 K) of rotaxane **NDIRot** with selected cross peaks for peak assignment.

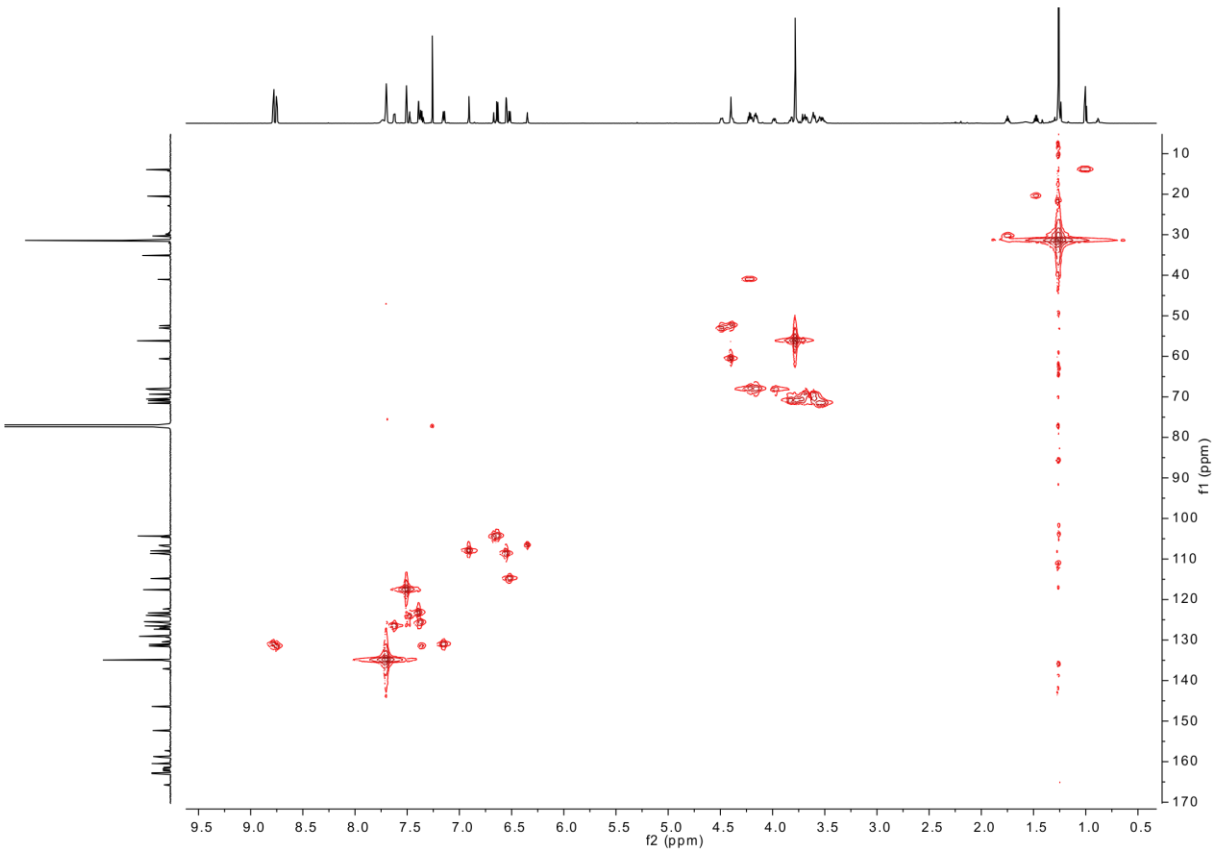

Figure S13: ^{1}H, ^{13}C HMQC NMR spectrum (700 MHz, $CDCl_3$, 298 K) of rotaxane **NDIRot**.

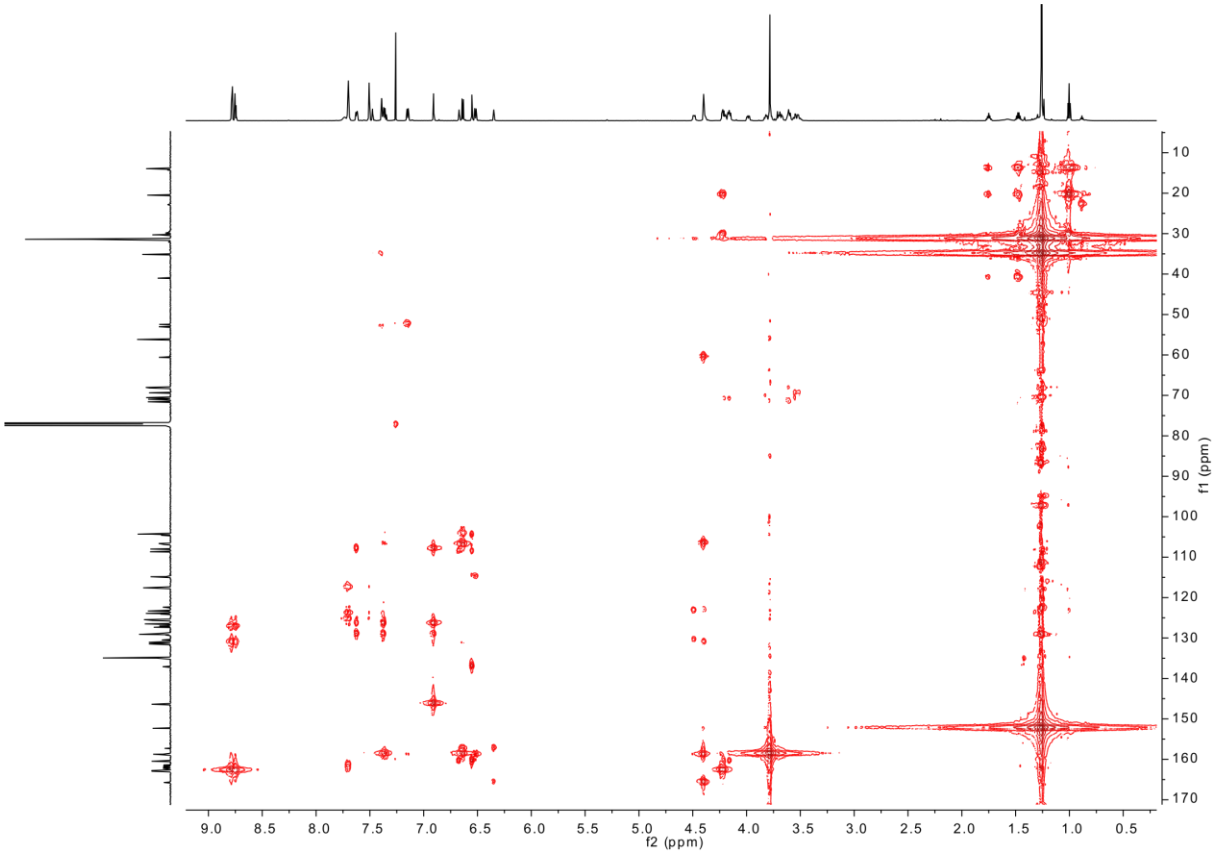

Figure S14: ^{1}H, ^{13}C HMBC NMR spectrum (700 MHz, $CDCl_3$, 298 K) of rotaxane **NDIRot**.

5.2. Tandem mass spectrometry

A Synapt G2-S HDMS (Waters Co., Milford, MA, USA) instrument with a quadrupole-time-of-flight high resolution mass detector was used to perform electrospray ionization tandem mass spectrometry. Employing collision-induced dissociation (CID) of mass-selected ions, using the following settings: flow rate 10 µL min^{-1}, capillary voltage 1.5 kV, sample cone voltage 34 V, source offset 54 V, source temperature 100 °C, desolvation temperature 20 °C, nebulizer gas 5 bar, desolvation gas flow 460 L h^{-1}. For CID, N_2 was used as the collision gas. Fragmentation experiments were conducted in the trap cell of the Synapt G2-S HDMS instrument with collision energies of 4–72 V. Data acquisition and processing was carried out using MassLynx™ (version 4.1).

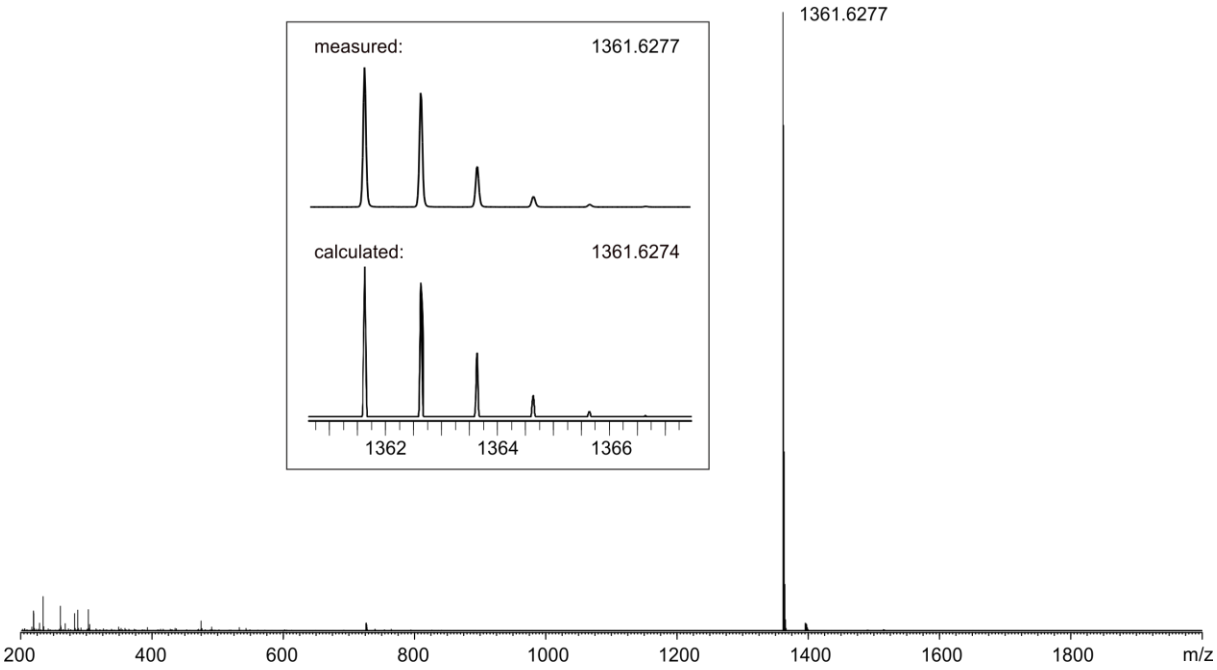

Figure S15: ESI-Q-TOF-HRMS spectrum of **NDIRot** (1 µM in CH_3CN); (inset) comparison of measured and calculated isotopic patterns.

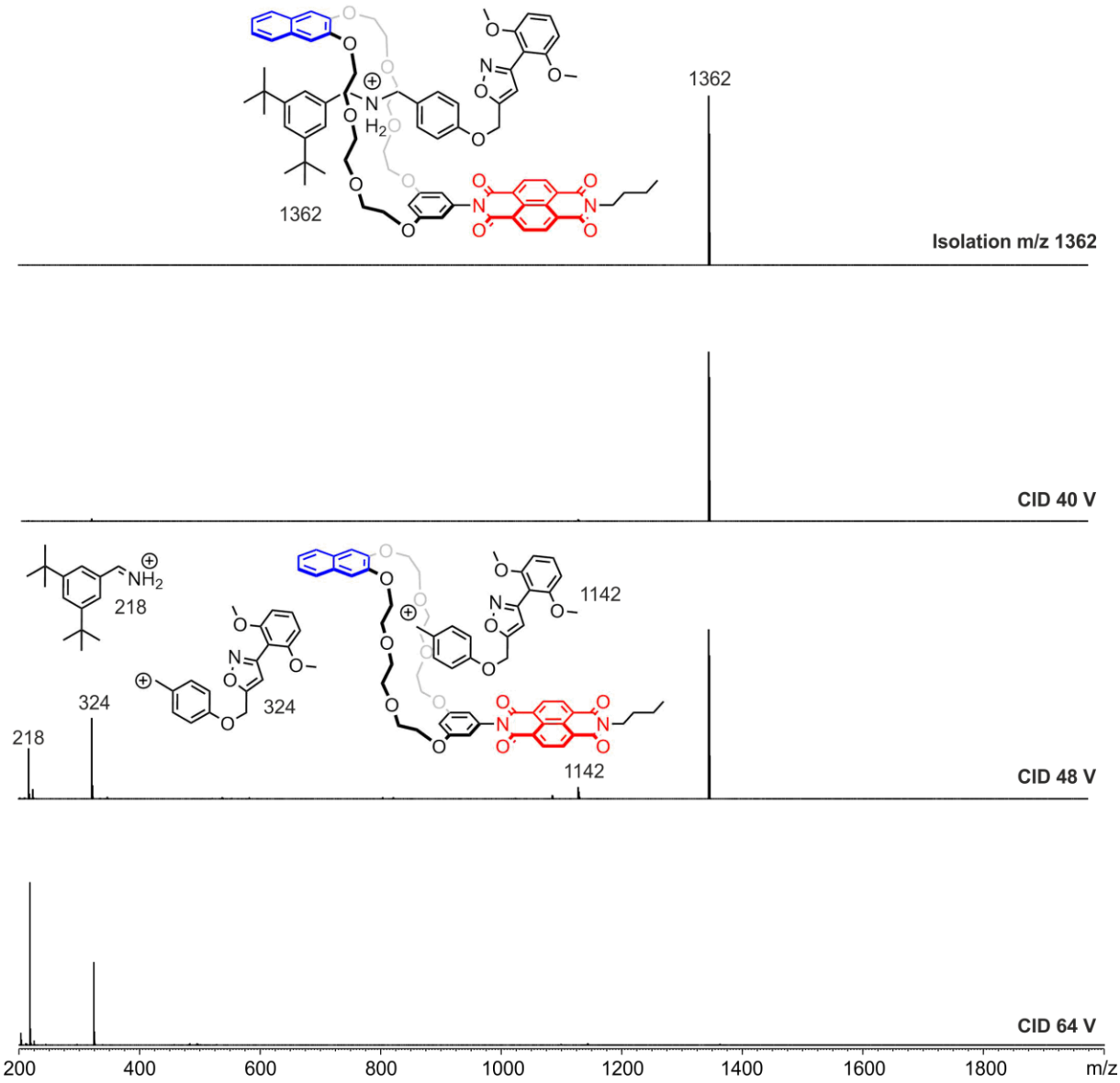

Figure S16: Collision-induced dissociation (CID) experiment with mass-selected rotaxane ions at *m/z* 1362 obtained from a CH_3CN solution (1 µM) of **NDIRot**: (top) after mass selection; (bottom) after fragmentation at different voltages. The fragment peaks could be assigned to ions formed by α-cleavage at the ammonium group of the axle. As no free axle (*m/z* 543) is observed in the fragmentation pattern, the interlocked structure of the selected rotaxane ion can be concluded.

6. Spectroelectrochemical measurements

UV–vis–NIR

The UV–vis–NIR spectroelectrochemistry measurements were performed on an Avantes spectrometer with an AvaLight-DH-S-Bal light source, an AvaSpec-ULS2048 UV/Vis detector, and an AvaSpec-NIR256-TEC NIR detector. Dry, freshly distilled and Argon purged solvents (CH_3CN and CH_2Cl_2) were used. The measurements were carried out in an optically transparent thin-layer electrochemical (OTTLE) cell (CaF_2 windows) with a platinum-mesh working electrode, a platinum-mesh counter electrode, and a silver-foil pseudoreference electrode. Voltammetric cycles between 0 and −1.2 V (vs. silver pseudoreference) were performed.

Table S3: Absorption maxima[a] (in nm) obtained by spectroelectrochemistry UV–vis–NIR measurements (0.1 M *n*-Bu_4PF_6, CH_2Cl_2/CH_3CN 1:1, 298 K).

oxidation state	NDIC7	NDIC8	NDIRot
NDI (0.0 V)	325, 342 (sh), 360, 380, 450 (sh)	324, 341 (sh), 359, 379	324, 341 (sh), 359, 379
$NDI^{\bullet-}$ (-0.6 V)	380, 402, 477, 528 (sh), 561 (sh), 592, 611, 674, 750	358, 380, 400, 476, 527 (sh), 589 (sh), 609, 685, 763	341, 359, 379, 399, 476, 527 (sh), 559 (sh), 589 (sh), 609, 689, 763
NDI^{2-} (-1.2 V)	379, 400, 422, 476, 549, 601, 675, 750	/[b]	/[b]

[a]sh = shoulder. [b]No significant band shifts and changes in absorbance were observed at more negative potential (−1.2 V vs silver wire), which can be explained by diffusion from the electrode and comproportionation of the doubly reduced species

Continuous-wave electron paramagnetic resonance spectroscopy

Continuous-wave electron paramagnetic resonance (CW-EPR) spectra at X-band frequency (ca. 9.5 GHz) were obtained with a Magnettech MS-5000 benchtop EPR spectrometer equipped with a rectangular TE 102 cavity and TC HO4 temperature controller. The measurements were carried out in synthetic quartz glass tubes. Dry, Argon purged and freshly distilled solvents were used. For the in situ preparation of the oxidized species, a three-electrode setup was employed using two Teflon-coated platinum wires (0.005″ bare, 0.008″ coated) as working and counter electrode and a Teflon-coated silver wire (0.005″ bare, 0.007″ coated) as pseudoreference electrode.

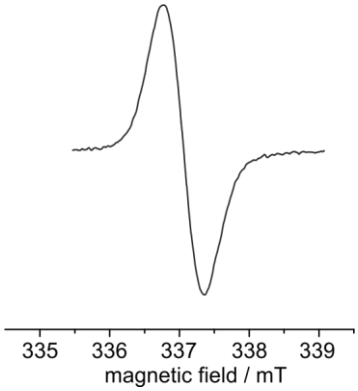

Figure S17: EPR spectroelectrochemistry measurements (0.1 M *n*-Bu_4PF_6, CH_2Cl_2/CH_3CN 1:1, 298 K) of radical species **NDIRot** (1 mM).

7. ^{1}H and ^{13}C NMR spectra

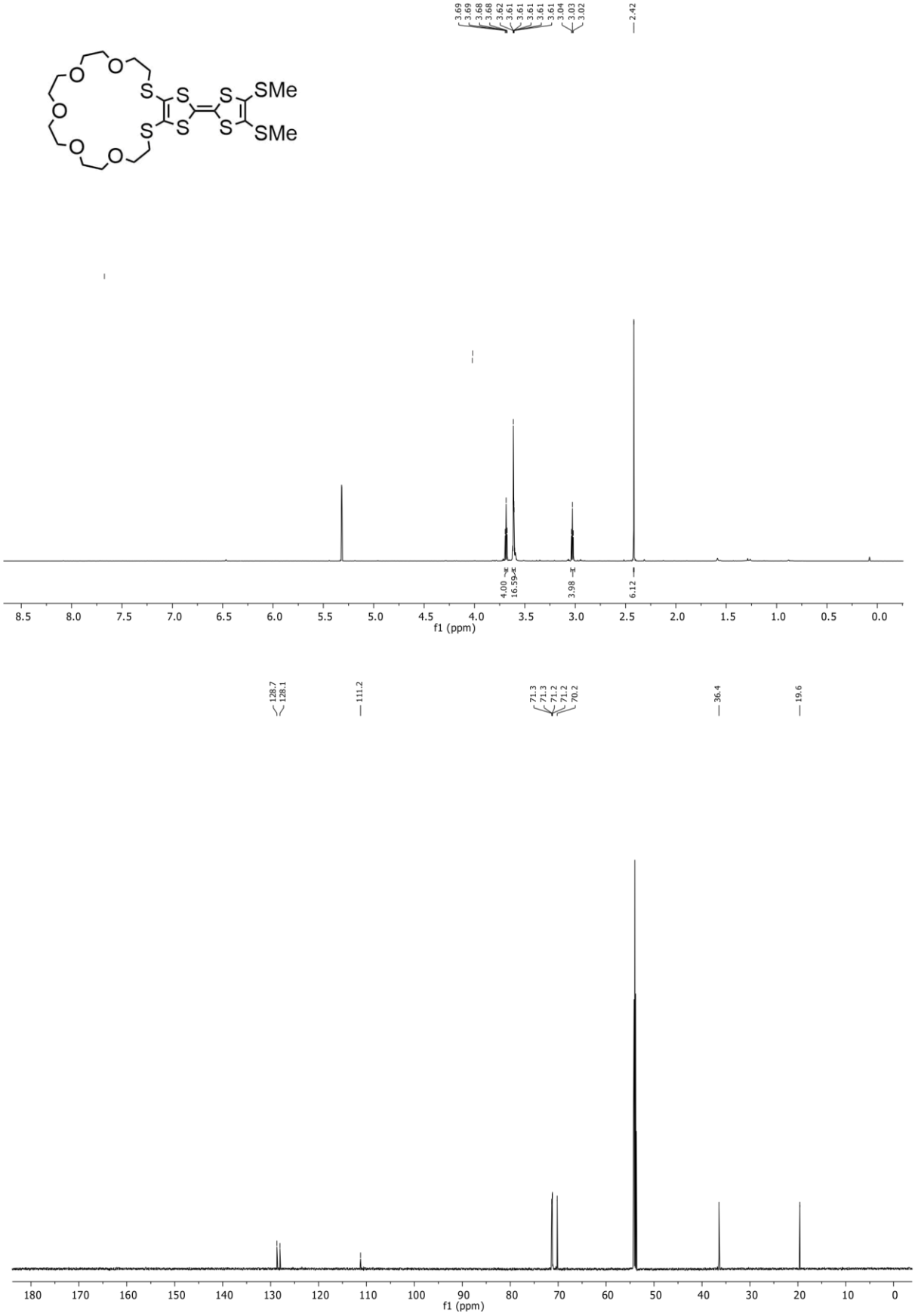

Figure S18: ^{1}H (top) and ^{13}C (bottom) NMR spectrum (700/176 MHz, CD_2Cl_2, 298 K) of **TTFC7**.

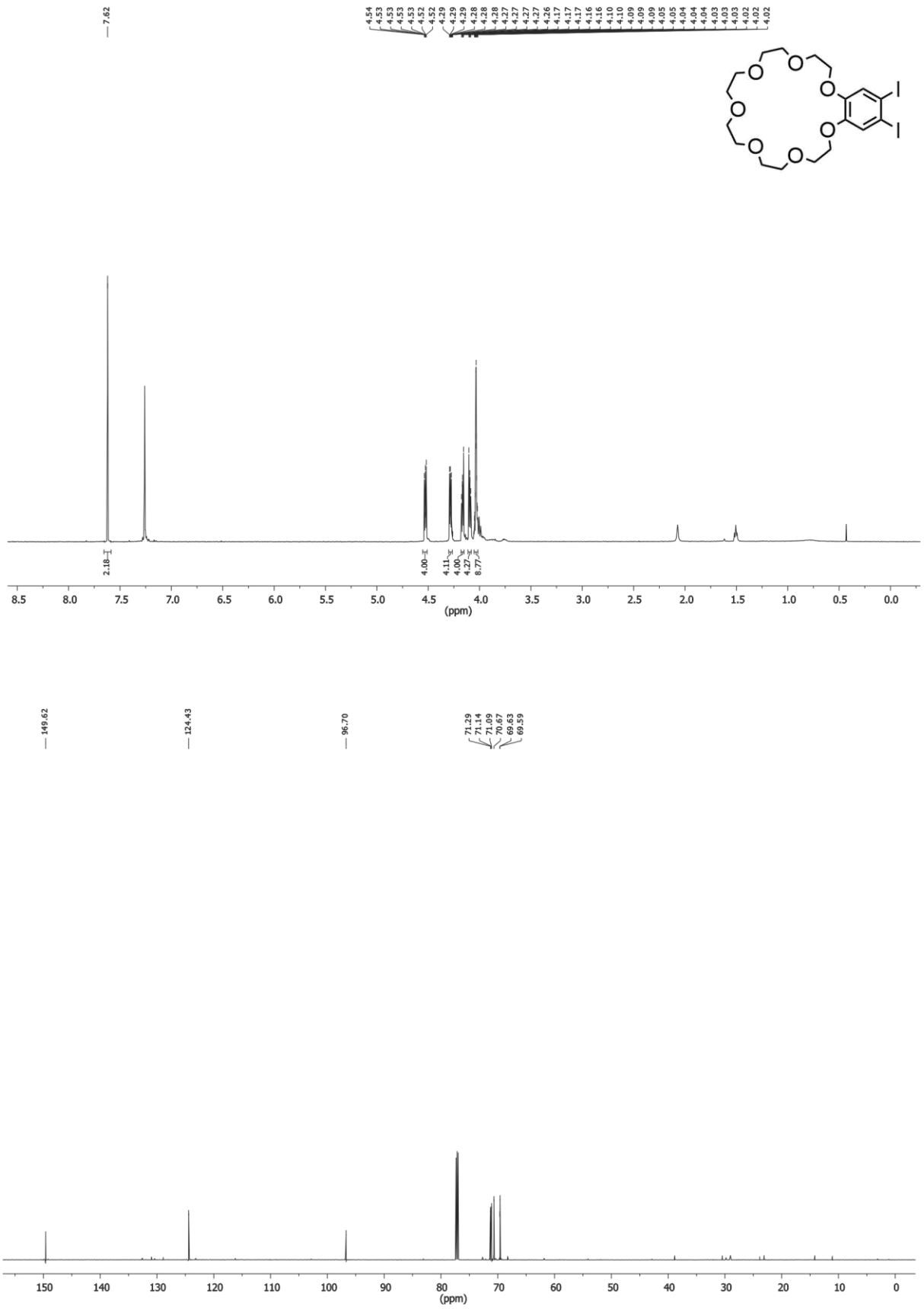

Figure S19: ^{1}H (top) and ^{13}C (bottom) NMR spectrum (500/176 MHz, $CDCl_3$, 298 K) of Diiodide **2**.

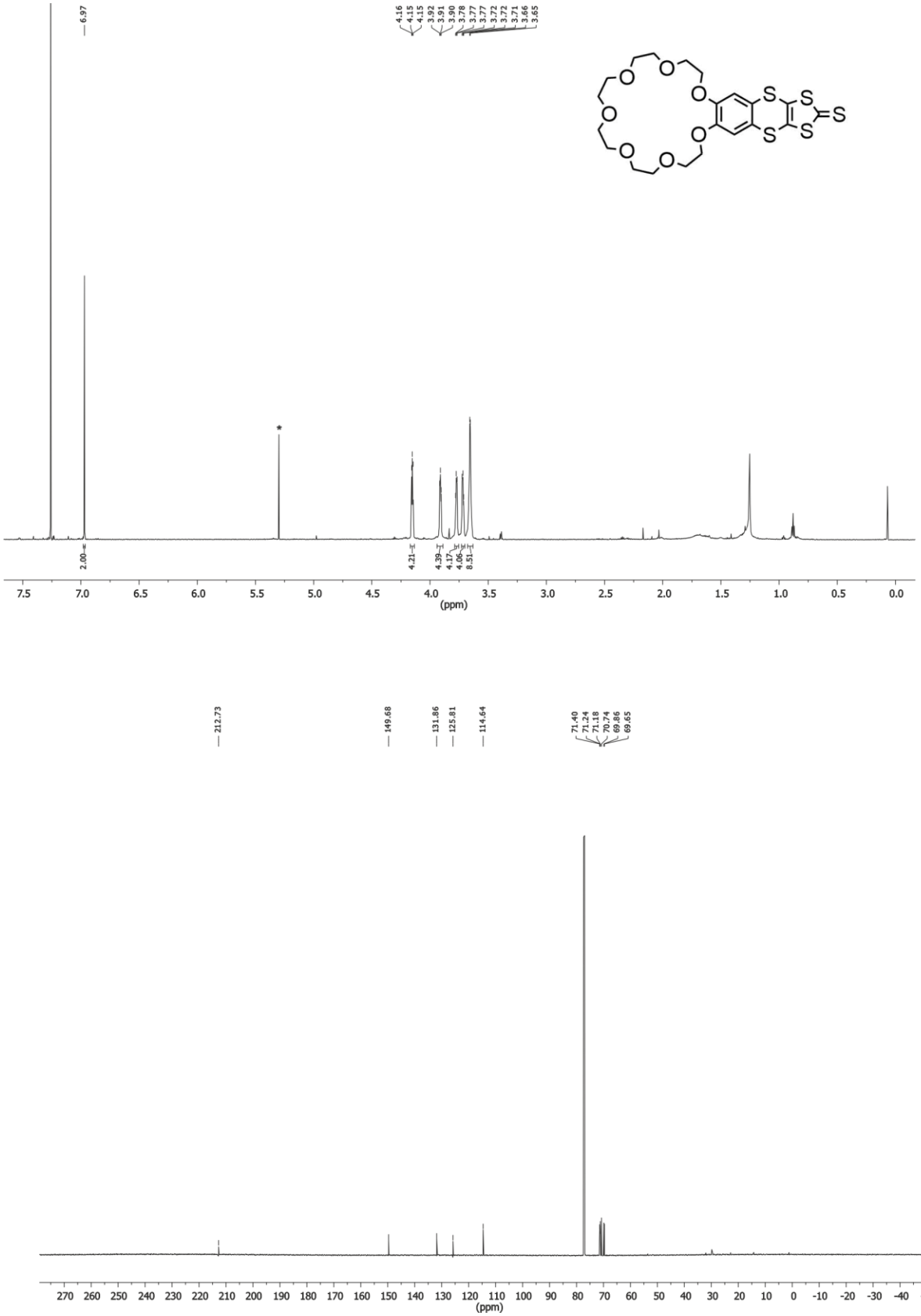

Figure S20: ^{1}H (top) and ^{13}C (bottom) NMR spectrum (500/176 MHz, $CDCl_3$, 298 K) of Thione **3**.

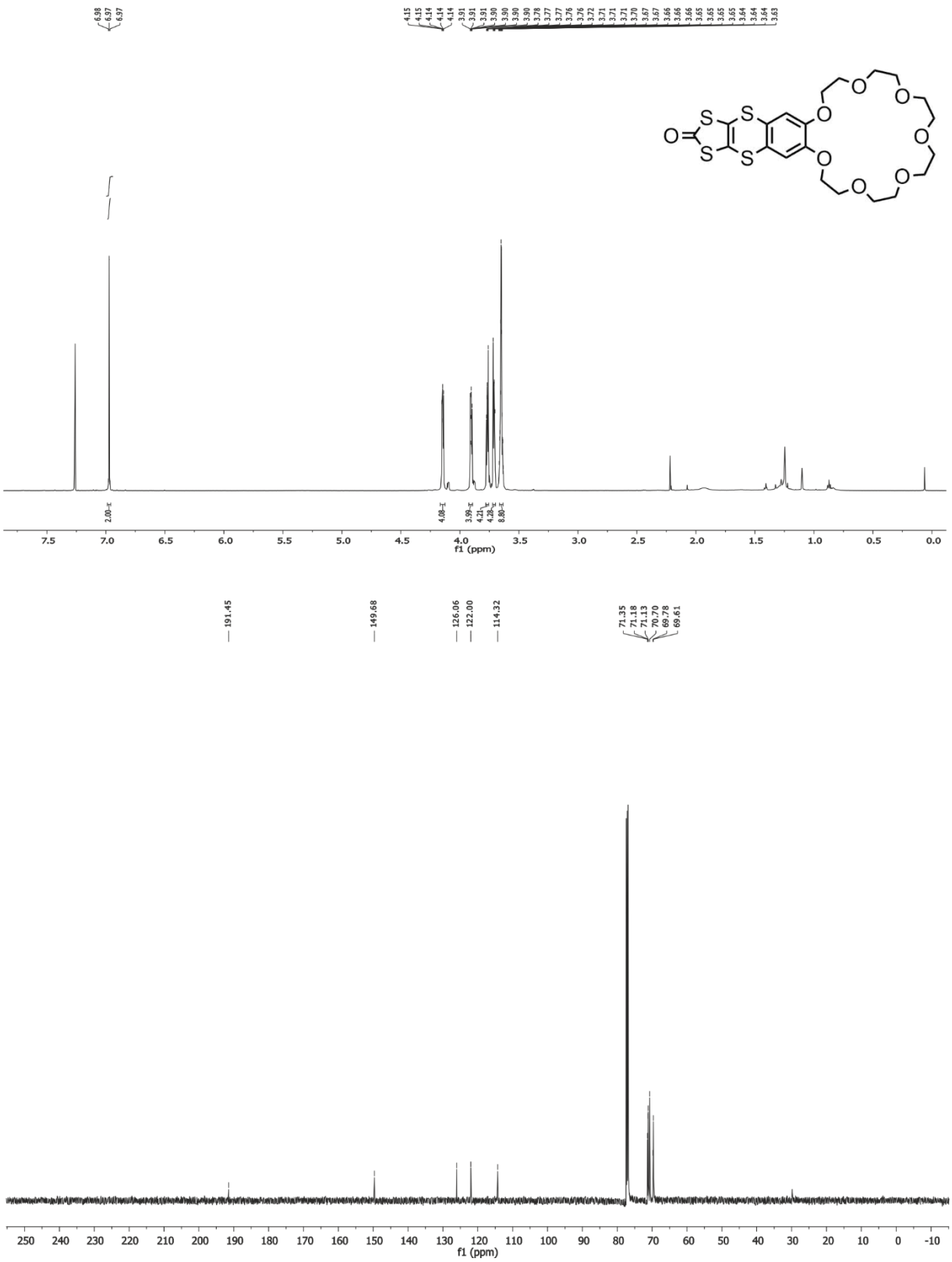

Figure S21: ^{1}H (top) and ^{13}C (bottom) NMR spectrum (500/176 MHz, $CDCl_3$, 298 K) of One **4**.

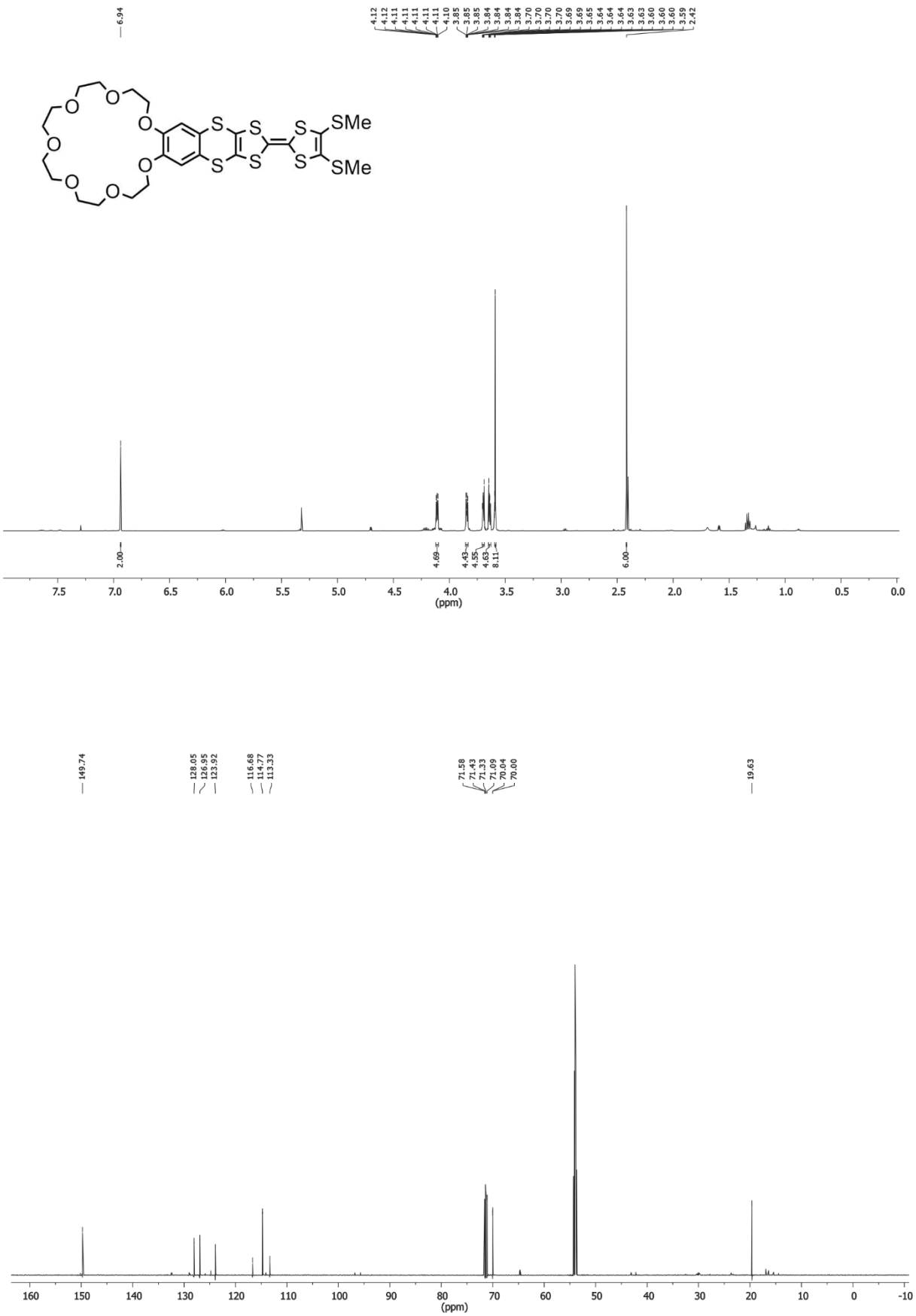

Figure S22: ^{1}H (top) and ^{13}C (bottom) NMR spectrum (700/176 MHz, CD_2Cl_2, 298 K) of **exTTFC7**.

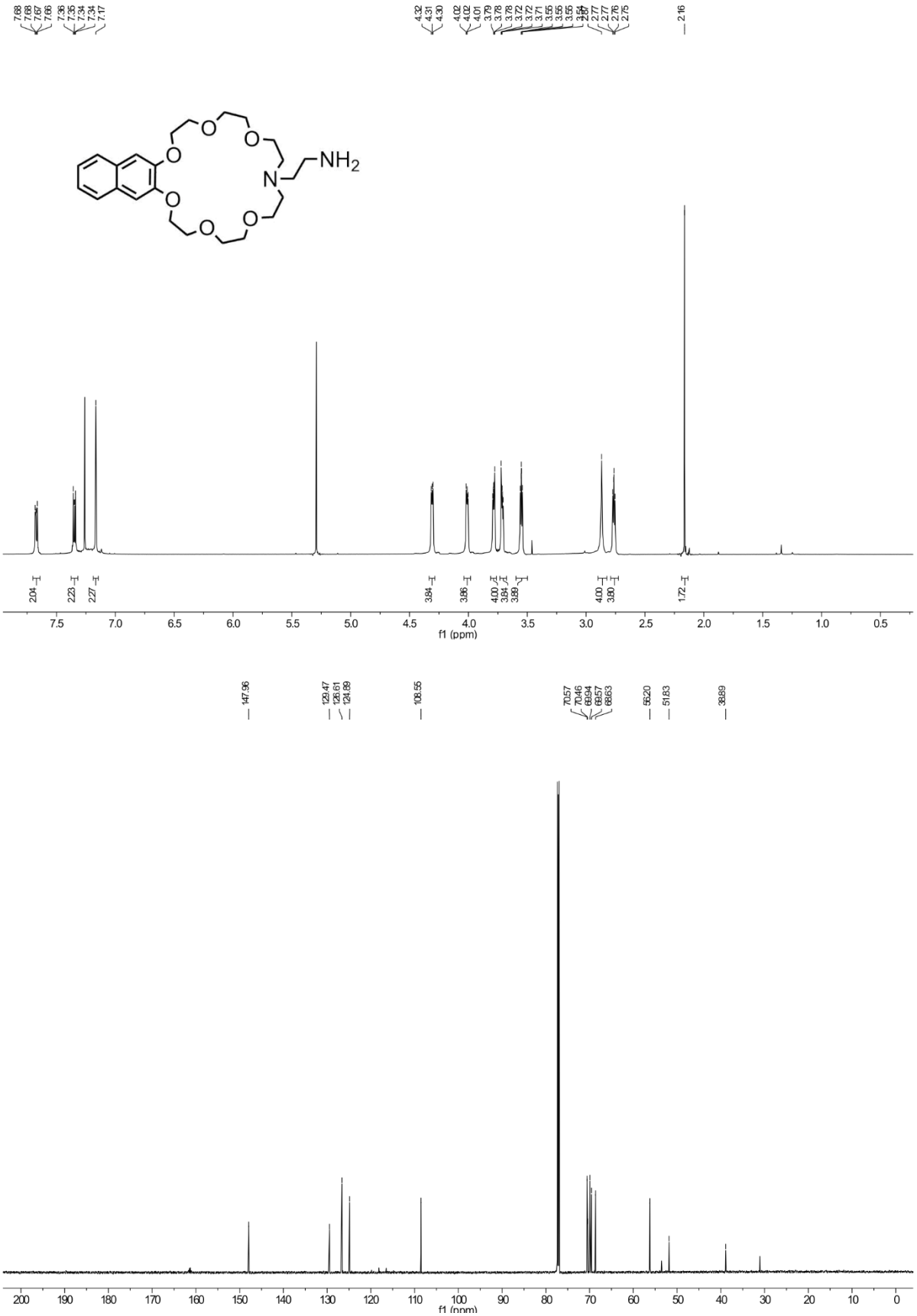

Figure S23: ^{1}H (top) and ^{13}C (bottom) NMR spectrum (500/176 MHz, $CDCl_3$ 298 K) of amine **6**.

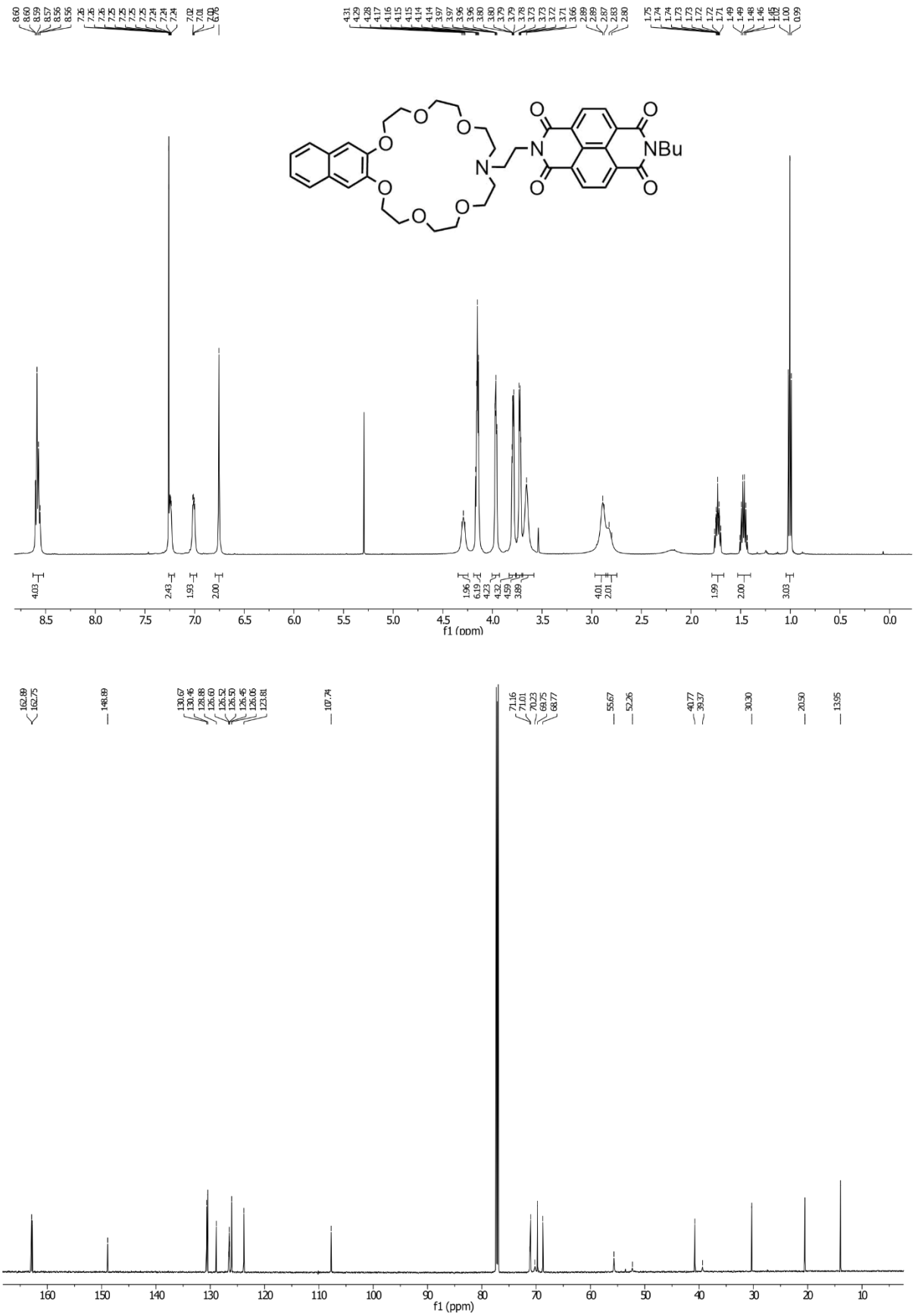

Figure S24: ^{1}H (top) and ^{13}C (bottom) NMR spectrum (500/176 MHz, $CDCl_3$, 298 K) of **NDIC7**.

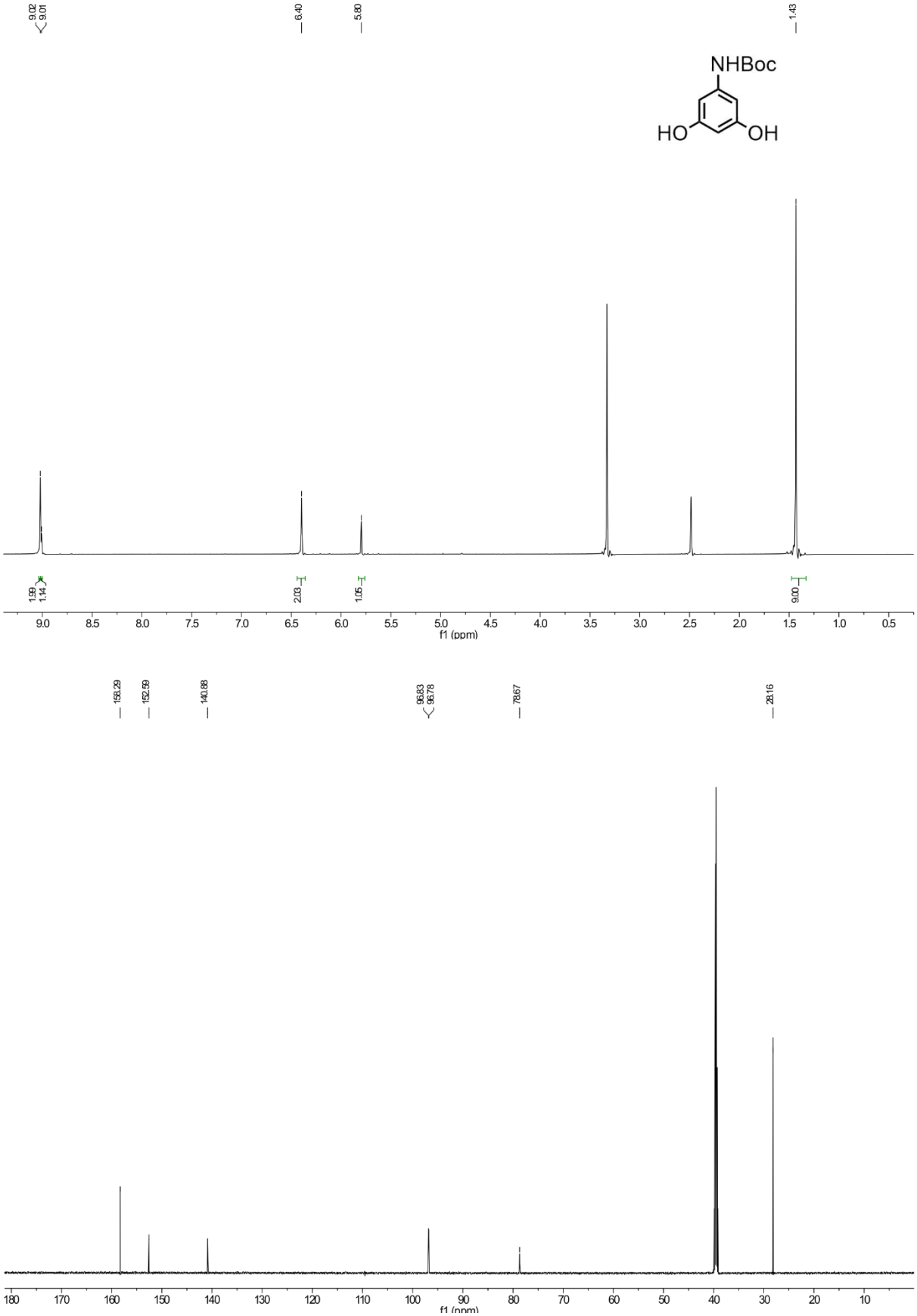

Figure S25: ^{1}H (top) and ^{13}C (bottom) NMR spectrum (700/176 MHz, $CDCl_3$, 298 K) of catechol **8**.

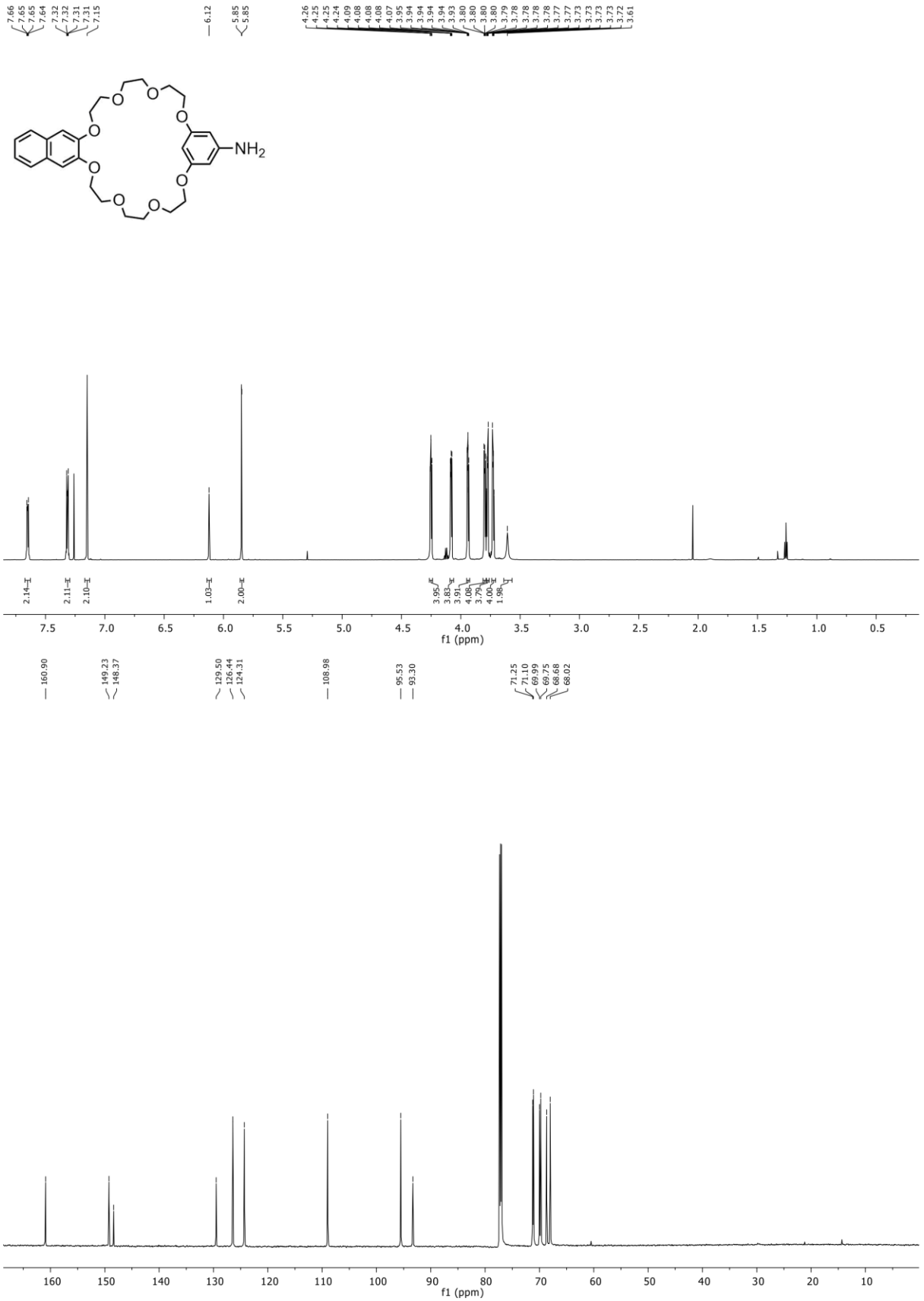

Figure S26: ^{1}H (top) and ^{13}C (bottom) NMR spectrum (700/176 MHz, $CDCl_3$, 298 K) of amine **9**.

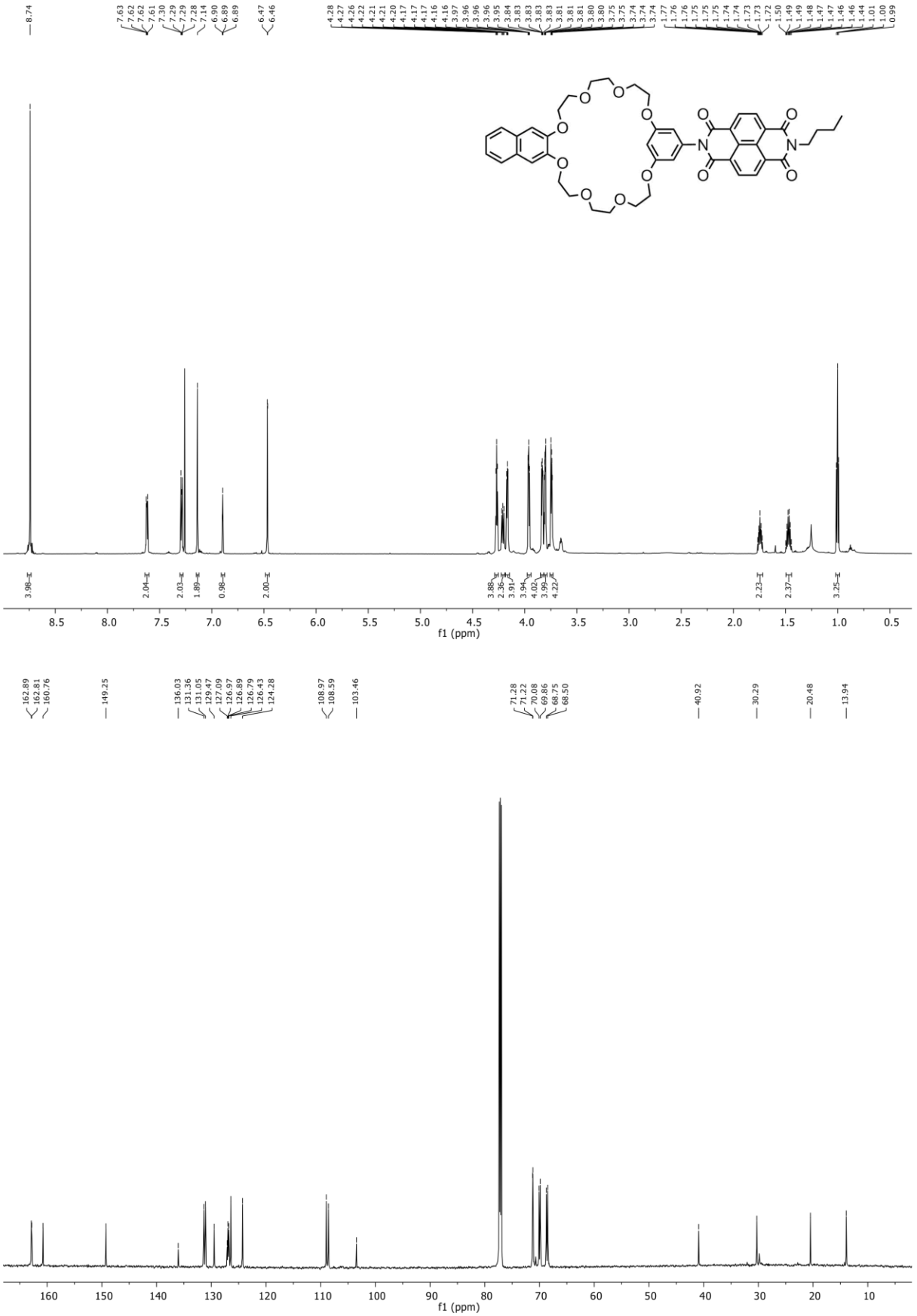

Figure S27: ^{1}H (top) and ^{13}C (bottom) NMR spectrum (700/176 MHz, $CDCl_3$, 298 K) of **NDIC8**.

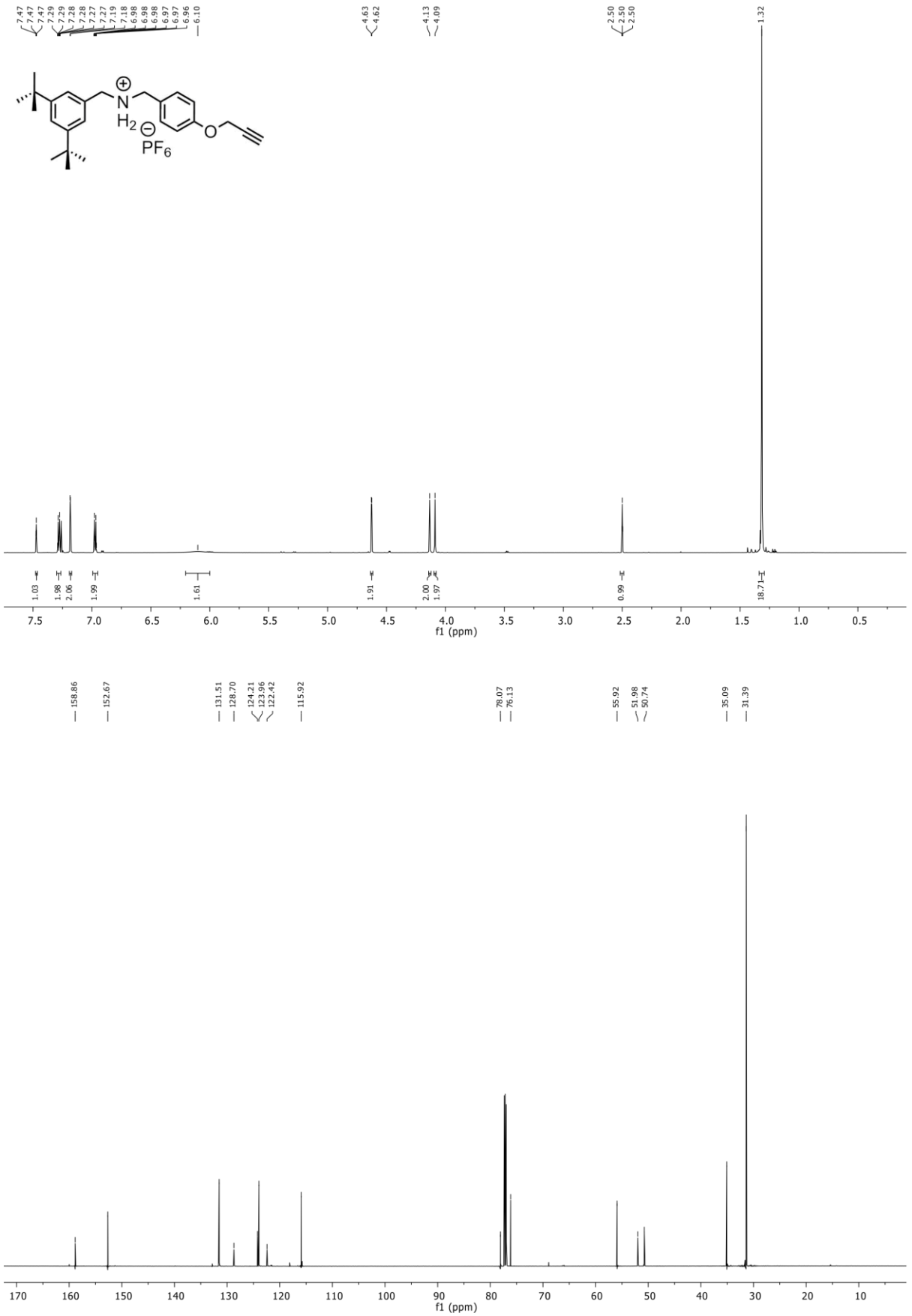

Figure S28: ^{1}H (top) and ^{13}C (bottom) NMR spectrum (700/176 MHz, $CDCl_3$, 298 K) of **A1**•PF_6.

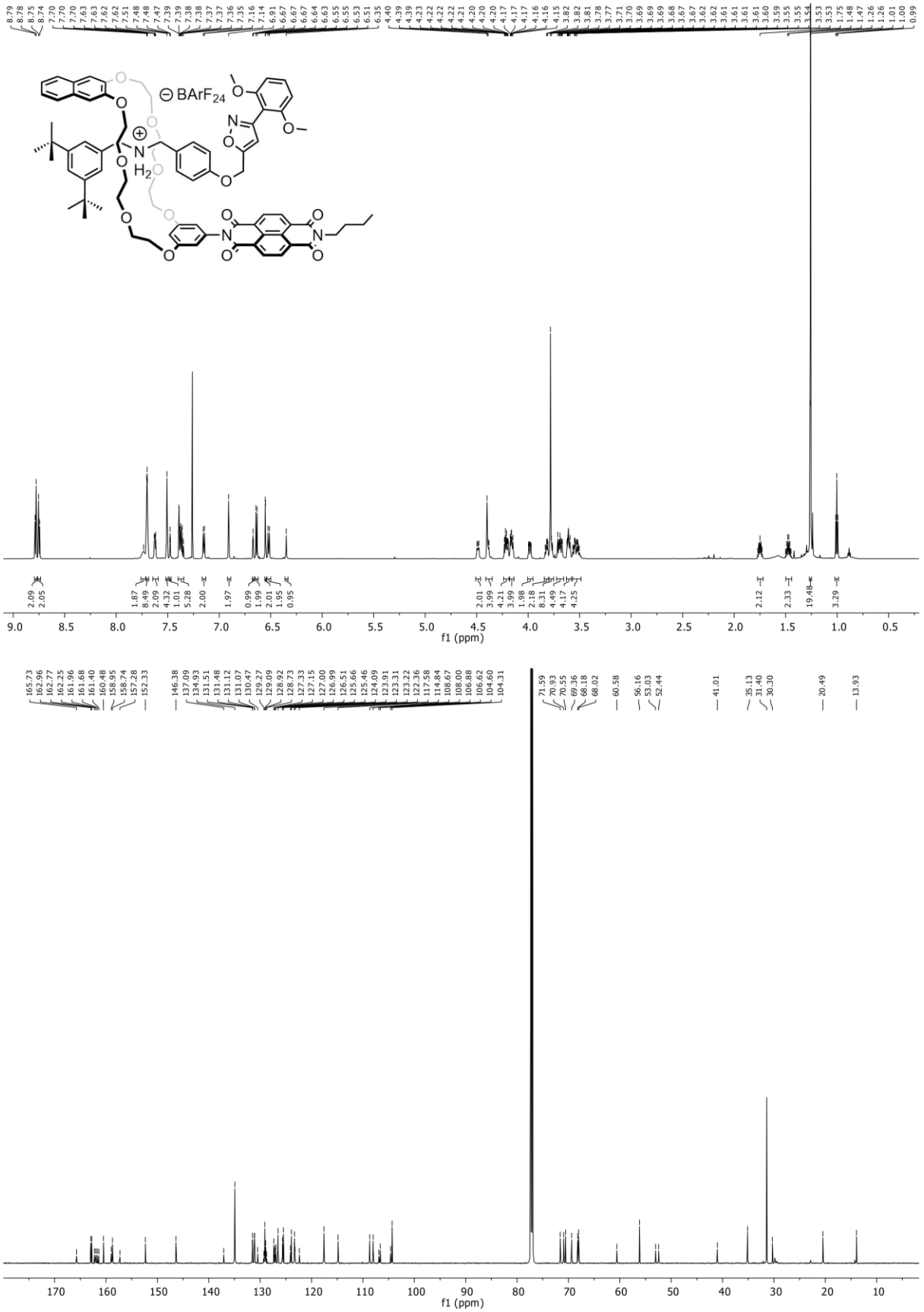

Figure S29: ^{1}H (top) and ^{13}C (bottom) NMR spectrum (700/176 MHz, $CDCl_3$, 298 K) of **NDIRot**.

8. References

1. N. Svenstrup, K. M. Rasmussen, T. K. Hansen, J. Becher, *Synthesis* **1994**, 809-812.

2. Y. Aoki, N. Umezawa, Y. Asano, K. Hatano, Y. Yano, N. Kato, T. Higuchi, *Bioorg. Med. Chem.* **2007**, *15*, 7108-7115.

3. W. Jiang, C. A. Schalley, *Beilstein J. Org. Chem.* **2010**, *6*, No. 14.

4. J. D. Badjic, C. M. Ronconi, J. F. Stoddart, V. Balzani, S. Silvi, A. Credi, *J. Am. Chem. Soc.* **2006**, *128*, 1489-1499.

5. H. Shao, T. Nguyen, N. C. Romano, D. A. Modarelli, J. R. Parquette, *J. Am. Chem. Soc.* **2009**, *131*, 16374-16376.

6. Z.-J. Zhang, H.-Y. Zhang, H. Wang, Y. Liu, *Angew. Chem. Int. Ed.* **2011**, *50*, 10834-10838.

7. C. Zhang, S. Li, J. Zhang, K. Zhu, N. Li, F. Huang, *Org. Lett.* **2007**, *9*, 5553-5556.

8. H. V. Schröder, S. Sobottka, M. Nößler, H. Hupatz, M. Gaedke, B. Sarkar, C. A. Schalley, *Chem. Sci.* **2017**, *8*, 6300-6306.

9. T. Matsumura, F. Ishiwari, Y. Koyama, T. Takata, *Org. Lett.* **2010**, *12*, 3828-3831.

10. *CrysAlisPro* (Version 1.171.39.43c.), Rigaku Oxford Diffraction, **2015**.

11. R. C. Clark, J. S. Reid, *Acta Crystallogr., Sect. A. Found. Crystallogr.* **1995**, *51*, 887-897.

12. G. M. Sheldrick, *Acta Crystallogr., Sect. A Found. Adv.* **2015**, *71*, 3-8.

13. G. M. Sheldrick, *Acta Crystallogr., Sect. C Struct Chem.* **2015**, *71*, 3-8.

14. G. M. Sheldrick, *Acta Crystallogr. , Sect. A Found. Crystallogr.* **2008**, *64*, 112-122.

15. C. B. Hübschle, G. M. Sheldrick, B. Dittrich, *J. Appl. Crystallogr.* **2011**, *44*, 1281-1284.

16. *in APEX3*, Bruker AXS Inc., Madison, Wisconsin, USA, **2015**.

17. G. M. Sheldrick, Version 2008/1, University of Göttingen, Germany, **2008**.

18. SAINT+, Version 8.27b © ed., Bruker AXS Inc., Madison, Wisconsin, USA, **1997-2012**.

19. G. M. Sheldrick, Version 2014/7 ed, University of Göttingen, Germany, **2014**.

20. J. R. Aranzaes, M.-C. Daniel, D. Astruc, *Can. J. Chem.* **2006**, *84*, 288-299.

ORGANIC CHEMISTRY FRONTIERS

RESEARCH ARTICLE

View Article Online
View Journal | View Issue

Cite this: *Org. Chem. Front.*, 2021, **8**, 3659

Dual-stimuli pseudorotaxane switches under kinetic control†‡

Marius Gaedke, [a] Henrik Hupatz,[a] Hendrik V. Schröder, §[a] Simon Suhr,[b] Kurt F. Hoffmann, [c] Arto Valkonen, [d] Biprajit Sarkar, [b] Sebastian Riedel, [c] Kari Rissanen [d] and Christoph A. Schalley *[a]

Received 31st March 2021,
Accepted 28th April 2021

DOI: 10.1039/d1qo00503k

rsc.li/frontiers-organic

A series of dumbbell-shaped *sec*-ammonium salts with bulky (pseudo)stoppers ('speed bumps') were tested for their ability to form pseudorotaxanes with a redox-switchable, tetrathiafulvalene (TTF)-decorated [24]crown-8 ether. Depending on the size of the pseudostoppers, fast (less than ten minutes), slow (hours to days) and very slow (no pseudorotaxanes observed) threading has been observed. NMR spectroscopy as well as tandem mass spectrometry indicate the formation of non-threaded face-to-face complexes prior to pseudorotaxanes formation. Both isomers can be distinguished by their substantially different stability in collision-induced dissociation (CID) experiments. Two external stimuli affect the stability of the pseudorotaxanes: Deprotonation of the ammonium ion results in fast dethreading, while dethreading is much slower when induced by the charge repulsion upon chemical oxidation of the TTF moiety. Remarkably, the same steric bulk of the pseudostopper thus leads to different dethreading rates depending on the stimulus applied. Based on these findings, two redox-switchable rotaxanes containing a 1-naphthyl and a phenyl moiety as sterically different 'speed bumps' in the axle centre were synthesised. Bulk electrolysis of the rotaxanes did not result in the expected macrocycle translocation on the axle independent of the 'speed bump' as a remarkable consequence of the mechanical bond.

Introduction

Artificial molecular switches[1] are controlled by external chemical,[2,3] light,[4,5] or electrochemical[6] stimuli. In mechanically interlocked molecules (MIMs) such as rotaxanes and catenanes, stimuli-induced switching manipulates the interactions of the wheels with their binding sites on the other component in a controlled manner.[7,8] Pseudorotaxanes are non-interlocked, but threaded axle-wheel complexes able to dissociate without breaking a covalent bond. Depending on the bulkiness of the axle end groups, they encompass a broad range of dethreading rates with the rotaxane at the very end, where no wheel exchange takes place (Fig. 1a).[9] Thus, (pseudo)rotaxanes allow us to study stimuli-induced switching with and without wheel exchange. In rotaxanes, the wheel's translational freedom is limited to the track provided by the axle[10] and switching can be converted into directed co-conformational changes, which can propel artificial molecular motors and machines.[7,8,11] The impact of the wheel exchange rate on dual-stimuli-induced switching has not been studied for kinetically hindered pseudorotaxanes, but rather for pseudorotaxanes with fast exchange or for rotaxanes (no exchange). This raises an interesting question: Can different stimuli applied to a dual-stimuli-responsive *and* kinetically hindered pseudorotaxane result in different timescales for dethreading over a 'speed bump' pseudostopper, even when the steric size of the 'speed bump' remains unchanged?

The energy landscapes of switchable (pseudo)[2]rotaxanes change, when stimuli are applied. In Fig. 1, which exemplarily depicts an acid/base- *and* redox-switchable pseudorotaxane (Fig. 1b and c) and its 'speed bump' containing rotaxane analogue (Fig. 1d and e), the yellow dots represent the (pseudo) rotaxane populations. Initially, the wheels reside on the binding site. Upon applying one of the two stimuli, the former binding site becomes disfavoured and the macrocycles migrate over the blue 'speed bump'. For the pseudo[2]rotaxane, the wheel is released from the axle over the barrier caused by the

[a]*Institut für Chemie und Biochemie der Freien Universität Berlin, Arnimallee 20, 14195 Berlin, Germany. E-mail: c.schalley@fu-berlin.de*
[b]*Lehrstuhl für Anorganische Koordinationschemie, Institut für Anorganische Chemie, Universität Stuttgart, Pfaffenwaldring 55, 70569 Stuttgart, Germany*
[c]*Institut für Chemie und Biochemie der Freien Universität Berlin, Fabeckstr. 34/36 14195, Berlin, Germany*
[d]*Department of Chemistry P.O. Box 35, 40014 Jyväskylä, Finland*

† Dedicated to Prof. Placido Neri upon the occasion of his 60th birthday.

‡ Electronic supplementary information (ESI) available. CCDC 2073308. For ESI and crystallographic data in CIF or other electronic format see DOI: 10.1039/d1qo00503k

§ Present address: Dr H. V. Schröder Department of Chemical and Biological Engineering, Princeton University, Princeton, NJ08544, USA

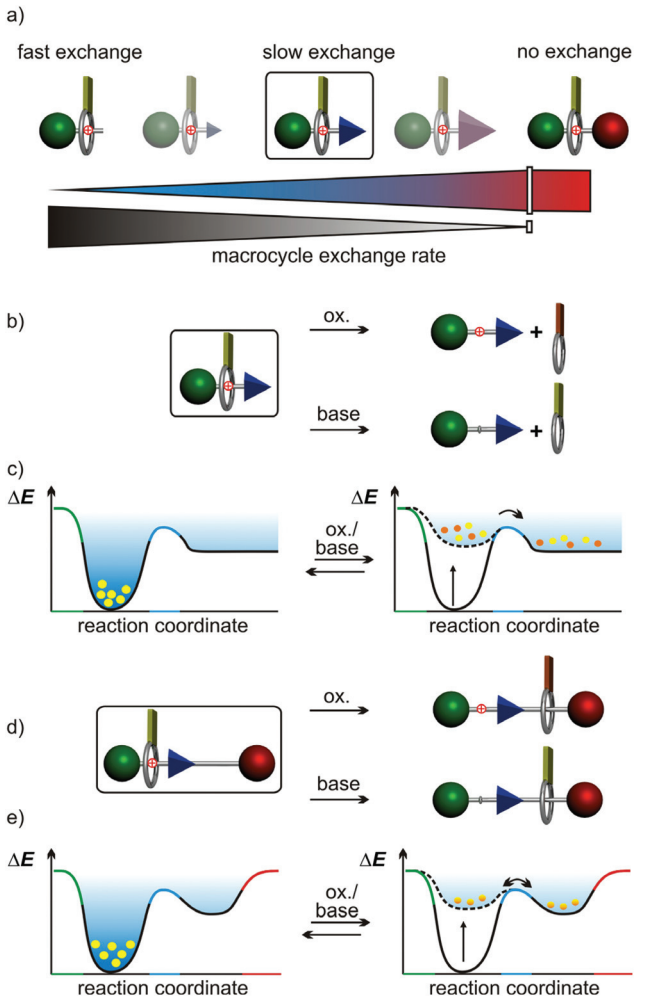

Fig. 1 (a) Range of macrocycle exchange rates from a quickly reversible pseudorotaxane formation (light blue, small 'speed bump') to a fully interlocked rotaxane (red stopper). (b) Stimuli-induced shuttling or unthreading and (c) the corresponding changes of the energy landscapes of a pseudorotaxane as well as (d and e) of a rotaxane (stoppers: green/red, steric 'speed bump' in the axle: blue, TTF oxidation states in yellow (reduced)/orange (oxidized to TTF^{2+}).

pseudostopper, while the wheel cannot escape from the axle in the [2]rotaxane. It will nevertheless move across the 'speed bump' back and forth and a new equilibrium distribution of positional isomers is finally reached on a time scale depending on the 'speed bump' size.

From the broad variety of available binding motifs,[12,13] *sec*-ammonium/crown ether (pseudo)rotaxanes provide an easy access to dual-stimuli-responsive compounds that allow us to investigate the above question in detail. In this motif, a crown ether encircles the ammonium ion with binding constants typically in the range of 10^2 to 10^6 M^{-1} in non-protic organic solvents. In thermodynamic terms, ammonium ions form threaded complexes depending on the number of hydrogen bonds (including C–H···O hydrogen bonds involving the methylene groups next to the ammonium ion), charge distribution and ion pair separation energies of the ammonium

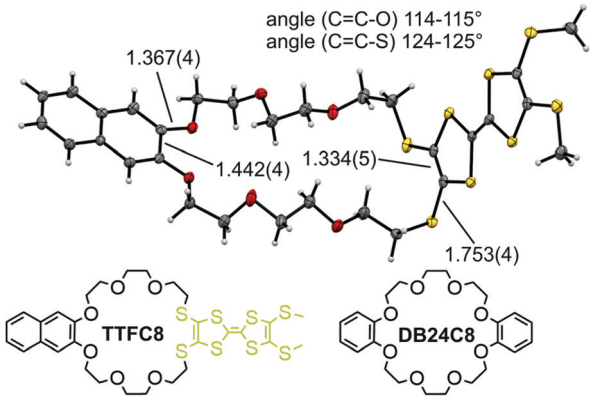

Fig. 2 Solid-state structure of **TTFC8** with selected bond lengths (Å) and angles.

salt.[14,15] Only face-to-face interactions are possible,[16] when the axle end groups are sterically too bulky. A large number of pseudo[2]rotaxanes with different crown ether sizes and different end groups have been reported to form in a broad variety of solvents.[17–19] In marked contrast, only few examples of rotaxanes with 'speed bumps' along their axles have been studied to unravel the influence of the mechanical bond.[20–25] The studies on shuttling in crown ether rotaxanes mostly focus on degenerate shuttles with two or more equivalent binding sites.[20,24] However, non-degenerate shuttles are more suitable for directional movement,[26] among which only very few are responsive to both acid/base and redox stimuli.[27]

Here, we make use of the *sec*-ammonium/crown ether binding motif and describe a series of pseudorotaxanes responsive to both stimuli with differently sized and differently shaped pseudostoppers. The ammonium/crown ether interaction can be disrupted by deprotonation of the ammonium group with a strong base.[28] Introducing a tetrathiafulvalene (TTF) into the crown ether (**TTFC8**, Fig. 2) implements also the second stimulus: Two-electron oxidation of the TTF unit to its dication induces coulombic repulsion between the wheel and the ammonium station and is expected to lead to dethreading as well.[29,30] Hence, these dual-stimuli-responsive pseudorotaxanes allow comparing the dethreading rates after deprotonation with those after oxidation, while maintaining the same steric bulk of the 'speed bump' pseudostopper. After identifying a suitable pseudostopper in pseudorotaxane dethreading experiments, this 'speed bump' can be integrated into a rotaxane axle to investigate co-conformational changes in the dual-stimuli-responsive [2]rotaxane, in which the mechanical bond prevents dethreading.

Results and discussion

The wheel: crystal structure of TTFC8

The redox-active wheel **TTFC8** used in this study was synthesized as reported earlier.[29] This macrocycle and the commercially available and widely used dibenzo[24]crown-8 ether (**DB24C8**) have the same number of 24 atoms along their cir-

cumference. Nevertheless, the substitution of two catechol oxygen by sulfur atoms affects both the structure and the conformational properties of the ring,[31] as becomes clear, when comparing the new solid state structure of **TTFC8** (Fig. 2, also see ESI section 8‡) with the known structure of **DB24C8**.[31]

The naphthalene-substituted side of **TTFC8** only shows a minor elongation in the central C=C bond (1.44 Å compared to 1.41 Å for **DB24C8**), the C–O bond lengths and C=C–O angles are virtually the same (1.37 Å and 115°). Although a shorter central C=C bond (1.33 Å) can be found on the TTF side, the C–S bond lengths (1.75 Å *vs.* 1.37 Å) and C=C–S bond angles (125° *vs.* 115°) notably enlarge the macrocycle cavity on the TTF-substituted side consistent with other published thiacrown derivatives.[32–34] The S atoms are *exo* to the ring rather than *endo*, like the oxygens on the other side. The effect of the structure on binding ammonium guests was investigated in our previous paper.[30]

Threading experiments

To test whether these differences in ring annulus lower the barrier to overcome bulky substituents, various *sec*-ammonium axles were synthesised as tetrakis(3,5-bis(trifluoromethyl) phenyl) borate ($BArF_{24}^-$) salts to compensate for the reduced binding constants of the thiacrown (see ESI section 5‡ for details).[29] Using $BArF_{24}^-$ with respect to PF_6^- results in a 10 to 20-fold increase of the binding constant.[30] The axles only differ in their terminal groups on one side (shown in blue in Fig. 3). As a guideline for the pseudostopper size and shape literature data available for **DB24C8**-based (pseudo–)rotaxanes with PF_6^- counterions was used.[16,19,35]

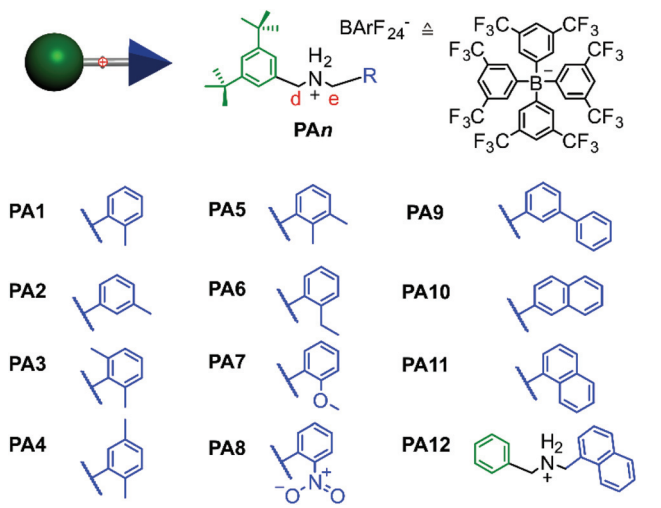

Fig. 3 The synthesised axles PA*n*.

The axles were mixed with either **DB24C8** or **TTFC8** in a 1 : 1 ratio in CD_2Cl_2. ^{1}H NMR spectra were taken at regular intervals to compare the half-lives ($t_{1/2}$) of the threading reactions for 4 mM solutions at room temperature by following the changing integrals of the $C\underline{H}_2$–NH_2–$C\underline{H}_2$ signals (see Table 1 and ESI section 2 Fig. S27–41‡ for the NMR spectra). Upon threading, the two methylene group signals shift downfield ($\Delta\delta \geq +0.2$ ppm). Furthermore, diastereotopic splitting of the crown ether methylene groups is observed for the pseudorotaxanes due to the directionality of the axle.[16,36]

An initial kinetic screening categorizes the axles into three groups. The first group (**PA1**, **PA2**, **PA4**, **PA8**, **PA9** and **PA10**) shows complete conversion into the threaded complex with **TTFC8** and **DB24C8** within less than 10 min. The second group (**PA5**, **PA6**, **PA7** and **PA11**) reveals half-lives in the range of hours to days. In addition, **PA5**, **PA6** and **PA7** form pseudorotaxanes with **TTFC8**, but not with **DB24C8** (even within 14 days). Both crown ethers can, however, pass the 1-naphthalene pseudostopper of **PA11** to form threaded complexes. Here, the slightly larger **TTFC8** threaded onto the axle approximately 120 times more quickly. Finally, no sign of threading is observed for **PA3** neither with **DB24C8** nor **TTFC8** within 14 days. These results are in good agreement with a recent study by Credi *et al.*[19] which also showed the 3,5-dimethyl phenyl moiety to be an efficient stopper in **DB24C8** containing rotaxanes[37–40] and identified the 2,6-dimethyl phenyl moiety as kinetically inert to threading of **DB24C8**.[19] Consequently, out of these candidates we chose **PA11** (1-naphthyl) as the most suitable pseudostopper for dual-stimuli-induced switching experiments, because threading occurs at time intervals that are conveniently observable by NMR spectroscopy.

In summary, the slight differences in size and shape apparent from the comparison of the crystal structures clearly affect the threading kinetics even though **TTFC8** and **DB24C8** share the same number of atoms in the wheel circumference.

Face-to-face complexes *vs.* pseudorotaxanes

In order to obtain some orienting insight into the thermodynamic binding properties of **PA11**, axle **PA12** has been synthesized, which allows fast threading of **TTFC8** over the phenyl group. The association constant obtained by isothermal titration calorimetry amounts to $K_a = (3.9 \pm 0.7)\ 10^5\ M^{-1}$ (ΔG° =

Table 1 Screening of threading timescales in model pseudo[2]rotaxanes PA*n*@MC and their corresponding half-lives $t_{1/2}$ for **DB24C8** and **TTFC8** threading monitored by ^{1}H NMR (4 mM in $CD_2Cl_2/CDCl_3$ 400/500 MHz at r.t.)

Entry[a]	PA1	PA2	PA3	PA4	PA5	PA6	PA7	PA8	PA9	PA10	PA11
DB24C8	<10 min	<10 min	≫14 days	<10 min	≫14 days	≫14 days	≫14 days	<10 min	<10 min	<10 min	10 days
TTFC8	<10 min	<10 min	≫14 days	<10 min	50 h	14 days	22 h	<10 min	<10 min	<10 min	2 h

[a] Axles denoted with "≫14 days" were considered to be not suitable for this study. It does not necessarily exclude a threaded complex to be achievable over time with suitable temperature and concentration.

(-31.9 ± 0.4) kJ mol^{-1}, ΔH° = (-44.1 ± 1.2) kJ mol^{-1}, $T\Delta S^{\circ}$ = (-12.2 ± 1.6) kJ mol^{-1}; also, see ESI section 5 and Table S2†). This binding data is very similar to that of the symmetrical dibenzylammonium axle (**DBA**) (K_a = (7.7 ± 1.0) 10^5 M^{-1} (ΔG° = (-33.6 ± 0.3) kJ mol^{-1}, ΔH° = (-39.8 ± 1.0) kJ mol^{-1}, $T\Delta S^{\circ}$ = (-6.2 ± 1.3) kJ mol^{-1}). We therefore assume the binding data for **PA11** to be in a similar range.

An ITC experiment with **PA11** was also attempted with titration intervals of 20 min to account for the slow threading. Remarkably, very sharp heat signals were observed. The quick heat evolution is not consistent with the slow pseudorotaxane formation as observed in ^{1}H NMR experiments. Obviously, the axle and the crown ether quickly form a non-threaded complex (Fig. 4a),[16] for which an upper limit for K_a of *ca.* 10^4 M^{-1} is estimated (see ESI section 5 and Fig. S53‡). ^{1}H NMR experiments confirm this face-to-face complex formation that is expressed in a minor shift for the methylene protons next to the ammonium moiety. These signals vanish slowly over time with the appearance of pseudorotaxane signals (Fig. S41‡).

Besides the evidence from ITC and NMR experiments, tandem mass spectrometry complements the picture. As one can expect the face-to-face complexes to easily dissociate in the gas phase upon collision-induced dissociation (CID), the dethreading of the pseudorotaxanes should require higher collision energies due to the steric barrier caused by the pseudostopper. Fig. 4b shows the survival yield curves for **PA11@TTFC8** separately prepared and isolated by column chromatography (blue) in comparison to a mixture of **PA11** and **TTFC8** subjected to the collision experiment 5 (red) and 135 minutes (black) after sample preparation. The red curve is indicative of a complex, which fragments at rather low collision voltages ($E_{1/2}$ = 9.8 ± 0.2 V). A small amount of 5% of the complex remains intact and half of it is fragmented at *ca.* 39 V. The blue curve shows only one, more stable complex ($E_{1/2}$ = 39.2 ± 0.4 V). For the sample taken after 135 min roughly 40% of the complex fragment at the lower collision voltage, while 60% fragment at the higher one. Clearly, two differently stable complexes form, *i.e.* the instantly forming face-to-face complex and the pseudorotaxane, which increases in abundance over time. This nicely shows the conversion of the instantly formed, but weaker non-threaded complex (lower equilibrium constant K_1, but higher rate constant k_1) into the pseudorotaxane (higher equilibrium constant K_2, but lower rate constant k_2).

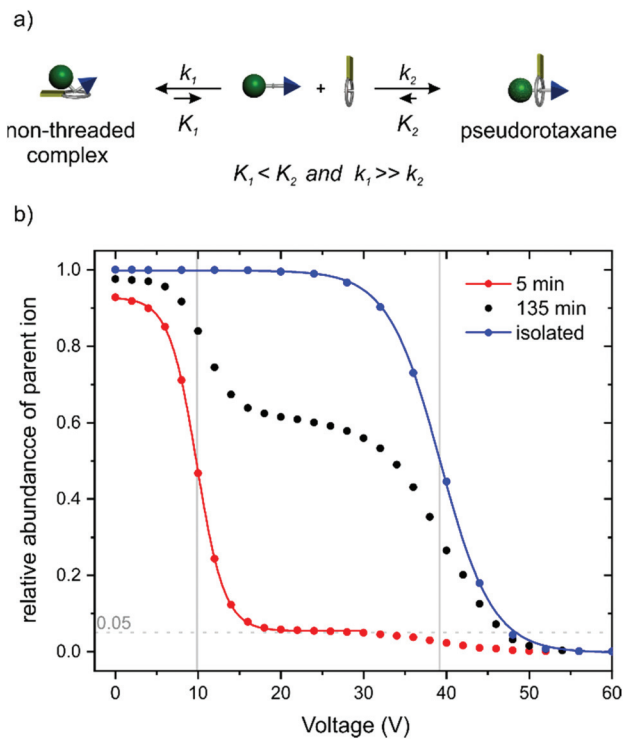

Fig. 4 (a) Schematic representation of the equilibrium for face-to-face complexation which competes with the formation of **PA11@TTFC8**. (b) Survival yield curves obtained for mass-selected [**PA11**·**TTFC8**]$^+$ ions (*m*/*z* 1108) at increasing collision voltages. Red curve: sample 5 min; black curve: sample 135 min after mixing of axle and wheel. Blue curve: pre-formed pseudorotaxane isolated by column chromatography before the experiment. The solid lines represent a sigmoidal fitting to determine 50% survival yield voltages $E_{1/2}$: red: $E_{1/2}$ = (9.8 ± 0.2) V; blue: $E_{1/2}$ = (39.2 ± 0.4) V (for experimental details, see ESI section 3‡).

Dual-stimuli responsiveness

When pseudo[2]rotaxane **PA11@TTFC8** is deprotonated with an excess of polystyrene-immobilized P2 base, quick dethreading is observed (Fig. 5b and ESI section 2 Fig. S32, S34, S36

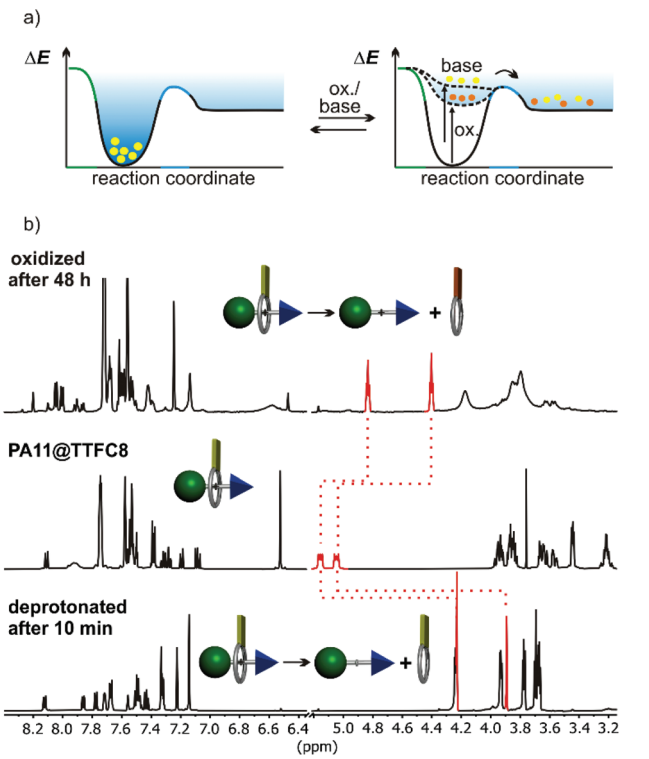

Fig. 5 (a) Dual-stimuli switching expressed in terms of the potential energy surface of the pseudorotaxane **PA11@TTFC8**. (b) ^{1}H NMR spectra (600 MHz, dry CD_2Cl_2, 298 K) of **PA11@TTFC8** (center), 48 hours after oxidation with excess $NOSbF_6$ (top), and 10 minutes after deprotonation with an excess of Schwesinger's P2 base immobilized on polystyrene (bottom).

and S42‡). No indication for hydrogen bonding of neutral **TTFC8** to the neutral axle was observed in the ^{1}H NMR spectra in contrast to earlier reports on complexes of neutral *primary* amines.[41] Dethreading is indicated by an emerging set of methylene proton signals (H_d, H_e), upfield shifted by $\Delta\delta \approx 0.8$ ppm upon deprotonation and dethreading. The pseudo[2]rotaxanes **PA5@TTFC8** (2,3-dimethylbenzyl end group), **PA6@TTFC8** (2-ethylbenzyl) and **PA7@TTFC8** (2-methoxybenzyl) were also subjected to deprotonation. Again, dethreading *via* deprotonation occurred immediately (see ESI Fig. S42 and Table S1‡).

The pseudorotaxane **PA11@TTFC8** can also successfully be oxidized with excess $NOSbF_6$ in dry CD_2Cl_2 under argon atmosphere. Two subsequent one-electron-oxidation steps lead to the TTF dication **PA11@TTFC8**$^{2+}$ easily recognizable from its instantaneously appearing deep blue colour. The oxidized macrocycle unthreads with a $t_{1/2}$ of 11 h (Fig. 5b, ESI section 2 Fig. S42‡). As the dication is again diamagnetic, unthreading can also be followed by integrating of a new set of methylene proton signals (H_d, H_e), upfield shifted by $\Delta\delta \approx 0.3$ and 0.6 ppm. This is confirmed by monitoring the dethreading of pseudo[2]rotaxanes **PA5@TTFC8**, **PA6@TTFC8** and **PA7@TTFC8** after oxidation. Complete dethreading occurred only for **PA7@TTFC8** and required a substantially longer time ($t_{1/2}$ = 22 h, see ESI section 2 Fig. S36‡).

These experiments clearly reveal that the dethreading rate does not only depend on the steric bulk of the axles' terminal groups, but also change significantly with the nature of the stimulus applied. Earlier, we reported attractive forces to still occur even between the doubly oxidized **TTFC8** and secondary ammonium axles.[29] Assuming that the ring circumference and conformational flexibility of **TTFC8** is not significantly altered upon oxidation[42] and taking into account that the oxidation itself occurs almost instantaneously, we therefore hypothesize that these residual interactions are the cause for the slower dethreading after oxidation. Fig. 5a qualitatively visualizes this in the framework of the energy landscapes after oxidation and after deprotonation: The oxidized pseudorotaxane resides in a somewhat lower local minimum on its potential energy surface as compared to the deprotonated pseudorotaxane.

Synthesis of 'speed bump' rotaxanes

Axle **6** (Fig. 6) features the bulky 1-naphthalene moiety and can easily be equipped with a stopper. After stirring **6** with **TTFC8** for three days at 40 °C (for **R1**, Fig. 6) or **S4** (axle of rotaxane **R2**) with **TTFC8** for 10 minutes at room temperature (for **R2**), nitrile-oxide stopper **St1**[43] was added and the mixtures were stirred at 35 °C overnight. Two rotaxanes (**R1** and **R2**) were isolated only differing by the size of the connecting blue 'speed bump'.

In the ^{1}H NMR spectra, successful rotaxane formation is evidenced by a downfield shift ($\Delta\delta$ = +0.5 ppm) of the methylene protons next to the ammonium, as well as the strong downfield shift ($\Delta\delta$ = +4.0 ppm) of the former alkyne proton that is incorporated in the newly formed isoxazole (H_p for **R1** and H_j for **R2**). Additionally, the methylene protons next to the

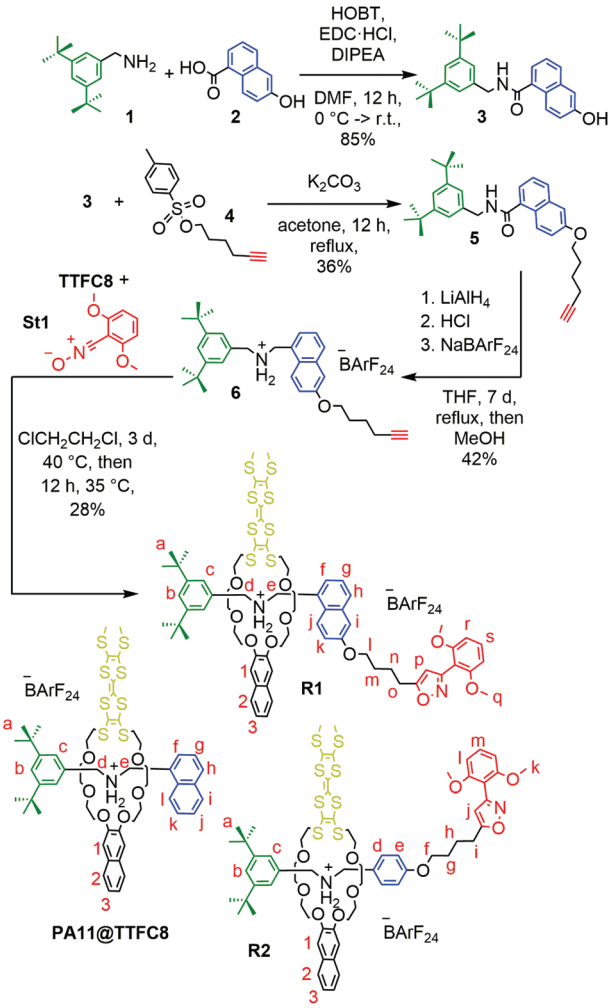

Fig. 6 Synthesis of rotaxane **R1**. Rotaxane **R2** and pseudo[2]rotaxane **PA11@TTFC8** are shown for comparison. For details of the synthesis of **R2**, see ESI, Scheme S3.‡

axle ether oxygen atom (H_l for **R1** and H_f for **R2**) shows an upfield shift ($\Delta\delta$ = 1.0 ppm) due to the close proximity to the naphthalene and/or TTF moiety of **TTFC8** (see ESI Fig. S19 and S26‡). The interlocked structure was further supported by tandem mass spectrometry. Collision-induced dissociation of mass-selected rotaxane parent ions occurred only at high collision energies. As the intact axle is not observed among the fragments, it is clear that dissociation of the two components is only possible after covalent bond cleavage within the axle, which excludes a non-threaded complex. Also, the collision energies required for dissociation as well as the observed fragment ions are comparable to other similar rotaxanes.[29]

Deprotonation of the rotaxanes

Deprotonation of **R1** with polystyrene-immobilized P2 base yields a neutral amine (Fig. 7d) which is indicated by a strong highfield shift of methylene protons $H_{d,e}$ ($\Delta\delta$ = 1 ppm solid line). The positions of these signals are similar to those of the deprotonated free axle (Fig. 7e). Other significant shifts

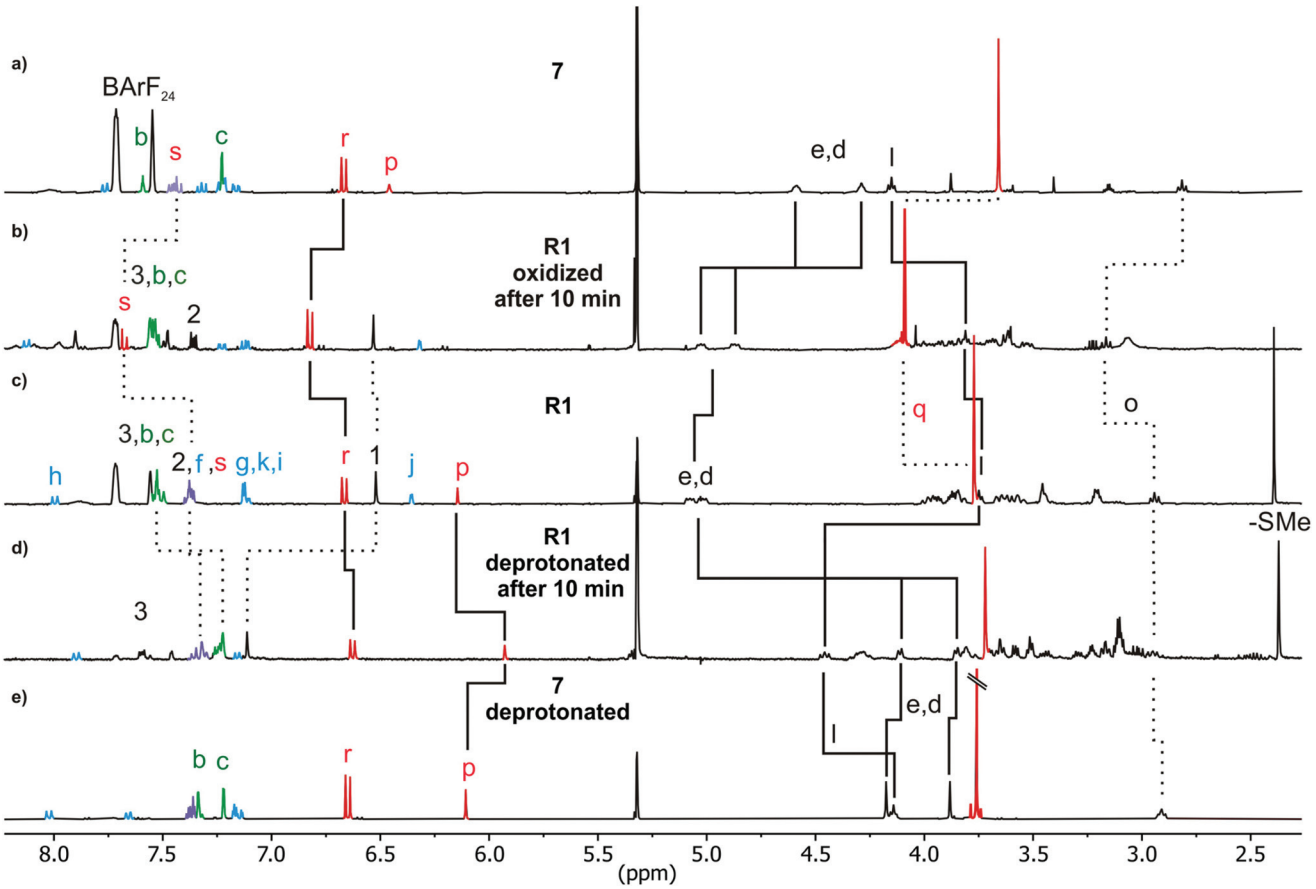

Fig. 7 ^{1}H NMR spectra (400 MHz, 298 K, CD_2Cl_2) of (a) stoppered axle **7** (b) **R1** 10 min after two-electron-oxidation (c) **R1** (d) **R1** 10 minutes after deprotonation and (e) deprotonated **7** with selected shifts highlighted.

include the isoxazole proton H_p ($\Delta\delta$ = −0.5 ppm), and alkyl chain methylene protons H_l ($\Delta\delta$ = +0.7 ppm solid line). Together with the downfield shift of H_l, this clearly indicates a deprotonation-induced shuttling away from the amine and towards the alkyl chain. No such shift of H_l is observed when free axle **7** (**6+St1**) is deprotonated (Fig. 7a/e). Rotaxane **R2** behaves similarly (Fig. S43 bottom‡). Variable temperature ^{1}H NMR experiments (see ESI, Fig. S51 and S52‡) performed with deprotonated **R1** and **R2** to test whether the two positional isomers of the wheel would be distinguishable unfortunately remained inconclusive.[24,44–50] Nevertheless, the NMR data is in agreement with a shift of the wheel across the 'speed bump' in the axle centre upon deprotonation.

Oxidation of the rotaxanes

The ^{1}H NMR spectrum of **R1** recorded 10 minutes after oxidation with $NOSbF_6$ to $\mathbf{R1}^{2+}$ is shown in Fig. 7b and did not change over the following 48 hours. The methylene protons $H_{d,e}$ next to the ammonium ion undergo only a small upfield shift ($\Delta\delta$ = −0.1 ppm). Also, proton H_l is shifted only by a small amount. As the small shifts can easily be rationalized by the additional charge induced through oxidation, these findings indicate that the wheel still occupies the ammonium station. However, protons H_r and H_s of the dimethoxyphenyl stopper at the opposite end of the axle shift downfield to some extent ($\Delta\delta$ = 0.2 to 0.25 ppm). Although this observation may at first glance seem inconsistent with the interpretation that the wheel remains on the ammonium side of the axle, these shift differences can be easily explained by invoking p-donor–p-acceptor complex formation between the strongly electron-deficient TTF^{2+} dication and the rather electron-rich dimethoxyphenyl stopper. The ^{1}H NMR spectrum of the oxidized rotaxane thus indicates that the macrocycle still encircles the ammonium ion, while refolding of the more remote axle half occurs.

More evidence can be obtained from cyclovoltammetric (CV) and differential pulse voltammetric (DPV) experiments with which the half-wave potentials of the two reversible TTF redox waves can be obtained. These potentials characteristically shift depending on the interactions between axle and wheel, as shown earlier for **TTFC8**-containing rotaxanes.[29,51,52] The correlation diagram in Fig. 8a contains the peak potentials obtained by DPV measurements in CH_2Cl_2 with n-Bu_4NBArF_{24} as the supporting electrolyte. Compared to the free wheel, the redox potentials $E^1_{1/2}(TTF^{0/+})$ and $E^2_{1/2}(TTF^{+/2+})$ are anodically shifted for all species bound to an axle. **PA12@TTFC8** is a diagnostic control compound, as two sets of TTF redox processes corresponding to the threaded ($E^1_{1/2}$, $E^2_{1/2}$) and unthreaded wheel ($E^1_{1/2}$, $E'_{1/2}$) are observed (see ESI Fig. S55‡). The low

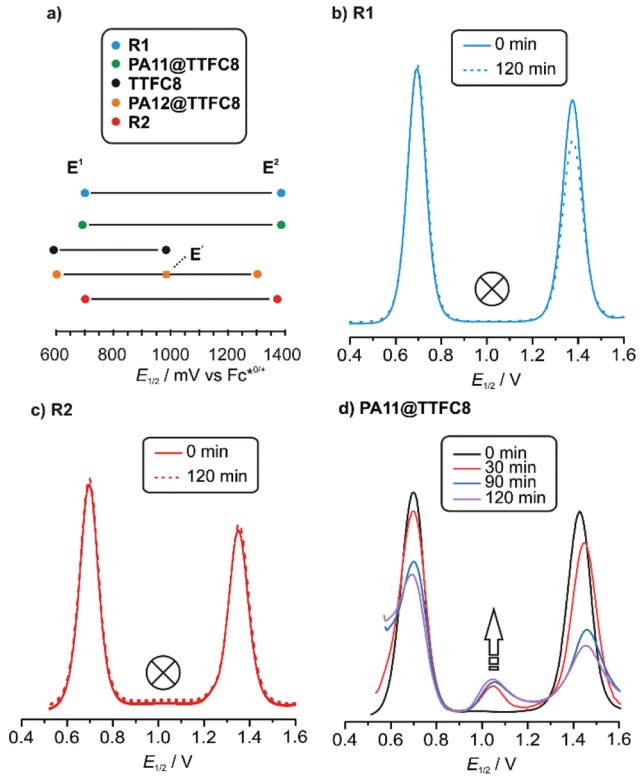

Fig. 8 Electrochemical data: (a) Correlation diagram of DPV peak potentials of all relevant (pseudo)rotaxane species, DPVs before and after electrolysis of (b) **R1**, (c) **R2**, (d) **PA11@TTFC8** (CH_2Cl_2, with *n*-Bu_4NBArF_{24} as the electrolyte (0.1 M), 298 K, 1 mM analyte, 25 mV modulation amplitude, 50 ms modulation time, 5 mV step potential, 0.5 s interval time).

steric bulk of the phenyl group allows fast interconversion between threaded and unthreaded on the CV timescale (in the DPV only one peak for $TTF^{0/+}$ redox couple is visible). In contrast, the isolated pseudorotaxane **PA11@TTFC8** only shows one redox couple for $TTF^{0/+}$ and $TTF^{+/2+}$ due to the sterically hindered unthreading. The mechanically interlocked structures **R1** and **R2** show no third feature ($E'_{1/2}$), meaning that the voltammograms indicate no significant wheel shuttling away from the ammonium station on the timescale of the experiment. Bulk electrolysis (Fig. 8b–d) of the (pseudo)rotaxanes for 2 h did not show a change in the DPV for **R1** and **R2**. However, for **PA11@TTFC8** signal broadening and lowered amperage in the course of electrolysis was observed. Bulk electrolysis gave rise to a new signal, which corresponds to the second oxidation of unbound **TTFC8**. The bulk electrolysis experiments suggest, that electrochemically–induced migration over the naphthalene moiety does take place for pseudorotaxane **PA11@TTFC8**. On the contrary, no such behavior was observed for the rotaxanes **R1** and **R2**. These results clearly support the ^{1}H NMR data, that no oxidation-induced shuttling occurs in the mechanically interlocked species.

Consequently, the behaviour of the rotaxanes parallels that of the pseudorotaxanes in that the two different stimuli cause significant differences in dethreading/shuttling rates despite of the steric barrier remaining unchanged. Also, the reason – a binding interaction of the crown ether wheel to the ammonium ion that is stronger than the effects of charge repulsion – is likely the same. Nevertheless, there are also differences: While the pseudorotaxane finally dethreads over 48 hours, no change is observed on a similar time scale for the rotaxane. This is an effect of the mechanical bond. While dethreading of the pseudorotaxane is entropically favoured by an increase in particle number, such wheel shuttling in the rotaxanes does not benefit from such entropic benefit.

Conclusions

A set of $BArF_{24}^-$ salts of *sec*-ammonium ions bearing different bulky end groups have been investigated with respect to their ability to form crown ether/ammonium pseudorotaxanes. The small differences in bond lengths between the two crown ethers **DB24C8** and **TTFC8** change the threading barrier significantly and threading occurs significantly faster for **TTFC8**. Three groups of quickly threading, kinetically hindered slowly threading, and non-threading axles can be distinguished. For the slowly and non-threading axle/wheel pairs, the formation of face-to-face crown ether/ammonium complexes occurs, which has been exemplarily studied in more detail for **PA11** by ^{1}H NMR, tandem MS and ITC experiments. To our knowledge this is the first time that an equilibrium of a threaded and non-threaded complex was quantitatively studied for the same axle macrocycle combination.

Deslipping of **TTFC8** from different axles could be achieved by deprotonation of the axle or by chemical oxidation of the macrocycle. Upon deprotonation, the pseudorotaxanes dissociate quickly. Chemical oxidation to the TTF dication lead to much slower dethreading. The difference in dethreading rates for the two stimuli can be explained by residual attractive interaction of the oxidized $\mathbf{TTFC8}^{2+}$ and the axle. It is quite remarkable that two different stimuli lead to so clearly different dethreading rates, even though the steric barrier remains unchanged. Clearly, an interplay between the steric barrier and the changes in the interactions between wheel and its binding stations is observed here which complicates the analysis of such steric 'speed bumps' in molecular interlocked switches and machines.

The shuttling of the wheel in the rotaxanes on one hand behaves similarly in that the two stimuli cause different effects on the shuttling. But the behaviour is not fully analogous. The comparison of rotaxanes and pseudorotaxanes clearly reveals a significant and non-negligible influence of the mechanical bond. At the end, the shuttling is affected by changing interactions between the wheel and the available binding stations as well as steric barriers on its way along the axle and the particular effects of the mechanical bond.

Conflicts of interest

There are no conflicts of interest to declare.

Acknowledgements

Gefördert durch die Deutsche Forschungsgemeinschaft (DFG) – Projektnummer 387284271 – SFB 1349 – und Projektnummer 434455294 (funded by the Deutsche Forschungsgemeinschaft – project-ID 387284271 – SFB 1349 and project-ID 434455294). A.V. kindly acknowledges the Academy of Finland (grant no. 314343) for financial support. We also thank Jennifer Anders for help with the synthesis.

Notes and references

1 J. D. Harris, M. J. Moran and I. Aprahamian, New molecular switch architectures, *Proc. Natl. Acad. Sci. U. S. A.*, 2018, **115**, 9414–9422.
2 J. D. Badjic, V. Balzani, A. Credi, S. Silvi and J. F. Stoddart, A molecular elevator, *Science*, 2004, **303**, 1845–1849.
3 D. Cao, Z. Liu, P. Verwilst, S. Koo, P. Jangjili, J. S. Kim and W. Lin, Coumarin-Based Small-Molecule Fluorescent Chemosensors, *Chem. Rev.*, 2019, **119**, 10403–10519.
4 D. Bleger and S. Hecht, Visible-Light-Activated Molecular Switches, *Angew. Chem., Int. Ed.*, 2015, **54**, 11338–11349.
5 D. Dattler, G. Fuks, J. Heiser, E. Moulin, A. Perrot, X. Yao and N. Giuseppone, Design of Collective Motions from Synthetic Molecular Switches, Rotors, and Motors, *Chem. Rev.*, 2020, **120**, 310–433.
6 A. Coskun, J. M. Spruell, G. Barin, W. R. Dichtel, A. H. Flood, Y. Y. Botros and J. F. Stoddart, High hopes: can molecular electronics realise its potential?, *Chem. Soc. Rev.*, 2012, **41**, 4827–4859.
7 S. Erbas-Cakmak, D. A. Leigh, C. T. McTernan and A. L. Nussbaumer, Artificial Molecular Machines, *Chem. Rev.*, 2015, **115**, 10081–10206.
8 E. R. Kay, D. A. Leigh and F. Zerbetto, Synthetic molecular motors and mechanical machines, *Angew. Chem., Int. Ed.*, 2007, **46**, 72–191.
9 T. Felder and C. A. Schalley, Secondary isotope effects on the deslipping reaction of rotaxanes: high-precision measurement of steric size, *Angew. Chem., Int. Ed.*, 2003, **42**, 2258–2260.
10 E. A. Neal and S. M. Goldup, Chemical consequences of mechanical bonding in catenanes and rotaxanes: isomerism, modification, catalysis and molecular machines for synthesis, *Chem. Commun.*, 2014, **50**, 5128–5142.
11 M. Baroncini, S. Silvi and A. Credi, Photo- and Redox-Driven Artificial Molecular Motors, *Chem. Rev.*, 2020, **120**, 200–268.
12 Z. Liu, S. K. M. Nalluri and J. F. Stoddart, Surveying macrocyclic chemistry: from flexible crown ethers to rigid cyclophanes, *Chem. Soc. Rev.*, 2017, **46**, 2459–2478.
13 A. Carrasco-Ruiz and J. Tiburcio, Electrostatic kinetic barriers in the threading/dethreading motion of a rotaxane-like complex, *Org. Lett.*, 2015, **17**, 1858–1861.
14 P. R. Ashton, P. J. Campbell, P. T. Glink, D. Philp, N. Spencer, J. F. Stoddart, E. J. T. Chrystal, S. Menzer, D. J. Williams and P. A. Tasker, Dialkylammonium Ion/Crown Ether Complexes: The Forerunners of a New Family of Interlocked Molecules, *Angew. Chem., Int. Ed. Engl.*, 1995, **34**, 1865–1869.
15 R. M. Izatt, J. D. Lamb, N. E. Izatt, B. E. Rossiter, J. J. Christensen and B. L. Haymore, A calorimetric titration study of the reaction of several organic ammonium cations with 18-crown-6 in methanol, *J. Am. Chem. Soc.*, 1979, **101**, 6273–6276.
16 P. R. Ashton, I. Baxter, M. C. T. Fyfe, F. M. Raymo, N. Spencer, J. F. Stoddart, A. J. P. White and D. J. Williams, Rotaxane or Pseudorotaxane? That Is the Question!†, *J. Am. Chem. Soc.*, 1998, **120**, 2297–2307.
17 C. J. Bruns and J. F. Stoddart, *The Nature of the Mechanical Bond: From Molecules to Machines*, John Wiley & Sons, Inc., 2016.
18 T. Clifford, A. Abushamleh and D. H. Busch, Factors affecting the threading of axle molecules through macrocycles: binding constants for semirotaxane formation, *Proc. Natl. Acad. Sci. U. S. A.*, 2002, **99**, 4830–4836.
19 J. Groppi, L. Casimiro, M. Canton, S. Corra, M. Jafari-Nasab, G. Tabacchi, L. Cavallo, M. Baroncini, S. Silvi, E. Fois and A. Credi, Precision Molecular Threading/Dethreading, *Angew. Chem., Int. Ed. Engl.*, 2020, **59**, 14825–14834.
20 P. G. Young, K. Hirose and Y. Tobe, Axle length does not affect switching dynamics in degenerate molecular shuttles with rigid spacers, *J. Am. Chem. Soc.*, 2014, **136**, 7899–7906.
21 M. Asakawa, P. R. Ashton, R. Ballardini, V. Balzani, M. Bělohradský, M. T. Gandolfi, O. Kocian, L. Prodi, F. M. Raymo, J. F. Stoddart and M. Venturi, The Slipping Approach to Self-Assembling [n]Rotaxanes†, *J. Am. Chem. Soc.*, 1997, **119**, 302–310.
22 B. Riss-Yaw, C. Clavel, P. Laurent and F. Coutrot, The relationship between the conformational degree of freedom of template-containing threads and slippage in the formation of [2]rotaxane building blocks, *Chem. Commun.*, 2017, **53**, 10874–10877.
23 Y. Yamashita, Y. Saito, S. Kikkawa, Y. Mutoh, S. Hosoya, I. Azumaya and S. Saito, Evaluation of the Steric Bulk of Substituents Utilizing the Shuttling Behavior of [2]Rotaxanes with N-Arylpyrrole Moieties, *Eur. J. Org. Chem.*, 2019, **2019**, 3412–3420.
24 G. Gholami, K. Zhu, G. Baggi, E. Schott, X. Zarate and S. J. Loeb, Influence of axle length on the rate and mechanism of shuttling in rigid H-shaped [2]rotaxanes, *Chem. Sci.*, 2017, **8**, 7718–7723.
25 A. C. Catalan and J. Tiburcio, Self-assembly of pseudorotaxane and rotaxane complexes using an electrostatic slippage approach, *Chem. Commun.*, 2016, **52**, 9526–9529.
26 C. Pezzato, C. Cheng, J. F. Stoddart and R. D. Astumian, Mastering the non-equilibrium assembly and operation of molecular machines, *Chem. Soc. Rev.*, 2017, **46**, 5491–5507.
27 G. Ragazzon, C. Schafer, P. Franchi, S. Silvi, B. Colasson, M. Lucarini and A. Credi, Remote electrochemical modu-

lation of pKa in a rotaxane by co-conformational allostery, *Proc. Natl. Acad. Sci. U. S. A.*, 2018, **115**, 9385–9390.

28 K. Nakazono and T. Takata, Neutralization of a sec-ammonium group unusually stabilized by the "rotaxane effect": synthesis, structure, and dynamic nature of a "free" sec-amine/crown ether-type rotaxane, *Chem. – Eur. J.*, 2010, **16**, 13783–13794.

29 H. V. Schröder, S. Sobottka, M. Nössler, H. Hupatz, M. Gaedke, B. Sarkar and C. A. Schalley, Impact of mechanical bonding on the redox-switching of tetrathiafulvalene in crown ether-ammonium [2]rotaxanes, *Chem. Sci.*, 2017, **8**, 6300–6306.

30 H. Hupatz, M. Gaedke, H. V. Schröder, J. Beerhues, A. Valkonen, F. Klautzsch, S. Müller, F. Witte, K. Rissanen, B. Sarkar and C. A. Schalley, Thermodynamic and electrochemical study of tailor-made crown ethers for redox-switchable (pseudo)rotaxanes, *Beilstein J. Org. Chem.*, 2020, **16**, 2576–2588.

31 A. Crochet, E. Kottelat, A. Fleury, M. Neuburger and K. M. Fromm, Polymorph of Dibenzo-24-Crown-8 and its Mercury Complex, *Z. Anorg. Allg. Chem.*, 2011, **637**, 672–675.

32 H. Nagai, Y. Suzaki and K. Osakada, Thiacrown Ethers with Oxygen and Sulfur for Coordination: Formation of the Pd and Pt Complexes and Pseudorotaxane with Dialkylammonium, *Eur. J. Inorg. Chem.*, 2014, **2014**, 4376–4384.

33 F. Le Derf, M. Mazari, N. Mercier, E. Levillain, P. Richomme, J. Becher, J. Garin, J. Orduna, A. Gorgues and M. Salle, Electroregulated Metal-Binding with a Crown Ether Tetrathiafulvalene Derivative: Toward Electrochemically Addressed Metal Cation Sponges, *Inorg. Chem.*, 1999, **38**, 6096–6100.

34 H. Nagai, Y. Suzaki and K. Osakada, Chemical Modification of a [2]Rotaxane Composed of Dithiacrown Ether and Dialkylammonium with Organic and Inorganic Compounds, *Chem. Lett.*, 2016, **45**, 834–836.

35 A. R. Williams, B. H. Northrop, K. N. Houk, J. F. Stoddart and D. J. Williams, The influence of constitutional isomerism and change on molecular recognition processes, *Chem. – Eur. J.*, 2004, **10**, 5406–5421.

36 S. J. Cantrill, D. A. Fulton, A. M. Heiss, A. R. Pease, J. F. Stoddart, A. J. P. White and D. J. Williams, The Influence of Macrocyclic Polyether Constitution upon Ammonium Ion/Crown Ether Recognition Processes, *Chem. – Eur. J.*, 2000, **6**, 2274–2287.

37 T. Takata, Stimuli-Responsive Molecular and Macromolecular Systems Controlled by Rotaxane Molecular Switches, *Bull. Chem. Soc. Jpn.*, 2019, **92**, 409–426.

38 S. Miyagawa, M. Kimura, S. Kagami, T. Kawasaki and Y. Tokunaga, Utilization of a Crown Ether/Amine-Type Rotaxane as a Probe for the Versatile Detection of Anions and Acids by Thin-Layer Chromatography, *Chem. – Asian J.*, 2020, **15**, 3044–3049.

39 J. Nishiyama, Y. Makita and N. Kihara, Rapid and Efficient Acylative Active Transport on a Rotaxane, *Asian J. Org. Chem.*, 2015, **4**, 1056–1064.

40 H. Sato, D. Aoki and T. Takata, Synthesis and Star/Linear Topology Transformation of a Mechanically Linked ABC Terpolymer, *ACS Macro Lett.*, 2016, **5**, 699–703.

41 S. D. P. Fielden, D. A. Leigh, C. T. McTernan, B. Perez-Saavedra and I. J. Vitorica-Yrezabal, Spontaneous Assembly of Rotaxanes from a Primary Amine, Crown Ether and Electrophile, *J. Am. Chem. Soc.*, 2018, **140**, 6049–6052.

42 H. V. Schröder, F. Witte, M. Gaedke, S. Sobottka, L. Suntrup, H. Hupatz, A. Valkonen, B. Paulus, K. Rissanen, B. Sarkar and C. A. Schalley, An aryl-fused redox-active tetrathiafulvalene with enhanced mixed-valence and radical-cation dimer stabilities, *Org. Biomol. Chem.*, 2018, **16**, 2741–2747.

43 T. Matsumura, F. Ishiwari, Y. Koyama and T. Takata, C-C bond-forming click synthesis of rotaxanes exploiting nitrile N-oxide, *Org. Lett.*, 2010, **12**, 3828–3831.

44 V. N. Vukotic, K. Zhu, G. Baggi and S. J. Loeb, Optical Distinction between "Slow" and "Fast" Translational Motion in Degenerate Molecular Shuttles, *Angew. Chem., Int. Ed.*, 2017, **56**, 6136–6141.

45 K. Hirose, Molecular brake systems controlled by light and heat, *J. Inclusion Phenom. Macrocyclic Chem.*, 2010, **68**, 1–24.

46 J. Dale and P. O. Kristiansen, Cyclic oligo-ethers related to ethylene oxide, *J. Chem. Soc., Chem. Commun.*, 1971, **13**, 670.

47 C. I. Ratcliffe, J. A. Ripmeester, G. W. Buchanan and J. K. Denike, A molecular merry-go-round: motion of the large macrocyclic molecule 18-crown-6 in its solid complexes studied by deuterium NMR, *J. Am. Chem. Soc.*, 1992, **114**, 3294–3299.

48 V. N. Vukotic, K. J. Harris, K. Zhu, R. W. Schurko and S. J. Loeb, Metal-organic frameworks with dynamic interlocked components, *Nat. Chem.*, 2012, **4**, 456–460.

49 K. Zhu, V. N. Vukotic, C. A. O'Keefe, R. W. Schurko and S. J. Loeb, Metal-organic frameworks with mechanically interlocked pillars: controlling ring dynamics in the solid-state via a reversible phase change, *J. Am. Chem. Soc.*, 2014, **136**, 7403–7409.

50 N. D. Suhan, L. Allen, M. T. Gharib, E. Viljoen, S. J. Vella and S. J. Loeb, Colour coding the co-conformations of a [2] rotaxane flip-switch, *Chem. Commun.*, 2011, **47**, 5991–5993.

51 M. Gaedke, F. Witte, J. Anhäuser, H. Hupatz, H. V. Schröder, A. Valkonen, K. Rissanen, A. Lützen, B. Paulus and C. A. Schalley, Chiroptical inversion of a planar chiral redox-switchable rotaxane, *Chem. Sci.*, 2019, **10**, 10003–10009.

52 H. V. Schröder, F. Stein, J. M. Wollschläger, S. Sobottka, M. Gaedke, B. Sarkar and C. A. Schalley, Accordion-Like Motion in Electrochemically Switchable Crown Ether/Ammonium Oligorotaxanes, *Angew. Chem., Int. Ed.*, 2019, **58**, 3496–3500.

Supporting Information

Dual-stimuli pseudorotaxane switches under kinetic control

Marius Gaedke,[a] Henrik Hupatz,[a] Hendrik V. Schröder,[a,b] Simon Suhr,[c] Kurt F. Hoffmann,[d] Arto Valkonen,[e] Biprajit Sarkar,[c] Sebastian Riedel,[d] Kari Rissanen,[e] and Christoph A. Schalley*[a]

[a] Institut für Chemie und Biochemie der Freien Universität Berlin, Arnimallee 20, 14195 Berlin, Germany.

[b] Present address: Department of Chemical and Biological Engineering, Princeton University, Princeton, NJ08544, USA

[c] Lehrstuhl für Anorganische Koordinationschemie, Institut für Anorganische Chemie, Universität Stuttgart, Pfaffenwaldring 55, 70569 Stuttgart, Germany

[d] Institut für Chemie und Biochemie der Freien Universität Berlin, Fabeckstr. 34/36 14195 Berlin, Germany.

[e] University of Jyvaskyla, Department of Chemistry, P.O. Box 35, 40014 Jyväskylä, Finland.

*Corresponding author e-mail: c.schalley@fu-berlin.de

Table of Contents

1. Experimental details

1.1. General methods

All reagents and solvents were obtained from commercial sources and used without further purification. Dry solvents were purchased from Acros Organics (Geel, Belgium) and either directly used or treated with the M. Braun solvent purification system SPS 800. **TTFC8**,[1] 2,6-dimethoxybenzonitrile oxide stopper **St1**,[2] (2,6-dimethylphenyl)methanaminium chloride,[3] (3,5-di-*tert*-butylphenyl)methanamine **1**,[4] 5-hexynyl tosylate **4**,[5] 4-(hex-5-yn-1-yloxyl)benzonitrile **S2**,[6] were synthesised according to literature procedures, naphthalen-2-ylmethanaminium hydrochloride was bought at Fluorochem (Hadfield, U.K.), 3,5-di-*tert*-butylbenzaldehyde, 2-methylbenzylamine hydrochloride, 3-methylbenzylamine hydrochloride, (3-phenylphenyl)methanamine hydrochloride, 2-naphthylmethanamine hydrochloride, 2,3-dimethylbenzylamine, 2,5-dimethylbenzylamine, 2-nitrobenzylamine hydrochloride, 2-ethylbenzylamine hydrochloride, sodium tetrakis[3,5-bis(trifluoromethyl)phenyl]borate ($NaBArF_{24}$), 6-hydroxy-1-naphthoic acid **2**, benzotriazol-1-ol (HOBT), 3-(ethyliminomethyleneamino)-*N*,*N*-dimethylpropan-1-amine hydrochloride (EDC·HCl), *N*-ethyl-*N*-(propan-2-yl)propan-2-amine (DIPEA) and polystyrene-immobilized phosphazene base P2 were bought at Sigma Aldrich (Taufkirchen, Germany) or TCI Chemicals (Eschborn, Germany). Thin-layer chromatography was performed on silica gel-coated plates with fluorescent indicator F254 (Merck KGaA, Darmstadt, Germany). For column chromatography, silica gel (0.04-0.063 mm, Merck), or Biotage (Uppsala, Sweden) SNAP and SNAP Ultra Cartridges were used on a Biotage Isolera One.

^{1}H and ^{13}C NMR experiments were performed on JEOL ECX 400, JEOL ECZ 600, Bruker AVANCE 500 or Bruker AVANCE 700 instruments. Residual solvent signals were used as the internal standards. All shifts are reported in ppm and NMR multiplicities are abbreviated as s (singlet), d (doublet), t (triplet), m (multiplet) and br (broad). Coupling constants *J* are reported in Hertz. Compounds containing the tetrakis[3,5-bis(trifluoromethyl)phenyl]borate ($BArF_{24}^{-}$) anion show ^{13}C NMR spectra with ^{19}F, ^{10}B and ^{11}B couplings. These signals are denoted as one signal.

Melting points were determined on a SMP 30 (Stuart) instrument and are uncorrected.

High-resolution ESI mass spectra were measured on an Agilent 6210 ESI-TOF device. CID experiments were performed on a Synapt G2-S HDMS (Waters Co., Milford, MA, USA) mass spectrometer. HPLC grade solvents were used for sample preparation.

UV/Vis spectra were recorded with a Varian Cary 50 Bio spectrometer equipped with a xenon lamp. Solvents with HPLC grade and Suprasil glass cuvettes with a path-length of 1 cm were used.

CV measurements were carried out with an Autolab PGSTAT302N potentiostat in a 2 mL measuring cell in dichloroethane with 0.1 M n-Bu_4NBArF_{24} as the conducting salt. The working electrode was made of glassy carbon, the reference Ag electrode was etched with conc. aq. HCl. A Pt wire worked as the counter electrode. The cyclic voltammograms were recorded with 10, 25, 50, 100, 250, 500, 1000 and 2500 mV/s scan rates, to ensure that the observed processes are reversible and diffusion-limited. In order to obtain the correct half-wave potentials, $FeCp_2^{*0}/FeCp_2^{*+}$ was used as the pseudo reference. These values were afterwards referenced to $FeCp_2/FeCp_2^{+}$ as described in the literature.[7] The raw data were treated with Nova 1.5 by Metrohm and the plots were made with Origin 2020 by OriginLab.

Bulk electrolysis experiments were conducted in a five-neck cell with a four-electrode set-up (see Figure S54 for a photograph) connected to an Autolab PGSTAT302N MBA potentiostat in bipotentiostat mode, using dry and degassed CH_2Cl_2 as the solvent and n-Bu_4NBArF_{24} as the supporting electrolyte. Electrolysis was performed with a cylindrical GC rod (3 mm diameter) at a potential of 1 V vs. the pseudo-reference. A silver wire was used as the pseudo-reference, a coiled Pt wire as the counter electrode. An additional GC disk electrode was employed to perform CV and DPV measurements every 30 minutes to determine the effect of electrolysis on the electrochemical response. The counter electrode was separated from the rest of the cell by glass wool soaked in analyte solution to suppress diffusion towards the working electrodes. Cyclic voltammograms were recorded at a scan rate of 100 mV/s. Differential pulse voltammograms were recorded with a step size of 0.005 V, a modulation amplitude of 0.025 V and modulation and interval times of 0.05 and 0.5 s, respectively. Measurements and treatment of raw data were performed within the Nova 2.1 software by Metrohm, while plots were made using Origin 2020 by OriginLab. The half-wave and peak potentials in CV and DPV experiments drifted between different measurements when recorded during electrolysis, but the diagnostic potential differences between the characteristic oxidation events remained constant. Potentials were afterwards normalized to the values obtained in regular CV measurements.

1.2. Synthesis of axles PA*n*

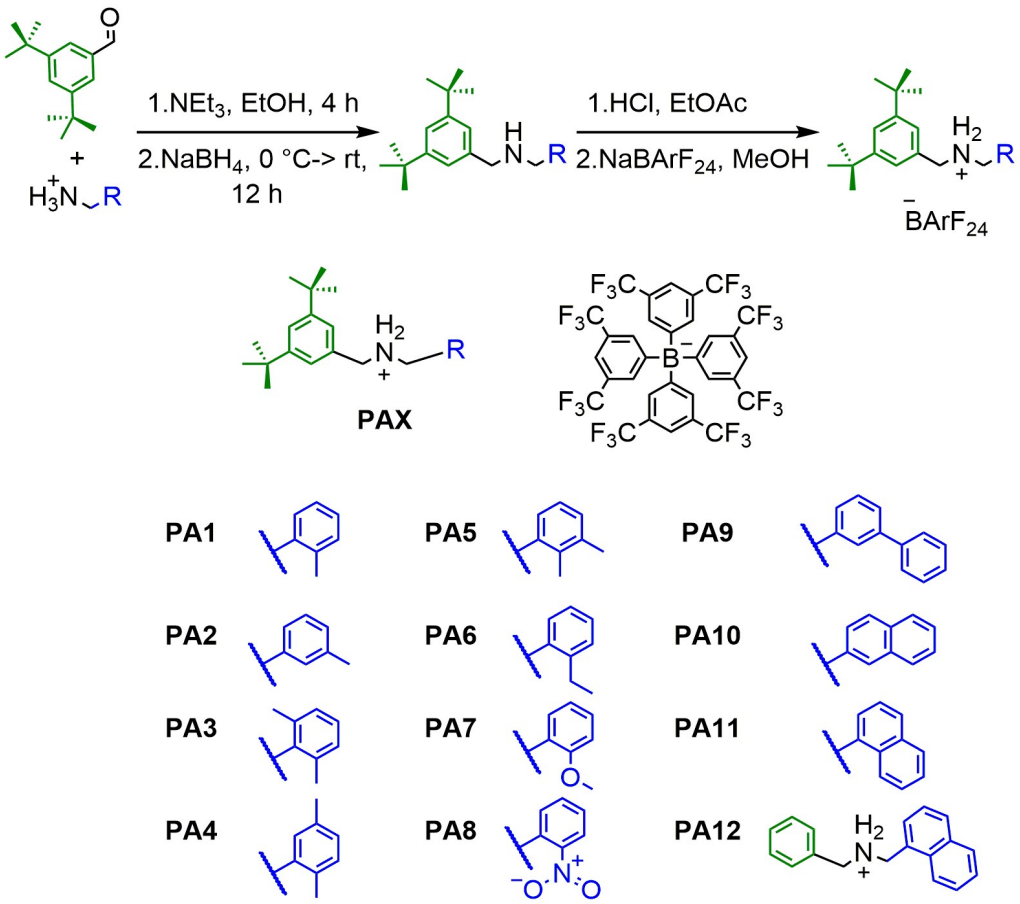

Scheme S1 Synthesis of axles **PA1-12**.

N-(3,5-di-tert-butylbenzyl)-1-(o-tolyl)methanaminium tetrakis(3,5-bis(trifluoromethyl)phenyl)borate

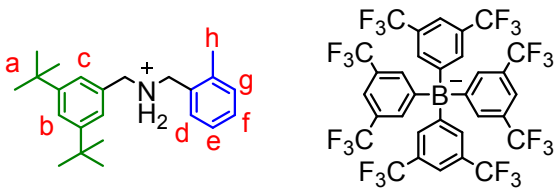

PA1

A solution of 190 mg (1.21 mmol, 1.0 equiv.) 2-methylbenzylamine hydrochloride, 263 mg (1.21 mmol, 1.0 equiv.) 3,5-di-*tert*-butylbenzaldehyde and 150 µL (1.08 mmol, 0.9 equiv.) NEt_3, in dry EtOH (30 mL) were refluxed under argon atmosphere for 4 h. Afterwards, the solution was cooled to 0 °C and 228 mg (6.03 mmol, 5.0 equiv.) $NaBH_4$ were slowly added. The mixture was stirred under argon atmosphere overnight in the thawing ice bath. The reaction was then quenched by slow addition of sat. $NaHCO_3$ solution and filtered. The solvent was removed from the filtrate under reduced pressure and the residue was dissolved in CH_2Cl_2 and then washed with sat. $NaHCO_3$ solution and brine. The organic phase was dried with $MgSO_4$ and the solvent removed again. The crude product was purified by column chromatography (SiO_2, CH_2Cl_2/MeOH = 100:1 -> 50:1, R_f ~ 0.3 in CH_2Cl_2/MeOH (100:1)) to obtain a yellowish oil. The oil was dissolved in EtOAc (5 ml) and acidified with HCl (conc.) until the solution reached pH = 1. The mixture was stirred for 1 h and afterwards the solvent was removed under reduced pressure. The residue was dissolved in MeOH (5 ml) and 195 mg (0.22 mmol, 1.0 equiv.) $NaBArF_{24}$ was added. The solution was left stirring overnight at room temperature, then the solvent was removed. The residue was taken up in CH_2Cl_2, washed with brine/water and dried over $MgSO_4$. The product **PA1** (222 mg, 0.19 mmol, 16 % overall) was obtained as off-white sticky solid.

^{1}H NMR (500 MHz, $CDCl_3$): δ = 1.31 (s, 18H, a), 2.14 (s, 3H, h), 4.26-4.32 (m, 4H, $C\underline{H_2}$-NH_2), 6.24 (s, 2H, $N\underline{H_2}$), 7.09-7.12 (m, 1H, d), 7.14 (d, *J*=1.7 Hz, 2H, c), 7.17-7.27(m, 2H, g), 7.33-7.37 (m, 1H, e), 7.55 (s_{br}, 4H, $BArF_{24}$), 7.66 (t, *J*=1.7Hz, 1H, b), 7.75 (s_{br}, 8H, $BArF_{24}$) ppm. **^{13}C NMR** (176 MHz, $CDCl_3$): δ = 18.4 31.1, 31.2, 31.4, 31.5, 35.2, 50.7, 54.4, 117.7, 117.8, 121.5, 123.3, 123.7, 125.9, 126.2, 126.3, 127.2, 128.1, 129.2, 130.0, 132.1, 132.4, 135.0, 154.3, 161.3, 161.7, 162.1, 162.5 ppm. **HRMS** (MeOH): *m/z* calcd. for $[C_{23}H_{34}N]^+$: 324.2686 $[M]^+$, found: 324.2704.

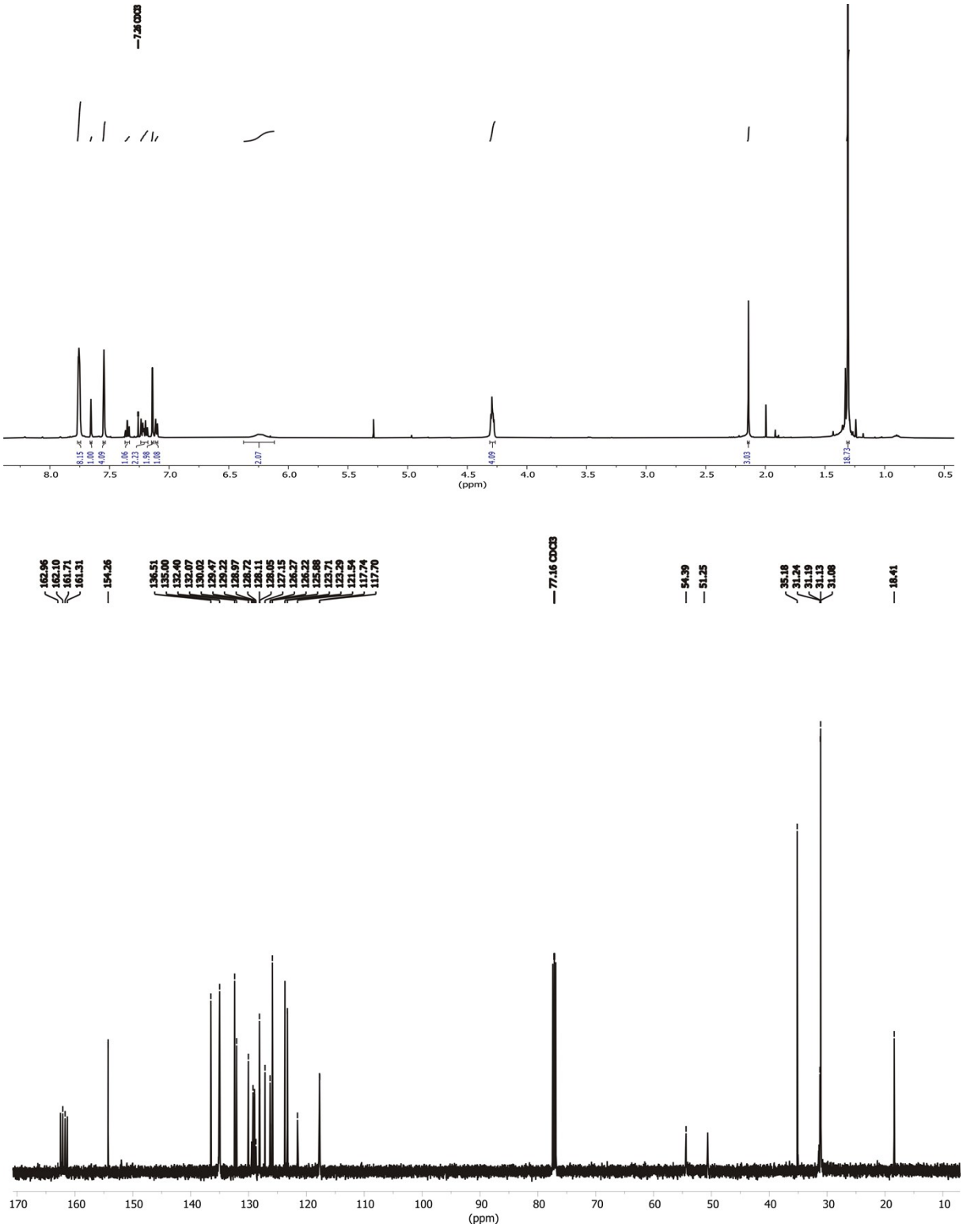

Fig. S1 ^{1}H (top) and ^{13}C (bottom) NMR spectra (500/176 MHz, $CDCl_3$, 298 K) of **PA1**.

N-(3,5-di-tert-butylbenzyl)-1-(*m*-tolyl)methanaminium tetrakis(3,5-bis(trifluoromethyl)phenyl)borate

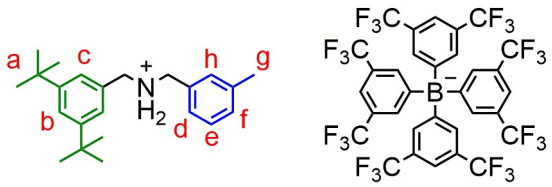

PA2

A solution of 53 mg (0.34 mmol, 1.0 equiv.) 3-methylbenzylamine hydrochloride, 73 mg (0.34 mmol, 1.0 equiv.) 3,5-di-*tert*-butylbenzaldehyde and 31 µL (0.30 mmol, 0.9 equiv.) NEt_3, in dry EtOH (20 mL) were refluxed under argon atmosphere for 4 h. Afterwards, the solution was cooled to 0 °C and 64 mg (1.7 mmol, 5.0 equiv.) $NaBH_4$ was slowly added. The mixture was left stirring under argon atmosphere overnight in the thawing ice bath. The reaction was quenched by slow addition of sat. $NaHCO_3$ solution and then filtered. The solvent was removed under reduced pressure from the filtrate and the residue was dissolved in CH_2Cl_2 and then washed with sat. $NaHCO_3$ solution and brine. The organic phase was dried with $MgSO_4$ and the solvent removed again. The crude product was purified by column chromatography (SiO_2, CH_2Cl_2/MeOH = 100:1 -> 50:1, R_f ~ 0.3 in CH_2Cl_2/MeOH (100:1)) to obtain a yellowish oil. The oil was dissolved in EtOAc (5 ml) and acidified with HCl (conc.) until the solution reached pH = 1. The mixture was stirred for 1 h and afterwards the solvent was removed under reduced pressure. The residue was dissolved in MeOH (5 ml) and 150 mg (0.17 mmol, 1.0 equiv.) $NaBArF_{24}$ was added. The solution was left stirring overnight at room temperature, then the solvent was removed. The residue was taken up in CH_2Cl_2, washed with brine/water and dried over $MgSO_4$. The product **PA2** (200 mg, 0.16 mmol, 47 % overall) was obtained as off-white sticky solid.

^{1}H NMR (500 MHz, $CDCl_3$): δ = 1.30 (s, 18H, a), 2.32 (s, 3H, g), 4.09-4.19 (m, 4H, C$\underline{H}_2$-NH_2), 7.00-7.05 (m, 2H, f,h), 7.09-7.12 (m, 2H, d,e), 7.19 (s, 2H, N$\underline{H}_2$), 7.28-7.30 (m, 2H, c), 7.52 (s_{br}, 4H, $BArF_{24}$), 7.57-7.58 (m, 1H, b), 7.70 (s_{br}, 8H, $BArF_{24}$) ppm. **^{13}C NMR** (176 MHz, $CDCl_3$): δ = 31.3, 35.8, 52.6, 53.3, 117.7, 123.4, 123.7, 125.6, 125.8, 126.2, 127.7, 128.0, 128.3, 129.1, 129.9, 130.2, 132.2, 135.0, 140.7, 153.7 161.8 ppm. **HRMS** (MeOH): *m/z* calcd. for $[C_{23}H_{34}N]^+$: 324.2686 $[M]^+$, found: 324.2708.

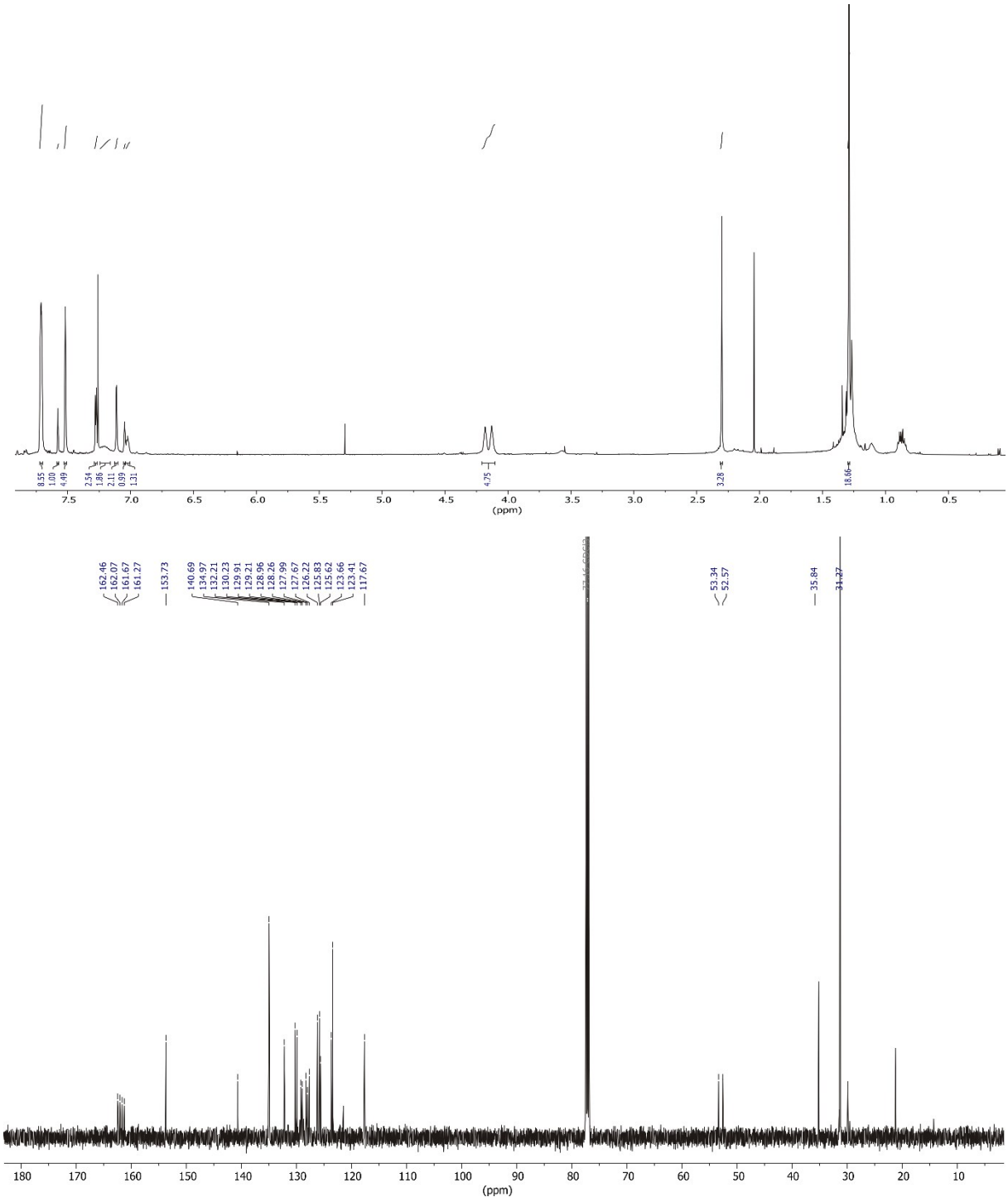

Fig. S2 ^{1}H (top) and ^{13}C (bottom) NMR spectra (500/176 MHz, $CDCl_3$, 298 K) of **PA2**.

N-(3,5-di-tert-butylbenzyl)-1-(2,6-dimethylphenyl)methanaminium tetrakis(3,5-bis(trifluoromethyl)phenyl)borate

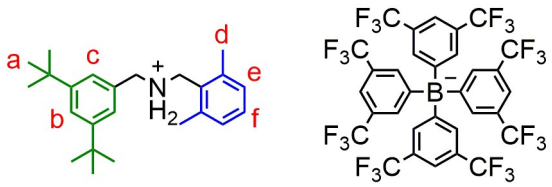

PA3

A solution of 433 mg (2.53 mmol, 1.0 equiv.) (2,6-dimethylphenyl)methanaminium chloride[3], 552 mg (2.53 mmol, 1.0 equiv.) 3,5-di-*tert*-butylbenzaldehyde and 310 µL (2.24 mmol, 0.9 equiv.) NEt_3, in dry EtOH (30 mL) were refluxed under argon atmosphere for 4 h. Afterwards, the solution was cooled to 0 °C and 479 mg (12.65 mmol, 5.0 equiv.) $NaBH_4$ was slowly added. The mixture was left stirring under argon atmosphere overnight in the thawing ice bath. The reaction was quenched by slow addition of sat. $NaHCO_3$ solution and then filtered. The solvent was removed under reduced pressure from the filtrate and the residue was dissolved in CH_2Cl_2 and then washed with sat. $NaHCO_3$ solution and brine. The organic phase was dried with $MgSO_4$ and the solvent removed again. The crude product was purified by column chromatography (SiO_2, CH_2Cl_2/MeOH = 100:1 -> 50:1, R_f ~ 0.3 in CH_2Cl_2/MeOH (100:1)) to obtain a yellowish oil. The oil was dissolved in EtOAc (15 ml) and acidified with HCl (conc.) until the solution reached pH = 1. The mixture was stirred for 1 h and afterwards the solvent was removed under reduced pressure. The residue was dissolved in MeOH (5 ml) and 1.15 g (1.24 mmol, 1.0 equiv.) $NaBArF_{24}$ was added. The solution was left stirring overnight at room temperature, then the solvent was removed. The residue was taken up in CH_2Cl_2, washed with brine/water and dried over $MgSO_4$. The product **PA3** (1.18 g, 0.98 mmol, 39 % overall) was obtained as colorless oil.

^{1}H NMR (500 MHz, $CDCl_3$): δ = 1.31 (s, 18H, a), 2.11 (s, 6H, d), 4.24-4.34 (m, 4H, C$\underline{H_2}$-NH_2), 6.55 (s, 2H, N$\underline{H_2}$), 7.05-7.08 (m, 2H, e), 7.15 (d, J = 1.7 Hz, 2H, c), 7.21-7.25 (m, 1H, f), 7.52 (s_{br}, 4H, $BArF_{24}$), 7.63 (t, J = 1.7 Hz, 1H, b), 7.70 (s_{br}, 8H, $BArF_{24}$) ppm. **^{13}C NMR** (176 MHz, $CDCl_3$): δ = 31.3, 35.2, 45.2, 54.3, 117.7, 122.4, 123.5, 123.6, 123.9, 125.4, 125.5, 125.9, 126.0, 129.0, 130.1, 132.2, 131.2, 134.9, 137.2, 153.1 161.8 ppm. **HRMS** (MeOH): *m/z* calcd. for $[C_{24}H_{36}N]^+$: 338.2842 $[M]^+$, found: 338.2871.

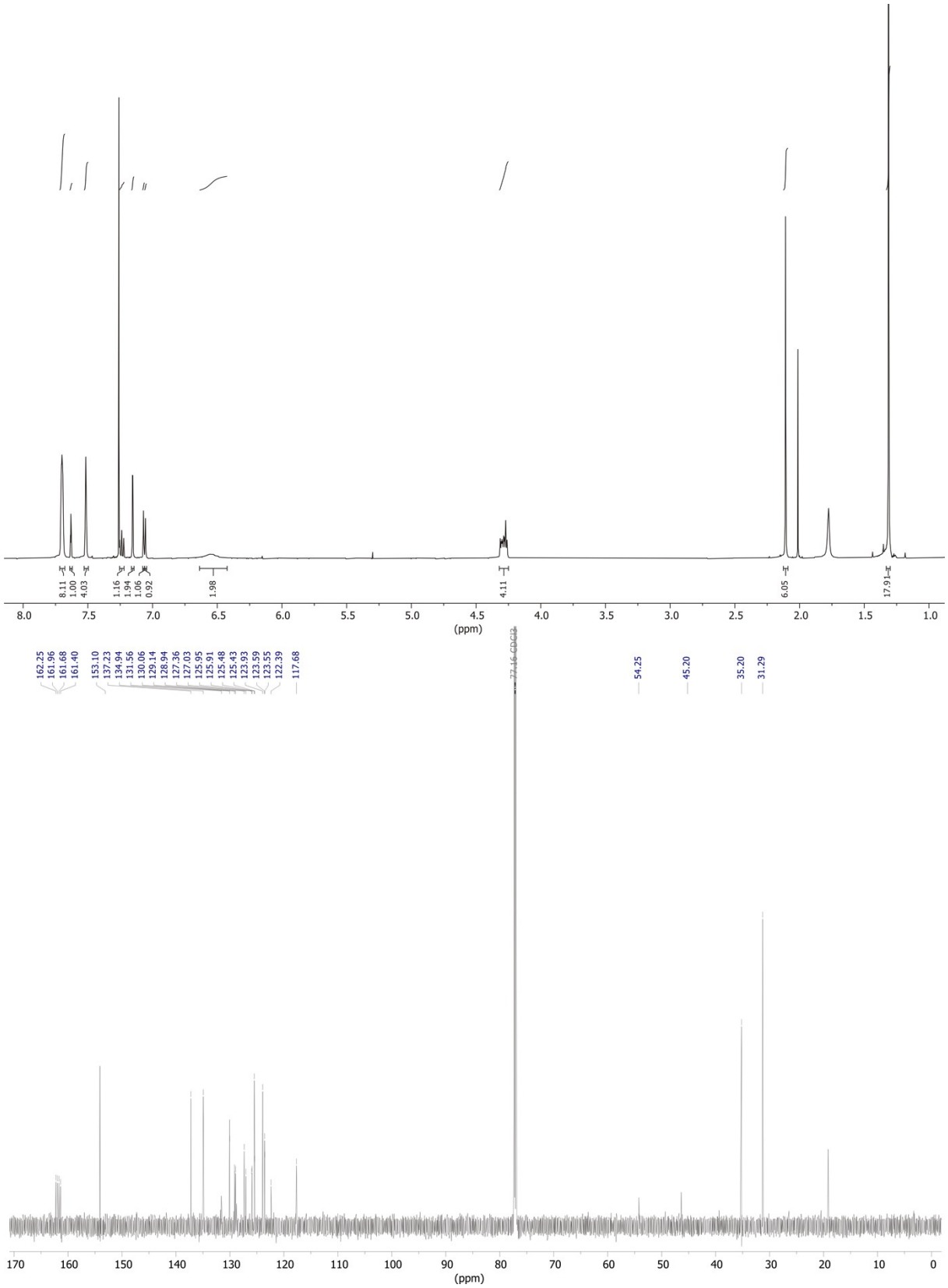

Fig. S3 ^{1}H (top) and ^{13}C (bottom) NMR spectra (500/176 MHz, $CDCl_3$, 298 K) of **PA3**.

N-(3,5-di-tert-butylbenzyl)-1-(2,5-dimethylphenyl)methanaminium tetrakis(3,5-bis(trifluoromethyl)phenyl)borate

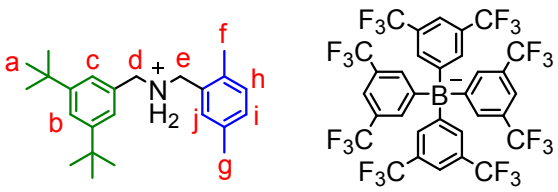

PA4

A solution of 250 mg (1.5 mmol, 1.0 equiv.) (2,5-dimethylphenyl)methanaminium chloride, 319 mg (1.5 mmol, 1.0 equiv.) 3,5-di-*tert*-butylbenzaldehyde and 180 µL (1.3 mmol, 0.9 equiv.) NEt_3, in dry EtOH (60 mL) were refluxed under argon atmosphere for 4 h. Afterwards, the solution was cooled to 0 °C and 275 mg (7.3 mmol, 5.0 equiv.) $NaBH_4$ was slowly added. The mixture was left stirring under argon atmosphere overnight in the thawing ice bath. The reaction was quenched by slow addition of sat. $NaHCO_3$ solution and then filtered. The solvent was removed under reduced pressure from the filtrate and the residue was dissolved in CH_2Cl_2 and then washed with sat. $NaHCO_3$ solution and brine. The organic phase was dried with $MgSO_4$ and the solvent removed again. The crude product was purified by column chromatography (SiO_2, CH_2Cl_2/MeOH = 100:1 -> 50:1, R_f ~ 0.7 in CH_2Cl_2/MeOH (50:1)) to obtain a yellowish oil. The oil was dissolved in Et_2O (15 ml) and acidified with HCl (conc.) until the solution reached pH = 1. The mixture was stirred for 3 h and afterwards the solvent was removed under reduced pressure. A fraction of the residue was dissolved in MeOH (10 ml) and 247 mg (0.27 mmol, 1.0 equiv.) $NaBArF_{24}$ was added. The solution was left stirring overnight at room temperature, then the solvent was removed. The residue was taken up in CH_2Cl_2, washed with brine/water and dried over $MgSO_4$. The product **PA4** (315 mg, 0.26 mmol, 88 % overall) was obtained as colorless oil.

^{1}H NMR (700 MHz, $CDCl_3$): δ = 1.33 (s, 18H, a), 2.12 (s, 3H, f), 2.27 (s, 3H, g), 4.16 - 4.24 (m, 4H, d,e), 6.95 – 6.98 (m, 1H, j), 7.13 - 7.16 (m, 2H, c,h), 7.19 – 7.22 (m, 1H, i), 7.54 (s_{br}, 4H, $BArF_{24}$), 7.62 (t, J = 1.7 Hz, 1H, b), 7.73 (s_{br}, 8H, $BArF_{24}$) ppm. **^{13}C NMR** (176 MHz, $CDCl_3$): δ = 18.1, 20.7, 31.3, 35.2, 49.9, 53.6, 117.7, 122.4, 123.4, 123.9, 125.5, 125.7, 126.6, 127.0, 127.6, 128.8, 129.0, 129.1, 129.3, 130.6, 132.2, 132.5, 133.4, 138.0, 153.9 161.9 ppm. **HRMS** (MeOH): *m/z* calcd. for $[C_{24}H_{36}N]^+$: 338.2842 $[M]^+$, found: 338.2858.

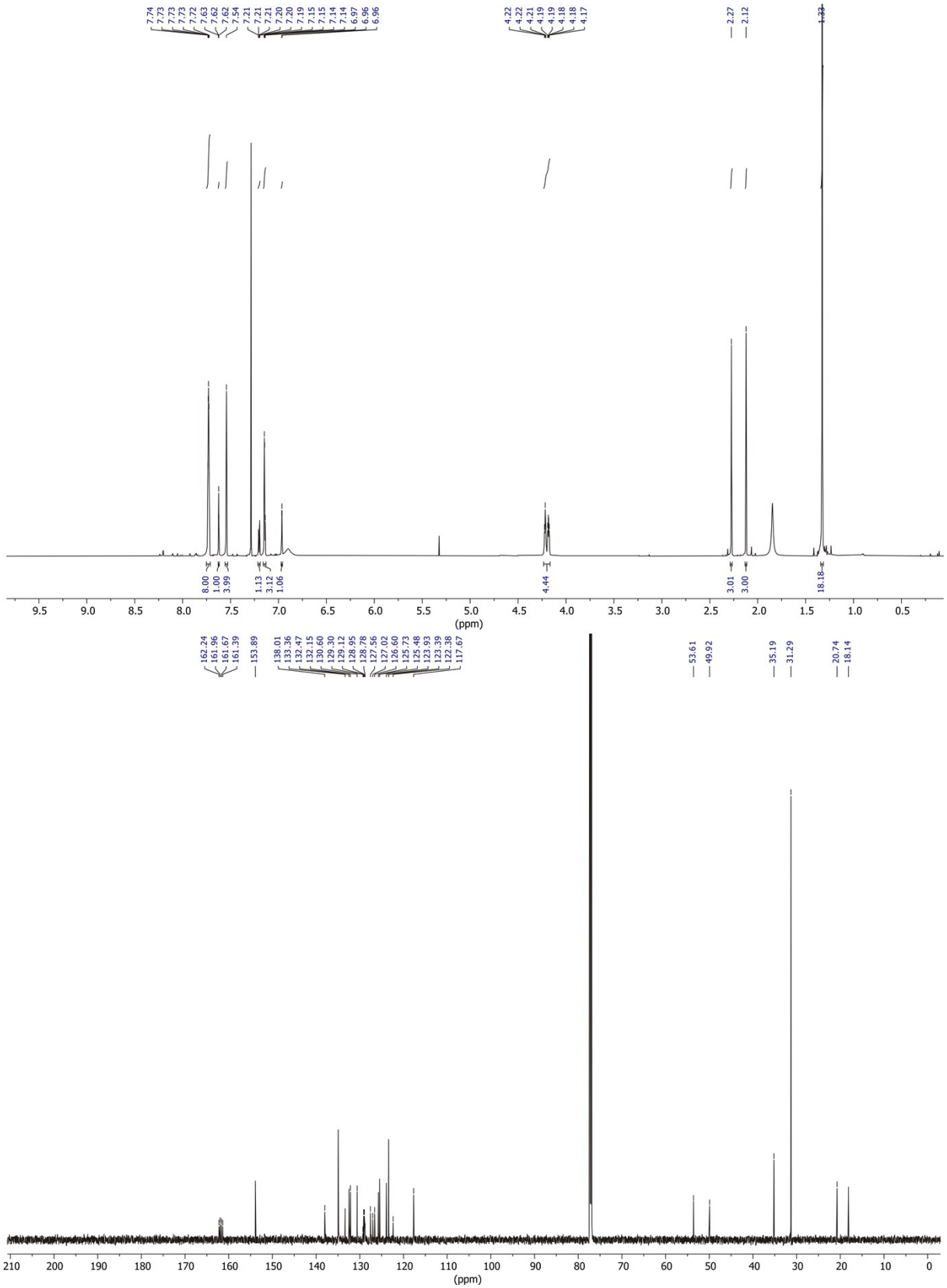

Fig. S4 ^{1}H (top) and ^{13}C (bottom) NMR spectra (700/176 MHz, $CDCl_3$, 298 K) of **PA4**.

N-(3,5-di-tert-butylbenzyl)-1-(2,3-dimethylphenyl)methanaminium tetrakis(3,5-bis(trifluoromethyl)phenyl)borate

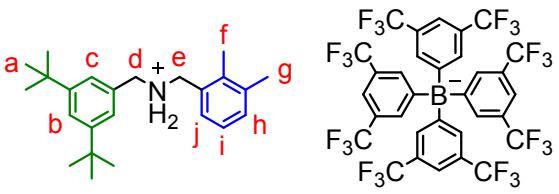

PA5

A solution of 250 mg (1.5 mmol, 1.0 equiv.) (2,3-dimethylphenyl)methanaminium chloride, 319 mg (1.5 mmol, 1.0 equiv.) 3,5-di-*tert*-butylbenzaldehyde and 180 µL (1.3 mmol, 0.9 equiv.) NEt_3, in dry EtOH (60 mL) were refluxed under argon atmosphere for 4 h. Afterwards, the solution was cooled to 0 °C and 275 mg (7.3 mmol, 5.0 equiv.) $NaBH_4$ was slowly added. The mixture was left stirring under argon atmosphere overnight in the thawing ice bath. The reaction was quenched by slow addition of sat. $NaHCO_3$ solution and then filtered. The solvent was removed under reduced pressure from the filtrate and the residue was dissolved in CH_2Cl_2 and then washed with sat. $NaHCO_3$ solution and brine. The organic phase was dried with $MgSO_4$ and the solvent removed again. The crude product was purified by column chromatography (SiO_2, CH_2Cl_2 -> CH_2Cl_2/MeOH = 50:1, R_f ~ 0.7 in CH_2Cl_2/MeOH (50:1)) to obtain a yellowish oil. The oil was dissolved in EtOAc (10 ml) and acidified with HCl (conc.) until the solution reached pH = 1. The mixture was stirred for 3 h and afterwards the solvent was removed under reduced pressure. A fraction of the residue was dissolved in MeOH (5 ml) and 247 mg (0.27 mmol, 1.0 equiv.) $NaBArF_{24}$ was added. The solution was left stirring overnight at room temperature, then the solvent was removed. The residue was taken up in CH_2Cl_2, washed with brine/water and dried over $MgSO_4$. The product **PA5** (324 mg, 0.27 mmol, 58 % overall) was obtained as colorless oil.

^{1}H NMR (700 MHz, $CDCl_3$): δ = 1.30 (s, 18H, a), 2.01 (s, 3H, f), 2.20 (s, 3H, g), 4.11-4.17 (m, 4H, d,e), 6.98 (d, J = 7.6 Hz, 1H, h), 7.08 (t, J = 7.6 Hz, 1H, i), 7.14 (d, J=1.8 Hz, 2H, c), 7.22 (d, J = 7.6 Hz, 1H, j), 7.51 (s_{br}, 4H, $BArF_{24}$), 7.58 (t, J = 1.5 Hz, 1H, b), 7.70 (s_{br}, 8H, $BArF_{24}$) ppm. **^{13}C NMR** (176 MHz, $CDCl_3$): δ = 14.9, 20.5, 31.3, 35.2, 50.0, 53.2, 117.6, 117.6, 117.7, 122.4, 123.5, 123.9, 125.4, 125.5, 127.0, 127.1, 127.9, 128.1, 128.8, 129.0, 129.1, 129.3, 133.0, 134.9, 135.2, 139.4, 153.7 161.9 ppm. **HRMS** (MeOH): *m/z* calcd. for $[C_{24}H_{36}N]^+$: 338.2842 $[M]^+$, found: 338.2847.

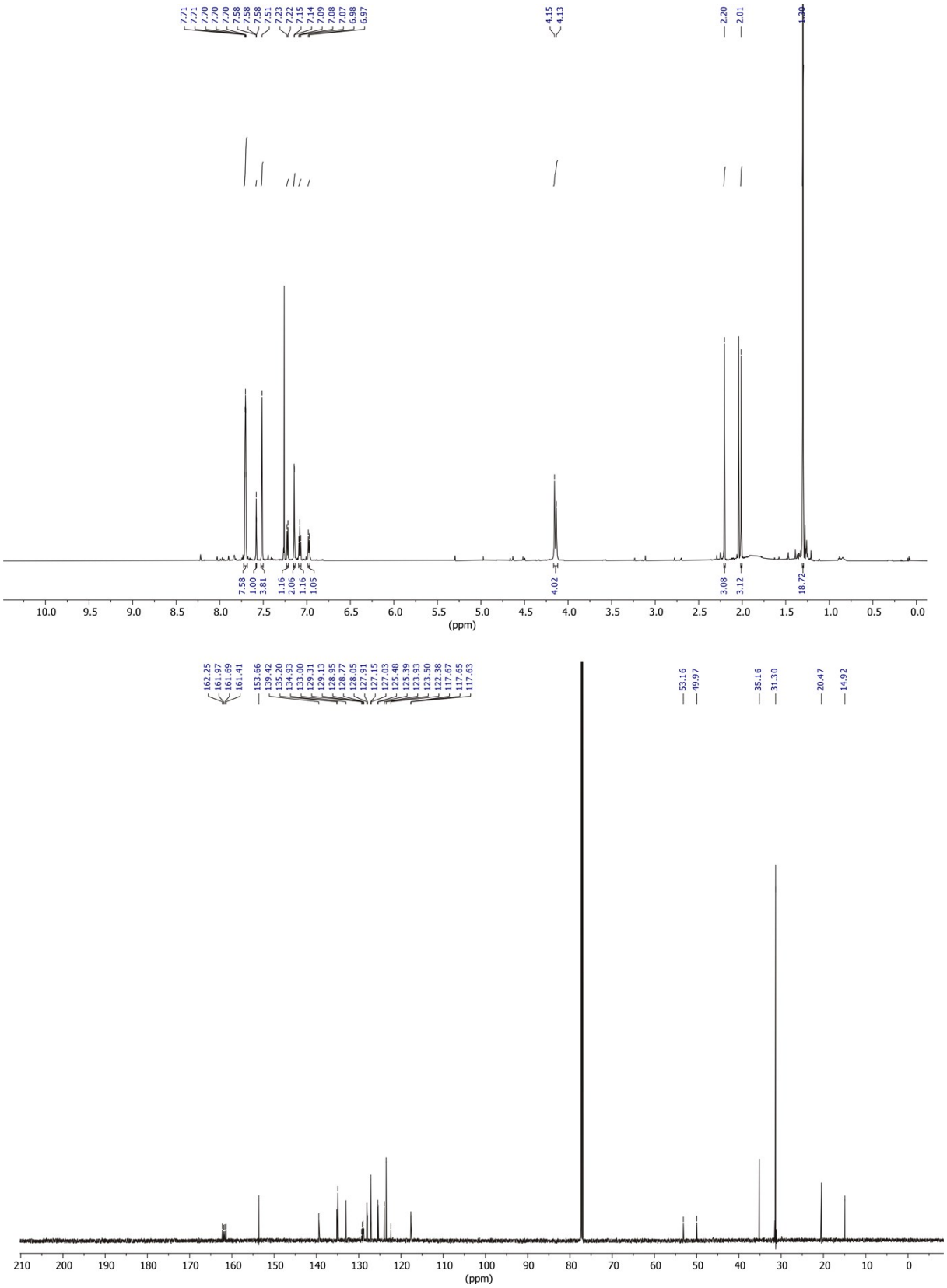

Fig. S5 ^{1}H (top) and ^{13}C (bottom) NMR spectra (700/176 MHz, $CDCl_3$, 298 K) of **PA5**.

N-(3,5-di-tert-butylbenzyl)-1-(2-ethylphenyl)methanaminium tetrakis(3,5-bis(trifluoromethyl)phenyl)borate

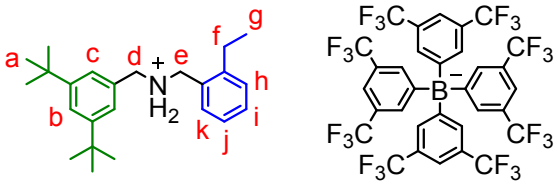

PA6

A solution of 250 mg (1.5 mmol, 1.0 equiv.) (2-ethylphenyl)methanaminium chloride[8], 319 mg (1.5 mmol, 1.0 equiv.) 3,5-di-*tert*-butylbenzaldehyde and 180 µL (1.08 mmol, 0.9 equiv.) NEt_3, in dry EtOH (60 mL) were refluxed under argon atmosphere for 4 h. Afterwards, the solution was cooled to 0 °C and 273 mg (7.3 mmol, 5.0 equiv.) $NaBH_4$ was slowly added. The mixture was left stirring under argon atmosphere overnight in the thawing ice bath. The reaction was quenched by slow addition of sat. $NaHCO_3$ solution and then filtered. The solvent was removed under reduced pressure from the filtrate and the residue was dissolved in CH_2Cl_2 and then washed with sat. $NaHCO_3$ solution and brine. The organic phase was dried with $MgSO_4$ and the solvent removed again. The crude product was purified by column chromatography (SiO_2, CH_2Cl_2 -> CH_2Cl_2/MeOH = 100:1, R_f ~ 0.3 in CH_2Cl_2/MeOH (100:1)) to obtain a yellowish oil. The oil was dissolved in EtOAc (10 ml) and acidified with HCl (conc.) until the solution reached pH = 1. The mixture was stirred for 1 h and afterwards the solvent was removed under reduced pressure. A fraction of the residue was dissolved in MeOH (10 ml) and 239 mg (0.27 mmol, 1.0 equiv.) $NaBArF_{24}$ was added. The solution was left stirring overnight at room temperature, then the solvent was removed. The residue was taken up in CH_2Cl_2, washed with brine/water and dried over $MgSO_4$. The product **PA6** (325 mg, 0.27 mmol, 58 % overall) was obtained as colorless oil.

^{1}H NMR (700 MHz, $CDCl_3$): δ = 1.04 (t, J = 7.6 Hz, 3H, g), 1.31 (s, 18H, a), 2.36 (q, J = 7.5 Hz, 2H, f), 4.13 - 4.22 (m, 4H, d,e), 7.15 - 7.17 (m, 3H, c,i), 7.17 - 7.20 (m, 1H, h), 7.21 - 7.30 (m, 1H, j), 7.36 - 7.39 (m, 1H, k), 7.45 - 7.50 (m, 1H, h), 7.52 (s_{br}, 4H, $BArF_{24}$), 7.59 – 7.60 (m, 1H, b), 7.70 (s_{br}, 8H, $BArF_{24}$) ppm. **^{13}C NMR** (176 MHz, $CDCl_3$): δ = 15.4, 25.5, 31.3, 35.2, 48.7, 53.4, 117.7, 122.4, 123.6, 123.9, 125.5, 125.5, 126.5, 127.0, 127.7, 127.8, 129.0, 129.1, 130.2, 130.3, 131.7, 134.9, 142.9, 153.8, 161.8 ppm. **HRMS** (MeOH): *m/z* calcd. for $[C_{24}H_{36}N]^+$: 338.2842 $[M]^+$, found: 338.2854.

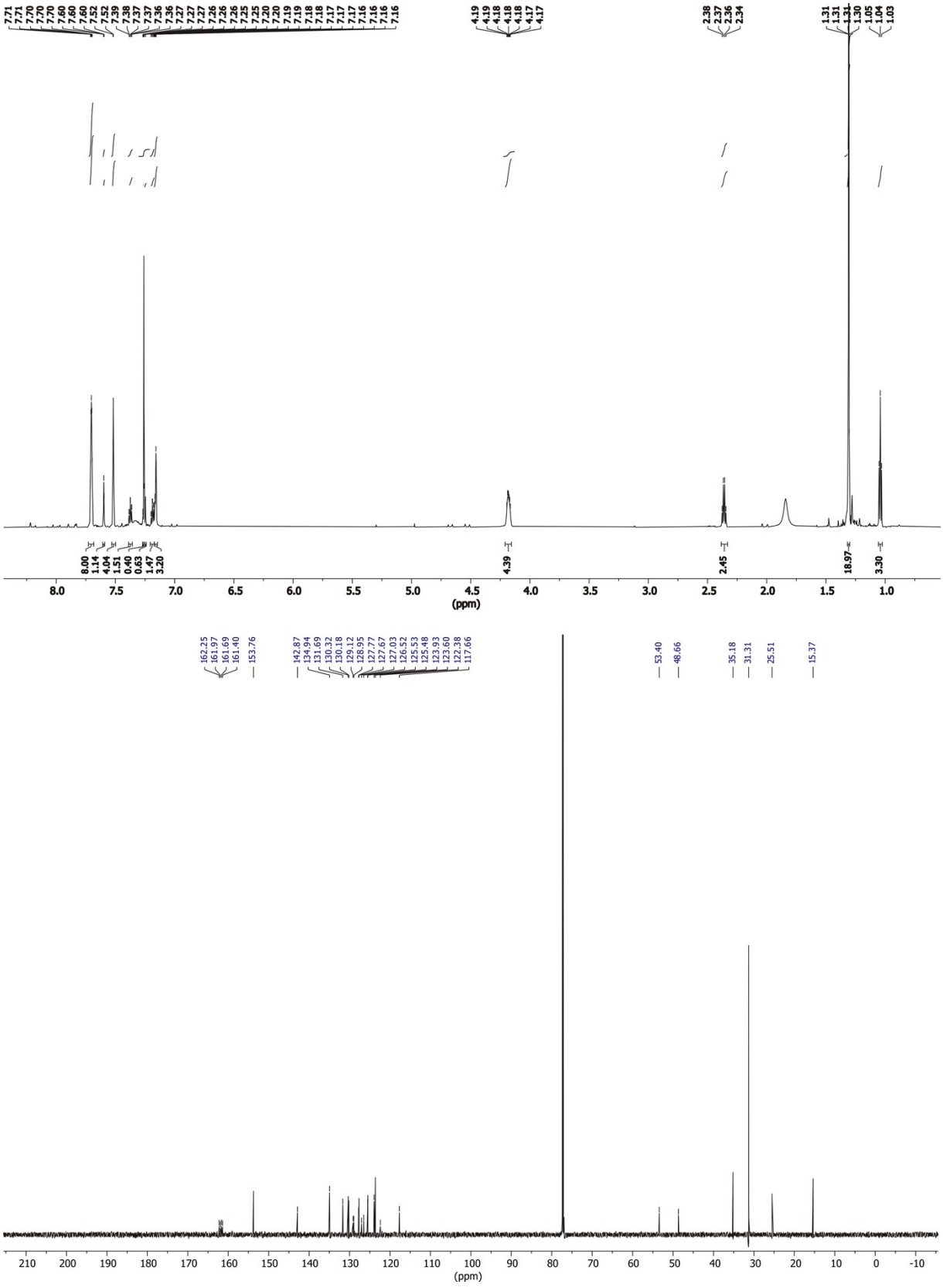

Fig. S6 ^{1}H (top) and ^{13}C (bottom) NMR spectra (700/176 MHz, $CDCl_3$, 298 K) of **PA6**.

N-(3,5-di-tert-butylbenzyl)-1-(2-methoxyphenyl)methanaminium tetrakis(3,5-bis(trifluoromethyl)phenyl)borate

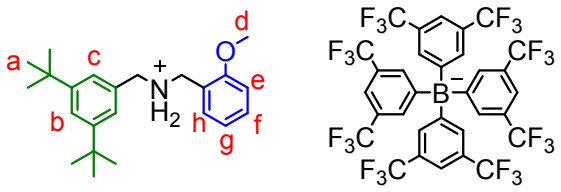

PA7

A solution of 190 mg (1.1 mmol, 1.0 equiv.) (2-methoxyphenyl)methanaminium chloride[8], 240 mg (1.1 mmol, 1.0 equiv.) 3,5-di-*tert*-butylbenzaldehyde and 150 µL (1.08 mmol, 0.9 equiv.) NEt_3, in dry EtOH (30 mL) were refluxed under argon atmosphere for 4 h. Afterwards, the solution was cooled to 0 °C and 207 mg (5.5 mmol, 5.0 equiv.) $NaBH_4$ was slowly added. The mixture was left stirring under argon atmosphere overnight in the thawing ice bath. The reaction was quenched by slow addition of sat. $NaHCO_3$ solution and then filtered. The solvent was removed under reduced pressure from the filtrate and the residue was dissolved in CH_2Cl_2 and then washed with sat. $NaHCO_3$ solution and brine. The organic phase was dried with $MgSO_4$ and the solvent removed again. The crude product was purified by column chromatography (SiO_2, CH_2Cl_2/MeOH = 100:1 -> 50:1, R_f ~ 0.3 in CH_2Cl_2/MeOH (100:1)) to obtain a yellowish oil. The oil was dissolved in EtOAc (10 ml) and acidified with HCl (conc.) until the solution reached pH = 1. The mixture was stirred for 1 h and afterwards the solvent was removed under reduced pressure. The residue was dissolved in MeOH (5 ml) and 478 mg (0.54 mmol, 1.0 equiv.) $NaBArF_{24}$ was added. The solution was left stirring overnight at room temperature, then the solvent was removed. The residue was taken up in CH_2Cl_2, washed with brine/water and dried over $MgSO_4$. The product **PA7** (603 mg, 0.50 mmol, 45 % overall) was obtained as colorless oil.

^{1}H NMR (500 MHz, $CDCl_3$): δ = 1.30 (s, 18H, a), 3.84 (s, 3H, d), 4.11-4.22 (m, 4H, C$\underline{H_2}$-NH_2), 6.84 (s, 2H, N$\underline{H_2}$), 6.95-7.04 (m, 2H, e,f), 7.06 (d, *J*=1.7 Hz, 2H, c), 7.07-7.11 (m, 1H, g), 7.45-7.50 (m, 1H, h), 7.52 (s_{br}, 4H, $BArF_{24}$), 7.59 (t, *J* = 1.7 Hz, 1H, b), 7.70 (s_{br}, 8H, $BArF_{24}$) ppm.

^{13}C NMR (176 MHz, $CDCl_3$): δ = 31.3, 35.2, 50.5, 53.3, 56.3, 111.8, 115.3, 117.7, 122.4, 122.9, 123.1, 123.9, 125.5, 126.0, 127.0, 127.4, 129.1, 131.2, 133.5, 134.9, 154.0, 157.0, 161.8 ppm.

HRMS (MeOH): *m/z* calcd. for $[C_{23}H_{34}NO]^+$: 340.2635 $[M]^+$, found: 340.2643.

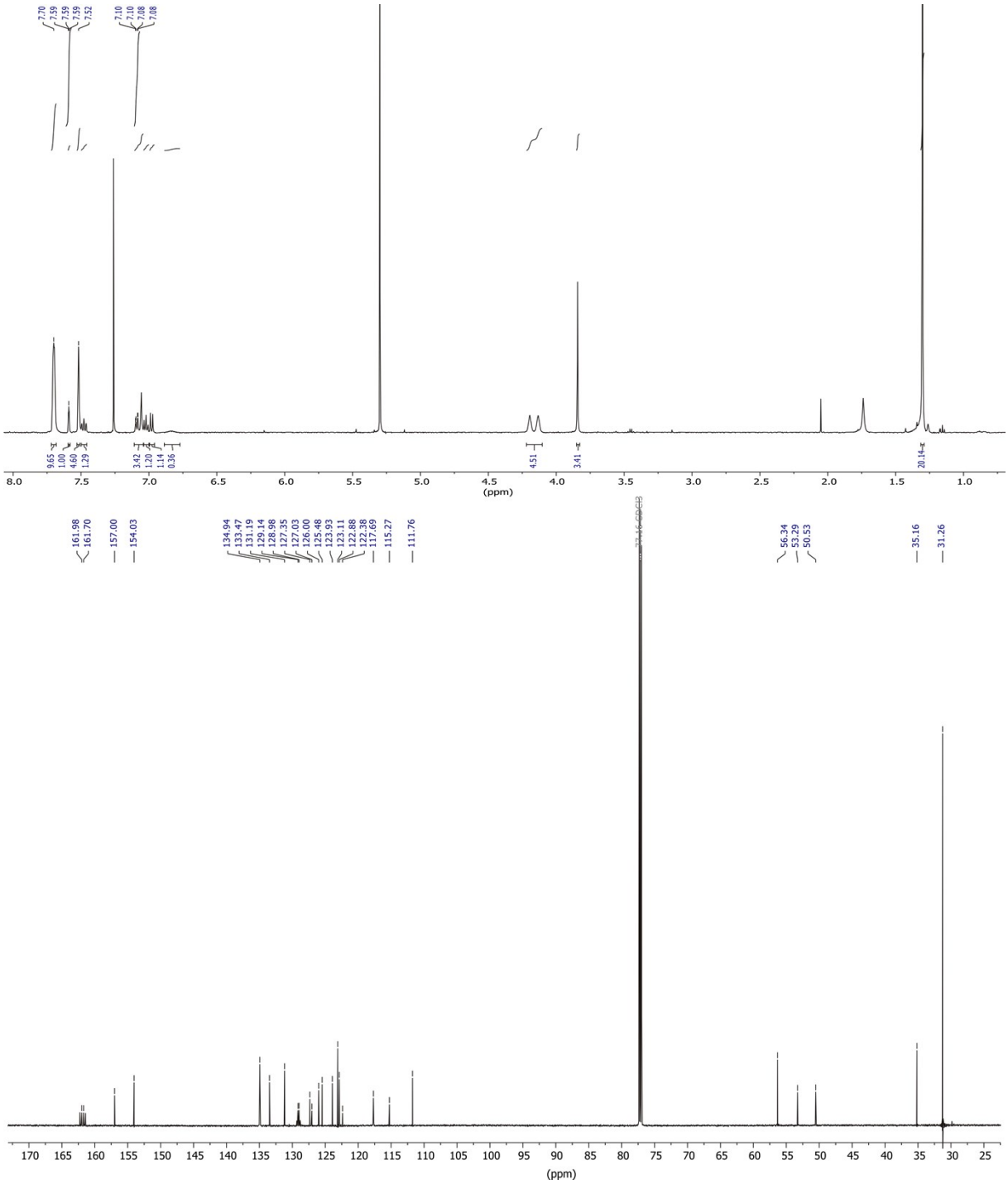

Fig. S7 ^{1}H (top) and ^{13}C (bottom) NMR spectra (500/176 MHz, $CDCl_3$, 298 K) of **PA7**.

N-(3,5-di-tert-butylbenzyl)-1-(2-nitrophenyl)methanaminium tetrakis(3,5-bis(trifluoromethyl)phenyl)borate

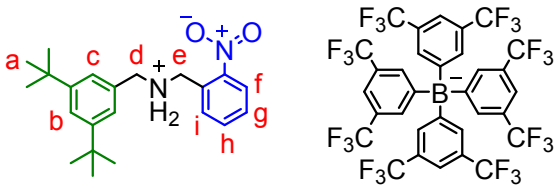

PA8

A solution of 250 mg (1.3 mmol, 1.0 equiv.) (2-nitrophenyl)methanaminium hydrochloride, 290 g (1.3 mmol, 1.0 equiv.) 3,5-di-*tert*-butylbenzaldehyde and 170 µL (0.9 mmol, 0.9 equiv.) dry NEt_3 in dry EtOH (60 mL) was left refluxing under argon atmosphere for 4 h. Afterwards, the solution was cooled to 0 °C in an ice bath and 252 mg (6.7 mmol, 5.0 equiv.) $NaBH_4$ was added. The mixture was left stirring under argon atmosphere in the thawing ice bath overnight. Then, the reaction was stopped by slow addition of sat. $NaHCO_3$ solution until no additional gas development occurred. The solvent was removed under reduced pressure and the residue was taken up in CH_2Cl_2. After washing with water, the organic phase was dried over $MgSO_4$. The crude product was then purified by column chromatography (SiO_2, CH_2Cl_2 → CH_2Cl_2/MeOH = 100:1, R_f ~ 0.2 in CH_2Cl_2/MeOH = 100:1) to get the desired oil, which was directly dissolved in Et_2O (10 mL) and acidified with conc. HCl, until the solution reached pH = 1. Afterwards, the solution was left stirring at r.t. for 3 h, then the solvent was removed under reduced pressure. A fraction of the yellow oil was dissolved in MeOH (10 mL) and 227 mg (0.26 mmol, 1.0 equiv.) $NaBArF_{24}$ was added. The solution was left stirring at r.t. overnight, then the solvent was removed under reduced pressure. Afterwards, the residue was taken up in CH_2Cl_2 and washed with water and dried over $MgSO_4$ to obtain the desired product **PA8** as yellow oil in a combined yield of 80% (327 mg, 0.26 mmol).

^{1}H NMR (500 MHz, $CDCl_3$) δ = 1.30 (s, 18H, a), 4.29 – 4.39 (m, 4H, d,e), 7.20 (d, J = 1.7 Hz, 2H, c), 7.21 – 7.30 (m, 1H, i), 7.34 (s_{br}, 2H, N$\underline{H}_2$), 7.51 (s_{br}, 4H, $BArF_{24}$), 7.52 - 7.55 (m, 1H, h), 7.60 (t, J = 1.8 Hz, 1H, b), 7.62 - 7.66 (m, 1H, g), 7.71 (s_{br}, 8H, $BArF_{24}$), 8.13 – 8.16 (m, 1H, f). ppm. **^{13}C NMR** (126 MHz, $CDCl_3$) δ [ppm] 31.5, 35.2, 50.9, 54.6, 117.7, 121.4, 123.3, 123.4, 123.6, 125.8, 126.0, 127.0, 127.1, 127.9, 128.9, 129.2, 133.4, 134.1, 134.9, 136.0, 149.1, 154.0, 161.9. **HRMS (MeOH):**m/z calcd. for $[C_{22}H_{31}N_2O_2]^+$: 355.2380 $[M]^+$, found: 355.2379.

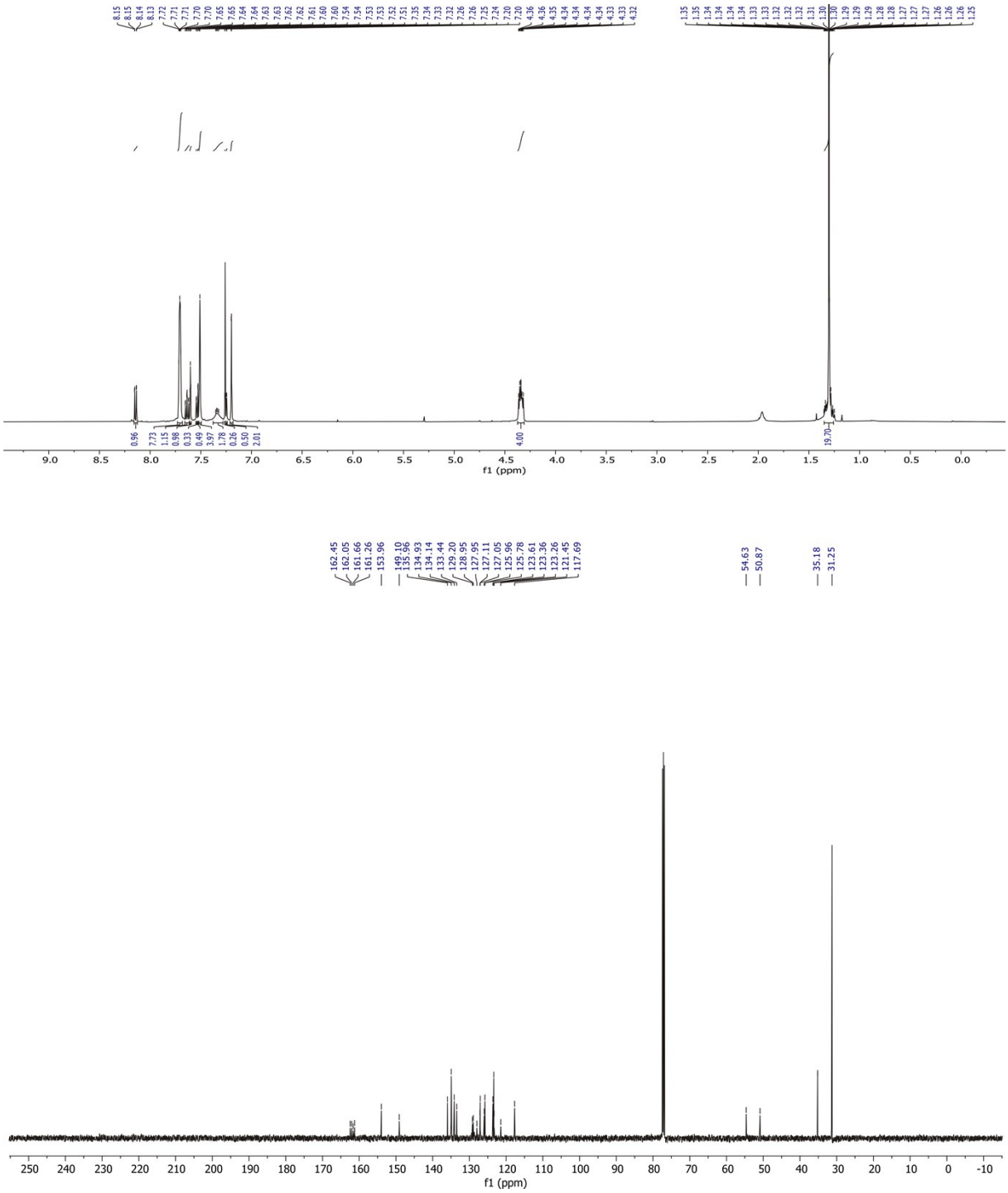

Fig. S8 ^{1}H (top) and ^{13}C (bottom) NMR spectra (500/126 MHz, $CDCl_3$, 298 K) of **PA8**.

1-([1,1'-biphenyl]-3-yl)-N-(3,5-di-tert-butylbenzyl)methanaminiumtetrakis(3,5-bis(trifluoromethyl)phenyl)borate

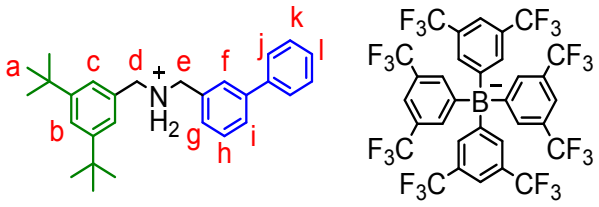

PA9

A solution of 200 mg (0.9 mmol, 1.0 equiv.) (3-Phenylphenyl)methanamine hydrochloride, 218 mg (0.9 mmol, 1.0 equiv.) 3,5-di-*tert*-butylbenzaldehyde and 115 µL (0.8 mmol, 0.9 equiv.) dry NEt_3 in dry EtOH (50 mL) was refluxed under argon atmosphere for 4 h. Afterwards, the solution was cooled to 0 °C in an ice bath and 172 mg (4.6 mmol, 5.0 equiv.) $NaBH_4$ was added. The mixture was left stirring under argon atmosphere in the thawing ice bath overnight. Then, the reaction was stopped by slow addition of sat. $NaHCO_3$ solution until no additional gas development occurred. The solvent was removed under reduced pressure and the residue was taken up in CH_2Cl_2. After washing with water, the organic phase was dried over $MgSO_4$. The crude product was then purified by column chromatography (SiO_2, CH_2Cl_2 → CH_2Cl_2/MeOH = 50:1, R_f ~ 0.2 in CH_2Cl_2/MeOH = 100:1) to obtain a yellowish oil, which was directly dissolved in EtOAc (10 mL) and acidified with conc. HCl, until the solution reached pH = 1. Afterwards, the solution was left stirring at r.t. for 3 h, then the solvent was removed under reduced pressure. The yellow solid was dissolved in MeOH (10 mL) and 361 mg (0.4 mmol, 1.0 equiv.) $NaBArF_{24}$ was added. The solution was left stirring at r.t. overnight, then the solvent was removed under reduced pressure. Afterwards, the residue was taken up in CH_2Cl_2 and washed with water and dried over $MgSO_4$ to obtain the desired product **PA9** as colorless oil in a combined yield of 43% (484 mg, 0.4 mmol).

^{1}H NMR (700 MHz, $CDCl_3$): δ = 1.29 (s, 18H, a), 4.17 - 4.22 (m, 4H, d,e), 7.17 (d, J = 1.8 Hz, 2H, c), 7.17 – 7.19 (m, 1H, j), 7.37 – 7.39 (m, 2H, g,i), 7.43 (t, J = 7.7 Hz, 1H, l), 7.45 - 7.47 (m, 2H, k), 7.52 (s_{br}, 4H, $BArF_{24}$), 7.55 (t, J = 1.9 Hz, 1H, f), 7.57 (t, J = 1.8 Hz, 1H, b), 7.68 (ddd, J = 1.0, 1.8, 7.8 Hz, 1H, h), 7.73 (s_{br}, 8H, $BArF_{24}$) ppm. **^{13}C NMR** (176 MHz, $CDCl_3$): δ = 31.3, 35.2,.1, 52.3, 53.3, 117.6, 117.7, 117.7, 117.7, 117.7, 122.4, 123.6, 124.0, 125.5, 127.1, 127.7, 128.0, 128.3, 128.6, 128.9, 128.9, 129.0, 129.0, 129.1, 129.1, 129.1, 129.1, 129.2, 129.3, 129.8, 129.9, 130.7, 135.0, 139.3, 143.4, 153.6, 161.8 ppm. **HRMS** (MeOH): *m/z* calcd. for $[C_{28}H_{36}N]^+$: 386.2842 $[M]^+$, found: 386.2848.

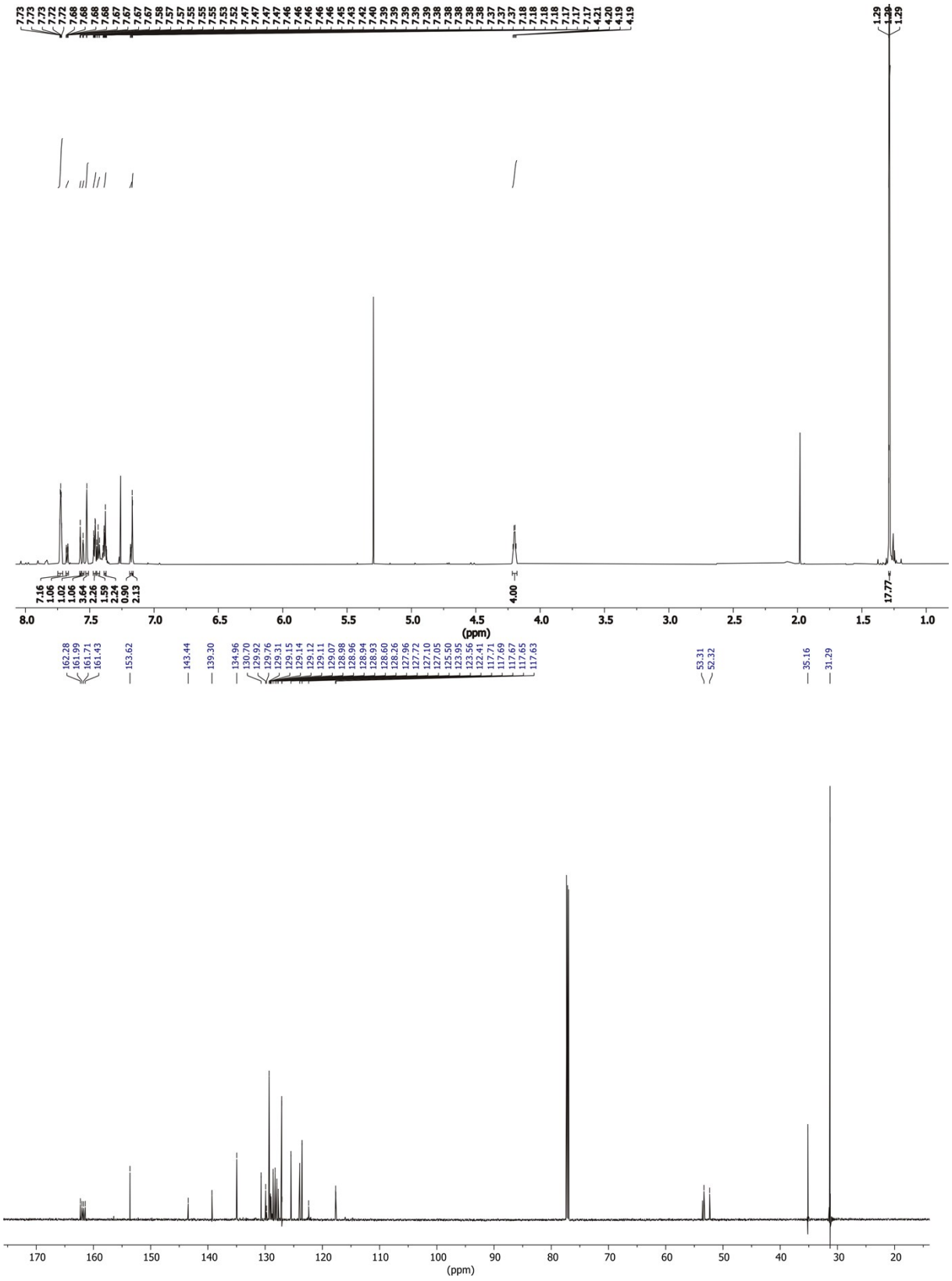

Fig. S9 ^{1}H (top) and ^{13}C (bottom) NMR spectra (700/176 MHz, $CDCl_3$, 298 K) of **PA9**.

N-(3,5-di-tert-butylbenzyl)-1-(naphthalen-2-yl)methanaminiumtetrakis(3,5-bis(trifluoromethyl)phenyl)borate

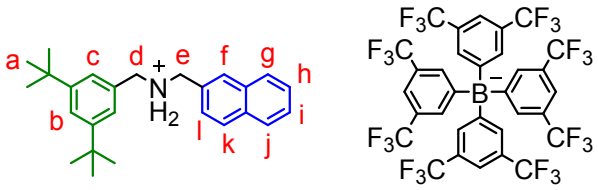

PA10

A solution of 200 mg (1.0 mmol, 1.0 equiv.) naphthalen-2-ylmethanaminium hydrochloride, 226 g (1.0 mmol, 1.0 equiv.) 3,5-di-*tert*-butylbenzaldehyde and 130 µL (0.9 mmol, 0.9 equiv.) dry NEt_3 in dry EtOH (50 mL) was left refluxing under argon atmosphere for 4 h. Afterwards, the solution was cooled to 0 °C in an ice bath and 200 mg (5.2 mmol, 5.0 equiv.) $NaBH_4$ was added. The mixture was left stirring under argon atmosphere in the thawing ice bath overnight. Then, the reaction was stopped by slow addition of sat. $NaHCO_3$ solution until no additional gas development occurred. The solvent was removed under reduced pressure and the residue was taken up in CH_2Cl_2. After washing with water, the organic phase was dried over $MgSO_4$. The crude product was then purified by column chromatography (SiO_2, CH_2Cl_2 → CH_2Cl_2/MeOH = 100:1, R_f ~ 0.2 in CH_2Cl_2/MeOH = 100:1) to get the desired oil, which was directly dissolved in EtOAc (10 mL) and acidified with conc. HCl, until the solution reached pH = 1. Afterwards, the solution was left stirring at r.t. for 3 h, then the solvent was removed under reduced pressure. The yellow solid was dissolved in MeOH (10 mL) and 599 mg (0.7 mmol, 1.0 equiv.) $NaBArF_{24}$ was added. The solution was left stirring at r.t. overnight, then the solvent was removed under reduced pressure. Afterwards, the residue was taken up in CH_2Cl_2 and washed with water and dried over $MgSO_4$ to obtain the desired product **PA10** as yellow oil in a combined yield of 61% (751 mg, 0.6 mmol).

^{1}H NMR (500 MHz, $CDCl_3$) δ = 1.29 (s, 18H, a), 4.19 – 4.25 (m, 2H, d), 4.29 – 4.38 (m, 2H, e), 7.12 (d, J = 1.8 Hz, 2H, c), 7.23 (dd, J = 8.5, 1.8 Hz, 1H, f), 7.52 (s_{br}, 4H, $BArF_{24}$), 7.56 - 7.60 (m, 2H, h, i), 7.60 – 7.64 (m, 1H, b), 7.73 (s_{br}, 8H, $BArF_{24}$), 7.74 – 7.77 (m, 2H, g, j), 7.84 – 7.91 (m, 2H, l, k) ppm.**^{13}C NMR** (176 MHz, $CDCl_3$) δ [ppm] 31.5, 35.2, 49.3, 50.1, 114.5, 116.0, 122.4, 122.8, 123.9, 124.0, 124.3, 125.5, 126.5, 127.1, 127.2, 127.5, 127.7, 127.9, 128.1, 128.7, 129.5, 129.8, 130.2, 132.9, 133.0, 133.1, 133.2, 133.2, 133.3, 133.6, 134.0, 135.0, 140.6, 152.5, 156.7.**HRMS (MeOH):**m/z calcd. for $[C_{26}H_{34}N]^+$: 360.2686 $[M]^+$, found: 360.2677.

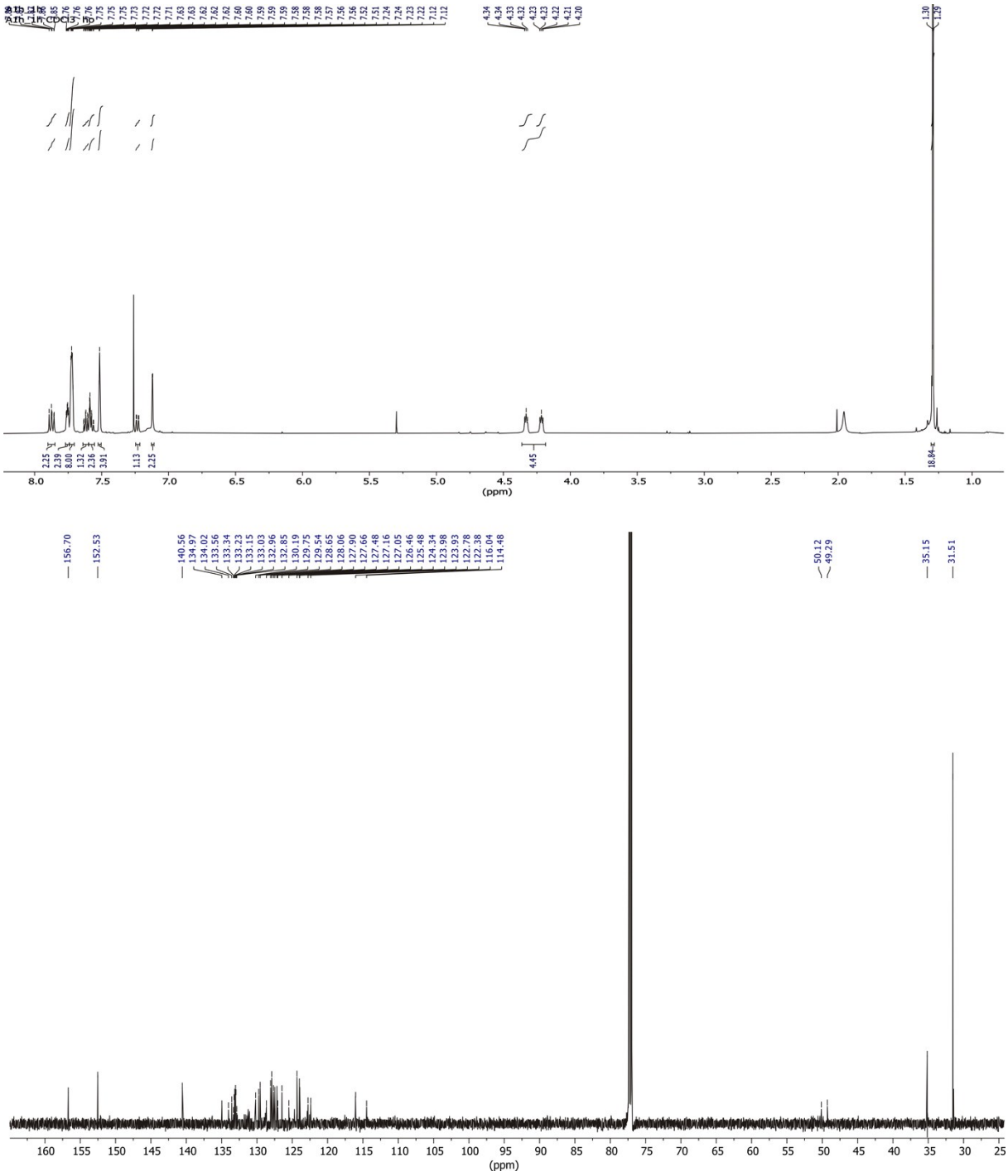

Fig. S10 ^{1}H (top) and ^{13}C (bottom) NMR spectra (500/176 MHz, $CDCl_3$, 298 K) of **PA10**.

N-(3,5-di-tert-butylbenzyl)-1-(naphthalen-1-yl)methanaminiumtetrakis(3,5-bis(trifluoromethyl)phenyl)borate

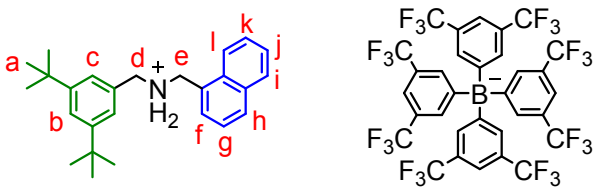

PA11

A solution of 200 mg (1.0 mmol, 1.0 equiv.) naphthalen-1-ylmethanaminium hydrochloride[9], 226 mg (1.0 mmol, 1.0 equiv.) 3,5-di-*tert*-butylbenzaldehyde and 130 µL (0.9 mmol, 0.9 equiv.) dry NEt_3 in dry EtOH (50 mL) was refluxed under argon atmosphere for 4 h. Afterwards, the solution was cooled to 0 °C in an ice bath and 195 mg (5.2 mmol, 5.0 equiv.) $NaBH_4$ was added. The mixture was left stirring under argon atmosphere in the thawing ice bath overnight. Then, the reaction was stopped by slow addition of sat. $NaHCO_3$ solution until no additional gas development occurred. The solvent was removed under reduced pressure and the residue was taken up in CH_2Cl_2. After washing with water, the organic phase was dried over $MgSO_4$. The crude product was then purified by column chromatography (SiO_2, CH_2Cl_2 → CH_2Cl_2/MeOH = 100:1, R_f ~ 0.2 in CH_2Cl_2/MeOH = 100:1) to obtain a yellowish oil, which was directly dissolved in EtOAc (10 mL) and acidified with conc. HCl, until the solution reached pH = 1. Afterwards, the solution was left stirring at r.t. for 3 h, then the solvent was removed under reduced pressure. The yellow solid was dissolved in MeOH (10 mL) and 599 mg (0.7 mmol, 1.0 equiv.) $NaBArF_{24}$ was added. The solution was left stirring at r.t. overnight, then the solvent was removed under reduced pressure. Afterwards, the residue was taken up in CH_2Cl_2 and washed with water and dried over $MgSO_4$ to obtain the desired product **PA11** as reddish oil in a combined yield of 63% (773 mg, 0.6 mmol).

^{1}H NMR (500 MHz, $CDCl_3$): δ = 1.30 (s, 18H, a), 4.20 (s, 2H, d), 4.31 (s, 2H, e), 7.12 (d, J = 1.7 Hz, 2H, c), 7.21 – 7.25 (m, 1H, f), 7.51 (s_{br}, 4H, $BArF_{24}$), 7.56 - 7.64 (m, 3H, b, g, k), 7.72 (s_{br}, 8H, $BArF_{24}$), 7.74 – 7.78 (m, 2H, h, j), 7.86 – 7.91 (m, 2H, l, i). **^{13}C NMR** (176 MHz, $CDCl_3$): δ = 31.5, 31.6, 35.1, 46.1, 51.0, 114.3, 116.0, 116.1, 116.1, 116.1, 121.7, 121.9, 122.4, 122.5, 122.6, 122.8, 122.9, 123.9, 124.0, 124.1, 124.3, 125.5, 125.8, 126.7, 127.6, 127.7, 127.7, 128.9, 129.4, 129.8, 130.0, 130.8, 130.9, 131.0, 131.1, 133.0, 133.8, 134.1, 135.0, 140.6, 152.7, 156.9 ppm. **HRMS** (MeOH): *m/z* calcd. for $[C_{26}H_{34}N]^+$: 360.2686 $[M]^+$, found: 360.2688.

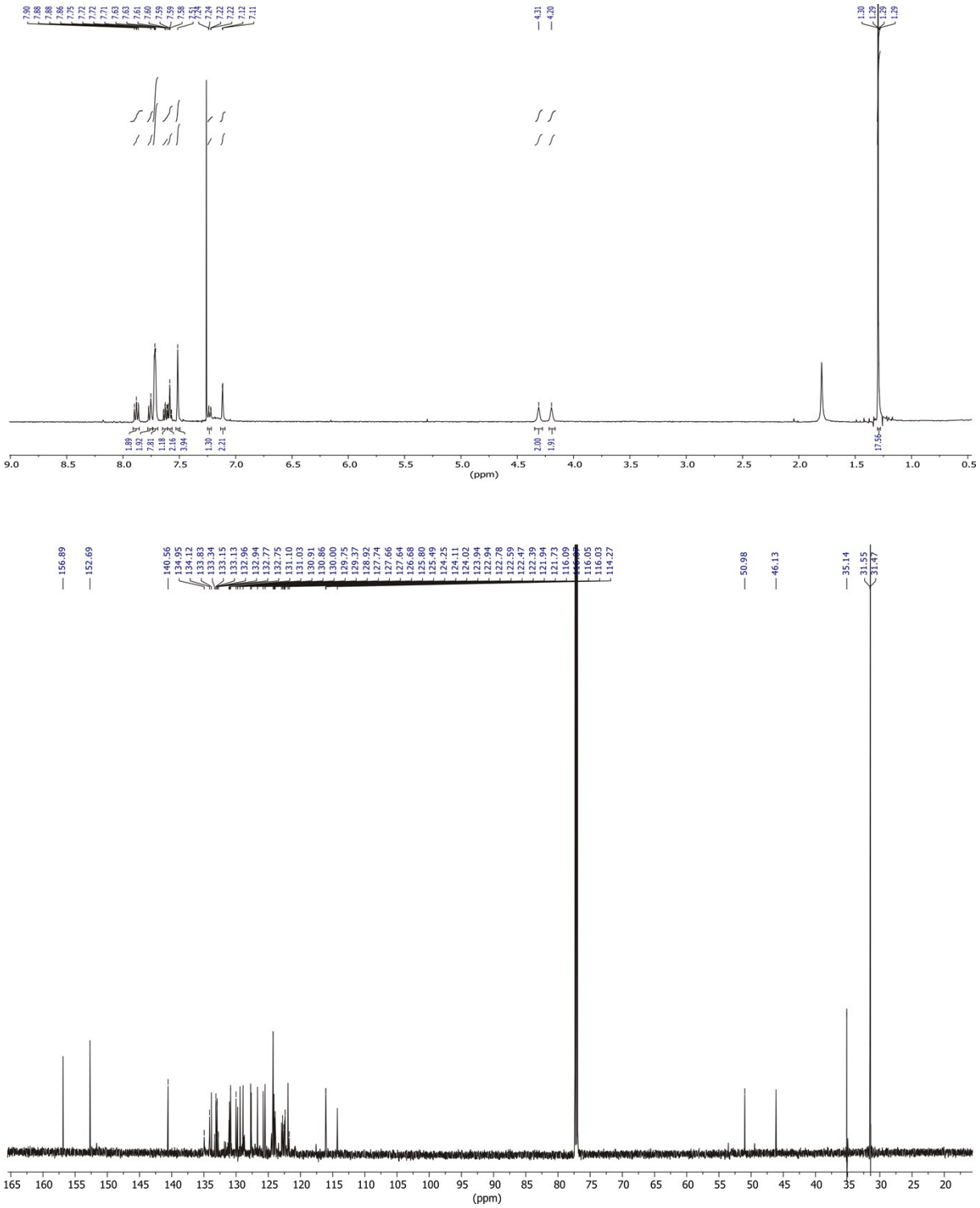

Fig. S11 ^{1}H (top) and ^{13}C (bottom) NMR spectra (500/176 MHz, $CDCl_3$, 298 K) of **PA11**.

N-benzyl-1-(naphthalen-1-yl)methanaminiumtetrakis(3,5-bis(trifluoromethyl)phenyl)borate

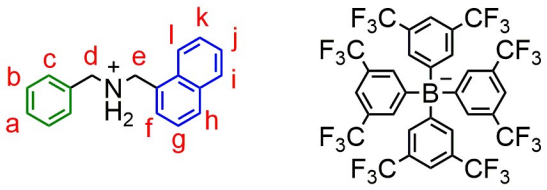

PA12

A solution of 52 mg (0.27 mmol, 1.0 equiv.) naphthalen-1-ylmethanaminium hydrochloride[9], 27 µL (0.27 mmol, 1.0 equiv.) benzaldehyde and 32 µL (0.24 mmol, 0.9 equiv.) dry NEt_3 in dry EtOH (15 mL) was refluxed under argon atmosphere for 4 h. Afterwards, the solution was cooled to 0 °C in an ice bath and 52 mg (1.3 mmol, 5.0 equiv.) $NaBH_4$ was added. The mixture was left stirring under argon atmosphere in the thawing ice bath overnight. Then, the reaction was stopped by slow addition of sat. $NaHCO_3$ solution until no additional gas development occurred. The solvent was removed under reduced pressure and the residue was taken up in CH_2Cl_2. After washing with water, the organic phase was dried over $MgSO_4$. The crude product was then purified by flash column chromatography (spherical SiO_2, CH_2Cl_2 → CH_2Cl_2/MeOH = 6%, R_f ~ 0.3 in CH_2Cl_2/MeOH = 1%) to obtain a yellow oil, which was directly dissolved in EtOAc (10 mL) and acidified with conc. HCl, until the solution reached pH = 1. Afterwards, the solution was left stirring at r.t. for 3 h, then the solvent was removed under reduced pressure. A fraction of the brown oil was dissolved in MeOH (5 mL) and 62 mg (70 µmol, 1.0 equiv.) $NaBArF_{24}$ was added. The solution was left stirring at r.t. overnight, then the solvent was removed under reduced pressure. Afterwards, the residue was taken up in CH_2Cl_2 and washed with water and dried over $MgSO_4$ to obtain the desired product **PA12** as brown oil in a combined yield of 54% (52 mg, 46 µmol).

^{1}H NMR (600 MHz, $CDCl_3$): δ = 4.20 (s, 2H, d), 4.41 (s, 2H, e), 7.08 – 7.11 (m, 2H, c), 7.23 (dd, J = 7.0, 1.2 Hz, 1H, f), 7.33 – 7.39 (m, 4H, g,k,b), 7.42 – 7.46 (m, 1H, a), 7.48 – 7.50 (m, 1H, h), 7.49 – 7.52 (s_{br}, 4H, $BArF_{24}$), 7.57 (m, 1H, j), 7.72 (s_{br}, 8H, $BArF_{24}$), 7.93 – 7.97 (m, 1H, i,l). **^{13}C NMR** (151 MHz, $CDCl_3$): δ = 49.79, 52.99, 117.68, 120.22, 122.01, 123.82, 125.62, 127.46, 128.67, 129.04, 129.34, 130.33, 130.47, 131.19, 132.15, 134.33, 134.95, 161.38, 161.70, 162.04, 162.36 ppm. **HRMS** (MeOH): *m/z* calcd. for $[C_{18}H_{18}N]^+$: 248.1434 $[M]^+$, found: 248.1431.

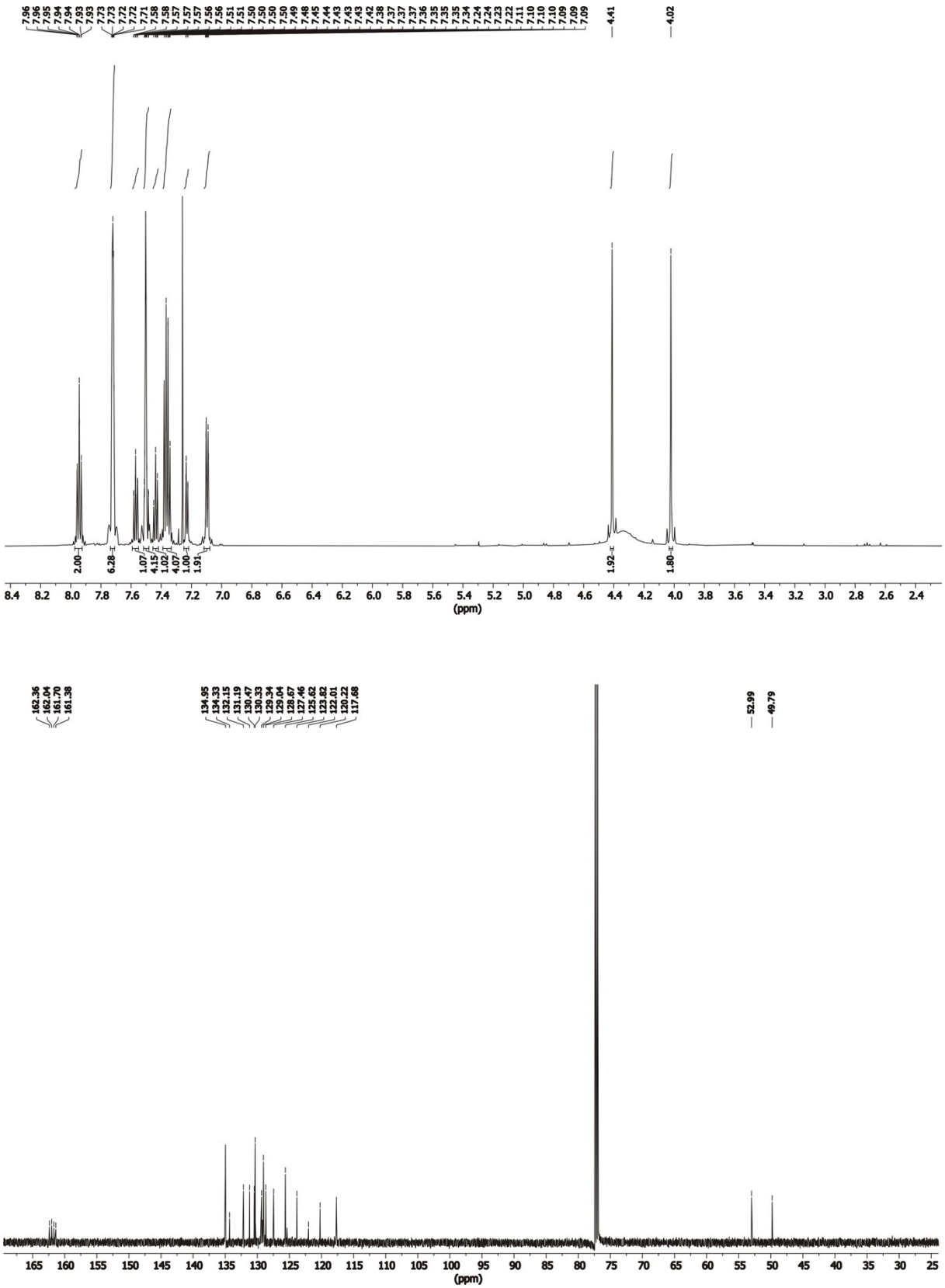

Fig. S12 ^{1}H (top) and ^{13}C (bottom) NMR spectra (600/151 MHz, $CDCl_3$, 298 K) of **PA12**.

1.3. Synthesis of [2]rotaxane R1, R2 and PA11@TTFC8

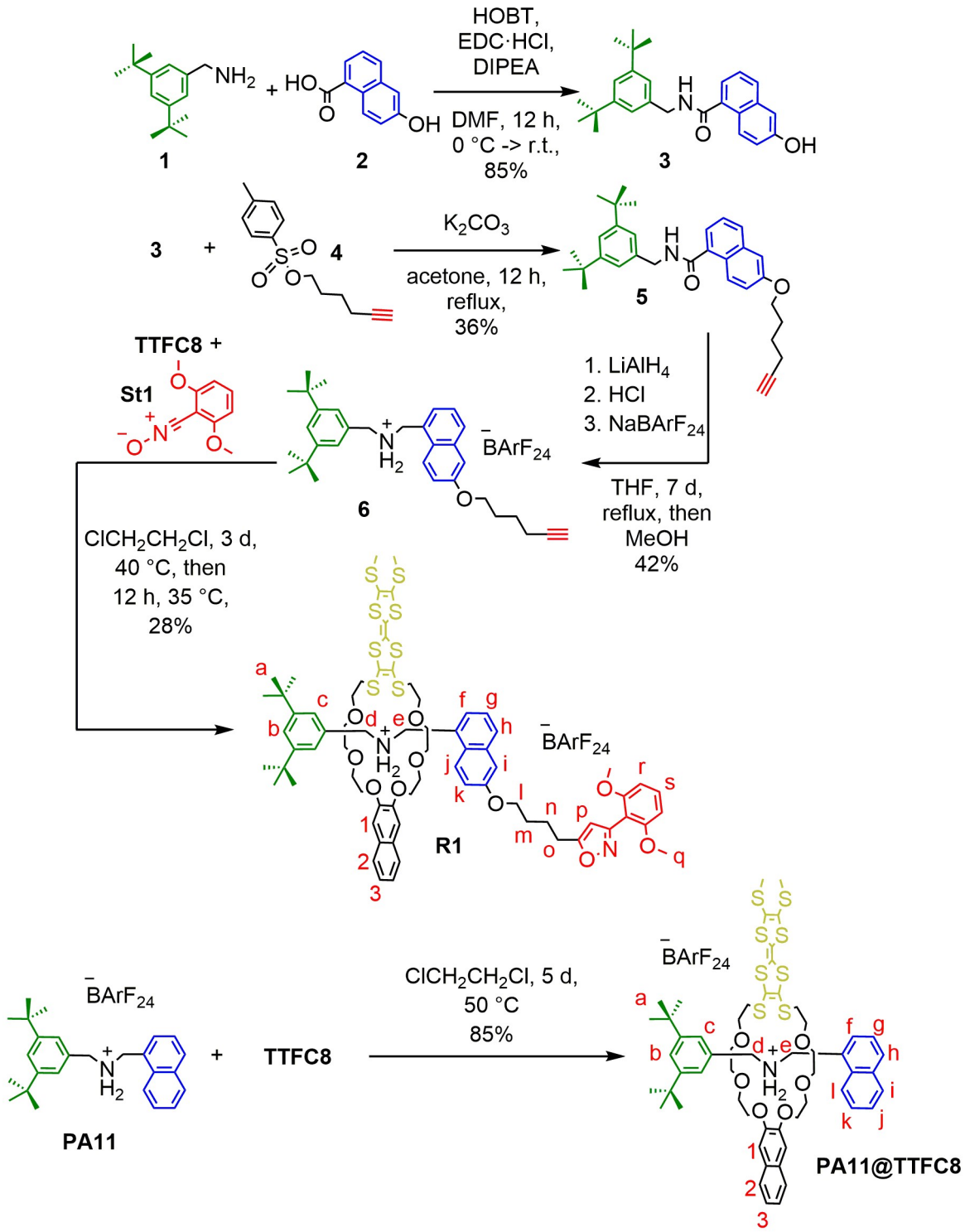

Scheme S2 Synthesis of **R1** and **PA11@TTFC8**.

N-(3,5-di-tert-butylbenzyl)-6-hydroxy-1-naphthamide 3

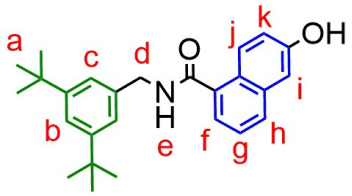

3

A solution of 58 mg (0.27 mmol, 1.0 equiv.) (3,5-di-*tert*-butylphenyl)methanamine **1**, 50 mg (0.27 mmol, 1.0 equiv.) 6-hydroxy-1-naphthoic acid **2** were dissolved in dry DMF (5 mL). In an ice bath 22 mg (0.16 mmol, 0.6 equiv.) HOBT, 66 mg (0.35 mmol, 1.3 equiv.) EDC·HCl and 72 µL (0.43 mmol, 1.6 equiv.) DIPEA were added. The mixture was stirred under argon atmosphere in the thawing ice bath overnight. Then, the mixture was diluted with 30 mL EtOAc and washed with water and brine. After drying over $MgSO_4$, the solvent was removed. Afterwards, the crude product was purified by column chromatography (SiO_2, CH_2Cl_2 -> CH_2Cl_2/MeOH 50:1, R_f ~ 0.4 in CH_2Cl_2/MeOH = 50:1) to get the desired product **3** as yellow sticky solid in 85% yield (85.7 mg, 0.22 µmol).

^{1}H NMR (500 MHz, acetone-d_6) δ = 1.33 (s, 18H, a), 4.68 (d, J = 6.2 Hz, 2H, d), 7.16 (dd, J = 9.1, 2.5 Hz, 1H, k), 7.23 (d, J = 2.5 Hz, 1H, i), 7.35 (d, J = 1.8 Hz, 2H, c), 7.37 – 7.42 (m, 2H, b, h), 7.46 (dd, J = 7.0, 1.3 Hz, 1H, g), 7.72 – 7.76 (m, 1H, f), 8.02 – 8.09 (s_{br}, 1H, e), 8.28 (d, J = 9.2 Hz, 1H, j), 8.83 (s_{br}, 1H, OH) ppm. **^{13}C NMR** (126 MHz, Acetone-d_6) δ = 31.8, 35.4, 44.3, 110.2, 119.8, 121.6, 122.5, 122.8, 126.1, 126.1, 128.4, 129.1, 136.2, 136.4, 139.8, 151.5, 156.4, 169.9 ppm. **HRMS** (CH_2Cl_2/MeOH): m/z calcd. for $[C_{26}H_{31}NO_2]$: 412.2247 $[M+Na]^+$, found: 412.2263.

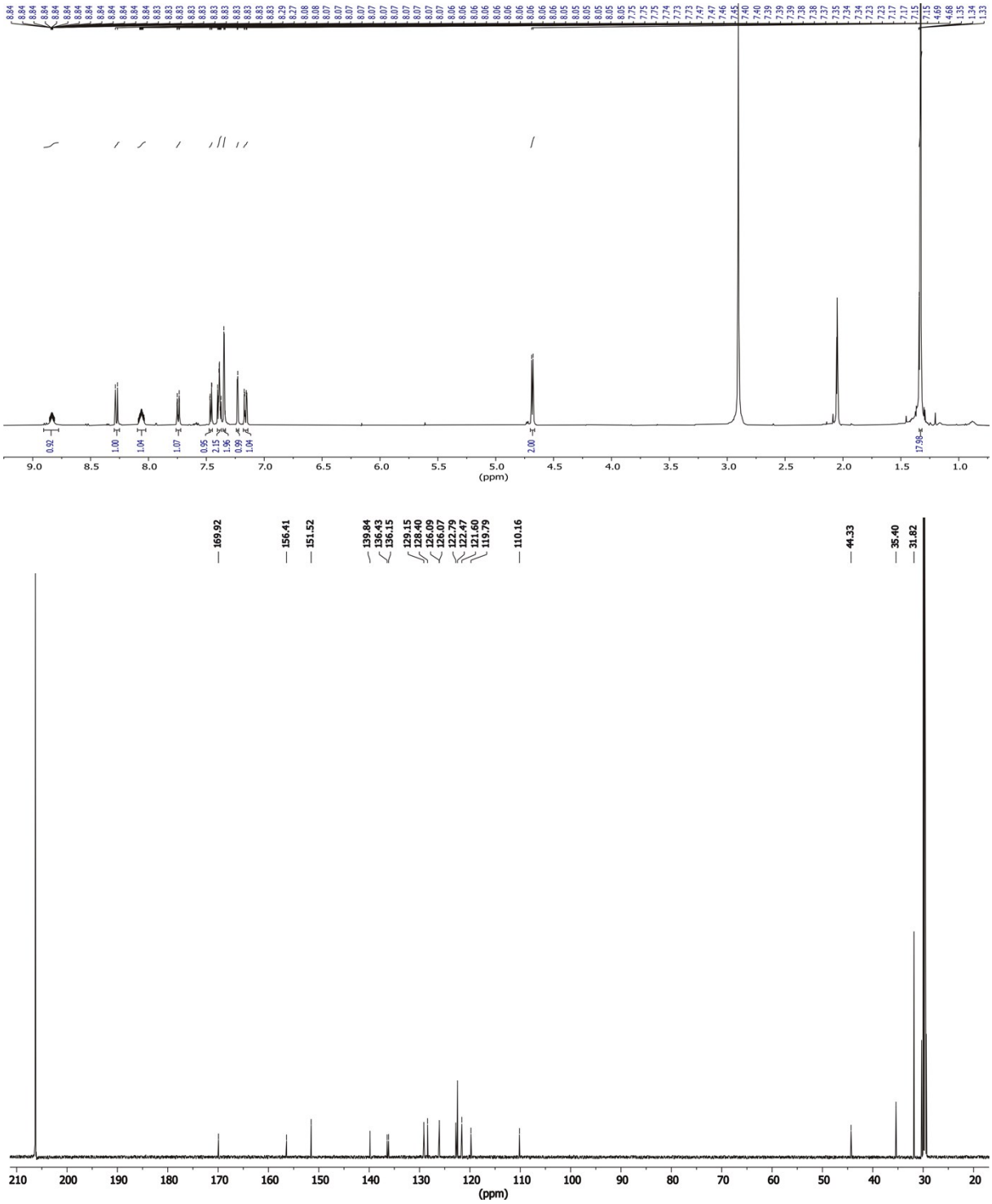

Fig. S13 ^{1}H (top) and ^{13}C (bottom) NMR spectra (500/126 MHz, Acetone-d_6, 298 K) of **3**.

N-(3,5-di-tert-butylbenzyl)-6-(hex-5-yn-1-yloxy)-1-naphthamide 5

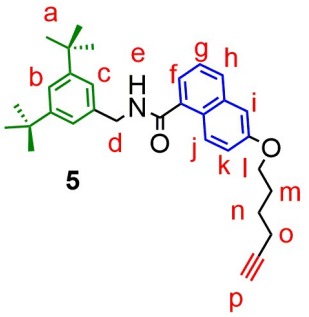

5

A solution of 194 mg (0.77 mmol, 1.2 equiv.) tosylate **4**, 250 mg (0.64 mmol, 1.0 equiv.) amide **3** and 177 mg (1.28 mmol, 2.0 equiv.) K_2CO_3 in acetone (10 mL) was refluxed for 12 h. Then, the mixture was filtered and the solvent was removed, the crude product was dissolved in CH_2Cl_2 and washed with water and brine. After drying over $MgSO_4$, the solvent was removed. Afterwards, the crude product was purified by column chromatography (SiO_2, CH_2Cl_2 -> CH_2Cl_2/MeOH 100:1, R_f ~ 0.8 in CH_2Cl_2/MeOH = 100:1) to get the desired product **5** as yellow sticky solid in 36% yield (108 mg, 0.23 mmol).

^{1}H NMR (500 MHz, $CDCl_3$) δ = 1.34 (s, 18H, a), 1.73 – 1.82 (m, 2H, n), 1.95 – 2.05 (m, 3H, m, p), 2.31 (td, *J* = 7.0, 2.7 Hz, 2H, o), 4.11 (t, *J* = 6.3 Hz, 2H, l), 4.72 (d, *J* = 5.7 Hz, 2H, d), 6.24 (t, *J* = 5.7 Hz, 1H, e), 7.14 (d, *J* = 2.6 Hz, 1H, i), 7.20 (dd, *J* = 9.2, 2.6 Hz, 1H, k), 7.25 (d, *J* = 1.9 Hz, 2H, c), 7.37 – 7.42 (m, 2H, b, g), 7.47 (dd, *J* = 7.1, 1.3 Hz, 1H, h), 7.75 – 7.79 (m, 1H, f), 8.30 (dt, *J* = 9.2, 0.6 Hz, 1H, j) ppm. **^{13}C NMR** (126 MHz, $CDCl_3$) δ = 18.3, 25.2, 28.3, 31.6, 35.0, 44.9, 67.5, 68.9, 84.2, 107.1, 120.2, 121.9, 122.3, 122.6, 125.4, 125.7, 127.2, 129.5, 134.6, 135.3, 137.3, 151.6, 157.4, 169.6 ppm. **HRMS (CH_2Cl_2/MeOH):** m/z calcd. for $[C_{32}H_{39}NO_2]$: 470.3059 $[M+H]^+$, found: 470.3028; 492.2879 $[M+Na]^+$, found: 492.2848; 508.2618 $[M+K]^+$, found: 508.2585.

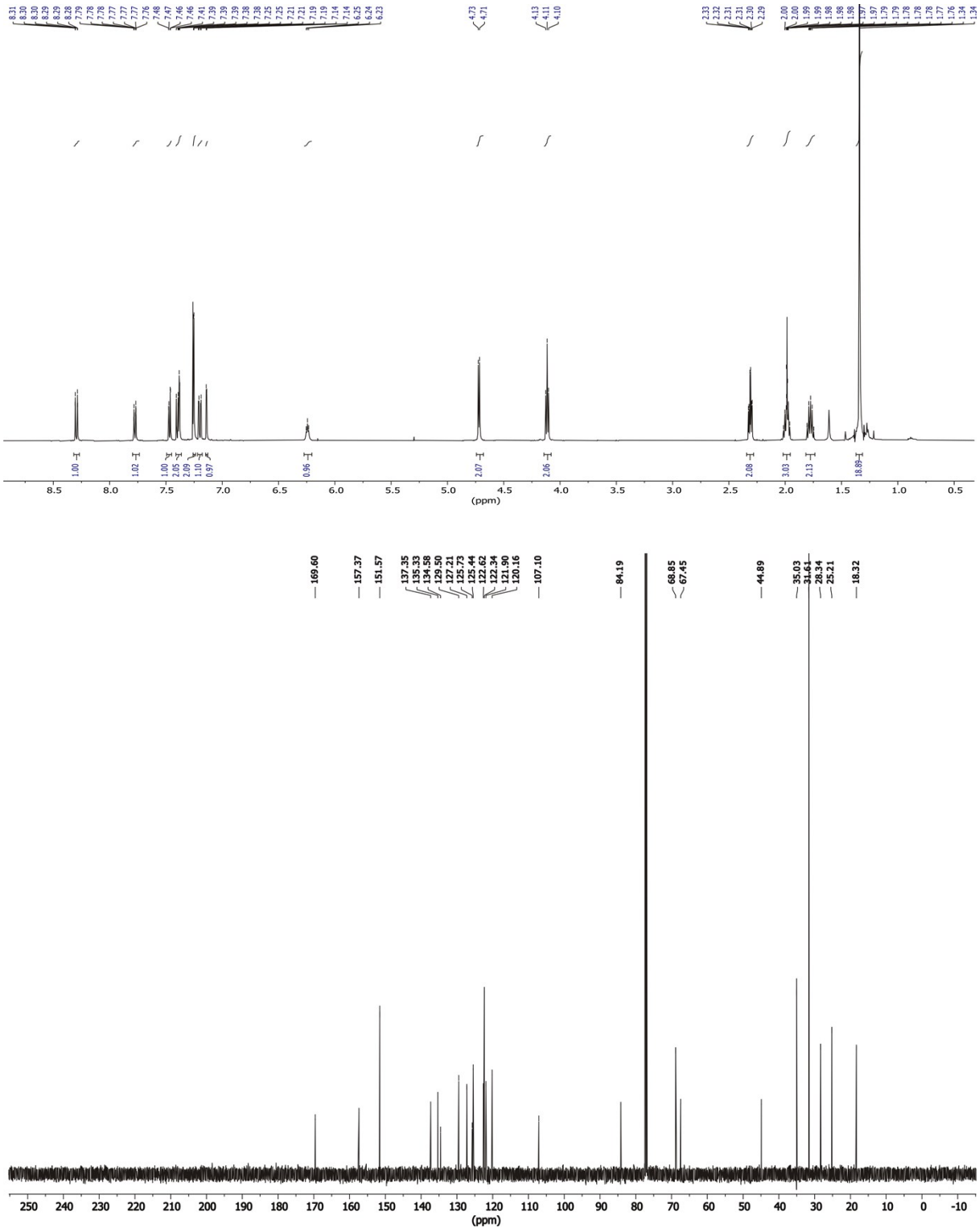

Fig. S14 ^{1}H (top) and ^{13}C (bottom) NMR spectra (500/126 MHz, $CDCl_3$, 298 K) of **5**.

N-(3,5-di-tert-butylbenzyl)-1-(6-(hex-5-yn-1-yloxy)naphthalen-1-yl)methanaminium tetrakis(3,5-bis(trifluoromethyl)phenyl)borate 6

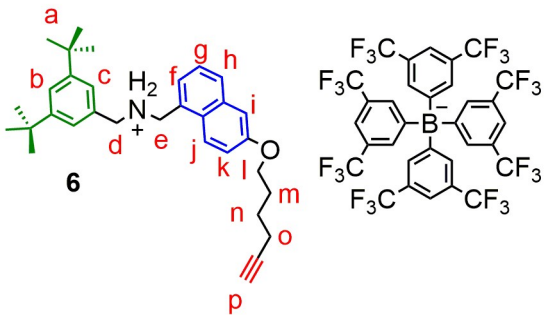

Amide **5** (382 mg, 0.813 mmol, 1 equiv.) and $LiAlH_4$ (124 mg, 3.25 mmol, 4 equiv.) were dissolved in 60 mL dry THF and refluxed for 7 days. Afterwards, the reaction was quenched with saturated aq. Na_2SO_4 solution. The white precipitate was filtered off and the solvent was removed. The residue was dissolved in CH_2Cl_2 (50 mL) and washed with brine (3x70 mL). The organic phase was dried over $MgSO_4$ and the solvent was removed. The crude product was purified by column chromatography (SiO_2, CH_2Cl_2 -> CH_2Cl_2/MeOH 100:1, R_f ~ 0.2 in CH_2Cl_2/MeOH = 100:1) to get the desired amine as a yellow oil, which was dissolved in diethylether (20 mL) and protonated with HCl conc. under cooling in an ice bath. The solvent was removed, 100 mg (0.2 mmol) of the brown sticky oil were dissolved in MeOH (10 mL) and $NaBArF_{24}$ (180 mg, 0.2 mmol, 1.0 equiv.) was added. After stirring overnight at room temperature, the solvent was removed, the residue was taken up in CH_2Cl_2 and washed with water (3x50 mL). The organic phase was dried over $MgSO_4$ and the solvent was removed. The crude salt was purified via column chromatography (SiO_2, CH_2Cl_2 -> CH_2Cl_2/acetone 10:1, R_f ~ 0.4 in CH_2Cl_2/acetone = 50:1) to get the desired axle **6** as brown oil in 42% overall yield (112.4 mg, 0.85 µmol).

^{1}H NMR (700 MHz, $CDCl_3$) δ = 1.33 (s, 18H, a), 1.74 – 1.79 (m, 2H, n), 1.97 – 2.02 (m, 3H, m,p), 2.31 (td, *J* = 7.0, 2.7 Hz, 2H, o), 4.10 (t, *J* = 6.3 Hz, 2H, l), 4.14 (s, 2H, d), 4.37 (s, 2H, e), 7.06 – 7.10 (m, 2H, j, f), 7.15 (d, *J* = 1.7 Hz, 2H, c), 7.17 – 7.20 (m, 2H, k, i), 7.26 – 7.29 (m, 1H, g), 7.52 (s, 4H, $BArF_{24}$), 7.61 (d, *J* = 1.8 Hz, 1H, b), 7.71 – 7.74 (m, 8H, $BArF_{24}$), 7.75 (d, *J* = 8.4 Hz, 1H, h) ppm.**^{13}C NMR** (176 MHz, $CDCl_3$) δ = 18.3, 25.1, 28.2, 31.0, 31.4, 35.2, 49.1, 53.5, 67.8, 68.9, 84.0, 108.5, 117.6, 121.4, 122.0, 122.4, 123.40, 123.9, 125.2, 125.5, 125.5, 126.2, 127.0, 129.1, 130.6, 135.0, 153.6, 157.8, 161.9, 212.8 ppm. **HRMS (MeOH):** m/z calcd. for $[C_{32}H_{42}NO]^+$: 456.3261 $[M]^+$, found: 456.3283

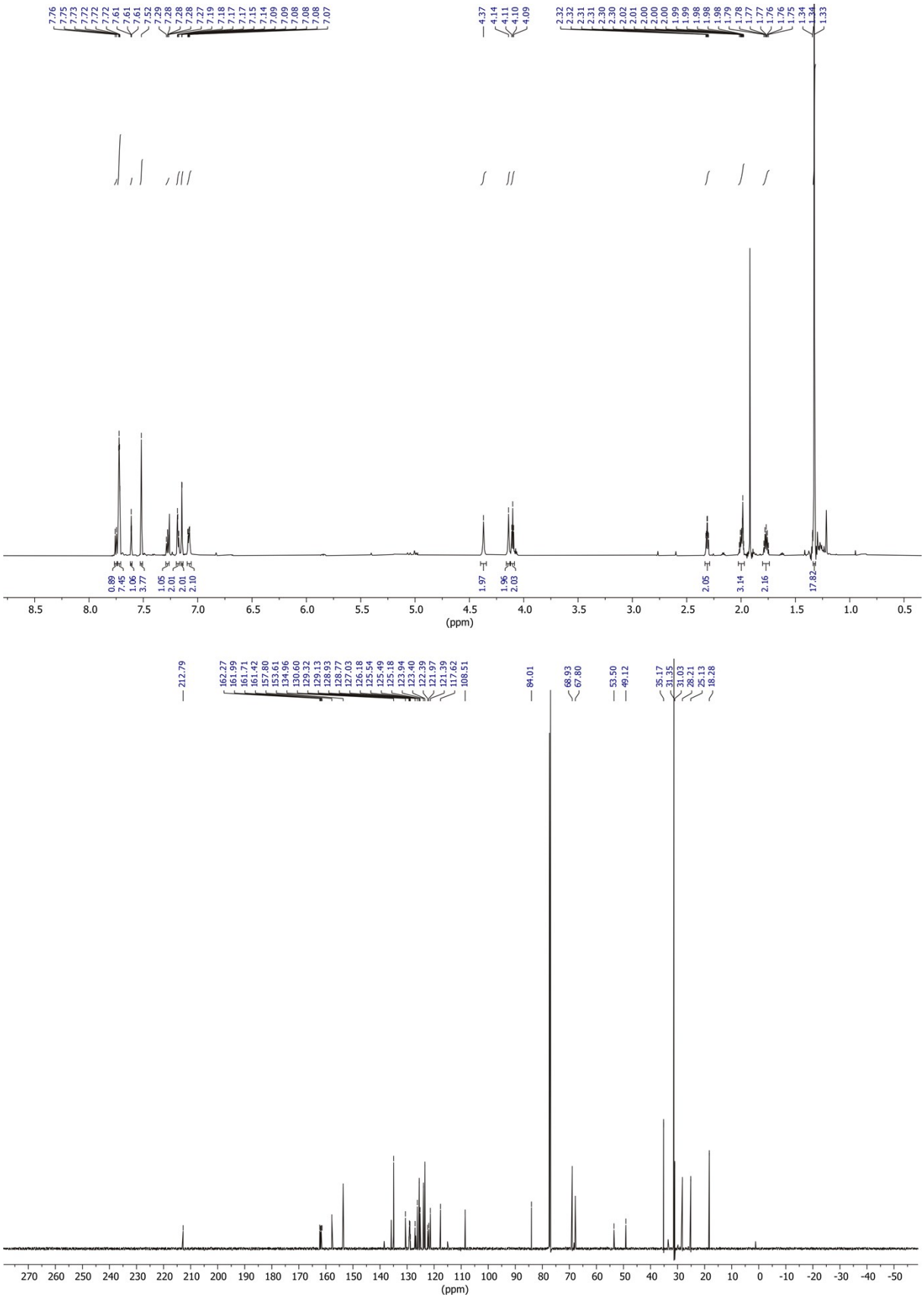

Fig. S15 ^{1}H (top) and ^{13}C (bottom) NMR spectra (700/176 MHz, $CDCl_3$, 298 K) of **6**.

N-(3,5-di-tert-butylbenzyl)-1-(6-(4-(3-(2,6-dimethoxyphenyl)isoxazol-5-yl)butoxy)naphthalen-1-yl)methanaminium tetrakis(3,5-bis(trifluoromethyl)phenyl)borate 7

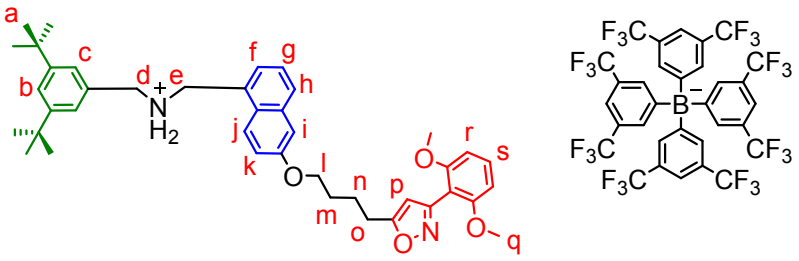

7

The axle **6** (20 mg, 15 µmol, 1.0 equiv.) and stopper **St1** (4 mg, 20 µmol, 1.3 equiv.) was added and the mixture heated to 35°C for 2 days. Then, the mixture was purified by column chromatography (SiO_2, CH_2Cl_2 + EtOH 3%, R_f ~ 0.3 in CH_2Cl_2) to obtain the desired product **7** (8 mg, 5 µmol, 30%) as an brown oil.

^{1}H NMR (400 MHz, CD_2Cl_2) δ = 1.28 (s, 18H, a), 1.80 – 1.92 (m, 4H, m,n), 2.82 (t, J = 7.0 Hz, 2H, o), 3.66 (s, 6H, q), 4.15 (t, J = 5.7 Hz, 2H, l), 4.29 (s, 2H, d,e), 4.59 (s, 2H, d,e), 6.46 (s, 1H, p), 6.65 – 6.69 (d, J = 8.5 Hz, 2H, r), 7.13 – 7.19 (m, 1H, j), 7.20 – 7.25 (m, 4H, c,f,i), 7.29 – 7.35 (m, 1H, g), 7.40 – 7.49 (m, 2H, s,k), 7.55 (s_{br}, 4H, $BArF_{24}$), 7.59 (t, J = 1.8 Hz, 1H, b), 7.71 (s_{br}, 8H, $BArF_{24}$), 7.77 (d, J = 8.3 Hz, 1H, h), 7.97 – 8.05 (s_{br}, 2H, NH_2) ppm. **^{13}C NMR** (176 MHz, CD_2Cl_2) δ = 24.2, 26.7, 28.5, 29.3, 30.1, 31.4, 35.3, 47.2, 49.3, 57.0, 67.9, 105.9, 106.0, 109.4, 117.9, 121.3, 122.7, 123.1, 124.2, 124.2, 125.4, 125.5, 125.8, 126.3, 126.4, 127.3, 127.5, 129.3, 130.7, 135.2, 153.6, 156.5, 157.5, 159.3, 162.2, 173.9 ppm. **HRMS (MeOH):**m/z calcd. for $[C_{41}H_{51}N_2O_4]^+$: 635.3849 $[M]^+$, found: 635.3868.

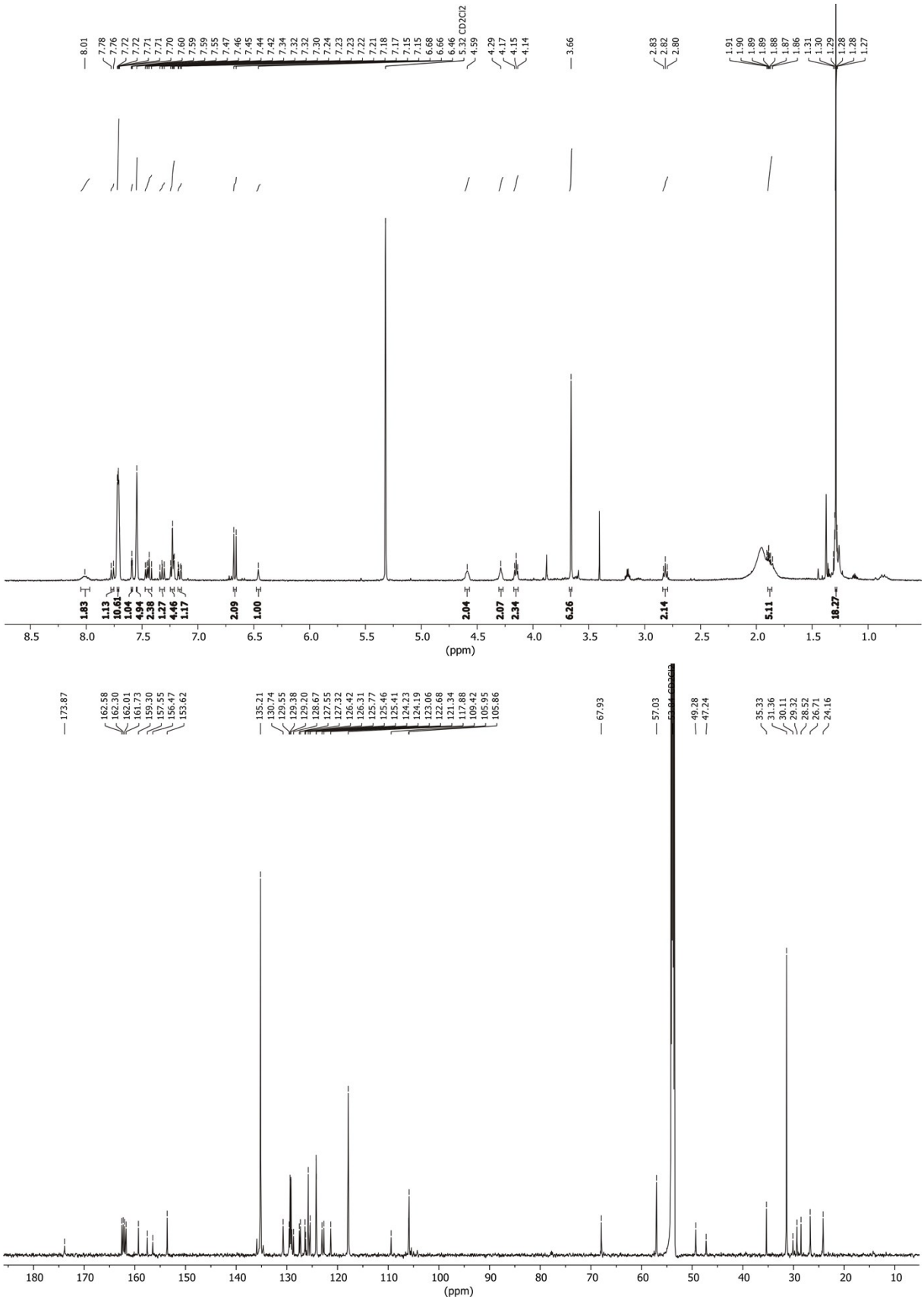

Fig. S16 ^{1}H (top) and ^{13}C (bottom) NMR spectra (400/176 MHz, CD_2Cl_2, 298 K) of **7**.

[2]Rotaxane R1

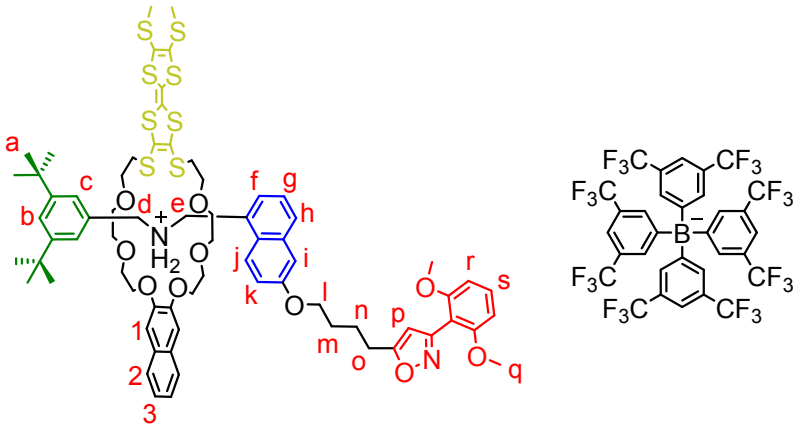

R1

The axle **6** (38 mg, 29 µmol, 1.0 equiv.) and macrocycle **TTFC8** (24 mg, 32 µmol, 1.1 equiv.) were dissolved in $ClCH_2CH_2Cl$ (2 mL) and stirred at 40 °C. for 3 days. Afterwards, the mixture was allowed to cool to room temperature, stopper **St1** (7 mg, 37 µmol, 1.3 equiv.) was added and the mixture heated to 35°C for 2 days. Then, the mixture was purified by column chromatography (SiO_2, CH_2Cl_2/hexane 8:2 -> CH_2Cl_2, R_f ~ 0.5 in CH_2Cl_2) to obtain the desired product **R1** (15 mg, 7 µmol, 23%) as an orange oil.

^{1}H NMR (700 MHz, CD_2Cl_2) δ = 1.28 (s, 18H, a), 1.90 – 1.95 (m, 2H, m), 1.97 – 2.03 (m, 2H, n), 2.40 (s, 6H, S-CH_3), 2.93 – 2.96 (m, 2H, o), 3.17 – 3.25 (m, 4H, S-CH_2-CH_2), 3.42 – 3.49 (m, 5H, O-CH_2-CH_2), 3.55 – 3.59 (m, 3H, O-CH_2-CH_2), 3.60 – 3.68 (m, 5H, O-CH_2-CH_2), 3.75 – 3.77 (m, 2H, l), 3.78 (s, 6H, q), 3.82 – 3.89 (m, 6H, O-CH_2-CH_2), 3.92 – 4.01 (m, 6H, O-CH_2-CH_2), 5.00 – 5.04 (m, 2H, d), 5.06 – 5.11 (m, 2H, e), 6.14 (t, *J* = 0.7 Hz, 1H, p), 6.38 (d, *J* = 2.6 Hz, 1H, j), 6.53 (s, 2H, 1), 6.67 (d, *J* = 8.4 Hz, 2H, r), 7.11 – 7.14 (m, 3H, g,k,i), 7.36 – 7.39 (m, 4H, 2,f,s), 7.50 (t, *J* = 1.7 Hz, 1H, b), 7.52 – 7.54 (m, 4H, 3, c), 7.55 – 7.57 (s_{br}, 4H, $BArF_{24}$), 7.70 – 7.74 (s_{br}, 8H, $BArF_{24}$), 7.98 – 8.01 (d, *J* = 9.2 Hz, 1H, h) ppm. **^{13}C NMR** (176 MHz, CD_2Cl_2) δ = 19.5, 25.0, 27.2, 29.3, 30.3, 31.7, 35.6, 39.1, 51.0, 56.5, 67.8, 68.8, 70.6, 71.2, 71.3, 72.8, 104.2, 104.7, 107.4, 108.0, 108.2, 109.2, 113.9, 118.0, 120.5, 122.8, 122.8, 123.4, 124.4, 124.5, 125.4, 125.8, 125.9, 126.6, 126.7, 127.0, 127.2, 127.5, 128.1, 128.9, 129.4, 129.5, 129.8, 130.1, 131.6, 135.4, 135.5, 147.5, 153.4, 157.4, 157.6, 159.2, 162.3, 173.1 ppm. **HRMS (MeOH):**m/z calcd. for $[C_{71}H_{87}N_2O_{10}S_8]^+$: 1383.4121 $[M]^+$, found: 1383.4156

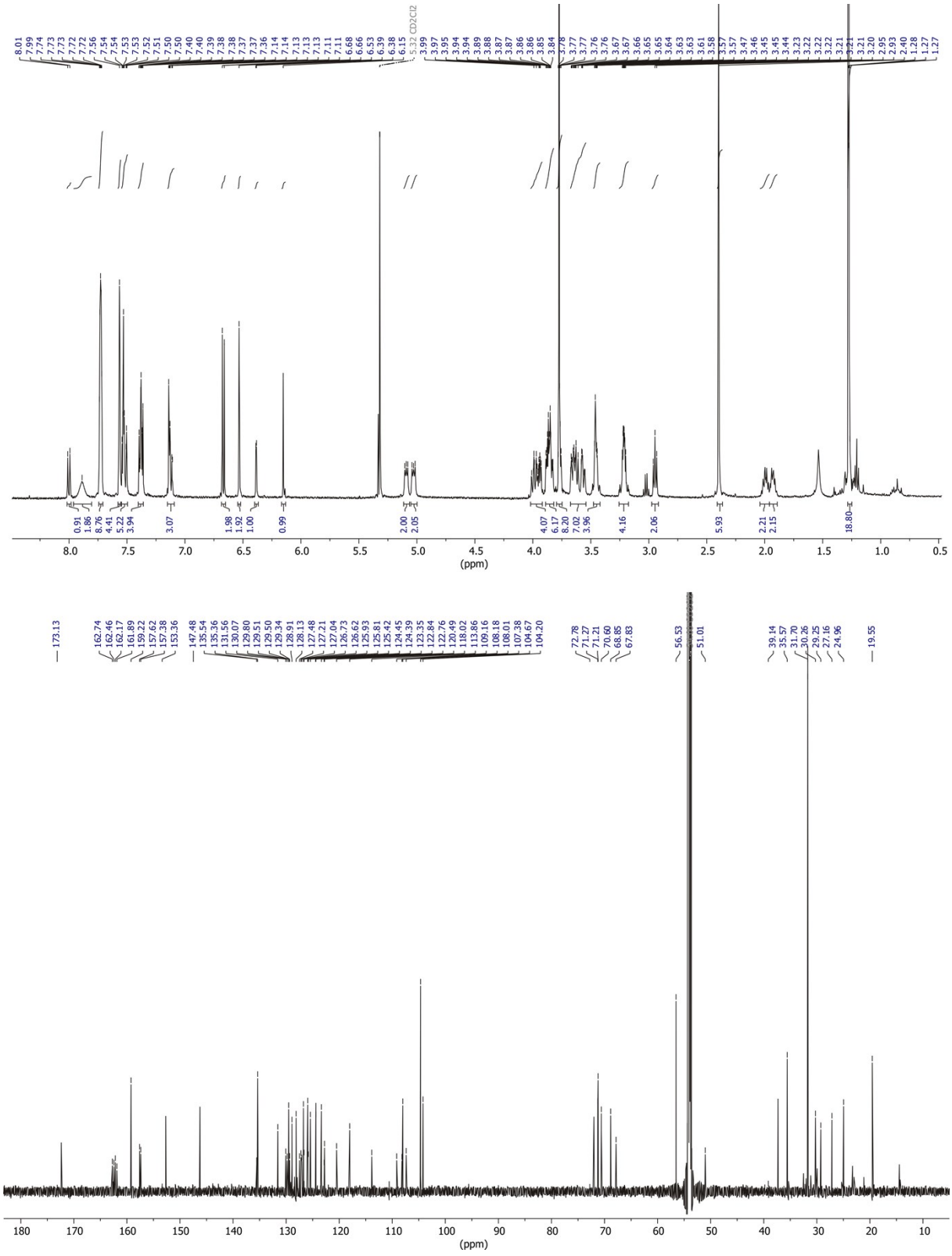

Fig. S17 ^{1}H (top) and ^{13}C (bottom) NMR spectra (700/176 MHz, CD_2Cl_2, 298 K) of **R1**.

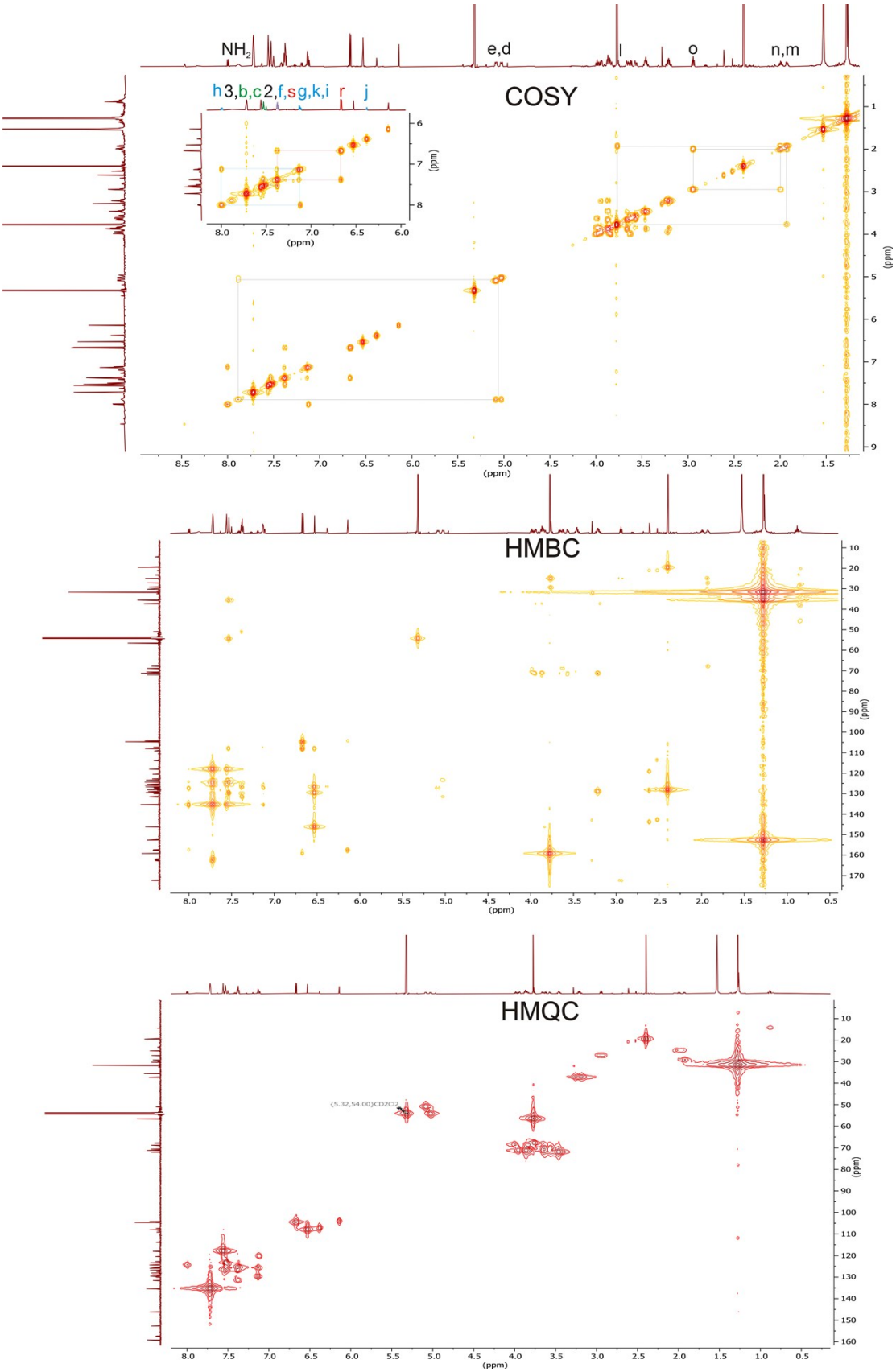

Fig. S18 COSY (top), HMBC (center) and HMQC (bottom) NMR spectra (700/176 MHz, CD_2Cl_2, 298 K) of **R1**.

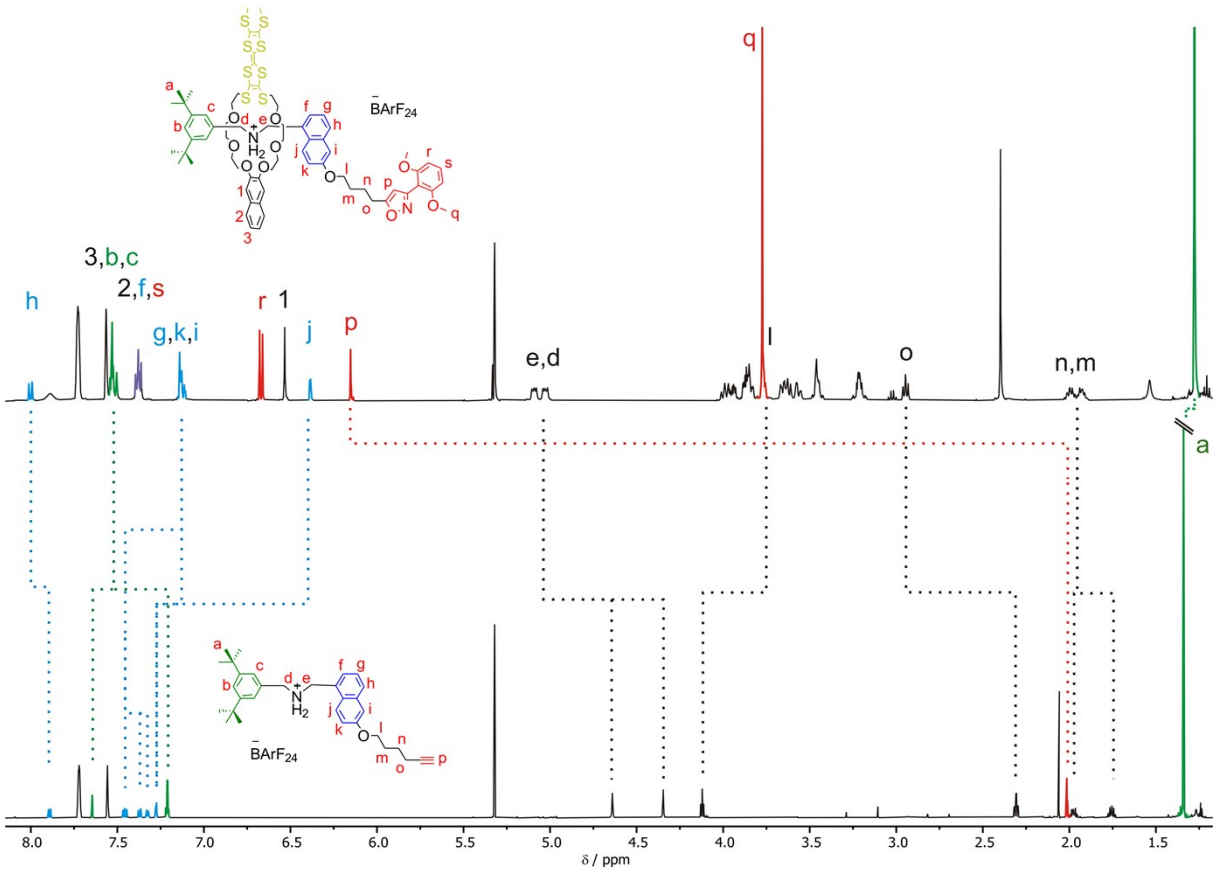

Fig. S19 [2]rotaxane **R1** (top) and axle **6** (bottom) NMR spectra (500 MHz, CD_2Cl_2, 298 K).

Pseudorotaxane PA11@TTFC8

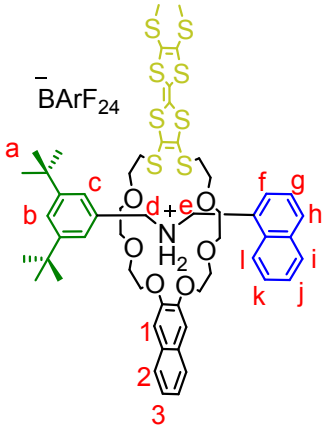

PA11@TTFC8

Axle **PA11** (50 mg, 41 µmol, 1.0 equiv.) and macrocycle **TTFC8** (31 mg, 41 µmol, 1.0 equiv.) were dissolved in $ClCH_2CH_2Cl$ (2 mL) and stirred at 50 °C for 5 days. The mixture was purified by column chromatography (SiO_2, CH_2Cl_2, R_f ~ 0.5 in CH_2Cl_2) to obtain the desired product **PA11@TTFC8** (65.2 mg, 33 µmol, 85%) as an orange sticky solid.

^{1}H NMR (700 MHz, CD_2Cl_2) δ = 1.27 (s, 18H, b), 2.40 (s, 6H, S-Me), 3.16 – 3.24 (m, 4H, S-$C\underline{H}_2$-CH_2), 3.43 – 3.45 (m, 4H, O-CH_2), 3.55 – 3.58 (m, 4H, O-CH_2), 3.61 – 3.68 (m, 4H, O-CH_2), 3.81 – 3.88 (m, 6H, O-CH_2), 3.90 – 3.97 (m, 4H, O-CH_2), 5.02 – 5.06 (m, 2H, d), 5.13 – 5.17 (m, 2H, e), 6.52 (s, 2H, 1), 7.08 (dd, *J* = 8.2, 7.0 Hz, 1H, j), 7.18 – 7.21 (m, 1H, k), 7.27 – 7.29 (m, 1H, f), 7.30 – 7.33 (m, 1H, l), 7.36 – 7.40 (m, 1H, 2), 7.49 (t, *J* = 1.8 Hz, 1H, a), 7.47 – 7.56 (m, 6H, 3, c, g, i), 7.55 – 7.57 (m, 4H, $BArF_{24}$), 7.71 – 7.74 (m, 8H, $BArF_{24}$), 7.91 (s_{br}, 2H, NH_2), 8.10 (d, *J* = 8.5, 0.9 Hz, 1H, h) ppm. **^{13}C-NMR** (176 MHz, CD_2Cl_2) δ = 19.6, 31.7, 35.5, 37.3, 44.5, 50.9, 54.2, 68.8, 70.6, 71.2, 71.3, 72.0, 108.1, 118.0, 122.9, 123.1, 123.4, 124.4, 124.5, 125.2, 125.5, 125.9, 126.7, 126.8, 127.2, 127.5, 127.5, 128.1, 128.8, 129.1, 129.4, 129.5, 130.9, 131.2, 131.5, 134.0, 135.4, 146.2, 152.7, 162.3 ppm. **HRMS (CH_2Cl_2):** m/z calcd. for $[C_{56}H_{70}NO_6S_8]^+$:1108.2963 $[M]^+$, found: 1108.2948

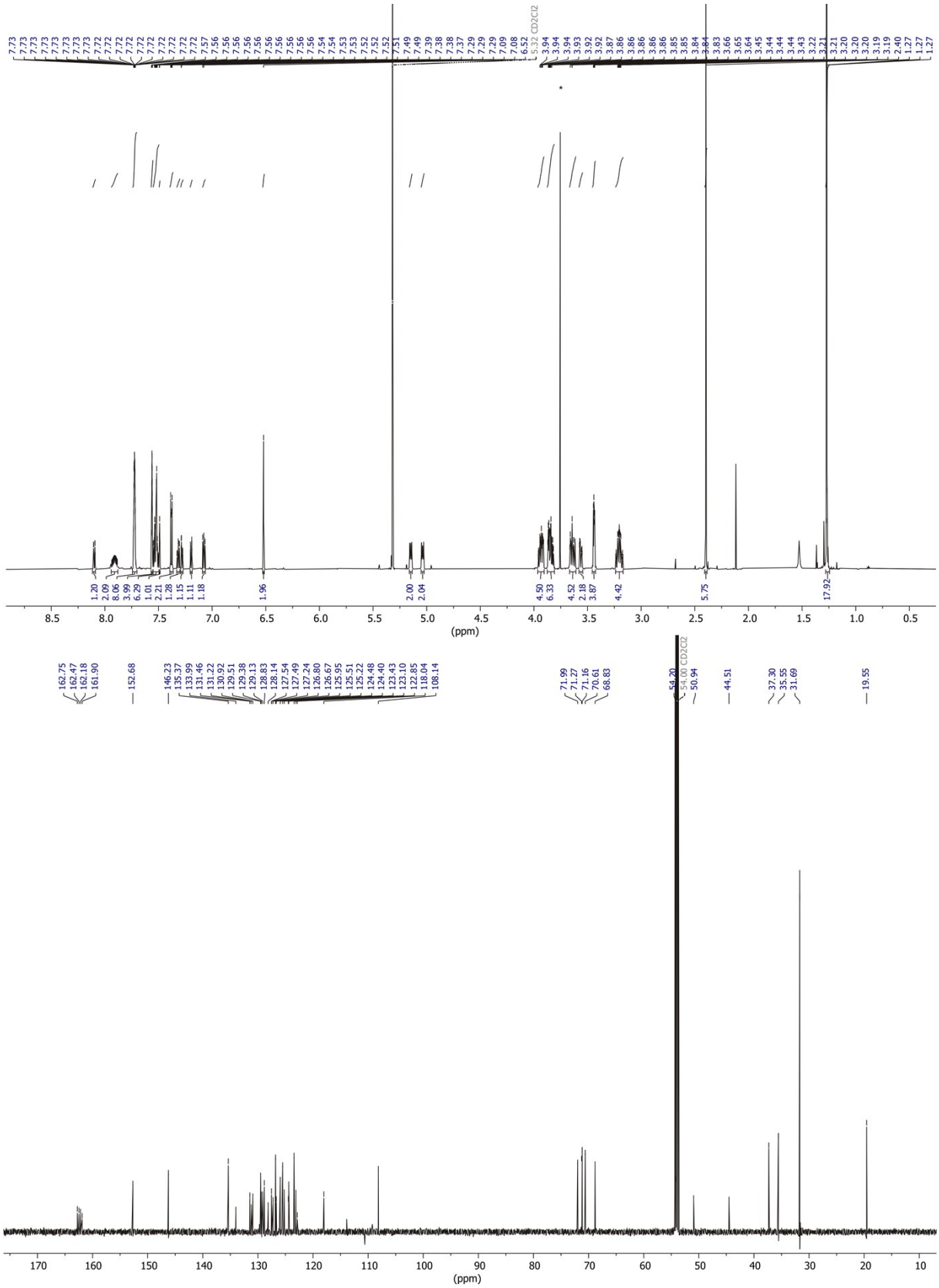

Fig. S20 ^{1}H (top) and ^{13}C (bottom) NMR spectra (700/176 MHz, CD_2Cl_2, 298 K) of **PA11@TTFC8**.

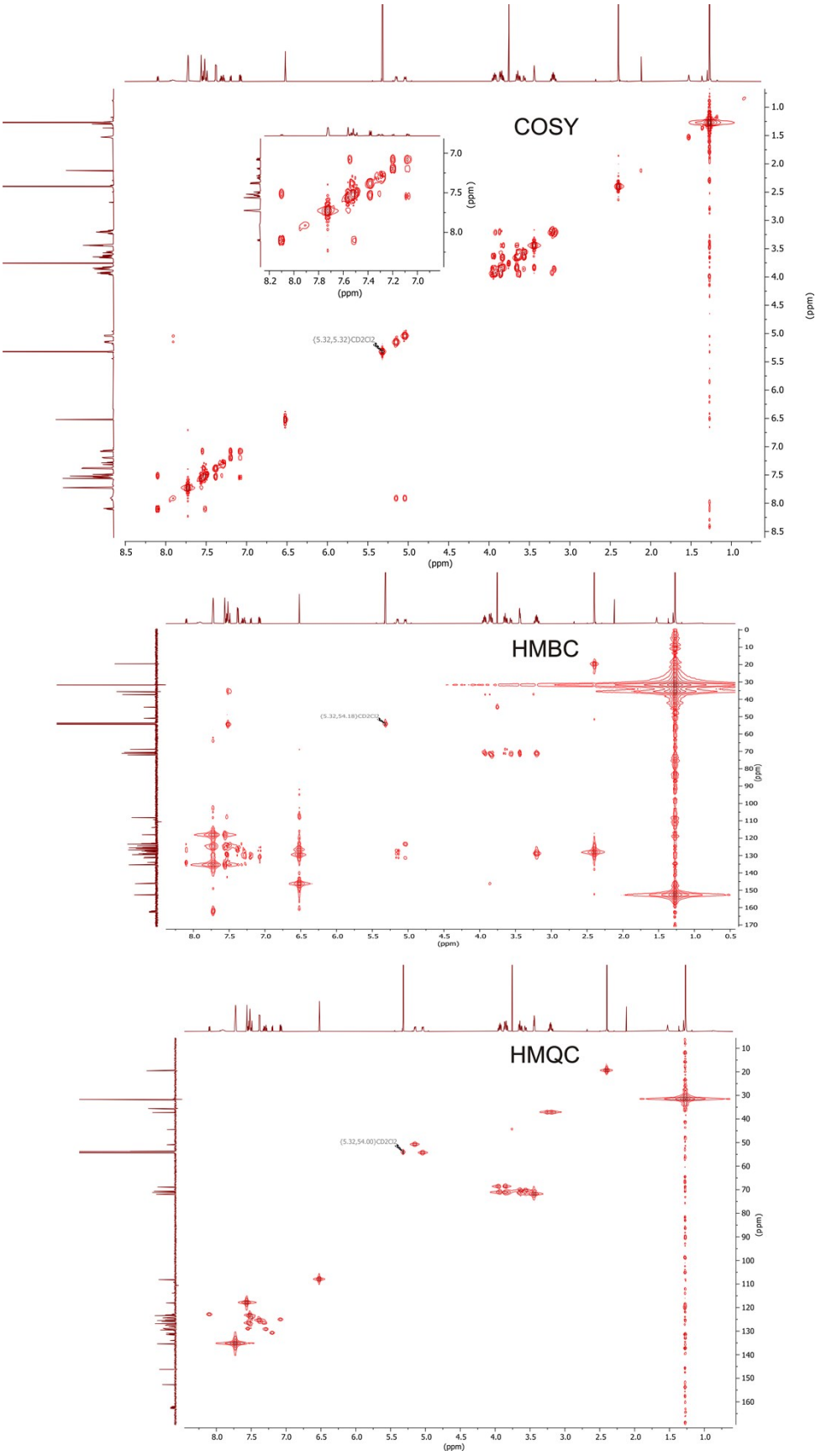

Fig. S21 COSY (top), HMBC (center) and HMQC (bottom) NMR spectra (700/176 MHz, CD_2Cl_2, 298 K) of **PA11@TTFC8**.

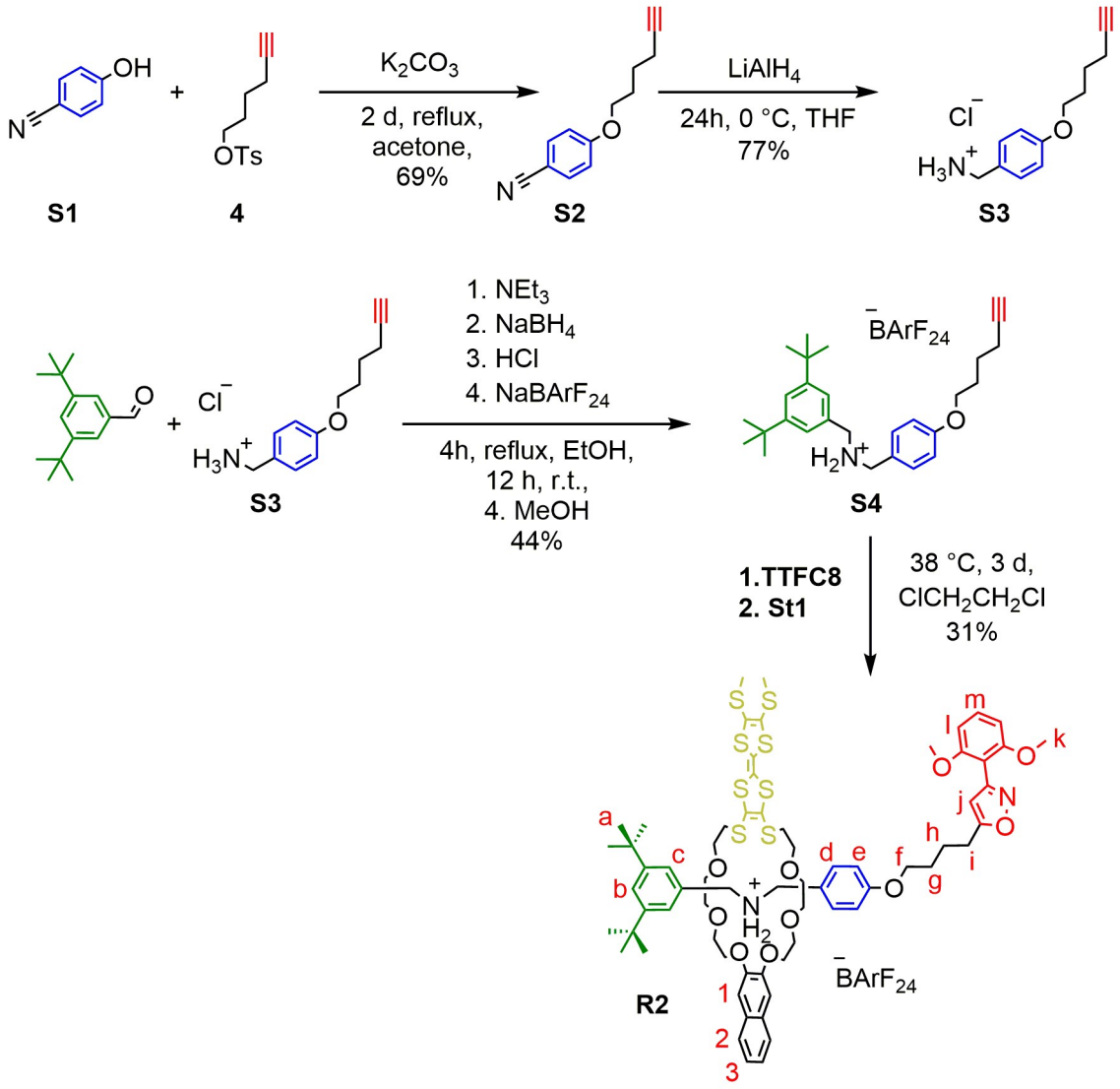

Scheme S3 Synthesis of **R2**.

(4-(Hex-5-yn-1-yloxy)phenyl)methanaminium chloride S3

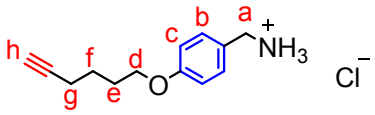

S3

To a solution of 400 mg (2.0 mmol, 1.0 equiv.) 4-(hex-5-yn-1-yloxy)benzonitrile **S2** in dry THF (100 mL), 380 mg (10 mmol, 5.0 equiv.) $LiAlH_4$ was added at 0 °C and stirred for 24 h in the thawing ice bath. The excess $LiAlH_4$ was quenched with saturated Na_2SO_4 solution. The solid parts were filtered off and the solvent was removed under reduced pressure. The oily residue was dissolved in CH_2Cl_2, washed with brine and dried with $MgSO_4$. After removal of the solvent, the crude product was purified by flash column chromatography (SiO_2, CH_2Cl_2 + 1% NEt_3 → CH_2Cl_2 + 1% NEt_3/ 5% EtOH, *Rf* ~ 0.5 in CH_2Cl_2 + 1% NEt_3/ 3% EtOH) to isolate the desired amine, which was dissolved in Et_2O and conc. HCl (aq.) was added until no more solid crushed out. After filtration the white solid was washed with cold acetone. The product is a white sticky solid, which could be isolated in 77% yield (370 mg, 1.5 mmol) over two steps.

^{1}H NMR (700 MHz, DMSO-d_6) δ = 1.55 – 1.61 (m, 2H, f), 1.76 – 1.81 (m, 2H, e), 2.22 (td, *J*=7.1, 2.7 Hz, 2H, g), 2.78 (t, *J*=2.6, 1H, h), 3.92 (s, 2H, a), 3.98 (t, *J*=6.4, 2H, d), 6.92 – 6.98 (m, 2H, c), 7.36 – 7.40 (m, 2H, b), 8.16 – 8.34 (s_{br}, 3H, NH) ppm. **^{13}C NMR** (176 MHz, DMSO-d_6) δ = 17.4, 24.6, 27.7, 41.7, 67.0, 71.4, 84.3, 114.5, 125.8, 130.5, 158.7 ppm. **HRMS (MeOH):** m/z calcd. for $[C_{13}H_{18}NO]$: $[M\text{-}NH_3]^+$, 187.1123 found: 187.1119.

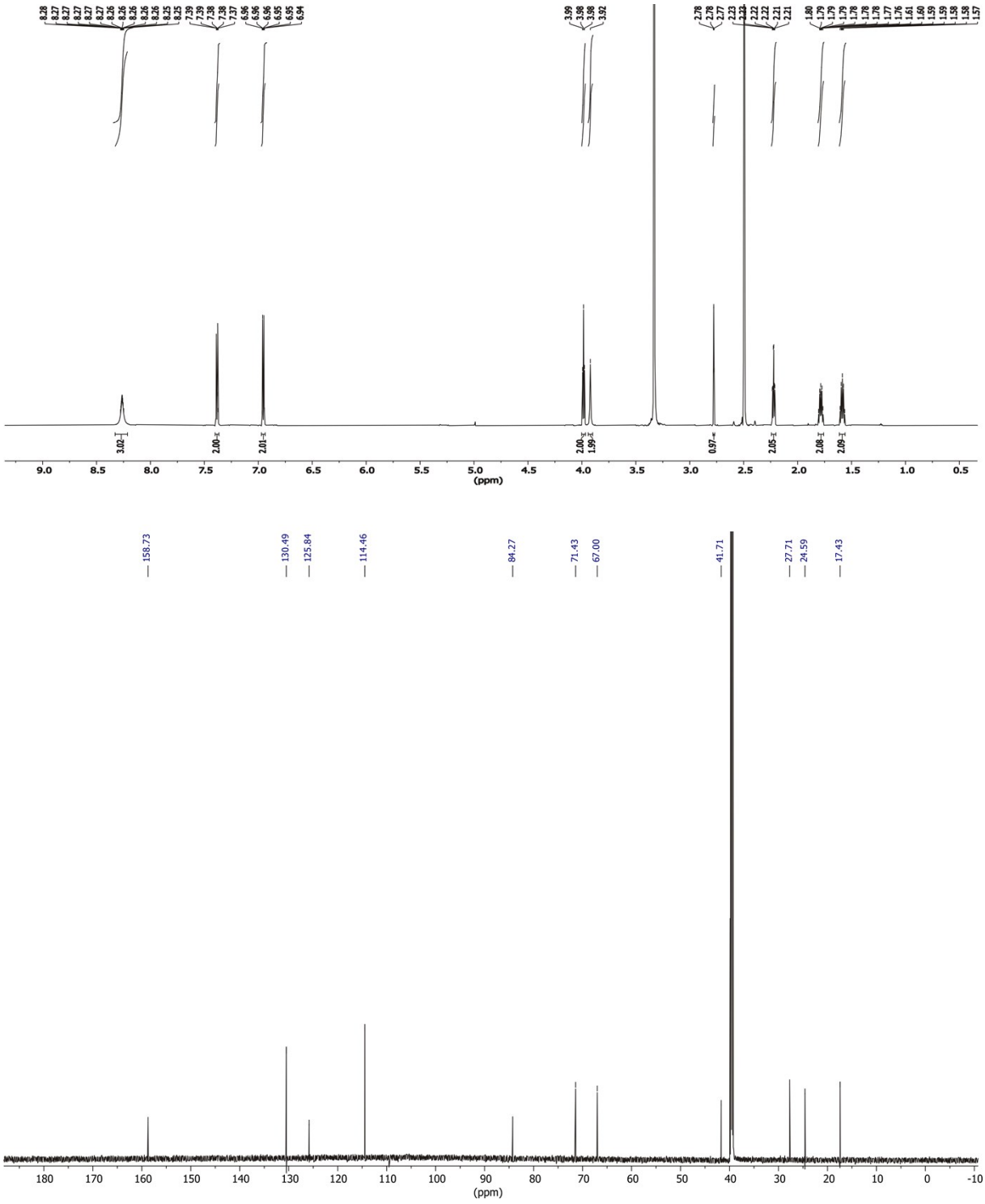

Fig. S22 ^{1}H (top) and ^{13}C (bottom) NMR spectra (700/176 MHz, DMSO-d_6, 298 K) of **S3**.

N-(3,5-di-tert-butylbenzyl)-1-(4-(hex-5-yn-1-yloxy)phenyl)methanaminium tetrakis(3,5-bis(trifluoromethyl)phenyl)borate S4

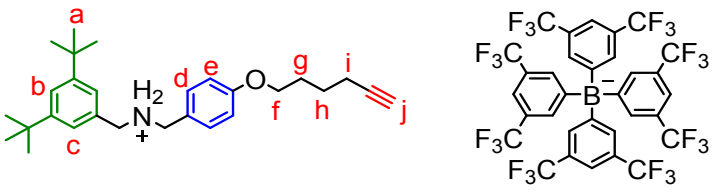

S4

Ammonium compound **S3** (150 mg, 0.63 mmol, 1 equiv.), 3,5-di-*tert*-butylbenzaldehyde (140.0 mg, 0.63 mmol, 1.0 equiv.) and NEt_3 (90 µL, 0.56 mmol, 0.9 equiv.) were dissolved in 30 mL dry EtOH and refluxed for 5.5 h. Then, the mixture was cooled to 0 °C and $NaBH_4$ (150.0 mg, 3.13 mmol, 5 equiv.) was added. The reaction stirred overnight in the thawing ice bath. Afterwards, the reaction was quenched with saturated aq. $NaHCO_3$ solution. The solvent was removed. The residue was taken up with CH_2Cl_2 (40 mL) and washed with Brine (3x50 mL). The organic phase was dried over $MgSO_4$ and the solvent was removed. The crude product was purified via flash column chromatography (SiO_2, CH_2Cl_2 -> CH_2Cl_2 + 10% EtOH, R_f ~ 0.5 in CH_2Cl_2 + 3% EtOH) to get the desired Amine as yellow oil, which was dissolved in EtOAc (10 mL) and protonated with HCl conc. under cooling in an ice bath. The solvent was removed and 60 mg (0.14 mmol) of the brown sticky oil were dissolved in MeOH (5 mL) and $NaBArF_{24}$ (120 mg, 0.14 mmol, 1.0 equiv.) was added. After stirring overnight at room temperature, the solvent was removed, the residue was taken up in CH_2Cl_2 and washed with water (3x50 mL). The organic phase was dried over $MgSO_4$ and the solvent was removed to get the desired axle **S4** as brown oil in 44% yield overall (160 mg, 0.13 mmol).

^{1}H NMR (700 MHz, CD_2Cl_2) δ = 1.32 (s, 18H, a), 1.68 – 1.73 (m, 2H, h), 1.89 – 1.94 (m, 2H, g), 2.00 (t, J = 2.7 Hz, 1H, j), 2.28 (td, J = 7.1, 2.7 Hz, 2H, i), 4.01 (t, J = 6.3 Hz, 2H, f), 4.22 (s, 2H, N-CH_2), 4.24 (s, 2H, N-CH_2), 6.97 – 7.01 (m, 2H, e), 7.15 (d, J = 1.8 Hz, 2H, c), 7.24 – 7.27 (m, 2H, d), 7.56 (s_{br}, 4H, $BArF_{24}$), 7.60 (t, J = 1.8 Hz, 1H, b), 7.72 (s_{br}, 8H, $BArF_{24}$) ppm. **^{13}C NMR** (176 MHz, CD_2Cl_2) δ = 18.6, 25.6, 28.7, 31.6, 35.5, 53.1, 68.4, 69.0, 84.5, 116.4, 118.0, 121.0, 122.9, 123.9, 124.4, 125.9, 125.9, 127.5, 128.9, 129.4, 131.5, 135.4, 153.9, 161.7, 162.3 ppm. **HRMS (MeOH):** m/z calcd. for $[C_{28}H_{40}NO]^+$: 406.3104 $[M]^+$, found: 406.3109

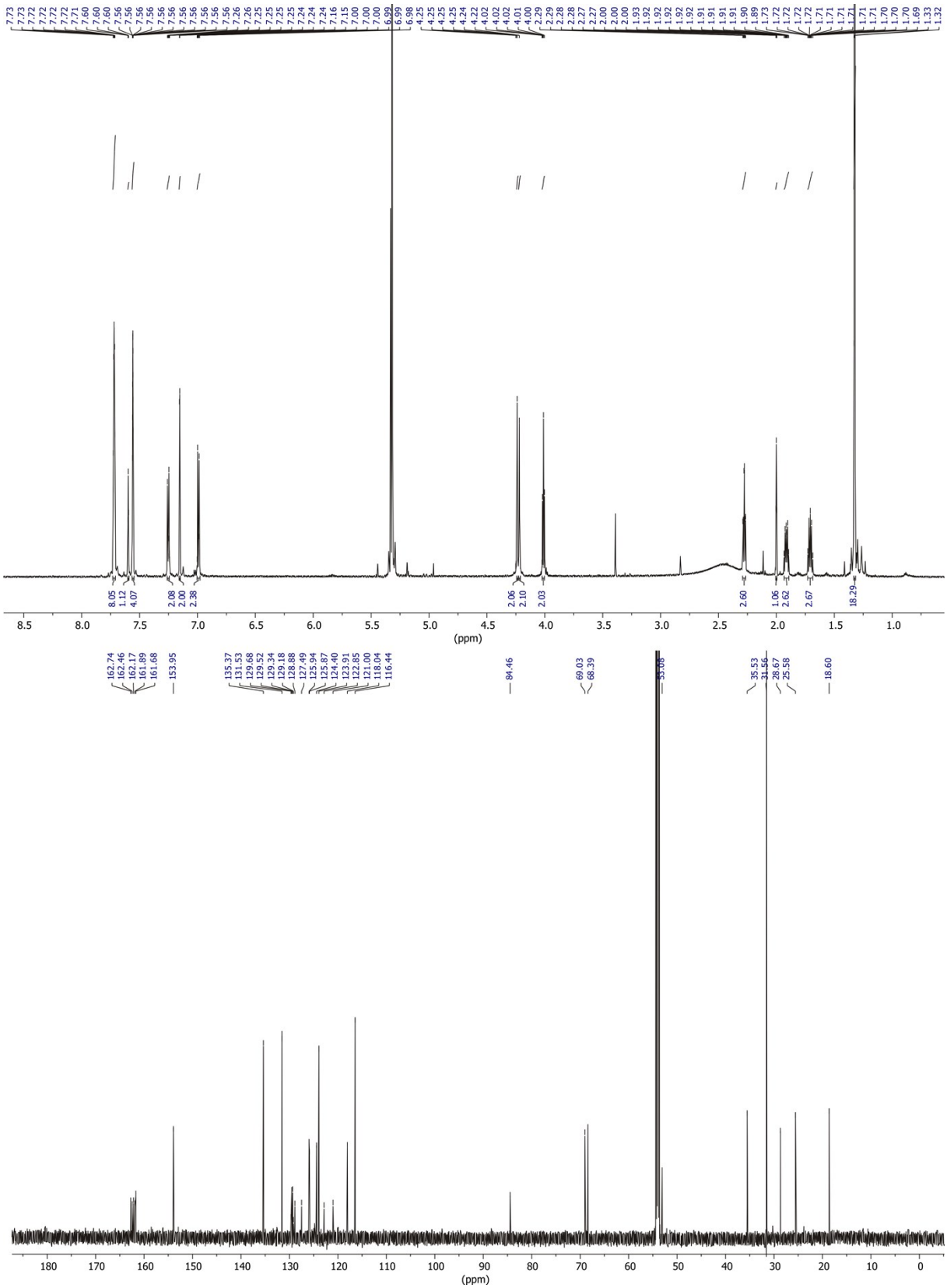

Fig. S23 ^{1}H (top) and ^{13}C (bottom) NMR spectra (700/176 MHz, CD_2Cl_2, 298 K) of **S4**.

[2]Rotaxane R2

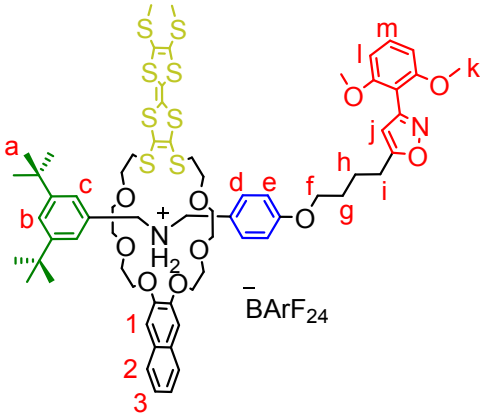

R2

A solution of 50 mg (39 µmol, 1.0 equiv.) axle **S4** and 32 mg (43 µmol, 1.1 equiv.) macrocycle **TTFC8** in $ClCH_2CH_2Cl$ (2 mL) was stirred at 38 °C. for 10 min. Afterwards, the mixture was allowed to cool to r.t. and 9 mg (50 µmol, 1.3 equiv.) stopper **St1** was added and the mixture was stirred at 38 °C for 36 h. Then, the mixture was purified by column chromatography (SiO_2, CH_2Cl_2/hexane 8:2-> CH_2Cl_2, R_f ~ 0.6 in CH_2Cl_2) to obtain the desired product **R2** (27 mg, 12 µmol, 31 %) as orange oil.

^{1}H NMR (700 MHz, CD_2Cl_2) δ = 1.27 (s, 18H, a), 1.54 – 1.59 (m, 2H, g), 1.66 – 1.72 (m, 2H, h), 2.41 (s, 6H, S-CH_3), 2.74 – 2.83 (m, 2H, i), 3.10 (t, *J* = 6.5 Hz, 2H, f), 3.18 (m, 4H, S-CH_2-), 3.46 – 3.54 (m, 4H, O-CH_2-), 3.59 – 3.65 (m, 6H, O-CH_2-), 3.73 – 3.78 (m, 8H, k, O-CH_2-), 3.79 – 3.83 (m, 2H, O-CH_2-), 3.84 – 3.90 (m, 2H, O-CH_2-), 4.00 - 4.04 (m, 2H, O-CH_2-), 4.19 – 4.24 (m, 2H, O-CH_2-), 4.55 – 4.60 (m, 2H, N-CH_2-), 4.78 – 4.82 (m, 2H, N-CH_2-), 6.09 (s, 1H, j), 6.32 – 6.35 (m, 2H, e), 6.67 (d, *J* = 8.4 Hz, 2H, l), 6.93 (s, 2H, 1), 7.10 – 7.12 (m, 2H, d), 7.35 – 7.40 (m, 2H, 3, m), 7.49 (dd, *J* = 7.5, 1.8 Hz, 3H, b, c), 7.56 (s_{br}, 4H, $BArF_{24}$), 7.65 (m, 2H, 2), 7.70 (s_{br}, 2H, NH_2), 7.72 (s_{br}, 8H, $BArF_{24}$) ppm.**^{13}C NMR** (176 MHz, CD_2Cl_2) δ = 19.6, 24.6, 27.0, 29.1, 31.7, 35.5, 37.3, 56.5, 67.5, 69.0, 70.4, 71.1, 71.2, 72.1, 104.2, 104.7, 108.1, 108.3, 114.7, 118.0, 122.8, 122.9, 123.7, 124.4, 124.4, 125.7, 125.9, 126.9, 127.5, 128.1, 129.0, 129.4, 129.6, 131.2, 131.5, 131.6, 135.4, 147.1, 152.7, 157.6, 159.2, 160.3, 162.3, 172.4 ppm. **HRMS (MeOH):** m/z calcd. for $[C_{67}H_{85}N_2O_{10}S_8]^+$: 1333.3964 $[M]^+$, found: 1333.3990 m/z.

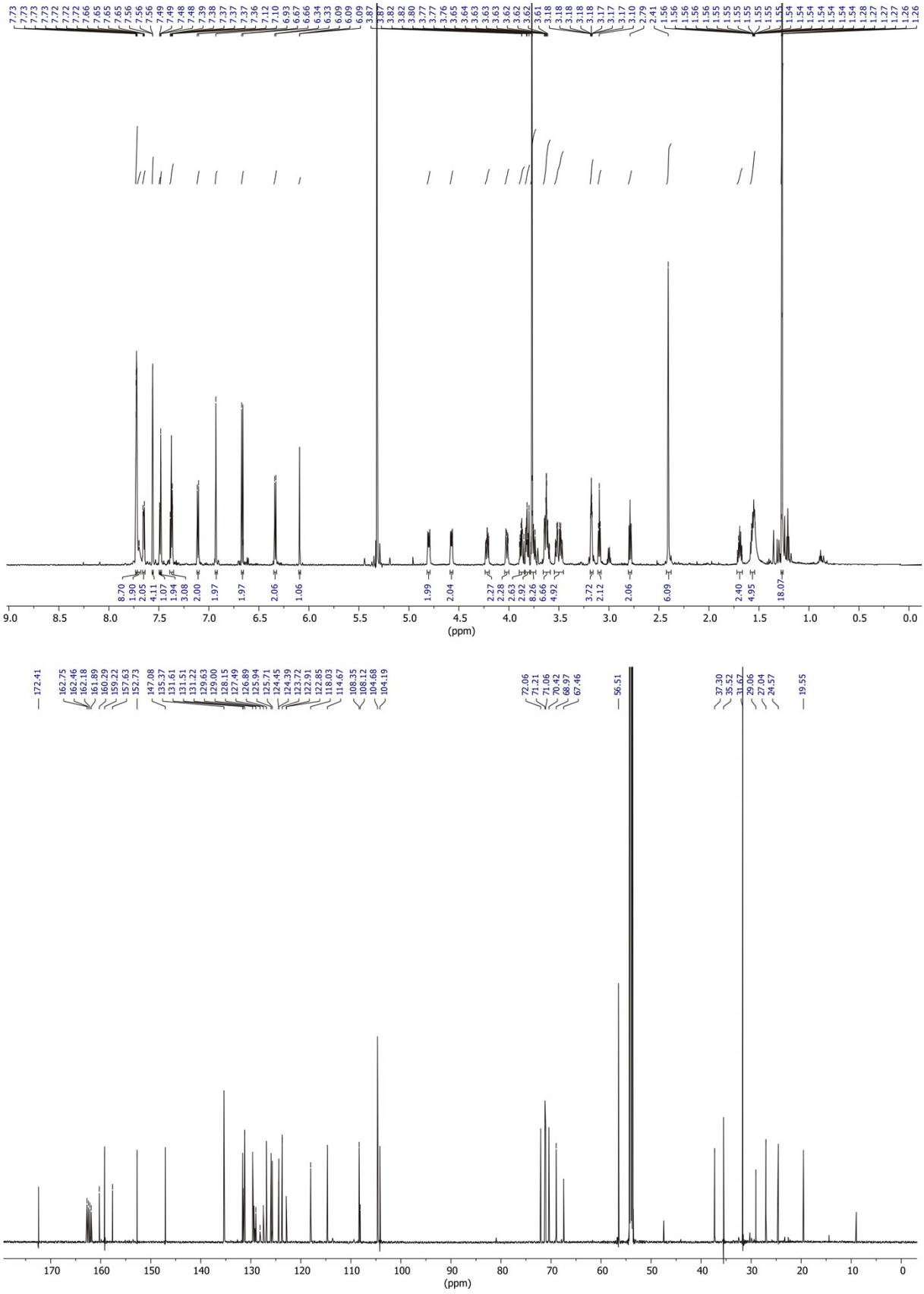

Fig. S24 ^{1}H (top) and ^{13}C (bottom) NMR spectra (700/176 MHz, CD_2Cl_2, 298 K) of **R2**.

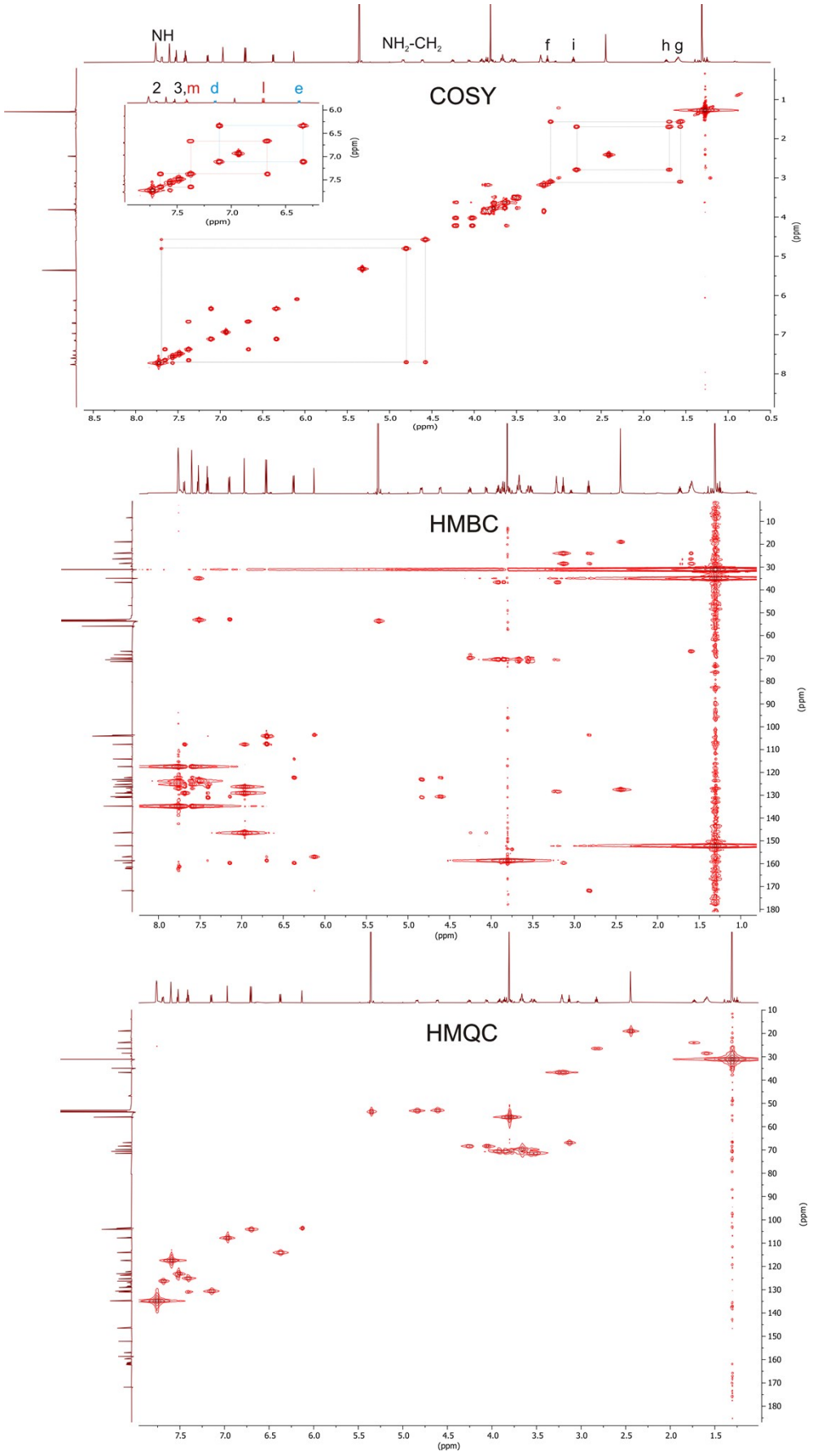

Fig. S25 COSY (top), HMBC (center) and HMQC (bottom) NMR spectra (700/176 MHz, CD_2Cl_2, 298 K) of **R2**.

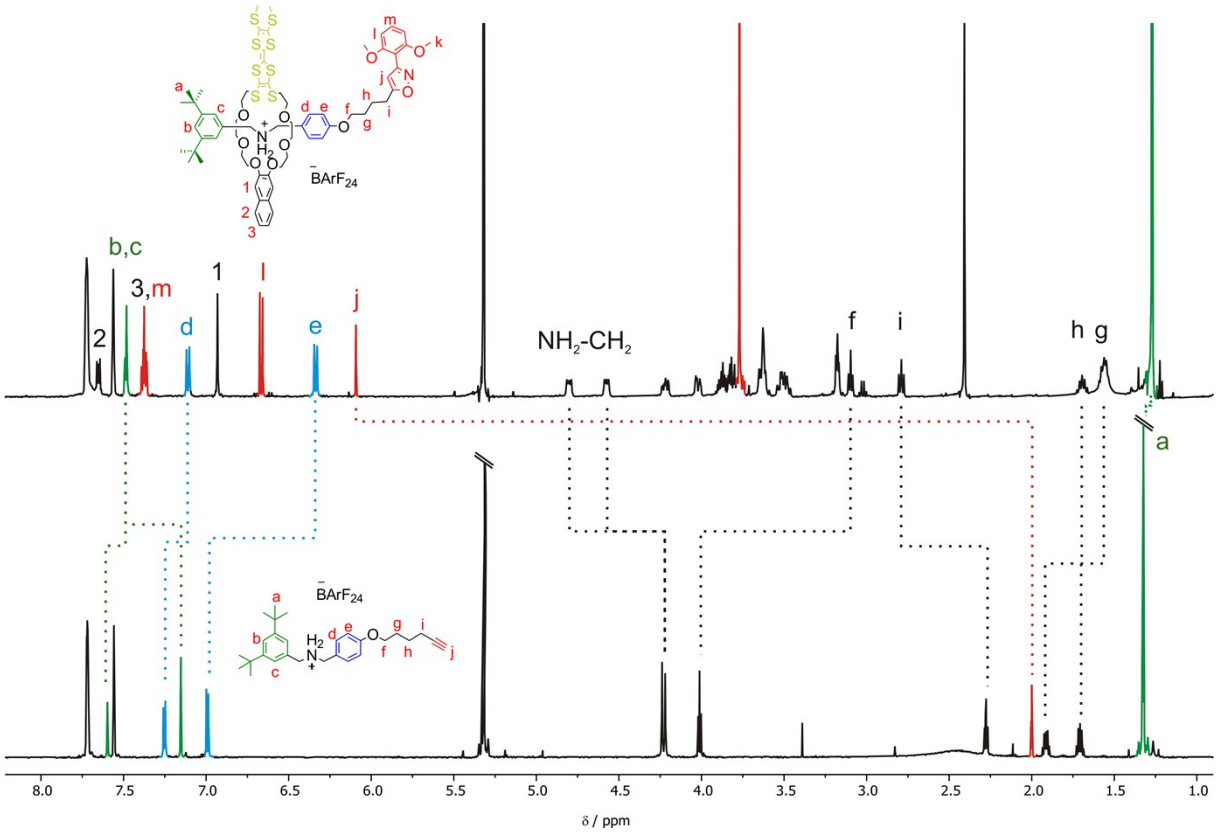

Fig. S26 [2]rotaxane **R2** (top) and axle **S4** (bottom) NMR spectra (500 MHz, CD_2Cl_2, 298 K).

2. Threading and dethreading: ^{1}H NMR experiments

Threading and unthreading experiments were performed at 4 mM concentration, deprotonation/oxidation was performed in dry CD_2Cl_2. Oxidation was performed by adding an excess of $NOSbF_6$ shaking gently, until the solution turned deep blue and subsequent filtration into a J. Young tube under argon atmosphere of residual $NOSbF_6$. Deprotonation was performed by adding an excess of polystyrene-immobilized P2 base, shaking and then filtration into a J. Young tube under argon atmosphere.

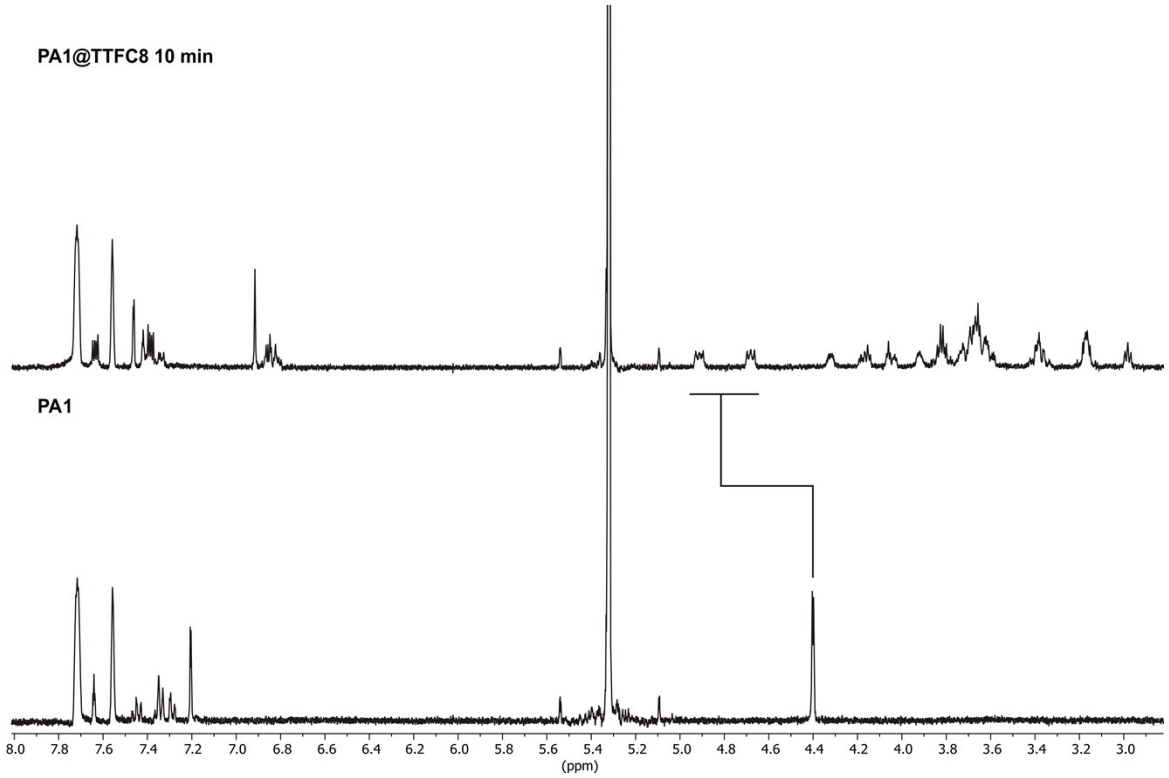

Fig. S27 Partial ^{1}H NMR spectra (400 MHz, CD_2Cl_2, 298 K) of **PA1** before (bottom) and after addition of **TTFC8** (top) the highlighted downfield shift and splitting of the methylene protons next to the ammonium is characteristic for a threaded complex.

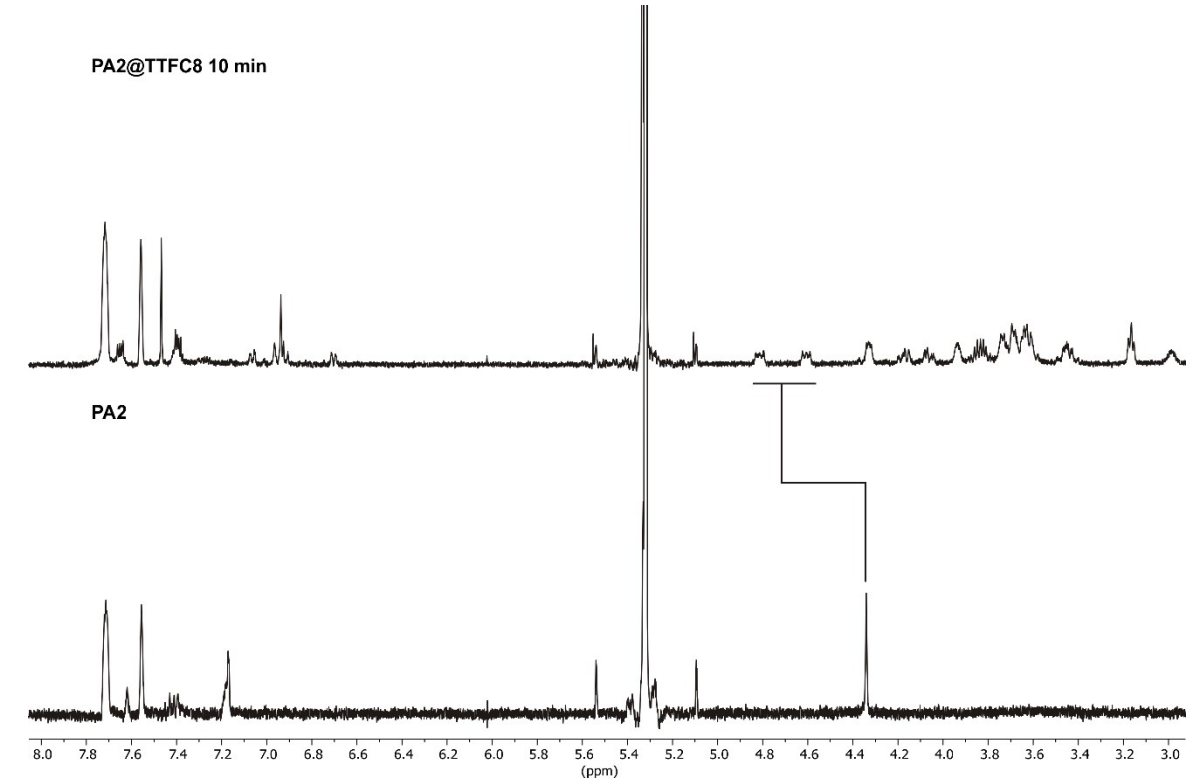

Fig. S28 Partial ^{1}H NMR spectra (400 MHz, CD_2Cl_2, 298 K) of **PA2** before (bottom) and after addition of **TTFC8** (top) the highlighted downfield shift and splitting of the methylene protons next to the ammonium is characteristic for a threaded complex.

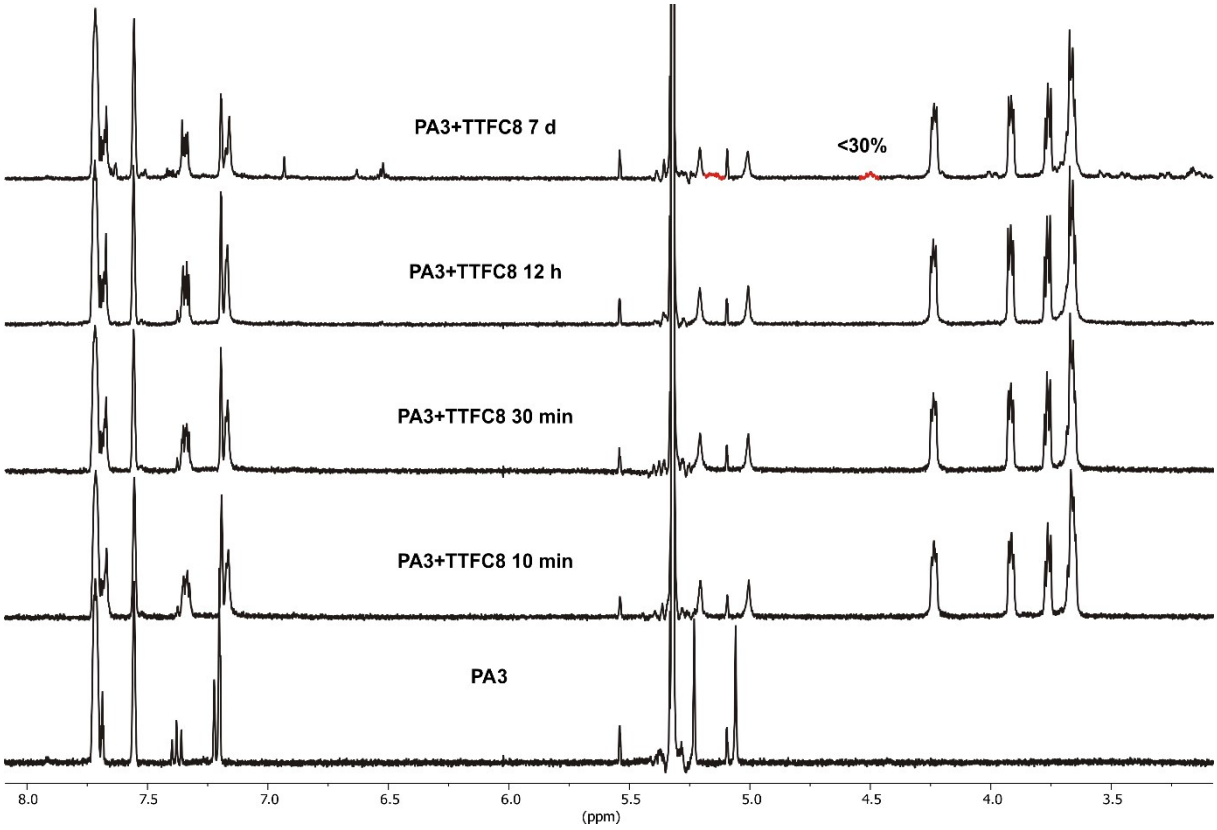

Fig. S29 Partial ^{1}H NMR spectra (400 MHz, CD_2Cl_2, 298 K) of **PA3** before (bottom) and after addition of **TTFC8** (top), the emerging peaks (red) correspond to the threaded complex.

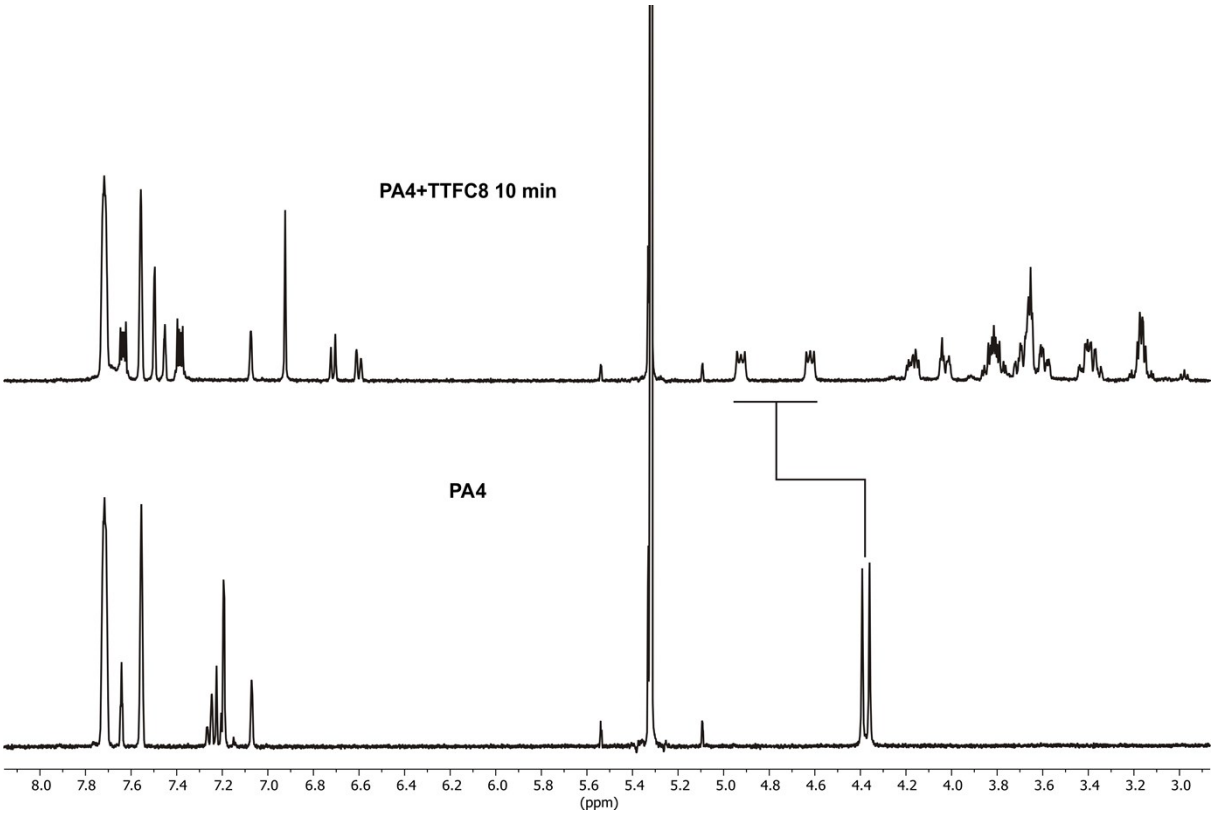

Fig. S30 Partial ^{1}H NMR spectra (400 MHz, CD_2Cl_2, 298 K) of **PA4** before (bottom) and after addition of **TTFC8** (top) the highlighted downfield shift and splitting of the methylene protons next to the ammonium is characteristic for a threaded complex.

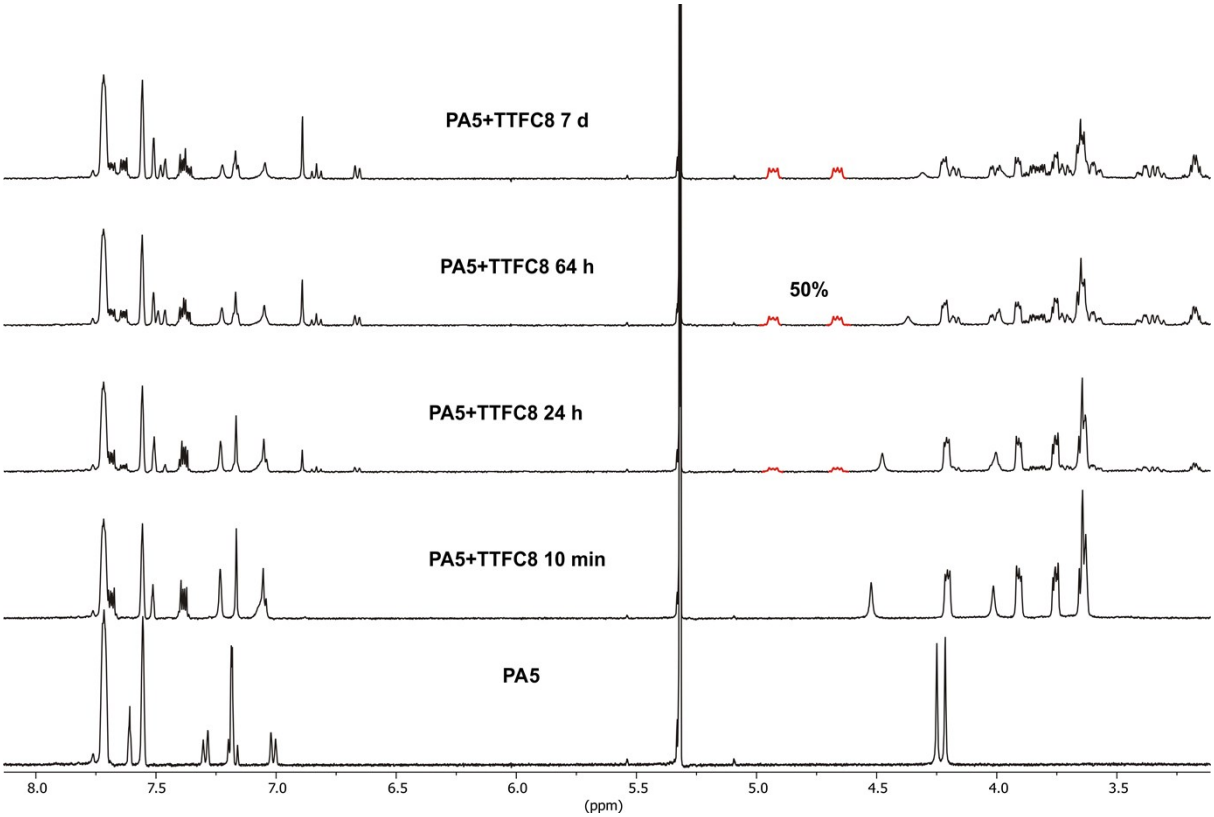

Fig. S31 Partial ^{1}H NMR spectra (400 MHz, CD_2Cl_2, 298 K) of **PA5** before (bottom) and after addition of **TTFC8** (top), the emerging peaks (red) correspond to the threaded complex.

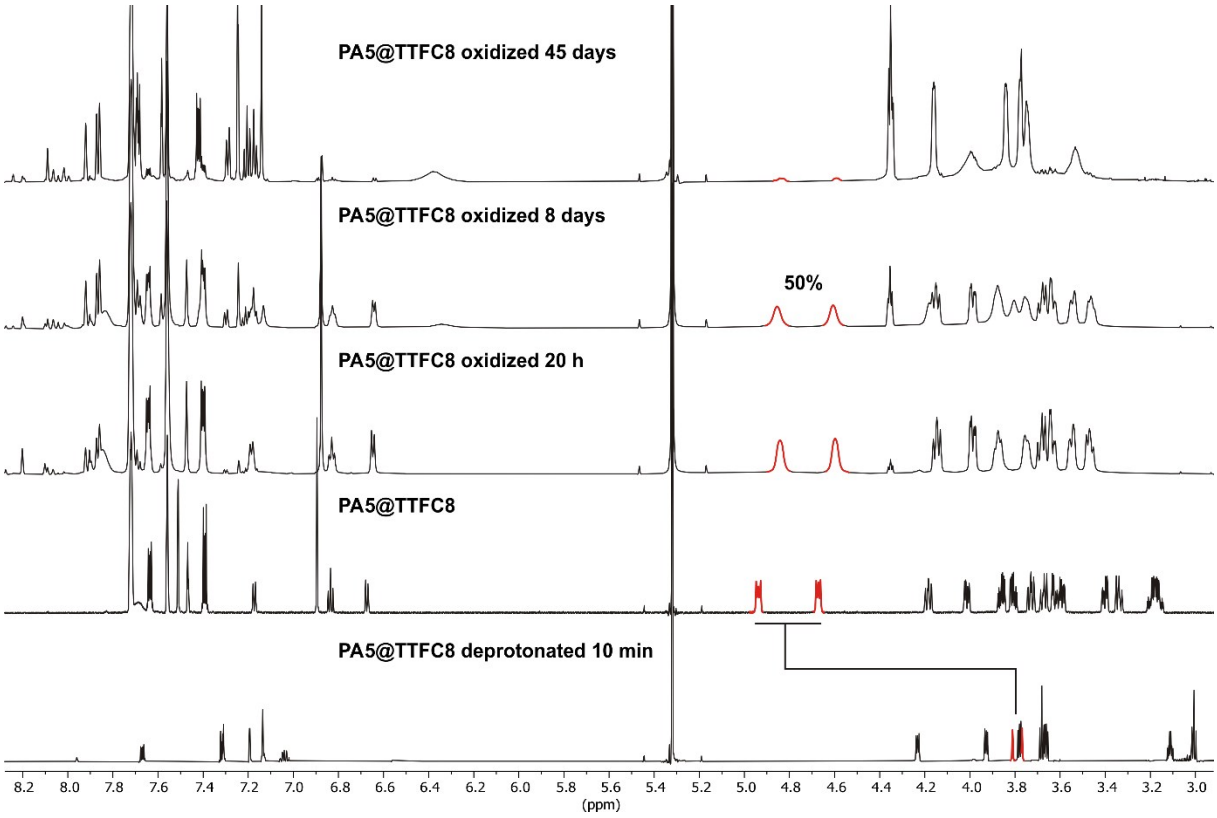

Fig. S32 Partial ^{1}H NMR spectra (700 MHz, CD_2Cl_2, 298 K) of **PA5@TTFC8** (center) after oxidation with $NO^{\cdot+}SbF_6^-$ (top) and after deprotonation with P2 base (bottom). The highlighted peaks in red correspond to the methylene protons next to the nitrogen.

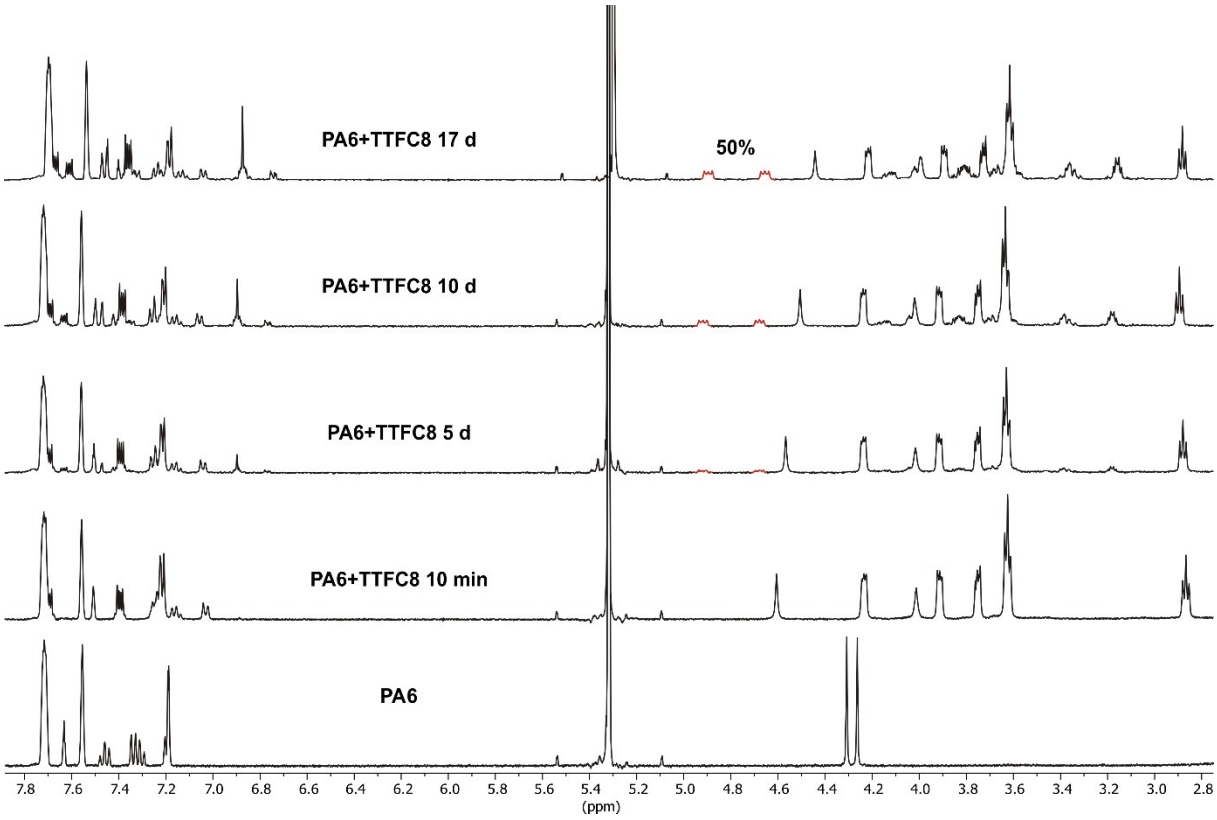

Fig. S33 Partial ^{1}H NMR spectra (400 MHz, CD_2Cl_2, 298 K) of **PA6** before (bottom) and after addition of **TTFC8** (top), the emerging peaks (red) correspond to the threaded complex.

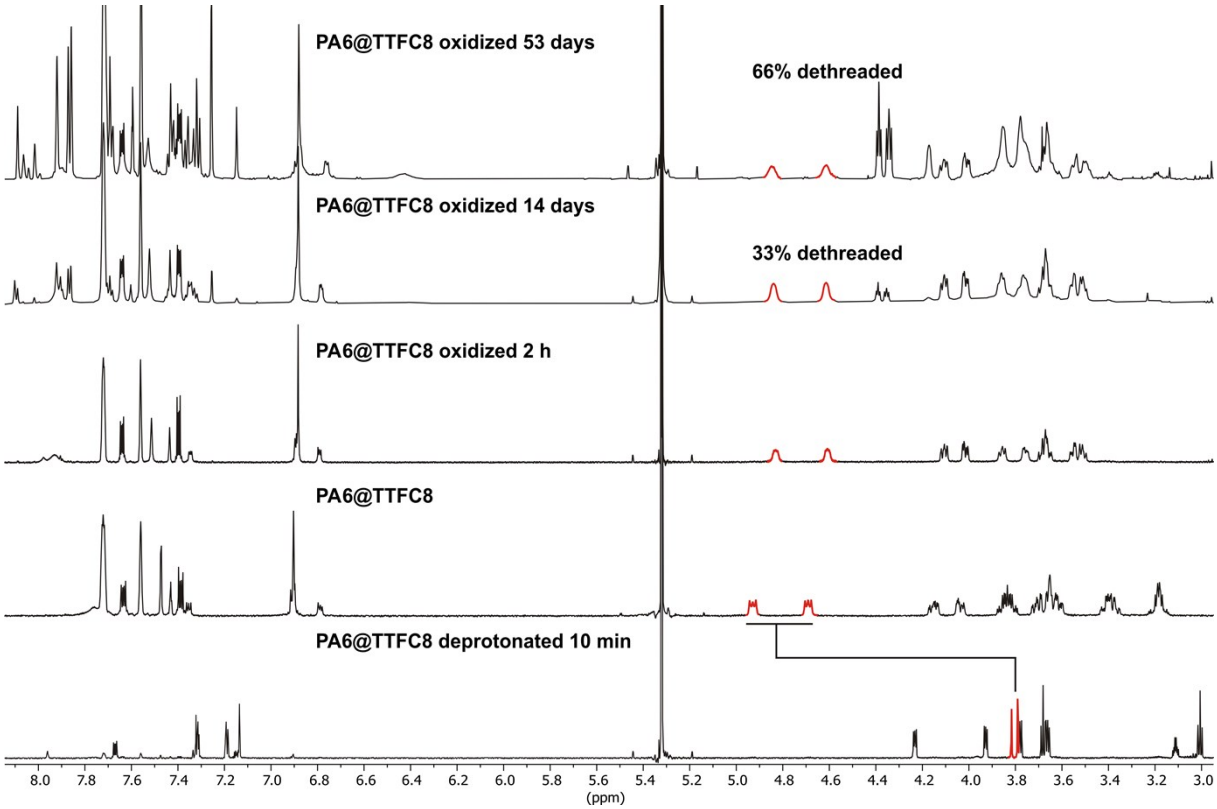

Fig. S34 Partial ^{1}H NMR spectra (700 MHz, CD_2Cl_2, 298 K) of **PA6@TTFC8** (center) after oxidation with $NO^{\cdot+}SbF_6^-$ (top) and after deprotonation with P2 base (bottom). The highlighted peaks in red correspond to the methylene protons next to the nitrogen.

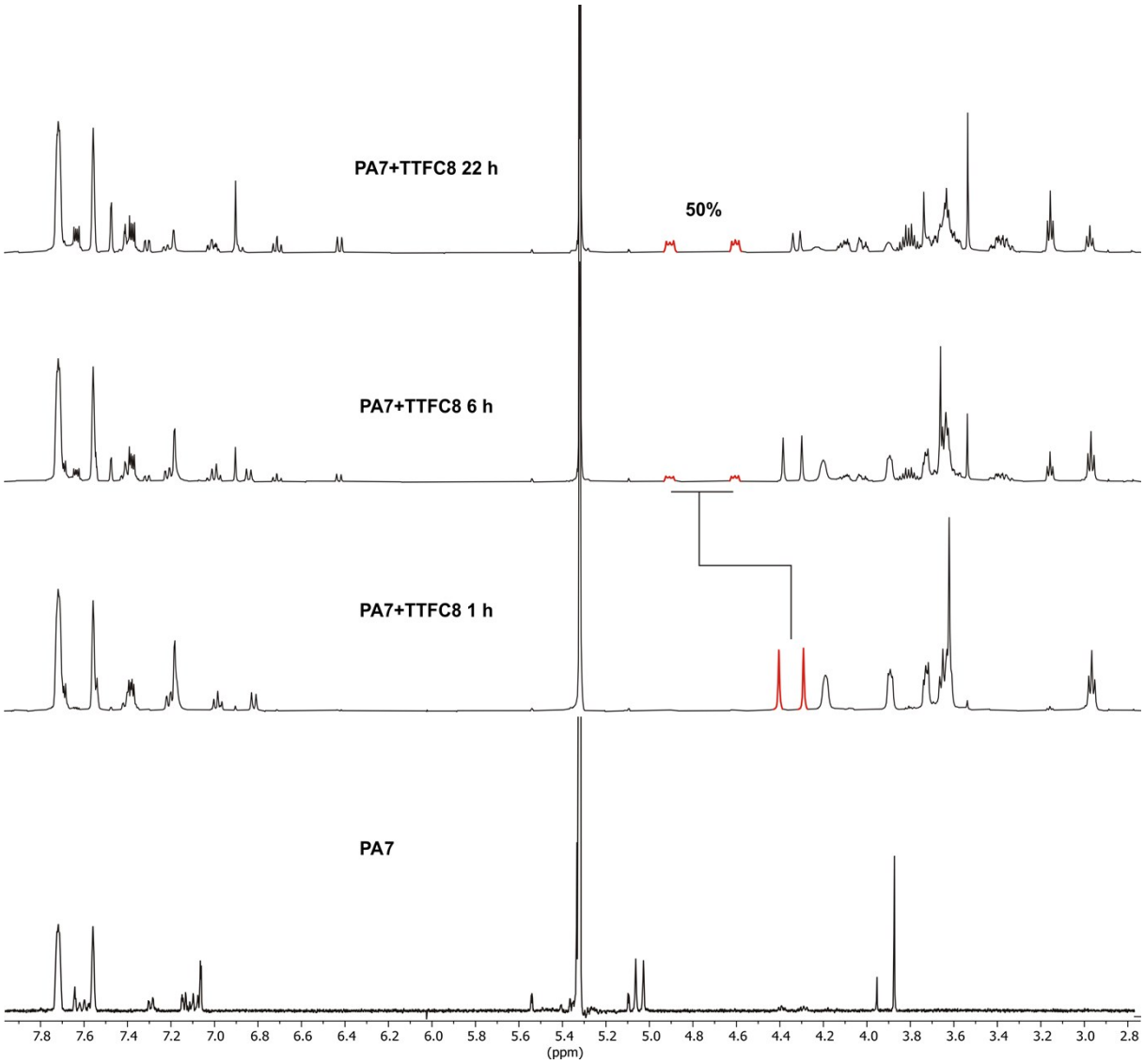

Fig. S35 Partial ^{1}H NMR (400 MHz, CD_2Cl_2, 298 K) spectra of **PA7** before (bottom) and after addition of **TTFC8** (top), the emerging peaks (red) correspond to the threaded complex.

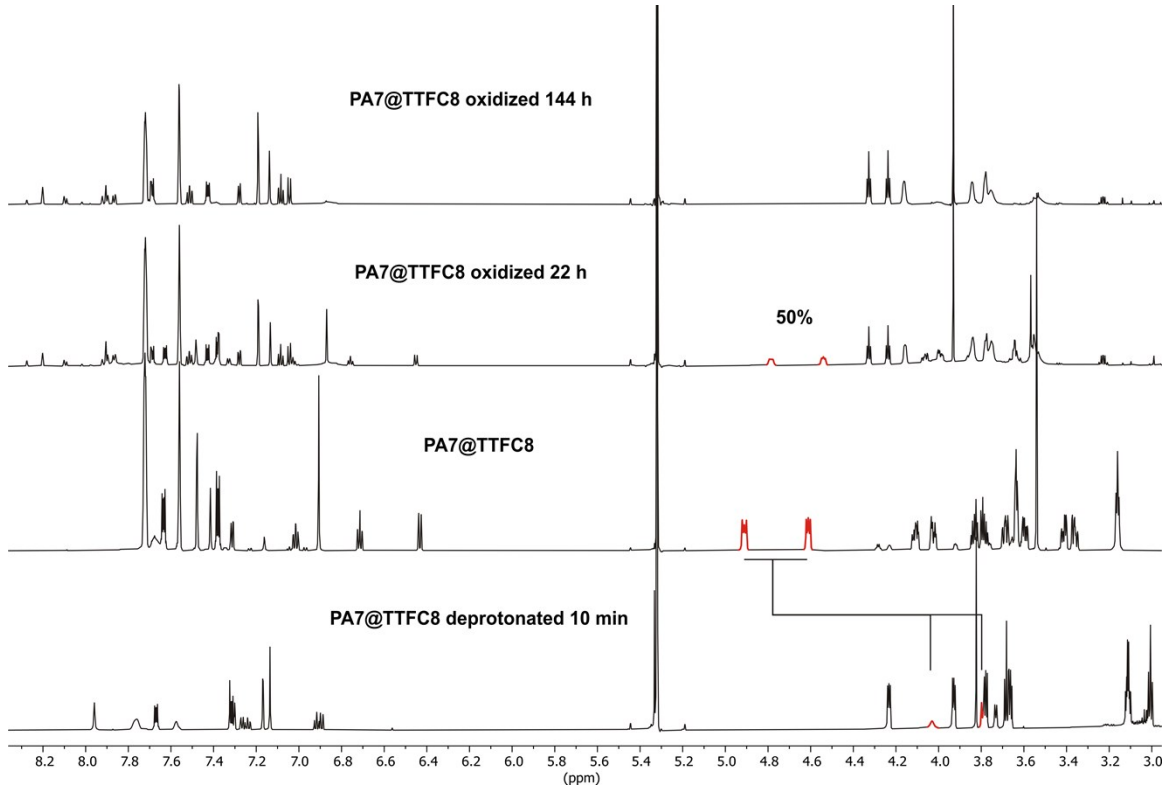

Fig. S36 Partial ^{1}H NMR spectra (700 MHz, CD_2Cl_2, 298 K) of **PA7@TTFC8** (center) after oxidation with $NO^{\cdot+}SbF_6^-$ (top) and after deprotonation with P2 base (bottom). The highlighted peaks in red correspond to the methylene protons next to the nitrogen.

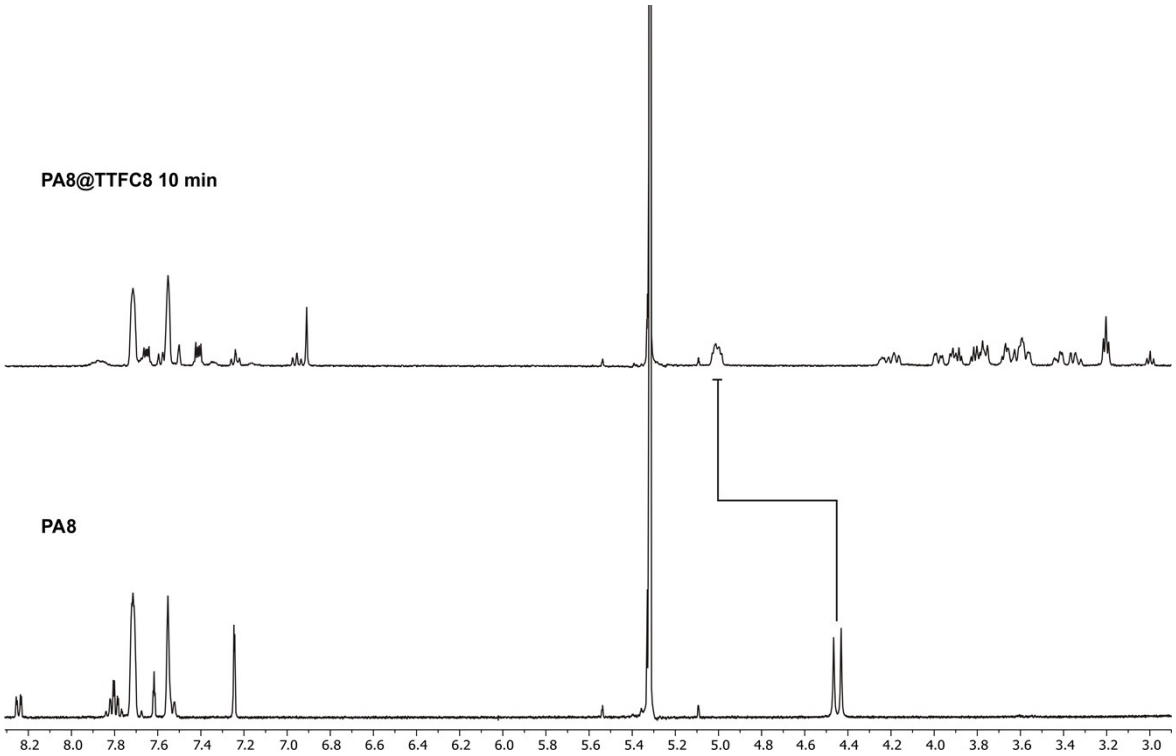

Fig. S37 Partial ^{1}H NMR spectra (400 MHz, CD_2Cl_2, 298 K) of **PA8** before (bottom) and after addition of **TTFC8** (top), the highlighted peaks correspond to the threaded complex.

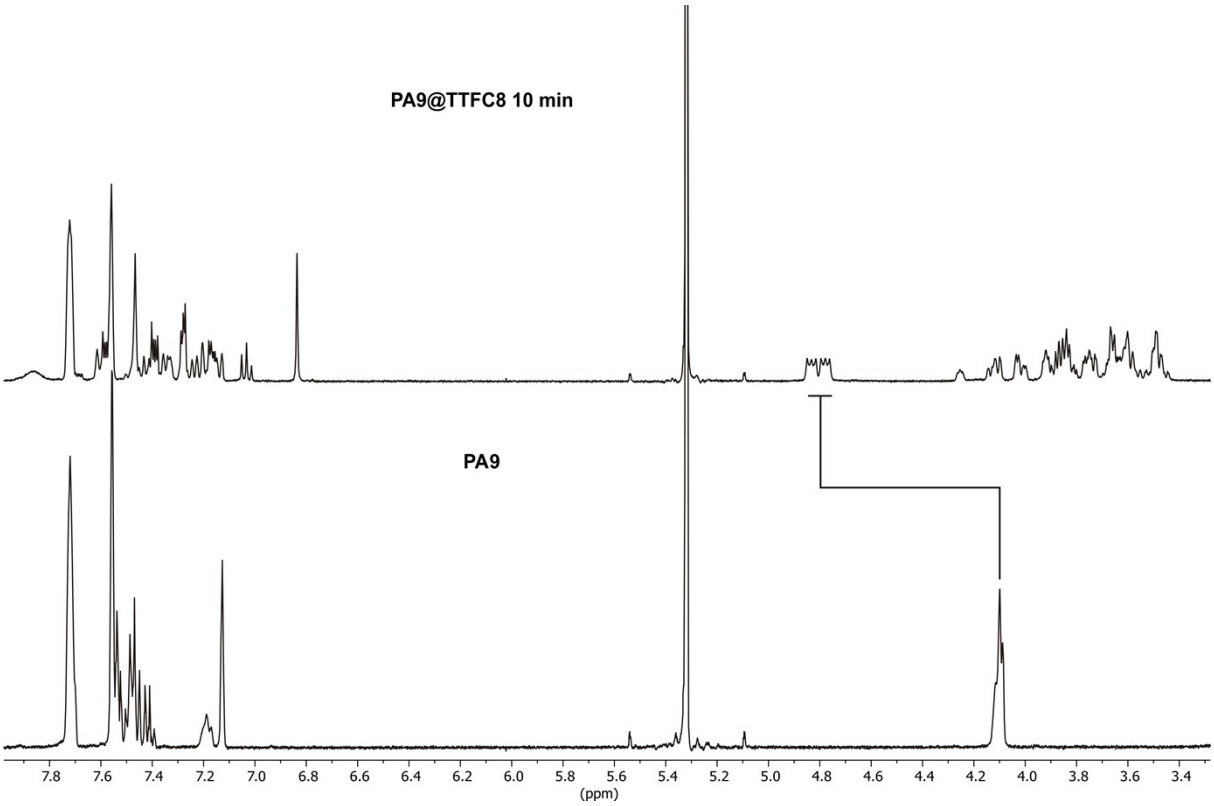

Fig. S38 Partial ^{1}H NMR spectra (400 MHz, CD_2Cl_2, 298 K) of **PA9** before (bottom) and after addition of **TTFC8** (top), the highlighted peaks correspond to the threaded complex.

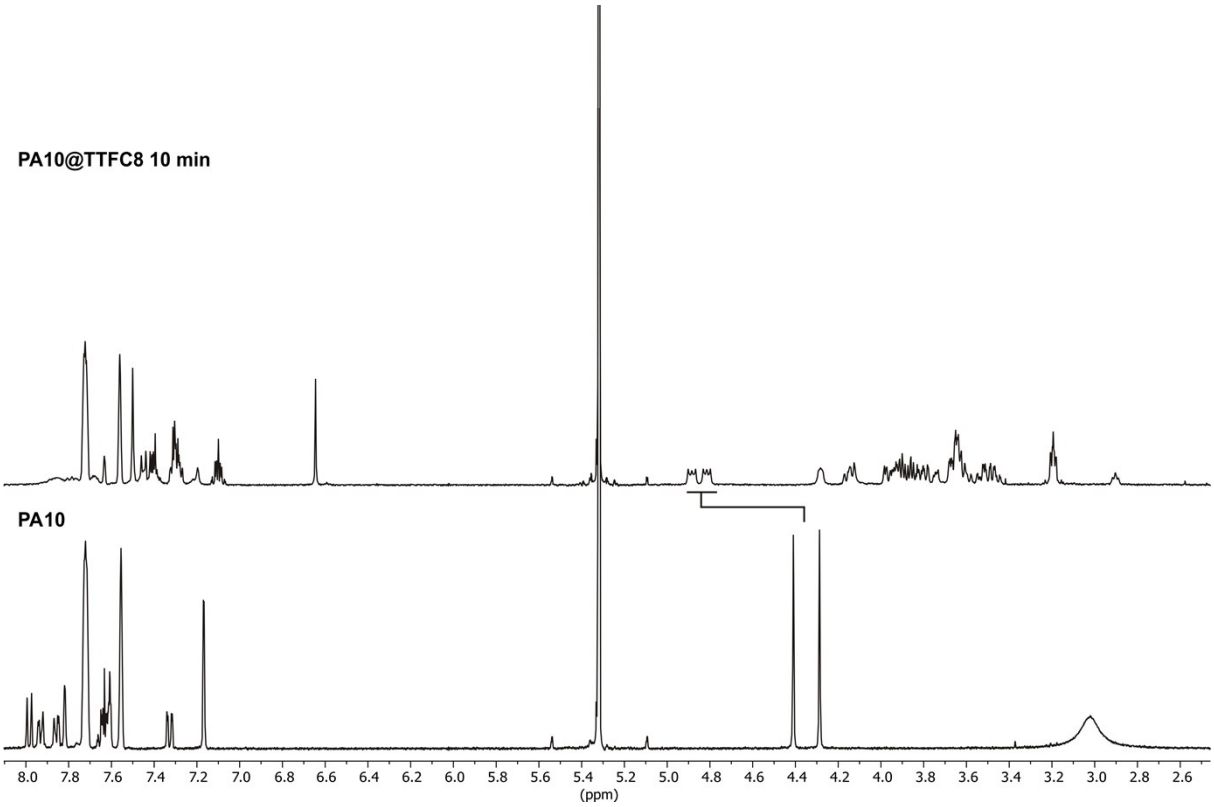

Fig. S39 Partial ^{1}H NMR spectra (400 MHz, CD_2Cl_2, 298 K) of **PA10** before (bottom) and after addition of **TTFC8** (top), the highlighted peaks correspond to the threaded complex

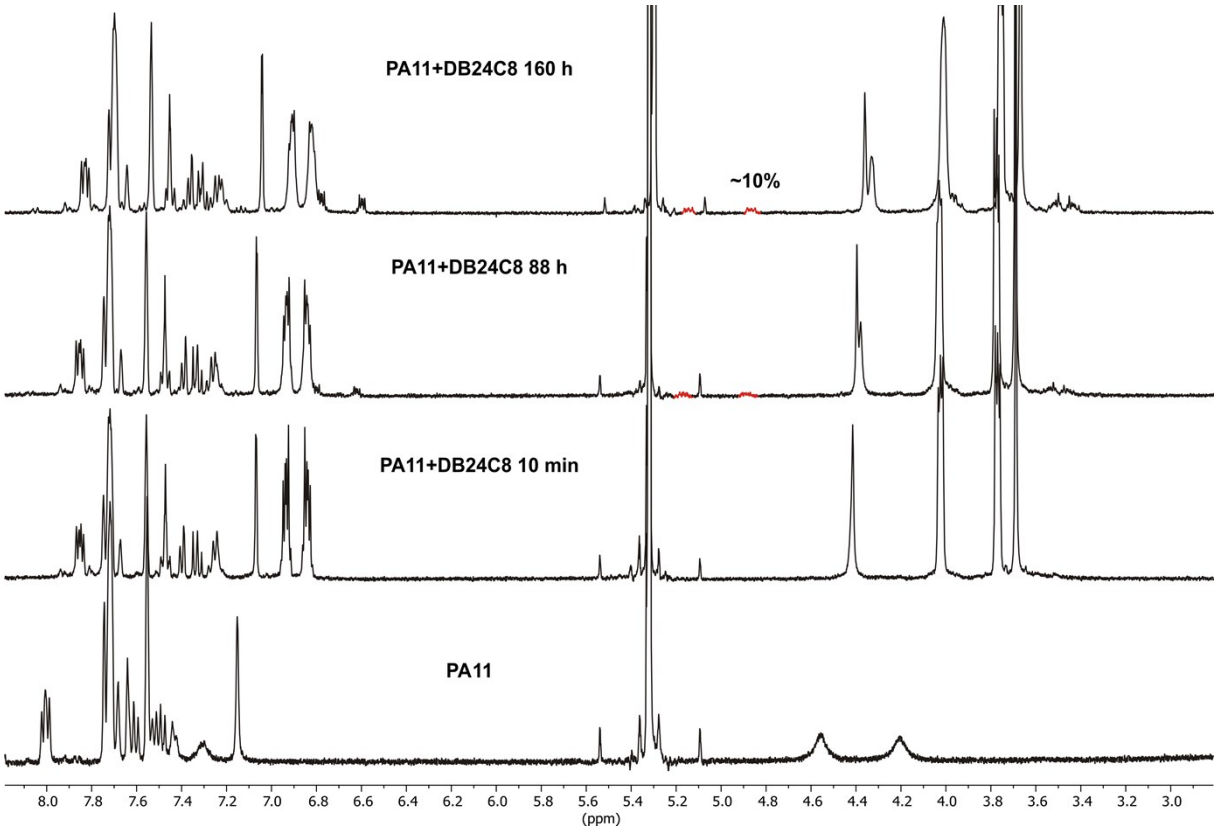

Fig. S40 Partial ^{1}H NMR spectra (400 MHz, CD_2Cl_2, 298 K) of **PA11** before (bottom) and after addition of **DB24C8** (top), the highlighted peaks correspond to the threaded complex.

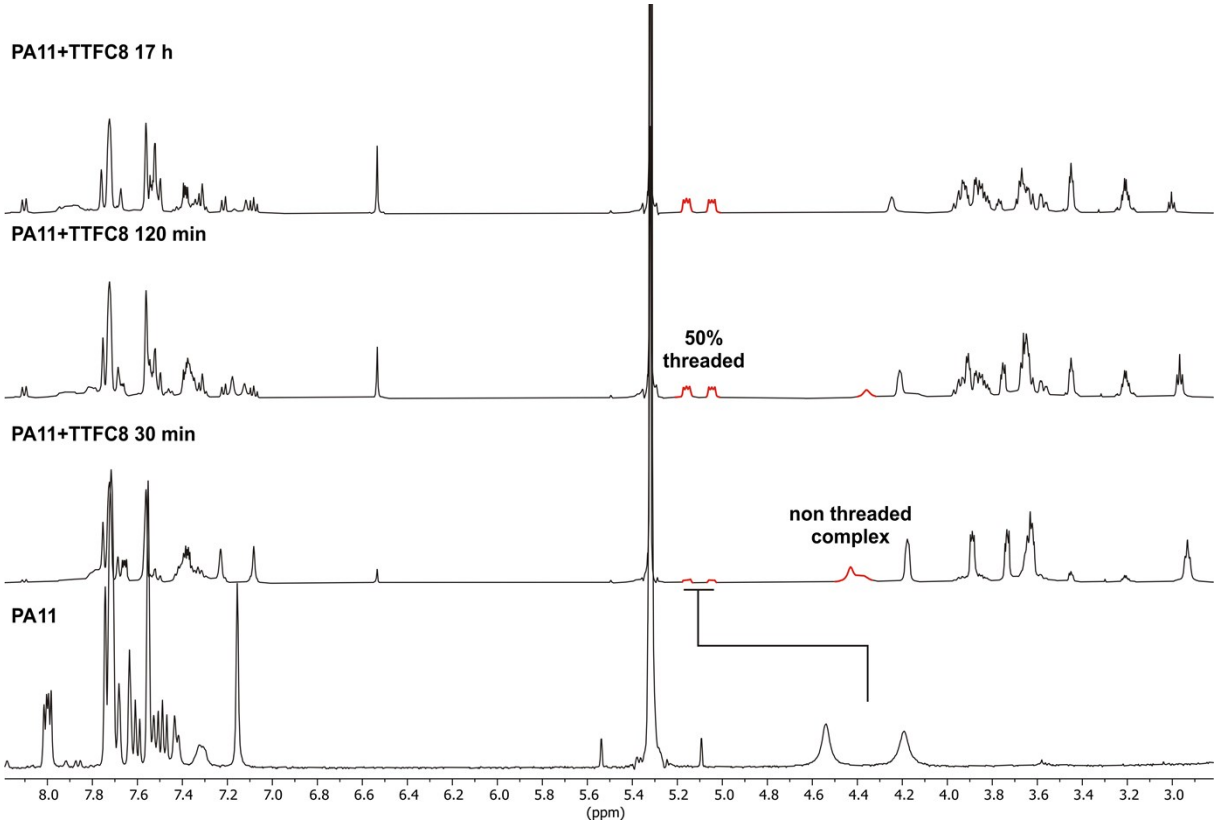

Fig. S41 Partial ^{1}H NMR spectra (500 MHz, CD_2Cl_2, 298 K) of **PA11** before (bottom) and after addition of **TTFC8** (top), the highlighted peaks correspond to the threaded complex.

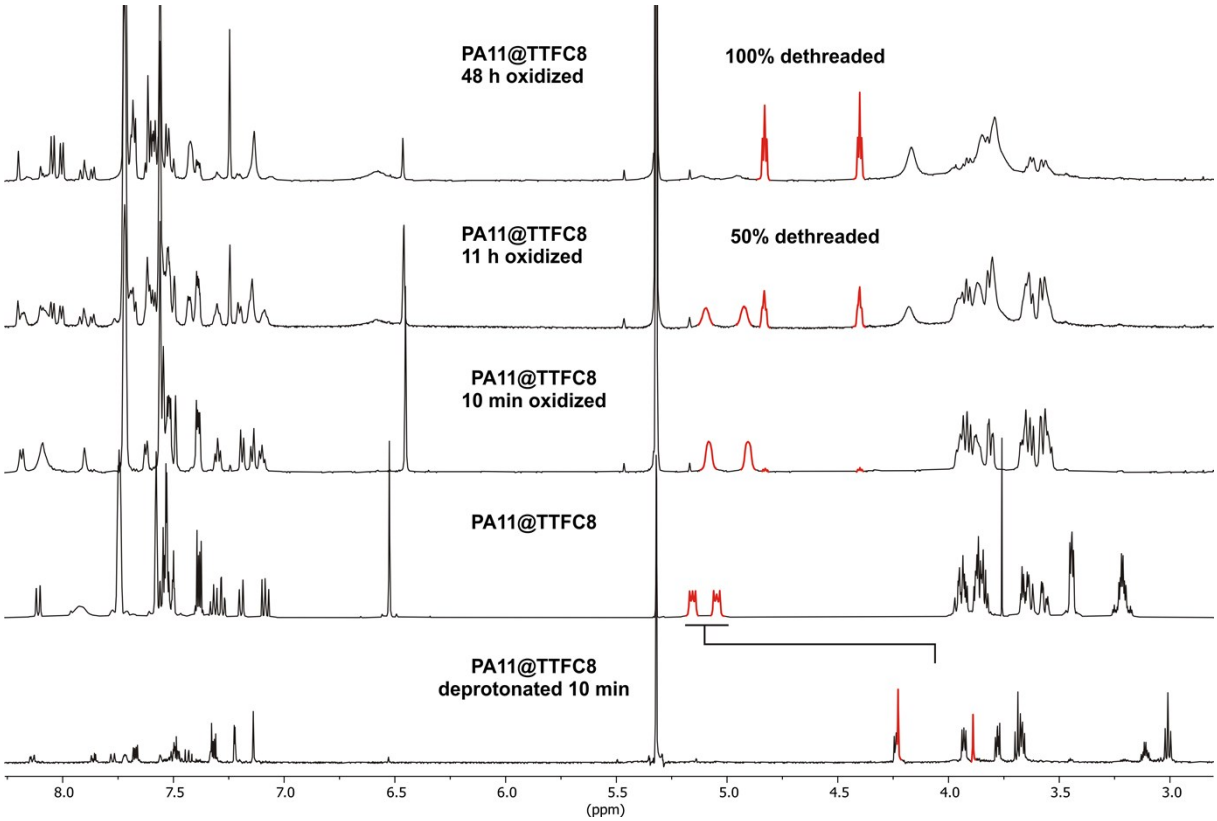

Fig. S42 ^{1}H NMR spectra (600 MHz, CD_2Cl_2, 298 K) of **PA11@TTFC8** (center) after oxidation with $NO^{\cdot+}SbF_6^-$ (top) and after deprotonation with P2 base (bottom). The highlighted peaks in red correspond to the methylene protons next to the nitrogen.

Tab. S1: Dethreading timescales in model pseudo[2]rotaxanes **PA*n*@TTFC8**: $t_{1/2}$, obtained via ^{1}H NMR (2 mM in CD_2Cl_2 400/600/700 MHz at r.t.).

	PA5@TTFC8	**PA6@TTFC8**	**PA7@TTFC8**	**PA11@TTFC8**
deprotonation (P2 base)	< 10 min	< 10 min	< 10 min	< 10 min
oxidation ($NO^{\cdot+}SbF_6^-$)	184 h	> 335 h	22 h	11 h

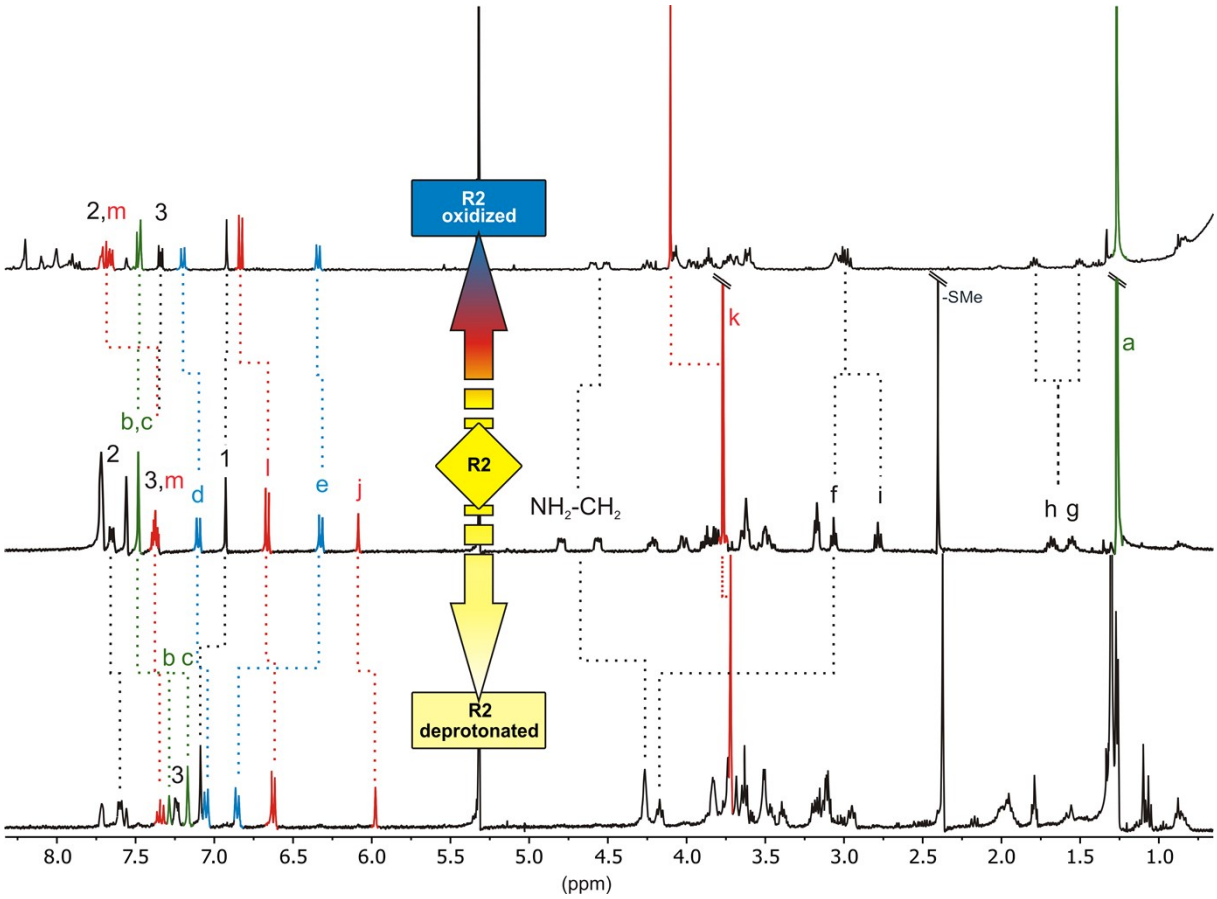

Fig. S43 ^{1}H NMR spectra (400 MHz, CD_2Cl_2, 298 K) with selected shifts highlighted of **R2** (center) 10 min after oxidation with $NO^{\cdot+}SbF_6^-$ (top) and 10 min after deprotonation with polystyrene-immobilized P2 base (bottom).

3. Tandem mass spectrometry

A Synapt G2-S HDMS (Waters Co., Milford, MA, USA) instrument with a quadrupole-time-of-flight high resolution mass detector was used to perform electrospray ionization tandem mass spectrometry. Collision-induced dissociation (CID) experiments of mass-selected ions, were performed using the following settings: flow rate 10 µL min^{-1}, capillary voltage 1.5 kV, sample cone voltage 34 V, source offset 54 V, source temperature 100 °C, desolvation temperature 20 °C, nebulizer gas 5 bar, desolvation gas flow 460 L h^{-1}. For CID, N_2 was used as the collision gas. Fragmentation experiments were conducted in the trap cell of the Synapt G2-S HDMS instrument with collision energies of 2 – 72 V. For the column chromatography isolated sample, 4 V steps were used and for the other samples 2 V steps. Data acquisition and processing was carried out using MassLynx™ (version 4.1).

For plotting of the survival yield curves the spectra were centered. For each spectrum at different collision voltages, the intensity of the ion with the selected mass (m/z 1108) was divided by the total ion intensity (only fragments with an intensity above 1% were considered) and then plotted against the collision voltage. Fitting was done by applying a sigmoidal Boltzmann equation using Origin Pro 2020 to obtain the 50%-survival yield voltages of threaded and non-threaded complex.

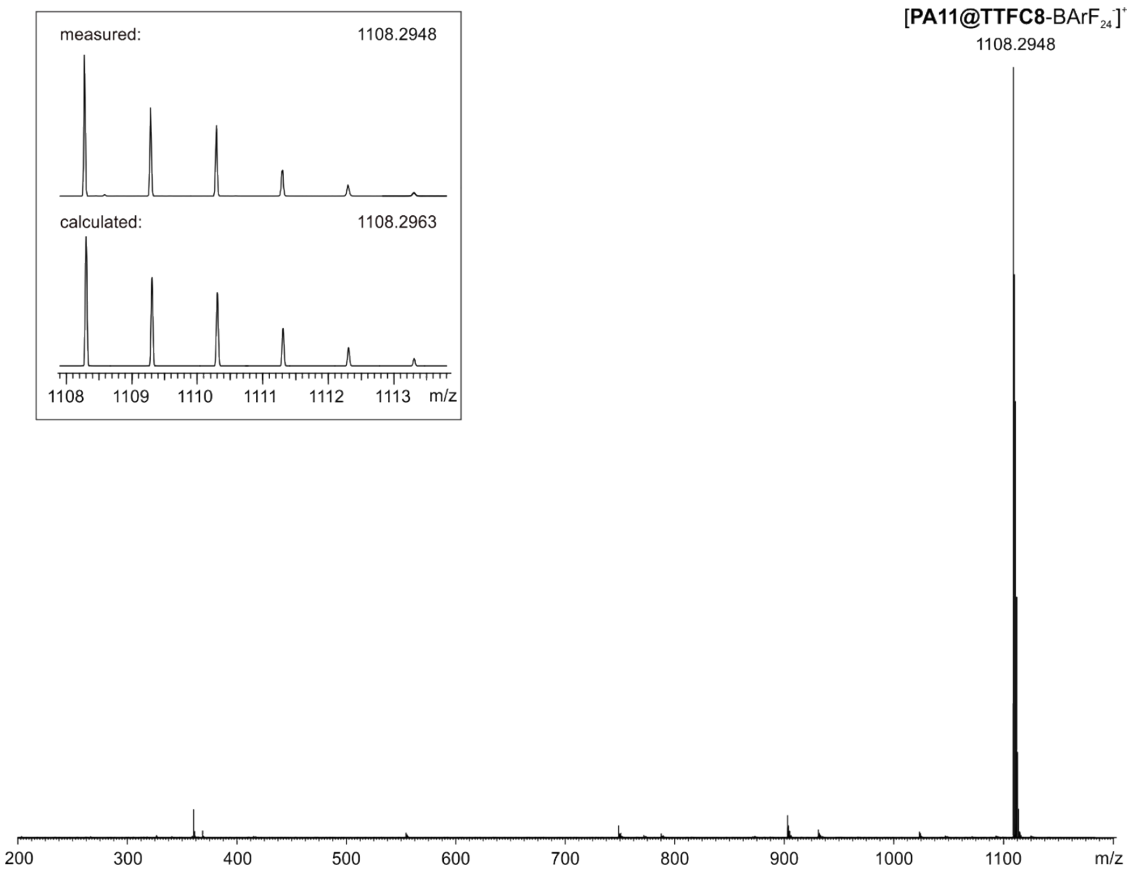

Figure S44 ESI-Q-TOF-HRMS spectrum of **PA11@TTFC8** (5 µM in CH_2Cl_2) isolated after column chromatography; (inset) comparison of measured and calculated isotopic patterns.

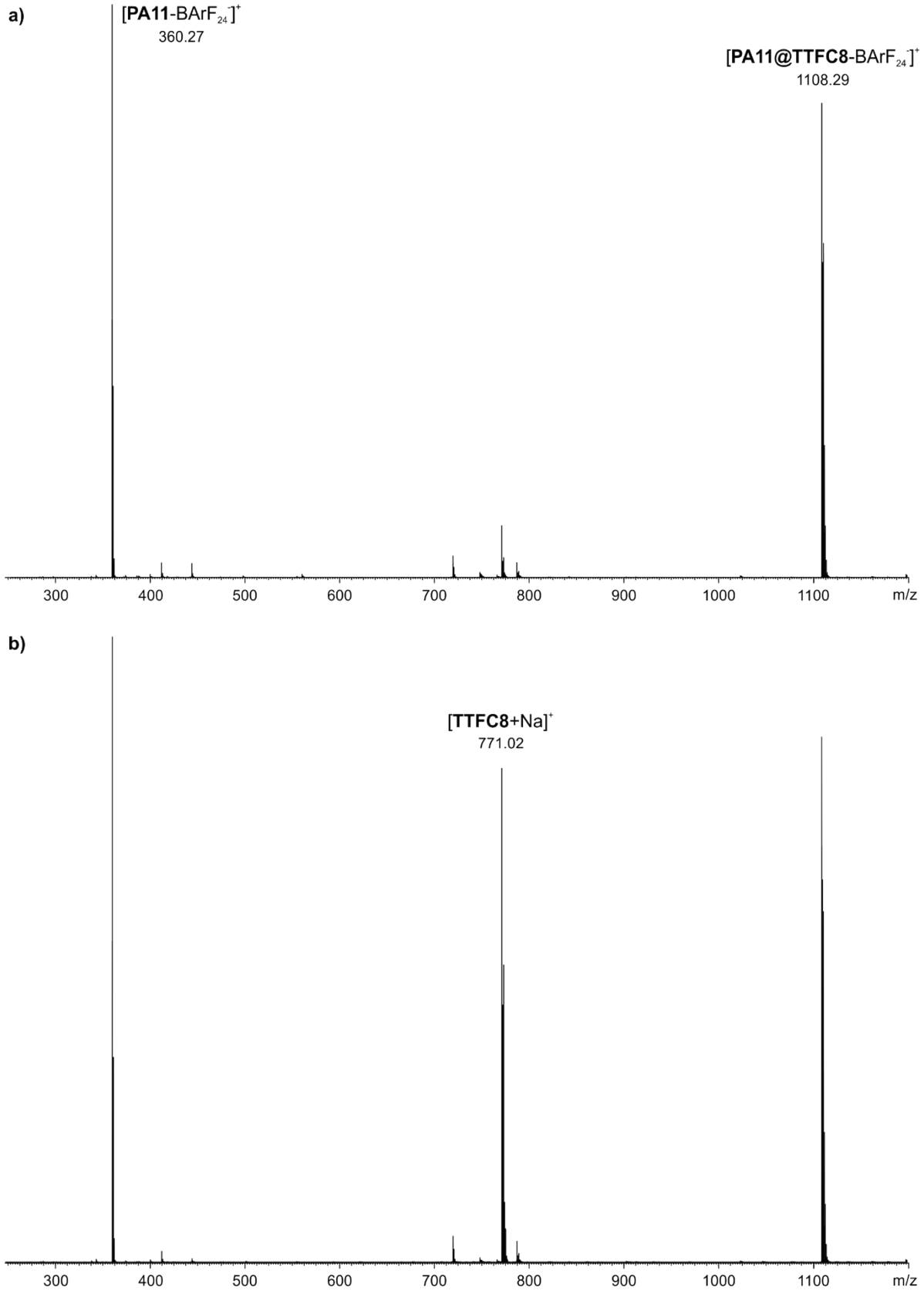

Figure S45 ESI-Q-TOF-HRMS spectrum of a mixture of **PA11** and **TTFC8** (500 µM in CH_2Cl_2), diluted before measuring to 50 µM after 5 min (a) and 135 min (b). Both solutions feature a complex of **TTFC8** and **PA11**, as well as **TTFC8**(+Na) and **PA11** individually. Which indicates that a non-threaded complex is formed within 5 min or during the ionization.

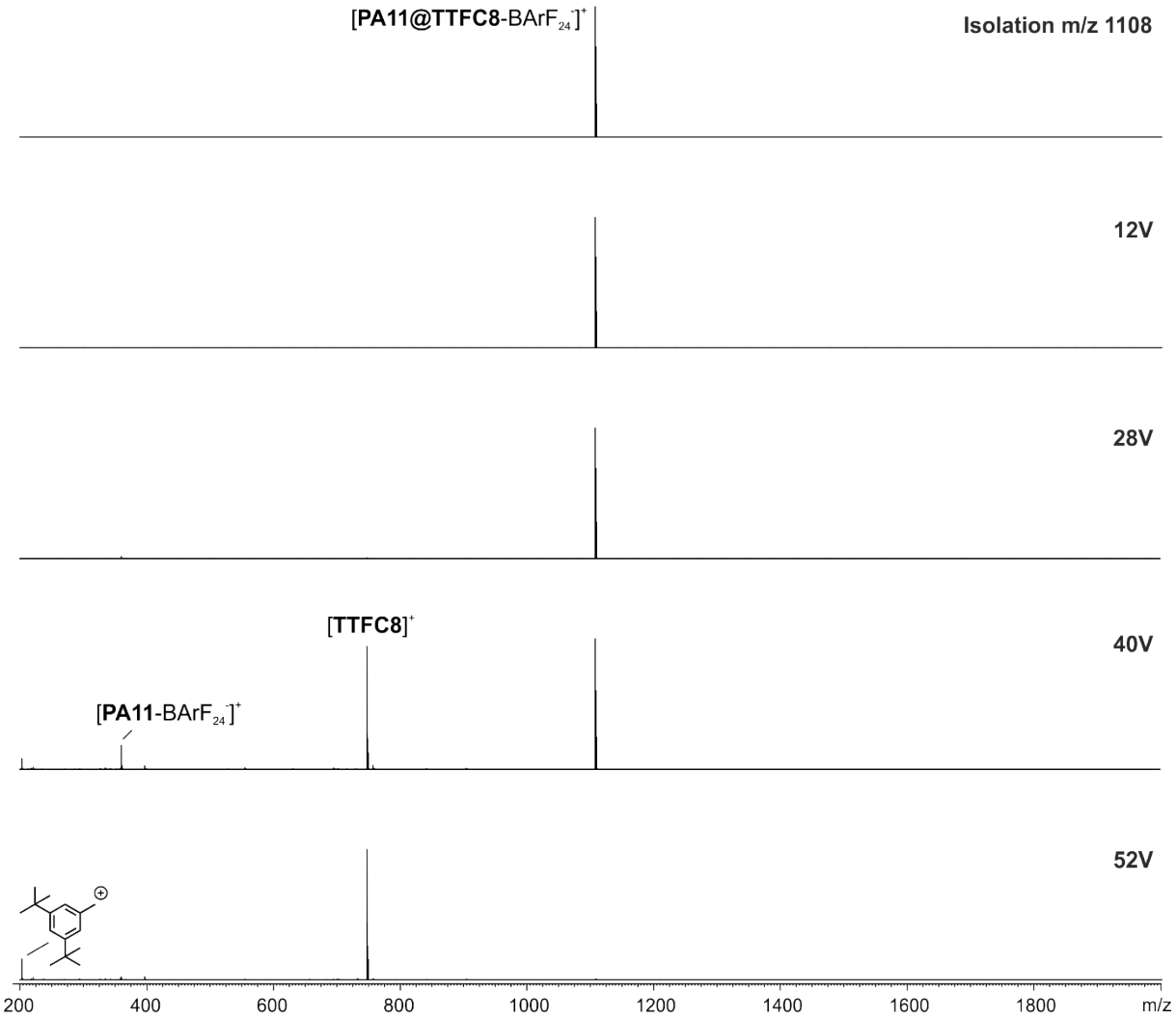

Figure S46 CID experiment with mass-selected ions at *m/z* 1108 obtained from a CH_2Cl_2 solution (50 nM) of **PA11@TTFC8** isolated after column chromatography: (top) after mass-selection; (bottom) after fragmentation at different voltages. Higher voltages are necessary to induce fragmentation and as a major fragment oxidized **TTFC8** is observed. This is diagnostic for a mechanically interlocked structure.[10]

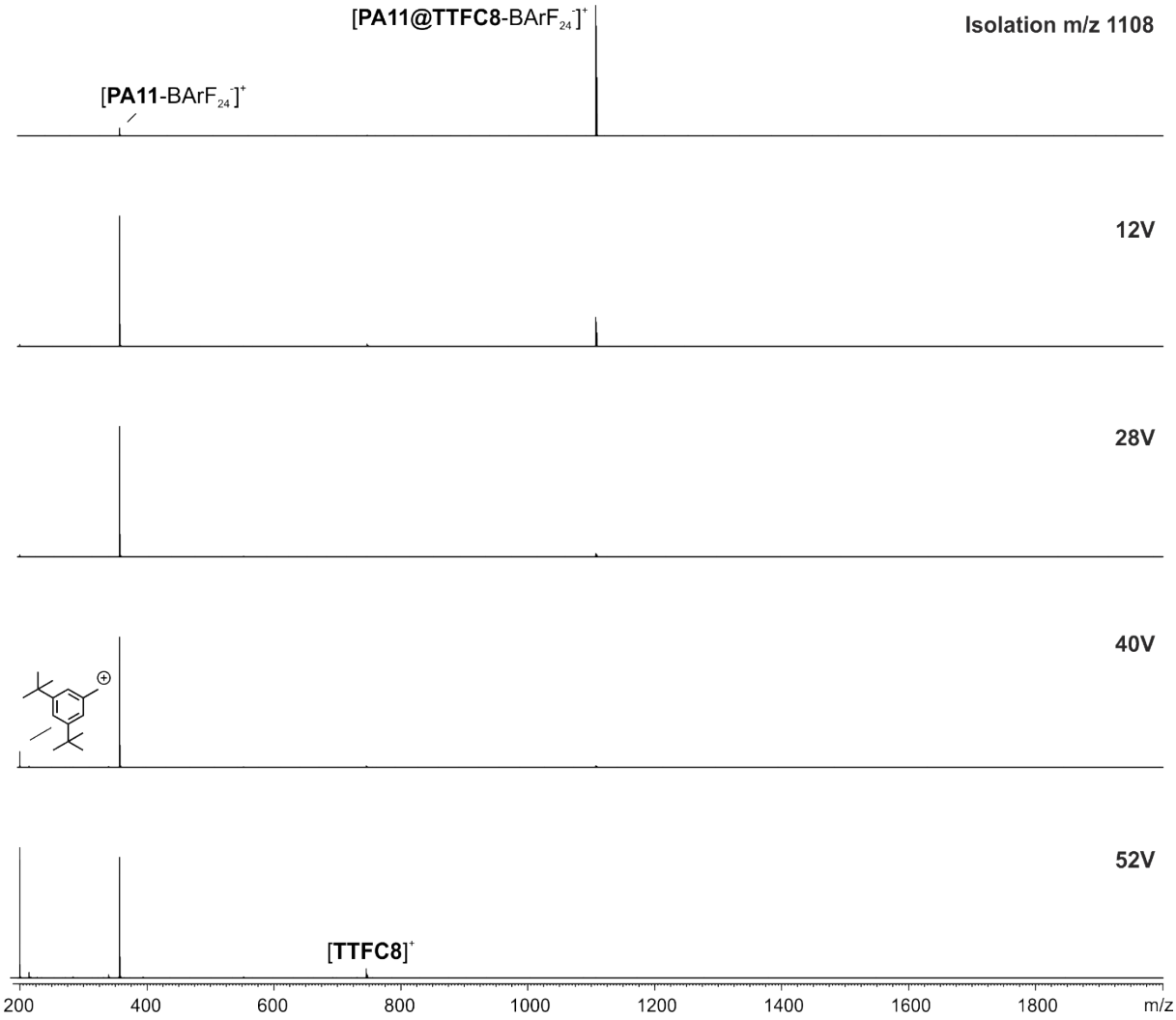

Figure S47 CID experiment with mass-selected ions at *m/z* 1108 obtained from a mixture of **PA11** and **TTFC8** (500 µM in CH_2CCl_2), diluted before measuring to 50 µM after 5 min (top) after mass-selection; (bottom) after fragmentation at different voltages. The complex fragments already appear at low collision voltages, which can be explained by the formation of a non-threaded complex. A minor amount of the complex is still existing at higher voltages (28 and 40 V), which represents the amount of threaded complex.

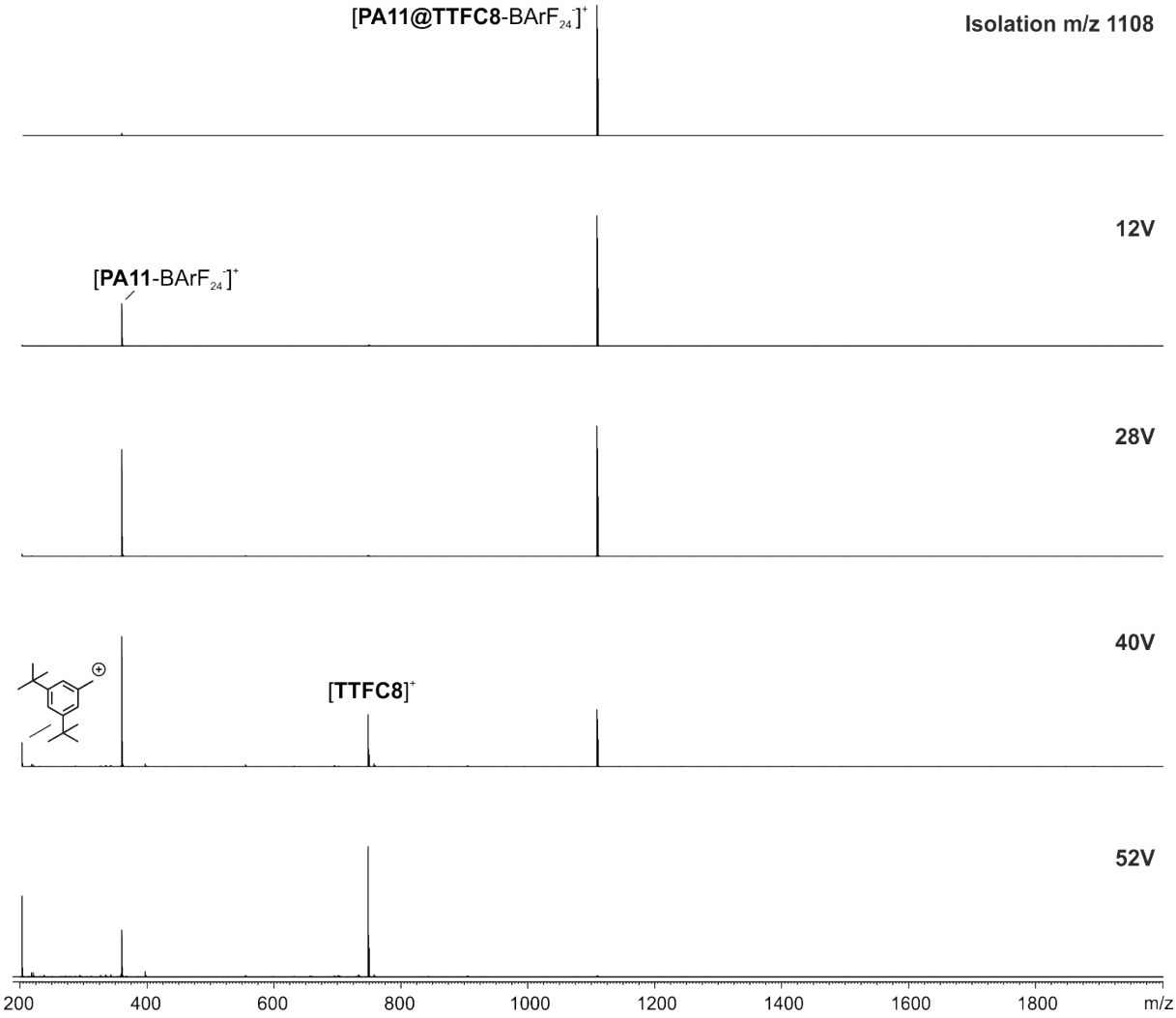

Figure S48 CID experiment with mass-selected ions at *m/z* 1108 obtained from a mixture of **PA11** and **TTFC8** (500 µM in CH_2Cl_2), diluted before measuring to 50 µM after 135 min (top) after mass-selection; (bottom) after fragmentation at different voltages. A fraction of the complex fragments appear already at low collision voltages, which can be explained by the formation of a non-threaded complex. A bigger amount of the complex is still existing at higher voltages (28 and 40 V), which represents the amount of threaded complex.

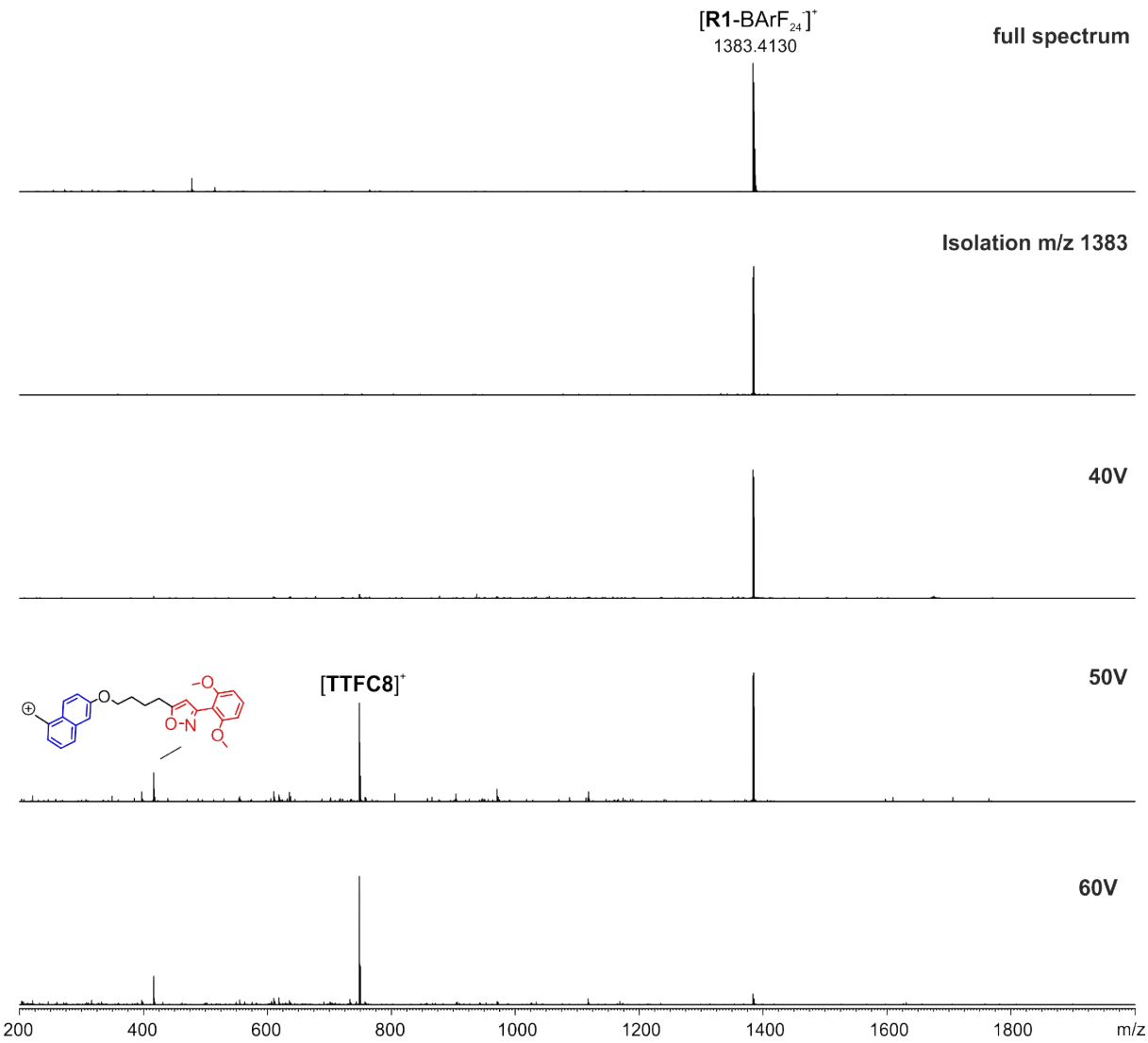

Figure S49 ESI-Q-TOF-HRMS spectrum (top) and CID experiment with mass-selected ions at *m/z* 1383 obtained from solution of **R1** (5 µM in acetonitrile). Higher voltages are necessary to induce fragmentation of **R1** and as major fragments oxidized **TTFC8** and axle fragments are observed. The free axle (m/z 635) is not observed as a fragment. This is diagnostic for a mechanically interlocked structure.[10]

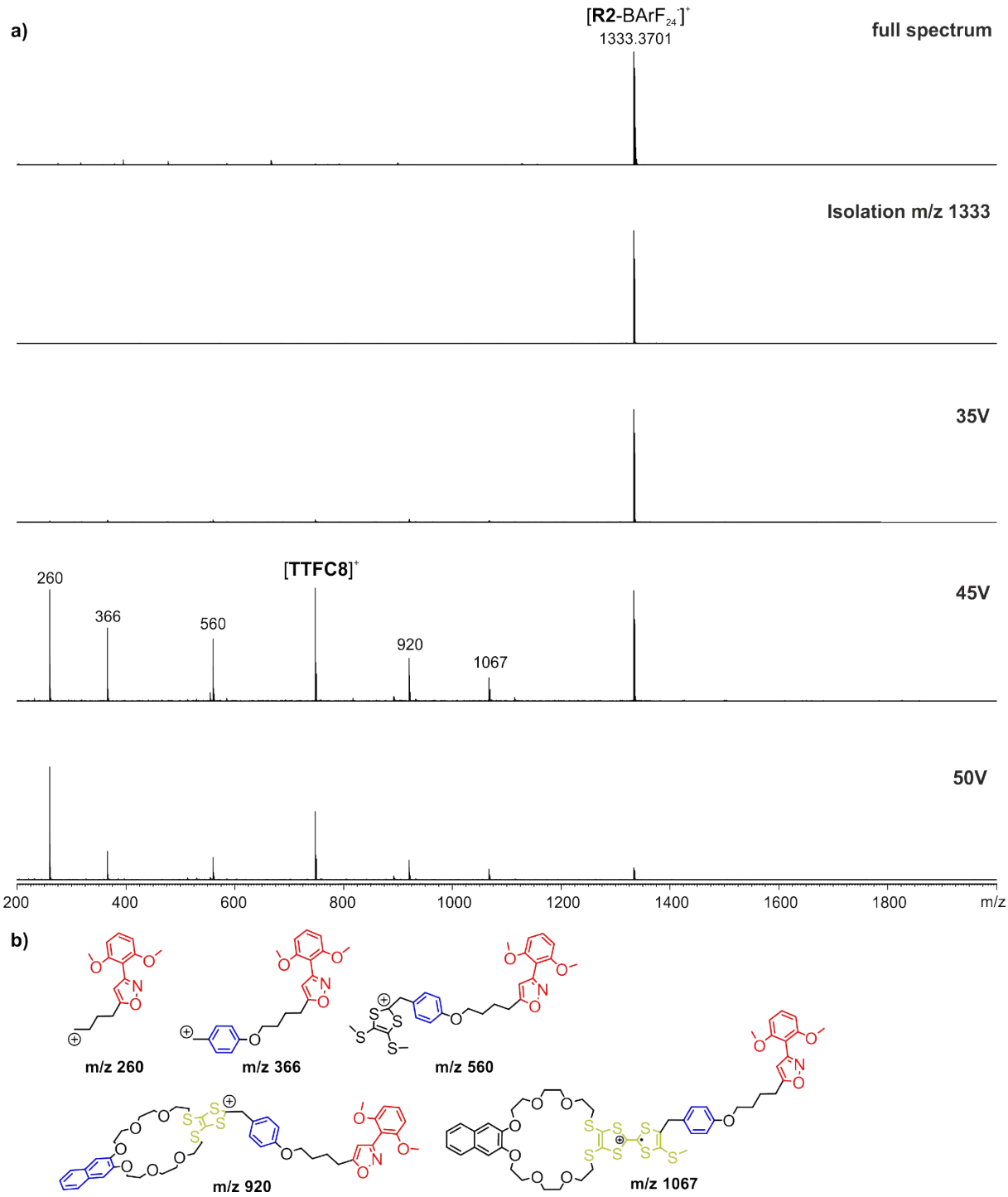

Figure S50 (a) ESI-Q-TOF-HRMS spectrum (top) and CID experiment with mass-selected ions at *m/z* 1333 obtained from solution of **R2** (5 µM in acetonitrile). Higher voltages are necessary to induce fragmentation of **R2** and as major fragments oxidized **TTFC8** and axle fragments are observed. The free axle (m/z 635) is not observed as a fragment. This is diagnostic for a mechanically interlocked structure. (b) Proposed structures for m/z values occurring in the fragmentation spectra. Similar fragments have been observed for other TTF crown/ammonium rotaxane.[10]

4. Variable-temperature ^{1}H NMR spectroscopy

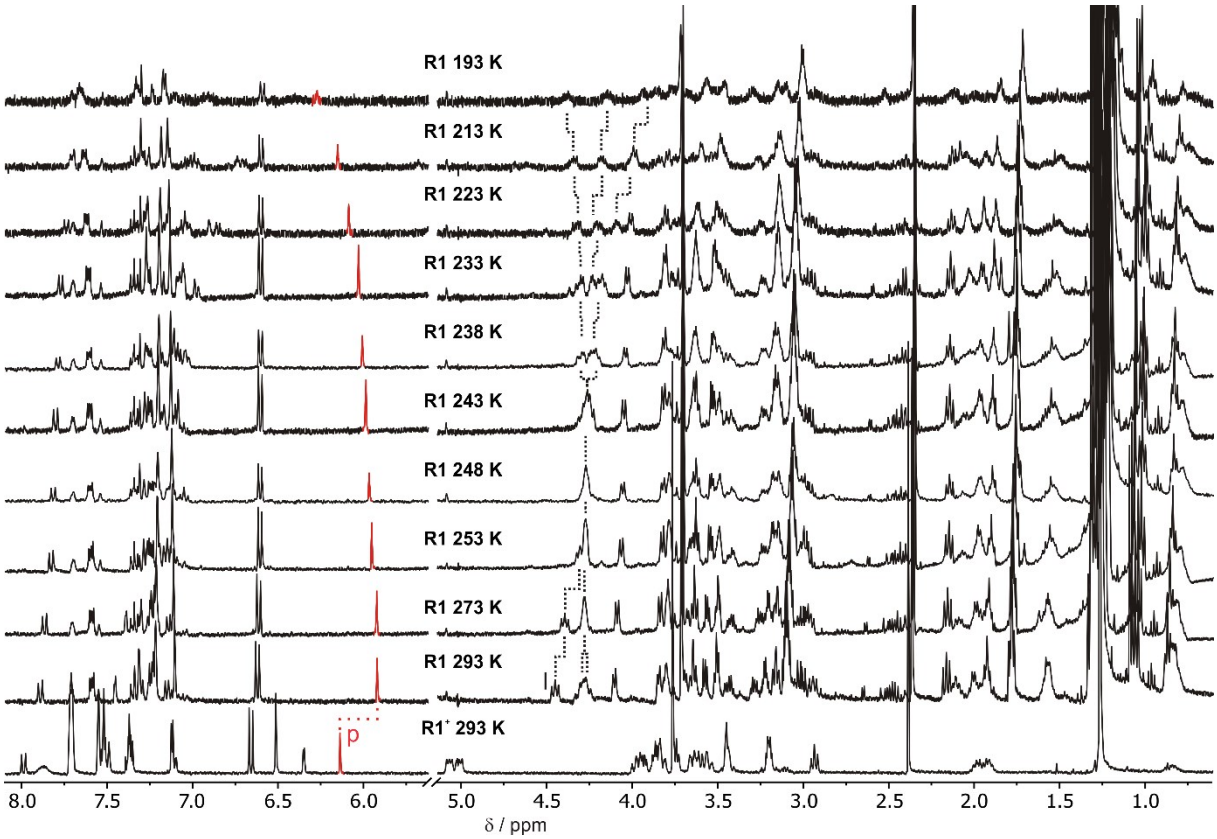

Fig. S51 VT ^{1}H NMR spectra (400 MHz, CD_2Cl_2) of [2]rotaxane **R1** before (bottom) and after deprotonation with P2 base (gradual cooling from 293 to 193 K), showing the shift of H_p (isoxazol).

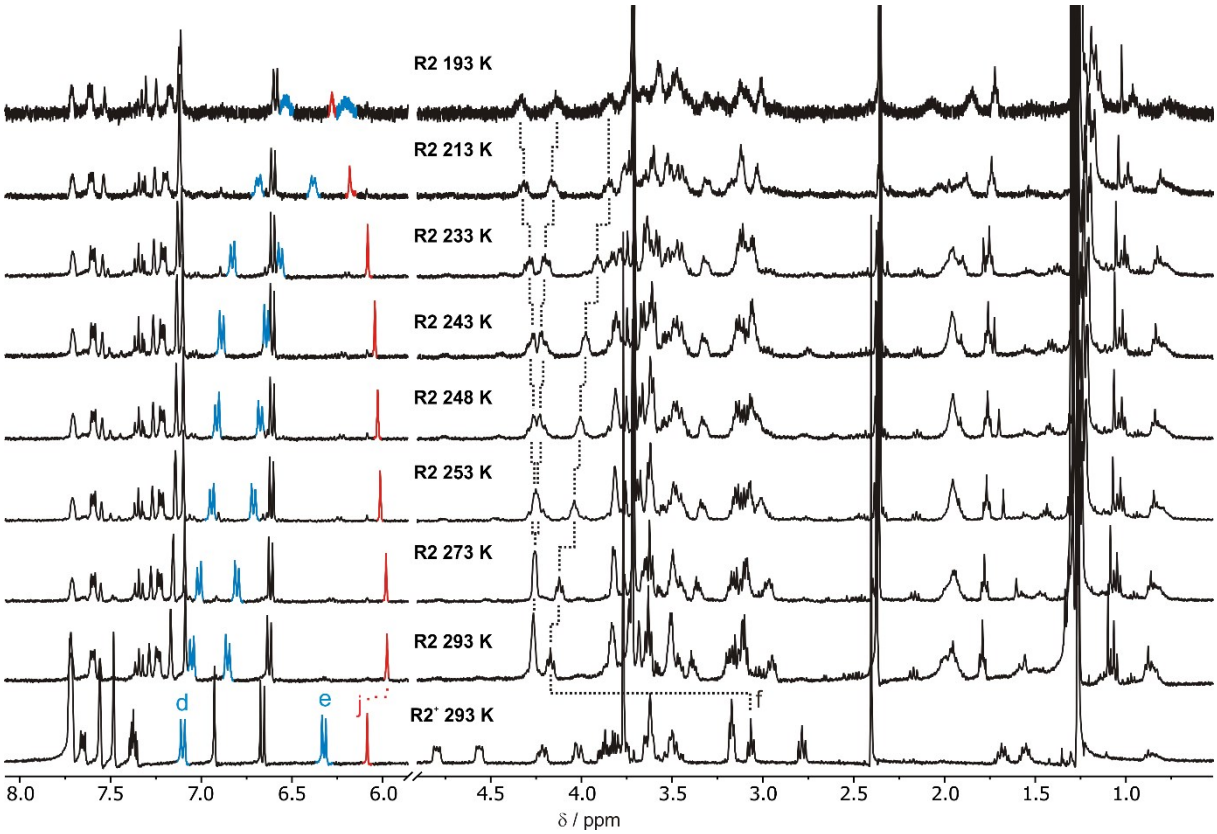

Fig. S52 VT ^{1}H NMR spectra (400 MHz, CD_2Cl_2) of [2]rotaxane **R2** before (bottom) and after deprotonation with P1 base (gradual cooling from 293 to 193 K), showing the shift of H_j (isoxazol), $H_{d,e}$ (phenyl).

5. Isothermal titration calorimetry

ITC experiments were carried out in dry 1,2-dichloroethane at 298 K on a TAM III microcalorimeter (Waters GmbH, TA Instruments, Eschborn, Germany). In a typical experiment, an 800 µL solution of crown ether was placed in the sample cell at a concentration of 1.1 mM, and 250 µL of a solution of the ammonium salt (7.0 mM) were put into the syringe. The titrations consisted of 32 consecutive injections of 8 µL each with a 20 min interval between injections. Heats of dilution were determined by titration of ammonium salt solutions into the sample cell containing blank solvent and were subtracted from each data set. The heat flow generated in the sample cell is measured as a differential signal between sample and reference cell. Hence, an exothermic event results in a positive and an endothermic in a negative heat flow. The data were analysed using the instrument's internal software package and fitted with a 1:1 binding model. Each titration was conducted three times and the measured values for K and ΔH were averaged.

Tab. S2: Thermodynamic data obtained from the ITC experiments.

	K_a /10^4 M^{-1}	ΔG / kJ mol^{-1}	ΔH / kJ mol^{-1}	$T\Delta S$ / kJ mol^{-1}
PA11@TTFC8	1.0 ± 0.3	-22.9 ± 0.6	-28.6 ± 2.0	-5.7 ± 2.6
PA12@TTFC8	39 ± 7	-31.9 ± 0.4	-44.1 ± 1.2	-12.2 ± 1.6
DBA@TTFC8	77 ± 10	-33.6 ± 0.3	-39.8 ± 1.0	-6.2 ± 1.3

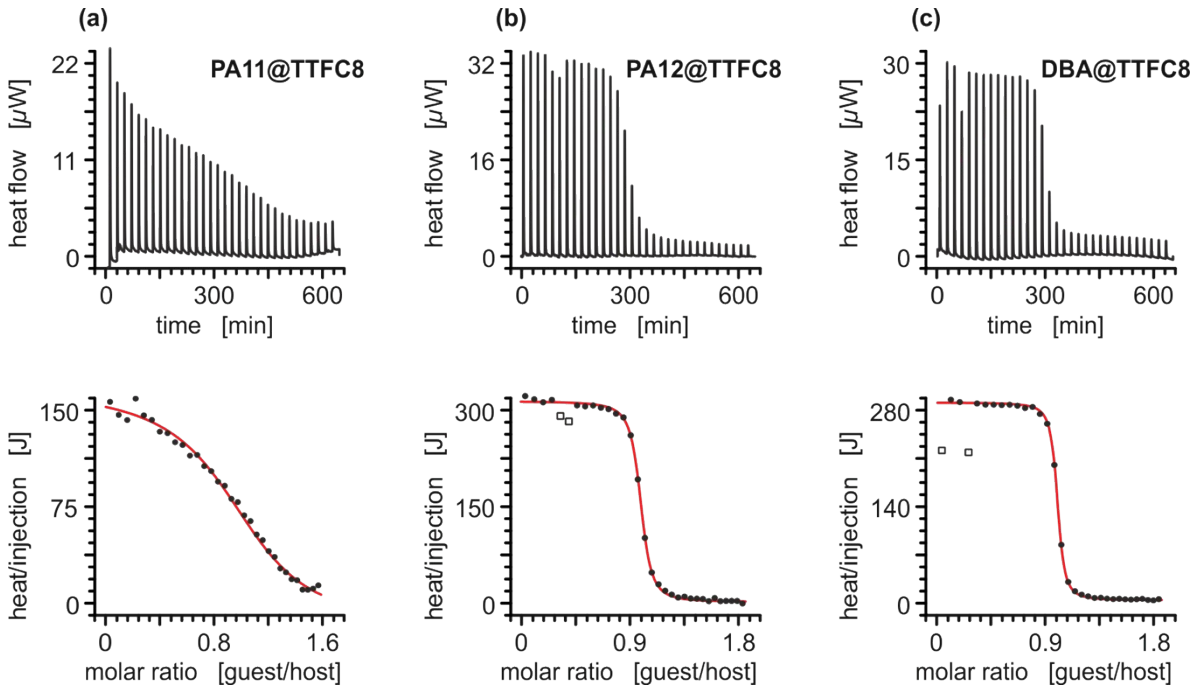

Figure S53. Titration plots (heat flow versus time and heat/volume versus guest/host ratio) obtained from ITC experiments at 298 K in 1,2-dichloroethane**: (a)** vial: **TTFC8**, syringe: axle **PA11**; **(b)** vial: **TTFC8**, syringe: axle **PA12**; **(c)** vial: **TTFC8**, syringe: axle **DBA** (dibenzylammonium $BArF_{24}$). Points marked with non-filled squares were not considered in the fitting process. **PA11@TTFC8** was fitted using a 1:1 binding model. However, for this axle the formation of a threaded complex happens over the course of hours and the formation of a non-threaded complex is observed on a minute timescale. The thermodynamic parameters obtained for this macrocycle/axle combination can therefore be interpreted as a combination of both equilibria (see Figure 3 main text) with the formation of the threaded complex contributing with a less time dependent heat flow. The obtained thermodynamic parameters can therefore be used as an upper limit for the values of K and ΔH of the non-threaded complex.

6. Electrochemical measurements

Redox-potentials reported in this study were obtained by DPV. All measurements were at least conducted twice. Measurements were conducted in CH_2Cl_2 with 0.1 M electrolyte and 2 mM analyte concentration.

Tab. S3 Electrochemical data obtained from DPV measurements (CH_2Cl_2, with n-Bu_4NBArF_{24} as the electrolyte, 298 K).

species	$E^1_{1/2}$ / mV	$E'_{1/2}$ / mV	$E^2_{1/2}$ / mV
TTFC8	594	/	987
PA12@TTFC8	599	987	1294
PA11@TTFC8	695	/	1385
R1	695	/	1380
R2	694	/	1349

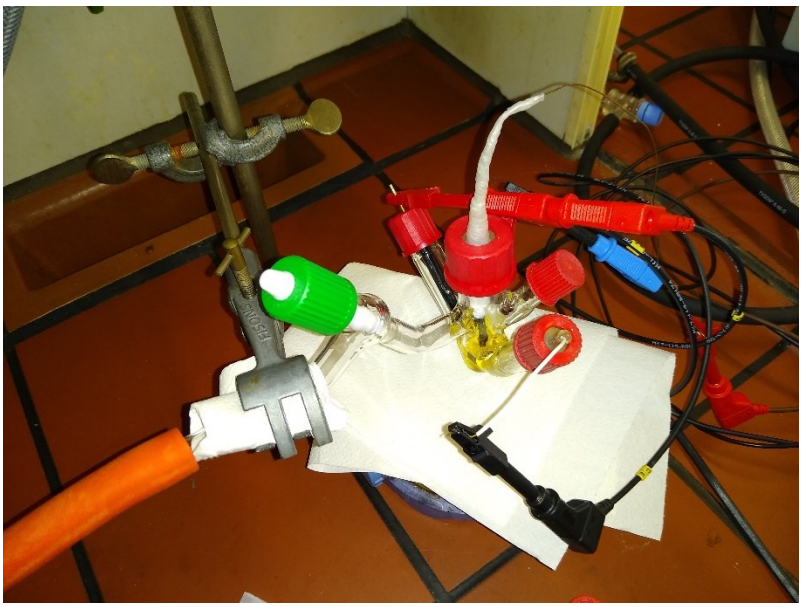

Fig. S54: General set-up for bulk electrolysis experiments.

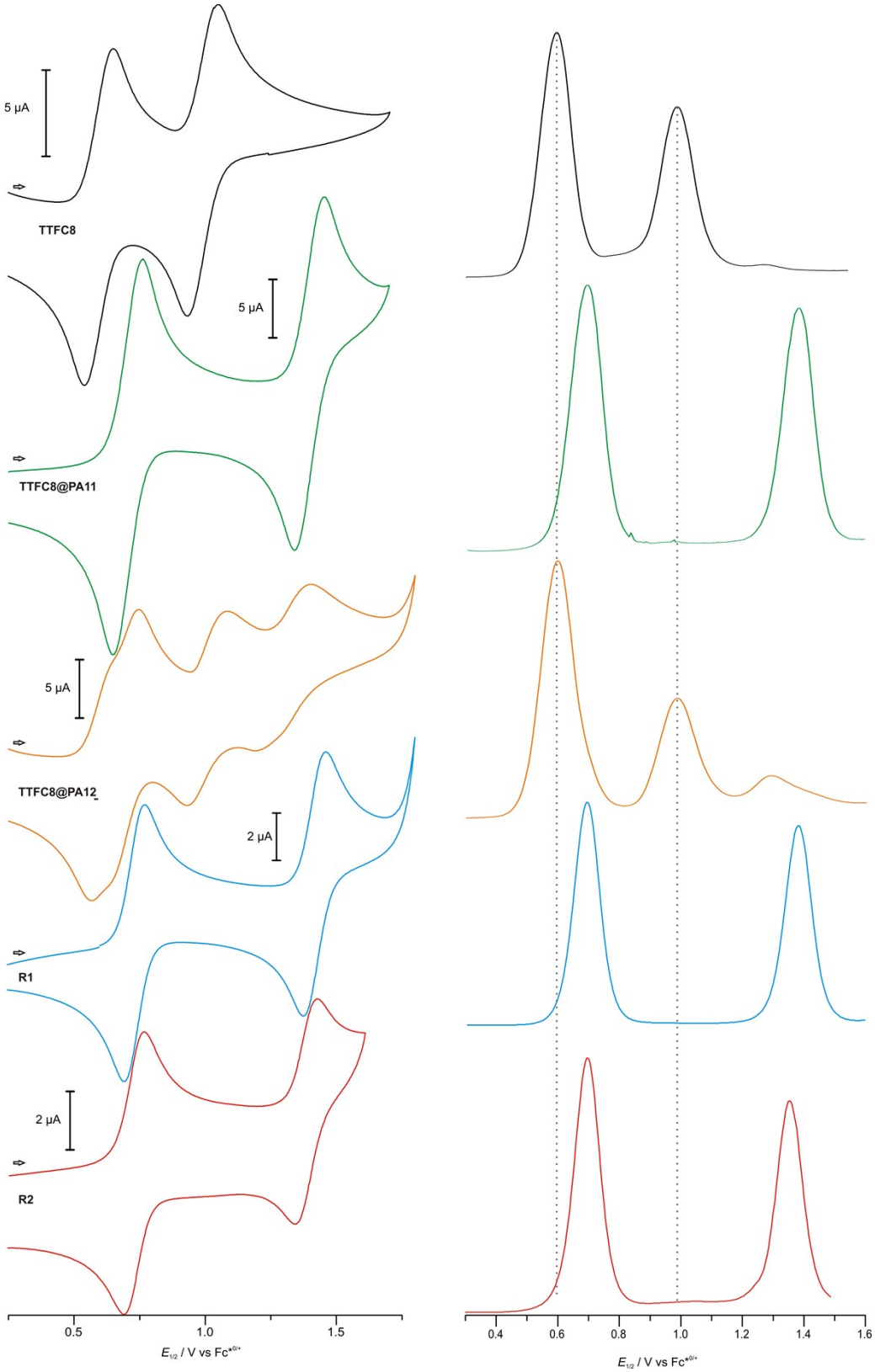

Fig. S55 Stacked cyclic voltammograms (100 mV/s scan rate) with corresponding differential pulse voltammograms (DPV, 10 mV/s scan rate, 25 mV modulation amplitude, 50 ms modulation time, 5 mV step potential, 0.5 s interval time) (CH_2Cl_2, n-Bu_4NBArF_{24}, 298 K) of **TTFC8, PA11@TTFC8, PA12@TTFC8, R1, R2.**

7. UV/Vis experiments

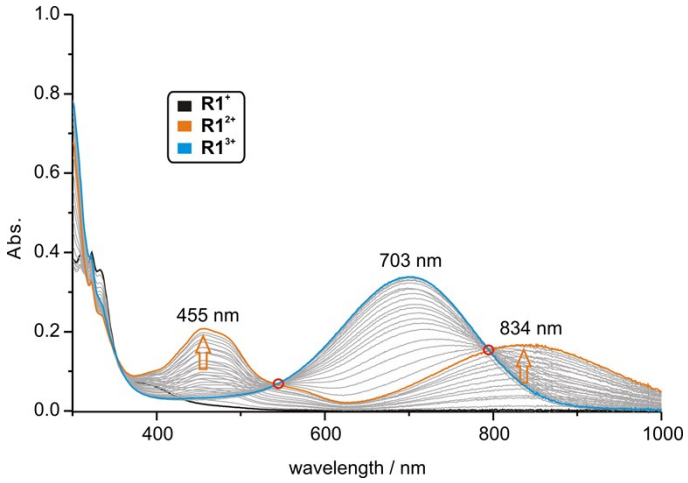

Fig. S56 UV/Vis spectra of **R1** (25 µM in CH_2Cl_2, 298 K, bulk $Fe(ClO_4)_3$ as the oxidant) in the TTF^0 (black), $TTF^{\bullet+}$ (orange) and TTF^{2+} (blue) state. The grey lines correspond to spectra taken in between full conversion to the radical cation or the doubly oxidized species, since the bulk $Fe(ClO_4)_3$ does not dissolve completely in CH_2Cl_2.

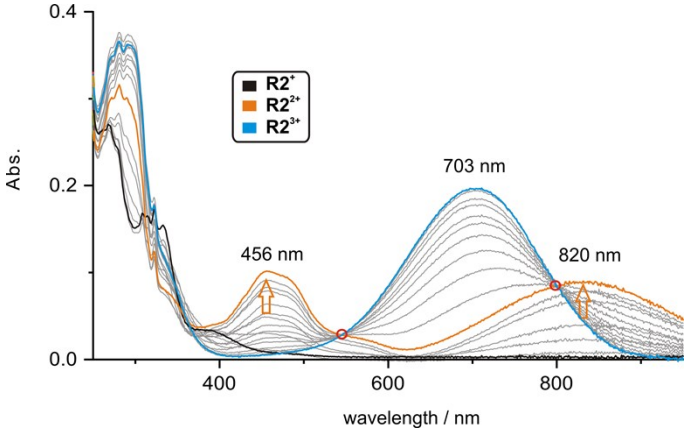

Fig. S57 UV/Vis spectra of **R2** (25 µM in CH_2Cl_2, 298 K, bulk $Fe(ClO_4)_3$ as the oxidant) in the TTF^0 (black), $TTF^{\bullet+}$ (orange) and TTF^{2+} (blue) state. The grey lines correspond to spectra taken in between full conversion to the radical cation or the doubly oxidized species, since the bulk $Fe(ClO_4)_3$ does not dissolve completely in CH_2Cl_2.

8. Crystallographic data

The data for **TTFC8** were collected on an Agilent SuperNova single-source diffractometer equipped with an Eos CCD detector at 123(2) K using mirror-monochromated Mo-Kα (λ = 0.71073 Å) radiation. Data collection (ω scans) and reduction was performed using the program CrysAlisPro. (Version 1.171.38.43, Rigaku Oxford Diffraction 2015) The analytical face-indexing-based absorption correction method was applied. The structure was solved by intrinsic phasing methods (SHELXT[11]) and refined by full-matrix least squares on F^2 using SHELXL-2017/1.[11, 12] Anisotropic displacement parameters were assigned to non-H atoms. All hydrogen atoms were constrained to their idealised positions and refined using riding models with U_{eq}(H) of 1.5U_{eq}(C) for terminal methyl groups and of 1.2U_{eq}(C) for other groups. Moderate geometric and anisotropic restraints were utilized to stabilize the refinement of disordered ethylene group and to make it chemically reasonable. Deposition Number CCDC-2073308 contain(s) the supplementary crystallographic data for this paper. These data are provided free of charge by the joint Cambridge Crystallographic Data Centre and Fachinformationszentrum Karlsruhe Access Structures service www.ccdc.cam.ac.uk/structures.

The slow diffusion of diisopropyl ether into a concentrated solution of **TTFC8** in CH_2Cl_2/CH_3CN (1:1) mixture yielded single crystals suitable for X-ray diffraction study (see Fig. 2). The solid state structure shows planar TTF moiety, as well as, typical bond lengths and angles of neutral TTF derivatives, like characteristically short C=C distance of 1.343(5) Å between the 1,3-dithiole rings and a distance range of 1.749(4) to 1.816(3) Å for C-S bonds.[13, 14] Almost orthogonal distortion of naphthalene unit out of TTF plane with 84.65° interplanar angle is resulting in bent boat-shaped conformation of the molecule. In the crystal packing, the molecules are arranged in columnar stacks with naphthalenes and TTFs on top of each other with plane-to-plane distances of 3.247 Å and 3.415 Å, shifted by 3.908 Å and 3.762 Å, respectively. There is a slight disorder in one ethylene group in the crown ether moiety, which is refined by splitting C and H atoms of that ethylene group over two spatial positions with approximately 63/37 ratio (major/minor).

Crystal data of **TTFC8**: $C_{30}H_{36}O_6S_8$, M = 749.07, triclinic, space group *P*-1 (no.2), a = 5.0805(3), b = 14.9091(10), c = 22.3719(14) Å, α = 98.267(5), β = 91.760(5), γ = 96.811(5)°, V = 1663.2(2) Å^3, Z = 2, ρ_{calc} = 1.496 Mgm^{-3}, μ = 0.579 mm^{-1} (T_{max} = 0.974 and T_{min} = 0.943), F(000) = 784, θ range = 3.27-26.50°, 10254 reflections collected, 6834 unique (R_{int} = 0.0328, I>2σ(I) = 4509), which were used in all calculations (418 parameters, 39 restraints), Goodness-of-fit (F^2) = 1.066. The final R indices [I>2σ(I)]: R1 = 0.0551 and wR2 = 0.1023. R indices (all data): R1 = 0.0947 and wR2 = 0.1248. Largest residual electron densities: 0.531 and -0.398 e.Å^{-3}.

9. References

1. H. V. Schröder, S. Sobottka, M. Nössler, H. Hupatz, M. Gaedke, B. Sarkar and C. A. Schalley, *Chem. Sci.*, 2017, **8**, 6300-6306.
2. T. Matsumura, F. Ishiwari, Y. Koyama and T. Takata, *Org. Lett.*, 2010, **12**, 3828-3831.
3. O. P. S. Rossi, F. Selva, *Farmaco. Ed. Sci.*, 1967, **22**, 172-176.
4. S. Grunder, D. Muñoz Torres, C. Marquardt, A. Błaszczyk, R. Krupke and M. Mayor, *Eur. J. Org. Chem.*, 2011, **2011**, 478-496.
5. J. Bucher, T. Wurm, K. S. Nalivela, M. Rudolph, F. Rominger and A. S. Hashmi, *Angew. Chem. Int. Ed.*, 2014, **53**, 3854-3858.
6. D. Y. Wang, Z. K. Yang, C. Wang, A. Zhang and M. Uchiyama, *Angew. Chem. Int. Ed.*, 2018, **57**, 3641-3645.
7. J. R. Aranzaes, M.-C. Daniel and D. Astruc, *Can. J. Chem.*, 2006, **84**, 288-299.
8. C. Bornschein, S. Werkmeister, K. Junge and M. Beller, *New J. Chem.*, 2013, **37**, 2061.
9. A. R. Salimi, M. Azizpoor Fard, H. Eshtiagh-Hosseini, M. A. M and H. R. Khavasi, *Acta Crystallogr Sect E Struct Rep Online*, 2010, **66**, o509.
10. M. Gaedke, F. Witte, J. Anhäuser, H. Hupatz, H. V. Schröder, A. Valkonen, K. Rissanen, A. Lützen, B. Paulus and C. A. Schalley, *Chem. Sci.*, 2019, **10**, 10003-10009.
11. G. M. Sheldrick, *Acta Crystallogr., Sect. A: Found. Adv.*, 2015, **71**, 3-8.
12. G. M. Sheldrick, *Acta Crystallogr., Sect. C: Struct. Chem.*, 2015, **71**, 3-8.
13. J. Sun, X. Lu, J. Shao, X. Li, S. Zhang, B. Wang, J. Zhao, Y. Shao, R. Fang, Z. Wang, W. Yu and X. Shao, *Chem. Eur. J.*, 2013, **19**, 12517-12525.
14. H. Kobayashi, R. Kato, T. Mori, A. Kobayashi, Y. Sasaki, G. Saito, T. Enoki and H. Inokuchi, *Mol. Cryst. Liq. Cryst.*, 2011, **107**, 33-43.

Sequence-sorted redox-switchable hetero[3]rotaxanes

Marius Gaedke,[‡a] Henrik Hupatz,[‡a] Felix Witte,[b] Susanne M. Rupf,[c] Clara Douglas,[a] Hendrik V. Schröder,[a,d] Lukas Fischer,[a] Moritz Malischewski,[c] Beate Paulus[b] and Christoph A. Schalley*[a]

[a] *Institut für Chemie und Biochemie der Freien Universität Berlin, Arnimallee 20, 14195 Berlin, Germany. E-mail: c.schalley@fu-berlin.de*
[b] *Institut für Chemie und Biochemie der Freien Universität Berlin, Arnimallee 22, 14195 Berlin, Germany.*
[c] *Institut für Chemie und Biochemie der Freien Universität Berlin, Fabeckstr. 34/36, 14195 Berlin, Germany.*
[d] *present address: Department of Chemical and Biological Engineering, Princeton University, Princeton, NJ 08544, USA*
[‡] These authors contributed equally to this work.

Abstract: From a library of five crown ether macrocycles with different ring sizes and redox-active moieties, such as tetrathiafulvalene (TTF) and naphthalene dimiide (NDI), directional heterocircuit[3]rotaxanes were constructed. Using an axle with two binding sites with different steric accessibility, the concept of integrative self-sorting was applied to program the sequence of functional units in heteropseudo[3]rotaxanes. Depending on binding strength and ring size of the smaller macrocycles, different heteropseudo[3]rotaxane selectivities and stabilities were determined by 2D NMR spectroscopy and tandem mass spectrometry. A heteropseudo[3]rotaxane with rotaxane-like behaviour was isolated chromatographically, displaying electrochemically "frustrated" properties. A robust synthetic procedure was developed allowing the synthesis of four new hetero[3]rotaxanes incorporating specific sequences of functional units. Sequence pseudoisomeric rotaxanes which have the naphthalene diimide subunit at two different positions show distinct electrochemical properties. DFT calculations suggest that this differences could arise from a folding of the structure, in which the redox-active moieties stack with a stopper unit. This study presents a blueprint for the construction of hetero[3]rotaxanes with sequential control of the functional units along the track of the axle and paves the way to extend the functionality of mechanically interlocked molecules.

Introduction

Mechanically interlocked molecules (MIMs) have shown great potential as artificial molecular switches and motors performing various tasks at the nanoscopic level and rudimentarily mimicking functions of natural molecules.[1-3] However, the molecular complexity and thereby accessible functions of MIMs are often limited by their symmetrical structures.[4-7] The asymmetrical and directional structure of functional biomolecules derives not only from the centrochirality of their molecular building blocks originating from a defined structural pool of building blocks, such as DNA nucleotides or amino acids, but also from the specific sequences in which these building blocks are connected. This sequence induces for example the secondary and tertiary structure formation in proteins.[8] The precise positional control of functional units in the natural assembly processes is remarkable. Only minor changes in the sequence can cause a significantly different structure and hence may change function.[9] Therefore, the precise control over the directionality and sequence of subcomponents in molecular assemblies is an important goal when constructing functional molecules.

Most MIMs described in the literature are [2]rotaxanes and some examples incorporate directional axles (Fig. 1, top left). Directional axles have been used to build sophisticated molecular machines which operate in a directional fashion. For example, so-called “ribosomal rotaxanes”, incorporate a sequence of amino acids on the track of a directional axle. This amino acid sequence is then sequentially connected to a macrocycle upon chemically induced and directional wheel translation.[10-12]

In a homocircuit[3]rotaxane, two identical macrocycles are threaded onto the axle and a directionality can again only be defined by the axle itself (Fig. 1, top right). Also, oligohomo[*n*]rotaxanes containing more than two macrocycles have been described.[13-16] In particular, molecular pumps, where multiple macrocycles are threaded onto an axle bringing the system to a higher energy state, are fascinating examples for the application of directional homocircuit[*n*]rotaxanes.[17-19]

If the two threaded macrocycles are not identical, a more complex picture arises. In heterocircuit[3]rotaxanes (Fig. 1, bottom), the directionality is additionally described by the order of macrocycles on the directional axle, consequently, sequence isomers may exist.[20-23] As a consequence of their unique structure, the isomer-specific synthesis of heterocircuit[3]rotaxanes is not trivial.[24] Hence, only few examples of heterocircuitrotaxanes have been described yet.[25] In 1995, the first heterorotaxane synthesis was reported by the group of Stoddart applying a sequential threading approach where a [2]rotaxane is synthesised first. In a second step, the second macrocycle is then threaded onto the axle.[26] A decade passed with minor advancements in this field due to the synthetic obstacles. However, in the last 15 years the interest in heterocircuitrotaxanes increased and outstanding examples could be realised via new synthetic approaches.[24, 27-34] The group of Loeb, for example, utilised a sequential threading-clipping method yielding a [3]rotaxane facilitating a ring-through-ring molecular shuttling.[35]

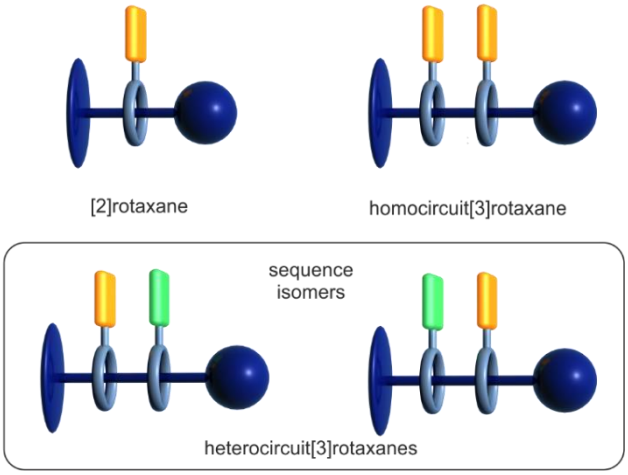

Fig. 1 Schematic representation of [2] and [3]rotaxanes containing a directional axle (dark blue) and one or two macrocycles (grey) carrying functional units (orange and green).

Fundamentally different are syntheses using the concept of self-sorting. Here, no sequential addition of components defines the sequences, but instead all components are present in one solution, and find their positions in the final structure through the sorting of orthogonal binding motifs.[36] Even though homorotaxanes or sequence isomers could form, the macrocycles and axles are structurally programmed to prefer one of the heterorotaxane isomers. The group of Goldup, for example, developed a kinetic self-sorting method to obtain heterocircuit[3]rotaxanes.[37] In 2008, the concept of integrative self-sorting was introduced by us for constructing heterorotaxanes using sufficiently different crown/ammonium binding motifs.[38, 39] This principle allows to program sequences of two macrocycles on one axle, for example by descending ring size accompanying binding site selectivity.[36] Later, it was also applied in the synthesis of a [c2]daisy-chain-containing hetero[4]rotaxane[40] and a hetero[6]rotaxane.[41] In a time-dependent mass spectrometric study of the self-sorting process, the crucial role of error correction and kinetic path selection was demonstrated.[42] So far, all examples of heterorotaxane have a narrow scope of macrocycle combinations and are mostly complex assemblies, but do not contain functional or stimuli-responsive units. The precise arrangement of functional units would pave the way to new molecular switches with emerging properties.

In our recent work on redox-active crown/ammonium complexes we observed that the combination of electron donor tetrathiafulvalene (TTF) and electron acceptor naphthalene diimide (NDI) in a divalent rotaxane yielded a donor-acceptor complex.[43] Furthermore, homooligorotaxanes incorporating TTF-decorated crown ethers enabled the understanding of new switching modes in donor-donor assemblies, such as synchronised pirouetting motion of two macrocycles[44] and an accordion-like motion of the crown ethers.[15] In a study on TTF- and NDI-decorated crown ethers with different cavity sizes, crown[8] ethers revealed a preference for dibenzylammonium and crown[7] wheels for benzyl alkyl ammonium stations, suggesting integrative self-sorting for more functional wheels.[45]

Herein, we propose a blueprint to sequence-sorted heterocircuit[3]rotaxanes using one directional axle and a library of five macrocycles carrying three different types of functional units. This approach allows for unrestricted selection and combination of the functional units in rotaxane structure. We investigate the influence of different ring sizes and binding strengths of the crown ethers involved on the self-sorting equilibrium and heteropseudo[3]rotaxane properties. We apply these findings to the synthesis of four redox-switchable hetero[3]rotaxanes and study the influence of the sequence of functional units on the spectroelectrochemical properties of the rotaxane assemblies.

Results and discussion

Design of molecular building blocks

The macrocycle library consists of three types of functionalised crown[8] ethers and two types of functionalised crown[7] ethers (Fig. 2): While **TTFC8** contains an electron-rich pro-aromatic tetrathiafulvalene with electron-donor property (yellow, "donor"), **DBC8** and **BC7** exhibit an aromatic system with no significant donor or acceptor properties (grey, "neutral"), and **NDIC8** and **NDIC7** incorporate an electron-poor aromatic system with electron-acceptor properties (green, "acceptor"). The axle **Ax** contains two secondary ammonium binding stations which are separated by a phenyl group to prevent threading of the crown[7] ethers to the dibenzyl ammonium station (Fig. 2).[38] The directionality of the axle is not only described by the two binding stations, but also, the di-*tert*-butyl stopper. This stopper prevents any wheel threading from this end of the axle and is crucial for programming the wheel sequence. Weakly coordinating tetrakis[3,5-bis(trifluoromethyl)phenyl]borate ($BArF_{24}^-$) counterions are used to facilitate a stable threaded complex of the weaker binding crown ethers

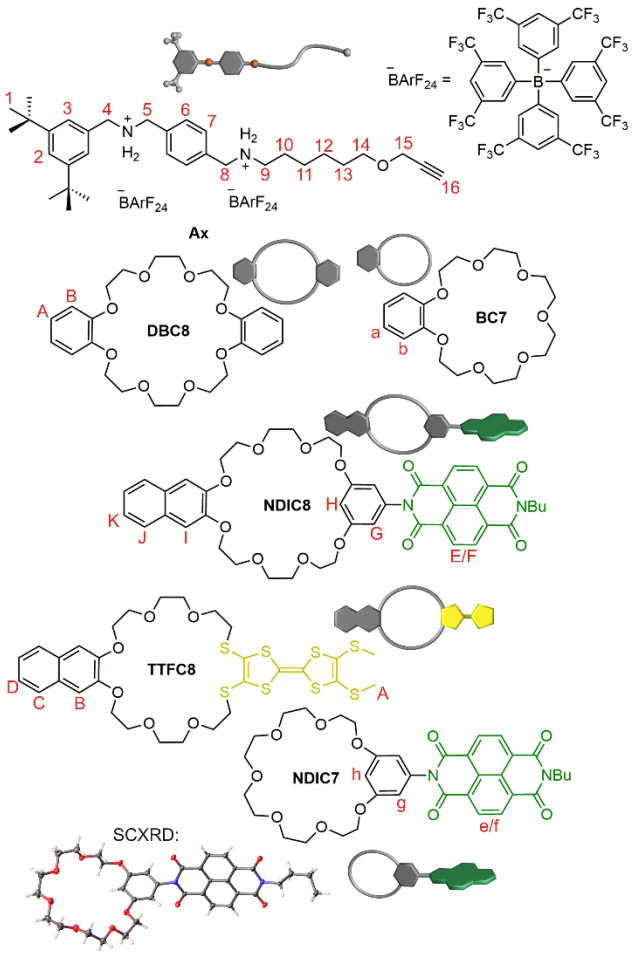

Fig. 2 Molecular Axle **Ax** and crown ether macrocycles used in this work. Protons of crown[8] wheels are denoted with capital letters, whereas crown[7] ether protons are denoted with small letters.

NDIC8, **TTFC8** and **NDIC7**. **NDIC7** and axle **Ax** are novel structures and were synthesised along the procedures given in the supporting information (ESI† section 1). For **NDIC7** we obtained a crystal structure (ESI† section 8). In the crystal, the dihedral angle between the phenyl group and the NDI is 70.01(11)°, which is considerably flatter than for **NDIC8**[45] (84.18(8)°), in order to facilitate π-π interactions between the NDIs of neighbouring **NDIC7** in the solid state. The ring sizes of **NDIC8**, **NDIC7** and **TTFC8** are wider than those of **DBC8** and **BC7**, respectively, as the 4.766(6) Å (**NDIC7**) / 4.730(4) Å (**NDIC8**) distance of the two phenolic O atoms in the NDI-substituted macrocycles as well as the S-S distance of 3.3136(13) Å in **TTFC8**[46] are substantially larger than the O-O distance of 2.5642(5) Å in **DBC8**.[47]

Recently, we have shown that the spectroelectrochemical properties of redox-active crown ethers are not significantly influenced by the crown ether size.[45] This allows us to use the crown ether sizes to program the position of the functional unit on the axle without changing the spectroelectrochemical properties of the functional units. Therefore, the hetero[3]rotaxane combinations carrying **DBC8** / **NDIC7** and **NDIC8** / **BC7** are considered as "sequence pseudoisomers".

The thermodynamics of pseudorotaxane formation has been studied for monovalent model axles by isothermal titration calorimetry, revealing a 10 times stronger binding for **DBC8** and **BC7** compared to **NDIC8** and **TTFC8**, as well as, **NDIC7**, respectively (for binding data, see ESI† table S1). Crown[8] ethers bind to the aliphatic ammonium slightly weaker than the crown[7] analogues.

Self-sorting of pseudorotaxanes

The intermediates and products of the self-assembly of equimolar mixtures of divalent axle and the two differently sized generic crown ethers **C8** (pink) and **C7** (blue) are shown schematically in Fig. 3a, where homopseudo[3]rotaxane **PRC8C8** and pseudo[2]rotaxane **PRC7** represent dead-ends on the way to the desired heteropseudo[3]rotaxane **PRC8C7**. Error-correction is necessary to overcome these dead-ends.

For all six combinations of one **C8**, one **C7** and **Ax**, equimolar solutions were equilibrated for 16 days at room temperature after which no further change in the NMR spectra was observed. Although a full assignment of all signals in the highly complex ^{1}H NMR spectra is not straightforward due to severe signal overlap (ESI† section 3), the four methylene signals (H(4), H(5), H(8) and H(9)) can be identified in the COSY spectra and are highly indicative for pseudorotaxane formation (Fig. 3b, e and ESI† section 3). For the mixture containing **TTFC8**, **BC7** and **Ax**, three major species could be identified and assigned by the chemical shift of their methylene protons to the heteropseudo[3]rotaxane **PRTTFC8BC7** (Fig. 3b, blue), homopseudo[3]rotaxane **PRTTFC8TTFC8** (Fig. 3b, red) and pseudo[2]rotaxane **PRBC7** (Fig. 3b, green). Changing the smaller macrocycle to the weaker binding **NDIC7** a higher amount of heteropseudo[3]rotaxane **PRTTFC8NDIC7** (Fig. 3e, blue) is observed. While the pseudo[2]rotaxane **PRNDIC7** cannot be identified, a small fraction of pseudo[2]rotaxane **PRTTFC8** (Fig. 3e, brown) is visible. The other four combinations show similar results (ESI† section 3). As calculated from the integrals of the methylene protons H(4) and H(5), the heteropseudo[3]rotaxanes are preferentially formed in all six cases (Table 1). The weaker binding macrocycle **NDIC7** forms the corresponding heteropseudo[3]rotaxanes with higher selectivity as compared to **BC7**.

Due to the charge inherent in all pseudorotaxanes under study, electrospray ionisation mass spectrometry (ESI-MS) is a valuable additional analytical technique to study the self-sorting equilibrium (Fig. 3c, f and ESI† section 4). Due to differences in ionisation efficiencies, the overall abundances cannot be directly related to solution concentrations, yet a semiquantitative overview of the formation of the pseudorotaxanes with reaction time can certainly be obtained. A solution of **Ax** and **TTFC8** was equilibrated for 1 h. In the ESI mass spectrum, pseudo[2]rotaxane **PRTTFC8** can be observed in the two +1 and +2 charge states (Fig. 3c). After addition of **BC7**, heteropseudo[3]rotaxane **PRTTFC8BC7** forms only slowly on an hour time scale, as the threading of **BC7** is a slow process. At the same time, also the dead-end pseudo[2]rotaxane **PRBC7** is formed.

In marked contrast, hetero[3]pseudorotaxane **PRTTFC8NDIC7** forms already within minutes upon addition of the wider **NDIC7** to the solution of **Ax** and **TTFC8**. After 4 h virtually no changes are observed in the spectrum (Fig. 3f). The same experiments with the other crown[8] ethers revealed that the

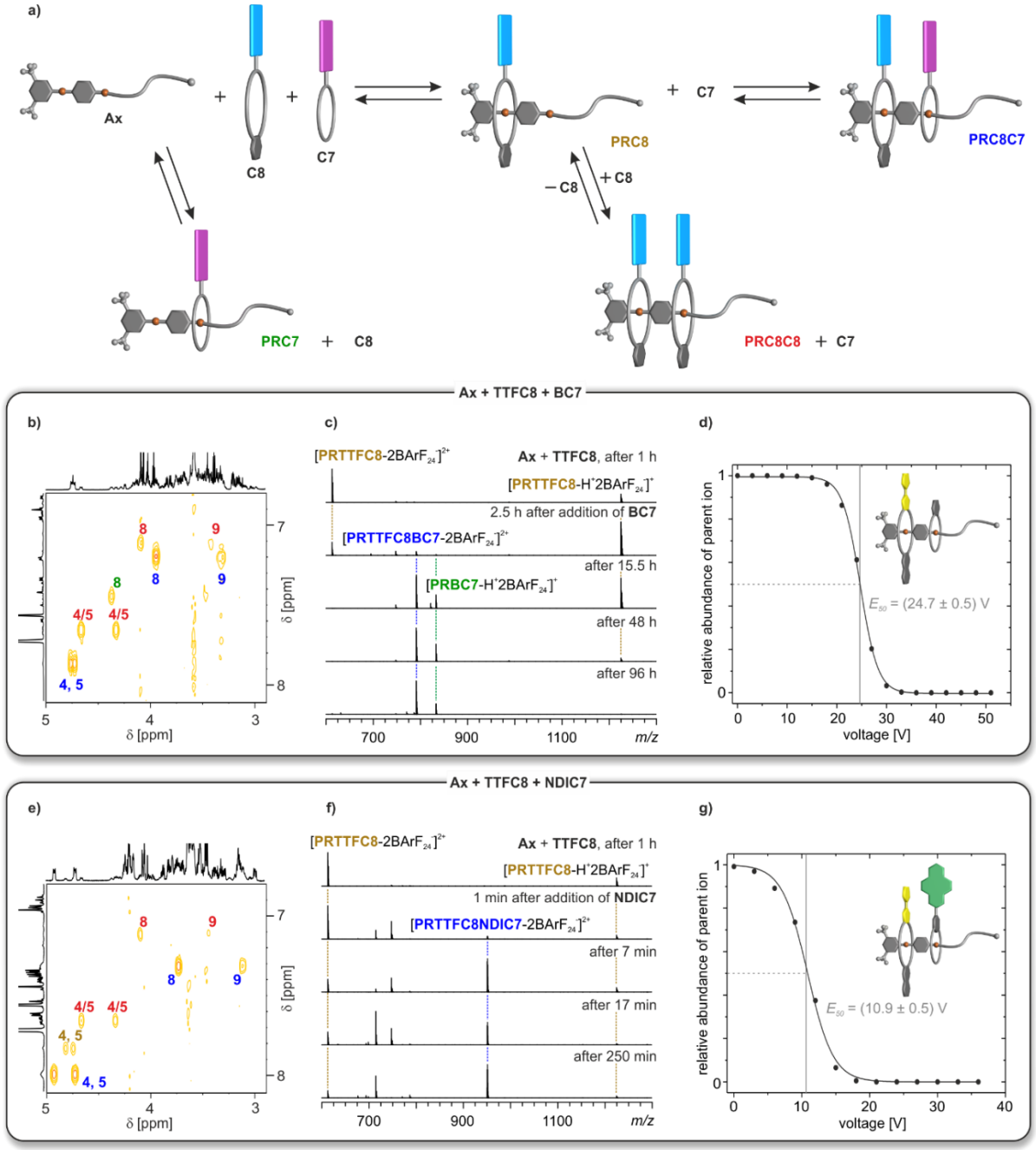

Fig. 3 a) Schematic representation of the self-sorting equilibrium for two generic crown ethers **C8** (pink) and **C7** (blue). Spectra in (b, c and d) use an equimolar solution of **TTFC8**, **BC7** and **Ax**; and in (e, f and g) of **TTFC8**, **NDIC7** and **Ax**. Signals of protons or ions for the heteropseudo[3]rotaxanes are labeled in blue, for the homopseudo[3]rotaxanes in red, for the pseudo[2]rotaxane **PRTTFC8** in brown and to the crown[7] pseudo[2]rotaxanes in green. (b, e) Partial ^{1}H,^{1}H COSY spectra (700 MHz, CD_2Cl_2, 298 K, 5 mM, 16 d). (c, f) Time-dependent ESI-MS spectra in CH_2Cl_2 at 293 K. Non-labeled peaks correspond to different crown ether ions (ESI† section 4). (d, g) Survival yield curves obtained for mass-selected ions of **PRTTFC8BC7** *m/z* 791 (d) and **PRNDIC8BC7** *m/z* 951 (g) obtained from CID experiments at increasing collision voltages. Solid lines represent a sigmoidal fitting to determine 50% survival yield voltages E_{50} (Table 1 and ESI† section 4).

equilibrium for **NDIC7**-containing mixtures are reached after a couple of hours, while mixtures including **BC7** take several days to equilibrate (Table 1 row 3 and ESI† section 4). This difference can be rationalised by the bigger ring size and thereby faster threading kinetics of **NDIC7**. Slower threading kinetics come together with a slower error correction process, as it can also be seen by the appearance of dead-end **PRBC7** in the mass spectrum as well as the ^{1}H NMR experiments. The different crown[8] ethers do not significantly alter the overall threading kinetics and heteropseudo[3]rotaxane **PRC8C7** selectivity, as their threading is comparably fast.[42]

Collision-induced dissociation (CID) experiments with mass-selected heteropseudo[3]rotaxane ions were used to establish the sequence of the pseudorotaxanes and to exclude non-threaded binding (ESI†

section 4). For all heteropseudo[3]rotaxanes incorporating **NDIC7**, the CID mass spectra showed the loss of the crown[7] ether as the first fragmentation step (ESI† Fig. S39–S41). In contrast, **BC7** containing heteropseudo[3]rotaxane ions fragment by breaking of a covalent bond first (ESI† Fig. S36 – S38). The 50% survival yield voltages E_{50} obtained from the CID mass spectra allow to compare the gas-phase stabilities of the heteropseudo[3]rotaxane assemblies (Fig. 3d, g, Table 1 and ESI† Fig. S42). **PRTTFC8BC7** exhibits a significantly higher gas phase stability as compared to **PRTTFC8NDIC7** (Fig. 3d, g). Also, E_{50} mainly is impacted by the threaded crown[7] ether (Table 1 row 4). Taking into account, that the isolated ions are doubly charged, the $E_{1/2}$ values of all six heteropseudo[3]rotaxane ions are significantly higher than for a non-threaded crown/*sec*-ammonium complex.[46] Overall, these observations evidence the desired sequence and threaded structures were achieved in all six heteropseudo[3]rotaxane combinations.

Table 1 Characterisation parameters for the self-sorting equilibrium of six macrocycle combinations with axle **Ax** in equimolar solutions obtained by ^{1}H NMR spectroscopy, time-dependent and tandem mass spectrometry (for full data set and experimental details see ESI† section 3 and 4).

macrocycle combination	**DBC8 BC7**	**TTFC8 BC7**	**NDIC8 BC7**	**DBC8 NDIC7**	**TTFC8 NDIC7**	**NDIC8 NDIC7**
hetero[3]pseudorotaxane amount[a]	58%	56%	57%	72%	70%	74%
threading timeframe[b]	days	days	days	hours	hours	hours
E_{50}[c]	21.7 V	24.7 V	27.1 V	9.4 V	10.9 V	11.4 V

[a] calculated from signal integration in ^{1}H NMR experiments (700 MHz, CD_2Cl_2, 298 K, 5 mM, 16 d). Amounts are given as percentages of all identified pseudorotaxane species (estimated error: 5%). [b] Qualitative estimation from time-dependent ESI-MS, when 90% of the maximum heteropseudo[3]rotaxane concentration is reached. [c] Estimated error amounts to 0.5 V.

These results clearly show that the second, smaller macrocycles **NDIC7** and **BC7** dominate the thermodynamic and kinetic properties of the self-sorting equilibrium. The benefit of faster threading kinetics for a self-sorting process can be highlighted by the observation of a higher selectivity for the **NDIC7** containing heteropseudo[3]rotaxanes. The higher binding constants achieved by using $BArF_{24}^-$ counterions compared to previous studies[38, 39, 42] where PF_6^- counterions were used, caused a higher kinetic barrier for the dethreading reaction of **BC7**, which is the crucial step for all error-correction processes, resulting in a comparably long equilibration time. Yet, the used conditions are robust and facilitate the formation of heteropseudo[3]rotaxanes for all combinations.

A cascade-stoppered pseudo[3]rotaxane

The slow self-sorting process together with the remarkably high gas phase stability of **BC7**-containing heteropseudo[3]rotaxanes motivated us to study **PRTTFC8BC7** in a greater detail. Although a few exceptions are known,[34, 46] crown/ammonium pseudorotaxanes are usually not sufficiently stable to survive column chromatography. Therefore, it is surprising that the pseudorotaxane **PRTTFC8BC7** was chromatographically isolated in 24% yield. For all other combinations of wheels under study here, the formed complexes dissociate on the silica column. Pseudo[3]rotaxanes with **NDIC7** dissociated quickly. The two other **BC7**-containing pseudo[3]rotaxanes required more polar mobile phases, which undermine their stability so that they also dissociate during chromatography. The stronger binding wheel **BC7** on the outer binding site acts as a stopper for the weaker binding wheel **TTFC8** on the dibenzyl ammonium binding site. Pseudo[3]rotaxanes of two **TTFC8** on **Ax** could not be isolated as they fell apart during the purification. This underlines the exceptional importance of the sequence in which the macrocycles are threaded on the one-side stoppered axle for the physico-chemical properties of the assembly.

For comparison, the rotaxane **RTTFC8BC7** was synthesised in 15% yield by adding 1.5 equiv. of 2,6-dimethoxybenzonitrile oxide stopper **St1** and stirring for one day at 35 °C. Fig. 4 shows the ^{1}H NMR shifts of **(P)RTTFC8BC7** in comparison to the axle **Ax**. Characteristic shifts include benzylic methylene protons H(4/5) and H(9), which shift downfield ($\Delta\delta \geq +0.4$ ppm and +0.2 ppm) upon threading of **TTFC8** and **BC7**. Additionally, methylene protons H(8) shift upfield by 0.3 ppm. Both is true for the pseudo[3]rotaxane

PRTTFC8BC7 and the [3]rotaxane **RTTFC8BC7**. A strong downfield shift by 3.9 ppm of the former alkyne proton H(16) is observed, as it is incorporated into the newly formed isoxazole moiety. The methylene group H(15) adjacent to the former alkyne also shifts by 0.4 ppm downfield. Except for the protons on stopper **St1** and H(15,16), the shifts of pseudorotaxane **PRTTFC8BC7** and rotaxane **RTTFC8BC7** are similar.

To test the stability in a more polar solvent, chromatographically isolated **PRTTFC8BC7** was dissolved in acetonitrile in high dilution (1 µM). After 6 h a significant amount of threaded **PRTTFC8BC7** could still be observed by ESI-MS (ESI† Fig. S43). It took multiple days to reach thermodynamic equilibrium in which virtually no complex has survived, evidencing the high kinetic stability and nearly rotaxane-like behaviour of **PRTTFC8BC7**.

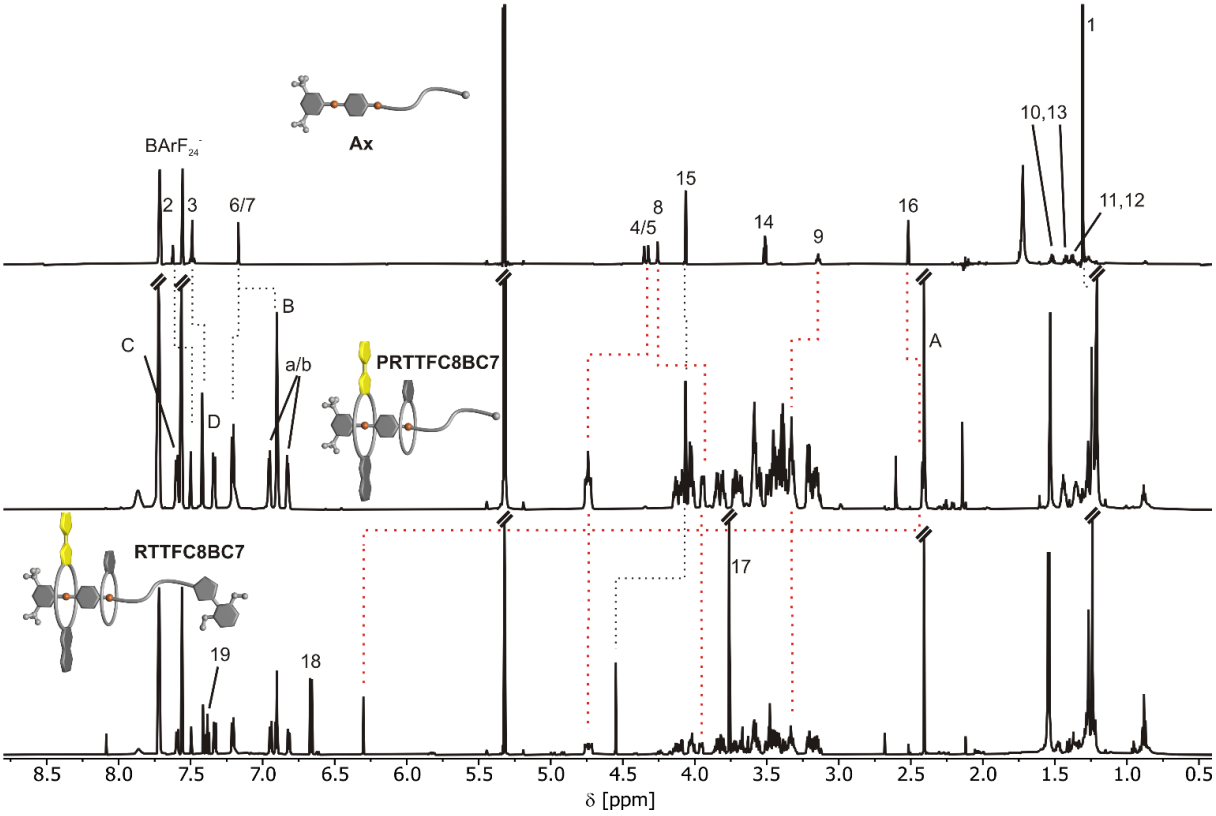

Fig. 4 ^{1}H NMR comparison of free axle **Ax**, **PRTTFC8BC7** and **RTTFC8BC7**. Characteristic shifts are highlighted by red dotted lines. (ESI† section 1.4 for full signal assignment)

Electrochemical characterisation of both species **(P)RTTFC8BC7,** by cyclic voltammetry (CV) and differential pulse voltammetry (DPV) show similar results (Fig. 5). The two reversible oxidations of TTF are anodically shifted, as expected for wheel **TTFC8** bound to an ammonium site.[48] In previous work, we reported that the ammonium site is expelled upon oxidation due to coulombic repulsion with the oxidised TTF unit. Electrochemically induced dethreading results in a new signal for the $TTF^{\cdot+/2+}$ redox couple of unbound **TTFC8** at ~1 V against decamethylferrocene / decamethylferrocenium ($Fc^{*0/+}$).[48] Sterically demanding end groups can kinetically hamper oxidation-induced dethreading efficiently.[46] However, for both, pseudorotaxane and rotaxane, no dethreading is observed and redox potentials vary only marginally. This underlines the remarkable stability, which is exceptional for a non-interlocked crown/ammonium complex, and rotaxane-like behaviour of **PRTTFC8BC7** as already observed in the CID measurements. The increased TTF oxidation potentials (+ 126 and 362 mV for first and second oxidation) together with its unability to dethread turn **PRTTFC8BC7** it into an electrochemically "frustrated" pseudorotaxane that is kinetically trapped in a metastable state.

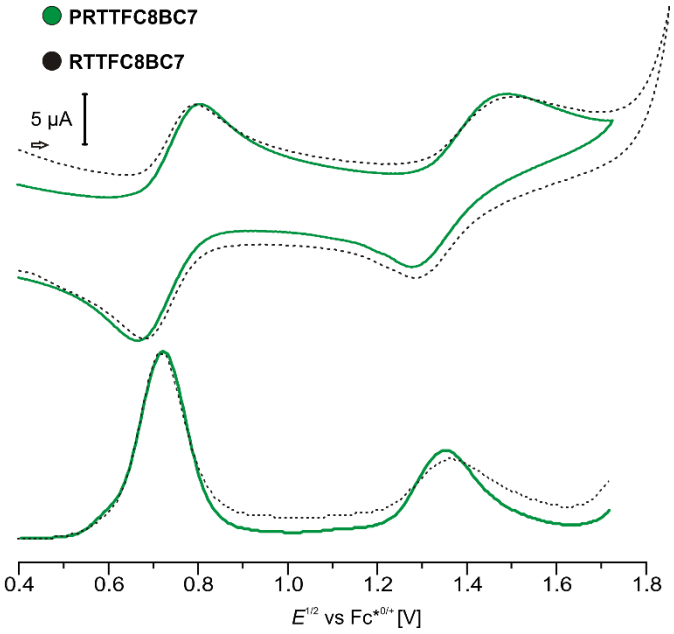

Fig. 5 CV and DPV of (pseudo)hetero[3]rotaxanes **(P)RTTFC8BC7** (1,2-dichloroethane with *n*-Bu_4NBArF_{24} as the electrolyte (0.1 M) 1.5 mM analyte, 25 mV/s scan rate for CV and 225 mV modulation amplitude, 50 ms modulation time, 5 mV step potential and 0.5 s interval time for DPV).

Hetero[3]rotaxane synthesis

The self-sorting experiments show pseudohetero[3]rotaxane formation to be prominent for all **C8**/**C7** macrocycle combinations. We therefore developed a generally applicable synthetic procedure for the synthesis of the corresponding hetero[3]rotaxanes, which does not depend on a prior chromatographic purification of the pseudo[3]rotaxane precursors. The pseudorotaxane mixtures were treated with the 2,6-dimethoxybenzonitrile stopper **St1**. This reaction was optimised by using up to six equivalents of the smaller macrocycle relative to the axle to reduce homo[3]rotaxane formation (for detailed synthetic procedures and characterisation data see ESI† section 1.4). Afterwards, the excess of the smaller macrocycle was recycled. Fig. 6 shows the isolated hetero[3]rotaxanes which all feature the diagnostic ^{1}H NMR shifts upon threading and rotaxanation as well as the diastereotopic splitting of the crown ether methylene groups as described in the previous chapter (ESI† Fig. S14, S17 and S20). The desired macrocycle sequence and the mechanically interlocked structure of the four hetero[3]rotaxanes was confirmed by CID experiments with mass-selected hetero[3]rotaxane ions, where at very high collision energies axle cleavage is observed as the major fragmentation pathway (ESI† Fig. S49 – S52). The isolated examples consist of a “donor-neutral” (yellow-grey), “donor-acceptor” (yellow-green) and the pseudo sequence isomers “acceptor-neutral” (green-grey) and “neutral-acceptor” (grey-green) hetero[3]rotaxanes. The isolated yields compare very well to the majority of isolated heterorotaxanes in the literature.[26, 28, 35, 37] Additionally, the isolation of hetero[3]rotaxanes with different wheel combinations without self-sorting would certainly be a very tedious process.

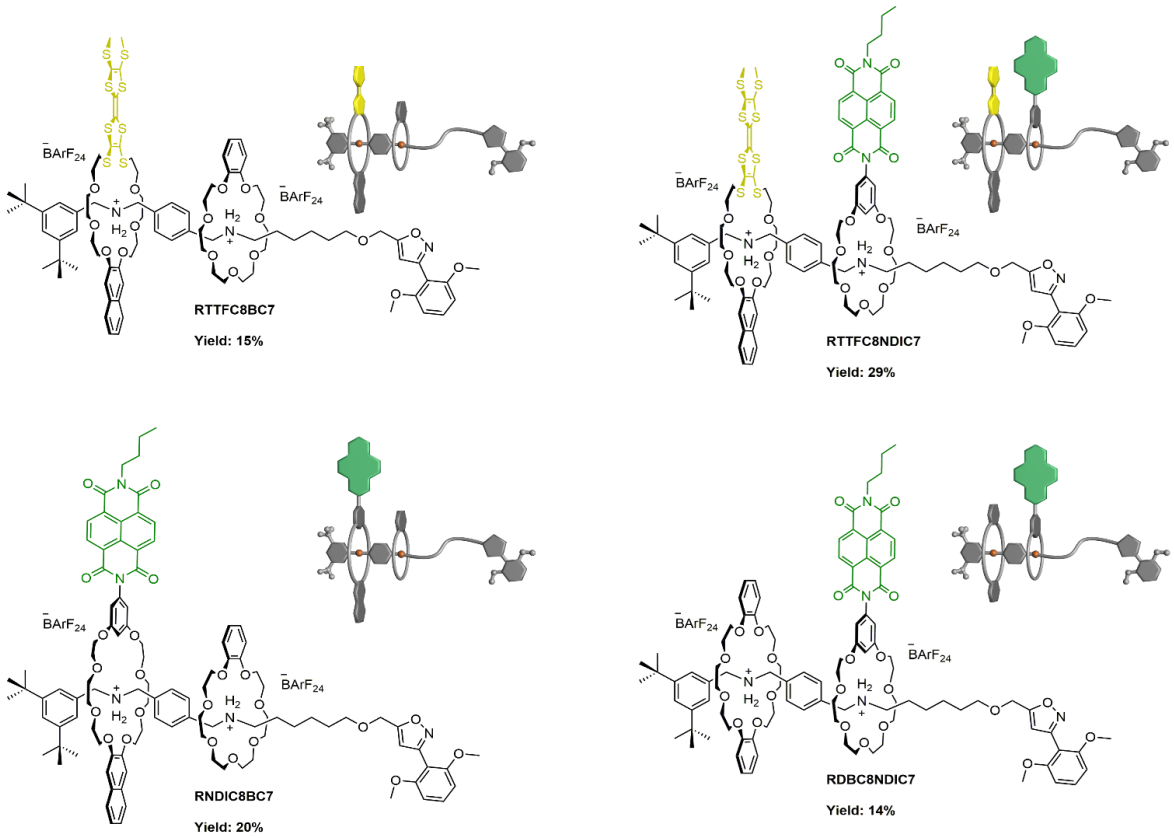

Fig. 6 Hetero[3]rotaxanes synthesised from the pseudorotaxane mixtures and their isolated yields.

Optoelectronic properties of sequence-sorted rotaxanes

A comparison between isolated hetero[3]rotaxanes and the free macrocycles **TTFC8**, **NDIC7** or **NDIC8** allow an assessment of the influence of the macrocycle sequence on the electrochemical properties. Fig. 7 summarises all peak potentials obtained by DPV measurements in 1,2-dichloroethane with *n*-Bu_4NBArF_{24} as supporting electrolyte (ESI† table S2). The potentials are referenced against the $Fc^{*0/+}$ redox-couple. The peaks at positive potentials can be attributed to the two reversible redox waves, $TTF^{(0/\cdot+)}$ and $TTF^{(\cdot+/2+)}$. As previously shown,[48] all species with **TTFC8** bound to an axle are shifted anodically in a comparable fashion. The second macrocycle does not have strong impact on the oxidation of **TTFC8** in the rotaxane as can be seen on the similar oxidation potentials of donor-acceptor rotaxane **RTTFC8NDIC7** and donor-neutral rotaxane **RTTFC8BC7**.

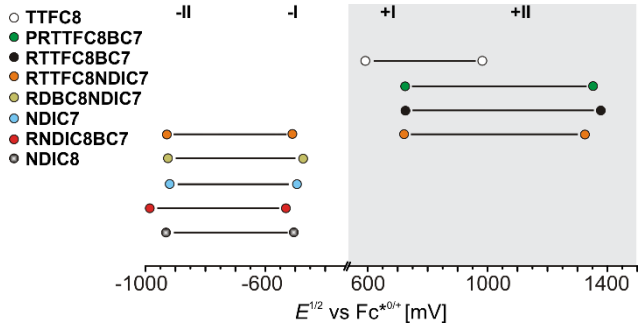

Fig. 7 Correlation diagram of half-wave potentials for hetero[3]rotaxanes and free macrocycles determined by DPV (table S2 the error is estimated to be ±10 mV).

In contrast, the peaks at negative potentials are the two reversible reductions $NDI^{(0/\cdot-)}$ and $NDI^{(\cdot-/2-)}$. For the free wheels **NDIC7** and **NDIC8** both reduction peaks are similar ($\Delta E^{1/2}$ = 11 mV for $NDI^{(0/\cdot-)}$ and $\Delta E^{1/2}$ = 16 mV for $NDI^{(\cdot-/2-)}$), as expected from their similar structures. For [3]rotaxane **RNDIC8BC7** a significant

cathodic shift of 20 mV for $NDI^{(0/\cdot-)}$ and 55 mV for $NDI^{(\cdot-/2-)}$ compared to wheel **NDIC8** is observed. In contrast, [3]rotaxanes **RTTFC8NDIC7** and **RDBC8NDIC7** only show minor differences in the reduction potentials ($\Delta E^{1/2} \leq 10$ mV for $NDI^{(0/\cdot-)}$ and $\Delta E^{1/2} \leq 11$ mV for $NDI^{(\cdot-/2-)}$) compared to wheel **NDIC7**. Consequently, the position of the NDI-unit on the axle indeed has a significant impact on the electrochemical properties. For **NDIC7** we could not determine a significant influence of the second larger macrocycle neither being neutral nor electron donor. The difference of electrochemical properties of the NDI sequence pseudoisomers **RNDCI8BC7** and **RDBC8NDIC7** presumably occurs as a consequence of the sequence rather than the macrocycle combination. Indeed, DFT calculations and conformational analysis at the PBEh-3c level[49] using the COSMO[50] solvation model provide a molecular structure for RNDIC8BC7, where the NDI-unit stacks with the dimethoxybenzene stopper (Fig. 8a and ESI† section 7).

For donor-acceptor hetero[3]rotaxane RTTFC8NDIC7 the calculated structure displays a stacked conformation of TTF- and NDI-unit as well as the dimethoxybenzene stopper (Fig. 8b and ESI† section 7). Yet, spin-density plots are TTF-localised for the oxidised species and NDI-localised for the reduced species (ESI† Fig S60 and S61). Chemical oxidation of **RTTFC8NDIC7** shows similar bands in the UV/Vis spectra as those of the free wheel **TTFC8** for the three redox states of TTF (ESI† section 6). Together with the electrochemical data, these observations demonstrate the spectroelectric properties of **TTFC8** to be retained within the mechanically interlocked assembly.

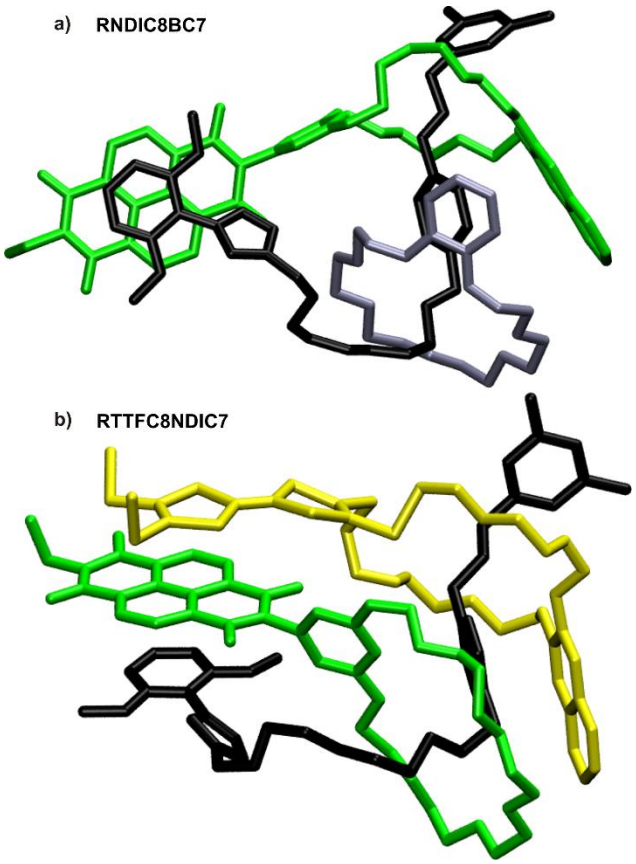

Fig. 8 Calculated structures of (a) **RNDIC8BC7** and (b) **RTTFC8NDIC7**, with the axle denoted in black, **TTFC8** in yellow, **BC7** in grey and **NDIC7** as well as **NDIC8** in green.

Conclusions

We demonstrated how integrative self-sorting can be applied as a molecular programming language to dictate the sequence of redox-switchable units along a molecular track. For the first time, we integrated functional redox-switchable units, namely TTF and NDI, into hetero[3]rotaxanes using this strategy.

The properties of the self-sorting process are dominated by the second macrocycle in the sequence. While the wider and weaker binding **NDIC7** facilitates fast threading kinetics, as well as good hetero[3]rotaxane selectivity, the smaller and stronger binding **BC7** results in slow threading kinetics and a slow error correction as well as in lower selectivities for the heteropseudo[3]rotaxane. The **BC7**-containing heteropseudo[3]rotaxanes show a surprising stability. The pseudorotaxane **PRTTFC8BC7**, could even be isolated by chromatography and thus shows rotaxane-like behaviour with **BC7** being a pseudostopper. Upon TTF oxidation, an electrochemically "frustrated" pseudorotaxane forms, in which the larger wheel experiences charge repulsion with the axle ammonium station, but is unable to dethread.

With the synthesis of four new hetero[3]rotaxanes, we demonstrate that different functional units can be placed in different sequences on the axle, as long as one crown[8] ether and one crown[7] ether is used. While for each individual hetero[3]rotaxane combination more selective conditions such as counterion, solvent or equilibration time, can be found, our synthetic approach is general and robust and facilitates the synthesis of hetero[3]rotaxanes with varying crown ether sizes, binding strength and functional units. This concept is applicable to other functionalised crown ethers. By the ease to decorate crown ethers[51] with various functional moieties, our approach represents a modular strategy to incorporate and combine a broad variety of such units using hetero[3]rotaxanes as the scaffold.

In our work the functional units were combined to generate a donor-neutral (**RTTFC8BC7**), a donor-acceptor (**RTTFC8NDIC7**), an acceptor-neutral (**RNDIC8BC7**) and a neutral-acceptor (**RDBC8NDIC7**) rotaxane. Studying the electrochemical properties of theses assemblies, we could show that the donor moiety (TTF) was marginally influenced. Instead, the acceptor moiety (NDI) showed shifted redox potentials depending on the position on the axle, probably depending on the availability of interactions to one of the stoppers. Regardless of their sequence, the redox-active units retain their reversible spectroelectrochemical properties upon incorporation into the mechanically interlocked structure. Using these results, highly directional functional molecules bearing different macrocycles can be envisioned and facilitate new switching modes or functions for rotaxane assemblies.

Author contributions

The project was developed by H. H. and M.G.. H. H., M. G. and C. A. S. wrote the manuscript with main contributions from H. H. and M. G.. The synthetic work was carried out by M. G., C. D., S. M. R., L. F. and H. H. with main contributions coming from M. G.. H. H. conducted and evaluated all time dependent NMR and tandem MS experiments. M. G. performed further NMR, UV/Vis and CV/DPV experiments and prepared the single crystals. H. V. S. helped with data evaluation and conception. H. H. measured and analysed the ITC data. All computational work was done by F. W. and B. P.. S. M. R. and M. M. measured and solved the SCXRD data. Both M. G. and H. H. contributed equally and have the right to list their name first in their CV. All Authors contributed to the final version of the manuscript.

Acknowledgements

We thank Sebastian Müller for help with the synthesis. We are grateful for funding from the Deutsche Forschungsgemeinschaft (DFG; project number 434455294) and acknowledge the assistance of the Core Facility BioSupraMol supported by the DFG. Furthermore, F. W. and B. P. acknowledge the DFG for funding (PA 1360/16-1) and the North-German Supercomputing Alliance (Norddeutscher Verbund für Hoch- und Höchstleistungsrechnen) for providing computational resources.

Notes and references

1. S. Erbas-Cakmak, D. A. Leigh, C. T. McTernan and A. L. Nussbaumer, *Chem. Rev.*, 2015, **115**, 10081-10206.
2. Y. Feng, M. Ovalle, J. S. W. Seale, C. K. Lee, D. J. Kim, R. D. Astumian and J. F. Stoddart, *J. Am. Chem. Soc.*, 2021, **143**, 5569-5591.

3. L. Zhang, V. Marcos and D. A. Leigh, *Proc. Natl. Acad. Sci. USA*, 2018, **115**, 9397-9404.
4. A. Coskun, M. Banaszak, R. D. Astumian, J. F. Stoddart and B. A. Grzybowski, *Chem. Soc. Rev.*, 2012, **41**, 19-30.
5. M. Xue, Y. Yang, X. Chi, X. Yan and F. Huang, *Chem. Rev.*, 2015, **115**, 7398-7501.
6. M. Baroncini, L. Casimiro, C. de Vet, J. Groppi, S. Silvi and A. Credi, *ChemistryOpen*, 2018, **7**, 169-179.
7. C. A. Schalley, K. Beizai and F. Vögtle, *Acc. Chem. Res.*, 2001, **34**, 465-476.
8. N. Badi and J. F. Lutz, *Chem. Soc. Rev.*, 2009, **38**, 3383-3390.
9. M. Kosloff and R. Kolodny, *Proteins*, 2008, **71**, 891-902.
10. B. Lewandowski, G. De Bo, J. W. Ward, M. Papmeyer, S. Kuschel, M. J. Aldegunde, P. M. Gramlich, D. Heckmann, S. M. Goldup, D. M. D'Souza, A. E. Fernandes and D. A. Leigh, *Science*, 2013, **339**, 189-193.
11. G. De Bo, S. Kuschel, D. A. Leigh, B. Lewandowski, M. Papmeyer and J. W. Ward, *J. Am. Chem. Soc.*, 2014, **136**, 5811-5814.
12. C. M. Wilson, A. Gualandi and P. G. Cozzi, *ChemBioChem*, 2013, **14**, 1185-1187.
13. A. J. Avestro, D. M. Gardner, N. A. Vermeulen, E. A. Wilson, S. T. Schneebeli, A. C. Whalley, M. E. Belowich, R. Carmieli, M. R. Wasielewski and J. F. Stoddart, *Angew. Chem. Int. Ed.*, 2014, **53**, 4442-4449.
14. D. Sluysmans, S. Hubert, C. J. Bruns, Z. Zhu, J. F. Stoddart and A. S. Duwez, *Nat. Nanotechnol.*, 2018, **13**, 209-213.
15. H. V. Schröder, F. Stein, J. M. Wollschläger, S. Sobottka, M. Gaedke, B. Sarkar and C. A. Schalley, *Angew. Chem. Int. Ed.*, 2019, **58**, 3496-3500.
16. H. Y. Zhou, Q. S. Zong, Y. Han and C. F. Chen, *Chem. Commun.*, 2020, **56**, 9916-9936.
17. C. Cheng, P. R. McGonigal, S. T. Schneebeli, H. Li, N. A. Vermeulen, C. Ke and J. F. Stoddart, *Nat. Nanotechnol.*, 2015, **10**, 547-553.
18. C. Pezzato, M. T. Nguyen, D. J. Kim, O. Anamimoghadam, L. Mosca and J. F. Stoddart, *Angew. Chem. Int. Ed.*, 2018, **57**, 9325-9329.
19. S. Amano, S. D. P. Fielden and D. A. Leigh, *Nature*, 2021, **594**, 529-534.
20. H. Y. Au-Yeung and A. W. H. Ng, *Synlett*, 2020, **31**, 309-314.
21. A. M. Fuller, D. A. Leigh and P. J. Lusby, *J. Am. Chem. Soc.*, 2010, **132**, 4954-4959.
22. E. A. Neal and S. M. Goldup, *Chem. Commun.*, 2014, **50**, 5128-5142.
23. C. Talotta, C. Gaeta, Z. Qi, C. A. Schalley and P. Neri, *Angew. Chem. Int. Ed.*, 2013, **52**, 7437-7441.
24. E. A. Wilson, N. A. Vermeulen, P. R. McGonigal, A. J. Avestro, A. A. Sarjeant, C. L. Stern and J. F. Stoddart, *Chem. Commun.*, 2014, **50**, 9665-9668.
25. X. Q. Wang, W. J. Li, W. Wang and H. B. Yang, *Chem. Commun.*, 2018, **54**, 13303-13318.
26. D. B. Amabilino, P. R. Ashton, M. Bělohradský, F. M. Raymo and J. F. Stoddart, *J. Chem. Soc., Chem. Commun.*, 1995, **7**, 747-750.
27. J. E. Lewis, J. Winn, L. Cera and S. M. Goldup, *J. Am. Chem. Soc.*, 2016, **138**, 16329-16336.
28. X. Zhao, X. K. Jiang, M. Shi, Y. H. Yu, W. Xia and Z. T. Li, *J. Org. Chem.*, 2001, **66**, 7035-7043.
29. A. Joosten, Y. Trolez, V. Heitz and J. P. Sauvage, *Chem. Eur. J.*, 2013, **19**, 12815-12823.
30. X. Hou, C. Ke and J. Fraser Stoddart, *Chem. Soc. Rev.*, 2016, **45**, 3766-3780.
31. C. Ke, R. A. Smaldone, T. Kikuchi, H. Li, A. P. Davis and J. F. Stoddart, *Angew. Chem. Int. Ed.*, 2013, **52**, 381-387.
32. C. Ke, N. L. Strutt, H. Li, X. Hou, K. J. Hartlieb, P. R. McGonigal, Z. Ma, J. Iehl, C. L. Stern, C. Cheng, Z. Zhu, N. A. Vermeulen, T. J. Meade, Y. Y. Botros and J. F. Stoddart, *J. Am. Chem. Soc.*, 2013, **135**, 17019-17030.
33. X. Hou, C. Ke, C. J. Bruns, P. R. McGonigal, R. B. Pettman and J. F. Stoddart, *Nat. Commun.*, 2015, **6**, 6884.
34. M. A. Soto, F. Lelj and M. J. MacLachlan, *Chem. Sci.*, 2019, **10**, 10422-10427.
35. K. Zhu, G. Baggi and S. J. Loeb, *Nat. Chem.*, 2018, **10**, 625-630.
36. Z. He, W. Jiang and C. A. Schalley, *Chem. Soc. Rev.*, 2015, **44**, 779-789.
37. E. A. Neal and S. M. Goldup, *Angew. Chem. Int. Ed.*, 2016, **55**, 12488-12493.
38. W. Jiang, H. D. Winkler and C. A. Schalley, *J. Am. Chem. Soc.*, 2008, **130**, 13852-13853.
39. W. Jiang and C. A. Schalley, *Proc. Natl. Acad. Sci. USA*, 2009, **106**, 10425-10429.
40. X. Fu, Q. Zhang, S. J. Rao, D. H. Qu and H. Tian, *Chem. Sci.*, 2016, **7**, 1696-1701.
41. S. J. Rao, Q. Zhang, J. Mei, X. H. Ye, C. Gao, Q. C. Wang, D. H. Qu and H. Tian, *Chem. Sci.*, 2017, **8**, 6777-6783.
42. W. Jiang, A. Schäfer, P. C. Mohr and C. A. Schalley, *J. Am. Chem. Soc.*, 2010, **132**, 2309-2320.
43. H. V. Schröder, H. Hupatz, A. J. Achazi, S. Sobottka, B. Sarkar, B. Paulus and C. A. Schalley, *Chem. Eur. J.*, 2017, **23**, 2960-2967.
44. H. V. Schröder, A. Mekic, H. Hupatz, S. Sobottka, F. Witte, L. H. Urner, M. Gaedke, K. Pagel, B. Sarkar, B. Paulus and C. A. Schalley, *Nanoscale*, 2018, **10**, 21425-21433.
45. H. Hupatz, M. Gaedke, H. V. Schröder, J. Beerhues, A. Valkonen, F. Klautzsch, S. Müller, F. Witte, K. Rissanen, B. Sarkar and C. A. Schalley, *Beilstein J. Org. Chem.*, 2020, **16**, 2576-2588.
46. M. Gaedke, H. Hupatz, H. V. Schröder, S. Suhr, K. F. Hoffmann, A. Valkonen, B. Sarkar, S. Riedel, K. Rissanen and C. A. Schalley, *Org. Chem. Front.*, 2021, **8**, 3659-3667.
47. I. R. Hanson, D. L. Hughes and M. R. Truter, *J. Chem. Soc., Perkin Trans. 2*, 1976, **8**, 972.
48. H. V. Schröder, S. Sobottka, M. Nössler, H. Hupatz, M. Gaedke, B. Sarkar and C. A. Schalley, *Chem. Sci.*, 2017, **8**, 6300-6306.
49. S. Grimme, J. G. Brandenburg, C. Bannwarth and A. Hansen, *J. Chem. Phys.*, 2015, **143**, 054107.

50. A. Klamt and G. Schüürmann, *J. Chem. Soc., Perkin Trans. 2*, 1993, **5**, 799-805.
51. F. Nicoli, M. Baroncini, S. Silvi, J. Groppi and A. Credi, *Org. Chem. Front.*, 2021, DOI: 10.1039/d1qo00699a.

Supporting Information

Sequence-sorted redox-switchable hetero[3]rotaxanes

Marius Gaedke, ǂ[a] Henrik Hupatz, ǂ[a] Felix Witte,[b] Susanne M. Rupf,[c] Clara Douglas,[a] Hendrik V. Schröder,[a,d] Lukas Fischer,[a] Moritz Malischewski,[c] Beate Paulus[b] and Christoph A. Schalley*[a]

[a] Institut für Chemie und Biochemie, Freie Universität Berlin, Arnimallee 20, 14195 Berlin, Germany.

[b] Institut für Chemie und Biochemie, Freie Universität Berlin, Arnimallee 22, 14195 Berlin, Germany.

[c] Institut für Chemie und Biochemie, Freie Universität Berlin, Fabeckstr. 34/36 14195 Berlin, Germany.

[d]present address: Department of Chemical and Biological Engineering, Princeton University, Princeton, NJ08544, USA

*Corresponding author e-mail: c.schalley@fu-berlin.de

ǂThese authors contributed equally to this work.

Table of Contents

1. Experimental details

1.1. General methods

All reagents and solvents were obtained from commercial sources and used without further purification. Dry solvents were purchased from Acros Organics (Geel, Belgium) and either directly used or treated with the M. Braun solvent purification system SPS 800. Wheel **TTFC8**,[1] 2,6-dimethoxybenzonitrile oxide stopper **St1**,[2] monovalent axle **A1**,[3] monovalent axle **A2**,[3] 1-bromo-6-(prop-2-yn-1-yloxy)hexane **S5**,[4] *tert*-butyl (3,5-dihydroxyphenyl)carbamate **S10**,[3] NDI building block **S13**,[5] **BC7**[6] and **NDIC8**[3] were synthesised according to literature procedures, sodium tetrakis[3,5-bis(trifluoromethyl)phenyl]borate ($NaBArF_{24}$), 3,5-di-*tert*-butylbenzaldehyde **S1**, (4-cyanophenyl)methanaminium chloride **S2**, di-*tert*-butyl-dicarbonate, were bought at Sigma Aldrich or TCI Chemicals. Thin-layer chromatography was performed on silica gel-coated plates with fluorescent indicator F254 (Merck). For column chromatography, silica gel (0.04-0.063 mm, Merck), or Biotage SNAP and SNAP Ultra Cartridges were used on a Biotage Isolera One.

^{1}H and ^{13}C NMR experiments were performed on JEOL ECX 400, JEOL ECZ 600, Bruker AVANCE 500 or Bruker AVANCE 700 instruments. Residual solvent signals were used as the internal standards. All shifts are reported in ppm and NMR multiplicities are abbreviated as s (singlet), d (doublet), t (triplet), m (multiplet) and br (broad). Coupling constants *J* are reported in Hertz. Compounds containing the tetrakis[3,5-bis(trifluoromethyl)phenyl]borate ($BArF_{24}^-$) anion show ^{13}C NMR spectra with ^{19}F, ^{10}B and ^{11}B couplings. These signals are denoted as one signal.

High-resolution ESI mass spectra were measured on an Agilent 6210 ESI-TOF device or a Synapt G2-S HDMS (Waters Co., Milford, MA, USA) mass spectrometer. HPLC grade solvents were used for sample preparation.

UV/Vis spectra were recorded with a Varian Cary 50 Bio spectrometer equipped with a xenon lamp. Solvents with HPLC grade and Suprasil glass cuvettes with a path-length of 1 cm were used.

CV measurements were carried out with an Autolab PGSTAT302N potentiostat in a 2 mL measuring cell in 1,2-dichloroethane with 0.1 M $n\text{-}Bu_4NBArF_{24}$ as the conducting salt. The working electrode was made of glassy carbon, the reference Ag electrode was etched with conc. aq. HCl. A Pt wire worked as the counter electrode. The cyclic voltammogram traces were recorded with 25, 50, 100, 250, 500, 1000 mV/s scan rates, to ensure that the observed processes are reversible and diffusion-limited. In order to obtain the correct half-wave potentials, $FeCp_2^{*0}/FeCp_2^{*+}$ (decamethylferrocene) was used as the reference. These values were afterwards referenced to $FeCp_2/FeCp_2^+$ (ferrocene) as described in the literature.[7] The

raw data were treated with Nova 1.5 by Metrohm and the plots were made with Origin 2020 by OriginLab.

1.2. Synthesis of axle Ax

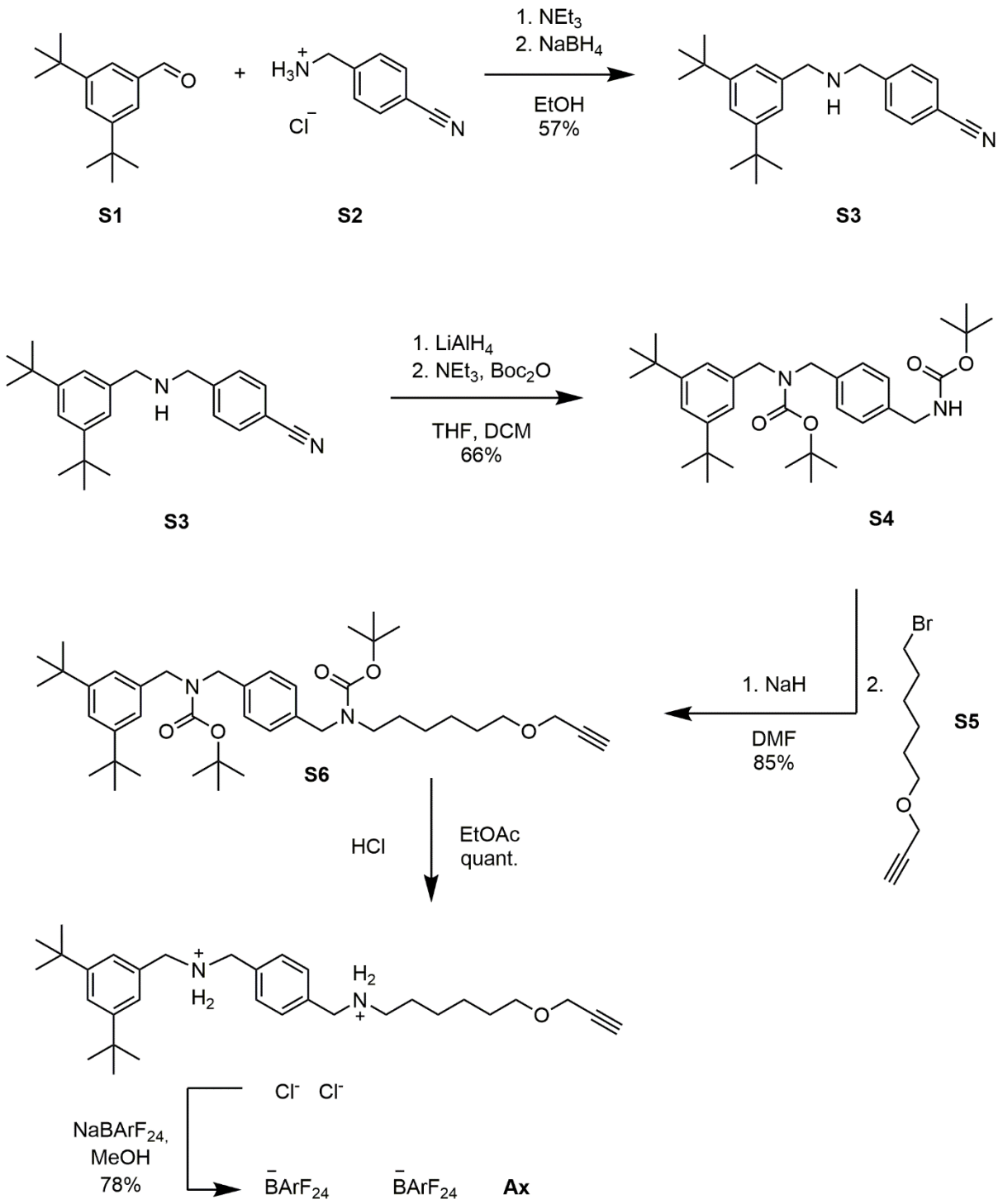

Scheme S1 General procedure for the synthesis of axle **Ax**.

4-(((3,5-di-tert-butylbenzyl)amino)methyl)benzonitrile S3

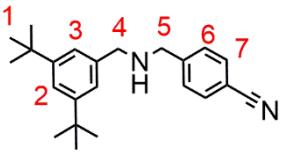

S3

3,5-Di-*tert*-butylbenzaldehyde (2.00 g, 9.16 mmol, 1.00 equiv.) and (4-cyanophenyl)-methanaminium chloride (1.53 g, 9.16 mmol, 1.00 equiv.) were dissolved in dry EtOH (400 ml) under argon atmosphere. Triethylamine (1.15 mL, 8.27 mmol, 0.90 equiv.) was added and the solution was refluxed for 5 h. After it was cooled to 0 °C, $NaBH_4$ (1.73 g, 45.8 mmol, 5.00 equiv.) was added and the solution was stirred under argon atmosphere overnight in the thawing ice bath. The reaction was then quenched by adding a concentrated aq. solution of $NaHCO_3$ until no more gas evolved. The solvent was removed under reduced pressure and the oily residue was dissolved in CH_2Cl_2 (100 ml). The organic layer was washed with brine and dried over $MgSO_4$. The solvent was removed under reduced pressure and the residue was purified by column chromatography (SiO_2, CH_2Cl_2/MeOH 100:1 → 50:1, R_f ~ 0.4 in CH_2Cl_2/MeOH = 50:1) yielding the amine as a white solid (1.76 g, 5.26 mmol, 57%).

^{1}H NMR (500 MHz, CD_2Cl_2): δ = 1.33 (s, 18H, 1), 3.76 (s, 2H, 5), 3.87 (s, 2H, 4), 7.16 (d, J = 1.8 Hz, 2H, 3), 7.32 (t, J = 1.9 Hz, 1H, 2), 7.48 – 7.52 (m, 2H, 6), 7.60 – 7.64 (m, 2H, 7) ppm. **^{13}C NMR** (125 MHz, CD_2Cl_2): δ = 31.8, 35.3, 111.1, 119.6, 121.6, 122.9, 129.2, 132.7, 139.9, 147.2, 151.4.ppm. **HRMS (MeOH)**: m/z calcd. for $[C_{23}H_{31}N_2]$+: 335.2482 [M+H]+, found: 335.2495

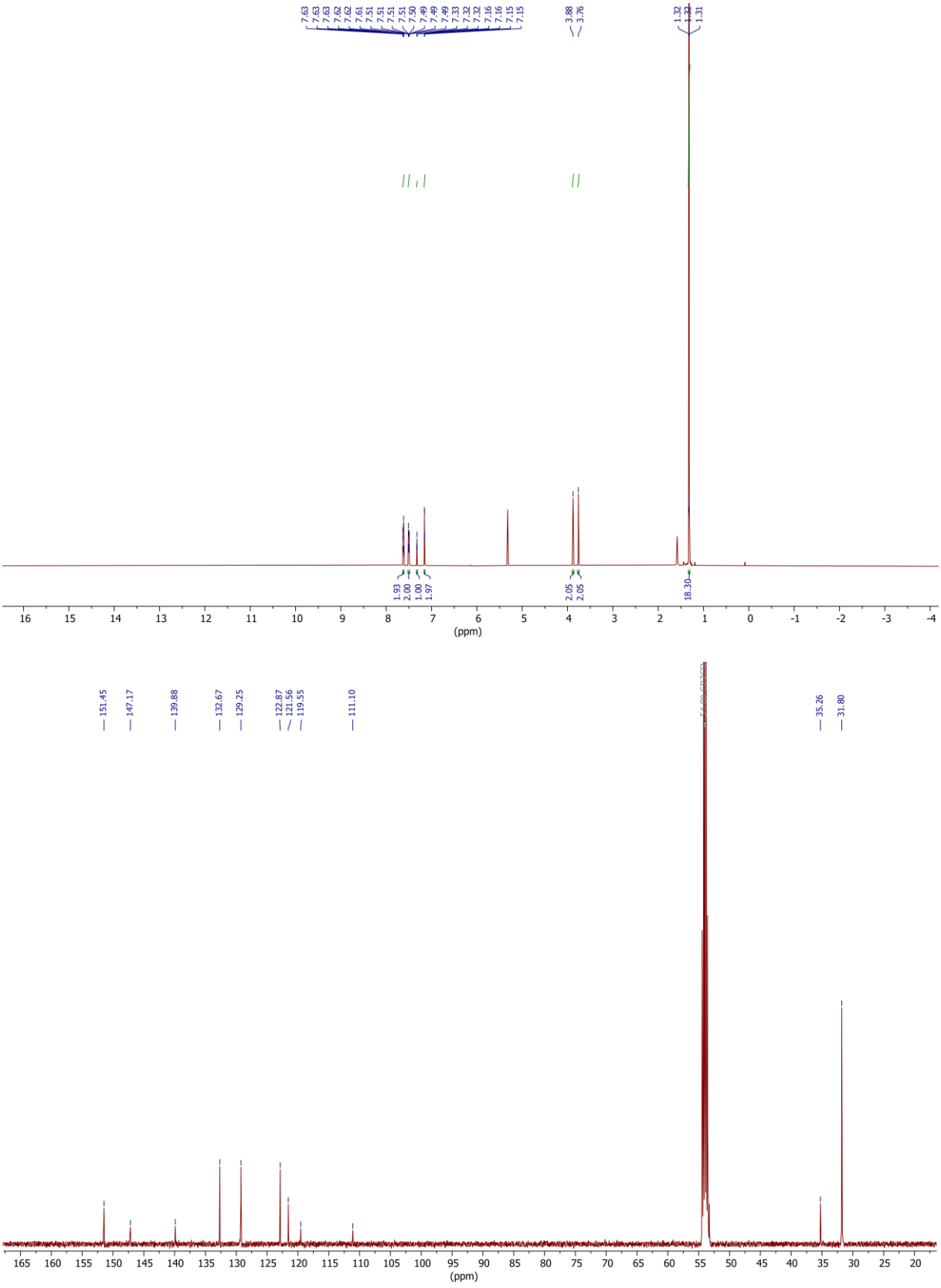

Fig. S1 ^{1}H (top) and ^{13}C (bottom) NMR spectra (500/126 MHz, CD_2Cl_2, 298 K) of amine **S3**.

tert-butyl (4-(((tert-butoxycarbonyl)amino)methyl)benzyl)(3,5-di-tert-butylbenzyl)carbamate S4

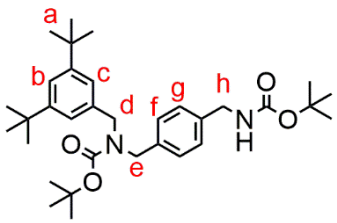

S4

Amine **S3** (1.76 g, 5.26 mmol, 1.00 equiv.) was dissolved in dry THF (400 ml) under argon atmosphere and cooled to 0 °C. $LiAlH_4$ (1.00 g, 26.3 mmol, 5.00 equiv.) was added and the solution was stirred under argon atmosphere for 24 h in the thawing ice bath. The reaction was quenched by adding a concentrated aq. solution of Na_2SO_4 until no more gas evolved. The precipitate was filtered off and the solvent was removed under reduced pressure. The residue was dissolved in CH_2Cl_2 (100 mL), washed with water and brine and dried over $MgSO_4$. The solvent was removed under reduced pressure. The raw product (1.75 g, 5.2 mmol, 1.00 equiv.) was dissolved in CH_2Cl_2 (50 mL) and cooled to 0 °C. Triethylamine (1.26 g, 12.4 mmol, 2.40 equiv.) and di-*tert*-butyl-dicarbonate (2.49 g, 11.4 mmol, 2.20 equiv.) was added. The reaction mixture was stirred overnight in the thawing ice bath. Afterwards, it was quenched by adding a concentrated aq. solution of $NaHCO_3$. The organic layer was washed with water and brine and dried over $MgSO_4$. The solvent was removed under reduced pressure and the residue was purified by column chromatography (SiO_2, CH_2Cl_2/MeOH 100:1 → 20:1, R_f ~ 0.4 in CH_2Cl_2/MeOH = 100:1) yielding the protected diamine as a colorless sticky oil (1.88 g, 3.48 mmol, 66%).

^{1}H NMR (700 MHz, $CDCl_3$): δ = 1.31 (s, 18H, 1), 1.47 (s, 9H, *tert*-butyl), 1.50 (s, 9H, *tert*-butyl), 4.30 (m, 4H, 4,5), 4.40 (s, 2H, 8), 4.40 (s_{br}, 1H, NH), 6.99 – 7.09 (m, 2H, 3), 7.11 – 7.25 (m, 4H, 6, 7), 7.31 (t, J = 1.9 Hz, 1H, 2) ppm. **^{13}C NMR** (176 MHz, $CDCl_3$): δ = 28.6, 31.8, 34.9, 44.6, 48.9, 49.2, 49.7, 50.2, 80.0, 121.3, 122.0, 122.4, 127.8, 128.5, 137.4, 137.9, 151.0, 154.9, 156.2 ppm. **HRMS (MeOH)**: m/z calcd. for $[C_{33}H_{50}N_2O_4]^+$: 577.3403 $[M+K]^+$, found: 577.3436; m/z calcd. for $[C_{33}H_{50}N_2O_4]^+$: 561.3663 $[M+Na]^+$, found: 561.3696.

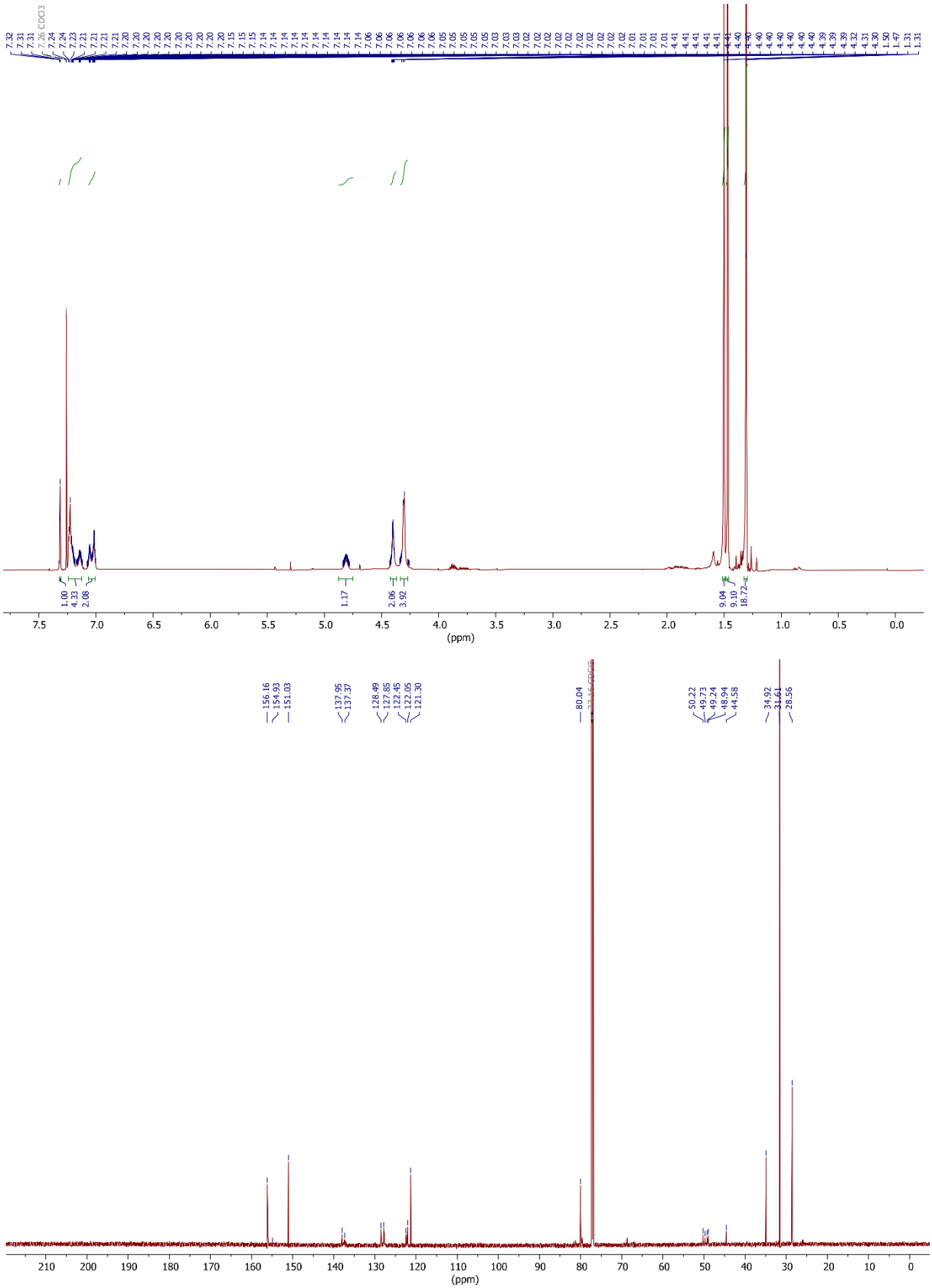

Fig. S2 ^{1}H (top) and ^{13}C (bottom) NMR spectra (700/176 MHz, $CDCl_3$, 298 K) of carbamate **S4**.

***tert*-butyl (4-(((*tert*-butoxycarbonyl)(6-(prop-2-yn-1-yloxy)hexyl)amino)methyl)benzyl)(3,5-di-*tert*-butylbenzyl)carbamate S6**

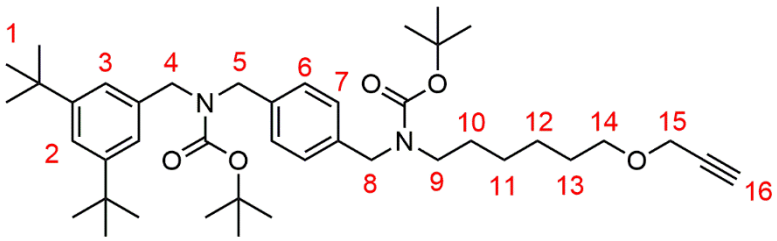

S6

Carbamate **S4** (1.99 g, 3.8 mmol, 1.00 equiv.) was dissolved in dry DMF (50 ml) under argon atmosphere and cooled to 0 °C. NaH (0.2 g, 4.9 mmol, 1.30 equiv.) was added slowly and portion-wise, the mixture stirred for 10 min in the ice bath and became pink. **S5** (1.00 g, 4.5 mmol, 1.20 equiv.) was added and the mixture was stirred under argon atmosphere in the thawing ice bath overnight. The reaction was quenched by adding H_2O (50 mL). The solvent was removed under reduced pressure and the residue was dissolved in CH_2Cl_2 (100 mL), washed with water and dried over $MgSO_4$. The solvent was removed under reduced pressure. The crude product was purified by column chromatography (SiO_2, cyclohexane/Et_2O 9:1 -> 8:2, R_f ~ 0.5 in cyclohexane/Et_2O 8:2) yielding **S6** as a colorless sticky oil (2.19 g, 3.23 mmol, 85%).

^{1}H NMR (700 MHz, $CDCl_3$): δ = 1.24 – 1.29 (m, 2H, 11), 1.31 (s, 18H, 1), 1.33 – 1.39 (m, 2H, 12), 1.42 – 1.53 (m, 20H, *tert*-butyl, 10), 1.55 – 1.62 (m, 2H, 13), 2.40 (t, J = 2.4 Hz, 1H, 16), 3.08 – 3.22 (m, 2H, 9), 3.49 (t, J = 6.6 Hz, 2H, 14), 4.12 (d, J = 2.4 Hz, 2H, 15), 4.25 – 4.33 (m, 2H, 4/5), 4.35 – 4.46 (m, 4H, 8,4/5), 7.00 – 7.08 (m, 2H, 3), 7.11 – 7.22 (m, 4H, 6,7), 7.32 (t, J = 1.9 Hz, 1H, 2) ppm. **^{13}C NMR** (176 MHz, $CDCl_3$): δ = 26.0, 26.8, 28.2, 28.6, 29.6, 30.5, 31.6, 34.9, 47.1, 48.9, 49.3, 50.0, 50.1, 58.2, 70.2, 74.2, 79.7, 80.0, 80.2, 121.3, 122.1, 122.5, 127.2, 127.8, 128.3, 137.1, 137.4, 137.8, 151.0, 156.2 ppm. **HRMS (MeOH)**: m/z calcd. for $[C_{42}H_{64}N_2O_5]^+$: 715.4452 $[M+K]^+$, found: 715.4473; m/z calcd. 699.4713 $[M+Na]^+$, found: 699.4732.

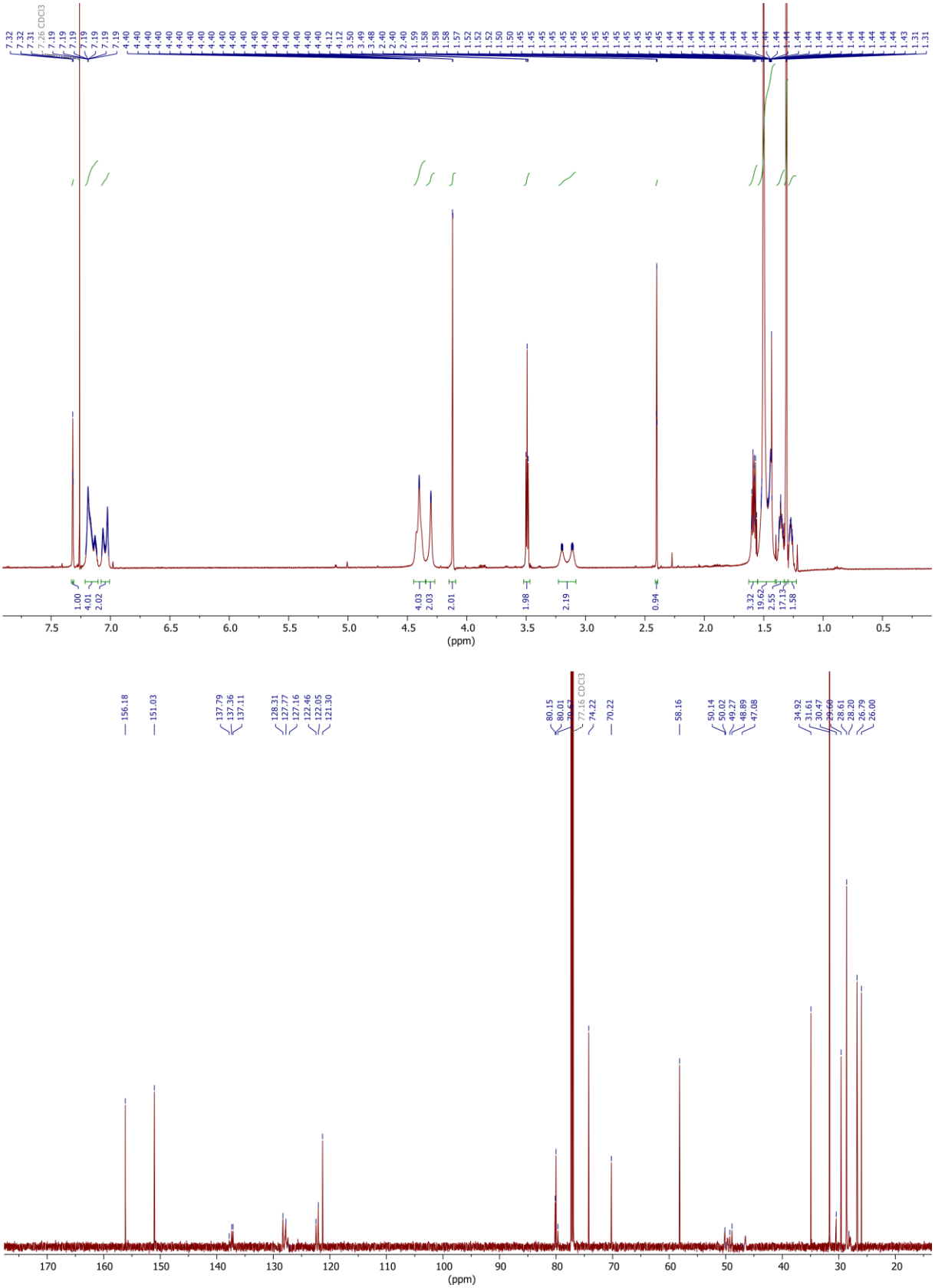

Fig. S3 ^{1}H (top) and ^{13}C (bottom) NMR spectra (700/176 MHz, $CDCl_3$, 298 K) of carbamate **S6**.

N-(4-(((3,5-di-tert-butylbenzyl)ammonio)methyl)benzyl)-6-(prop-2-yn-1-yloxy)hexan-1-aminium tetrakis(3,5-bis(trifluoromethyl)phenyl)borate Ax

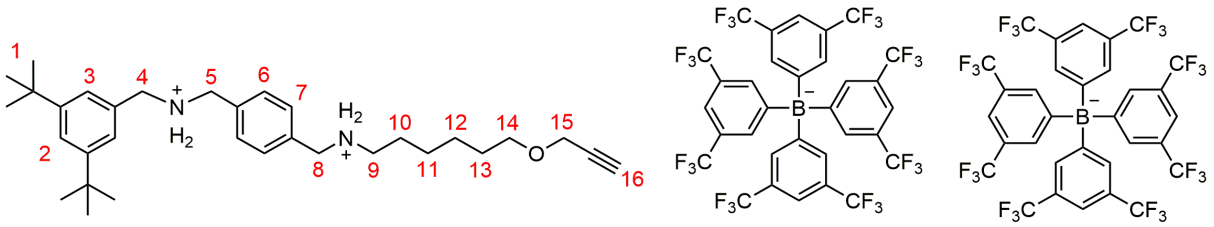

Ax

Carbamate **S6** (0.43 g, 0.61 mmol, 1.00 equiv.) was dissolved in EtOAc (20 ml) and cooled to 0 °C. conc. HCl (3 mL) was added. The mixture was stirred in the thawing ice bath overnight. The solvent was removed under reduced pressure and a portion (0.10 g, 0.18 mmol, 1.00 equiv.) was dissolved in MeOH (20 mL). $NaBArF_{24}$ (0.32 g, 0.36 mmol, 2.00 equiv.) was added and the mixture stirred for 3 h at r.t.. The solvent was removed under reduced pressure, the crude product was dissolved in CH_2Cl_2 (50 mL), washed with water and dried over $MgSO_4$. Removal of the solvent yielded **Ax** as a colorless sticky oil (0.31 g, 0.14 mmol, 78% combined). **^{1}H NMR** (700 MHz, CD_2Cl_2): δ = 1.31 (s, 18H, 1), 1.35 – 1.40 (m, 2H, 12), 1.40 – 1.46 (m, 2H, 11), 1.51 (tt, *J* = 7.0, 5.5 Hz, 2H, 13), 1.74 (m, 2H, 10), 2.53 (t, *J* = 2.4 Hz, 1H, 16), 3.16 (t, *J* = 6.9 Hz, 2H, 9), 3.52 (t, *J* = 5.7 Hz, 2H, 14), 4.06 (d, *J* = 2.4 Hz, 2H, 15), 4.27 (s, 2H, 8), 4.35 (s, 2H, 4/5), 4.37 (s, 2H, 4/5), 7.18 (d, *J* = 1.8 Hz, 2H, 3), 7.49 (m, 4H, 6,7), 7.56 (s_{br}, 8H, $BArF_{24}$), 7.64 (t, *J* = 1.8 Hz, 1H, 2), 7.72 (s_{br}, 16H, $BArF_{24}$). **^{13}C NMR** (151 MHz, CD_2Cl_2): δ = 24.6, 25.2, 25.6, 28.3, 31.4, 35.5, 48.8, 52.3, 52.4, 54.7, 58.2, 71.3, 75.7, 79.8, 118.1, 122.5, 124.0, 125.0, 126.1, 126.4, 127.7, 127.9, 129.4, 131.7, 131.8, 132.0, 132.0, 135.4, 154.2, 162.3 ppm. **HRMS (MeOH)**: m/z calcd. for $[C_{32}H_{50}N_2O]^{2+}$: 477.3845 $[M\text{-}H]^+$, found: 477. 3849.

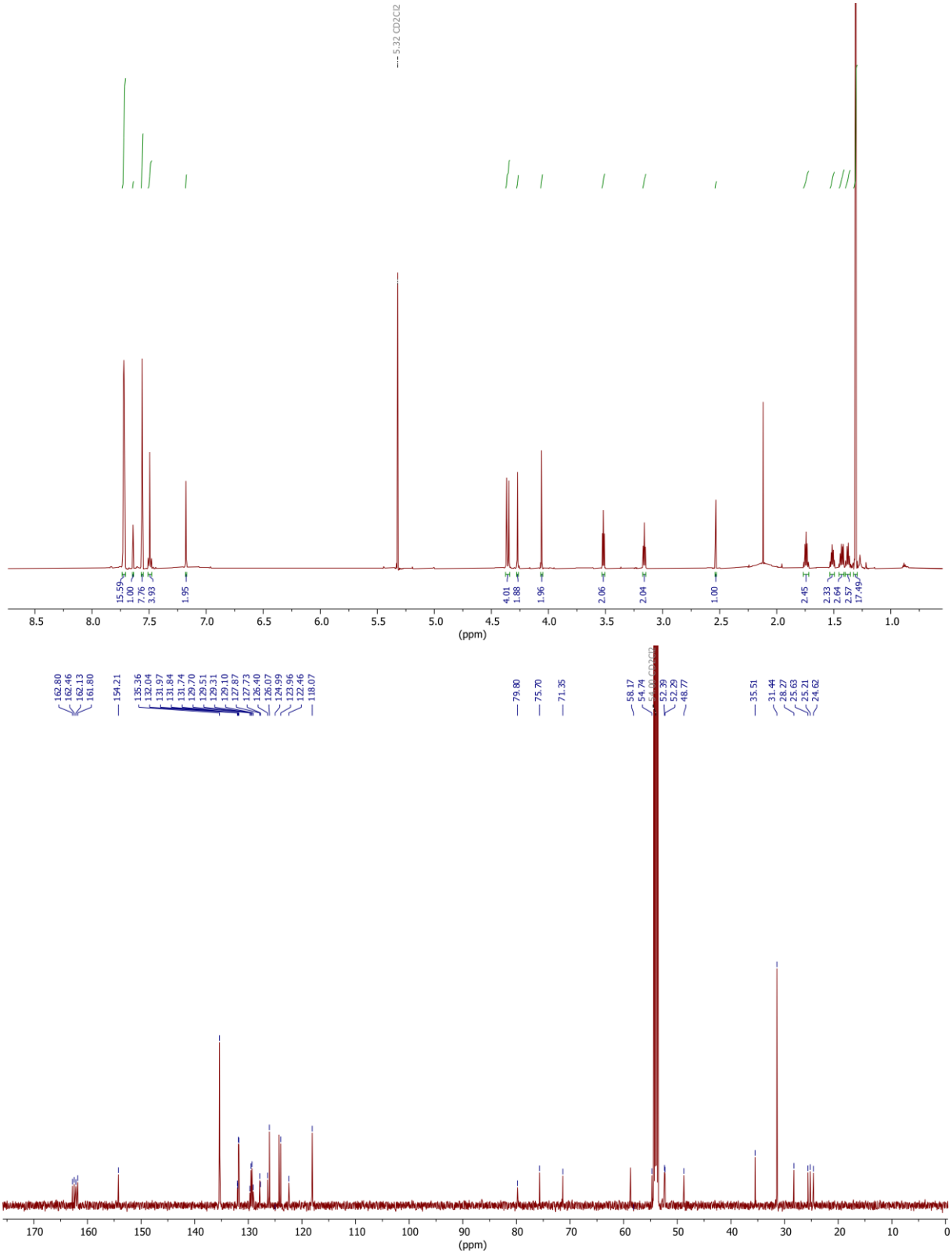

Fig. S4 ^{1}H (top) and ^{13}C (bottom) NMR spectra (700/151 MHz, CD_2Cl_2, 298 K) of axle **Ax**.

1.3. Synthesis of macrocycle NDIC7

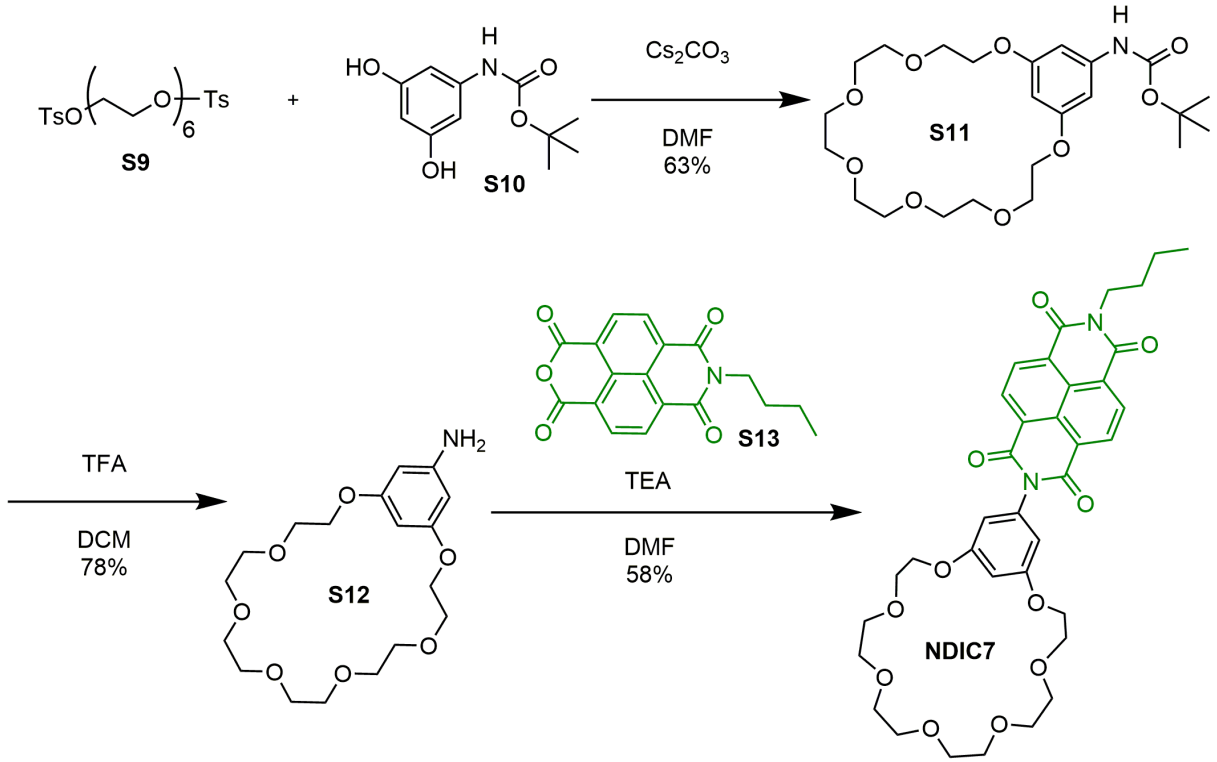

Scheme S2 General procedure for macrocycle **NDIC7**.

***tert*-butyl 2,5,8,11,14,17,20-heptaoxa-1(1,3)-benzenacycloicosaphane-15-ylcarbamate S11**

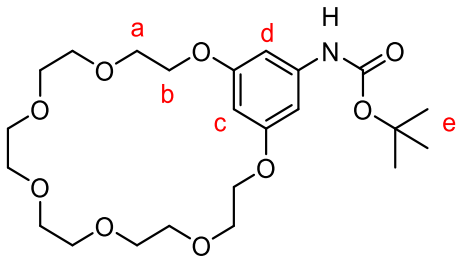

Ditosylate **S9** (525 mg, 0.89 mmol, 1.00 equiv.) was dissolved in dry DMF (100 mL) under argon atmosphere. In a separate vessel, K_2CO_3 (492 mg, 3.56 mmol, 4.00 equiv.) and diol **S10** (201 mg, 0.89 mmol, 1.00 equiv.) were dissolved in dry DMF (200 mL) and stirred at 60 °C under argon atmosphere. The ditosylate solution was added portion-wise over 2 h, afterwards the solution was stirred for 5 days at 80 °C. The solution was cooled to r.t. and filtered. The solvent was removed under reduced pressure. The residue was dissolved in CH_2Cl_2 (100 mL) and washed with water and brine and dried over $MgSO_4$. The solvent was removed under reduced pressure and the residue was purified by column chromatography (SiO_2, CH_2Cl_2/EtOAc 30% → 100% EtOAc, R_f ~ 0.2 in CH_2Cl_2/EtOAc = 1:1) yielding **S11** as a yellowish oil (256 mg, 0.56 mmol, 63%).

^{1}H NMR (500 MHz, $CDCl_3$): δ = 1.49 (s, 9H, e), 3.61 – 3.65 (m, 12H, CH_2-O), 3.68 (m, 4H, CH_2-O), 3.76 – 3.81 (m, 4H, a), 4.12 – 4.16 (m, 4H, b), 6.35 (t, *J* = 2.2 Hz, 1H, c), 6.48 (s, 1H, NH), 6.59 (d, *J* = 2.2 Hz, 2H, d) ppm. **^{13}C NMR** (176 MHz, $CDCl_3$): δ = 28.4, 67.9, 69.7, 70.7, 70.7, 71.1, 71.3, 80.6, 97.9, 98.1, 140.2, 152.6, 160.4 ppm. **HRMS (MeOH)**: m/z calcd. for $[C_{23}H_{37}NO_9]^+$: 494.2366 $[M+Na]^+$, found: 494.2389; 510.2105 $[M+K]^+$, found: 510.2131.

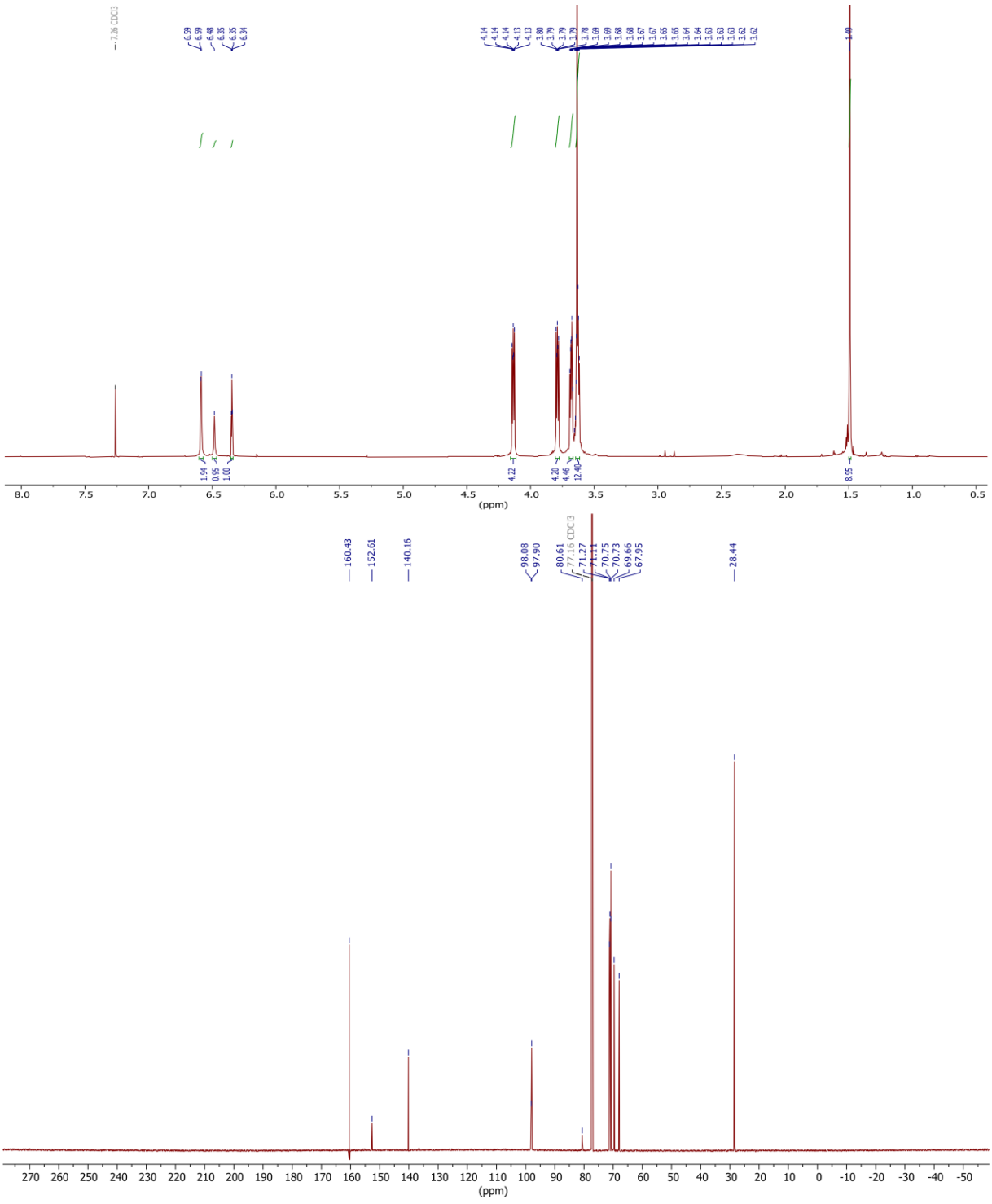

Fig. S5 ^{1}H (top) and ^{13}C (bottom) NMR spectra (500/176 MHz, $CDCl_3$, 298 K) of crown ether **S11**.

***2,5,8,11,14,17,20-heptaoxa-1(1,3)-benzenacycloicosaphan-15-amine* S12**

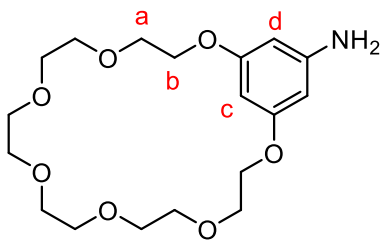

Crown ether **S11** (264 mg, 0.56 mmol, 1.00 equiv.) was dissolved in CH_2Cl_2 (30 mL). After cooling to 0 °C, trifluoroacetic acid (0.86 mL, 11.20 mol, 20.0 equiv.) was added and the mixture was stirred overnight in the thawing ice bath. The solvent was removed and the residue was taken up in aq. sat. $NaHCO_3$ solution. The solution was extracted with CH_2Cl_2 and the combined organic layers were washed with brine and dried over $MgSO_4$. The solvent was removed under reduced pressure and the residue was purified by column chromatography (SiO_2, CH_2Cl_2 → CH_2Cl_2/EtOH 10:1, R_f ~ 0.4 in CH_2Cl_2) yielding **S12** as a brown oil (162 mg, 0.44 mmol, 78%).

^{1}H NMR (700 MHz, $CDCl_3$): δ = 3.65 (d, J = 4.5 Hz, 12H, CH_2-O), 3.69 – 3.71 (m, 4H, CH_2-O), 3.80 – 3.82 (m, 4H, a), 4.10 – 4.13 (m, 4H, b), 5.88 (d, J = 2.1 Hz, 2H, d), 6.10 (t, J = 2.2 Hz, 1H, c) ppm. **^{13}C NMR** (176 MHz, $CDCl_3$): δ = 67.9, 69.8, 70.8, 70.9, 71.2, 71.3, 93.5, 95.3, 125.0, 148.3, 161.1 ppm. **HRMS (MeOH)**: m/z calcd. for $[C_{18}H_{29}NO_7]^+$: 372.2022 $[M+H]^+$, found: 372.2030; 394.1842 $[M+Na]^+$, found: 394.1853; 410.1581 $[M+K]^+$, found: 410.1595.

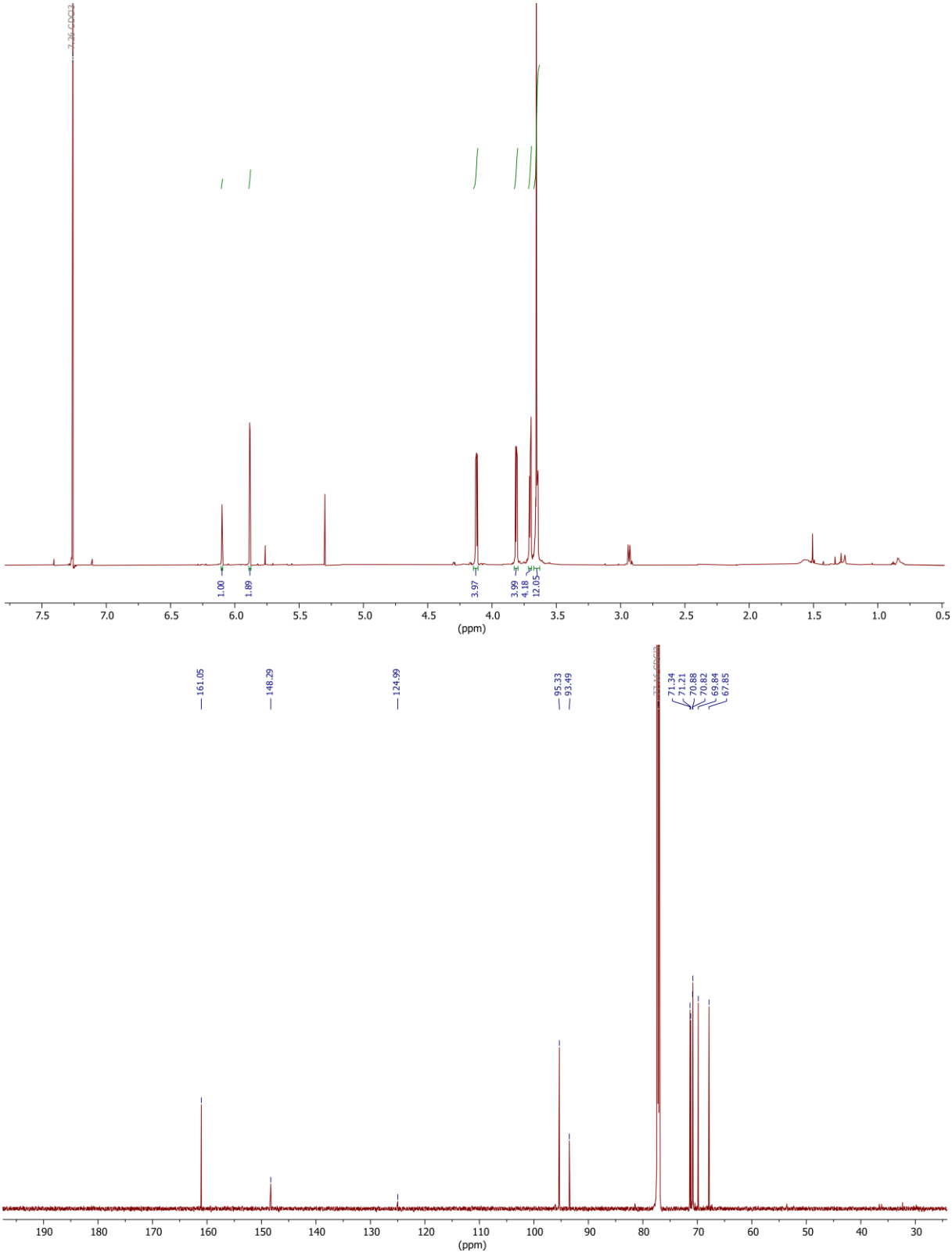

Fig. S6 ^{1}H (top) and ^{13}C (bottom) NMR spectra (700/176 MHz, $CDCl_3$, 298 K) of crown ether **S12**.

2-(2,5,8,11,14,17,20-heptaoxa-1(1,3)-benzenacycloicosaphane-15-yl)-7-butylbenzo[lmn][3,8]phenanthroline-1,3,6,8(2H,7H)-tetraone NDIC7

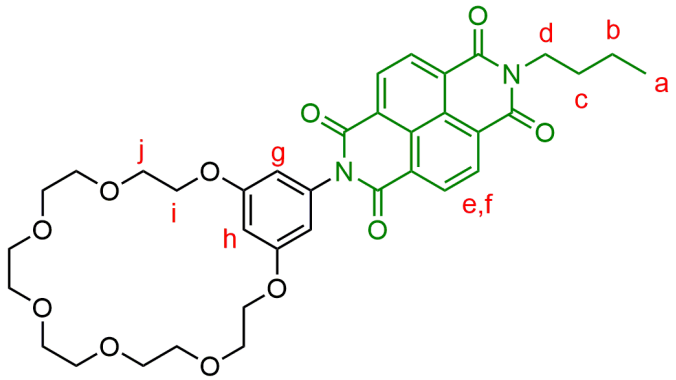

NDI **S13** (146 mg, 0.48 mmol, 1.10 equiv.) was dissolved in dry DMF (18 mL) and stirred for 20 min at 70°C under argon. Triethylamine (0.18 mL, 1.31 mmol, 3.00 equiv.) and crown ether **S12** (162 mL, 0.44 mmol, 1.00 equiv.) were added and the mixture was refluxed overnight. The solvent was removed under reduced pressure and the residue was taken up in CH_2Cl_2 (50 mL). The solution was washed with water and brine and dried over $MgSO_4$. The solvent was removed under reduced pressure and the residue was purified by column chromatography (SiO_2, CH_2Cl_2 → CH_2Cl_2/ACN 2.6:1, R_f ~ 0.3 in CH_2Cl_2) yielding **NDIC7** as a greenish brown solid (170 mg, 0.25 mmol, 58%).

^{1}H NMR (700 MHz, $CDCl_3$): δ = 1.01 (t, J = 7.4 Hz, 3H, a), 1.44 – 1.51 (m, 2H, b), 1.72 – 1.78 (m, 2H, c), 3.66 – 3.74 (m, 16H, CH_2-O), 3.83 – 3.86 (m, 4H, j), 4.19 – 4.21 (m, 4H, i), 4.21 – 4.24 (m, 2H, d), 6.47 (d, J = 2.2 Hz, 2H, g), 6.86 (t, J = 2.2 Hz, 1H, h), 8.80 (s, 4H, e,f) ppm. **^{13}C NMR** (176 MHz, $CDCl_3$): δ = 14.0, 20.5, 30.3, 41.0, 68.3, 69.8, 70.8, 70.9, 71.3, 71.4, 103.6, 108.3, 126.9, 127.1, 131.2, 131.5, 136.1, 160.9, 162.9, 163.0 ppm. **HRMS (MeOH)**: m/z calcd. for $[C_{36}H_{40}N_2O_{11}]^+$: 699.2529 $[M+Na]^+$, found: 699.2507; 715.2269 $[M+K]^+$, found: 715.2252.

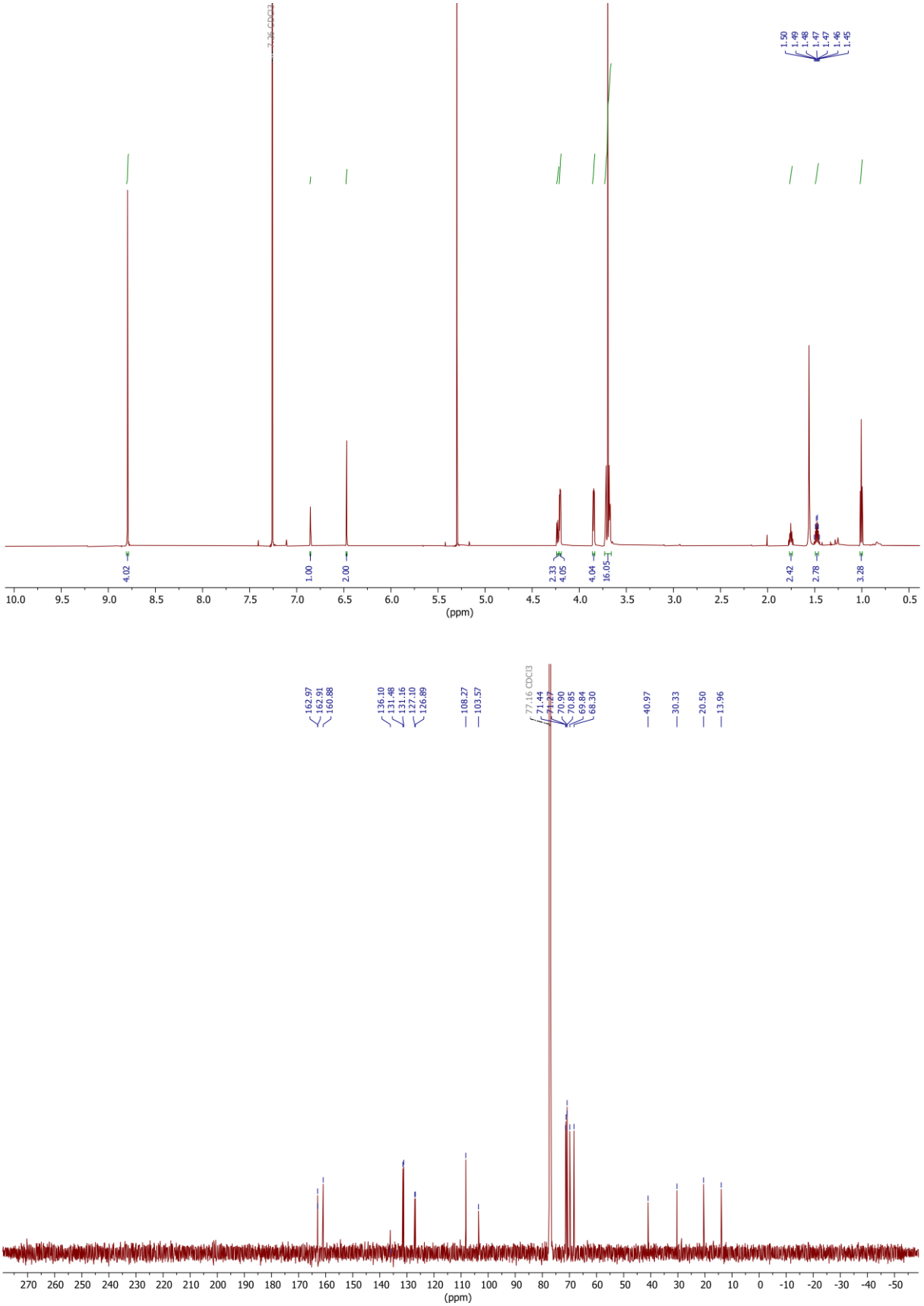

Fig. S7 ^{1}H (top) and ^{13}C (bottom) NMR spectra (700/176 MHz, $CDCl_3$, 298 K) of wheel **NDIC7**.

1.4. Synthesis of (pseudo)[3]rotaxanes

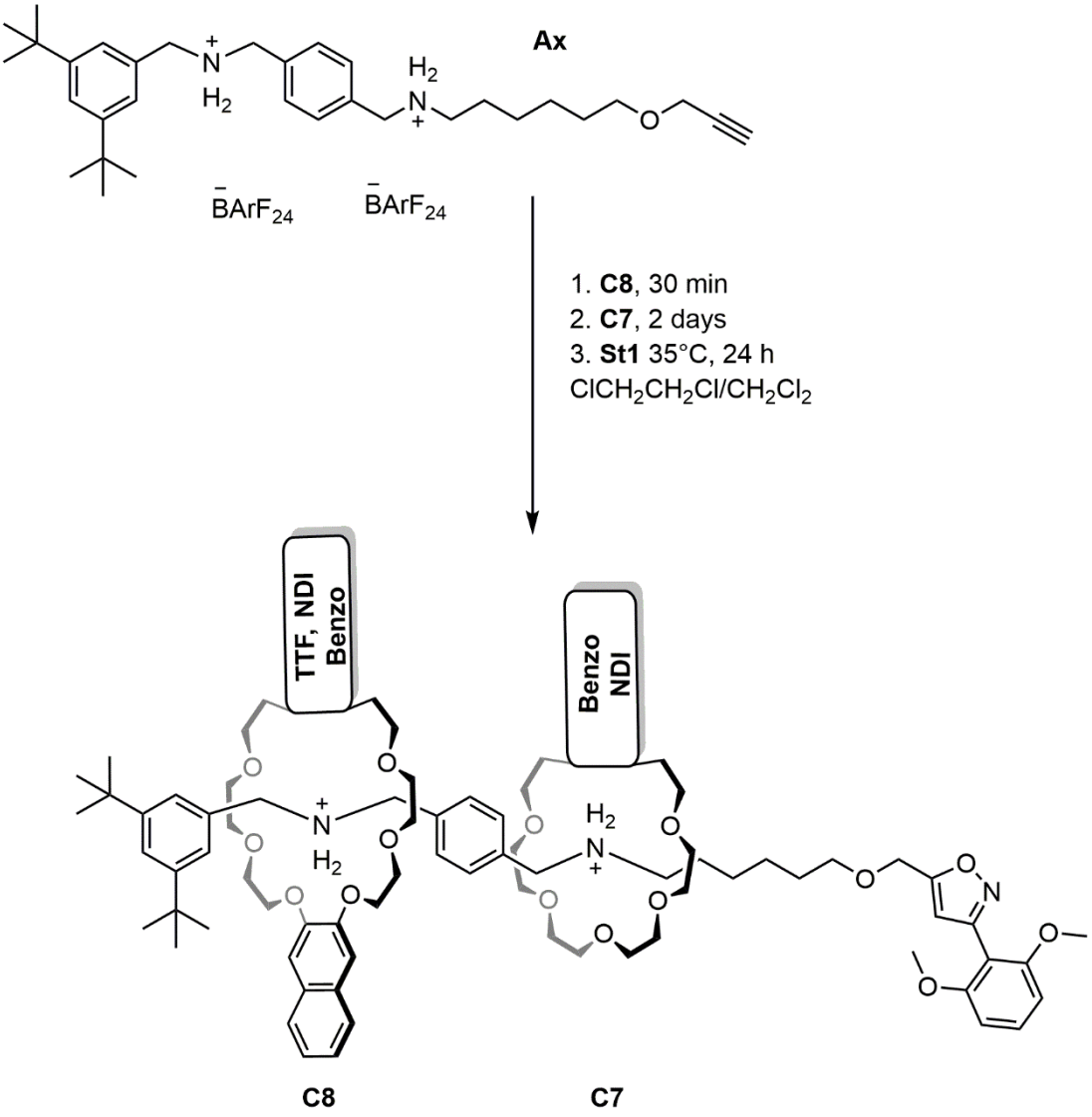

RC8C7

Scheme S3 General synthesis procedure for hetero[3]rotaxanes **RC8C7**.

Pseudo[3]rotaxane PRTTFC8BC7

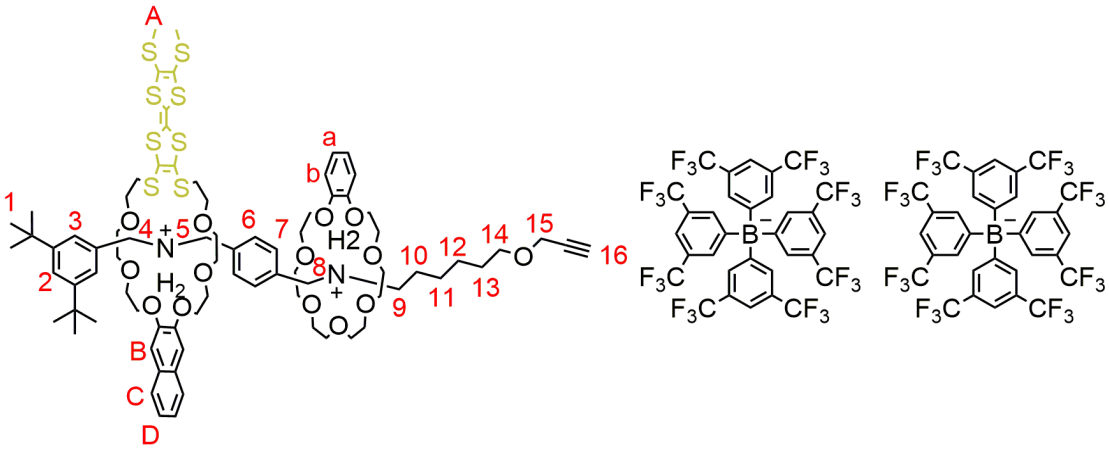

PRTTFC8BC7

The axle **Ax** (50 mg, 23 μmol, 1.00 equiv.) and macrocycle **TTFC8** (15 mg, 20 μmol, 0.90 equiv.) were dissolved in $ClCH_2CH_2Cl$ (2 mL) and stirred for 30 min, then macrocycle **BC7** (49 mg, 136 μmol, 6.00 equiv.) was added. After 2 days, the mixture was purified by column chromatography (SiO_2, CH_2Cl_2, R_f ~ 0.9 in CH_2Cl_2) to obtain the desired product **PRTTFC8BC7** (16 mg, 5 μmol, 24%) as an orange oil.

^{1}H NMR (700 MHz, CD_2Cl_2) δ = 1.23 – 1.25 (s, 18H, 1), 1.25 – 1.32 (m, 4H, 11,12), 1.32 – 1.38 (m, 2H, 10), 1.41 – 1.47 (m, 2H, 13), 2.40 (s, 6H, A), 2.41 – 2.43 (t, *J* = 2.4 Hz, 1H, 16), 3.11 – 3.24 (m, 8H, O-CH_2-CH_2), 3.29 – 3.52 (m, 20H, O-CH_2-CH_2, 9,14), 3.53 – 3.63 (m, 8H, O-CH_2-CH_2), 3.66 – 3.75 (m, 4H, O-CH_2-CH_2), 3.77 – 3.87 (m, 4H, O-CH_2-CH_2), 3.92 – 3.97 (m, 2H, 8), 4.00 – 4.05 (m, 4H, O-CH_2-CH_2), 4.06 (d, *J* = 2.4 Hz, 2H, 15), 4.08 – 4.11 (m, 2H, O-CH_2-CH_2), 4.11 – 4.17 (m, 2H, O-CH_2-CH_2), 4.70 – 4.78 (m, 4H, 4,5), 6.81 – 6.85 (m, 2H, b), 6.88 – 6.92 (m, 4H, B, 6/7), 6.94 – 6.98 (m, 2H, a), 7.17 – 7.23 (m, 4H, 6/7,NH_2), 7.31 – 7.37 (m, 2H, D), 7.42 (d, *J* = 1.8 Hz, 2H, 3), 7.50 (t, *J* = 1.8 Hz, 1H, 2), 7.56 (s_{br}, 8H, $BArF_{24}$), 7.58 – 7.61 (m, 2H, C), 7.70 – 7.77 (s_{br}, 16H, $BArF_{24}$), 7.82 – 7.90 (s, 2H, NH_2) ppm. **^{13}C NMR** (176 MHz, CD_2Cl_2) δ = 19.4, 26.0, 26.9, 27.0, 29.5, 29.6, 31.4, 35.3, 37.2, 47.6, 50.3, 53.1, 58.3, 68.4, 68.9, 70.0, 70.1, 70.1, 70.8, 71.0, 71.2, 71.3, 71.7, 71.8, 74.1, 80.5, 108.2, 108.3, 112.2, 114.5, 117.9, 122.0, 122.7, 123.7, 124.2, 124.8, 125.8, 126.7, 127.3, 128.0, 128.6, 129.3, 130.2, 130.6, 132.7, 134.5, 135.2, 146.9, 147.0, 152.8, 162.2 ppm. **HRMS (CH_2Cl_2):**m/z calcd. for $[C_{80}H_{114}N_2O_{14}S_8]^{++}$: 791.3012 $[M]^{++}$, found: 791.3034.

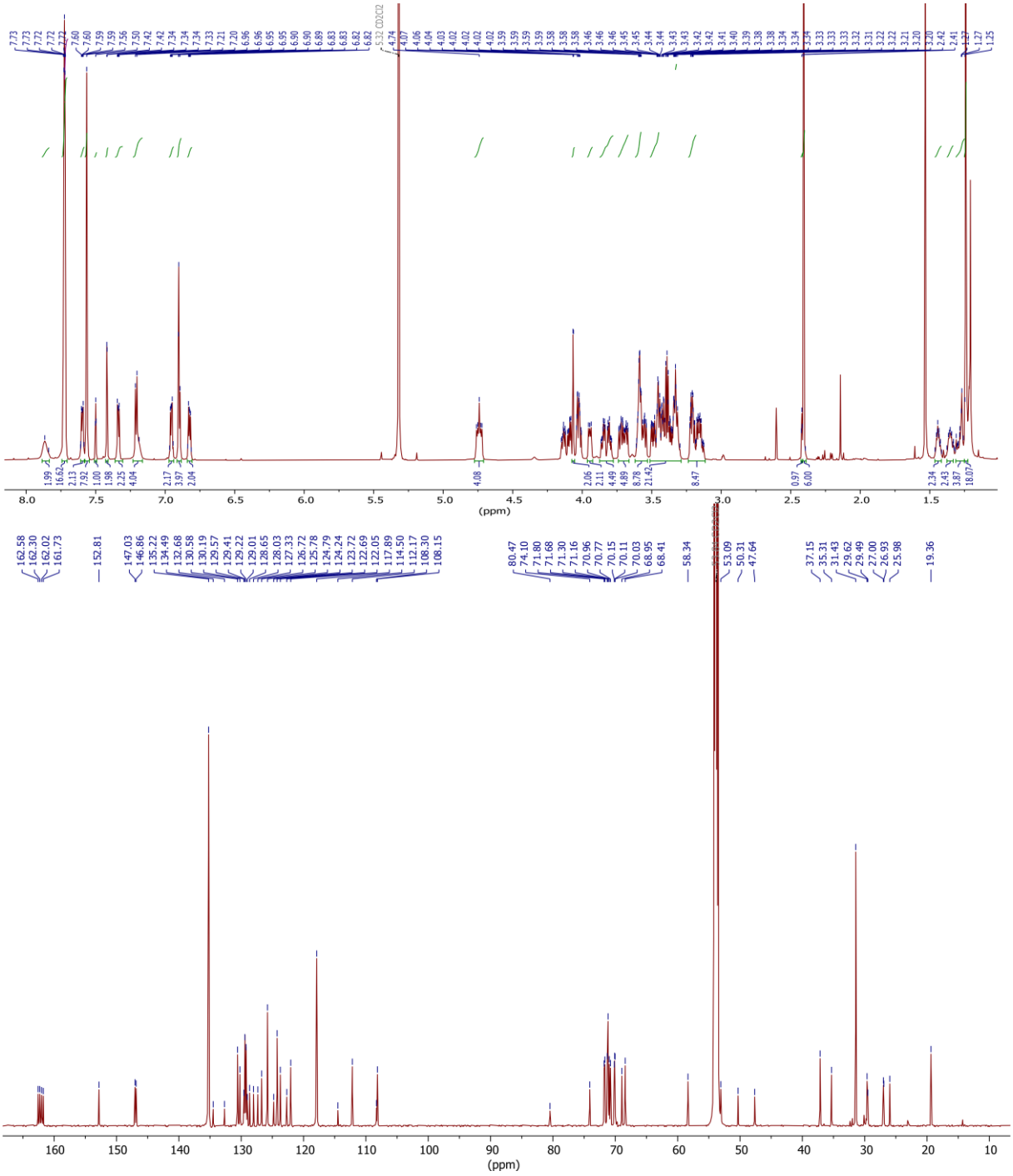

Fig. S8 ^{1}H (top) and ^{13}C (bottom) NMR spectra (700/176 MHz, CD_2Cl_2, 298 K) of pseudo[3]rotaxane **PRTTFC8BC7**.

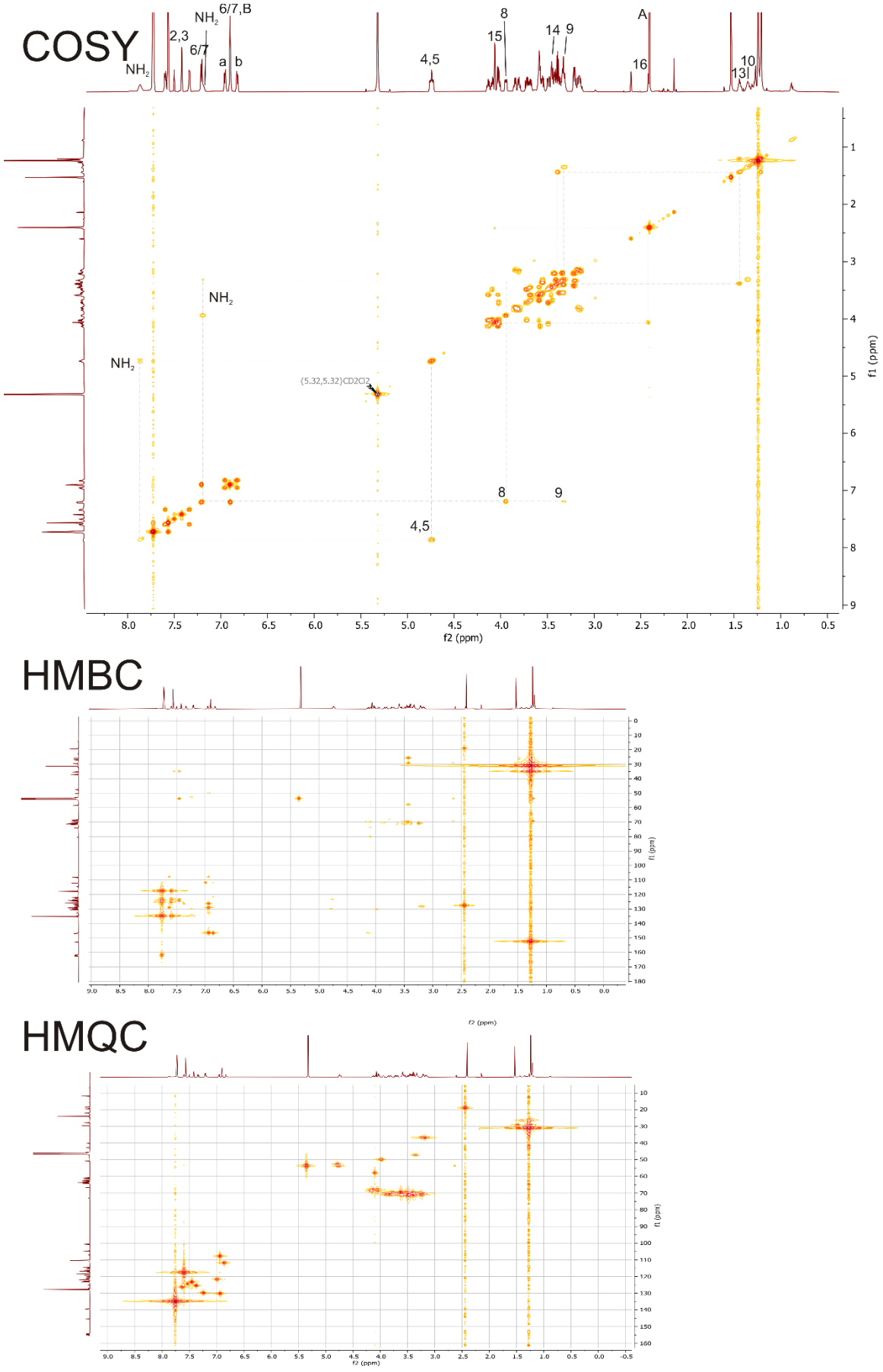

Fig. S9 COSY (top), HMBC (center) and HMQC (bottom) NMR spectra (700/176 MHz, CD_2Cl_2, 298 K) of pseudo[3]rotaxane **PRTTFC8BC7**.

RTTFC8BC7

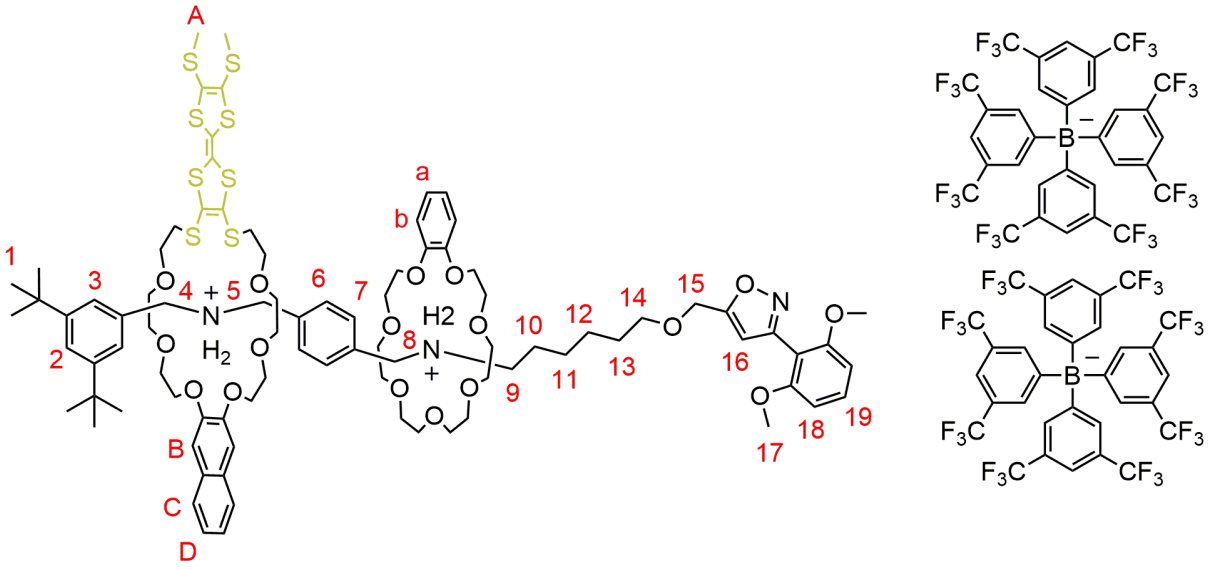

Axle **Ax** (60.0 mg, 27 µmol, 1.00 equiv.) and **TTFC8** (18 mg, 24 µmol, 0.90 equiv.) were dissolved in 1,2-dichloroethane (3 mL) and stirred for 30 min, then **BC7** (58 mg, 163 µmol, 6.00 equiv.) were added and stirred at 35° C. After 2 days, N-oxide **St1** (7 mg, 41 µmol, 1.50 equiv.) was added to the mixture and stirred for an additional 18 h at 35° C. The crude product was purified by preparative thin-layer chromatography (SiO_2, CH_2Cl_2, R_f ~ 0.3 in CH_2Cl_2). The product was obtained as an orange oil (12 mg, 3.6 µmol, 15%).

^{1}H NMR (700 MHz, CD_2Cl_2) δ = 1.23 – 1.25 (s, 18H, 1), 1.34 – 1.39 (m, 6H, 10,11,12), 1.45 – 1.50 (m, 4H, 13), 2.40 – 2.41 (s, 6H, A), 3.11 – 3.23 (m, 8H, O-CH_2-CH_2), 3.28 – 3.39 (m, 10H, 9, O-CH_2-CH_2), 3.40 – 3.52 (m, 14H, 14,O-CH_2-CH_2), 3.54 – 3.64 (m, 10H, O-CH_2-CH_2), 3.66 – 3.71 (m, 4H, O-CH_2-CH_2), 3.71 – 3.75 (m, 3H, O-CH_2-CH_2), 3.75 – 3.76 (s, 6H, 17), 3.76 – 3.83 (m, 3H, O-CH_2-CH_2), 3.83 – 3.88 (m, 3H, O-CH_2-CH_2), 3.93 – 3.98 (m, 2H, 8), 3.99 – 4.05 (m, 4H, O-CH_2-CH_2), 4.08 – 4.16 (m, 4H, O-CH_2-CH_2), 4.55 (s, 2H, 15), 4.70 – 4.77 (m, 4H, 4,5), 6.29 – 6.31 (s, 1H, 16), 6.65 – 6.68 (d, J = 8.5 Hz, 2H, 18), 6.80 – 6.84 (m, 2H, a/b), 6.89 – 6.92 (m, 4H, 7,B), 6.93 – 6.97 (m, 2H, a/b), 7.17 – 7.24 (m, 4H, 6, NH_2), 7.32 – 7.34 (m, 2H, D), 7.36 – 7.41 (t, J = 8.5 Hz, 1H, 19), 7.41 – 7.42 (d, J = 1.8 Hz, 2H, 3), 7.49 – 7.50 (t, J = 1.8 Hz, 1H, 2), 7.55 – 7.57 (s_{br}, 8H, $BArF_{24}$), 7.58 – 7.61 (m, 2H, C), 7.71 – 7.73 (s_{br}, 16H, $BArF_{24}$), 7.81 – 7.90 (s_{br}, 2H, NH_2) ppm. **^{13}C NMR** (176 MHz, CD_2Cl_2) δ = 14.3, 19.4, 23.1, 25.9, 26.9, 27.0, 29.8, 30.1, 31.4, 32.3, 35.3, 37.1, 47.6, 50.3, 53.1, 56.3, 63.9, 68.4, 68.9, 70.0, 70.1, 70.8, 71.0, 71.1, 71.2, 71.3, 71.4, 71.6, 71.8, 104.5, 106.4, 107.4, 108.2, 112.2, 114.2, 114.5, 117.9, 122.0, 122.7, 123.7, 124.2, 124.8, 125.8, 126.7, 127.3, 128.0, 128.6, 129.3, 130.2, 130.6, 131.7, 132.7, 134.5, 135.2, 146.8, 147.0, 152.8, 157.4, 159.0, 162.1, 168.2 ppm. **HRMS (acetonitrile):**m/z calcd. for $[C_{89}H_{123}N_3O_{17}S_8]^{++}$: 881.3319 $[M]^{++}$, found: 881.3325.

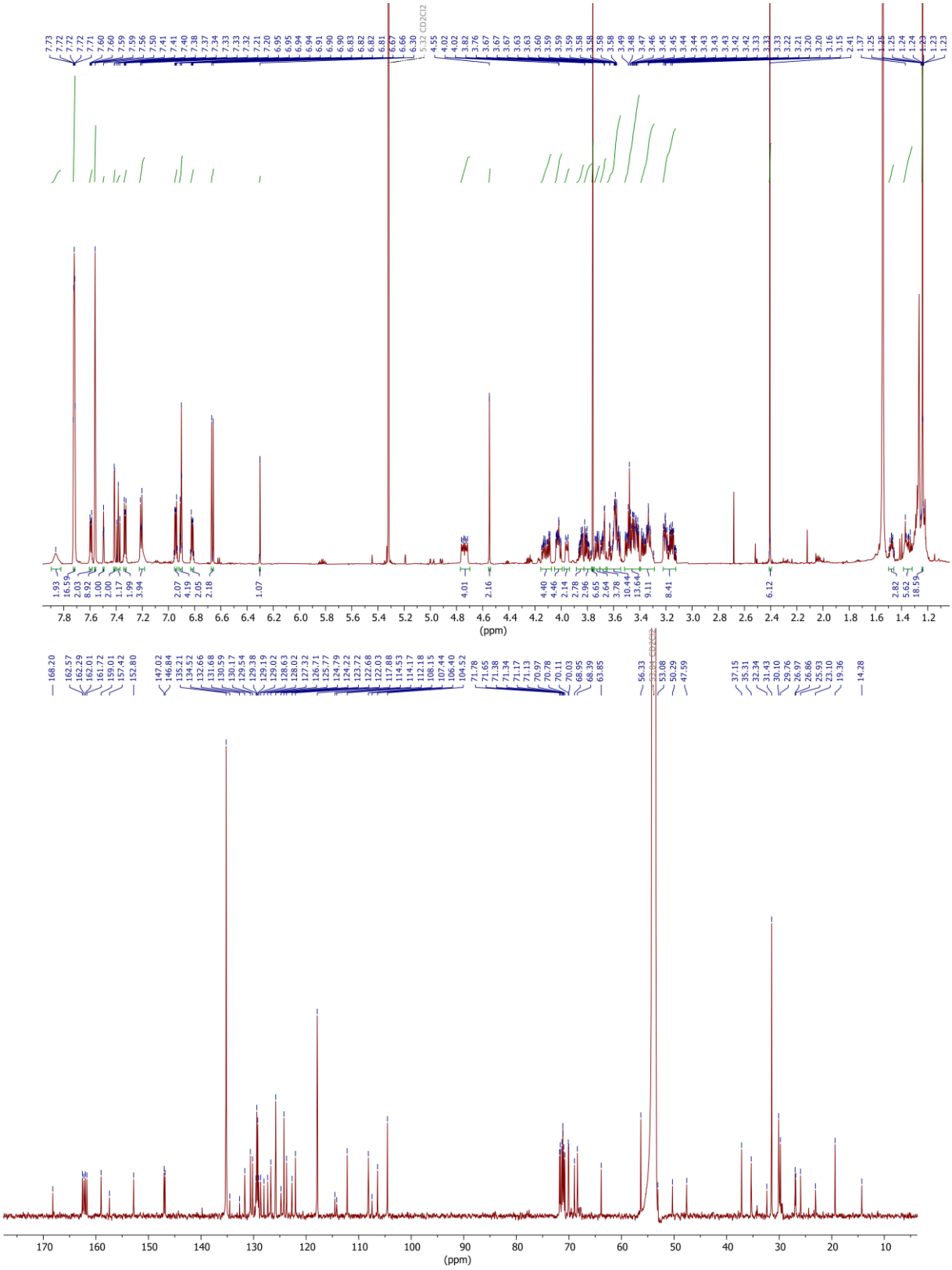

Fig. S10 ^{1}H (top) and ^{13}C (bottom) NMR spectra (700/176 MHz, CD_2Cl_2, 298 K) of [3]rotaxane **RTTFC8BC7**.

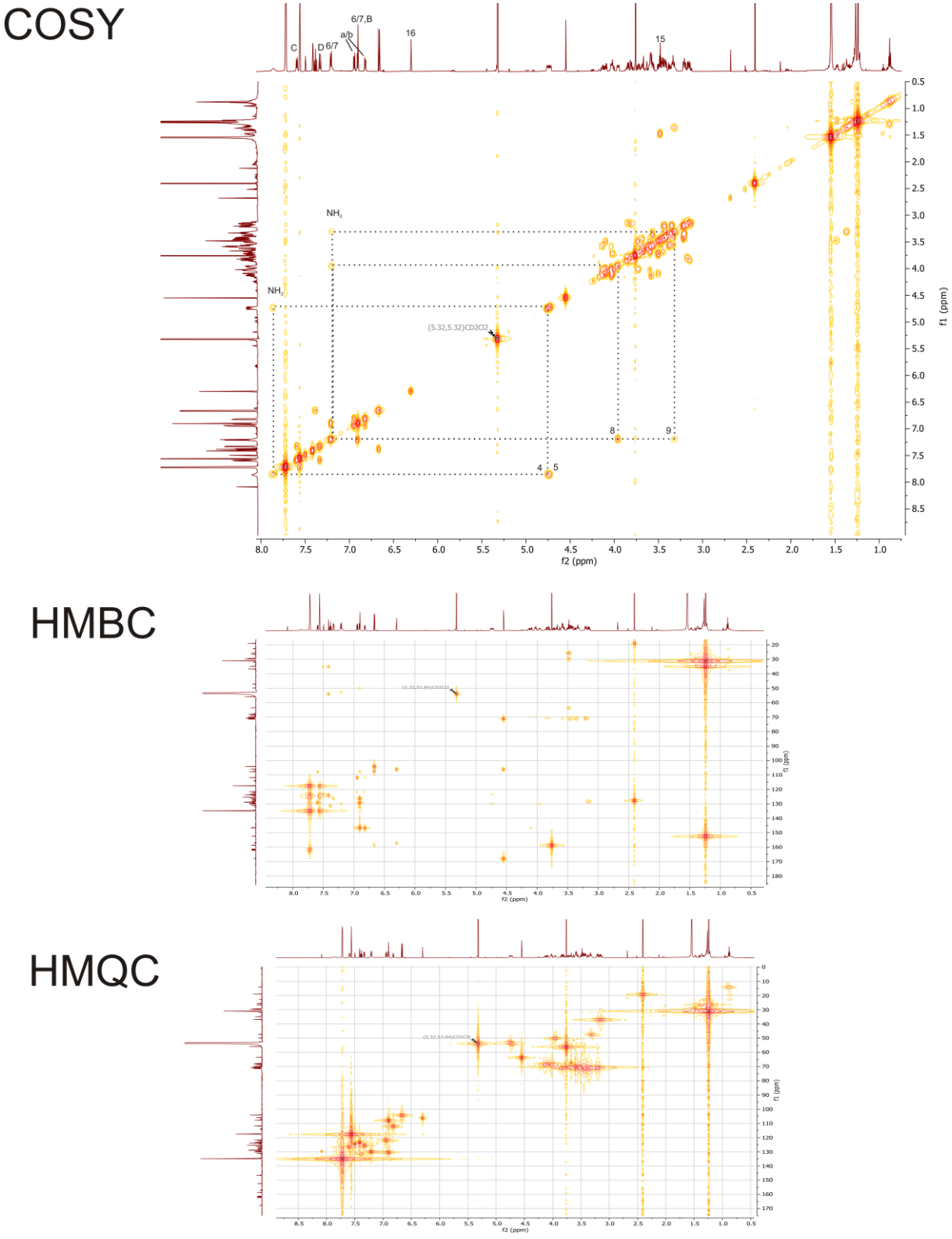

Fig. S11 COSY (top), HMBC (center) and HMQC (bottom) NMR spectra (700/176 MHz, CD_2Cl_2, 298 K) of [3]rotaxane **RTTFC8BC7**.

[3]rotaxane RTTFC8NDIC7

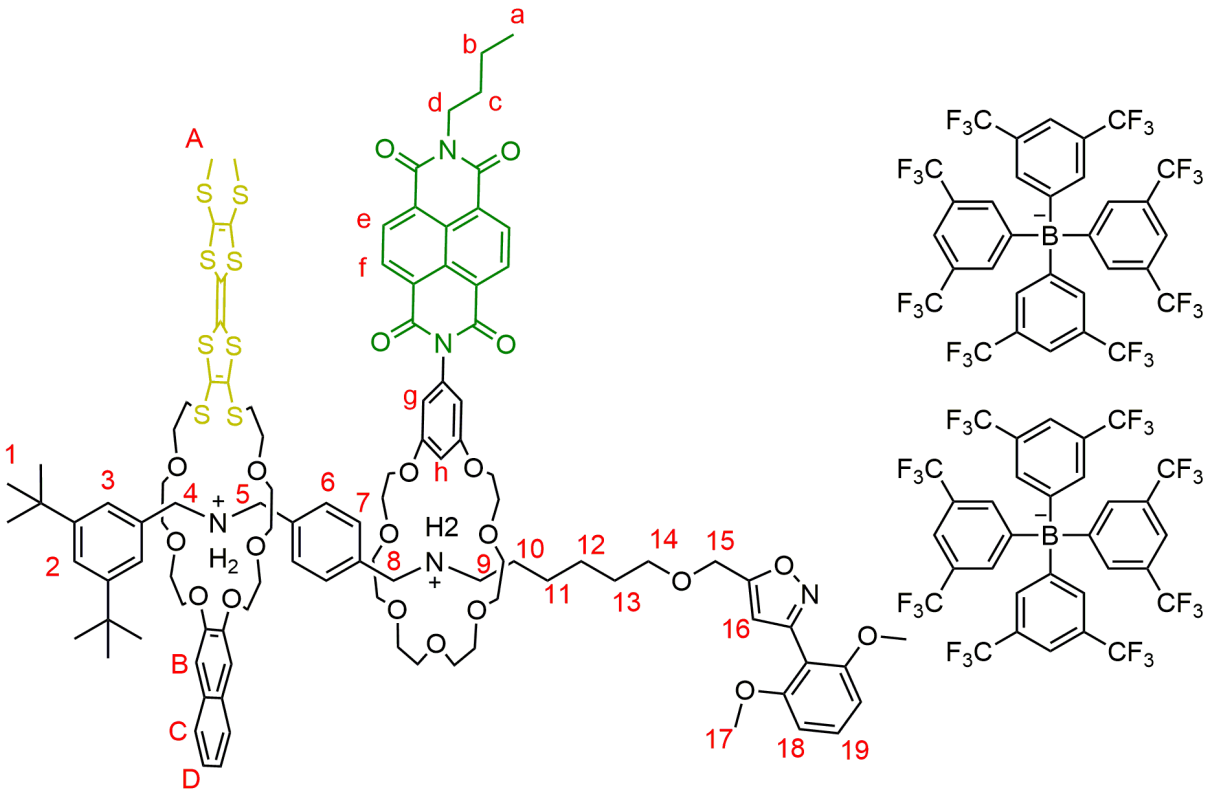

RTTFC8NDIC7

The axle **Ax** (60 mg, 27 µmol, 1.00 equiv.) and **TTFC8** (18 mg, 24 µmol, 0.90 equiv.) were dissolved in CH_2Cl_2 (3 mL) and stirred for 30 min. **NDIC7** (110 mg, 163 µmol, 6.00 equiv.) was added and stirred for another 2 days. Finally, N-oxide **St1** (7 mg, 41 µmol, 1.50 equiv.) was added to the mixture and stirred for an additional 24 h at 35° C. The crude product was purified via preparative thin-layer chromatography (SiO_2, CH_2Cl_2/EtOH 50:1, R_f ~ 0.25 in CH_2Cl_2/EtOH 100:1) The product was obtained as a greenish brown oil (27 mg, 7 µmol, 29%).

^{1}H NMR (700 MHz, CD_2Cl_2) δ =1.00 (t, J = 7.4 Hz, 3H, a), 1.27 (s, 18H, 1), 1.34 – 1.38 (m, 4H, 11,12), 1.42 – 1.45 (m, 2H, 10), 1.45 – 1.49 (m, 2H, b), 1.58 – 1.62 (m, 2H, 13), 1.74 – 1.76 (m, 2H, c), 2.40 (s, 6H, A), 2.96 – 3.03 (m, 4H, O-CH_2-CH_2), 3.07 – 3.19 (m, 10H, O-CH_2-CH_2, 9), 3.26 – 3.30 (m, 2H, O-CH_2-CH_2), 3.32 – 3.35 (m, 2H, O-CH_2-CH_2), 3.38 – 3.42 (m, 2H, O-CH_2-CH_2), 3.46 – 3.50 (m, 4H, O-CH_2-CH_2), 3.50 – 3.56 (m, 10H, O-CH_2-CH_2, 14), 3.58 – 3.67 (m, 16H, O-CH_2-CH_2,), 3.67 – 3.69 (m, 4H, O-CH_2-CH_2), 3.70 – 3.71 (s, 6H, 17), 3.73 – 3.77 (m, 6H, O-CH_2-CH_2, 8), 3.79 – 3.90 (m, 8H, O-CH_2-CH_2,), 4.04 – 4.08 (m, 2H, O-CH_2-CH_2), 4.16 – 4.22 (m, 6H, O-CH_2-CH_2, d), 4.22 – 4.28 (m, 6H, O-CH_2-CH_2), 4.53 (s, 2H, 15), 4.71 – 4.74 (m, 2H, 4/5), 4.90 – 4.94 (m, 2H, 4/5), 6.23 (s, 1H, 16), 6.43 (t, J = 2.3 Hz, 1H, h), 6.56 (d, J = 8.4 Hz, 18H), 6.61 (d, J = 2.2 Hz, 2H, g), 6.94 – 6.97 (m, 4H, B, 6/7), 7.27 – 7.37 (m, 5H, D, 19, NH_2), 7.36 – 7.38 (m, 2H, 6/7), 7.44 (d, J = 1.8 Hz, 2H, 3), 7.54 (t, J = 1.8 Hz, 1H, 2), 7.56 (s_{br}, 8H, $BArF_{24}$), 7.60 – 7.64 (m, 2H, C), 7.72 (s_{br}, 16H, $BArF_{24}$), 7.99 (s_{br}, 2H, NH_2),

8.69 – 8.77 (m, 4H, e,f) ppm. **^{13}C NMR** (176 MHz, CD_2Cl_2) δ = 8.9, 14.0, 14.3, 19.3, 20.8, 23.1, 25.2, 26.1, 26.2, 26.7, 26.8, 26.9, 27.6, 29.5, 29.8, 29.9, 29.9, 30.1, 30.5, 31.4, 31.6, 32.0, 32.3, 33.5, 34.5, 35.4, 37.2, 41.1, 47.1, 48.4, 51.1, 56.2, 63.8, 67.8, 68.0, 68.9, 70.0, 70.2, 70.6, 70.8, 70.9, 71.3, 71.4, 71.9, 103.7, 104.4, 106.5, 107.2, 108.0, 108.2, 108.6, 109.2, 114.7, 117.9, 122.7, 123.5, 124.2, 124.8, 125.8, 126.1, 126.5, 126.7, 126.9, 127.3, 127.4, 127.7, 128.0, 128.8, 129.0, 129.2, 129.4, 129.5, 129.7, 130.1, 130.3, 130.5, 130.6, 130.7, 131.1, 131.4, 131.5, 133.1, 133.5, 135.2, 138.5, 146.6, 152.9, 157.2, 158.9, 159.7, 159.9, 161.7, 162.0, 162.3, 162.6, 163.1, 163.3, 168.0 ppm. **HRMS (acetonitrile):**m/z calcd. for $[C_{107}H_{135}N_5O_{21}S_8]^{++}$: 1041.3719 $[M]^{++}$, found: 1041.3729.

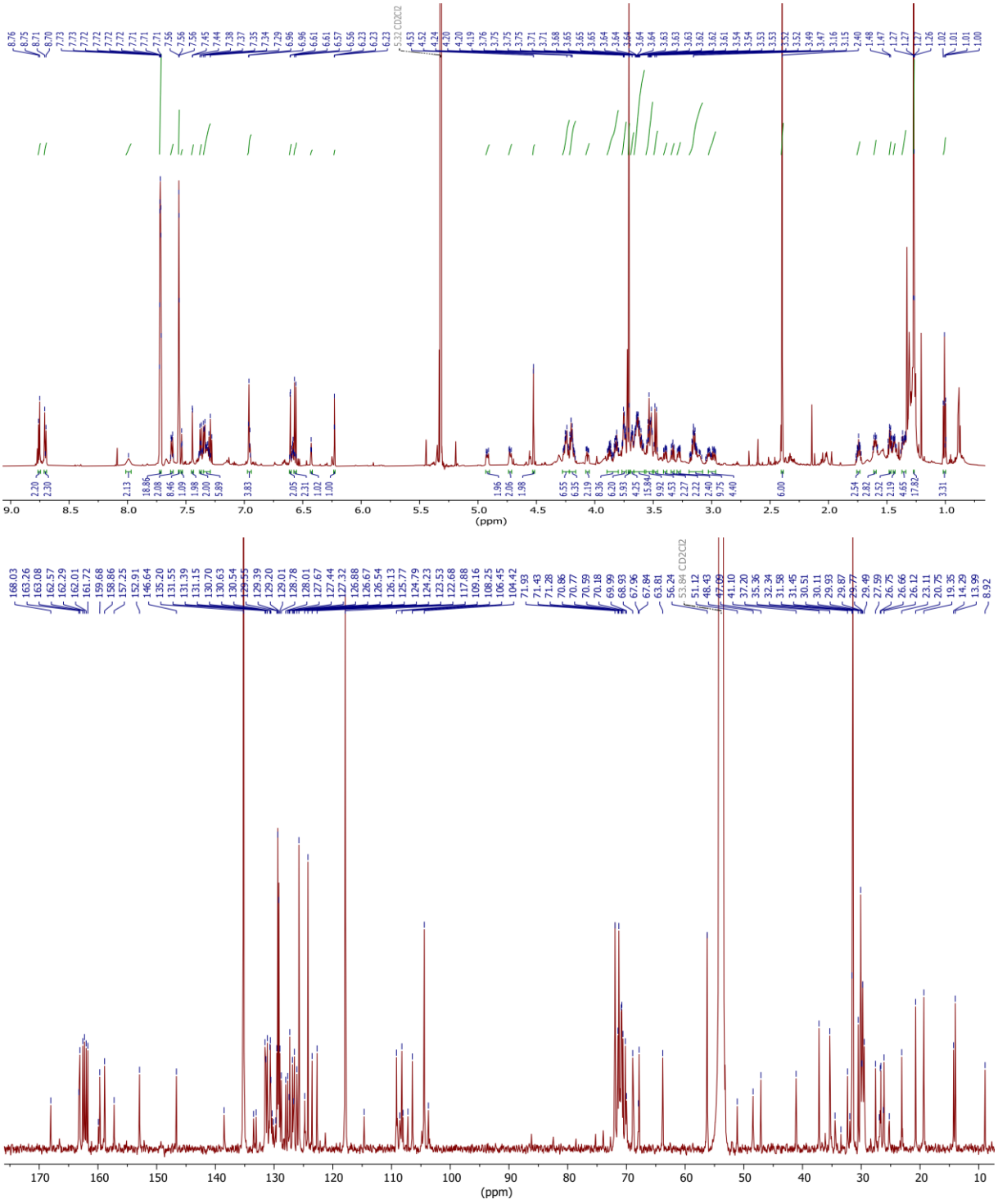

Fig. S12 ^{1}H (top) and ^{13}C (bottom) NMR spectra (700/176 MHz, CD_2Cl_2, 298 K) of [3]rotaxane **RTTFC8NDIC7**

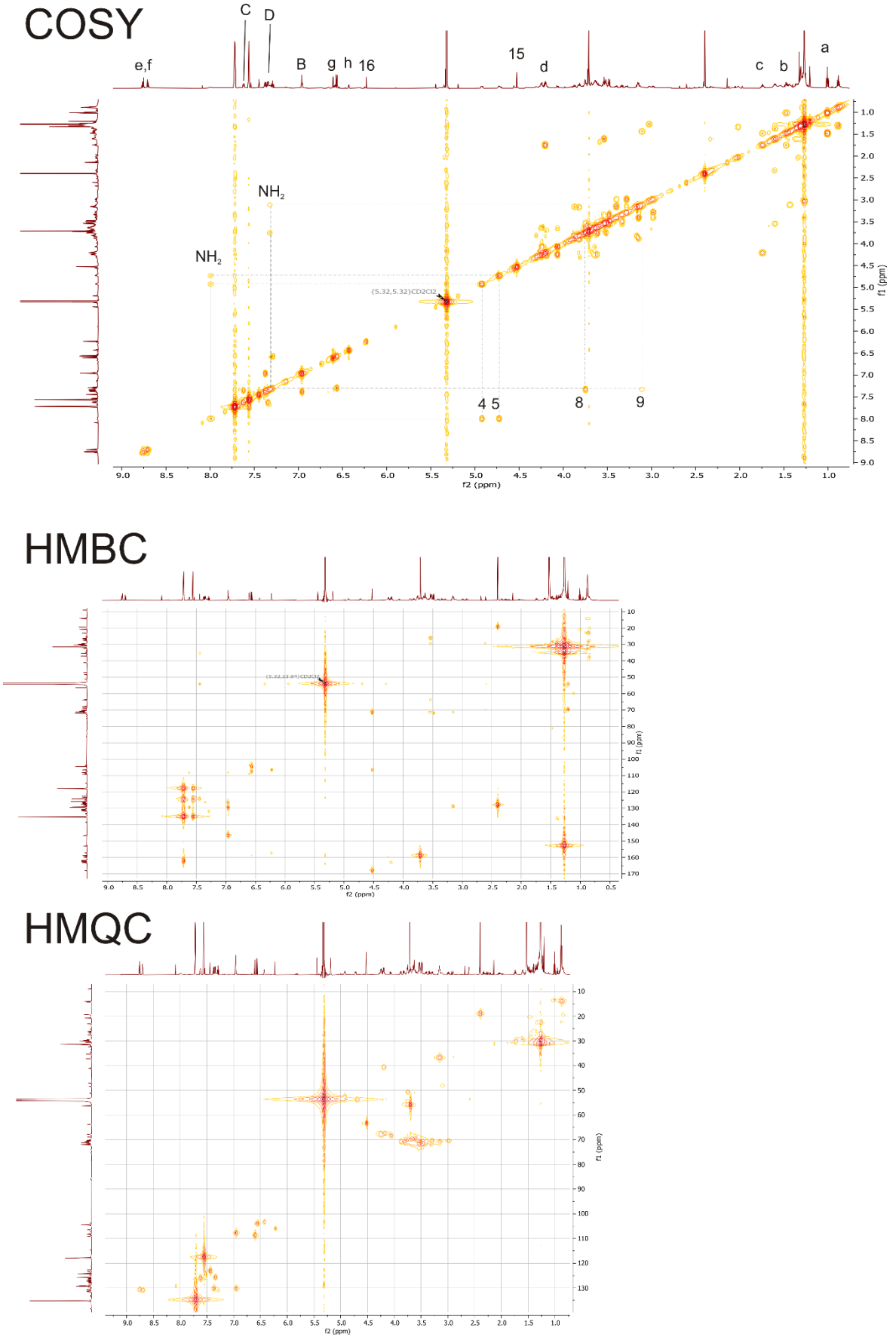

Fig. S13 COSY (top), HMBC (center) and HMQC (bottom) NMR spectra (700/176 MHz, CD_2Cl_2, 298 K) of [3]rotaxane **RTTFC8NDIC7**

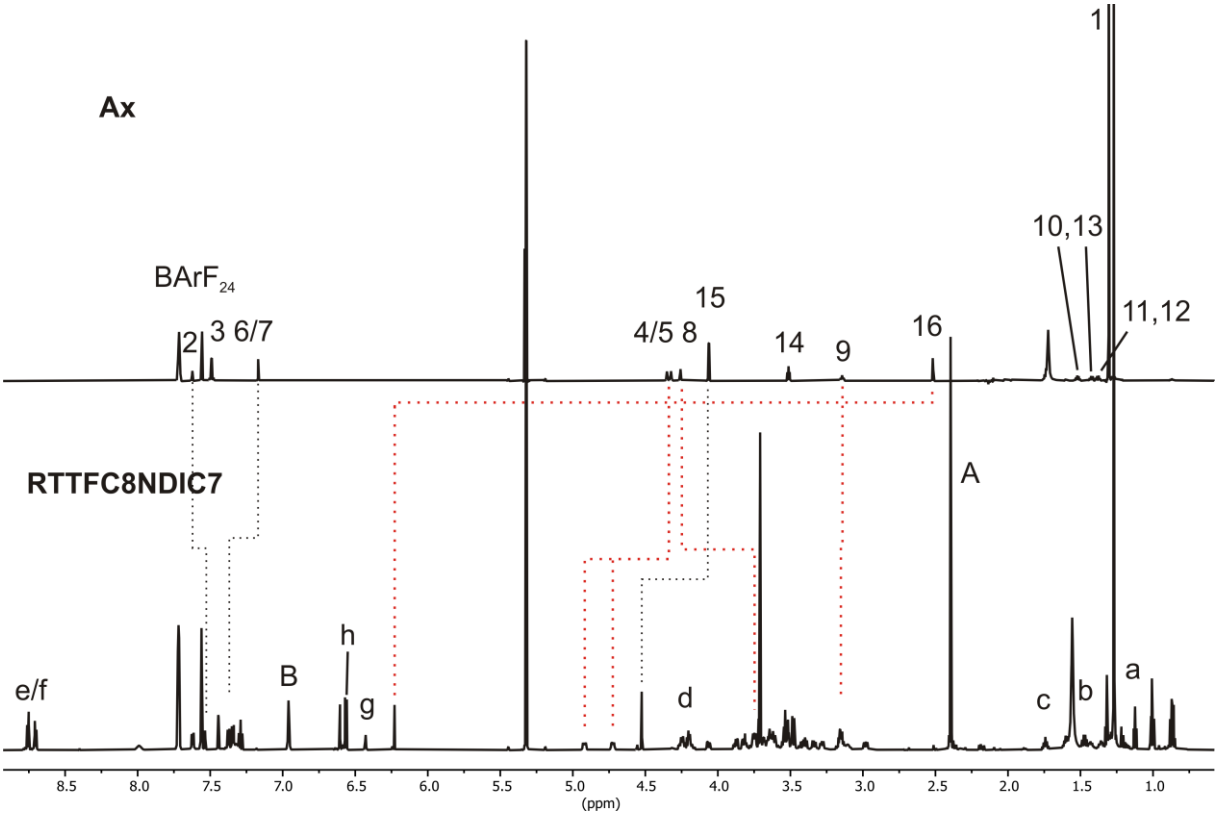

Fig. S14 [3]rotaxane **RTTFC8NDIC7** (bottom) and axle **Ax** (top) NMR spectra (700 MHz, CD_2Cl_2, 298 K).

[3]rotaxane RNDIC8BC7

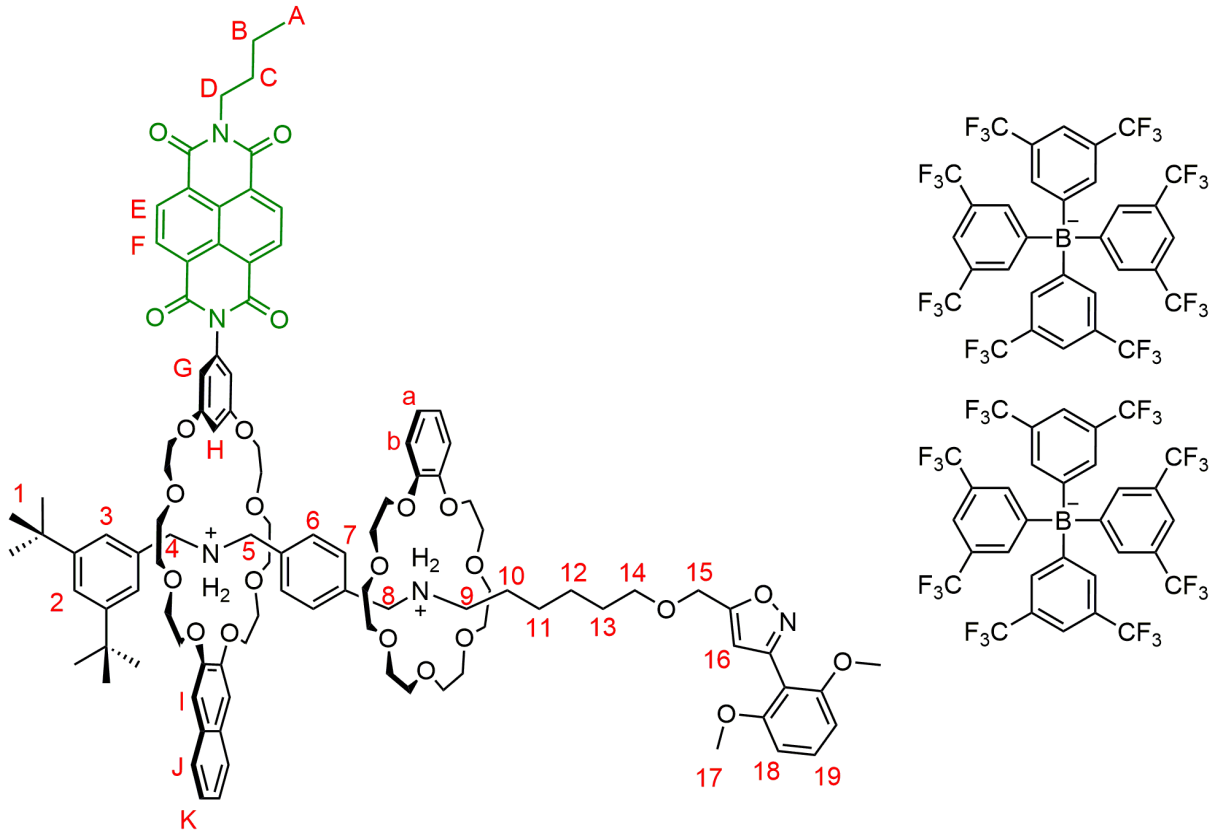

RNDIC8BC7

The axle **Ax** (60 mg, 27 µmol, 1.00 equiv.) and macrocycle **NDIC8** (20 mg, 25 µmol, 0.90 equiv.) were dissolved in CH_2Cl_2 (3 mL) and stirred for 30 min, then macrocycle **BC7** (15 mg, 41 µmol, 1.50 equiv.) was added. After 3 days, stopper **St1** (7 mg, 41 µmol, 1.50 equiv.) was added and the mixture was heated to 35°C for 24 h. Then, the mixture was purified by preparative TLC (SiO_2, 2000 µm, CH_2Cl_2/ACN 10:1, R_f ~ 0.4 in CH_2Cl_2/ACN 10:1) to obtain the desired product **RNDIC8BC7** (17 mg, 5 µmol, 20 %) as yellow oil.

^{1}H NMR (700 MHz, CD_2Cl_2) δ = 0.99 (t, J = 7.4 Hz, 3H, A), 1.24 (s, 18H, 1), 1.33 – 1.40 (m, 6H, 10,11,12),1.43 – 1.46 (m, 4H, B, 13), 1.68 – 1.75 (m, 2H, C), 3.12 – 3.17 (m, 4H, O-CH_2-CH_2), 3.25 – 3.39 (m, 16H, 9, O-CH_2-CH_2), 3.41 – 3.46 (m, 5H, 14, O-CH_2-CH_2), 3.46 – 3.52 (m, 5H, O-CH_2-CH_2), 3.52 – 3.62 (m, 10H, O-CH_2-CH_2), 3.62 – 3.70 (m, 10H, O-CH_2-CH_2), 3.73 (s, 6H, 17), 3.75 – 3.78 (m, 1H, O-CH_2-CH_2), 3.78 – 3.83 (m, 3H, O-CH_2-CH_2), 3.85 - 3.89 (m, 2H, O-CH_2-CH_2), 3.96 – 4.04 (m, 6H, 8, O-CH_2-CH_2), 4.04 – 4.08 (m, 2H, O-CH_2-CH_2), 4.08 – 4.12 (m, 3H, O-CH_2-CH_2), 4.12 – 4.16 (m, 2H, O-CH_2-CH_2), 4.17 – 4.20 (m, 2H, D), 4.21 – 4.27 (m, 3H, O-CH_2-CH_2), 4.53 (s, 2H, 15), 4.60 – 4.64 (m, 4H, 4,5), 6.50 (s, 1H, 16), 6.56 (d, J = 2.2 Hz, 2H, G), 6.63 (t, J = 2.2 Hz, 1H, H), 6.69 (d, J = 8.5 Hz, 2H, 18), 6.78 - 6.82 (m, 2H, a/b), 6.90 – 6.95 (m, 6H, a/b, I, 6/7), 7.22 (s_{br}, 2H, NH_2), 7.29 (dd, J = 8.8, 2.5 Hz, 2H, 6/7), 7.33 – 7.35 (m, 2H, K), 7.37 (t, J = 8.4 Hz, 1H, 19), 7.41 (d, J = 1.8 Hz, 2H, 3), 7.51 (t, J = 1.8

Hz, 1H, 2), 7.55 (s_{br}, 8H, $BArF_{24}$), 7.58 - 7.62 (m, 2H, J), 7.71 (s_{br}, 16H, $BArF_{24}$), 8.00 (s_{br}, 2H, NH_2), 8.67 – 8.80 (m, 4H, E,F) ppm. **^{13}C NMR** (176 MHz, CD_2Cl_2) δ = 1.2, 14.0, 14.3, 20.7, 25.9, 27.0, 27.1, 29.7, 30.1, 30.5, 31.3, 31.4, 32.3, 35.3, 41.2, 47.7, 50.3, 52.4, 57.2, 63.8, 68.4, 68.4, 68.8, 69.5, 70.0, 70.9, 71.1, 71.2, 71.6, 71.7, 71.8, 77.6, 77.7, 77.9, 104.4, 106.2, 106.7, 107.0, 108.1, 108.9, 112.1, 117.9, 122.0, 122.7, 123.9, 124.2, 124.9, 125.8, 126.7, 126.9, 127.3, 127.6, 128.1, 129.3, 130.3, 130.4, 130.7, 131.3, 131.5, 132.6, 134.7, 135.2, 137.9, 146.8, 147.0, 152.8, 157.9, 158.5, 160.6, 162.1, 163.3, 164.8, 168.9 ppm. **HRMS (acetonitrile):** m/z calcd. for $[C_{105}H_{133}N_5O_{23}]^{++}$: 916.4707 $[M]^{++}$, found: 916.4714

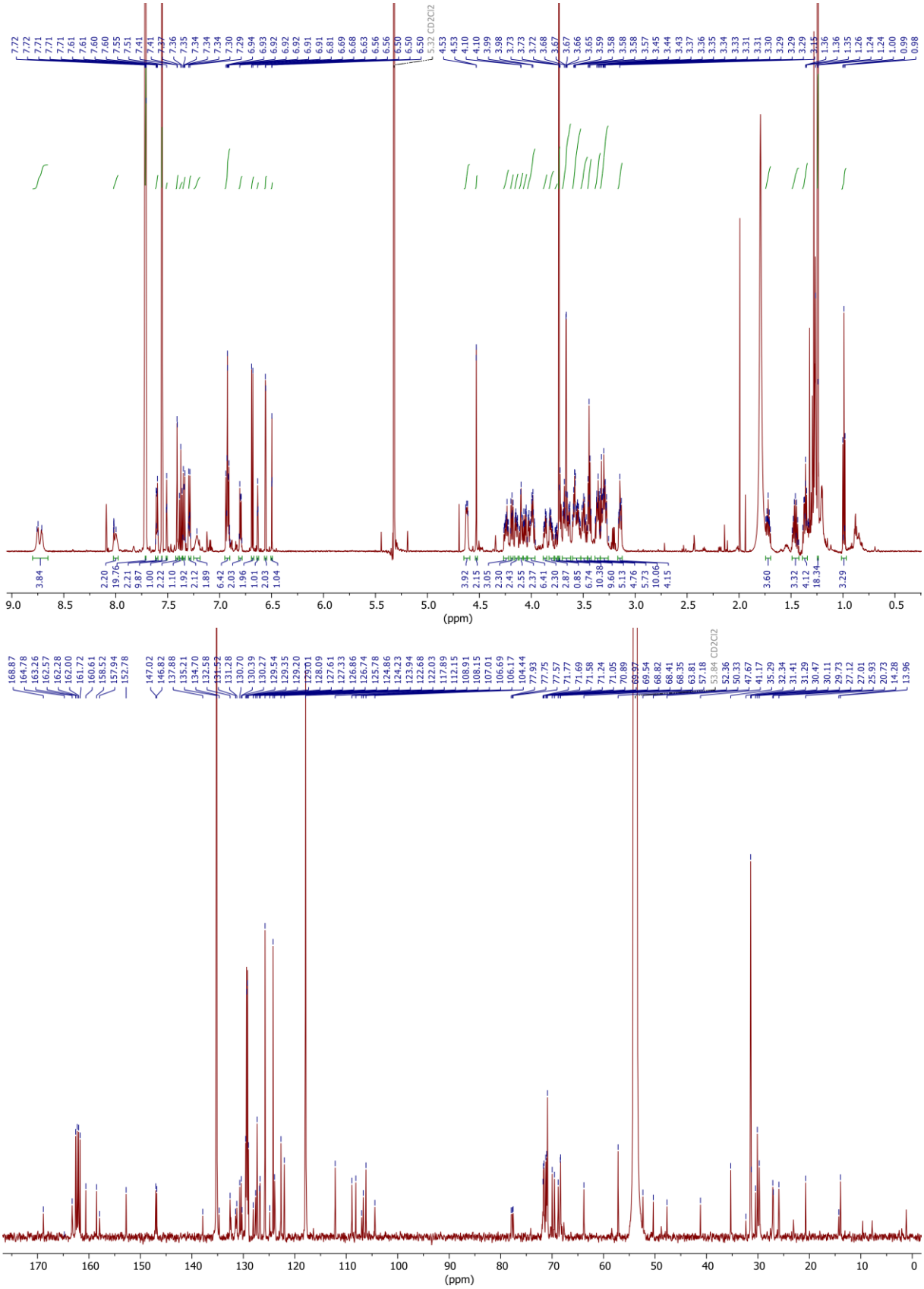

Fig. S15 ^{1}H (top) and ^{13}C (bottom) NMR spectra (700/176 MHz, CD_2Cl_2, 298 K) of [3]rotaxane **RNDIC8BC7**.

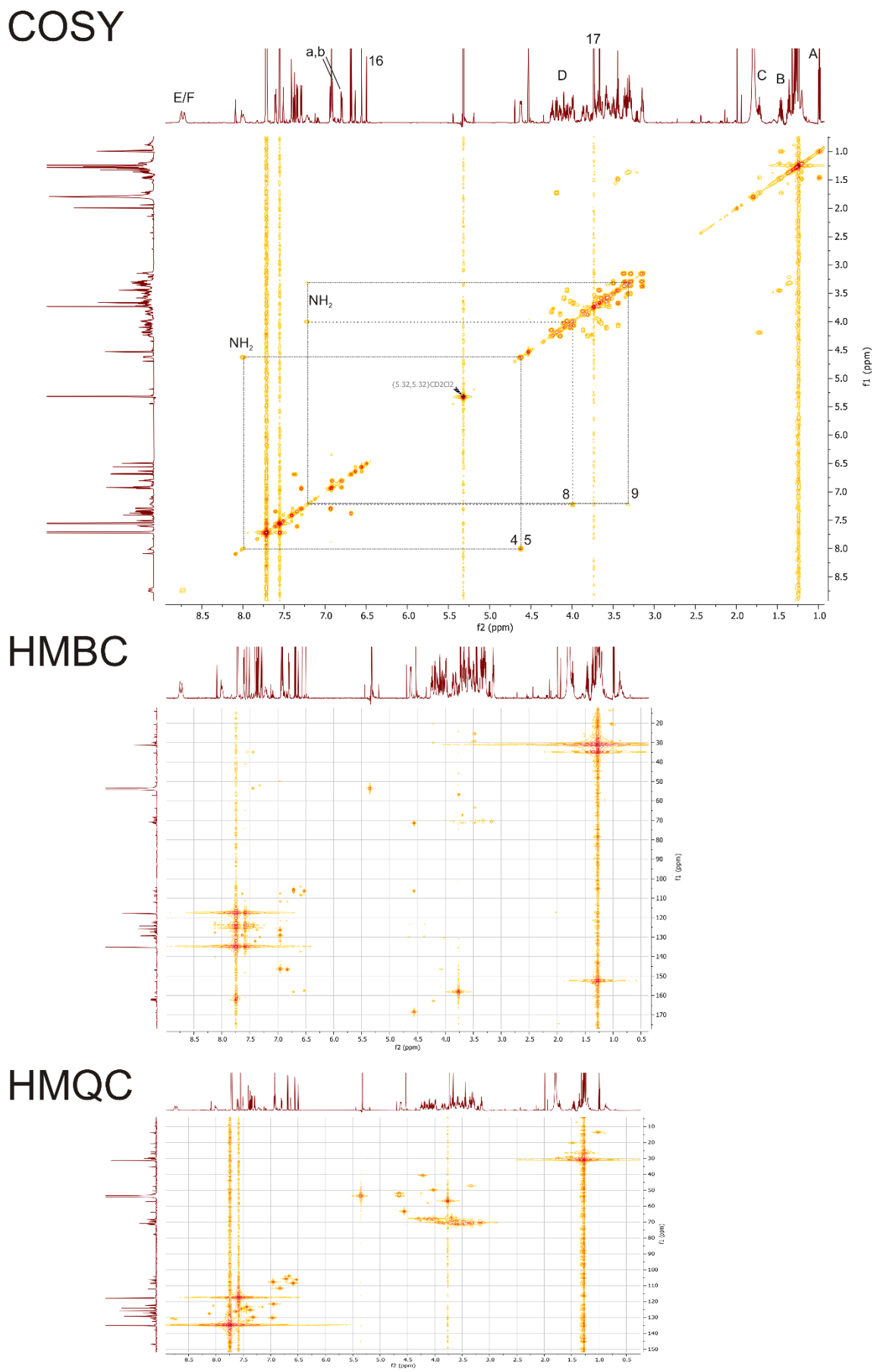

Fig. S16 COSY (top), HMBC (center) and HMQC (bottom) NMR spectra (700/176 MHz, CD_2Cl_2, 298 K) of [3]rotaxane **RNDIC8BC7**.

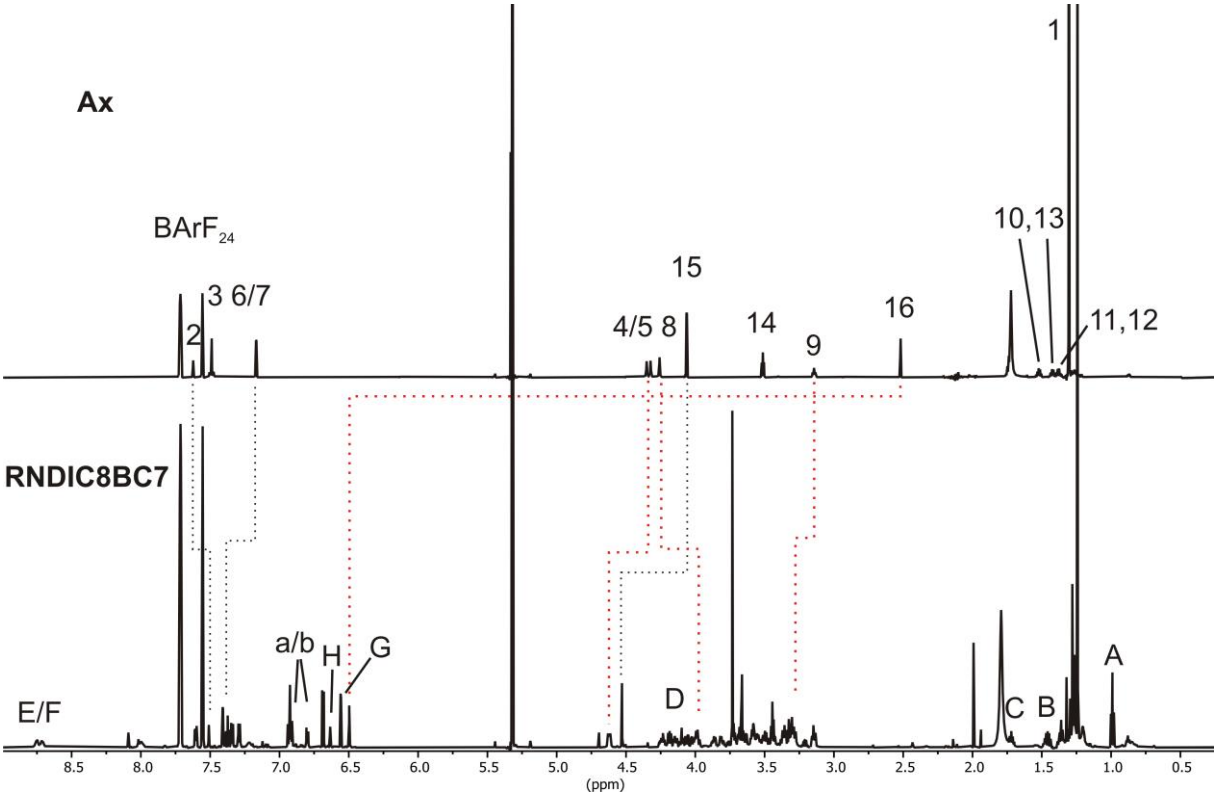

Fig. S17 [3]rotaxane **RNDIC8BC7** (bottom) and axle **Ax** (top) NMR spectra (700 MHz, CD_2Cl_2, 298 K).

[3]rotaxane RDBC8NDIC7

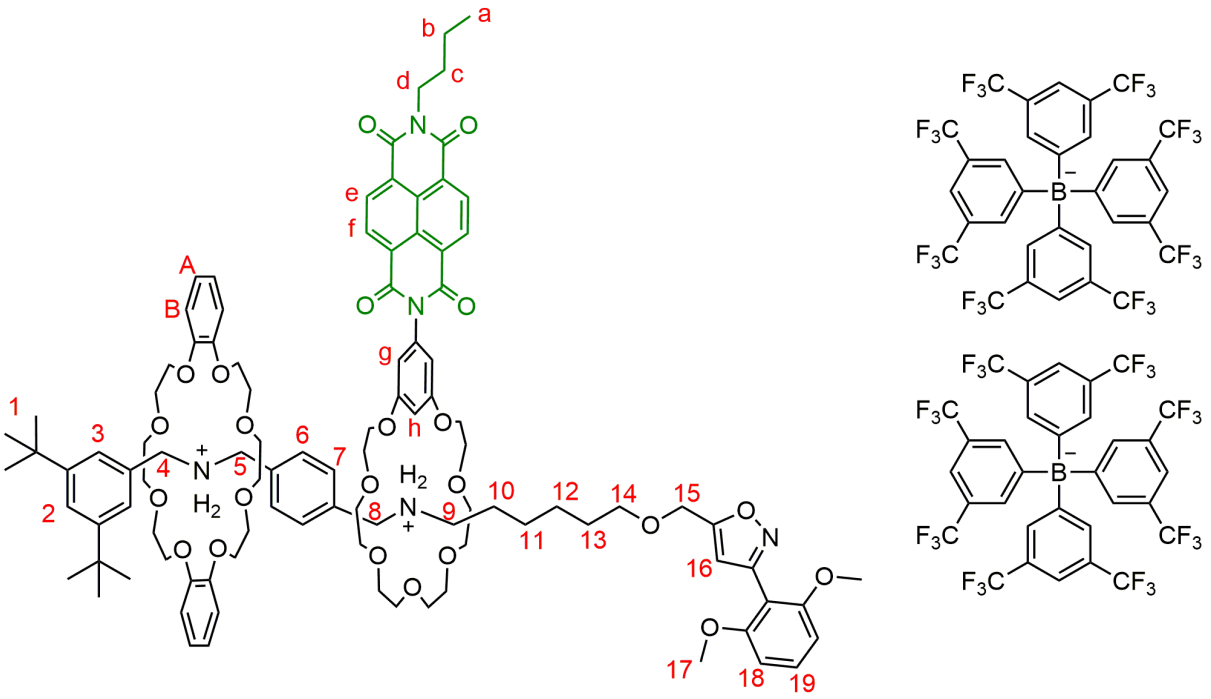

RDBC8NDIC7

The axle **Ax** (60 mg, 27 µmol, 1.00 equiv.) and macrocycle **DBC8** (11 mg, 25 µmol, 0.90 equiv.) were dissolved in CH_2Cl_2 (3 mL) and stirred for 30 min, then macrocycle **NDIC7** (110 mg, 163 µmol, 6.00 equiv.) was added. After 2 days, stopper **St1** (7 mg, 41 µmol, 1.50 equiv.) was added and the mixture was heated to 35°C for 24 h. Then, the mixture was purified by preparative TLC (SiO_2, 2000 µm, CH_2Cl_2/ACN 10:1, R_f ~ 0.4 in CH_2Cl_2/ACN 10:1) to obtain the desired product **RDBC8NDIC7** (12 mg, 3 µmol, 14 %) as yellow oil.

^{1}H NMR (700 MHz, CD_2Cl_2) δ = 0.99 (t, J = 7.4 Hz, 3H, a), 1.24 (s, 18H, 1), 1.33 – 1.38 (m, 1H, c, 11, 12), 1.42 – 1.51 (m, 2H, 10, b), 1.65 (tt, J = 14.3, 6.3 Hz, 2H, 13), 1.69 – 1.75 (m, 2H, c), 2.96 – 3.00 (m, 2H, O-CH_2-CH_2), 3.09 – 3.15 (m, 4H, 9, O-CH_2-CH_2), 3.24 – 3.29 (m, 2H, O-CH_2-CH_2), 3.34 – 3.43 (m, 6H, O-CH_2-CH_2), 3.48 – 3.52 (m, 6H, O-CH_2-CH_2), 3.53 – 3.62 (m, 7H, 14, O-CH_2-CH_2), 3.63 – 3.67 (m, 5H, O-CH_2-CH_2), 3.71 (s, 6H, 17), 3.72 – 3.80 (m, 12H, O-CH_2-CH_2), 4.02 – 4.11 (m, 10H, 8, O-CH_2-CH_2), 4.16 – 4.20 (m, 2H, d), 4.29 – 4.33 (m, 4H, O-CH_2-CH_2), 4.55 (s, 2H, 15), 4.71 – 4.75 (m, 2H, 4/5), 4.79 – 4.83 (m, 2H, 4/5), 6.28 (s, 1H, 16), 6.56 (d, J = 8.5 Hz, 2H, 18), 6.62 (d, J = 2.2 Hz, 2H, g), 6.68 (t, J = 2.3 Hz, 1H, h), 6.74 (m, 4H, A/B), 6.85 (m, 4H, A/B), 6.96 – 7.00 (m, 2H, 6/7), 7.24 – 7.30 (m, 3H, 19, 6/7), 7.33 (d, J = 1.8 Hz, 2H, 3), 7.39 – 7.44 (m, 2H, NH_2), 7.49 (t, J = 1.8 Hz, 1H, 2), 7.54 – 7.57 (m, 8H, $BArF_{24}$), 7.60 (s_{br}, 2H, NH_2), 7.69 – 7.74 (m, 16H, $BArF_{24}$), 8.67 – 8.78 (m, 4H, e/f) ppm. **^{13}C NMR** (176 MHz, CD_2Cl_2) δ = 14.0, 14.3, 19.5, 20.7, 23.1, 26.2, 26.7, 26.9, 29.8, 29.9, 30.1, 30.5, 31.4, 32.3, 35.3, 36.7, 41.1, 48.5, 49.8, 51.4, 52.5, 56.3, 63.8, 68.0, 68.3, 70.6,

70.8, 71.1, 71.2, 71.5, 71.9, 72.0, 103.9, 104.6, 106.6, 107.1, 109.1, 112.9, 117.9, 122.0, 122.7, 123.8, 124.2, 124.3, 125.8, 126.9, 127.3, 127.6, 129.3, 130.4, 130.6, 131.2, 131.4, 131.6, 132.7, 133.9, 135.2, 138.6, 147.9, 152.5, 157.3, 158.8, 159.8, 162.2, 163.1, 163.2, 168.0 ppm. **HRMS (acetonitrile):** m/z calcd. for $[C_{101}H_{131}N_5O_{23}]^{++}$: 891.4629 $[M]^{++}$, found: 891.4639.

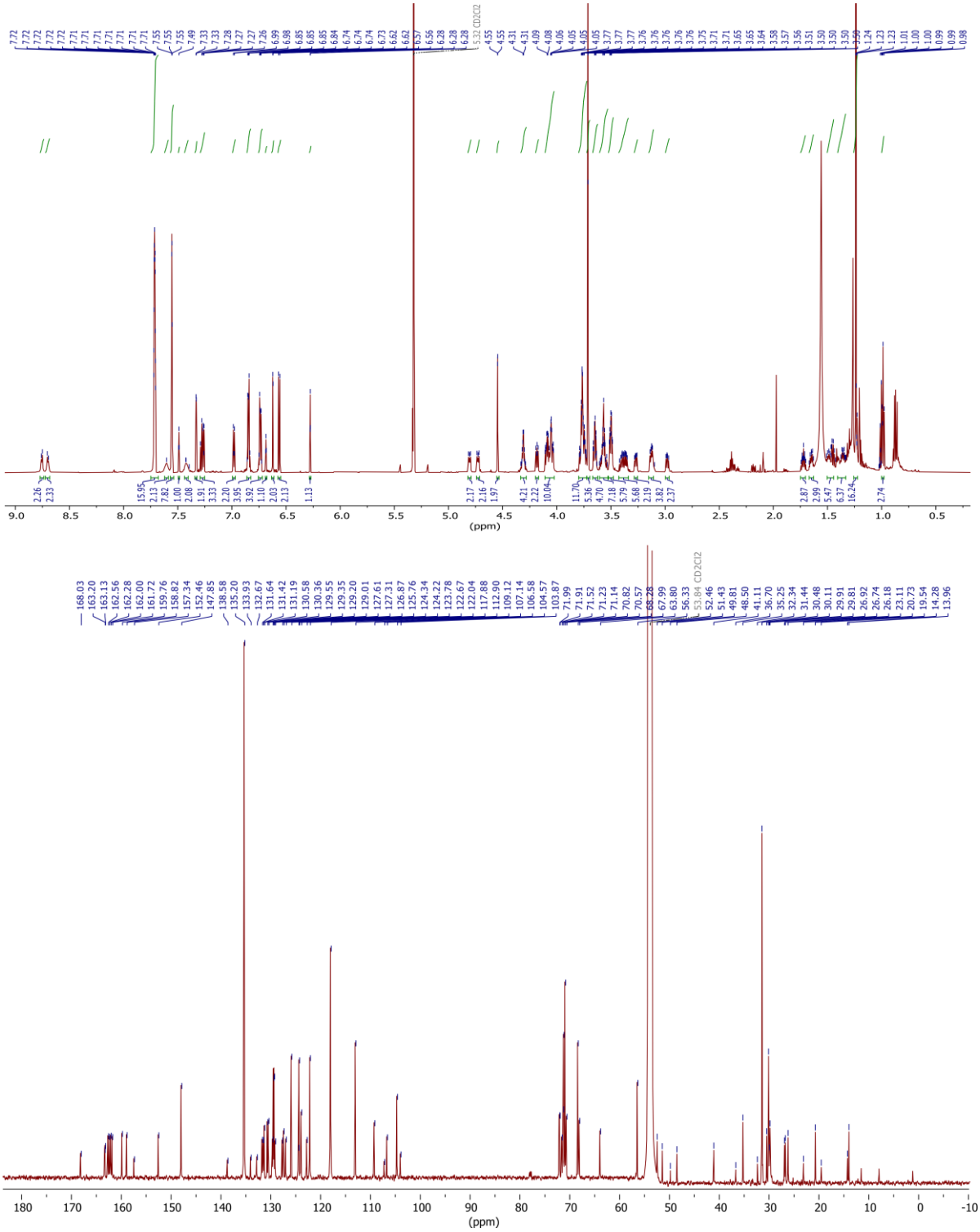

Fig. S18 ^{1}H (top) and ^{13}C (bottom) NMR spectra (700/176 MHz, CD_2Cl_2, 298 K) of [3]rotaxane **RDBC8NDIC7**.

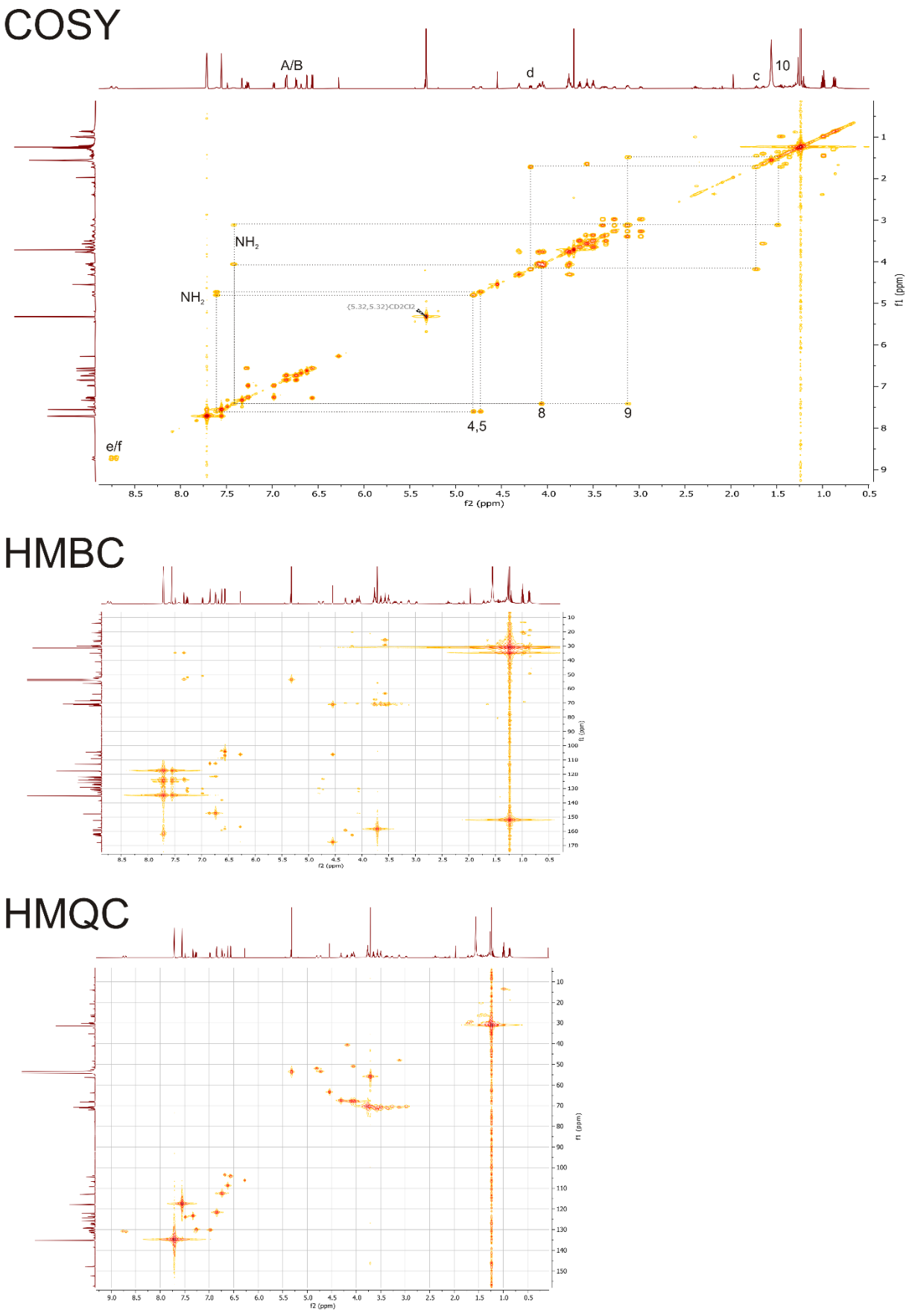

Fig. S19 COSY (top), HMBC (center) and HMQC (bottom) NMR spectra (700/176 MHz, CD_2Cl_2, 298 K) of [3]rotaxane **RDBC8NDIC7**.

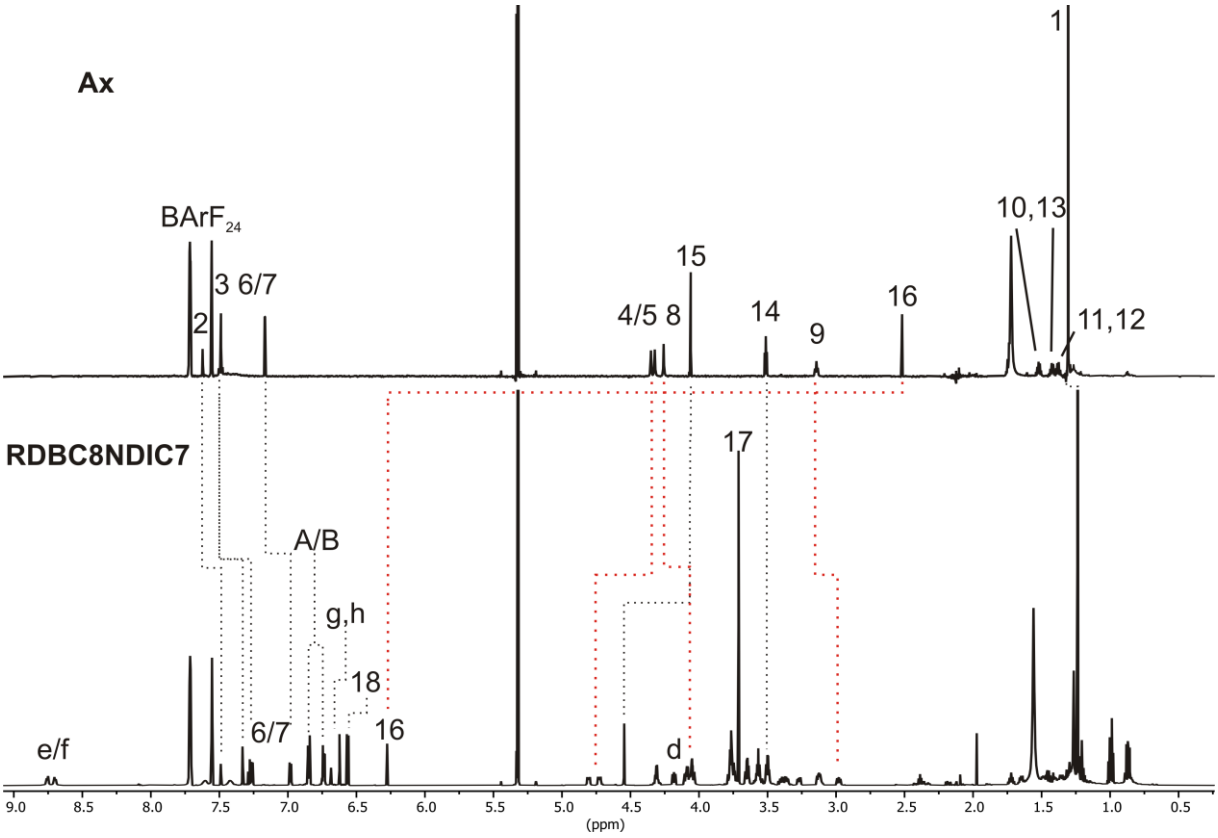

Fig. S20 [3]rotaxane **RDBC8NDIC7** (bottom) and axle **Ax** (top) NMR spectra (700 MHz, CD_2Cl_2, 298 K).

2. Isothermal titration calorimetry

ITC titrations were carried out in dry 1,2-dichloroethane (DCE) at 298 K on a TAM III microcalorimeter (Waters GmbH, TA Instruments, Eschborn, Germany). In a typical experiment, an 800 µL solution of crown ether was placed in the sample cell at a concentration of 1.1 mM, and 260 µL of a solution of the ammonium salt (8.0 mM) were put into the syringe. The titrations consisted of 32 consecutive injections of 8 µL each with a 20 min interval between injections. Heats of dilution were determined by titration of ammonium salt solutions into the sample cell containing blank solvent and were subtracted from each data set. The heat flow generated in the sample cell is measured as a differential signal between sample and reference cell. Hence, an exothermic event results in a positive and an endothermic in a negative heat flow. The data were analysed using the instrument's internal software package and fitted with a 1:1 binding model. Each titration was conducted at least three times and the measured values for *K* and Δ*H* were averaged.

Instead of divalent axle **Ax**, two monovalent model compounds **A1** and **A2** were titrated to the five macrocycles (Figure S21) of this study. Hexafluorophosphate PF_6^- was used as counter ion, as the binding constants are too high with $BArF_{24}^-$ anions to be determined with ITC. Earlier studies showed that the binding constant is roughly 15 – 20 times higher with $BArF_{24}$-anions and that trends are similar for both counterions.[3]

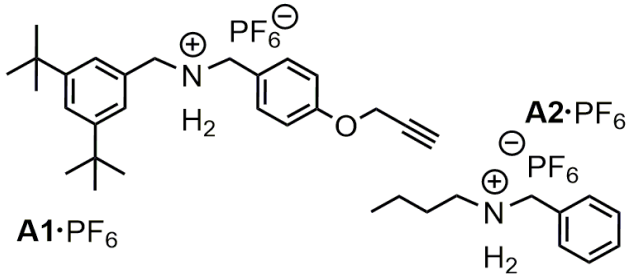

Fig. S21 Chemical structures of the monovalent model ammonium axles used to determine thermodynamic binding data for all five macrocycles.

Table S1. Thermodynamic binding data of different crown ether/secondary ammonium axle complexes obtained by ITC titrations in 1,2-dichloroethane at 298 K.

axle	macrocycle	K_a / 10^3 M^{-1}	ΔG^0 / kJ/mol	ΔH^0 / kJ/mol	$T\Delta S^0$ / kJ/mol
A2·PF_6	**BC7**[a]	1200 ± 100	-34.6 ± 0.2	-63.0 ± 0.5	-28.3 ± 0.7
	NDIC7	7.0 ± 1.0	-22.1 ± 0.2	-51.2 ± 2.0	-29.2 ± 2.2
A2·PF_6	**DBC8**[a]	480 ± 70	-32.4 ± 0.3	-60.4 ± 1.5	-28.0 ± 1.8
	NDIC8[a]	13 ± 1	-23.4 ± 0.2	-48.1 ± 1.0	-24.7 ± 1.2
	TTFC8[a]	7.0 ± 1.0	-22.1 ± 0.2	-50.3 ± 1.0	-28.3 ± 1.2
A1·PF_6	**DBC8**[a]	1300 ± 100	-34.8 ± 0.3	-60.9 ± 2.0	-26.1 ± 2.3
	NDIC8[a]	49 ± 6	-26.7 ± 0.3	-46.6 ± 2.0	-19.9 ± 2.3
	TTFC8[a]	33 ± 3	-25.7 ± 0.2	-51.5 ± 0.9	-25.9 ± 1.1

[a] Taken from a previous report.[3]

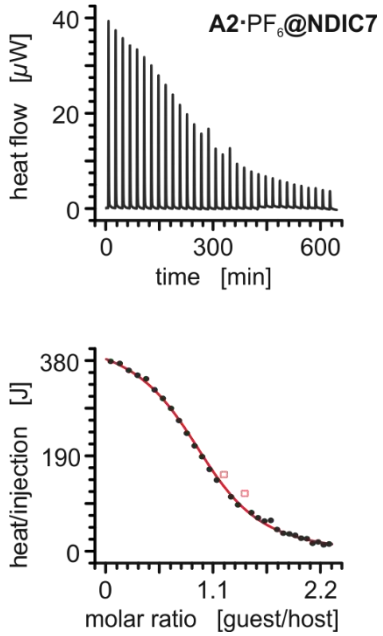

Fig. S22 Titration plots (heat flow versus time and heat/volume versus guest/host ratio) obtained from ITC experiments at 298 K in 1,2-dichloroethane: vial: **NDIC7**, syringe: axle **A2**·PF_6. Points marked with non-filled squares were not considered in the fitting process. Titration plots for the other combinations are part of a previous report. [3]

3. Heteropseudo[3]rotaxane ^{1}H NMR experiments

Equimolar solutions of divalent axle **Ax** and macrocycles gave complex ^{1}H NMR spectra. When a crown ether is bound to ammonium units, the methylene protons (H_4, H_5, H_8 and H_9) exhibit unambiguous cross coupling signals in the COSY spectrum to the corresponding ammonium protons. The characteristic shifts of these methylene protons were used to identify the pseudorotaxane species present in solution and the integrals of these signals were used to calculate the ratio of the species, which is given in percent of all identified pseudorotaxane species. Due to imprecise integration, the given percentages have experimental errors of 5%.

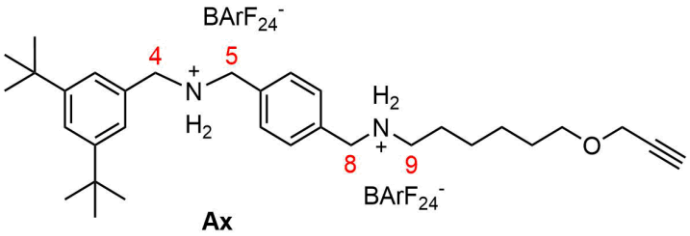

Ax

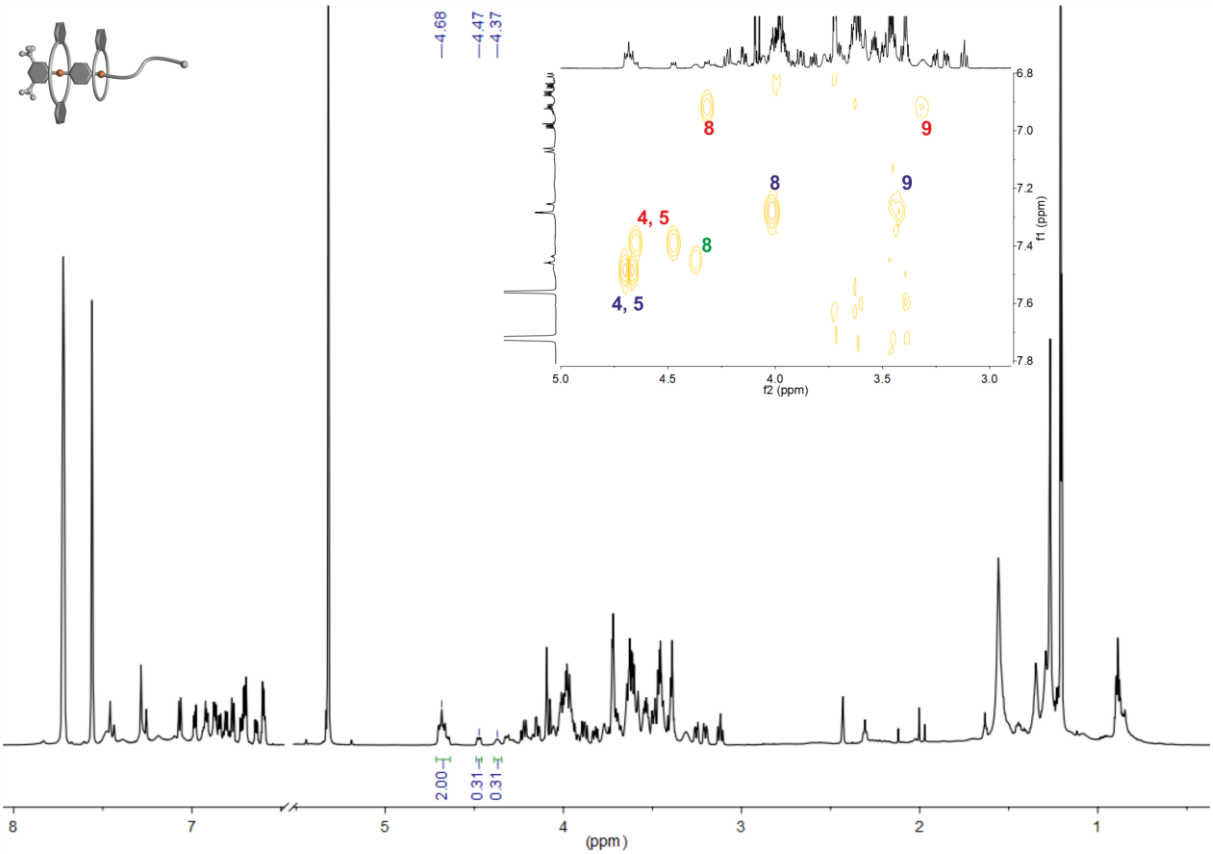

Fig. S23 ^{1}H NMR and partial COSY spectra (700 MHz, CD_2Cl_2, 298 K, 5 mM) of an equimolar solution of **Ax**, **DBC8** and **BC7** 16 d after mixing. Signals of protons corresponding to the heteropseudo[3]rotaxane **PRDBC8BC7** (58%) are labeled in blue, those corresponding to the homopseudo[3]rotaxane **PRDBC8DBC8** (21%) in red and those of the pseudo[2]rotaxane **PRBC7** (21%) in green.

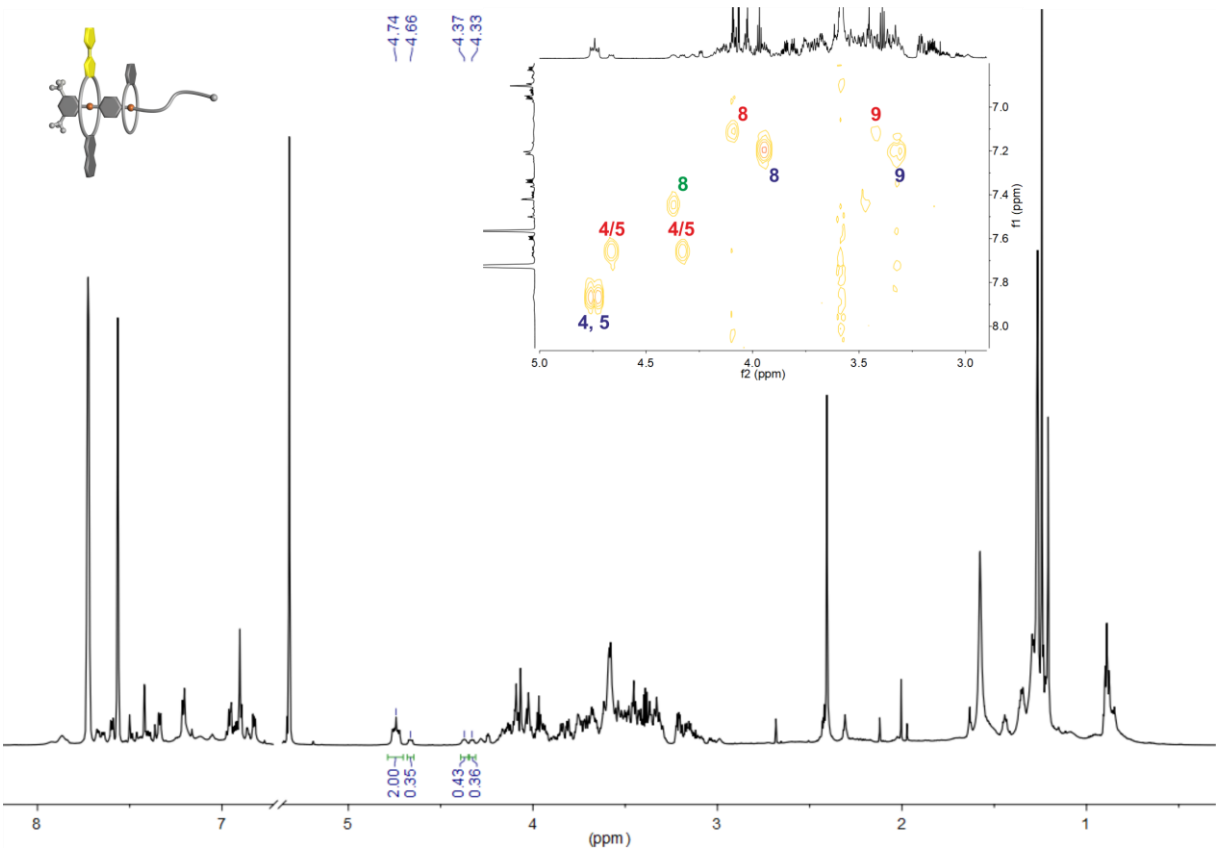

Fig. S24 ^{1}H NMR and partial COSY spectra (700 MHz, CD_2Cl_2, 298 K, 5 mM) of an equimolar solution of **Ax**, **TTFC8** and **BC7** 16 d after mixing. Signals of protons corresponding to the heteropseudo[3]rotaxane **PRTTFC8BC7** (56%) are labeled in blue, those corresponding to the homopseudo[3]rotaxane **PRTTFC8TTFC8** (20%) in red and those of the pseudo[2]rotaxane **PRBC7** (24%) in green.

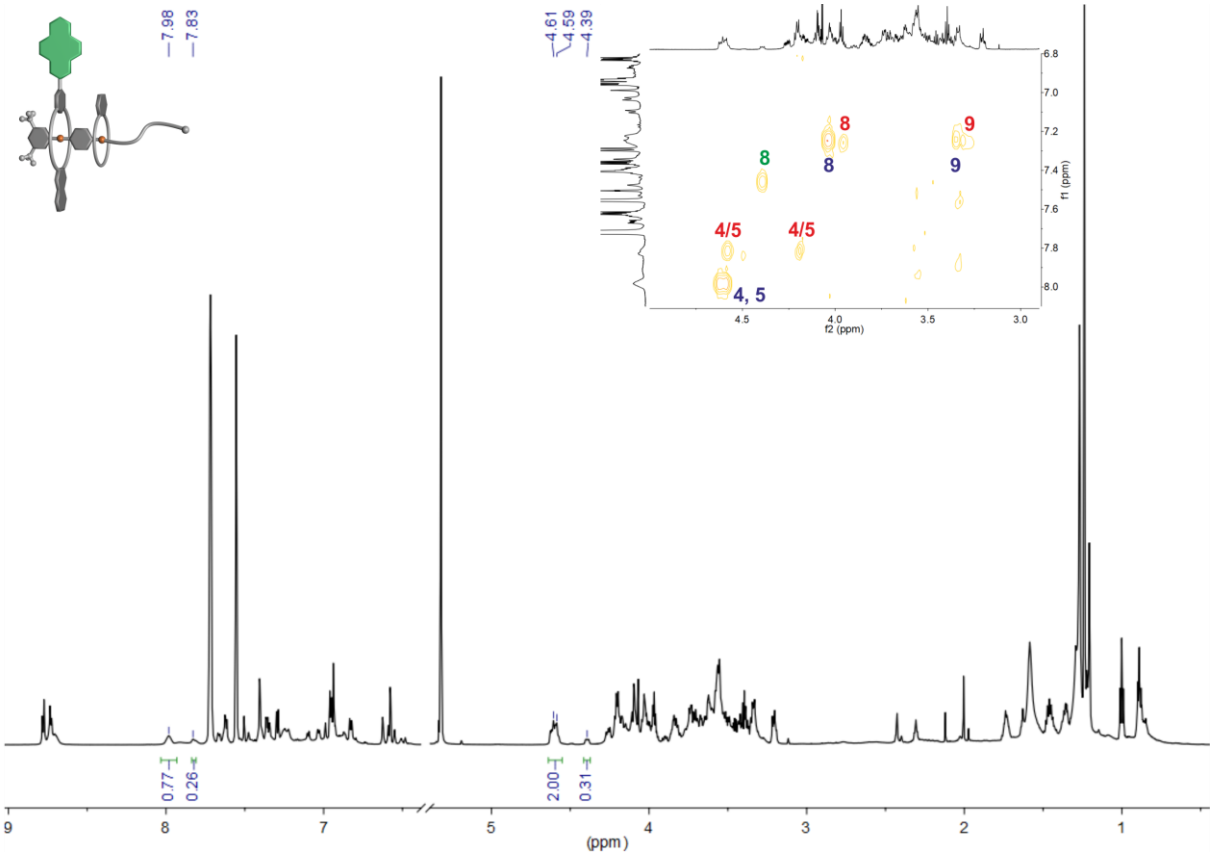

Fig. S25 ^{1}H NMR and partial COSY spectra (700 MHz, CD_2Cl_2, 298 K, 5 mM) of an equimolar solution of **Ax**, **NDIC8** and **BC7** 16 d after mixing. Signals of protons corresponding to the heteropseudo[3]rotaxane **PRNDIC8BC7** (57%) are labeled in blue, those corresponding to the homopseudo[3]rotaxane **PRNDIC8NDIC8** (19%) in red and those to the pseudo[2]rotaxane **PRBC7** (24%) in green. The methylene protons of **PRNDIC8NDIC8** overlap with **PRNDIC8BC7** and crown ether signals, therefore, the integrals of the ammonium protons were used to calculate the ratios.

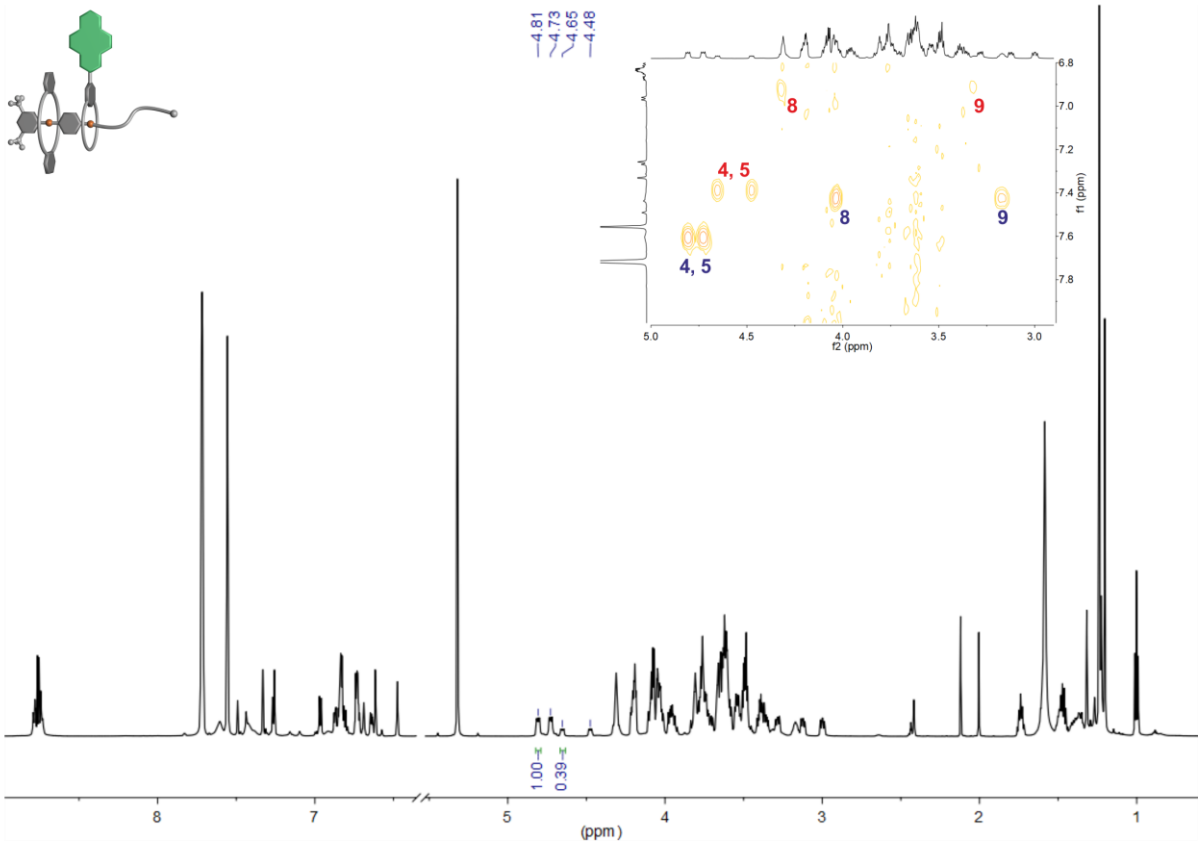

Fig. S26 ^{1}H NMR and partial COSY spectra (700 MHz, CD_2Cl_2, 298 K, 5 mM) of an equimolar solution of **Ax**, **DBC8** and **NDIC7** 16 d after mixing. Signals of protons corresponding to the heteropseudo[3]rotaxane **PRDBC8NDIC7** (72%) are labeled in blue and those corresponding to the homopseudo[3]rotaxane **PRDBC8DBC8** (28%) in red.

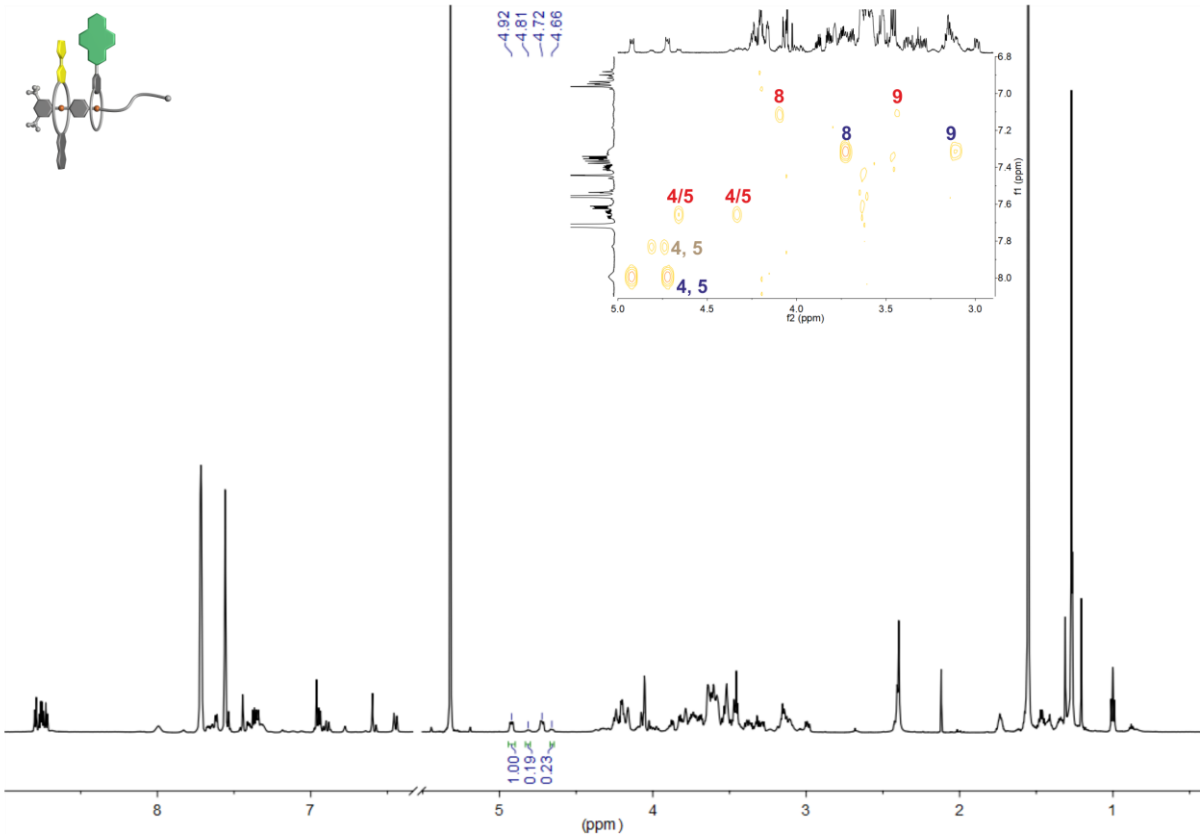

Fig. S27 ^{1}H NMR and partial COSY spectra (700 MHz, CD_2Cl_2, 298 K, 5 mM) of an equimolar solution of **Ax**, **TTFC8** and **NDIC7** 16 d after mixing. Signals of protons corresponding to the heteropseudo[3]rotaxane **PRTTFC8NDIC7** (70%) are labeled in blue, those corresponding to the homopseudo[3]rotaxane **PRTTFC8TTFC8** (16%) in red and those to the pseudo[2]rotaxane **PRTTFC8** (13%) in brown.

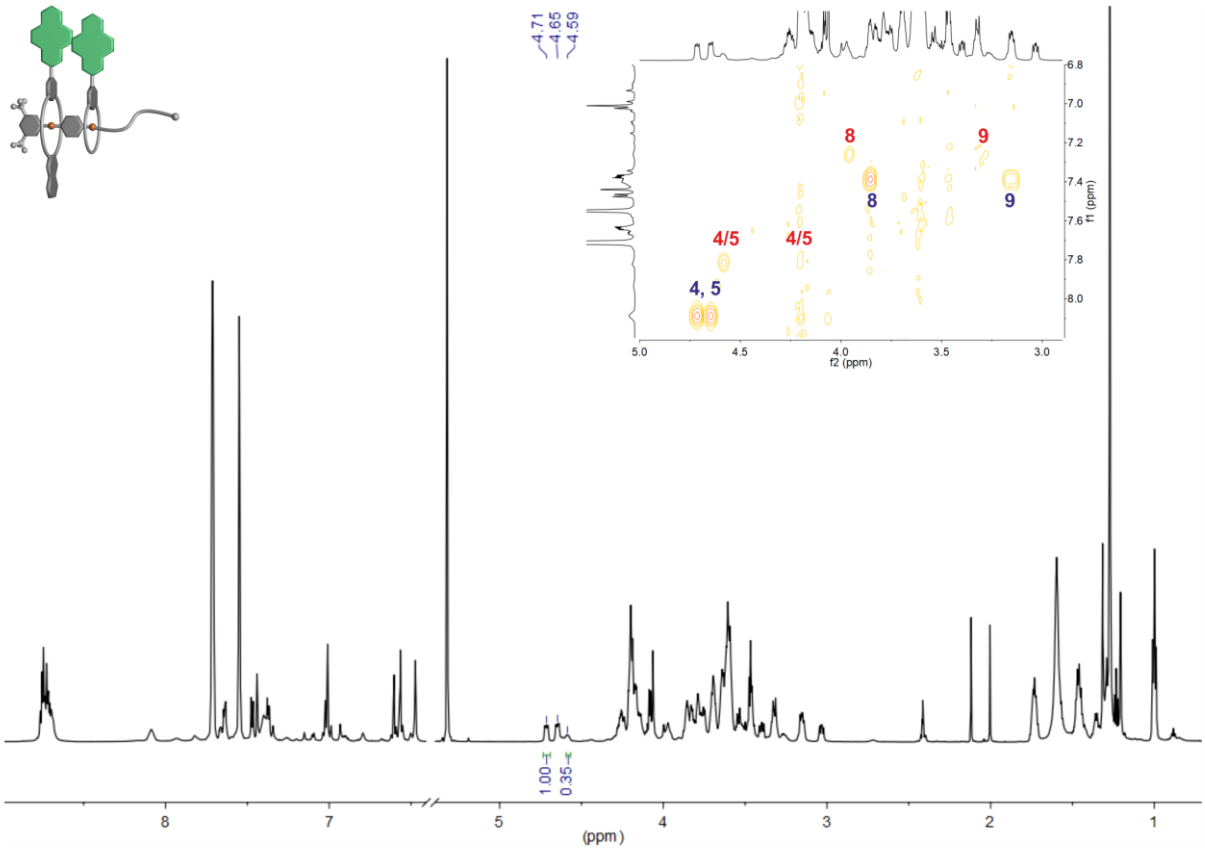

Fig. S28 ^{1}H NMR and partial COSY spectra (700 MHz, CD_2Cl_2, 298 K, 5 mM) of an equimolar solution of **Ax**, **NDIC8** and **NDIC7** 16 d after mixing. Signals of protons corresponding to the Heteropseudo[3]rotaxane **PRNDIC8NDIC7** (74%) are labeled in blue and those corresponding to the Homopseudo[3]rotaxane **PRNDIC8NDIC8** (26%) in red.

4. Tandem mass spectrometry

A Synapt G2-S HDMS (Waters Co., Milford, MA, USA) instrument with a quadrupole-time-of-flight high-resolution mass analyser was used to perform electrospray ionization tandem mass spectrometry. One of the following ionization conditions were used: a) For pseudorotaxane mixtures in dichloromethane or acetonitrile: flow rate 8 µL min^{-1}, capillary voltage 1.5 or 2.5 kV, sample cone voltage 34 V, source offset 54 V, source temperature 100 °C, desolvation temperature 220 °C, nebulizer gas 3.0 bar, desolvation gas flow 450 L h^{-1}. b) For sample solutions of the isolated rotaxane in acetonitrile: flow rate 8 µL min^{-1}, capillary voltage 2.5 kV, sample cone voltage 80 V, source offset 54 V, source temperature 100 °C, desolvation temperature 220 °C, nebulizer gas 2.5 bar, desolvation gas flow 700 L h^{-1}.

For collision-induced dissociation (CID) experiments of mass-selected ions, N_2 was used as the collision gas. Fragmentation experiments were conducted in the trap cell of the Synapt G2-S HDMS instrument with collision energies of 3 – 55 V. For the isolated rotaxane, 5 V steps were used and for the pseudorotaxane mixtures 3 V steps. Data acquisition and processing was carried out using MassLynx™ (version 4.1).

For plotting of the survival yield curves the spectra were centroided. For each spectrum at different collision voltages, the intensity of the ion with the selected mass was divided by the total ion intensity (only fragments with an intensity above 1% were considered) and then plotted against the collision voltage. Fitting was done with applying a sigmoidal Boltzmann function using Origin Pro 2020 to obtain the 50% survival yield voltages.

For time-dependent measurements, a solution of the axle **Ax** and one kind of crown[8] ether was prepared and stirred for 1 h (10 mM, 1,2-dichloroethane, 20 °C). One kind of crown[7] ether was added to yield an equimolar solution of 5 mM. The pseudorotaxane equilibrium in solution was monitored by HRMS. Prior to each measurement the sample was diluted to a concentration of 2.5 µM using dichloromethane. The absolute intensities of the ions do not necessarily correlate with the concentrations of the species in solution, as the ionization efficiencies of the involved species may differ significantly. Especially, all ions involving **BC7** ionize very efficiently at the conditions used in the experiment. For a better visibility of the signals of interest the mass range of these ions (m/z < 450) is not shown. Nevertheless, a good qualitative picture may be derived from these experiments.

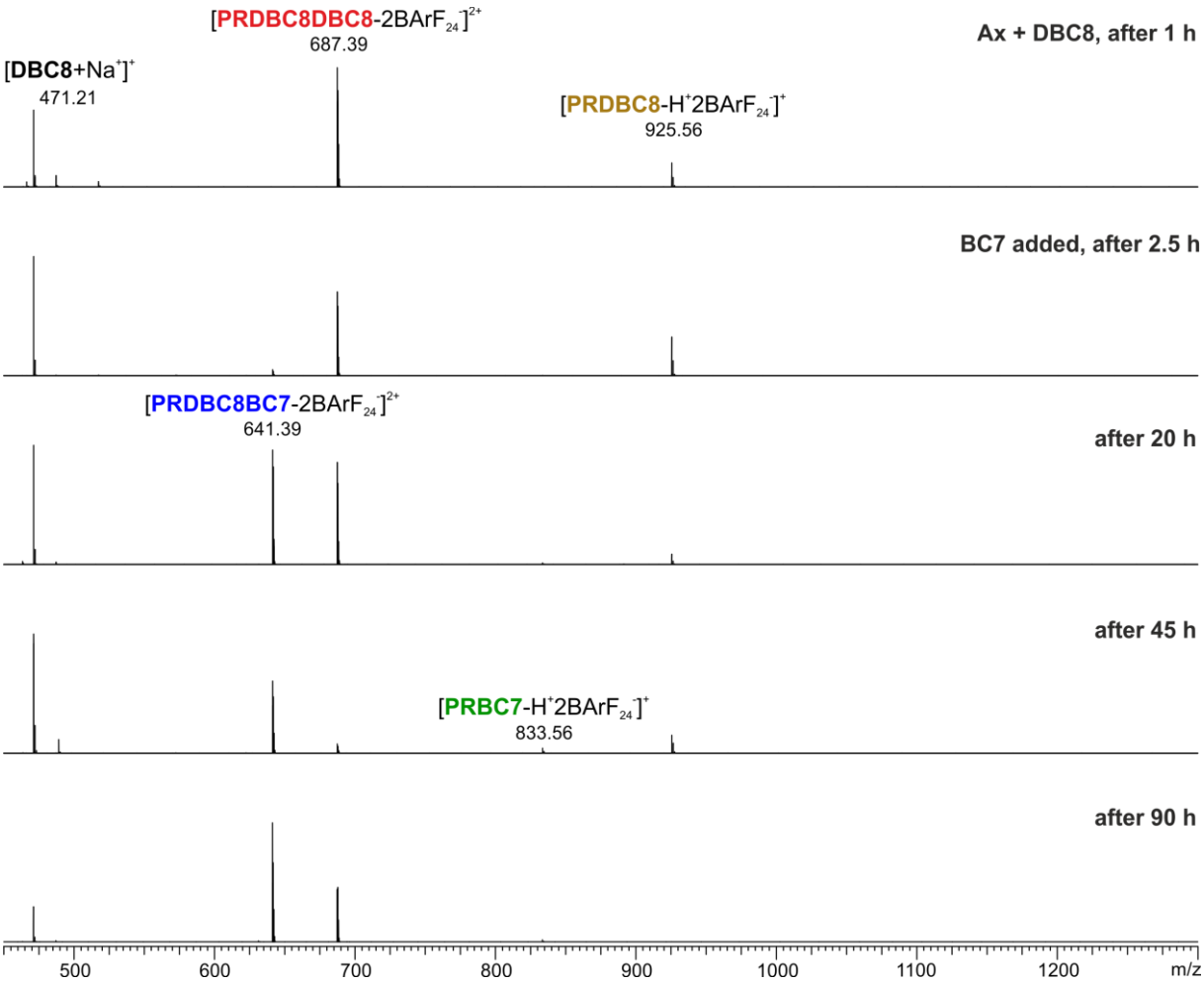

Figure S29 ESI-Q-TOF-HRMS spectra of a solution containing **Ax**, **DBC8** and **BC7** at different times. Prior to each measurement the solution was diluted to 2.5 µM using dichloromethane. Signals belonging to the heteropseudo[3]rotaxane **PRDBC8BC7** are labeled in blue, to the homopseudo[3]rotaxane **PRDBC8DBC8** in red, to the pseudo[2]rotaxane **PRDBC8** in brown and to the pseudo[2]rotaxane **PRBC7** in green.

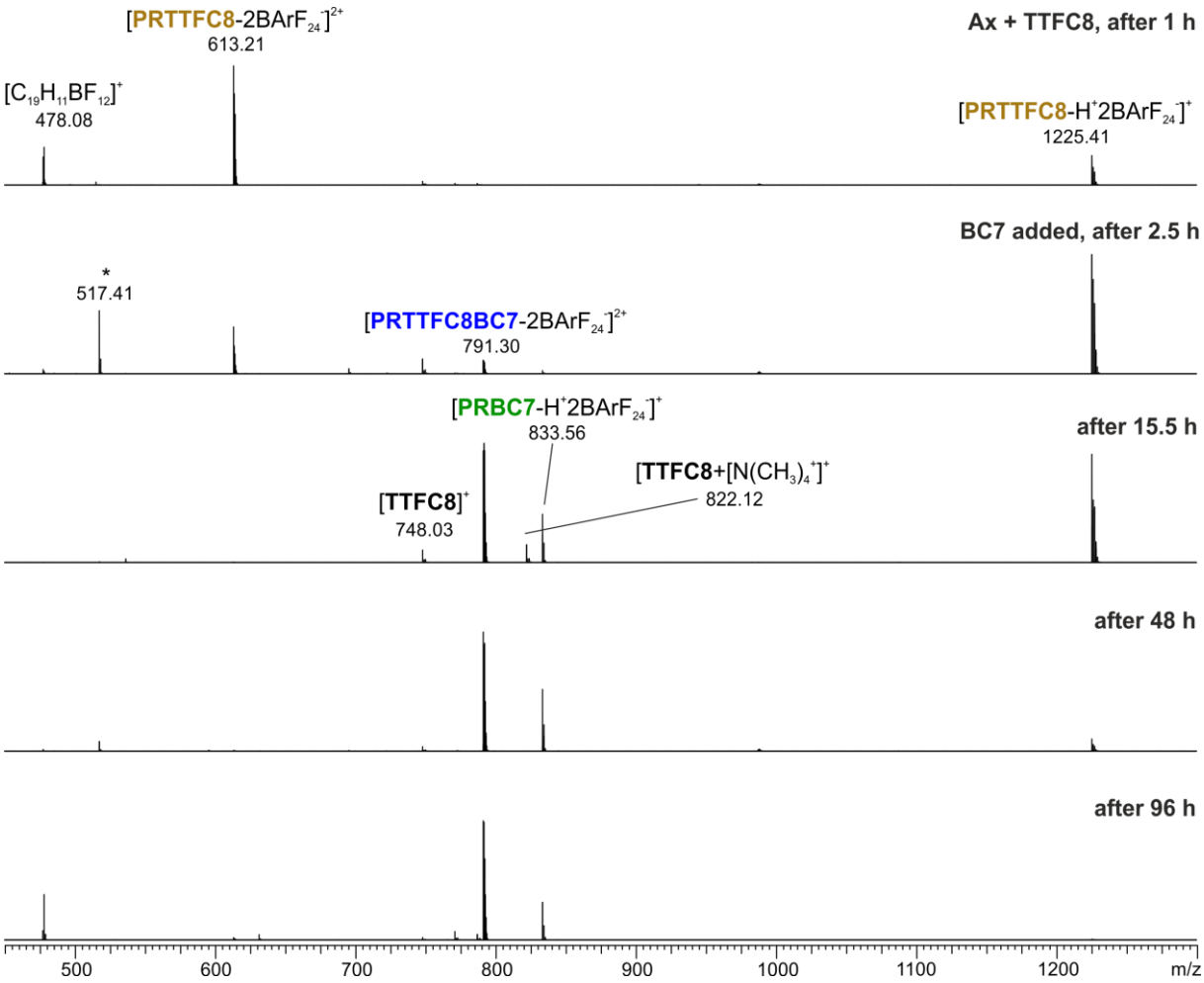

Figure S30 ESI-Q-TOF-HRMS spectra of a solution containing **Ax**, **TTFC8** and **BC7** at different times. Prior to each measurement the solution was diluted to 2.5 µM using dichloromethane. Signals belonging to the heteropseudo[3]rotaxane **PRTTFC8BC7** are labeled in blue, to the pseudo[2]rotaxane **PRTTFC8** in brown and to the pseudo[2]rotaxane **PRBC7** in green. The ion m/z 478.08 represents a fragment of the $BArF_{24}^-$ counterion. Peak marked with a * are impurities present in the instrument.

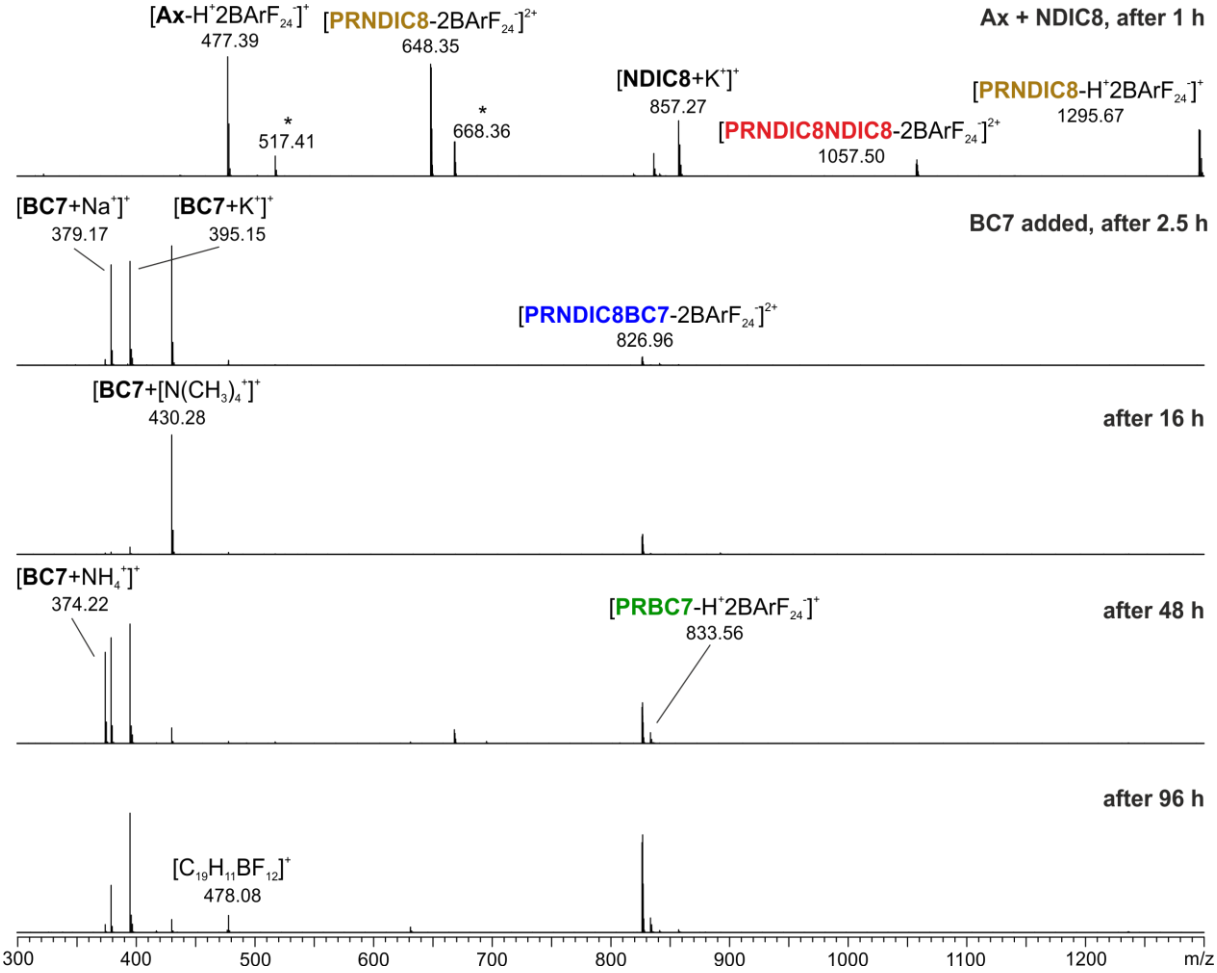

Figure S31 ESI-Q-TOF-HRMS spectra of a solution containing **Ax**, **NDIC8** and **BC7** at different times. Prior to each measurement the solution was diluted to 2.5 µM using dichloromethane. Signals belonging to the heteropseudo[3]rotaxane **PRNDIC8BC7** are labeled in blue, to the homopseudo[3]rotaxane **PRNDIC8NDIC8** in red, to the pseudo[2]rotaxane **PRNDIC8** in brown and to the pseudo[2]rotaxane **PRBC7** in green. The ion m/z 478.08 represents a fragment of the $BArF_{24}$-counterion. Peaks marked with a * are impurities present in the instrument.

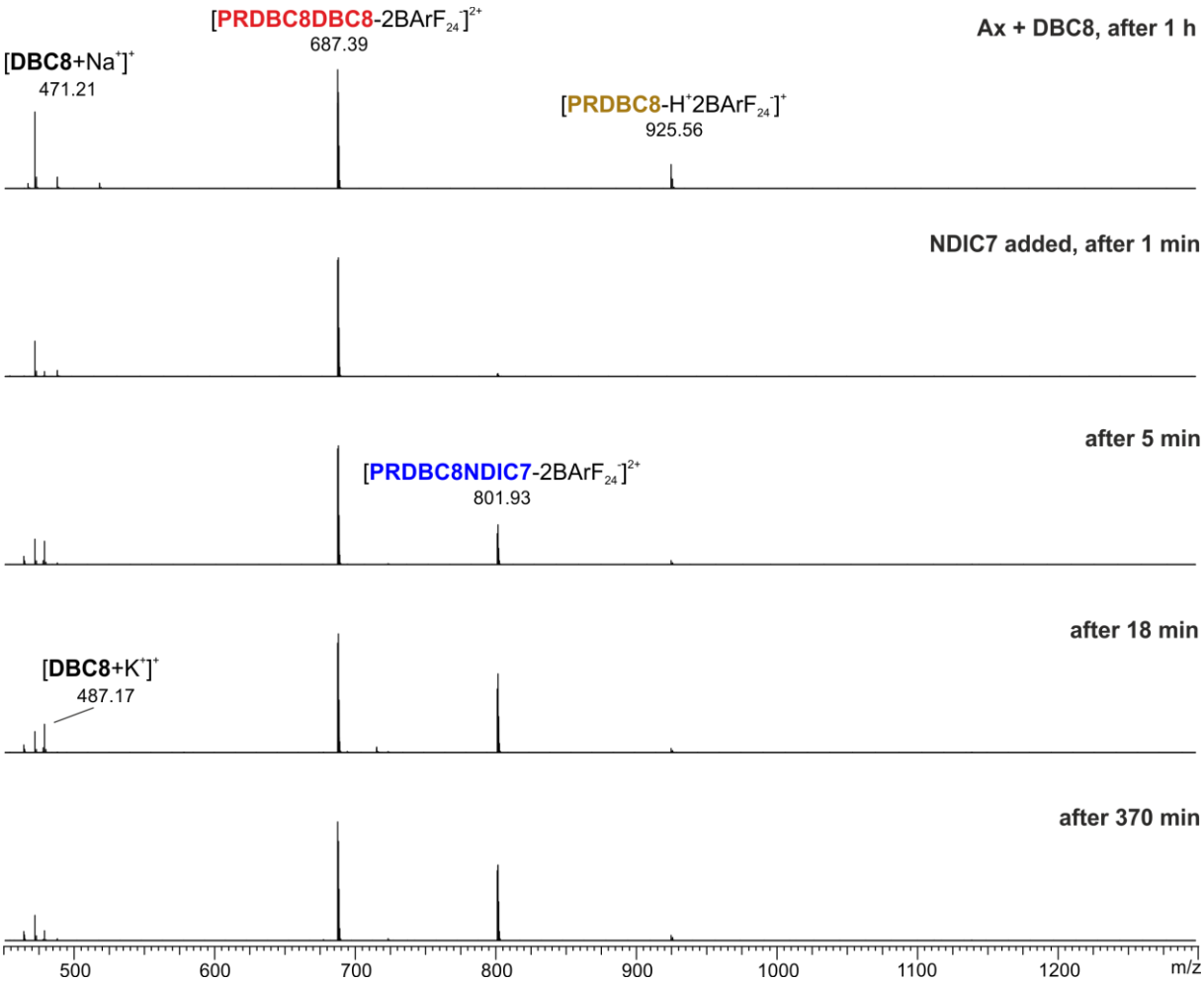

Figure S32 ESI-Q-TOF-HRMS spectra of a solution containing **Ax**, **DBC8** and **NDIC7** at different times. Prior to each measurement the solution was diluted to 2.5 µM using dichloromethane. Signals belonging to the heteropseudo[3]rotaxane **PRDBC8NDIC7** are labeled in blue, to the homopseudo[3]rotaxane **PRDBC8DBC8** in red and to the pseudo[2]rotaxane **PRDBC8** in brown.

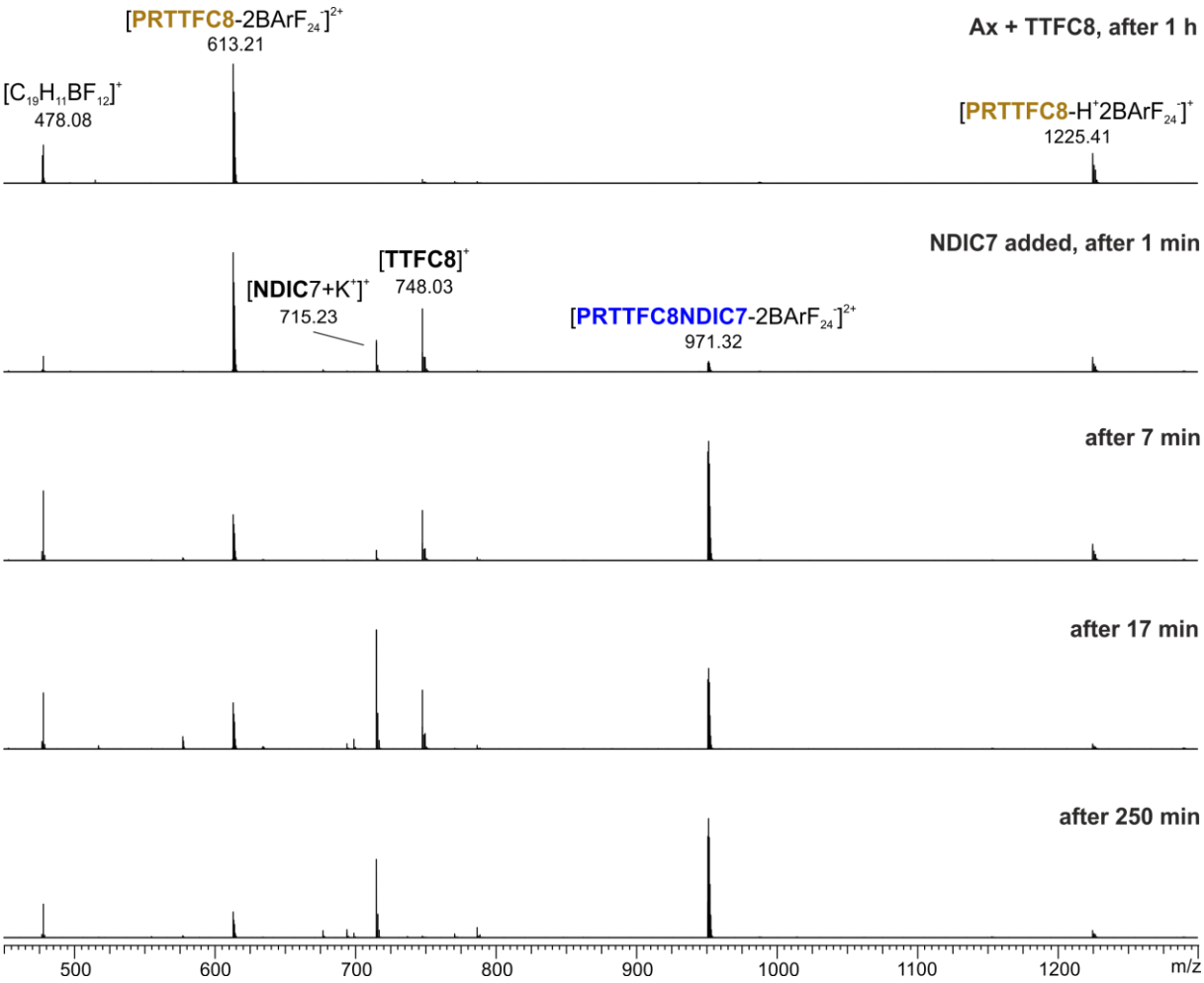

Figure S33 ESI-Q-TOF-HRMS spectra of a solution containing **Ax**, **TTFC8** and **NDIC7** at different times. Prior to each measurement the solution was diluted to 2.5 µM using dichloromethane. Signals belonging to the heteropseudo[3]rotaxane **PRTTFC8NDIC7** are labeled in blue and to the pseudo[2]rotaxane **PRTTFC8** in brown. The ion m/z 478.08 represents a fragment of the $BArF_{24}$-counterion.

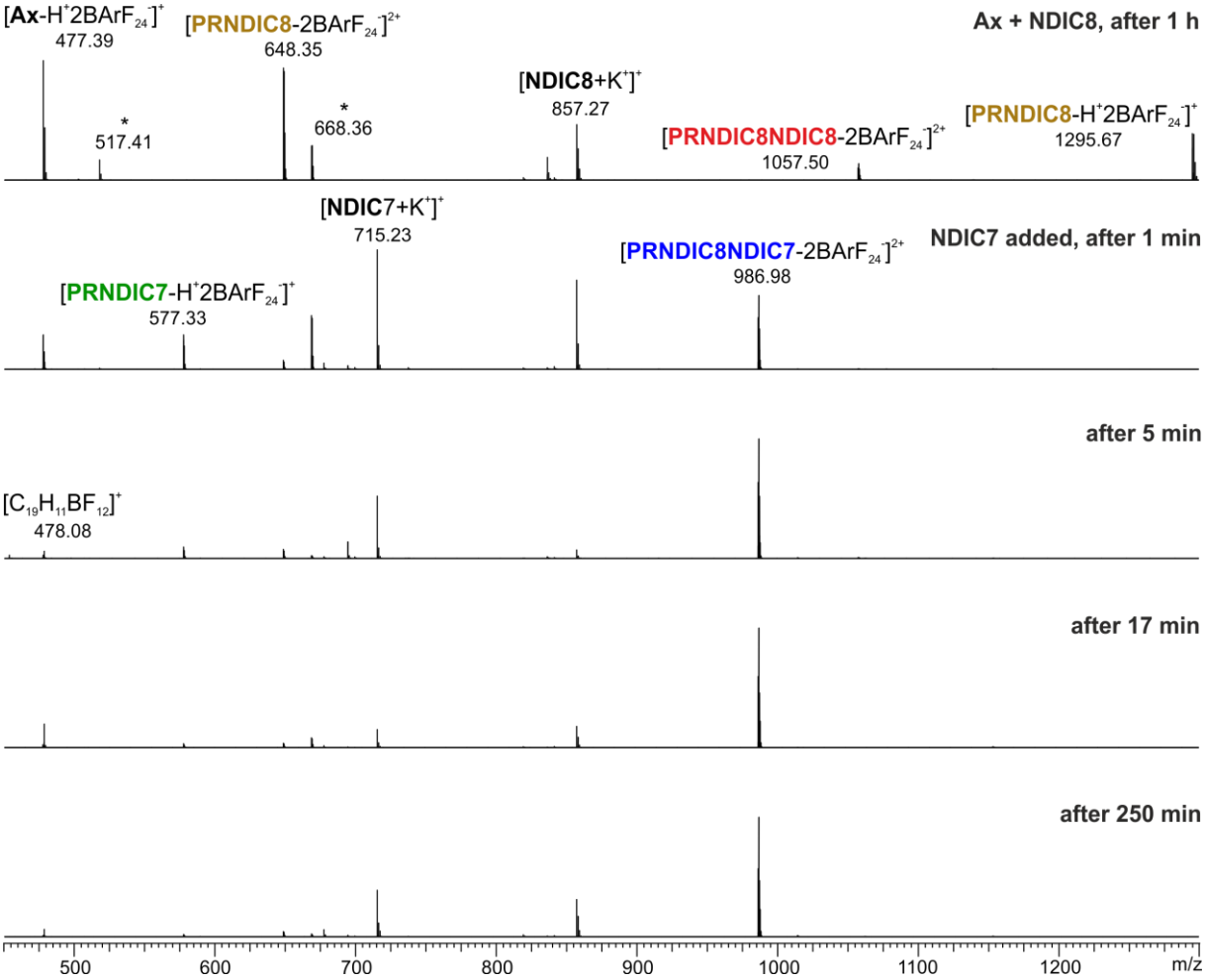

Figure S34 ESI-Q-TOF-HRMS spectra of a solution containing **Ax**, **NDIC8** and **NDIC7** at different times. Prior to each measurement the solution was diluted to 2.5 µM using dichloromethane. Signals belonging to the heteropseudo[3]rotaxane **PRNDIC8NDIC7** are labeled in blue, to the homopseudo[3]rotaxane **PRNDIC8NDIC8** in red, to the pseudo[2]rotaxane **PRNDIC8** in brown and to the pseudo[2]rotaxane **PRBC7** in green. The ion m/z 478.08 represents a fragment of the $BArF_{24}$-counterion. Peaks marked with a * are impurities present in the instrument.

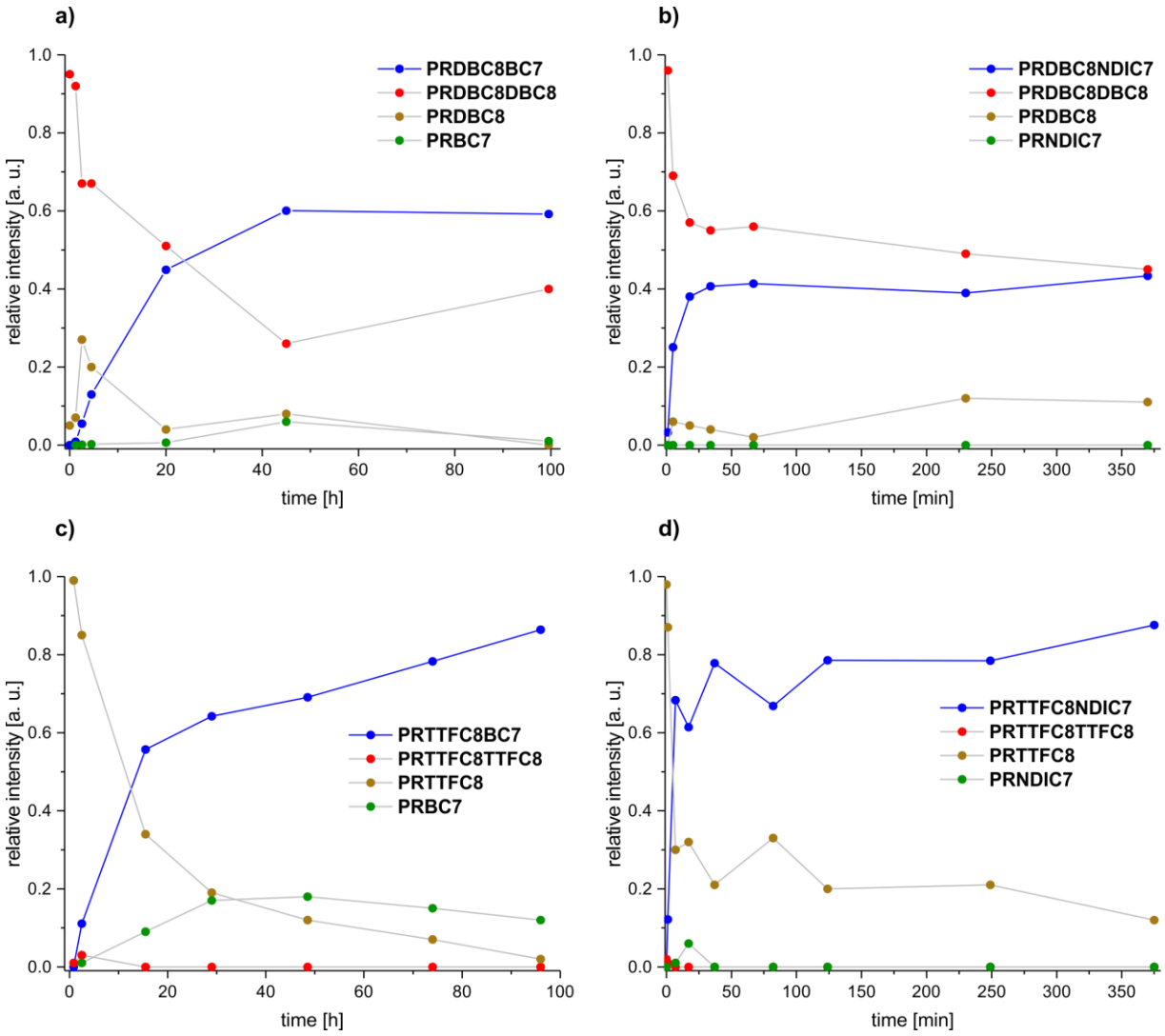

Figure S35 Plots summarising the changes of the hetero- and homopseudo[3]rotaxanes signal intensities and those of their pseudorotaxane precursors over reaction time from equimolar solutions of **Ax**, crown[8] ether and crown[7] ether at 20 °C. The relative intensities are taken from ESI-Q-TOF-HRMS spectra. The absolute intensities of the ions are not representative for the concentrations of the species in solution, as the ionization efficiencies of the involved species differ significantly. For full spetra see above.

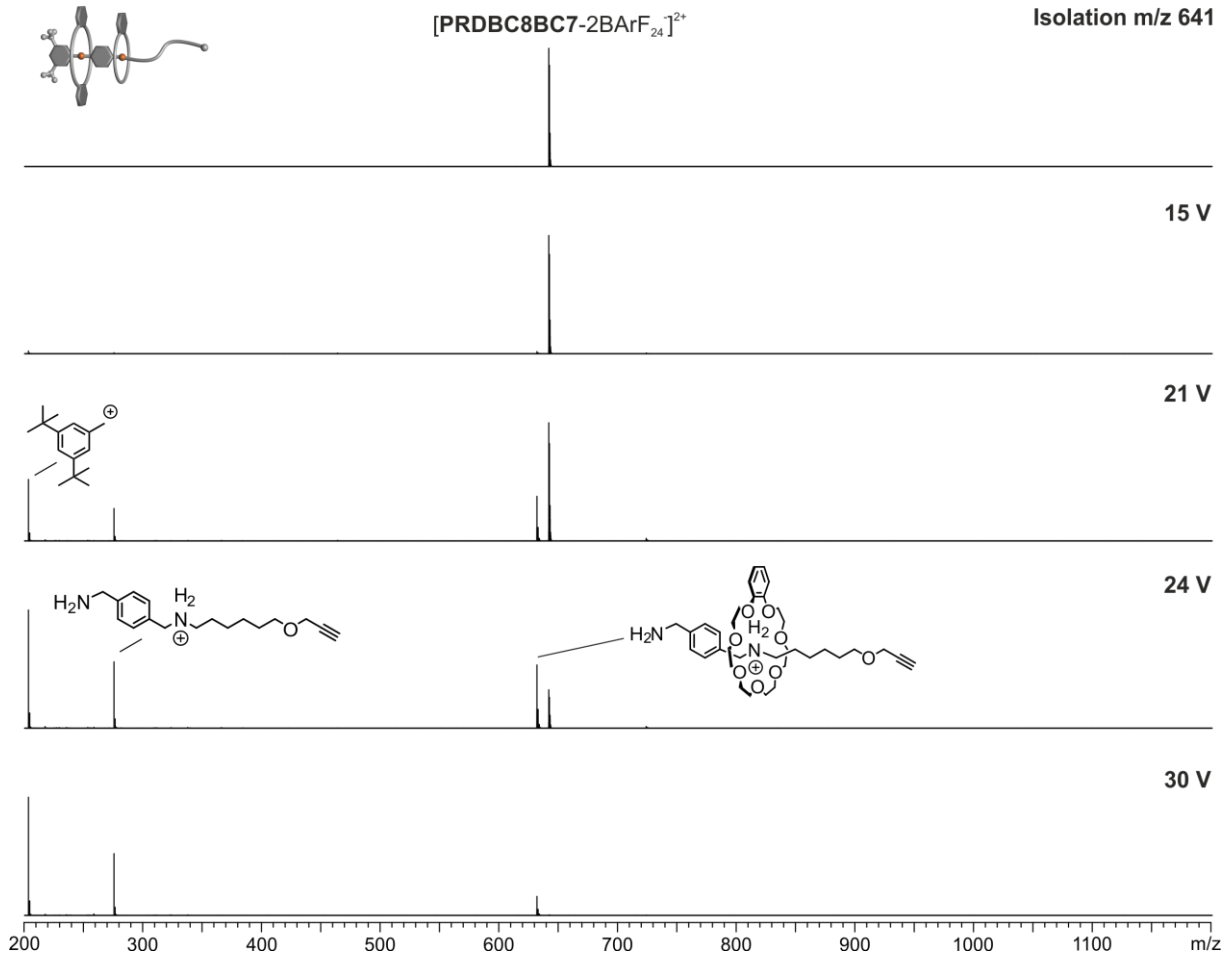

Figure S36 CID experiment with mass-selected [**PRDBC8BC7**-2BArF$_{24}^-$]$^{2+}$ ions at *m/z* 641 obtained from a CH_2Cl_2 solution (2.5 µM). Due to the remarkably strong binding of **BC7**, the first fragmentation at high collision voltages is the cleavage of a covalent bond in the axle rather than dissociation of the crown ether. The loss of **DBC8** upon axle cleavage at the western ammonium station evidences the desired sequence in the **PRDBC8BC7** pseudo[3]rotaxane.

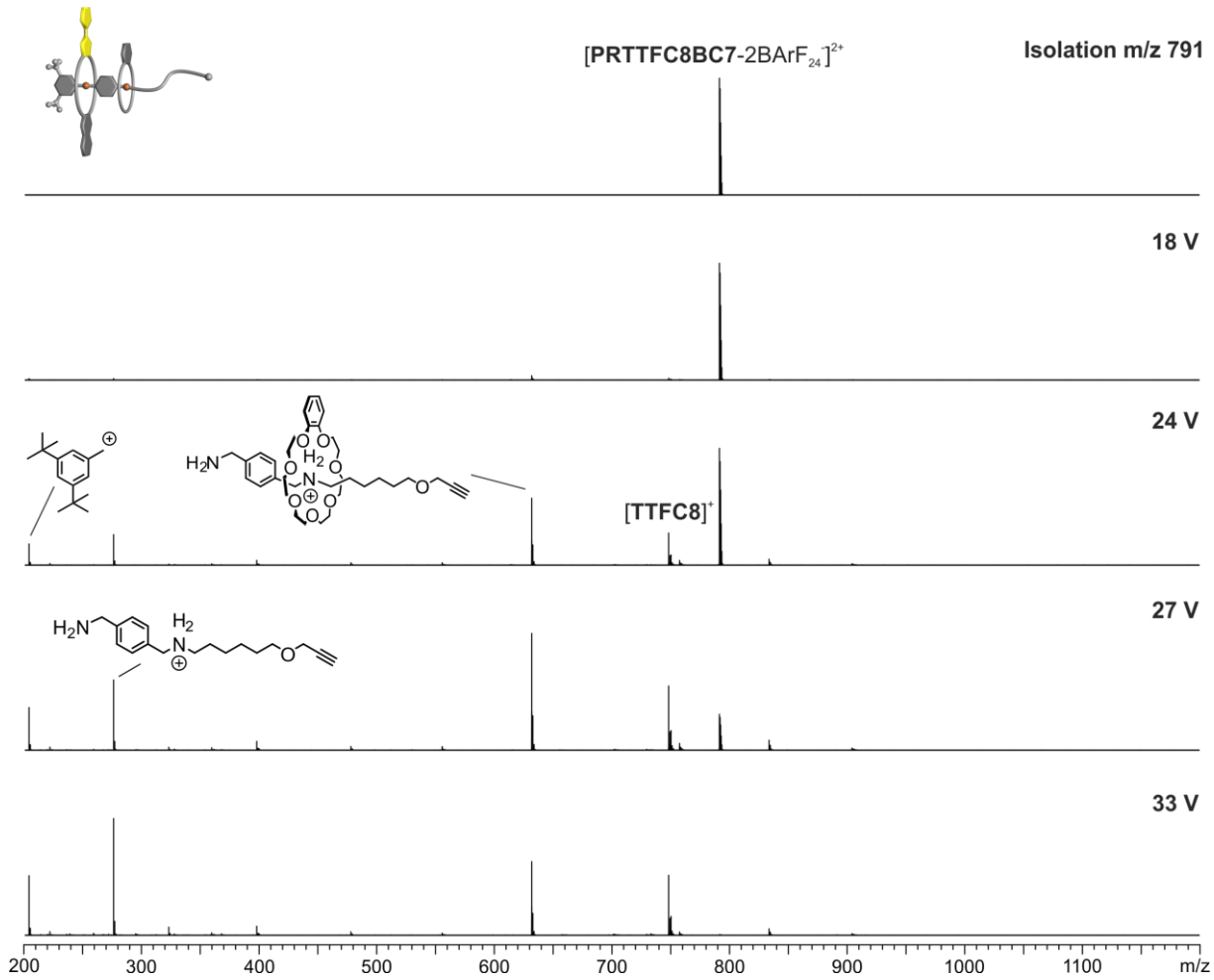

Figure S37 CID experiment with mass-selected [**PRTTFC8BC7**-2BArF$_{24}$$^{-}$]$^{2+}$ ions at *m/z* 791 obtained from a CH_2Cl_2 solution (2.5 μM). Due to the remarkably strong binding of **BC7**, the first fragmentation at high collision voltages is the cleavage of a covalent bond in the axle rather than dissociation of the crown ether. The loss of **TTFC8** upon cleavage of the axle at the western ammonium station evidences the desired sequence in the **PRTTFC8BC7** pseudo[3]rotaxane. The appearance of **TTFC8^{+}** as a fragment has been observed for other mechanically interlocked structures containing **TTFC8.**[1, 8]

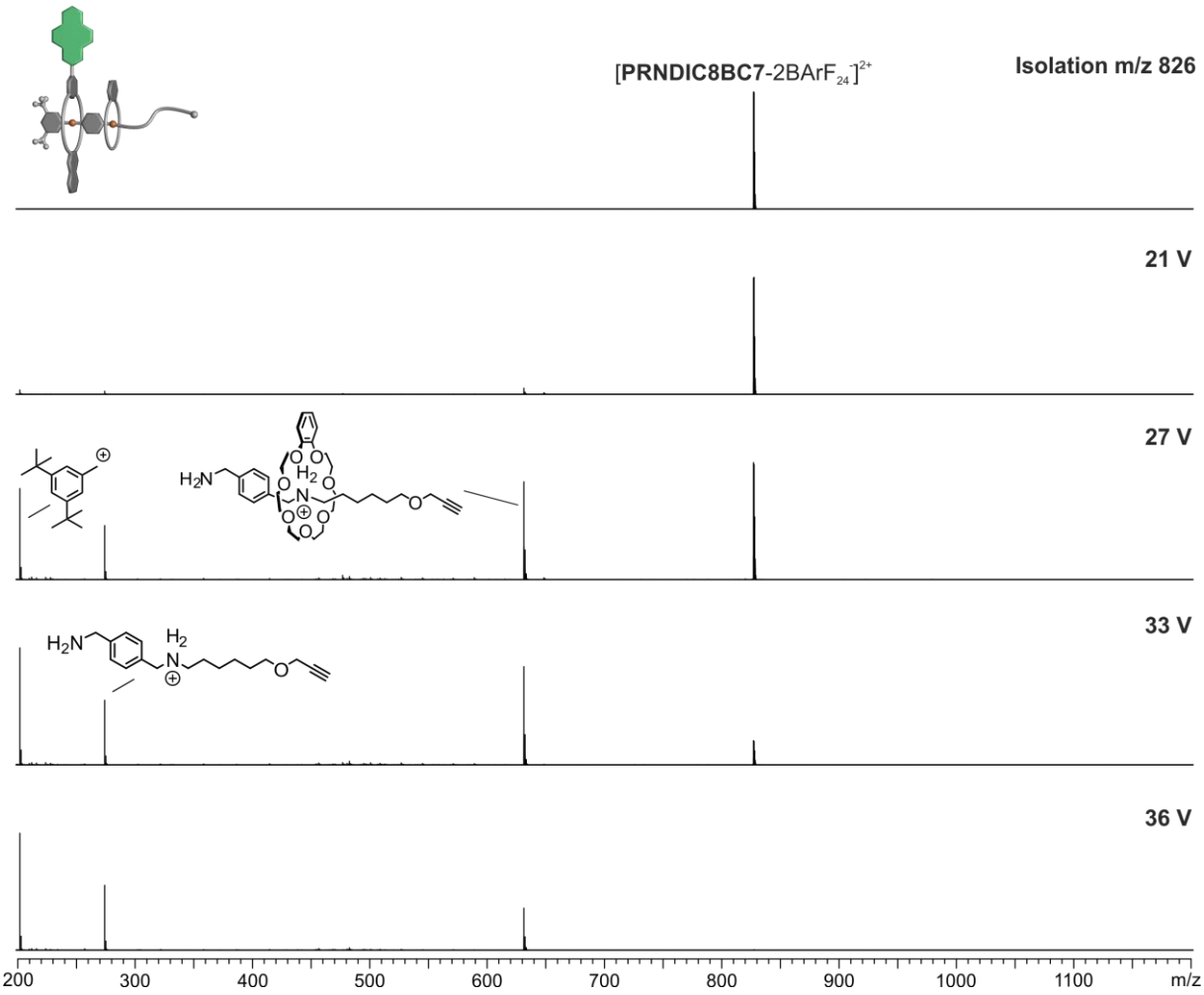

Figure S38 CID experiment with mass-selected [**PRNDIC8BC7**-2BArF$_{24}$]$^{2+}$ ions at *m/z* 826 obtained from a CH_2Cl_2 solution (2.5 µM). Due to the remarkably strong binding of **BC7**, the first fragmentation at high collision voltages is the cleavage of a covalent bond in the axle rather than dissociation of the crown ether. The loss of **NDIC8** upon cleavage of the axle at the western ammonium station evidences the desired sequence in the **PRNDIC8BC7** pseudo[3]rotaxane.

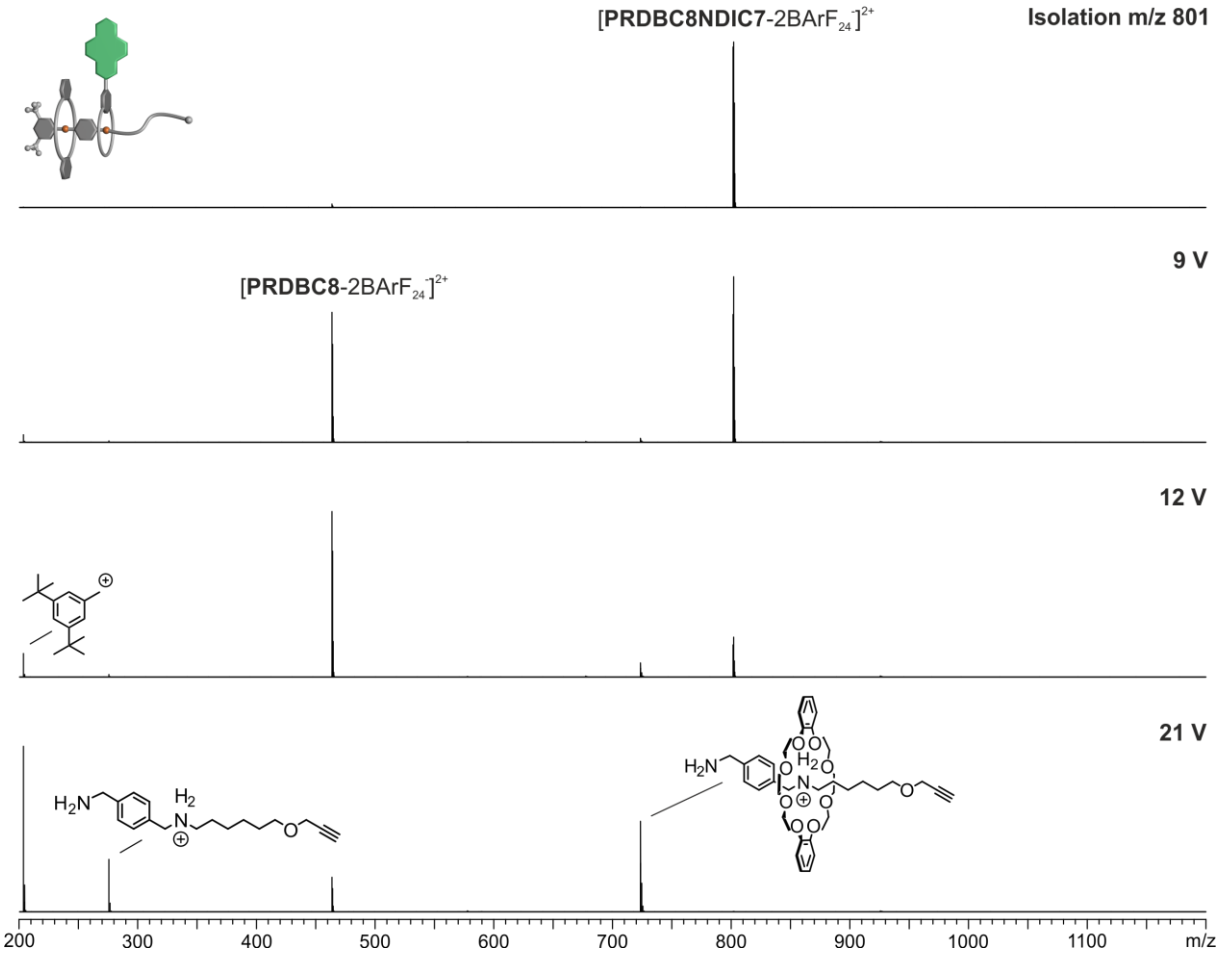

Figure S39 CID experiment with mass-selected [**PRDBC8NDIC7**-2BArF$_{24}^-$]$^{2+}$ ions at *m/z* 801 obtained from a CH_2Cl_2 solution (2.5 μM). The first fragmentation step at lower collision energies is the cleaving of the non-covalent bond to **NDIC7** to form the pseudo[2]rotaxane **PRDBC8**, which evidences the desired sequence in the **PRDBC8NDIC7** pseudo[3]rotaxane.

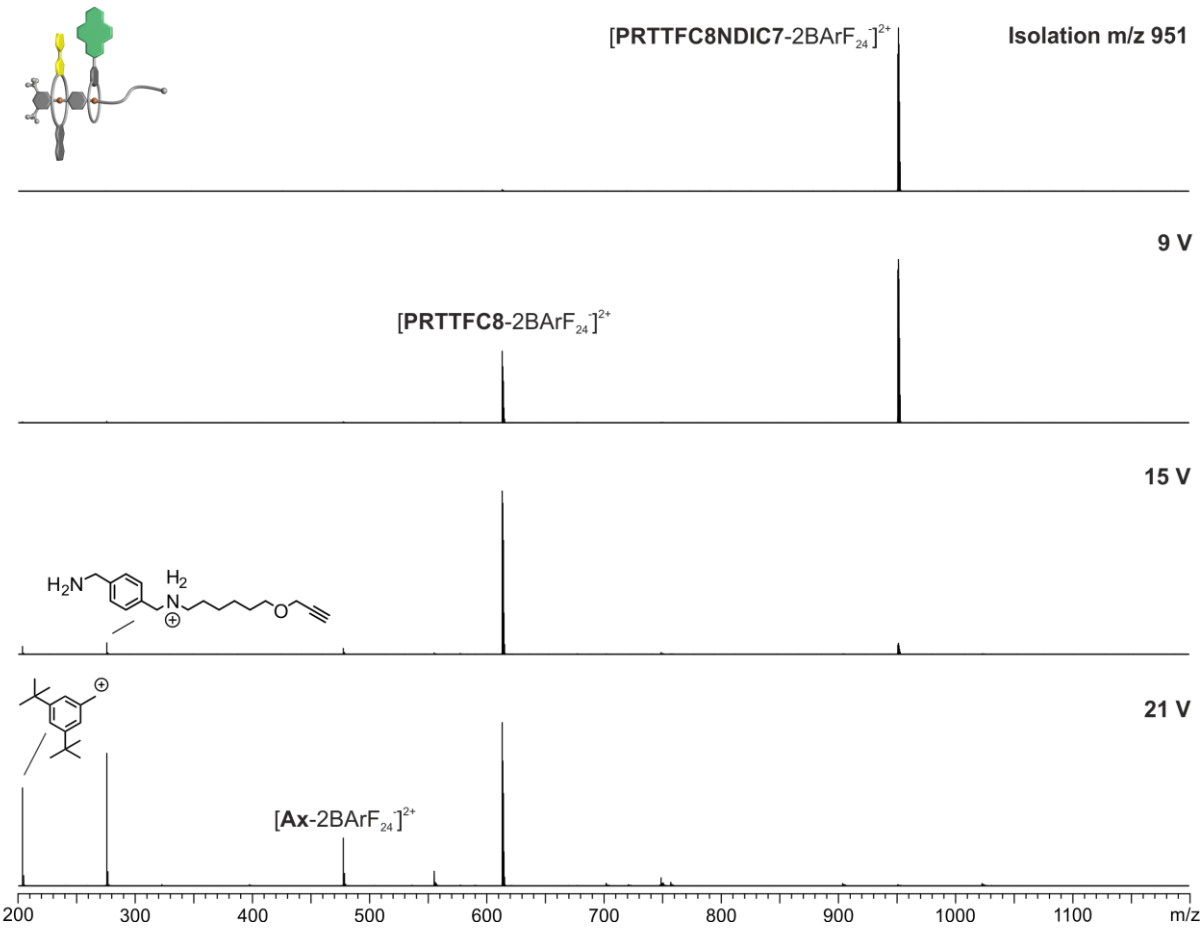

Figure S40 CID experiment with mass-selected [**PRTTFC8NDIC7**-2BArF$_{24}^-$]$^{2+}$ ions at *m/z* 951 obtained from a CH_2Cl_2 solution (2.5 μM). The first fragmentation step at lower collision energies is the cleavage of the non-covalent bond to **NDIC7** to form the pseudo[2]rotaxane **PRTTFC8**, which evidences the desired sequence in the **PRTTFC8NDIC7** pseudo[3]rotaxane.

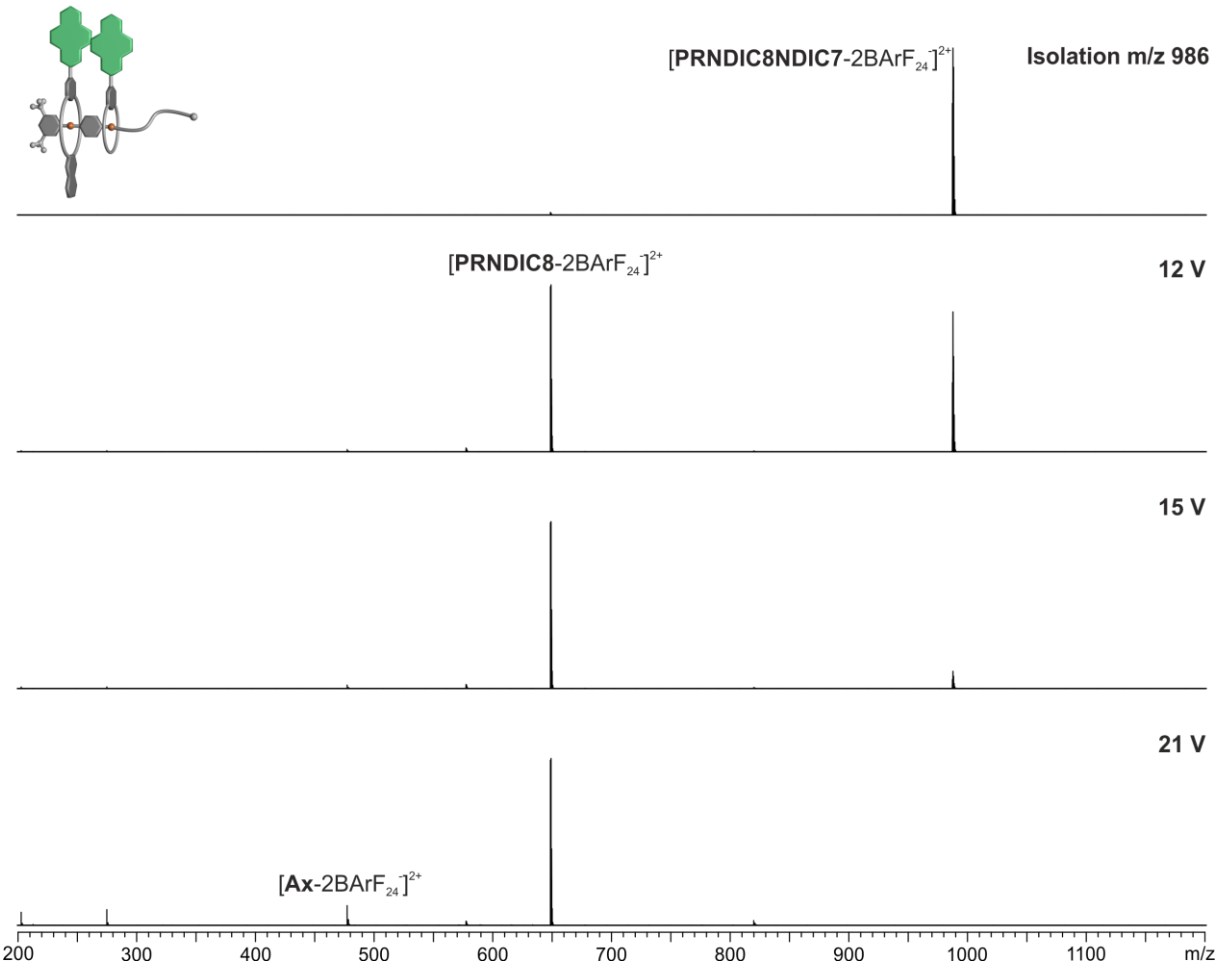

Figure S41 CID experiment with mass-selected [**PRNDIC8NDIC7**-2BArF$_{24}^-$]$^{2+}$ ions at *m/z* 951 obtained from a CH_2Cl_2 solution (2.5 µM). The first fragmentation step at lower collision energies is the cleavage of the non-covalent bond to **NDIC7** to form the pseudo[2]rotaxane **PRNDIC8**, which evidences the desired sequence in the **PRNDIC8NDIC7** pseudo[3]rotaxane.

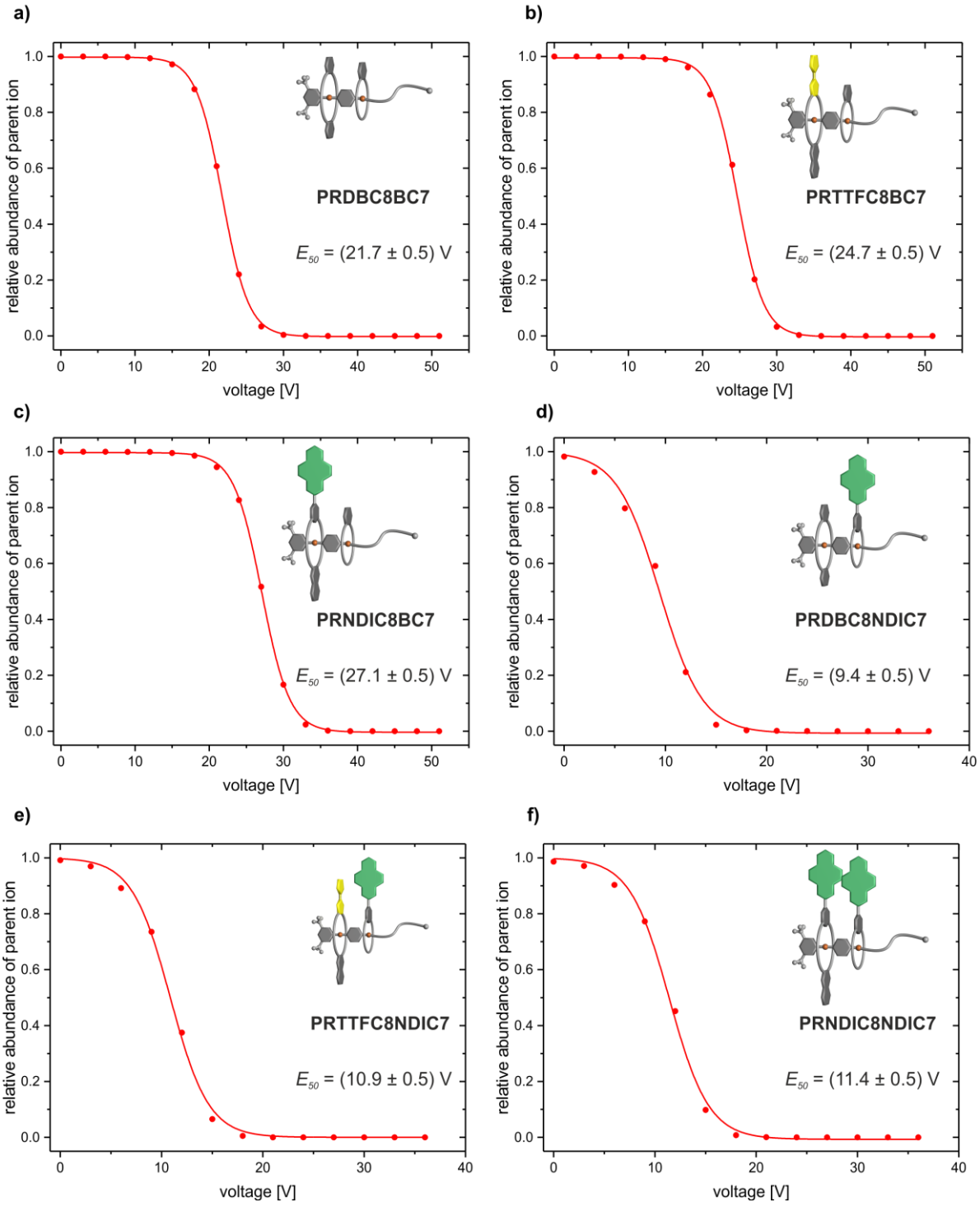

Figure S42 Survival yield curves for the different hetero[3]pseudorotaxane under study. Dications of hetero[3]pseudorotaxanes were mass-selected and fragmented at increasing collision voltages. The solid lines represent a sigmoidal fitting to determine 50% survival yield voltages.

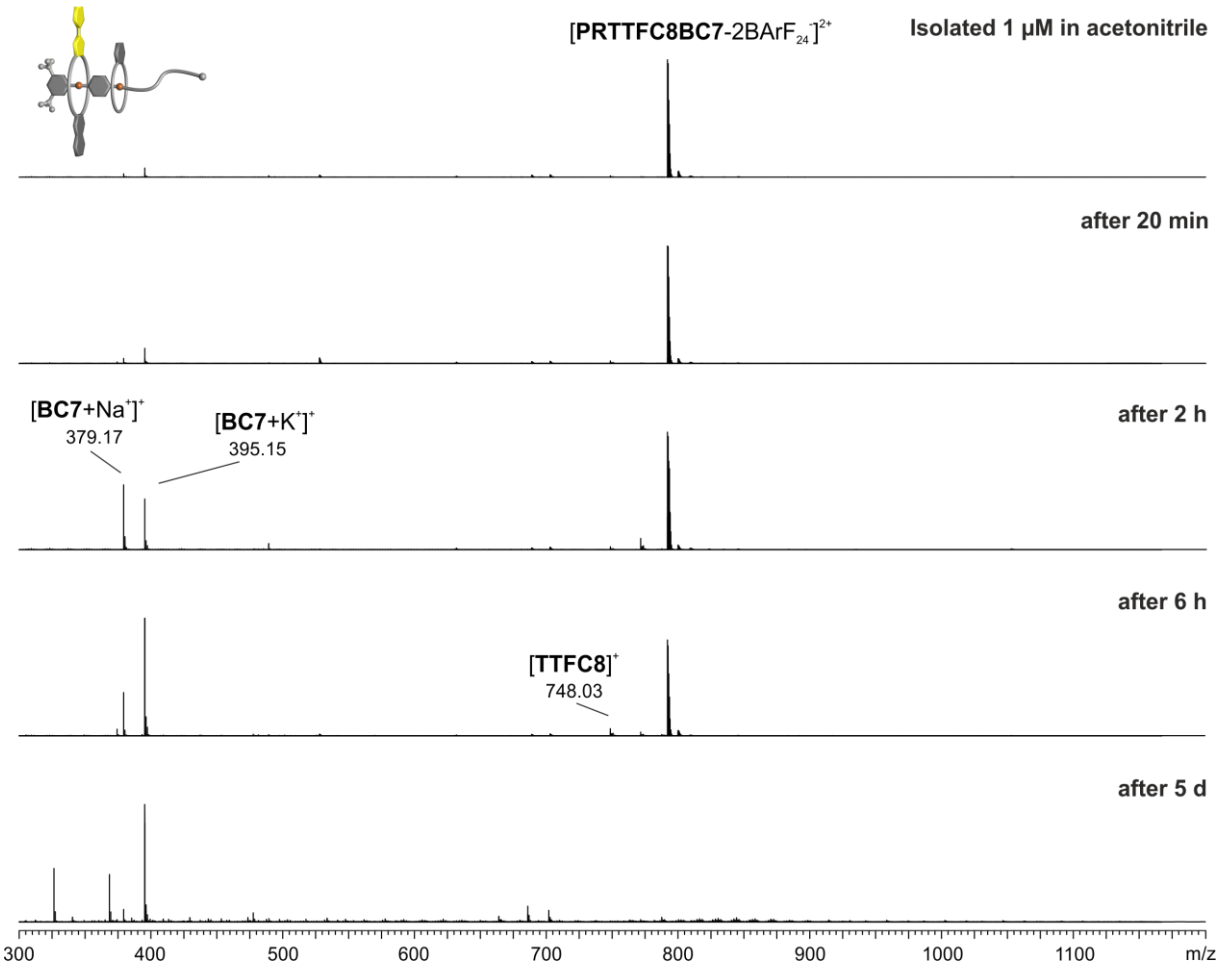

Figure S43 ESI-Q-TOF-HRMS spectra of a **PRTTFC8BC7** solution in acetonitrile at different times (1 µM, 25°C). The pronounced peak of **PRTTFC8BC7** after 6 h indicates the kinetic hinderance for dethreading of **BC7** and the kinetic stability of the pseudorotaxane **PRTTFC8BC7** in acetonitrile at low concentrations.

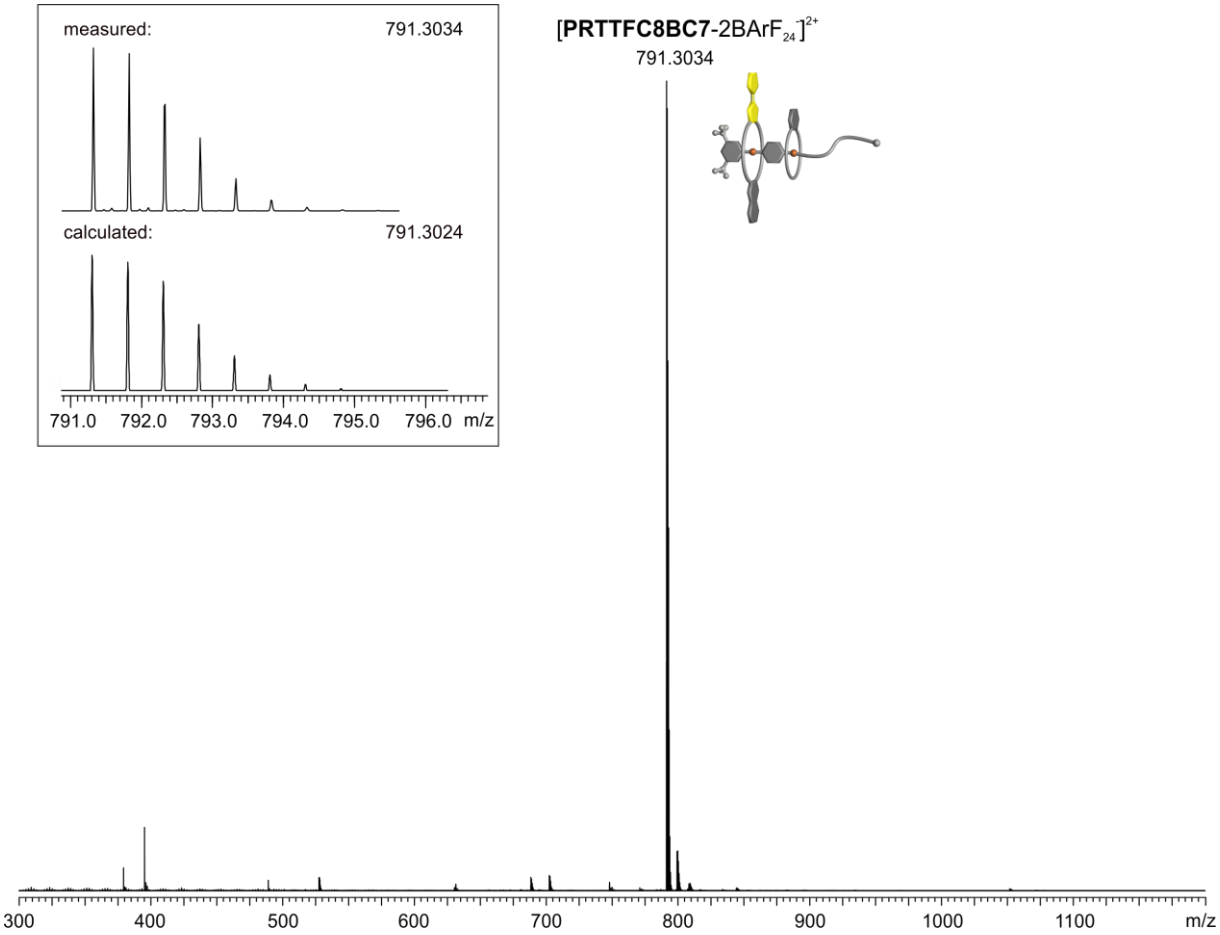

Figure S44 ESI-Q-TOF-HRMS spectrum of **PRTTFC8BC7** (1 µM in acetonitrile) isolated after column chromatography; inset: comparison of measured and calculated isotopic patterns.

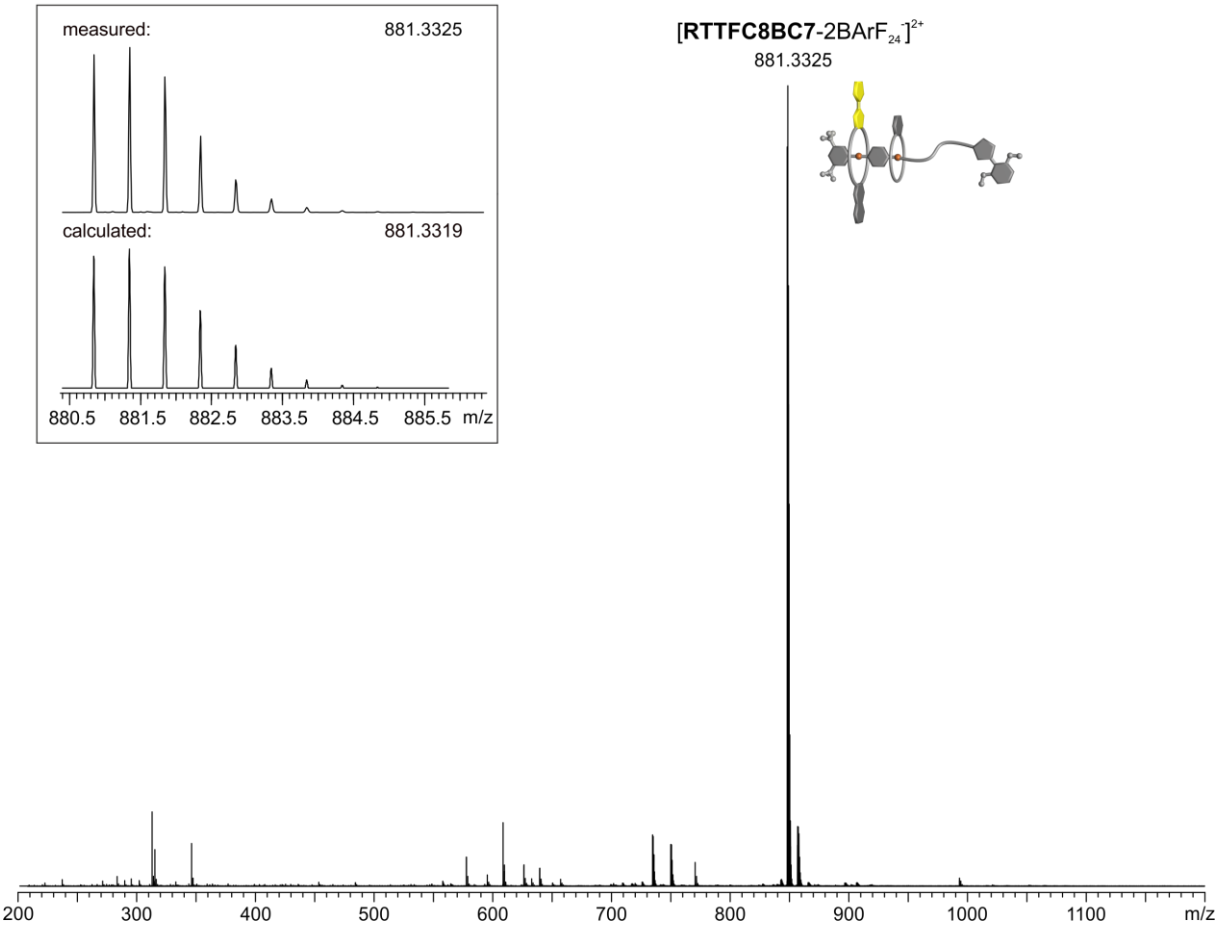

Figure S45 ESI-Q-TOF-HRMS spectrum of **RTTFC8BC7** (1 µM in acetonitrile); inset: comparison of measured and calculated isotopic patterns.

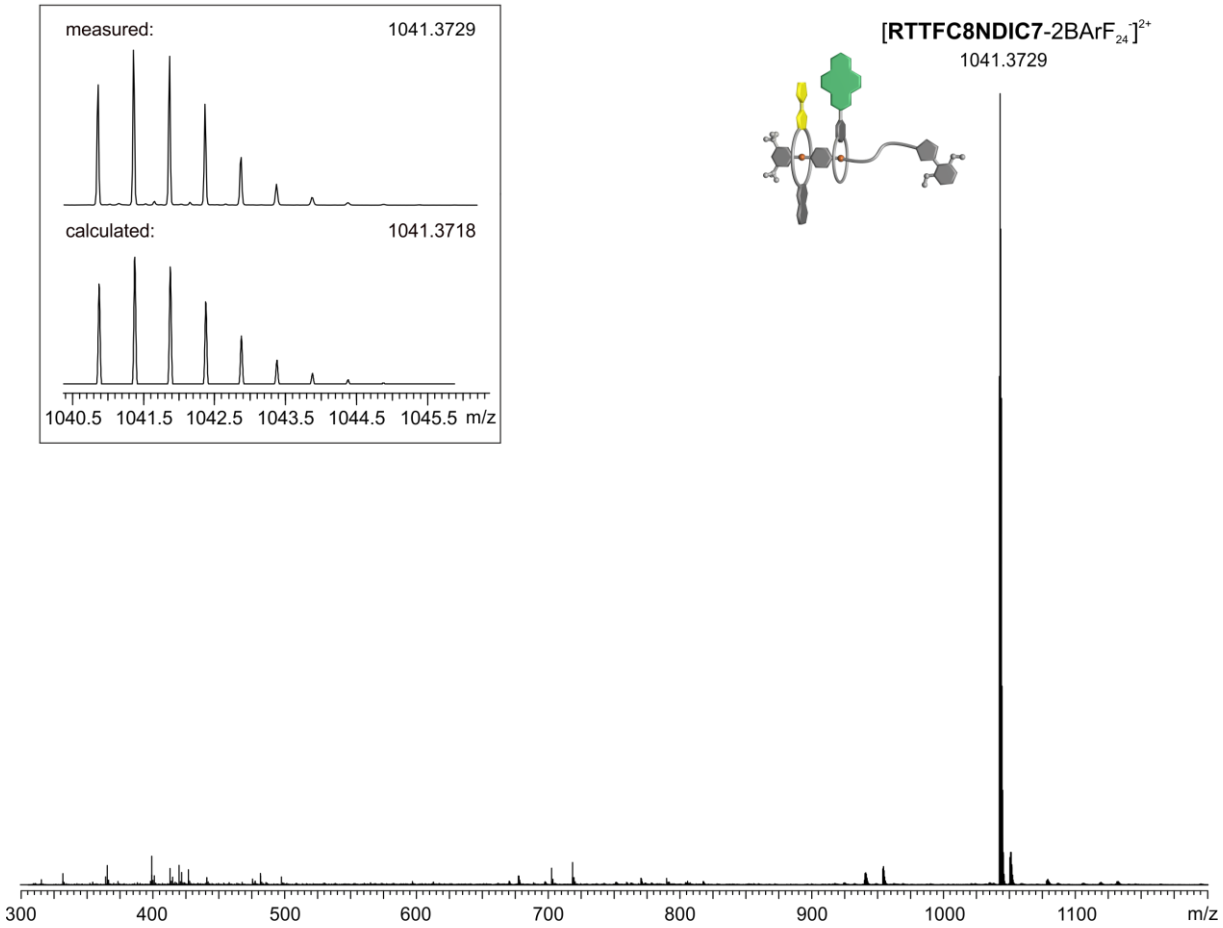

Figure S46 ESI-Q-TOF-HRMS spectrum of **RTTFC8NDIC7** (1 µM in acetonitrile); inset: comparison of measured and calculated isotopic patterns.

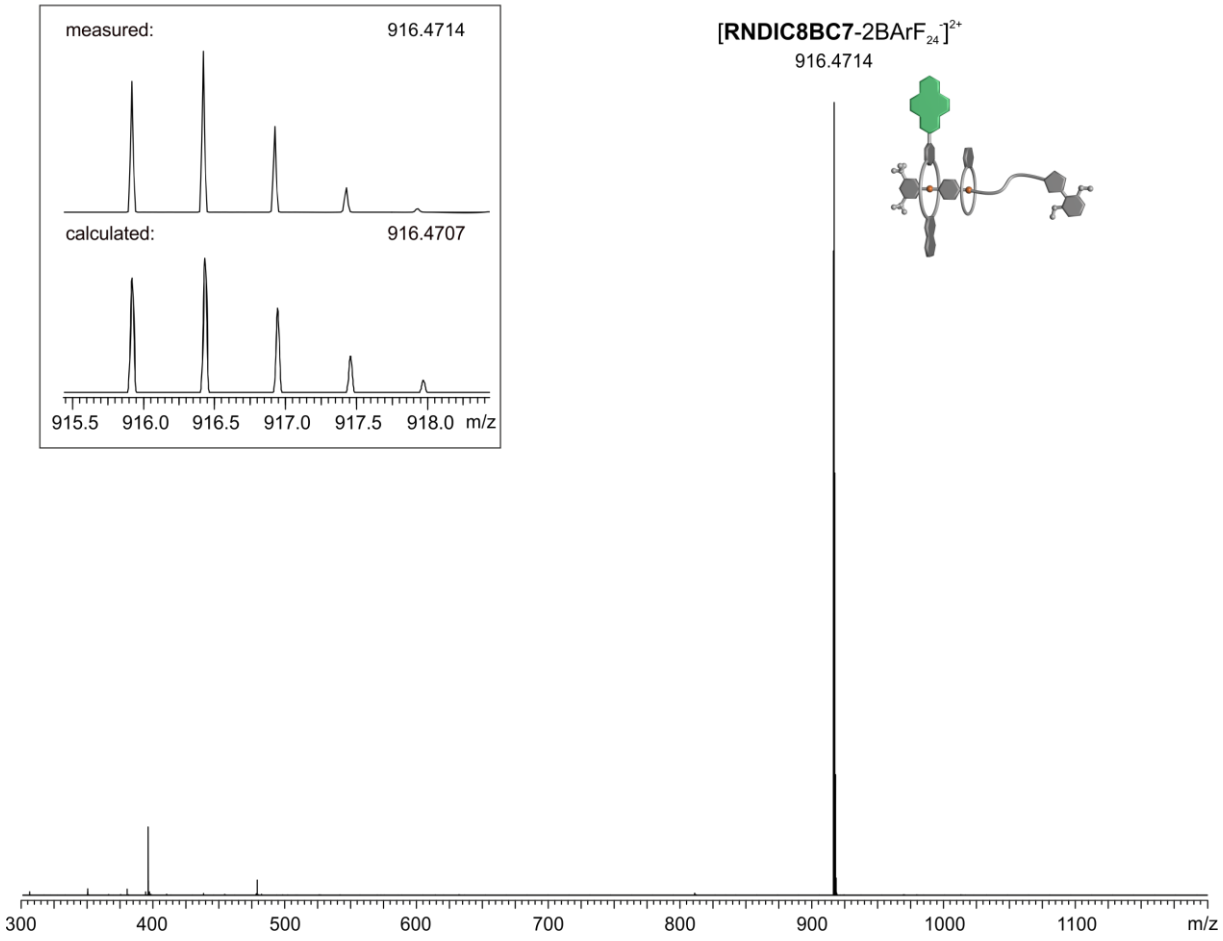

Figure S47 ESI-Q-TOF-HRMS spectrum of **RNDIC8BC7** (1 µM in acetonitrile); inset: comparison of measured and calculated isotopic patterns.

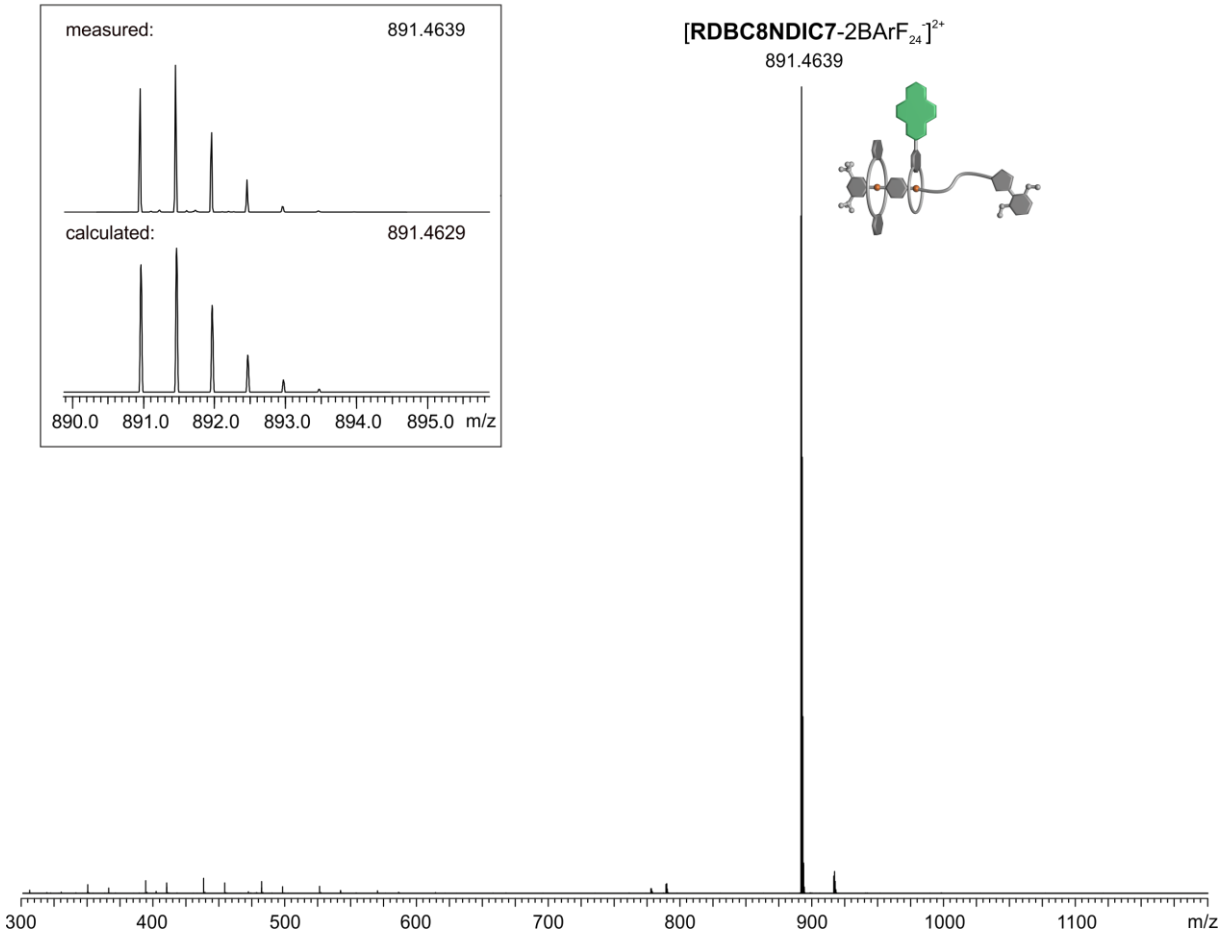

Figure S48 ESI-Q-TOF-HRMS spectrum of **RDBC8NDIC7** (1 µM in acetonitrile); inset: comparison of measured and calculated isotopic patterns.

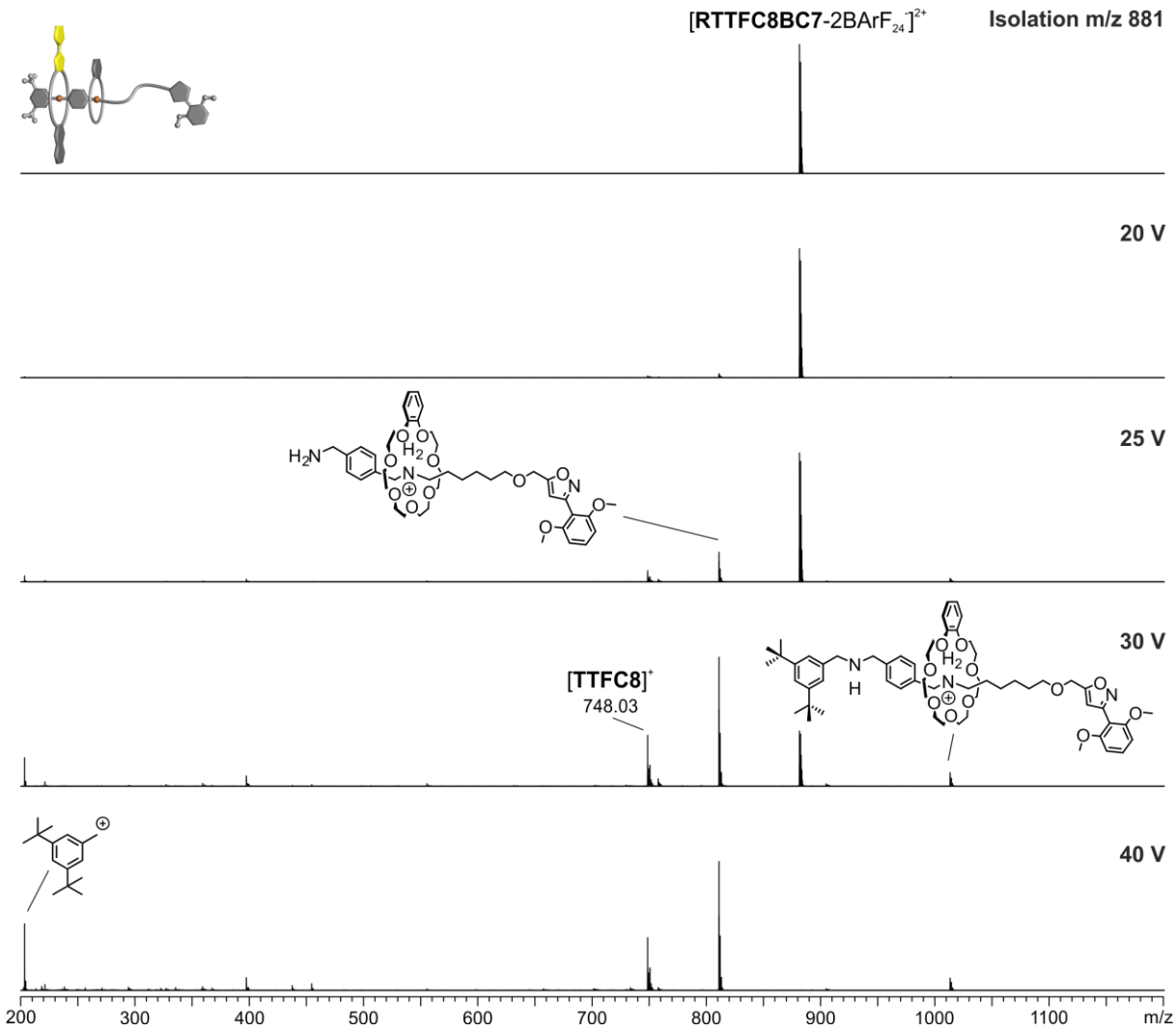

Figure S49 CID experiment with mass-selected ions at *m/z* 881 obtained from solution of **RTTFC8BC7** (1 µM in acetonitrile). Higher voltages are necessary to induce fragmentation of **RTTFC8BC7** and as major fragments oxidized **TTFC8** and axle fragments are observed. This is diagnostic for a mechanically interlocked structure.[8, 9] The small amount of [2]rotaxane fragment at *m/z* 1012 is formed by the opening and loss of **TTFC8** at high collision energies. The loss of **TTFC8** upon cleavage of the axle at the western ammonium station proves the desired sequence in the **RTTFC8BC7** [3]rotaxane.

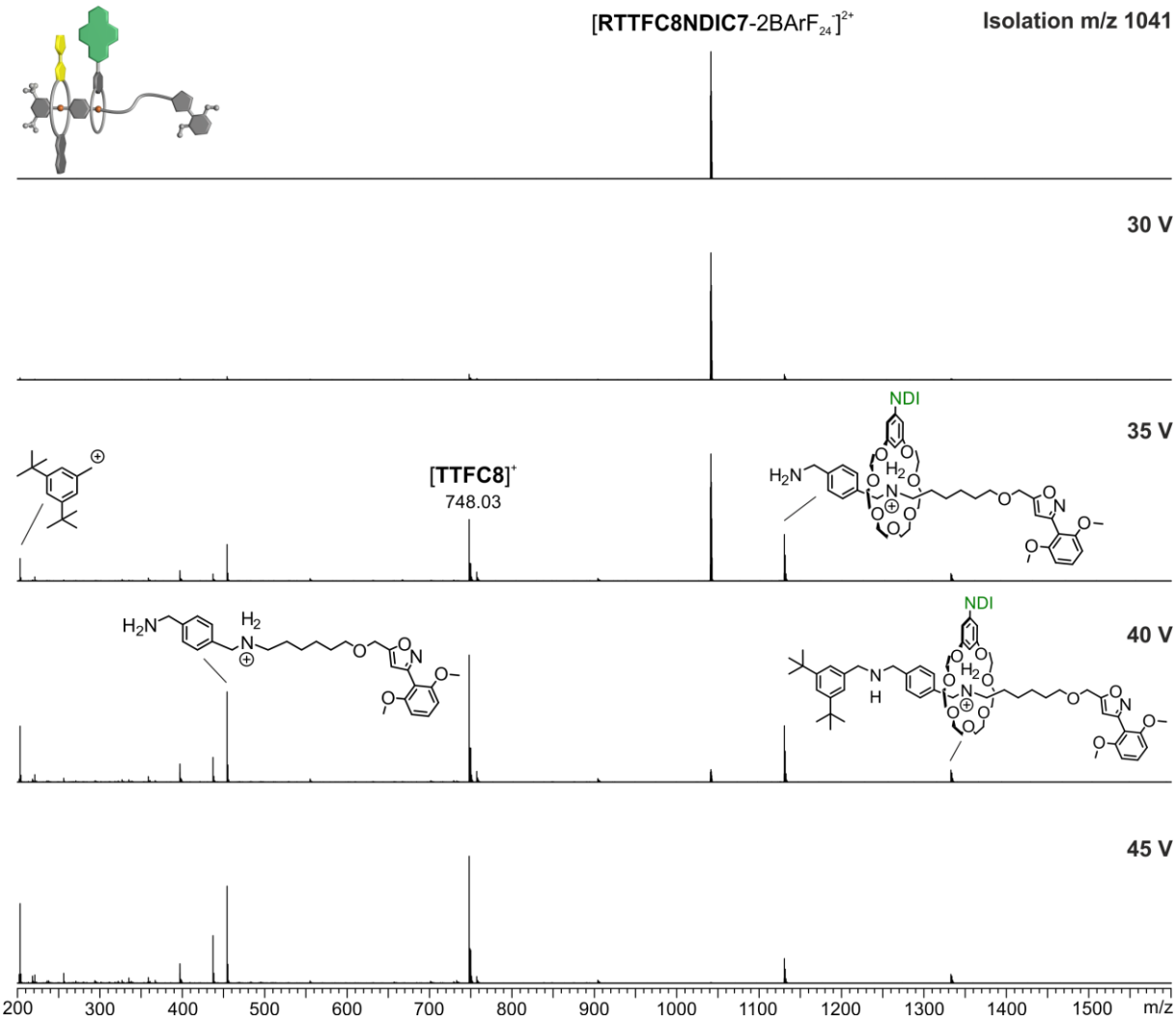

Figure S50 CID experiment with mass-selected ions at *m/z* 1041 obtained from solution of **RTTFC8NDIC7** (1 µM in acetonitrile). Higher voltages are necessary to induce fragmentation of **RTTFC8NDIC7** and as major fragments oxidized **TTFC8** and axle fragments are observed. This is diagnostic for a mechanically interlocked structure.[8, 9] The small amount of [2]rotaxane fragment at *m/z* 1332 is formed by the opening and loss of **TTFC8** at high collision energies. The loss of **TTFC8** upon cleavage of the axle at the western ammonium station proves the desired sequence in the **RTTFC8NDIC7** [3]rotaxane.

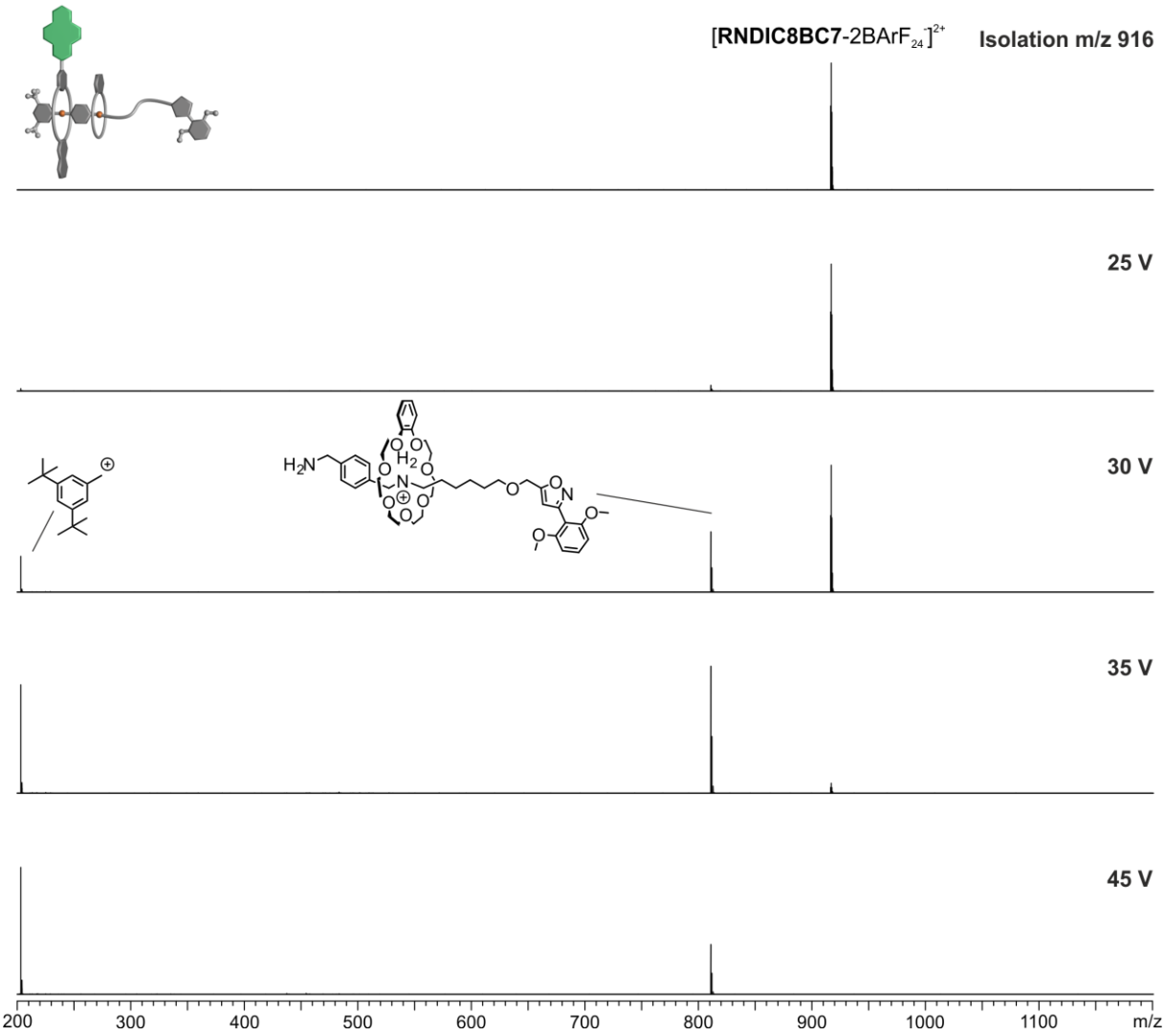

Figure S51 CID experiment with mass-selected ions at *m/z* 916 obtained from solution of **RNDIC8BC7** (1 µM in acetonitrile). Higher voltages are necessary to induce fragmentation of **RNDIC8BC7** and only axle fragments are observed. This is diagnostic for a mechanically interlocked structure.[3] The loss of **NDIC8** upon cleavage of the axle at the western ammonium station proves the desired sequence in the **RNDIC8BC7** [3]rotaxane.

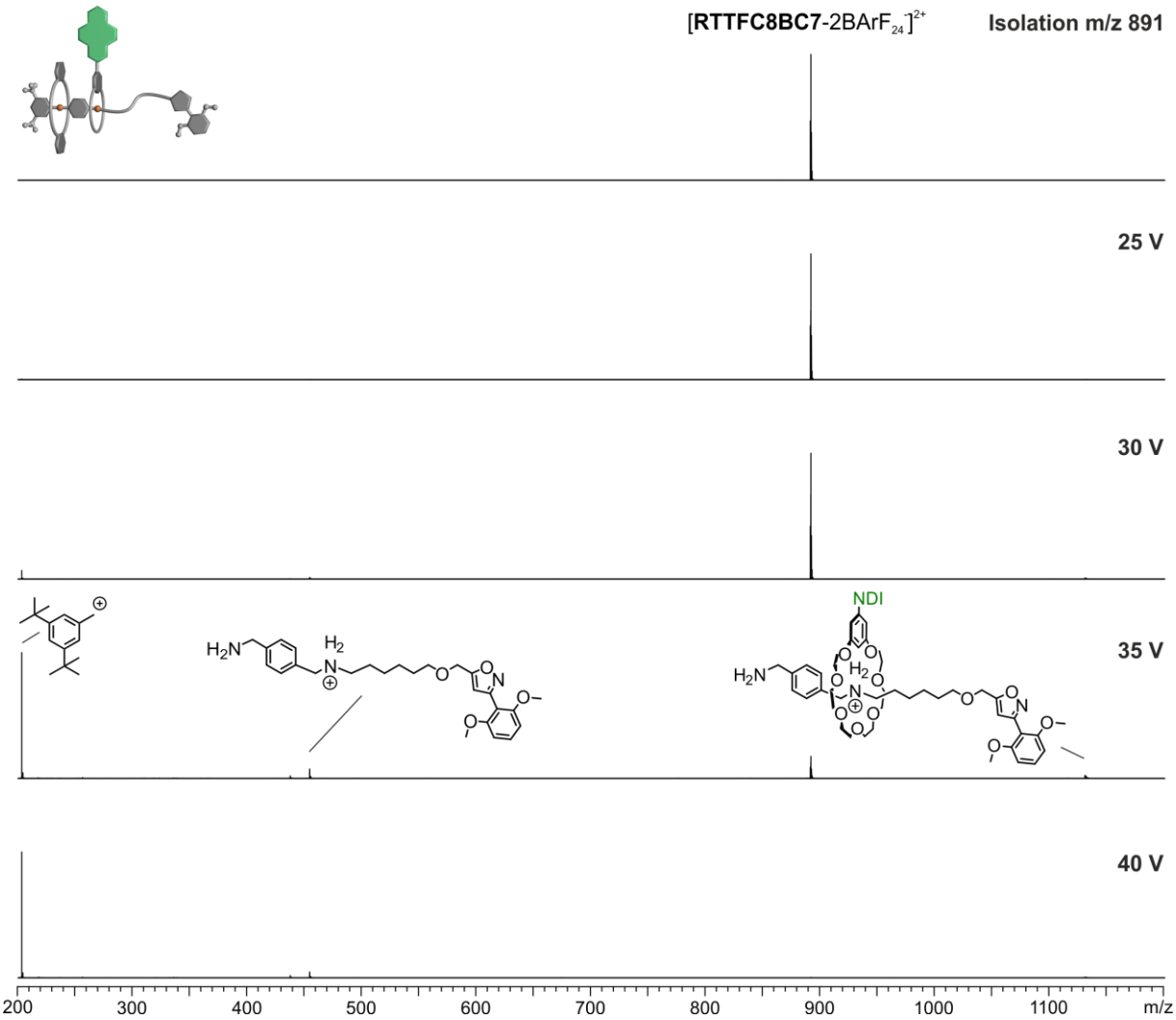

Figure S52 CID experiment with mass-selected ions at *m/z* 891 obtained from solution of **RDBC8NDIC7** (1 µM in acetonitrile). Higher voltages are necessary to induce fragmentation of **RDBC8NDIC7** and only axle fragments are observed. This is diagnostic for a mechanically interlocked structure.[3] The loss of **DBC8** upon cleavage of the axle at the western ammonium station proves the desired sequence in the **RDBC8NDIC7** [3]rotaxane.

5. Electrochemical measurements

Redox-potentials reported in this study were obtained by DPV. All measurements were at least conducted twice. Measurements were conducted in 1,2-dichloroethane (DCE) with 0.1 M electrolyte and 1.5 mM analyte concentration.

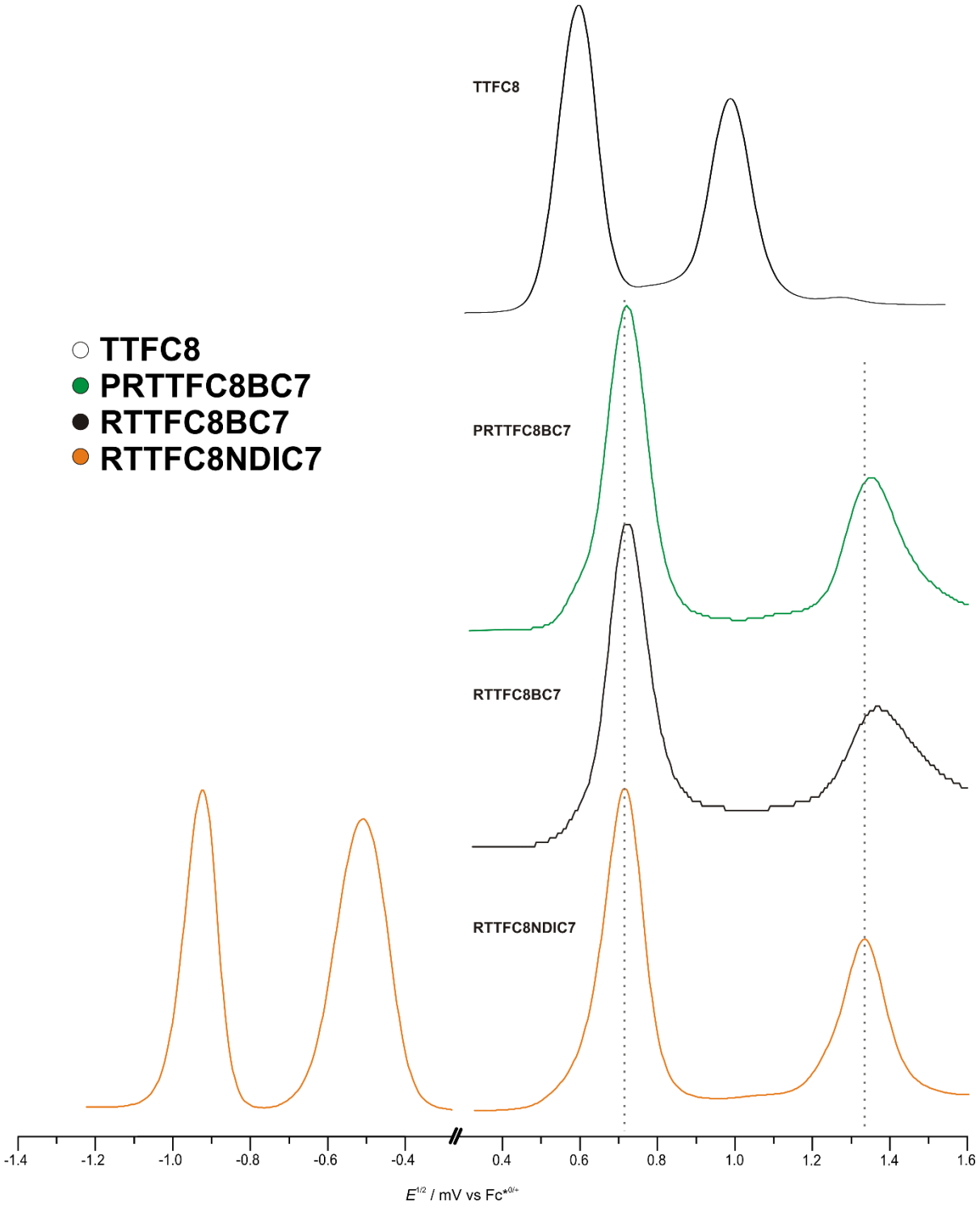

Fig. S53 Stacked differential pulse voltammograms (DPV, 10 mV/s scan rate, 25 mV modulation amplitude, 50 ms modulation time, 5 mV step potential, 0.5 s interval time) (DCE, n-Bu_4NBArF_{24}, 298 K) of **TTFC8**, **PRTTFC8BC7, RTTFC8BC7**, **RTTFC8NDIC7**.

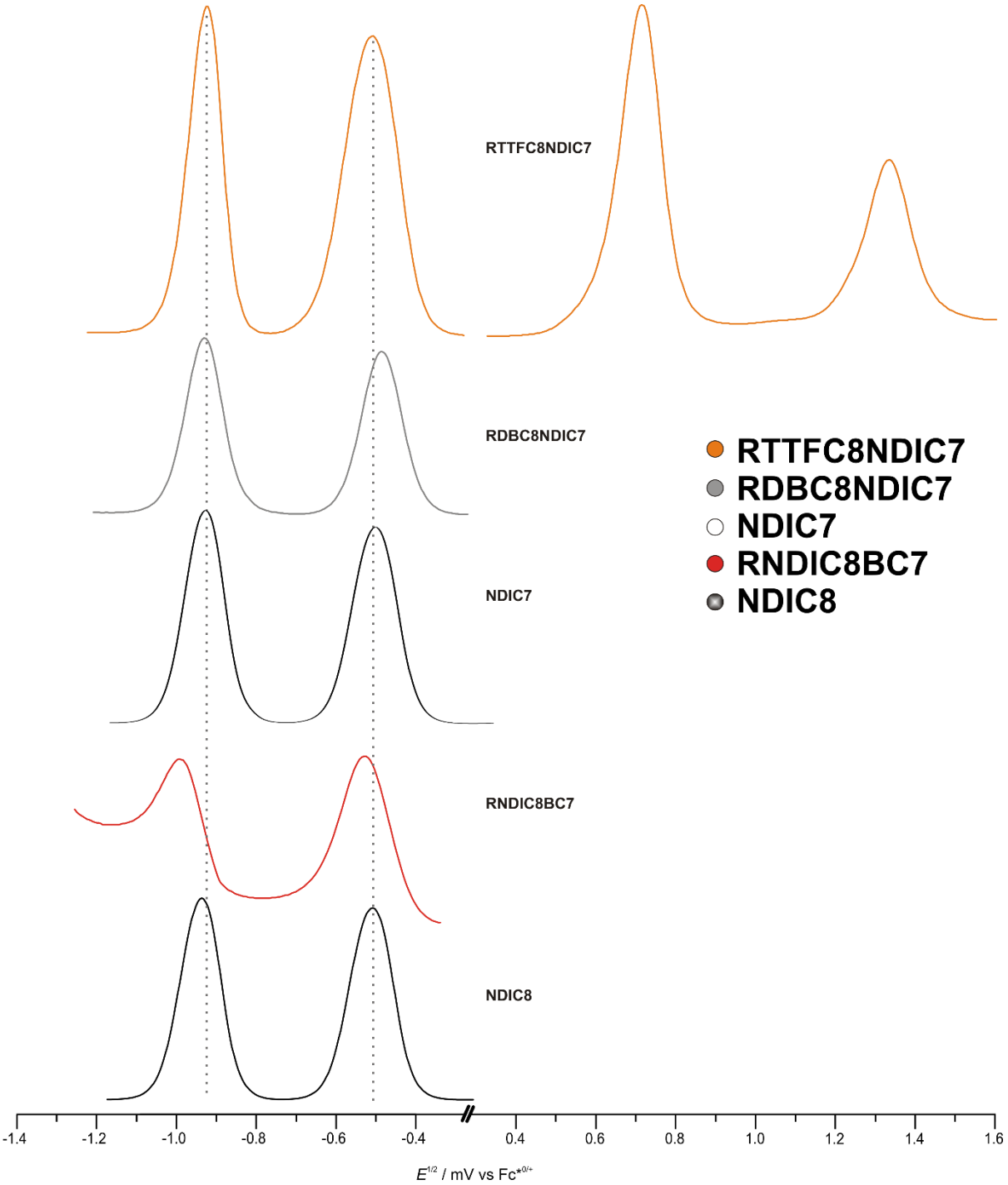

Fig. S54 Stacked differential pulse voltammograms (DPV, 10 mV/s scan rate, 25 mV modulation amplitude, 50 ms modulation time, 5 mV step potential, 0.5 s interval time) (DCE, n-Bu_4NBArF_{24}, 298 K) of **RTTFC8NDIC7**, **RDBC8NDIC7**, **NDIC7**, **RNDIC8BC7**, **NDIC8**.

Tab. S2 Electrochemical data obtained from DPV measurements (DCE, with n-Bu_4NBArF_{24} as the electrolyte, 298 K).

-II / mV	-I / mV	species	+I / mV	+II / mV
		TTFC8	594	987
		RTTFC8[8]	694	1349
		PRTTFC8BC7	720	1349
		RTTFC8BC7	725	1369
-921	-508	**RTTFC8NDIC7**	720	1329
-932	-489	**RDBC8NDIC7**		
-921	-498	**NDIC7**		
-992	-529	**RNDIC8BC7**		
-937	-509	**NDIC8**		

6. UV/Vis experiments

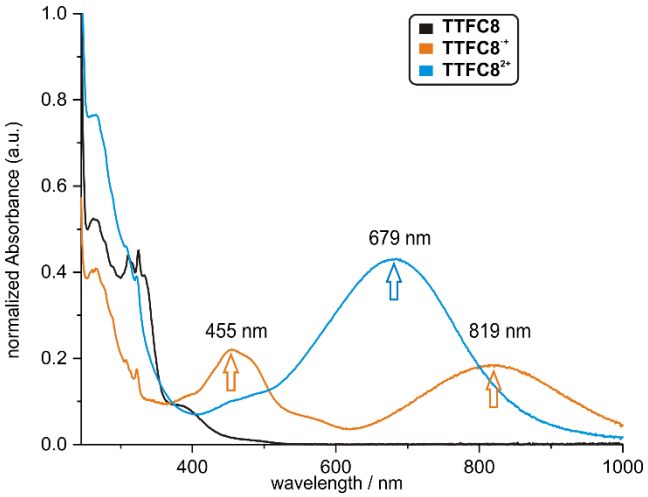

Fig. S55 UV/Vis spectra of **TTFC8** (15 µM in CH_2Cl_2, 298 K, excess bulk $Fe(ClO_4)_3$ as the oxidant) in the TTF^0, $TTF^{\bullet+}$ and TTF^{2+} state.

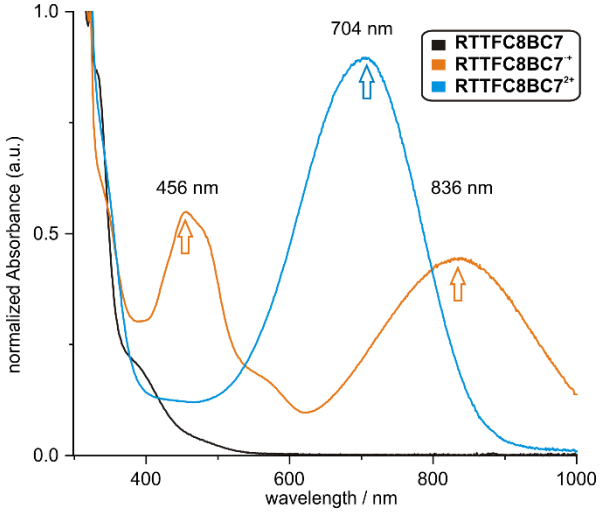

Fig. S56 UV/Vis spectra of **RTTFC8BC7** (15 µM in CH_2Cl_2, 298 K, excess bulk $Fe(ClO_4)_3$ as the oxidant) in the TTF^0, $TTF^{\bullet+}$ and TTF^{2+} state.

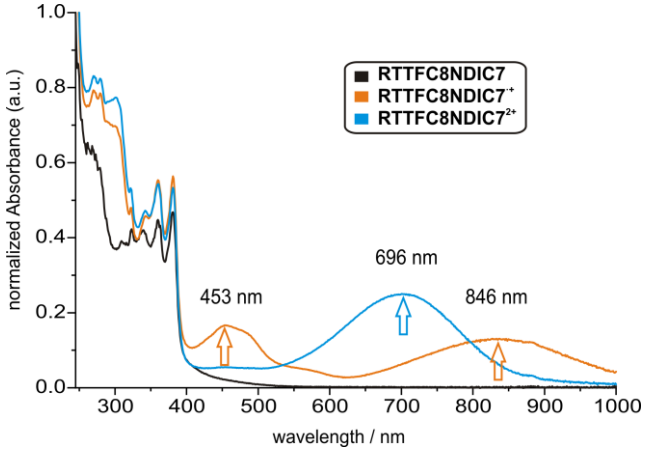

Fig. S57 UV/Vis spectra of **RTTFC8NDIC7** (15 µM in CH_2Cl_2, 298 K, excess bulk $Fe(ClO_4)_3$ as the oxidant) in the TTF^0, $TTF^{\bullet+}$ and TTF^{2+} state.

Tab. S3 Absorption maxima of $TTF^{\bullet+}$ and TTF^{2+} in different species(15 µM in CH_2Cl_2, 298 K, bulk $Fe(ClO_4)_3$ as the oxidant).

species	+I / nm	+II / nm
TTFC8	455, 819	679
RTTFC8BC7	456, 836	704
RTTFC8NDIC7	453, 846	696

The photometric titrations of hetero[3]rotaxanes **RTTFC8BC7** and **RTTFC8NDIC7** with $Fe(ClO_4)_3$ show bands similar to those of free wheel **TTFC8** for the three redox states (TTF, TTF·+ and TTF^{2+}).[10] In contrast to a fixed conformation divalent donor-acceptor rotaxane[11] with TTF and NDI, no intramolecular charge transfer band is observable.

7. Computational details

A conformational scan of the potential energy surface using Grimme's GFN2-xTB code[12] was conducted for compound **RTTFC8NDIC7** and **RNDIC8BC7** to obtain the most stable structures. Compound **RTTFC8NDIC7** was optimised in charge states 1+, 2+, and 3+, respectively, at the PBEh-3c[13] level of DFT in combination with the COSMO[14] solvation model (ε = 8.9 for CH_2Cl_2)[15] employing the Turbomole programm package (Version 7.4).[16] Subsequent single point calculations for an accurate description of the electronic structure were performed at the ωB97X-D3/def2-TZVP[17] level using the CPCM[18] solvent model and the ORCA programm package.[19] Spin densities were generated with ORBKIT.[20]

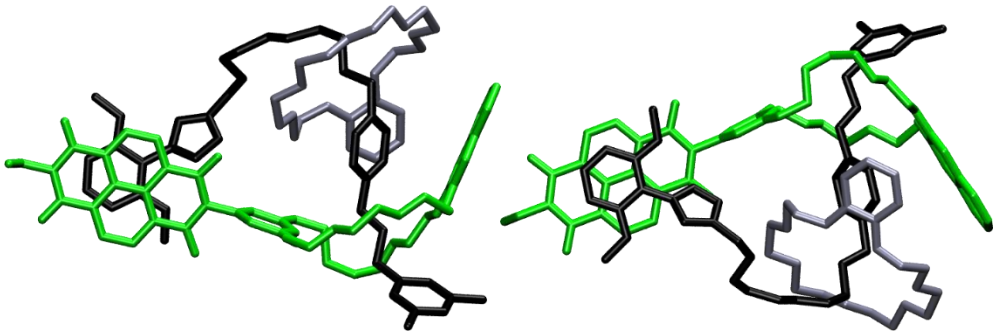

Fig. S58 Optimised structure of compound **RNDIC8BC7** illustrating the efficient stacking between the NDI and stopper moiety.

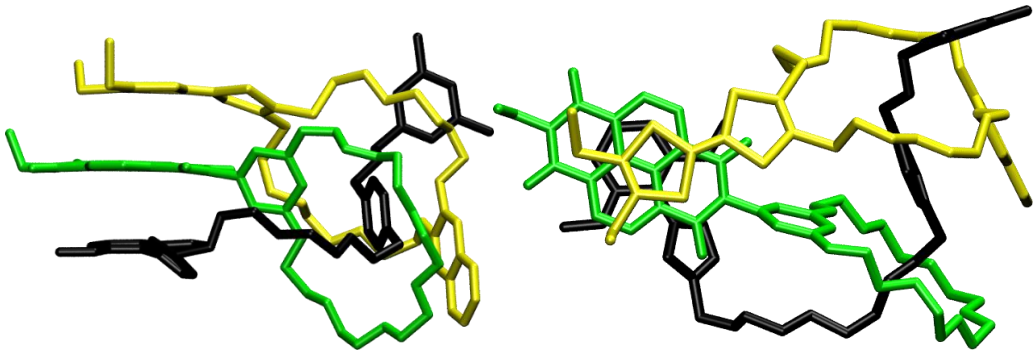

Fig. S59 Optimised structure of compound **RTTFC8NDIC7** illustrating the efficient stacking between the TTF, NDI and stopper moieties.

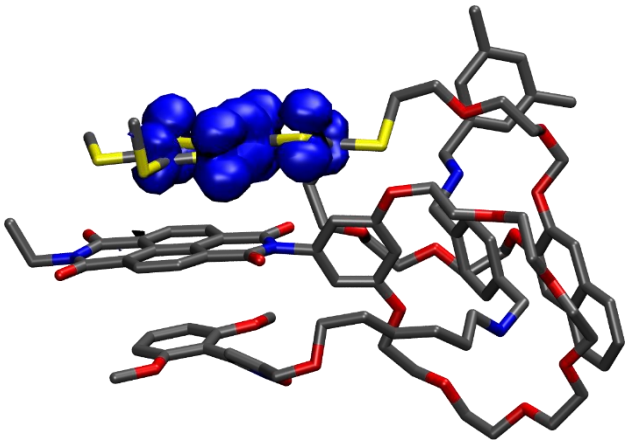

Fig. S60 Spin density of **RTTFC8NDIC7**$^{\cdot+}$ localised on the TTF moiety, isovalue = 0.001 a_0^{-3}.

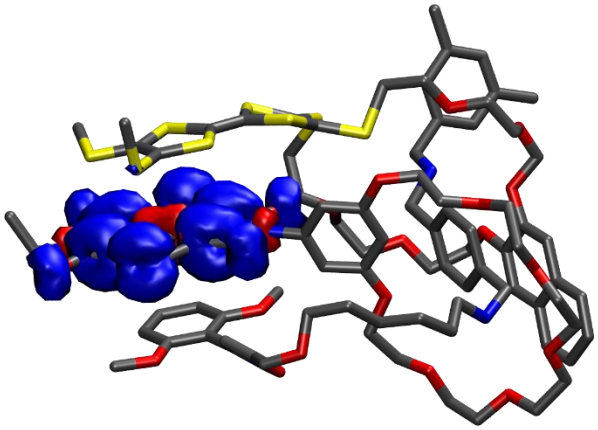

Fig. S61 Spin density of **RTTFC8NDIC7**$^{\cdot-}$ localised on the NDI moiety, isovalue = 0.001 a_0^{-3}.

The spin density plots confirm the retained redox-behaviour of the macrocycles within the rotaxane.

8. Crystallographic data

The crystals were grown by diffusing pentane into a sat. acetonitrile solution of **NDIC7**. X-ray data were collected on a BRUKER D8 Venture system. Data were collected at 100(2) K using graphite-monochromated Mo K_α radiation (λ_α = 0.71073 Å). The strategy for data collection was evaluated by using the Smart software. The data were collected by the standard "*ψ-ω* scan techniques" and were scaled and reduced using Saint+software. The structures were solved by using Olex2,[21] the structure was solved with the XT[22] structure solution program using Intrinsic Phasing and refined with the XL refinement package[23] using Least Squares minimization. Bond length and angles were measured with Diamond Crystal and Molecular Structure Visualization Version 4.6.2.[24] Drawings were generated with POV-Ray.[25] Deposition number CCDC 2047286 contains the supplementary crystallographic data for this paper. These data are provided free of charge by the joint Cambridge Crystallographic Data Centre and Fachinformationszentrum Karlsruhe Access Structures service www.ccdc.cam.ac.uk/structures.

Tab. S4 Crystal data of **NDIC7**.

Compound	**NDI-MC • ACN**
Empirical formula	$C_{38}H_{43}O_{11}N_3$
Formula weight	717.75
Temperature/K	100
Crystal system	triclinic
Space group	$P\bar{1}$
a/Å	8.908(11)
b/Å	8.969(9)
c/Å	26.350(3)
α/°	84.32(7)
β/°	85.34(6)
γ/°	64.95(7)
Volume/Å³	1896(4)
Z	2
ρ_{calc}/g·cm³	1.257
μ/mm^{-1}	0.093
F(000)	760.0
Crystal size/mm³	0.871 x 0.531 x 0.381
Crystal shape	plate
Radiation	MoKα (λ = 0.71073)
2Θ range for data collection/°	4.664 to 50.996
Index ranges	-10 ≤ h ≤ 10, -10 ≤ k ≤ 10, -31 ≤ l ≤ 31
Reflections collected	42858
Independent reflections	6884 [R_{int} = 0.0560, R_{sigma} = 0.0363]
Data/restrains/parameters	6884/0/625
Goodness-of-fit on F^2	1.057
Final R indexes [I>=2σ(I)]	R_1 = 0.0553, wR_2 = 0.1315
Final R indexes [all data]	R_1 = 0.0673, wR_2 = 0.1385
Largest diff. peak/hole / e·Å³	0.26/−0.35

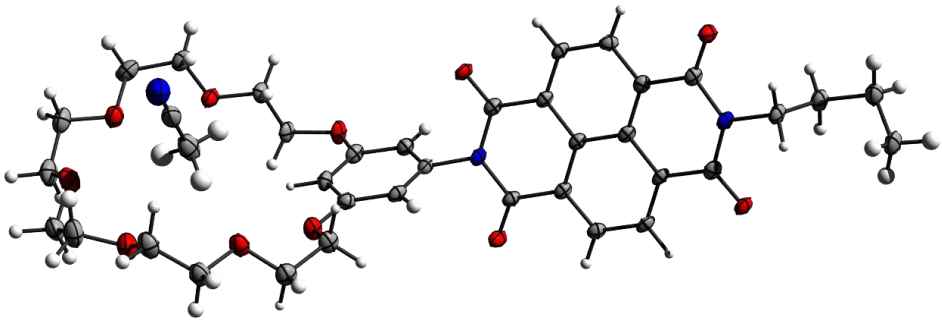

Fig. S62 Asymmetric unit cell of **NDIC7**.

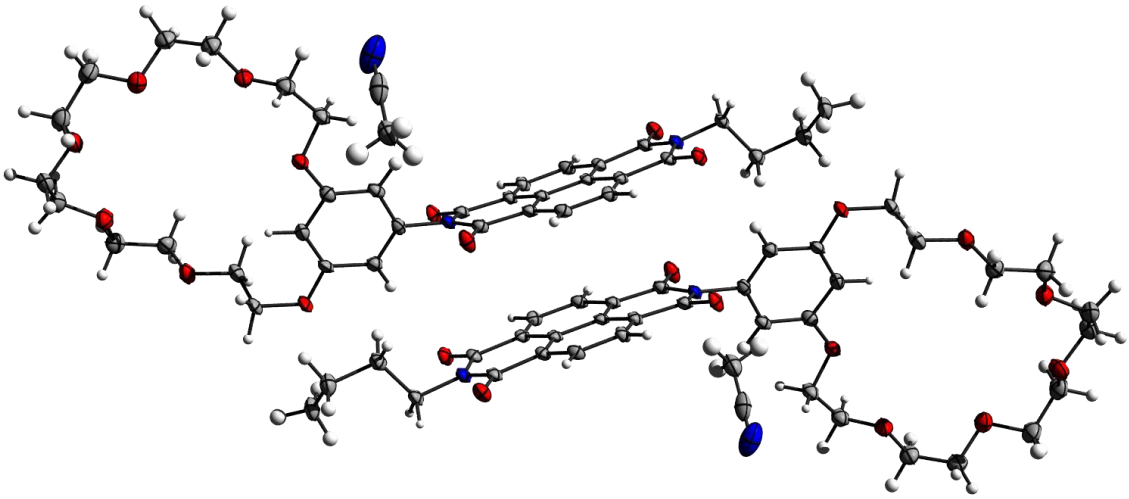

Fig. S63 Crystal packing of two **NDIC7**, with NDI-NDI plane distance of 3.27 Å.

9. References

1. H. V. Schröder, S. Sobottka, M. Nößler, H. Hupatz, M. Gaedke, B. Sarkar and C. A. Schalley, *Chem. Sci.*, 2017, **8**, 6300-6306.
2. T. Matsumura, F. Ishiwari, Y. Koyama and T. Takata, *Org. Lett.*, 2010, **12**, 3828-3831.
3. H. Hupatz, M. Gaedke, H. V. Schröder, J. Beerhues, A. Valkonen, F. Klautzsch, S. Müller, F. Witte, K. Rissanen, B. Sarkar and C. A. Schalley, *Beilstein J. Org. Chem.*, 2020, **16**, 2576-2588.
4. L. Zou and M. J. Webber, *Chem. Commun.*, 2019, **55**, 9931-9934.
5. H. Shao, T. Nguyen, N. C. Romano, D. A. Modarelli and J. R. Parquette, *J. Am. Chem. Soc.*, 2009, **131**, 16374-16376.
6. W. Jiang and C. A. Schalley, *Beilstein J. Org. Chem.*, 2010, **6**, 14.
7. J. R. Aranzaes, M.-C. Daniel and D. Astruc, *Can. J. Chem.*, 2006, **84**, 288-299.
8. M. Gaedke, H. Hupatz, H. V. Schröder, S. Suhr, K. F. Hoffmann, A. Valkonen, B. Sarkar, S. Riedel, K. Rissanen and C. A. Schalley, *Org. Chem. Front.*, 2021, **8**, 3659-3667.
9. M. Gaedke, F. Witte, J. Anhäuser, H. Hupatz, H. V. Schröder, A. Valkonen, K. Rissanen, A. Lützen, B. Paulus and C. A. Schalley, *Chem. Sci.*, 2019, **10**, 10003-10009.
10. S. V. Rosokha and J. K. Kochi, *J. Am. Chem. Soc.*, 2007, **129**, 828-838; M. B. Kirketerp, L. A. Leal, D. Varsano, A. Rubio, T. J. Jørgensen, K. Kilsa, M. B. Nielsen and S. B. Nielsen, *Chem. Commun.*, 2011, **47**, 6900-6902.
11. H. V. Schröder, H. Hupatz, A. J. Achazi, S. Sobottka, B. Sarkar, B. Paulus and C. A. Schalley, *Chem. Eur. J.*, 2017, **23**, 2960-2967.
12. C. Bannwarth, S. Ehlert and S. Grimme, *J. Chem. Theory Comput.*, 2019, **15**, 1652-1671.
13. S. Grimme, J. G. Brandenburg, C. Bannwarth and A. Hansen, *J. Chem. Phys.*, 2015, **143**, 054107.
14. A. Klamt and G. Schüürmann, *J. Chem. Soc., Perkin Trans. 2*, 1993, **5**, 799-805.
15. I. M. Smallwood, *Handbook of Organic Solvent Properties*, Butterworth-Heinemann, Oxford, 1996.
16. R. Ahlrichs, M. Bär, M. Häser, H. Horn and C. Kölmel, *Chem. Phys. Lett.*, 1989, **162**, 165-169.
17. J. D. Chai and M. Head-Gordon, *J. Chem. Phys.*, 2008, **128**, 084106; F. Weigend and R. Ahlrichs, *Phys. Chem. Chem. Phys.*, 2005, **7**, 3297-3305.
18. V. Barone and M. Cossi, *J. Phys. Chem. A*, 1998, **102**, 1995-2001.
19. F. Neese, *WIREs Comput. Mol. Sci.*, 2017, **8:e1327**.
20. G. Hermann, V. Pohl, J. C. Tremblay, B. Paulus, H. C. Hege and A. Schild, *J. Comput. Chem.*, 2016, **37**, 1511-1520.
21. O. V. Dolomanov, L. J. Bourhis, R. J. Gildea, J. A. K. Howard and H. Puschmann, *J. Appl. Crystallogr.*, 2009, **42**, 339-341.
22. G. M. Sheldrick, *Acta Cryst.*, 2015, **A71**, 3-8.
23. G. M. Sheldrick, *SHELXL Version 2014/7, Programm for Crystal Structure Solution and Refinement, University of Göttingen*, 2014; G. M. Sheldrick, *Acta Cryst.*, 2008, **A64**, 112-122.
24. K. Brandenburg, *"Diamond: Crystal and Molecular Structure Visualization" can be found under* http://www.crystalimpact.com/diamond, 2017.
25. *Persistence of Vision. Ltd., retrieved from* http://www.povray.org/download/, 2004.